

© 2013 Thomas Michael Frankie

IMPACT OF COMPLEX SYSTEM BEHAVIOR ON
SEISMIC ASSESSMENT OF RC BRIDGES

BY

THOMAS MICHAEL FRANKIE

DISSERTATION

Submitted in partial fulfillment of the requirements
for the degree of Doctor of Philosophy in Civil Engineering
in the Graduate College of the
University of Illinois at Urbana-Champaign, 2013

Urbana, Illinois

Doctoral Committee:

Professor Daniel A. Kuchma, Co-Chair and Co-Director of Research
Professor Amr S. Elnashai, Co-Chair and Co-Director of Research
Professor Billie F. Spencer
Professor Paolo Gardoni
Professor Yanfeng Ouyang

ABSTRACT

The damage to reinforced concrete (RC) bridges observed in the 1971 San Fernando, 1994 Northridge, and 1995 Kobe earthquakes prompted significant research efforts within the earthquake engineering community. Strides were made in capturing the true inelastic seismic response of RC bridge piers, and improvements were made to seismic design methods. However, several characteristics of complex RC bridge response are not yet fully understood. The challenge of assessing risk posed to bridges with irregular or curved geometry subjected to multi-directional loading is non-trivial. The effect of the resulting combined interactions on structural response and its implications on system-level bridge vulnerability are assessed in this study.

Fragility curves generated for bridges with varying parameters provides a means for assessing the probabilistic impact of these parameters on bridge response. A set of fragility curves capable of representing the true impact of complex geometry, modeling assumptions, and multi-directional system-level response on the vulnerability of RC bridges is developed. These relationships are an improvement over existing curves developed using observational, opinion-based, or uncalibrated numerical approaches. They also avoid inaccuracies that can arise in experimental testing or calibrated numerical analyses due to assumptions made in test set-up, modeling simplifications, and disregard of system-level interaction.

Nonlinear time-history analyses are performed on a set of bridge models subjected to a suite of carefully selected seismic records. Fragility relationships are developed from the resulting structural response data. The models are carefully calibrated using a high quality experimental data set from a large-scale hybrid test successfully completed in the Illinois Network for Earthquake Engineering Simulation (NEES) facility. The hybrid simulation of a curved four-span bridge captures the complex interactions generated by combined axial, flexural, shear, and torsional loading. An advanced six degree-of-freedom control scheme and hybrid simulation platform ensures accurate control and full system-level response. Extensive traditional and advanced instrumentation methods provide dense sets of data that can be visualized and processed for assessing structural response and performing model calibration.

Curved and straight analytical models are developed using the same set of calibrated model parameters. A suite of records representing a wide array of seismic hazards are applied to these models under varying uni-directional and multi-directional loading conditions. Nonlinear time history analyses are performed for straight and curved bridges with varying 3D loading effects and modeling assumptions. Statistical analysis is performed on the resulting structural response data to generate fragility curves. Variations in these curves represent the individual and combined influence of these parameters on system-level behavior and RC bridge vulnerability. Results further the understanding of complex seismic response of RC bridge systems, while providing an improved set of vulnerability relationships that accurately represent the potential risk posed to these critical components of our infrastructure.

To my son, Silas

ACKNOWLEDGMENTS

This work would not have been possible without the efforts of numerous individuals, thus many thanks are in order. The author would first like to express his sincere thanks to Professors Amr S. Elnashai, Daniel A. Kuchma, and Billie F. Spencer (EKS) for their professional and personal support throughout the course of the research presented here. Without their expert knowledge and guidance, this dissertation could not have been completed. Additional thanks to Professors Paolo Gardoni and Yanfeng Ouyang for their valuable contributions through their role on my doctoral committee. Finally, the recommendations and guidance provided by Professors David Sanders and Pedro Silva, and their role in directing the experimental program presented in this work, are recognized.

Many thanks go to the students and staff at the Illinois Network for Earthquake Engineering Simulation (NEES) facility, both past and present, as well as the professional staff of the CEE machine shop, led by Tim Prunkard. Specifically, the efforts of Dr. Chia-Ming Chang and Dr. Adel Abdelnaby are noted for their valuable and generous assistance in developing many of the experimental and analytical tools utilized in this work.

It is particularly important to thank my incredible wife, Erin, for her loving patience and support throughout my doctoral studies; my son, Silas, whose smile means the world to me; my parents, for introducing me to the joy of learning and discovery, while modeling compassion for others; and to the Lord who is over all and through all and in all of these things (*Eph. 4:6*). May my life and work be a testimony to the gospel of Jesus Christ. I pray also that my efforts presented here may contribute in some way to the benefit of those affected by the threat of natural disasters.

The Multi-axial Full-scale Substructure Testing and Simulation (MUST-SIM) facility at the University of Illinois at Urbana-Champaign is a part of the National Science Foundation (NSF) George E. Brown, Jr. Network for Earthquake Engineering Simulation (NEES), Award Number CMMI-0927178. The hybrid simulation research is conducted as a part of the NEESR-SG Combined Actions on Bridge Earthquake Response (CABER) program sponsored by NSF Grant CMS-0530737.

TABLE OF CONTENTS

CHAPTER 1: INTRODUCTION	1
1.1 Background and Motivation.....	4
1.2 Summary of Contents.....	7
CHAPTER 2: LITERATURE REVIEW	10
2.1 RC Bridge Fragilities	11
2.2 Testing and Analysis of RC Columns and Piers	18
CHAPTER 3: HYBRID TEST OF CURVED FOUR-SPAN BRIDGE.....	31
3.1 Bridge Design and Construction	32
3.2 Earthquake Input Motion	37
3.3 Hybrid Simulation Procedure.....	39
3.4 Advanced Capabilities and Experimental Methods	42
3.5 Dense Data Acquisition.....	54
3.6 Test Results	63
CHAPTER 4: ANALYTICAL ENVIRONMENT	66
4.1 Initial Un-Calibrated Model.....	67
4.2 Model Calibration	72
4.3 Suite of Earthquake Records.....	83
4.4 Set of Analytical Cases Examined	90
4.5 Structural Analyses	93
CHAPTER 5: BRIDGE FRAGILITY RELATIONSHIPS	100
5.1 Fragility Generation Procedure	101
5.2 Impact of Varying Parameters on Bridge Vulnerability	104
5.3 Methodology for Simulating Complex Bridge Effects	115
CHAPTER 6: CONCLUSIONS	119
6.1 Main Findings	119

6.2 Future Work	124
6.3 Future Work with Broad Impact	129
APPENDIX A. HYBRID SIMULATION TEST PREPARATION	134
A.1 Large-Scale Specimen Design and Fabrication.....	134
A.2 Small-Scale Specimen Design and Fabrication.....	139
A.3 Material Properties	144
APPENDIX B. HYBRID SIMULATION TEST SETUP	150
B.1 Large-Scale Test Setup.....	150
B.2 Instrumentation Plans	155
B.3 Small-Scale Test Setup.....	163
APPENDIX C. HYBRID SIMULATION RESULTS	164
C.1 Global Response.....	164
C.2 Data Acquisition Summary	174
C.3 Description of Key Event Points	186
C.4 Summary of Structural Response at Key Events.....	189
APPENDIX D. OVERVIEW OF INITIAL ANALYTICAL MODEL	242
D.1 Model Details	242
D.2 Results of Preliminary Analysis.....	251
D.3 Results with Adjustments for Hysteretic Damping.....	255
APPENDIX E. CALIBRATED MODEL DEVELOPMENT STAGES.....	260
E.1 Identifying Stiffness Degradation Behavior	260
E.2 Sample Generic Calibration Results.....	266
E.3 Slight and Moderate Calibrated Models	272
E.4 Severe Calibrated Model	283
APPENDIX F. SUITE OF SEISMIC RECORDS	292
APPENDIX G. STRUCTURAL ANALYSIS RESULTS.....	355

APPENDIX H. STATISTICAL ANALYSIS RESULTS.....	368
H.1 Limit States for Each Case.....	369
H.2 Influence of Geometry	379
H.3 Influence of Load Application	383
H.4 Influence of Model Calibration	390
H.5 Modification Factors	394
APPENDIX I. DIGITAL APPENDICES.....	401
BIBLIOGRAPHY	402

CHAPTER 1: INTRODUCTION

It is widely accepted that earthquakes continue to present a significant level of risk to populations and communities around the world. The seismic events occurring in only the past decade (2003 Bam, 2004 Sumatra, 2005 Kashmir, 2008 Sichuan, 2010 Haiti, 2010 Maule, and 2011 Tohoku) demonstrate the levels of loss that can result from seismic vulnerability of infrastructure. These events have revealed the importance of continuing to pursue methods that enable improved understanding of structural response under seismic loading. Advancements are particularly needed in the ability to accurately assess the true performance of complex hazard-structure interaction that occurs in the field. In addition to developing improved methods for design of new construction, significant research efforts are needed to improve the ability to accurately assess the performance of existing structures. The potential risk faced by current as-built infrastructure is very pertinent in terms of societal impact. The research described here attempts to improve the accuracy of the tools and processes currently utilized in assessment of seismic performance. These experimental and analytical methods are used to develop accurate data sets and models which can be utilized by various researchers and decision-makers. The results are presented in the form of fragility relationships that are often employed by loss assessment software packages. In the work presented here, these vulnerability relationships will serve to illustrate the varying degrees of influence that multiple geometric, modeling, and loading parameters have on structural assessment results. By improving simulation and modeling methods for assessing the seismic risk to populations, subsequent mitigation and response planning decisions can be based upon a more complete understanding of the true response of bridges subjected to earthquake loading.

Bridges are typically considered the most seismically vulnerable components of a highway transportation network. Therefore, probabilistic predictions of the resilience of these structures provide valuable information for updating of infrastructure prior to severe events, as well as restoring functionality of transportation networks following disasters. Improving models that provide estimates of the potential severity of damage to bridges under a particular level of seismic input are therefore pursued in this study as well. Loss estimation can be performed at any level, from individual structures such as bridges that serve as a lifeline to a large urban population, to regional levels of assessment for determining needs of large populations due to loss of water or power. These studies commonly use a probabilistic method for predicting damage to structures and the resulting societal

impacts. Current software programs such as the Federal Emergency Management Agency's (FEMA's) Hazards U.S. (HAZUS) and the Mid-America Earthquake Center's MAE-Viz estimate a wide variety of losses based off of the structural response of a community's infrastructure. These programs use vulnerability relationships, in the form of fragility curves, to relate seismic input to the statistical probability of a particular structural response. The level of severity for this structural response is then mapped to several societal parameters to define the resulting risk that the population is subject to when structures respond in this manner. These various types of societal risk, and loss, can be characterized in terms of the following three categories:

- i. Life safety (casualties, including fatalities, due to structural damage or collapse)
- ii. Societal function (including impacts of loss of shelter, hospitals, schools, transportation networks, utilities, and other critical infrastructure)
- iii. Monetary losses (direct losses due to cost of repairing and replacing damaged structures and their contents, as well as indirect losses due to closure, down time, and business interruptions)

The key method for accomplishing these improvements is to ensure that the methods for representing the vulnerability of structures are rooted in the most advanced and realistic structural testing and analyses methods. Improving our understanding of the true nature of complex structural behavior under seismic excitation will enable us to develop more accurate models. The study described here focuses on developing a method to account for these complexities for a specific category of reinforced concrete bridge infrastructure. This is due to the critical role that RC bridges serve in highway transportation systems, as well as the aspects of RC bridge pier response under combined actions that are not yet fully understood. Examining this case yields insight into the potential performance of additional bridge classifications subject to complex loading conditions. Additionally, improvements are made to experimental and numerical simulation methods utilized to inform these assessments.

There are numerous sources in the literature on the response of reinforced concrete bridges. Most have specifically focused on the seismic response of the gravity load-bearing piers of these structural systems. These studies include numerous experimental tests and numerical analyses. A selection of notable research programs are highlighted in Chapter 2. A review of the literature reveals many areas where significant improvements can be made to more accurately evaluate the full response of complex structural bridge systems. The technical challenge of assessing risk posed to bridges with

irregular or curved geometry and subjected to multi-directional loading is non-trivial. Additionally, the influence of assumptions and simplifications made in many experimental tests and numerical analyses on the reliability of response data is not fully known. The impact of accounting for or neglecting complex geometry, loading, and system-level effects when assessing RC bridge vulnerability therefore remains unclear.

With this in mind, the research presented here investigates and addresses the following topics:

- i. The extent to which complex bridge geometry and combined loading effects impact the seismic vulnerability of RC bridge systems.
- ii. The changes in perceived vulnerability that result from various assumptions and simplifications commonly made when testing or analyzing structural components, particularly in simplified experimental programs and uncalibrated numerical models.
- iii. The individual and combined effect that the above parameters have on RC bridge vulnerability relationships.
- iv. Identification of geometry, loading, and modeling scenarios that most critically affect the resulting fragility or perceived vulnerability of RC bridges.
- v. The ability to statistically account for these effects when examining experimental and analytical results developed for other scenarios through the application of modification factors to existing fragility relationships.

An overview of the work performed to investigate these topics is provided at the end of this chapter. It is suggested that the resulting fragility relationships be considered primarily in the context of evaluating the influence of these parameters on structural response. The curves do entail many inherent improvements in terms of what is captured in the vulnerability relationships. While these results have potential application to appropriate RC bridge infrastructure within loss assessment studies, the primary proposed purpose of the curves in this investigation is an evaluation of the influence of each parameter on structural response and seismic vulnerability. In addition to developing fragility curves for the assessment of straight and RC bridges under various conditions, a series of adjustment factors which account for variations in geometry, loading, and modeling techniques are developed. These factors are intended to illustrate the changes in vulnerability and dispersion parameters of the fragility relationships that result from varying geometry, model calibration, and loading conditions. It is proposed that these factors could then be implemented to modify existing relationships developed in other fragility assessments. Further work can be performed to provide researchers the flexibility of assessing seismic vulnerability for many levels of complex bridge response for a wide range of potential hazard scenarios. These factors, if fully

developed and further tested, could be developed into more comprehensive functions used to modify existing vulnerability relationships in the literature. Doing so could account for the influence of interaction effects not captured in previous studies, and potentially correct for other assumptions made in the initial experimental or analytical testing program from which the original curves were developed. The objective of this work is to improve the understanding of combined actions due to complex seismic response of RC bridge systems, while enhancing the resources available for performing loss-estimation studies that more reliably represent the potential risk posed to these critical components of infrastructure.

1.1 Background and Motivation

Damage to reinforced concrete bridges following natural disasters such as the 1971 San Fernando, 1994 Northridge, 1995 Kobe, and 2010 Maule earthquakes provided motivation for efforts to further the conceptual understanding of structural response of RC bridges. Much focus has been placed on capturing the true inelastic seismic response of bridge piers. The response of these gravity-supporting components clearly contributes to the behavior of the overall bridge system and the ability to function as intended. Findings from observations in the field, as well as an extensive effort in the earthquake engineering community, have improved modeling capabilities and current design practices for RC piers.

However, the influence of pier performance on the full response of RC bridge structures subjected to complex actions is not yet completely understood. This is largely due to the challenges associated with assessing the impact of interaction effects that result from combined loading applied to a bridge with complex geometry. This is particularly true for bridges with curved or skewed geometry, uneven pier heights, or uneven span lengths. Recently, significant work has been performed to analyze how interaction effects due to combined loading can precipitate failure in RC bridge piers. These studies are discussed at further length in Chapter 2. Few previous studies, however, have considered the effects of combined loading within the context of the full structural response of the bridge, including its deck, supports and abutments.

The experimental work that produced the data set utilized in this work is the hybrid simulation of a curved four-span RC bridge at the Network for Earthquake Engineering Simulation (NEES) Illinois

Multi-axial Full-scale Substructure Testing and Simulation (MUST-SIM) facility. The test culminated several years of research conducted at the universities of Missouri S&T, Nevada Reno, and Illinois as a part of the Investigation of Combined Actions on Reinforced Concrete Bridge Piers (CABER) project. The objective of the NEES CABER project was to develop a fundamental understanding of the effects of these combined actions on the performance of reinforced concrete (RC) columns and the resulting system response of the bridge. The investigations are motivated by the inadequacy of existing analytical solutions and lack of experimental data for use in improving model behavior under complex actions.

The experimental test conducted as a culmination of the CABER program includes combinations of bending, shear, axial load, and torsion. Combined actions occur in these piers as a result of the application of multi-directional earthquake motions and the geometric configuration of the bridge. It should be noted here that combined actions do occur even in cases of regular geometries subjected to uni-directional loading, particularly as nonlinearities develop. However, the influence of torsional moments can be particularly significant in the combined actions observed in columns of bridges that are skewed, curved, and have either unequal spans or column heights (Li, Belarbi, & Prakash, 2010). The findings from these studies in the literature, including the effects of torsion and other combined effects on structural response, are addressed further in Chapter 2. The geometry and loading of the curved RC bridge discussed in this study was specifically selected to produce and examine the effects of complex interaction effects, including torsion. The resulting data set allows for accurate calibration of analytical models that are tested with varying geometry and loading conditions, to ensure that the effects of these changes on structural response can be captured in the work described below.

The procedure presented herein entails developing a mechanism for identifying the statistical influence of various complex load and boundary conditions, bridge geometry (namely curvature), and numerical modeling assumptions on the vulnerability of reinforced concrete bridges. Fragility curves, which represent the probability of a structure reaching a certain damage state given a particular intensity of seismic demand, are widely accepted as a useful format for representing vulnerability to earthquake damage. Unfortunately, many of the curves existing in the literature are not rooted in high quality experimental and analytical results. This is due to the limited availability of high quality test data or calibrated models capable of fully representing the effects of combined interactions on system-level response. If the structural response data utilized to develop vulnerability

relationships does not come from simulations that accurately represent the complex system response under three-dimensional load and boundary conditions experienced in the field, then the resulting relationships may be unreliable.

Early methods in developing fragility relationships used empirical or experiential methods which do not account for individual bridge characteristics. In other cases, individualized fragility curves are developed based on rigorous computational simulation of a single bridge, therefore being unreliable for broad application. Fragility relationships that are developed for full bridge systems, taking into account the entire structural response of all components, may still rely on un-calibrated analytical models. Even fragility curves based in experimental or calibrated numerical testing and analyses are potentially unreliable due to assumptions made in test set-up or modeling, simplifications in load and boundary conditions, or again through disregard to the influence of full system-level response.

Although this is the case for much of the historical work in development of vulnerability relationships, significant advances have been made in capacity and demand models, as well as the probabilistic methods utilized in developing fragility relationships. Improvements in methods for developing and updating reliable experimentally-based fragility relationships have been recently achieved. A discussion of both historical development and recent advances in the literature is provided in Chapter 2.

With this in mind, it is again stated that the purpose of the research presented here is not to introduce a new method for statistical analysis. Instead, the goal is to utilize high-fidelity data and methods to illustrate the influence of various parameters often excluded from consideration in experimental and analytical testing programs. This is important because it is from these programs that various statistical methods obtain structural response data for developing vulnerability relationships. In this work, a set of fragility relationships developed from models calibrated from advanced hybrid simulation data are presented. These curves accurately represent the influence of various parameters on system-level bridge response. In addition, they are uniquely capable of reliably representing seismic vulnerability for this class of RC bridge.

1.2 Summary of Contents

A framework for the research described above is now presented. The methods employed in order to accomplish this work are laid out in this section by chapter. A brief overview of the content and work associated with each chapter of the dissertation is subsequently provided.

Chapter 2 contains a summary of past and current literature on two important topics addressed in this research. First, the past work that has been performed to develop fragility curves for bridges and RC bridge components (namely piers) is described. The implications of these developments on bridge impact assessment capabilities are discussed. Secondly, a survey is performed of the experimental and analytical work that has been conducted to improve understanding of combined actions on structural response of RC piers and columns. Tests on RC bridge piers under various levels of loading conditions and combined actions are discussed in detail. For both subjects of the literature review, focus is placed on the various assumptions that are often made in past works. These shortcomings are highlighted as areas for future improvement in the ability of fragility curves to represent seismic vulnerability for bridges with piers subjected to combined actions. These are discussed in the context of the improved capabilities introduced in this work. Namely, this includes accurately assessing system-level performance through careful testing and modeling that accounts for realistic behavior of RC bridges under complex loading.

In Chapter 3, a carefully designed experimental hybrid test of a curved four-span bridge is described. The bridge is tested in the Illinois NEES MUST-SIM laboratory using several advanced control and instrumentation methods. The design of the bridge is discussed and the properties of its components are provided. The procedure for conducting a hybrid test with one small-scale and two large-scale experimental piers is laid out. The earthquake record used for the pseudo-dynamic testing at four performance-based scaling levels is introduced. A description of the advanced loading units and control algorithms required for precise control of the test are given. The capabilities for six degree of freedom control and full-system interaction enabled by this complex hybrid simulation are highlighted. Finally, descriptions of data acquisition methods are provided, including the use of extensive traditional and advanced non-contact instrumentation. The resulting structural response data sets are discussed. The procedures involved in examining global and local responses are described. Various methods for interpretation and visualization of the structural response are

presented. Examples of results are presented and highlights of findings are summarized. Finally, the suitability of this data set for use in model calibration is discussed.

Chapter 4 provides a description of the analytical environment of the research program. The Zeus-NL model utilized in the hybrid simulation outlined in CHAPTER 3: is discussed further. The procedure implemented for calibration of this analytical model is described. Focus is placed on improvements made to the modeling assumptions revealed through comparison of purely numerical analysis to the structural response data from the hybrid test. The impact of the initial assumptions is also noted as a parameter for consideration when examining the potential influence of shortcomings in conventional understanding of bridge vulnerabilities. The parameters of this calibrated model are discussed and presented for use at three different levels of seismic loading, and a straight bridge is constructed using the same model parameters. A set of nonlinear time-history analyses are performed in Zeus-NL. Each of the models is subjected to a suite of carefully selected earthquake records varying in spectral content, site condition, and magnitude. These analyses are performed with various levels of complexity in terms of loading and boundary conditions in order to capture the influence of neglecting out-of-plane, vertical, and combined loading on both curved and straight bridges.

In Chapter 5, the method for developing fragility relationships from the structural response data obtained in CHAPTER 4: is discussed. The results are used to generate a set of two-parameter lognormal fragility curves. These curves are presented to identify the individual and combined influence of each of the varying parameters on actual or perceived seismic vulnerability. A set of modification factors are proposed for representing the statistical influence of varying geometric, load, and model parameters. A method for using these factors to modify the parameters of previously developed fragility curves without conducting new experimentally or analytically-based reliability studies is then presented.

Chapter 6 provides a set of conclusions that examine and address the significance of the findings in this study. Focus is placed on what has been learned about the effects of varying parameters on structural response of RC bridge systems, and the resulting implications of this response on vulnerability relationships. Recommendations for use of these findings in informing future experimental and analytical studies are provided. The contribution to the application of future loss assessment programs for an appropriate subset of RC bridge infrastructure is also provided. Future work is described as well. Highlights include expansion of the scope of parameters studied in this work, as well as recommendations for improvement of methods and validation of results presented.

Proposed modifications include improved model calibration techniques, more comprehensive limit state definitions, and further improvement to statistical representation of vulnerability functions. Finally, the use of the results of this study in performing Bayesian updating to existing fragility relationships is proposed. Additionally, implementation of a Bayesian updating procedure to improve the relationships presented here is also possible upon increased availability of high quality experimental data. The broad impact of the future work on design and assessment of RC bridges is finally summarized.

CHAPTER 2: LITERATURE REVIEW

In this chapter, a summary of key works in the literature is provided regarding two important topics. First, past research that has been conducted to develop fragility curves for bridges and RC bridge components (namely piers) is presented, along with the implications of these developments on bridge impact assessment capabilities. The various methods of fragility curve development are presented in order to highlight the potential for improvement through the use of structural capacity models rooted in experimental testing or calibrated numerical analyses. The importance of considering full bridge system-level response is also discussed. A brief discussion of advancements in probabilistic methods for generating and presenting fragility relationships is provided, and the methods used in this study are presented with their appropriate limitations and purposes stated. Secondly, a survey of experimental and analytical work that has been performed as the basis for understanding of structural response of bridges and their components are discussed at length. Tests on RC bridge piers under various levels of loading conditions and combined actions are discussed and used to underscore the numerous challenges toward conducting high fidelity experimental tests. Again, the importance of assessing vulnerability of bridges following rigorous structural testing programs and model calibration procedures is highlighted.

In both cases, shortcomings due to assumptions made in past and current literature are presented as motivation for improving capabilities to accurately represent risk to bridge infrastructure through modeling more realistic behavior of RC bridges. It is through these efforts, that a set of reliable fragility curves can be developed to illustrate the influence of the complexity of bridge geometry, loading, and modeling assumptions on seismic performance. The discussion of these works reveals much of the motivation behind investigating a means for assessing the individual and combined effects of these varying parameters on vulnerability of bridges. This is the reason that the work presented here includes the development of a set of modification factors for updating fragility curve parameters. The potential use of these factors for the modification of previous results developed for numerous bridge classifications and hazard scenarios is proposed. Vulnerability relationships resulting from analysis of simple straight bridges subjected to uni-directional loading conditions could be potentially modified to more closely represent the seismic vulnerability of bridges subjected to the more complex conditions that they are realistically expected to experience.

2.1 RC Bridge Fragilities

Bridge fragility curves are an essential tool in conducting pre- and post-earthquake assessments of risk for transportation systems. In order to evaluate the resulting impact to populations, the seismic hazard, roadway and bridge fragilities and functionalities must be assessed. Fragility curves allow for a method of representing this risk probabilistically, for instance as a function of seismic intensity. As an example, the Federal Emergency Management Agency (FEMA) implements a program entitled Hazards U.S. – Multi-Hazard (HAZUS-MH), as described in (FEMA, 2003), to perform impact assessment. Fragility descriptions of multiple bridge classes found in the national bridge inventory (NBI) are required in order to perform loss estimations in HAZUS-MH.

Table 2.1 Early bridge fragility assessment methods

Source	Method
ATC, 1985	Expert opinion
ATC, 1991	Expert opinion
Mander, 1998	NL static analyses
Basoz & Kiremidjian, 1999	Empirical
Yamazaki et al., 1999	Empirical
Hwang et al., 2000	Elastic spectral analyses
Shinozuka et al., 2000	NL static analyses

The recognized need for fragility relationships to assess, manage, and prioritize efforts to reduce seismic risk has led to developments of several different fragility curve generation methods. Early work included various expert opinion-based [(ATC, 1985), (ATC, 1991)] and empirically-based methods [(Basoz & Kiremidjian, 1999), (Yamazaki, Hamada, Motoyama, & Yamauchi, 1999)]. It was recognized that there were many limitations to the application of these curves, particularly for bridge designs in regions lacking modern seismic events to produce observation-based data on which to base these methods. As a result, various analytical methods have also been extensively studied. These include elastic spectral analyses (Hwang, Jernigan, & Lin, 2000), nonlinear static analyses [(Mander, 1998), (Shinozuka, Feng, Kim, & Kim, 2000), (Banerjee & Shinozuka, 2007)], and

nonlinear time-history analyses [(Hwang, Liu, & Chiu, 2001), (Choi, DesRoches, & Nielson, 2004)]. Table 2.1 lists several notable opinion-based, empirical, and early analytically-based works. Later work has also been performed to compare resulting fragility relationships produced from nonlinear static analyses with those of nonlinear time-history analyses, and were found to represent similar levels of vulnerability (Banerjee & Shinozuka, 2007).

It should be noted that many of these methods are often developed for a single bridge model, making their implementation over large numbers of bridges in the inventory challenging. Other sources in the literature have employed methods to develop fragility relationships by bridge class without requiring extensive numerical simulation of individual bridge structures. The work performed by (Mander & Basoz, 1999) served as the basis for the set of bridge classifications defined in HAZUS-MH. A study by (Nielson & DesRoches, 2007) develops a larger set of bridge classes, which are extensively compared to this earlier work by (Mander & Basoz, 1999). These studies, additional follow-up work, and their methods are described below in further detail, along with other notable works in the literature related to the development or application of bridge fragility relationships.

i. Generation of Bridge Pier Fragility Curves

When considering the vulnerability of bridges, there are various components of the structures that impact the overall bridge fragility relationships. Among the most critical components are the bridge piers themselves. As the primary gravity load-bearing element of RC bridges, the RC bridge piers are often considered the critical component to evaluate when assessing system performance. Thus, there are numerous studies that have established experimental, analytical, and mechanics-based methods to develop fragility curves for RC bridge piers with varying parameters, notably (Gardoni, Der Kiureghian, & Mosalam, 2002), (Gardoni, Mosalam, & Der Kiureghian, 2003) and (Choe, Gardoni, & Rosowsky, 2007). In the first two papers, probabilistic capacity and demand models are developed, respectively. Bayesian updating is used to account for unknown model parameters based on existing deterministic relationships, as well as observational data. The third work presents a procedure for Bayesian updating of existing probabilistic models with new data. This procedure is proposed in the future work discussed in Section 6.2 . Developing increasingly accurate probabilistic models for structural capacity based off of advanced experimental testing of structures, such as the

one presented in CHAPTER 3:, are essential for improving the reliability of seismic impact assessment efforts.

For several bridge types, the fragility curves for the piers have been considered to be adequately representative of the overall fragility of the bridge system itself [(Kim & Shinozuka, 2004), (Mackie & Stojadinovic, 2004)]. However, research from other sources has shown that this assumption is inaccurate in many cases. Varying superstructures supported with the same bridge piers can result in significantly different fragility relationships. Additionally, it is noted that the assumption often results in underestimation of bridge system fragility, particularly for multi-span simply-supported bridges. This is because the controlling factors for overall fragility for these systems can also be the bearings between the bridge piers and superstructure (Choi, DesRoches, & Nielson, 2004). For this reason, the remaining sources examined in this survey of RC bridge fragility development are those that consider, to various degrees, additional components of the bridge structure in their analyses. Additionally, an expansion to the limit state definitions utilized in the research presented in this paper is suggested in Section 6.2 on future work.

ii. Generation of Bridge Fragility Curves

The approach currently used for defining fragility curves in FEMA's HAZUS-MH was developed for a highway project conducted by the Multidisciplinary Center for Earthquake Engineering Research (MCEER) and described in (Mander, 1998), (Dutta, 1999), and (Mander & Basoz, 1999). This approach sought to develop dependable site-specific and bridge-specific fragility curves for various bridge types using data available from the National Bridge Inventory (NBI). First, a standard bridge fragility curve was developed for a generic "long" bridge with no appreciable 3D characteristics. This was developed for each bridge category, distinguishing between conventionally and seismically designed bridges. Fragility curve format was the standard two-parameter lognormal cumulative distribution function. Relationships were developed for slight, moderate, extensive, and complete limit states. A standard deviation value of $\beta=0.6$ was assumed from the literature. Median values for five different damage states were determined using spectral values of ground motion acceleration demand and structural displacement capacity. The capacity spectrum method was utilized to perform nonlinear static analysis to generate these parameters. A method was proposed for developing modification factors for skew (K_{skew}) and 3D effects (K_{3D}), again using details from the NBI database.

This method is proposed for use in a rapid-screening method for state transportation departments as a tool for post-disaster planning and scheduling. There are many positive features to this work, and it stands as a vast improvement upon empirical and experiential approaches. However, while the underlying theory for conducting nonlinear analysis is the same as that used in detailed analysis of individual components, the structural capacity utilized in this study is not rooted in a reliable data set based off of mature system-level experimental testing of a complex bridge structure. Instead, properties and attributes of the bridges and ground motion are supposed, while randomness and uncertainty are modeled to account for an assumed distribution of these parameters.

As an alternative to static analysis using the capacity spectrum method, structural response data can be obtained through statistical analysis of analytical results. A series of non-linear time history analyses were performed on variations of a particular straight four-span bridge with a continuous cast-in-place deck supported by four-pier bents (Hwang, Liu, & Chiu, 2001). The RC bridge was analyzed for ground motions in the New Madrid seismic zone. Uncertainties in the modeling parameters for the earthquakes, soil site conditions, and bridge are identified and varied to establish a set of ten bridge-site cases, each subjected to ten acceleration time histories. Nonlinear time history analyses are performed for each of the cases to establish a set of bridge response data. Regression analysis of the simulated response data is performed to obtain structural demand as a function of ground motion intensity. Fragility curves are developed from the conditional probability of demand exceeding specific damage states. The uncertainties associated with bridge modeling are significant given that response data is only obtained analytically. It is noted in the paper that the results rely on verifying and refining these model parameters. Additionally, the acceleration time history is applied only in the transverse direction of the straight bridge, simplifying the structural response in many ways with unknown impact on the resulting fragility relations.

A separate study employing regression analysis on analytical response data for a different straight four-span bridge to develop fragility curves is performed by (Karim & Yamazaki, 2003). Variations of four pier types and two bridge structures are analyzed. The size of the square bridge piers and level of reinforcement are varied, and both seismically isolated and non-isolated connections between piers and superstructure are considered. The non-linear time history analyses are performed on the various cases by subjecting them to 250 strong-motion records from five different events. However, the results are based in simplified single degree-of-freedom and two-degree-of-freedom models. Additionally, strong motion records are applied only in the longitudinal direction of the straight

bridge, neglecting the effects of out-of-plane motion on bridge vulnerability. The resulting fragility curves are inspected and a strong correlation is found between the structural parameters and resulting vulnerability. A relationship is developed between over-strength ratios of the structures and the parameters of the fragility curves. The use of over-strength ratios of bridges is proposed as a means for rapid and simplified development of fragility relationships for non-isolated bridges in Japan.

Another variant for producing analytically based fragility curves is introduced in (Choi, DesRoches, & Nielson, 2004) for four different bridge types commonly found in the Central and Southeastern United States. The four bridge types assessed are steel and concrete multi-span simply supported (MSSS) and multi-span continuous (MSC) girder bridges. For each bridge type, 10 sample bridges are used to represent variability in bridge properties. A set of 100 synthetic ground motion records of varying magnitudes and distances are selected to perform analyses in the longitudinal direction of the bridge. The curves are first generated for individual components by developing damage states for subcomponents of the columns and bearings. This is conservatively measured relative to the most vulnerable subcomponent. Then, these individual component fragilities are combined to create a lower and upper bound of the overall fragility curve for the full bridge system. The lower bound assumes that all components are fully dependent, while the upper bound considers the components completely independent. These fragility relationships are developed for use in both economic loss estimation applications, and as a tool for assigning retrofit priorities for bridges.

An extension of the work above is later performed, and includes expansion to a total of nine classes of bridges with improved numerical analyses through three dimensional modeling (Nielson & DesRoches, 2007). The new classes include MSC slab, MSSS slab and concrete box girder, as well as single span (SS) concrete and steel girder bridges. Analytically based fragility curves are developed in a similar method, this time using 3-D models for the nonlinear time-history analyses performed. The synthetic records, considered to represent the geometric mean of two orthogonal components, are used to generate the two perpendicular ground motions using the methodology presented in (Baker & Cornell, 2006). Thus, multi-directional loading is included in the analytical model, and response is accounted for through springs in the abutments, foundation, and bearings in both primary directions. Additionally, the performance of abutments is included as one of the components used to generate the full system-level bridge fragility relationships. The results from this study are compared the curves currently used in HAZUS-MH and developed, as described above, by (Mander & Basoz, 1999). It is found that for single-span and multi-span simply supported bridges,

the fragilities developed in this study indicate lower seismic vulnerability than current HAZUS values. On the other hand, continuous span bridges are shown to be more vulnerable as defined by this study than in relationships previously used in HAZUS. It should be noted however, that the comparisons are not identical, as bridge categories developed in this study are a much more specific set of classifications with greater resolution than was previously distinguished in HAZUS-MH.

At the beginning of this introduction, an important study by (Gardoni, Der Kiureghian, & Mosalam, 2002) was mentioned as it established experimental, analytical, and mechanics-based methods to develop fragility curves for RC bridge piers with varying parameters. The work developed probabilistic capacity models for deformation and shear capacity of circular reinforced concrete columns subjected to cyclic loading. These models are based off of a group of significant experimental tests and observations, and are used to estimate the fragility of structural components in terms of maximum deformation and shear demand. A follow-up work is presented in (Gardoni, Mosalam, & Der Kiureghian, 2003) which presents a methodology for developing probabilistic seismic demand models for use in conjunction with the already developed capacity models. Application of the approach for two examples of modern bridges typical to California is then presented. In both cases, Bayesian updating is used to assess the unknown model parameters based on existing deterministic models as well as observational data.

Other recent research programs developing fragility curves for multi-span continuous (MSC) and multi-span simply supported (MSSS) bridges with varying superstructure materials have been performed by (Ramanathan, DesRoches, & Padgett, 2012) and (Tavares, Padgett, & Paultre, 2012). In (Ramanathan, DesRoches, & Padgett, 2012), similar procedures to those already described are used to generate component-based fragilities. Three-dimensional nonlinear finite element analysis (FEA) is employed. Component fragilities were combined to generate system-level fragilities of four steel and concrete MSC and MSSS bridge classes. The central purpose of the study was to examine bridges in each of these categories that are designed with and without seismic detailing. In (Tavares, Padgett, & Paultre, 2012), three-dimensional nonlinear finite element analysis is used to assess bridges that are representative of the Province of Quebec, Canada. Vulnerability relationships are developed based on performance of critical components at varying peak ground accelerations.

Table 2.2 Key aspects of modern bridge fragility development efforts

Source	Geometry	Deck	Record	Loading	Method	Calibrate	System
Mander, 1998	Varies	Varies	Spectrum	3D mod. Factor	NL static CSM	N/A	No
Hwang et al., 2001	Straight 4-span	Cast deck on girder	10 Synthetic	Transv only	NL time hist only	No	Transv only
Karim & Yamazaki, 2003	Straight 4-span	Cast deck on girder	250 Strong Motion	Long only	NL Dyn & Pushvr	No	No
Gardoni, Mosalam, & Der Kiureghian, 2003	Straight 2- & 3-span	Cast in place concrete box girder	N/A	Transv only	NL Pushover	Yes	Yes
Choi et al., 2004	Straight MSC/MSSS	Deck on RC/ Steel girder	100 Synthetic	Long only	NL time hist only	No	Partly
Nielson & DesRoches, 2007	Straight SS/ MSC/MSSS	Box girder and deck on girder	96 Synthetic	Long & Transv	NL time hist only	No	Yes
Taveres et al., 2012	Straight SS/ MSC/MSSS	Slab, timber, RC, steel	Synthetic	Long & Transv	NL time hist only	No	Yes
Ramanathan et al., 2012	Straight MSC/MSSS	Deck on RC/ Steel girder	240 Synthetic	Transv only	NL time hist only	Bearing model	Yes
This Study	Curved 4-span	RC box girder	Strong Motion	Vert/Long/ Transv	NL time hist only	Yes	Yes

Key aspects of the studies described above are summarized in Table 2.2 in order to illustrate key features of works in the literature and to compare with the work performed in this study. The comparison reveals that, despite advances in analytical models and risk assessment methods, there still remain shortcomings in many existing fragility relationships. These are typically due to basing the structural capacity model on un-calibrated analytically-based structural response data, or on experimental data where numerous features are lacking. There is a need for implementation of high-fidelity experimental testing of bridge structures in order to obtain data sets that capture more complex parameters. This data can then be used to calibrate analytical models in order to perform the analyses necessary for statistical evaluation of vulnerability. It is proposed that the need for calibrated models is most essential in cases where irregularities in geometry, as well as multi-directional load and boundary conditions, result in complex load combinations on structures and their components. It should be noted that in Table 2.2, a source is not considered to have utilized an experimentally calibrated model if the only application of past experimental work is in developing damage state definitions. It is also critical to have these experimentally-based relationships represent full system-level response for these complex bridge systems, since the impact of neglecting superstructure and abutment response for these cases is not fully known.

Identifying the extent to which each of these aspects influences the resulting system-level bridge fragilities is one of the main objectives of this study. This is important as there are not any specific improvements to techniques utilized for developing fragility curves from a statistical methods perspective. Therefore, the strength of the research program presented here lies in the carefully planned and executed hybrid simulation that is capable of accurately capturing combined interaction effects. The accuracy of the results present also relies on the precise calibration of analytical models and thorough development of a suite of seismic records. It is a result of these efforts that the curves provide an improved set of fragility relationships with the potential application toward impact assessment studies of this specific bridge typology. Still, the resulting fragility relationships are chiefly developed for the purpose of evaluating the influence of the above parameters on structural response. Through the relative comparison of these vulnerability functions, the influence that various testing and modeling decisions have on the resulting seismic assessment and potential loss estimation results can be made. The influence of each of these parameters is incredibly important for informing future researchers of the degree in which assumptions made in terms of geometry, loading, and modeling will impact the results of a study.

2.2 Testing and Analysis of RC Columns and Piers

The first research topic introduced in this study is with respect to the effects of curved bridge geometry and multi-directional loading on the seismic vulnerability of bridge systems. Therefore, an understanding of the structural response resulting from combined actions is important when considering the impact of curved bridge geometry and multi-directional loading on RC bridge vulnerability. Throughout this section, select experimental tests of reinforced concrete piers and columns from the literature are presented. Due to the vast quantity of experimental and analytical research programs conducted on this topic, this review is far from exhaustive. However, the broad range of pier design, geometry, details and loading of the piers explored in these studies is representative of the full breadth of research available in the literature. These works are discussed in increasing order of complexity, from uni-directional lateral load capacity tests up through experiments assessing axial, shear, flexure, and torsion interactions. Studies on building columns are included in cases where certain parameters are investigated more thoroughly than in comparable studies of bridge piers in the literature. It should be noted though that building columns and bridge

piers can be subjected to very different types of demands due to their location and function within a structural system. Often, building columns are part of a system with a higher level of redundancy and are subjected to different levels of applied vertical load in terms of axial capacity. It can be noted here that it is not common for bridge piers to be subjected to greater than 15% of axial compressive capacity (Priestley & Benzoni, 1996). Therefore, if similar studies are performed on bridge piers as those existing for building columns, and effort is made to present the research on bridge piers.

In addition to experimental testing of RC bridge piers and columns under combined actions, there are numerous efforts to invoke numerical modeling to capture these effects. Several of these works in the literature are highlighted in this section, and include models developed to capture various degrees of combined actions. Some of these efforts utilize experimental testing programs to develop models. Others are based solely on numerical analysis, relying heavily on understanding of mechanics and material behavior. Numerous methods are employed to capture the complex response of bridge piers subjected to combined loading. These are included to survey various methods for capturing these effects, as well as to highlight the importance of calibrating models to represent physical behavior.

It should be noted that in this extensive survey of pier and column testing and analysis results, many of the components are assessed without full consideration made to the response of the entire structural system and its influence on pier behavior. Even when piers are subjected to complex actions that result from combined loading of the structural system, the interaction between pier performance and the structural system is typically not assessed. The details and capabilities of the hybrid test of a curved four-span RC bridge that is the origin of the data set utilized in this study is contrasted to the studies surveyed in the literature (Table 2.3). This serves to highlight that the level of complexity and realism accomplished in the hybrid test discussed in this study is rarely achieved elsewhere in the literature. This provides additional motivation for pursuing a simple set of modification factors to account for bridge structure, load conditions, and modeling assumptions. The vast array of tests that have been performed on various pier geometries subjected to numerous seismic events could be modified to account for these effects as desired.

i. Uni-directional Lateral Loading

The most basic of experimental tests on reinforced concrete piers and columns involves uni-directional lateral loading of these components, often under static vertical load. These tests serve as a basis for understanding the lateral load resistance provided to structures. Still, the variations in response and failure modes are non-trivial. Aspect ratio, longitudinal and transverse reinforcement ratio, as well as other geometric, design and detailing of the structures govern varying response behavior. Typically, responses are classified along the spectrum of pure shear to pure flexural response, which are influenced by each of these factors, as well as the level of vertical load. Still, the assessment of response due to uni-directional loading, whether monotonic or cyclic in nature, does not adequately address the likely range of complex stresses and loads imposed on RC bridge piers in the field.

Experimental uni-directional tests that provide significant results for consideration in the context of this study include the work performed by (Kunnath, El-Bahy, Taylor, & Stone, 1997). Twelve identical 1:4 scale circular RC bridge piers are tested monotonically and under cyclic loading in one direction. The research was performed to investigate the impact of cumulative damage and low-cycle fatigue. The failure modes observed included fatigue of longitudinal reinforcing bars at large displacement amplitudes (in excess of 4% lateral drift) and confinement failure due to rupture in the spiral transverse reinforcement. The latter failure mode was observed in specimens subjected to larger numbers of small amplitude cycles. Results were interpreted to assess the effectiveness of predicting seismic damage based solely on energy dissipation when failure is due to fatigue rather than limitations in ductility.

Another test program is conducted on twelve full-scale columns under severe displacement cycles (Acun & Sucuoglu, 2010). In this program, two typical designs of square cross-sections for building columns are subjected to flexural failure at different levels of displacement history. One design conforms to modern seismic design codes, while the other is considered substandard, or not conforming to these codes. Results are compared to the deformation-based performance limits proposed in (ASCE/SEI-41, 2007), which are shown to be conservative in predicting performance of plastic hinges. Results highlight the importance of modeling realistic degradation behavior of columns under severe displacement histories. The results from these tests are later employed to

develop an energy-based hysteresis model for more accurate moment-rotation response accounting for deterioration of energy dissipation capacity, strength, and stiffness (Sucuoglu & Acun, 2012).

ii. Pure Torsional Loading

For bridge systems with curved or irregular geometries, considerations must be made to the influence of torsion on the structural response of piers. In order to investigate the nature of the torque-twist relation for RC piers, as well as the formation and propagation of torsional cracks, the following studies on RC members subjected to pure torsion are presented and discussed.

Mechanisms for the development of stresses and propagation of failure in torsion are conducted on RC cylinders in (Subramaniam, Popovics, & Shah, 1998). The tension and shear-type stresses and strains induced on the specimens as a result of torsional loading are examined. Particular focus is placed on the formation of cracks and instability of the post-peak region of the torsional moment-rotation response. This relationship is also often referred to as the torque-twist relationship here and in other studies.

Various models have been developed in order to simplify and predict this torque-twist relationship. These empirical formulas often require a complicated iterative solution algorithm, and vary in accuracy in predicting response. A simplified version of a common model employed for this purpose is presented in (Jeng, 2010). The Softened Membrane Model for Torsion (SMMT) is simplified by proposing a direct calculation of cracking torque and tracking twist, and is validated with experimental tests of over 90 rectangular specimens. It should be noted that the relationships will likely differ between rectangular and circular members. This is due to concentrations of stresses from twisting on the non-uniform rectangular surfaces as compared to the uniform circular surfaces.

A set of 18 circular concrete members of 8 inch diameter with lengths varying from 16 to 39 inches and spiral spacing of 1 to 3.5 inches are tested in pure reverse cyclic torsional loading by (Hindi & Browning, 2011). These members are also analyzed with two different methods of transverse reinforcement. The first being a traditional single spiral confinement, and the second a new technique composed of twin opposing spirals, referred to as cross-spirals.

The conventional single spiral results represent piers most similar in nature to the small- and large-scale piers assessed in the hybrid experimental test described in this study. In the above studies, the stiffness and performance of piers subjected to pure torsional loading is vastly different than what is observed in combined loading. However, in the future work section of this paper, the cross-spirals mentioned above, as well as the interlocking spirals of (Prakash & Belarbi, 2010) are discussed as potential design improvements for providing improved transverse reinforcement in piers subjected to combined actions. The influence of torsional loading on other actions, and vice versa, is described in the following sections reviewing the literature on this subject. Significant reduction in stiffness, deformation, and load capacity in the torsional response, and the important influence this has on lateral response of the piers is also observed in the hybrid simulation presented in this study.

iii. Combined Loading without Torsion

Many of the initial investigations into combined loading effects involved some combination of shear, flexure, and axial loading. Torsional loading is added as a consideration in the following section, due to its prominence in the behavioral response of the structural tests serving as the base data set in this work, as well as its implications on response of curved bridges. Prior to considering these effects, however, it is prudent to first examine the literature on the effects of combined loading, excluding torsion.

Testing of ten RC columns subjected to cyclic lateral deflections and axial loads was conducted by (Abrams, 1987). These tests revealed that axial load variations can influence lateral strength, stiffness, and deformation capacities of RC columns. The assumed relationships between axial force and moment interaction, as well as axial force and lateral deflection were examined. It was concluded that frames with asymmetrical layouts of columns should be designed and analyzed with considerations made for possible axial force variations during lateral loading. These results could be extrapolated to at the very least indicate that bridges with complex geometry are more significantly affected by lateral-vertical interaction effects.

The importance of considering the effects of vertical ground motion specifically on the design of RC highway bridges, particularly those located near seismic faults is examined in (Saadeghvaziri & Foutch, 1991). Modeling of deck and piers to account for complex combined vertical and horizontal

earthquake motion is performed. It is shown that vertical motions generate fluctuating axial forces in the bridge columns. Furthermore, these fluctuating axial forces are capable of creating instability in the hysteretic behavior and an increase in ductility demand. In several cases, tests indicated that these resulted in exceedance of force design levels in the abutments and foundations.

It is typically agreed upon that the influence of axial stress on flexural response of RC members is better understood than the influence of axial stress on shear response. (Xie, Bentz, & Collins, 2011) Shear-axial interactions are specifically examined in (Lee & Elnashai, 2002). In this study, a hysteretic axial-shear interaction model was developed and implemented in a nonlinear FEA program. The model is based off of experimental tests performed on shear-dominant RC bridge piers under axial force variation (Maruyama, Ramirez, & Jirsa, 1984). It is shown that conventional FE models based on axial-flexural interaction were inadequate. The importance of modeling shear behavior on RC bridge piers is supported by the 1994 Northridge earthquake. Discussed specifically in this study is the damage to bridge piers of the I-10 Santa Monica Collector-Distributor 36 displaying shear and axial failure modes. It was concluded that flexure-shear-axial interaction should be accounted for when assessing the behavior of RC bridge piers, particularly in cases of high vertical ground motion.

A shear-axial interaction model that was later developed by (Lee, Choi, & Zi, 2005) is also capable of representing shear stiffness transitions that result from axial force variation. Strength, stiffness and deformation characteristics of a shear-axial interaction model capable of representing shear stiffness transitions are compared to experimental results from (Saatcioglu & Ozcebe, 1989) and (Maruyama, Ramirez, & Jirsa, 1984). A nonlinear time-history analysis is performed on a bridge damaged by the Kobe earthquake, which validates the applicability of the model. It was demonstrated that lateral displacement is significantly larger when considering the effects of shear, leading to greater ductility demands, overall stiffness degradation, and period elongation, all correctly identifying the damage patterns of the observed piers.

In a similar study, the potential for previous models to underestimate deformation response in RC structures is also shown to result from neglecting the effects of combined flexure-shear interaction (Lee & Elnashai, 2001). The importance of predicting strength and stiffness of RC columns subjected to lateral cyclic deformations under constant axial force is discussed. The study involves development of a simple model to capture flexural-shear interaction effects. Development of the model is based in results obtained from four large-scale flexurally dominant RC test columns (Park,

Priestley, & Gill, 1982), as well as eighteen shear dominant columns (Maruyama, Ramirez, & Jirsa, 1984). It was shown that neglecting to account for shear deformation in the analysis of many RC structures may lead to overestimating the energy dissipation capacity and underestimation of total deflection. This is because flexural deformation is overestimated due to the elimination of shear failure consideration, while shear component of lateral deformation is ignored. Additionally, underestimation of total deformation reduces the assumed impact of P-delta effects, resulting in overly optimistic assessment of structural stability. In the future work section of this work, the models developed in the above study are suggested for improved calibration to capture the full flexural-shear interaction effects in the longitudinal directions of the piers tested in the hybrid simulation program.

An additional shear-flexure interaction model of RC bridge piers is introduced by (Zhiguo, Bingjun, Dongsheng, & Xun, 2008). Experimental research is performed on six circular RC bridge piers. The piers exhibit stable flexural response up to a displacement ductility level of four, which is then followed by brittle shear failure. Modeling approaches toward describing the hysteretic behavior of the piers are developed for comparison with the experimental results in the ANSYS finite element analysis program.

One final shear-flexure interaction model of RC piers for seismic response assessment of bridges is developed in (Xu & Zhang, 2011). This is a for a coupled hysteretic model that accounts for shear-flexure interaction at both the section and element levels and is calibrated against a large number of experimental specimens, including static cyclic and dynamic shake table tests. The shear hysteretic model is based off of the work by (Ozcebe & Saatcioglu, 1989), while the flexure hysteretic model is based on that of (Takeda, Sozen, & Nielsen, 1970). A follow-up expansion to this study is conducted to include variable axial loads (Zhang, Xu, & Tang, 2011). Shear-flexure-axial combined actions on RC bridge piers under multi-directional seismic shaking are examined. Inelastic displacement is again shown to increase in comparison to previous models, due to shear-flexure interaction. A demand model for estimating the ductility displacement based on nonlinear time history analyses of 24 full-scale bridge piers is proposed to demonstrate pinching behavior, stiffness degradation, and strength deterioration under these combined actions.

Additional combined axial-shear-flexure interaction models are developed in (Mostafaei & Kabeyasawa, 2007) and (Mostafaei, Vecchio, & Kabeyasawa, 2009). In the former study, displacement-based analysis of RC columns is performed. Shear behavior is modeled through

applying the MCFT and flexural behavior modeled by sectional analysis. These mechanisms are modeled by springs in series. Axial deformation interaction and concrete strength degradation are considered. A simplified approach is proposed using a single section analysis and single shear model for the entire element. Analytical results are obtained for columns previously tested by these and other authors, and resulting comparisons are made to the experimental data to show consistent agreement in terms of ultimate lateral loads, drift, and post-peak responses. The latter follow-up work develops an approach for estimating the ultimate deformation and load capacity of RC columns is developed based off of the principles of axial-shear-flexure interaction.

iv. Combined Loading with Torsion

The importance of considering the effects of torsional loading on the combined actions of bridge pier response is now discussed. There are relatively fewer sources in the literature that include torsion when examining interaction effects, as many have focused on various combinations of shear, axial, and bending moment interactions. It is recognized that inelastic response of structural bridges are influenced heavily by the hysteretic behavior of the bridge piers. Therefore, in order to assess the seismic response of bridge systems, it is critical to examine the complex load combinations of flexure, shear, axial load, and torsion in the piers, which are due to constraints of structural and geometric configurations of the bridge subjected to multi-directional earthquake motions (Zhang & Xu, 2009). Improving understanding of torsional contribution is important when assessing seismic performance of piers subjected to flexure and shear loading, as the contribution of torsion increases the likelihood of brittle shear failure (Belarbi, Prakash, & You, 2009).

It is known that significant levels of torsion can result in skewed or curved bridges and bridges with unequal spans or pier heights (Li, Belarbi, & Prakash, 2010). These irregular geometric configurations are often necessitated by site constraints. It is also possible for abutment restraints or non-uniform soil conditions to cause combined loading effects that include torsion. Studies on RC piers of multi-span bridges have demonstrated that the torsion-to-bending ratio of bridge piers closest to abutments are significantly higher than those of piers closer to the center of the bridge (Belarbi, Prakash, & Silva, 2008). These findings are significant in light of the bridge design and test setup selected for this study.

One of the first experimental programs designed to assess the interaction effects of bending and torsion under axial load is introduced in (Otsuka, et al., 2004). A set of nine square RC columns are tested under pure bending, pure torsion, and combined loading of bending and torsion under axial force of 10% compressive strength. Varying levels of bending and torsion are applied, and pitch of transverse hoop reinforcement is varied. Load deformation relationships, strain relations, curvature distribution, and energy absorption are obtained.

Another early experimental investigation of RC columns subjected to combined bending and torsion is conducted by (Tirasit & Kawashima, 2007). Seven columns of the same properties were subjected to cyclic torsion, cyclic uniaxial bending, and combined bending and torsion with and without constant axial load. Several combinations of rotation-drift ratio were applied in order to study the interaction effects between torsion and flexural capacity of the columns tested. Results from this test showed that flexural capacity was reduced and damage on the columns shifted up from the plastic hinge region as increasing levels of torsion were applied. A model for flexural and torsional hysteretic behavior based on these experimental results is then proposed. An analytical investigation of skewed bridges is later performed using this nonlinear torsional hysteretic model (Kawashima & Tirasit, 2008). Torsion is considered to be resulting from rotation of the deck, which is due to the restraint conditions between the deck and abutments. Deterioration of torsional strength due to combined flexure is accounted for and it is concluded that the effect on torsion is significant and cannot be neglected in its contribution to the seismic performance of the skewed bridge.

It has been shown in (Li, Belarbi, & Prakash, 2010) that torsional moment can play a significant role in the response of bridge piers that are skewed, curved, and have either unequal column heights or spans. In this study on the behavior of RC bridge columns, four half-scale experimental specimens were tested under cyclic flexural moment and shear force, cyclic pure torsion, and combined cyclic shear, bending, and torsional moments. The four square columns were of the same aspect ratio, and varied only in loading conditions. The study revealed that combined loading under torsion can result in complex flexural and shear failures. It also supported conclusions from previous works in that 1) both flexural and torsional capacity are reduced as a result of combined loading, with failure modes and deformation capacities changed significantly and 2) the damage zone trends away from the typical flexural plastic hinge zone with an increasing level of torsional moment.

A series of experimental tests on RC bridge piers have been performed under various combinations of multi-directional bending, shear, axial load, and torsion as a part of the Combined Actions on

Bridge Earthquake Response (CABER) Program. Columns are tested quasi-statically at the Missouri University of Science and Technology (MST), pseudo-dynamically at the University of Illinois at Urbana-Champaign (UIUC), and dynamically at the University of Nevada, Reno (UNR) prior to the hybrid simulation of the curved 4-span RC bridge at UIUC presented in Chapter 3. Select papers in the literature resulting from this extensive program are now reviewed. These specific works are chosen to illustrate the recent developments in understanding of combined loading of RC piers under combined loading with torsion. These efforts provide the context within which decisions and plans are made for conducting a hybrid test of a curved four-span RC bridge utilized throughout this work.

Behavior of seven circular RC bridge piers are tested under combined loading including torsion and described in (Belarbi, Prakash, & You, 2009). The piers are subjected to cyclic bending and shear, cyclic torsion, and various levels of combined cyclic bending, shear, and torsion. The impact of the detailing and level of spiral reinforcement (0.73% and 1.32%) on the torsional resistance under combined loading is examined. It is demonstrated that both the flexural and torsional capacities are reduced due to the combined loading effects. The failure mode and deformation characteristics are affected greatly by a change in spiral reinforcement ratio, with an increase leading to significant improvements in strength and ductility.

Additional circular RC piers of similar design are tested under cyclic bending and shear, pure cyclic torsion, and various levels of combined cyclic bending, shear, and torsion (Prakesh, Belarbi, & You, 2010). Here, the specimens added to those considered above include changes in aspect ratio of the columns considered (height to diameter ratios of 3 and 6). The experimental results of these specimens subject to various ratios of torsion-to-bending moment, and bending moment-to-shear ratios are examined. Results are compared to FE analyses of the columns. Experimental tests showed no appreciable change in flexural or torsional capacity with a decrease in aspect ratio to the column, though this behavior was observed in the analyses. It is believed that this was due to the relatively low level of longitudinal reinforcement in the specimens. There were however significant changes in the failure mode, energy dissipation, and reduction of deformation levels reached due to the reduction in aspect ratio and influence of shear-torsion response.

Based on these evaluations of the combined response of bending, shear, axial and torsional loading, a damage index model is proposed to allow decoupling of these actions according to defined limit states (Prakash & Belarbi, 2010). Interaction of damage indices for bending and torsion in terms of progression of damage are developed. The proposed damage index models are validated from the test

results discussed above. The effects of transverse reinforcement ratios and shear span are also investigated. It is shown that an increase in torsion amplifies the progression of damage in the RC bridge column. However, an increase in transverse reinforcement ratio can delay this damage progression under combined bending and torsion, changing the torsional dominant behavior to be dominated primarily by flexure. Finally, the work proposes limits on damage index for designs to be capable of achieving various performance levels under combined loadings.

The above works all seek to expand understanding of the interaction effects of combined loading conditions and complex failure modes of circular and square RC bridge columns subjected to flexural, axial, shear, and torsional loading under earthquake excitation. Specifically, the influence of interaction for each loading condition should be examined individually in order to appropriately improve seismic design. The series of experimental testing at Missouri University of Science and Technology as a part of the CABER program served to produce data sets of circular and square cross-sections tested under various torsion-to-bending moment ratios. An overall evaluation of the influence of cross-sectional shape, torsional and flexural hysteretic response, damage distribution, and ductility characteristics for various torsion-to-bending ratios as determined from these studies are provided in (Prakash, Li, & Belarbi, 2012). This work also produces a set of interaction diagrams established on the basis of the experimental results and work listed above.

A summary of key aspects of the above tests are now provided in Table 2.3. The work presented in this study builds upon the understanding that has already been established in the works summarized above. That is, that torsional moment can play a significant role in the response of bridge piers that are skewed, curved, and have either unequal column heights or spans. The results obtained from these previous works serve to inform decisions made in the hybrid test conducted in this research. Therefore, they affect the resulting data set used to calibrate an analytical model capable of capturing the various combined effects highlighted above. While producing many significant results, a noteworthy shortcoming of many past experimental testing programs is the absence of testing in six degree of freedom control or considerations made to full system-level response. These two elements have a potential for significant impact on the seismic response of the members considered. It should be noted that in Table 2.3, the consideration of loads existing in the field and subsequent application of this static axial load throughout the loading protocol is not considered as incorporating system-level response into the response of the experimental piers.

Table 2.3 Key aspects of RC pier and column testing programs

Source	Struct Type	Test	Cross-Section	No. Cases	V	M	P	T	DOF	System Response
Park et al. ,1982	Building	Expt	Rect	4		X	X		3	No
Maruyama et al. ,1984	Building	Expt	Rect	18	X		/		3	No
Abrams, 1987	Building	Expt	Rect	10		X	X		3	Axial Load Variation
Saatcioglu & Ozcebe, 1989	Building	Expt	Rect	14	X	X	/		3-5	No
Saadeghvaziri & Foutch, 1991	Bridge	Anly	Rect	6	X	X	X		2-3	Deck
Priestley & Benzoni, 1996	Bridge	Expt	Circular	2	X	X	X		3	No
Kunnath et al., 1997	Bridge	Expt	Circular	12	X	X			3	No
Furlong et al., 2004	Building	Anly/ Lit	Rect	11		X	X		2-5	No
Otsuka et al., 2004	Bridge	Expt	Rect	9	X	X	X	X	1-4	No
Tirasit & Kawashima, 2007	Bridge	Expt	Rect	7	X	X	X	X	1-4	No
Zhiguo et al., 2008	Bridge	Both	Circular	6	X	X	X		3	No
Belarbi et al., 2009	Bridge	Expt	Circular	7	X	X	X	X	≤ 6	No
Acun & Sucuogul, 2010	Building	Expt	Rect	12		X			3	No
Jeng, 2010	Either	Emp*	Rect	90*				X	1	No
Li, Belarbi, & Prakash, 2010	Bridge	Expt	Rect	4	X	X	X	X	1-4	No
Hindi & Browning, 2011	Bridge	Expt	Circular	18				X	1	No
Zhang et al., 2011	Bridge	Anly/ Lit	Circular	24	X	X	X	X	≤ 6	Yes
Prakash, Li, & Belarbi, 2012	Bridge	Expt	Both	8	X	X	X	X	1-4	No
This Study	Bridge	Expt/ Anly	Circular	3	X	X	X	X	6	Yes

An important aspect of the work presented in this paper involves basing the measures of structural capacity used to develop fragility relationships on high quality experimental testing. This testing should include realistic 6DOF loading and boundary conditions that consider three-dimensional effects. This feature is relatively unique to this study, since the 6DOF hybrid test provides a data set that adequately represents the response characteristics of all components of the bridge's structural system. The importance of validating models through experimental work is made clear through the above review of existing literature on the influence of combined interaction effects. Through the use of reliable structural data capturing these features, analytical models can be developed and calibrated with greater levels of accuracy regarding structural response. Nonlinear dynamic time history analyses for a suite of records can then be performed on these resulting models. Varying the model parameters will produce sets of fragility curves that allow for identification of individual and combined effects of geometry, loading, and modeling assumptions on structural response of entire complex RC bridge systems. Exploring these results makes it possible to begin a realistic assessment of the vulnerability of complex RC bridges under various conditions. Considerations can then be made regarding improvements to existing methods for structural and risk assessment of these important components of civil infrastructure. The process outlined above, beginning with a description of the advanced 6DOF hybrid simulation of the curved four-span RC bridge, is now presented.

CHAPTER 3: HYBRID TEST OF CURVED FOUR-SPAN BRIDGE

In this chapter, a summary of the preparation and execution of a complex hybrid experimental test of a curved four-span bridge is provided. Circular reinforced concrete piers of a four-span curved bridge are investigated experimentally through large-scale hybrid simulation under multi-directional earthquake loading. The boundary conditions of the piers are controlled in all six degrees of freedom (6DOF). The experiment is performed through the unique capabilities of the NEES Multi-Axial Full-Scale Sub-Structures Testing and Simulation (MUST-SIM) Facility at the University of Illinois, Urbana-Champaign. The bridge is controlled and monitored carefully in order to produce a data set that can be utilized in rigorous calibration of analytical models for use in bridge vulnerability assessment. The experimental test program is novel in the fact that it accurately accounts for the effects of the following geometric, loading and boundary conditions of the curved bridge structure:

- Geometric irregularities and varying pier response characteristics due to uneven spans and pier heights
- Multi-directional motion of the applied earthquake record
- Curved bridge deck and combined actions including torsion that result in the structural members
- System-level interaction between three experimental piers in two testing facilities with numerical models of deck, restraints, and abutments

In this test, the hybrid bridge structure is composed of one small-scale and two large-scale experimental piers. The curved bridge deck and abutments are modeled analytically in Zeus-NL. Extensive traditional and advanced non-contact data acquisition methods are used to monitor performance of bridge piers under complex loading. The hybrid curved bridge is tested pseudo-dynamically under an earthquake record at four performance-based scaling levels. A description of the bridge design, earthquake input motion, hybrid simulation platform, experimental control capabilities, and data acquisition methods follows.

Structural response data and experimental results are presented and discussed. Global bridge response and associated data, as well as the impact of combined loading on local pier response are examined. Various methods for interpretation and visualization of the structural response data are presented. This detailed overview of the test features and associated data set is provided to verify the quality and accuracy of the methods used throughout this experimental program. This is necessary to

justify the extensive use of this data set to perform model calibration in Chapter 4, as well as to provide an overview of the range of data available for this purpose.

3.1 Bridge Design and Construction

Overall geometry of the prototype bridge is based on a seismic design example from NCHRP Project 12-49. The example is a five-span bridge with varying pier lengths, and was developed to provide design recommendations on multi-span bridges for seismic regions along the west coast of the United States. Modifications are made to this design example in order to investigate the influence of multi-directional earthquake loading on combined actions for bridge piers. Most significantly, this includes the removal of one span length, reduction to one-pier bents, varying span lengths and introducing curved geometry. This curved geometry, with non-uniform spacing of single-pier bents along the bridge, is selected to induce a non-trivial level of combined response in the structure, including torsion. An analytical parametric study is performed to select the pier locations, while still retaining span lengths that could feasibly be necessitated by site requirements. A rendering of the bridge geometry as defined in the analytical Zeus-NL model is displayed in Figure 3.1.

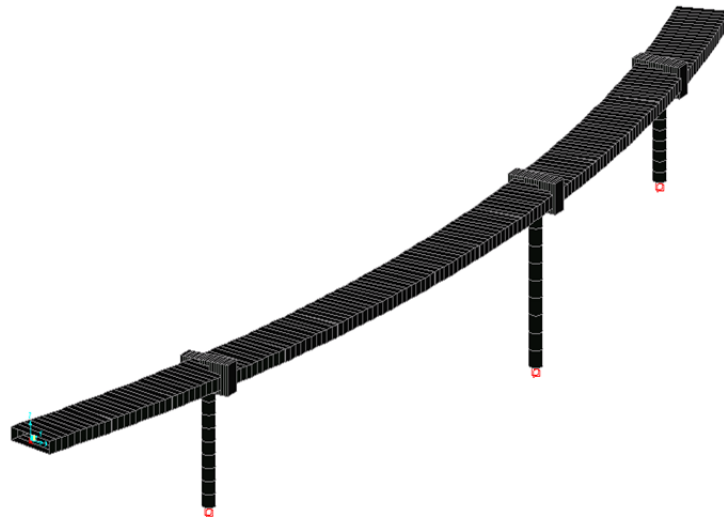


Figure 3.1 Rendering of overall bridge geometry (Zeus-NL)

This geometry develops torsional, flexural, shear, and axial stresses in the RC piers under combined loading. In the hybrid simulation, the outer two piers are tested in the NEES MUST-SIM facility at a scale of 1:3, while the inner pier are tested simultaneously at 1:20 scale in the small-scale facility located at the same site. The superstructure, abutments, and restraints are all modeled computationally at full scale. A description of the structural details of small- and large-scale specimens, as well as the hybrid simulation procedure for tying together these components is provided below. A thorough treatment of the analytical modeling, including details of the superstructure, restraints and abutments, can be found in Chapter 4. A graphical representation of these components of the hybrid simulation with scale and coordinate axes indicated is displayed in Figure 3.2.

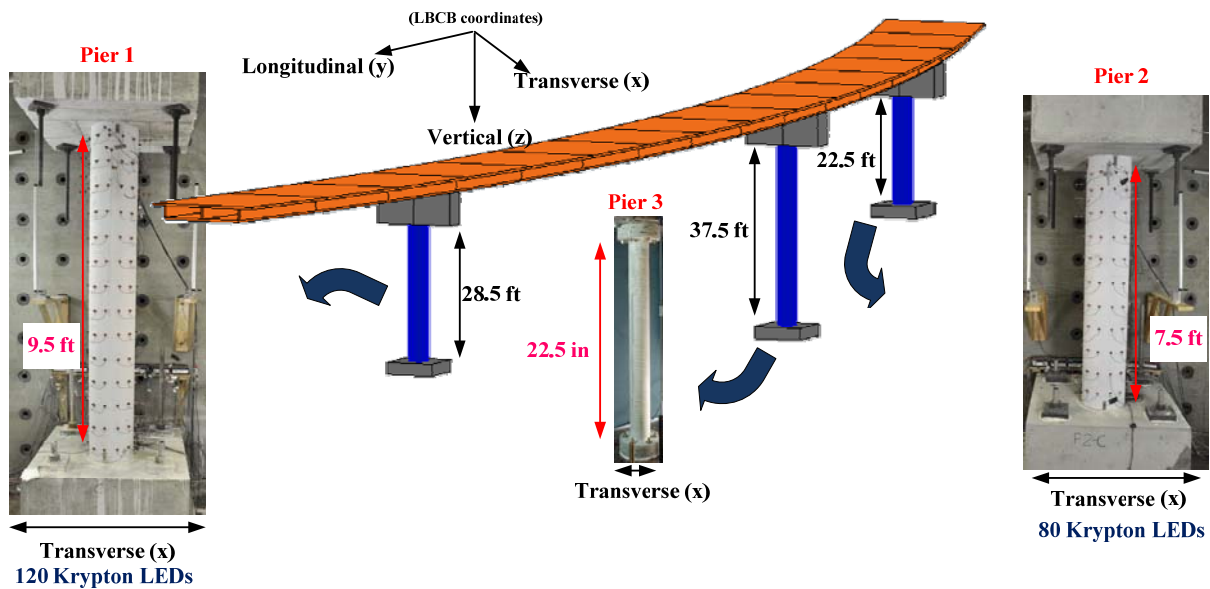


Figure 3.2 Experimental components of hybrid test

i. Basis of Bridge Design

Overall geometry of the prototype bridge is based on a seismic design example (Figure 3.3) used by the National Cooperative Highway Research Program (NCHRP) Project 12-49 to illustrate recommended design and analysis methods for bridges with varying pier heights. Bents range in height in order to illustrate the effect of irregularities in geometry in increasing complex nonlinear

response. Ratios are recommended for retaining sufficiently balanced stiffness and frame geometry to reduce the likelihood of out-of-phase response of the structure. This issue is also addressed for a very similar bridge in Section 7 of the Caltrans Seismic Design Criteria Guidelines (Caltrans, 2006). This original structure was the 500-ft bridge described in the unpublished Design Example No. 8. The bridge is composed of five continuous spans of 100 ft. each, with four two-pier bents. A crossbeam was used to connect the box girder superstructure to the piers.

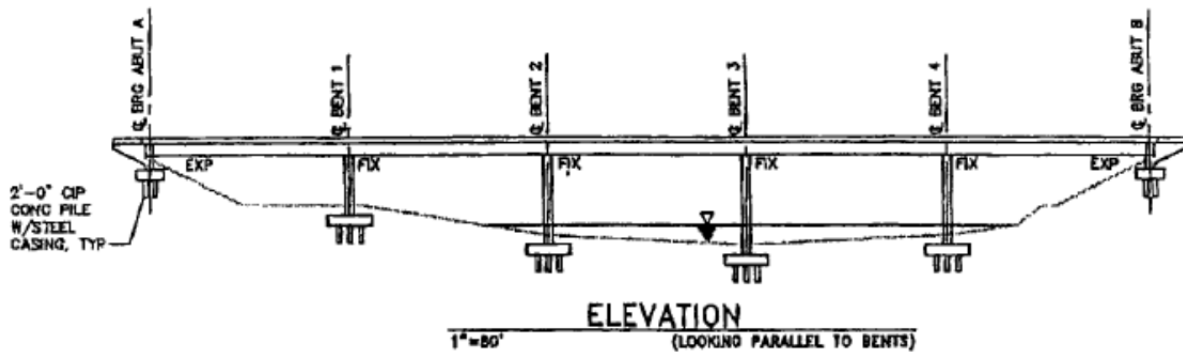


Figure 3.3 Origin of bridge model (NCHRP Project 12-49)

The features modified for this study include reducing from five to four spans and shortening the overall length appropriately, creating non-uniform span lengths, adding curvature to the bridge, and moving to single-pier bents. These decisions were made in an effort to generate a realistic curved bridge structure with similar deck and abutment properties, retaining average span length, traffic load, and overall functionality. The resulting geometry was selected via an analytical parametric study to identify a case that generated sufficient torsional response in the piers to investigate higher levels of combined loading. It should be noted that the original site selected by this project team was the Puget Sound region of Washington State. However, in NCHRP Report 489, Appendix H, the same bridge was analyzed for the seismic region used in this study, which corresponds to Seattle, WA.

ii. Details of Deck and Bridge Bents

The bridge superstructure is 400 ft. in total length with a radius of 660 ft. The cross section of the deck is a box girder with surface width of 22 ft. and dimensions displayed in Figure 3.4. Loads on the deck during analysis and hybrid testing include structural self-weight (pavement, utilities, and finishing). This is represented through lumped masses at nodes along the length of the deck and bent caps, as described in the description of the analytical model in Chapter 4 and displayed in Figure D.15.

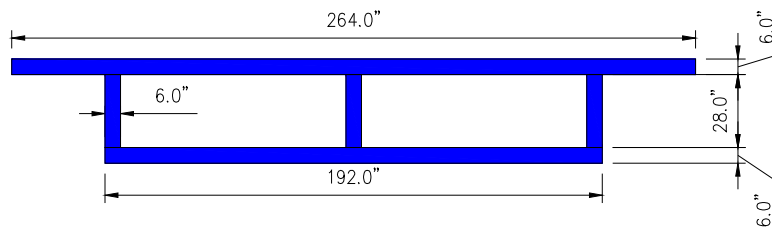


Figure 3.4 Cross-sectional details of bridge box girder

Single pier bents are used in order to develop torsional response in these members. A parametric study was performed using an OpenSees model to determine the most reasonable column locations that generate maximum torsional moments in the piers. This arrangement of piers was selected to obtain a bridge system with a higher level of torsion contributing to the overall interaction effects, as examining this contribution was of particular interest in this study. During this analytical study, it was shown that the highest torsional demands would be placed on the outer two piers of the curved bridge, which are modeled at 1:3 scale. Special effort was made to ensure that the distribution of piers represents a realistic and viable structural design option that could be seen on highway interchanges and exchanges throughout the country. The differences in span lengths and pier heights could easily be necessitated by project site conditions and restraints. The resulting piers are positioned along the curved bridge so that span lengths range from 50' to 150'. Above each pier, the box girder is supported by a 16' cap beam with cross-sectional properties displayed in Figure 3.5.

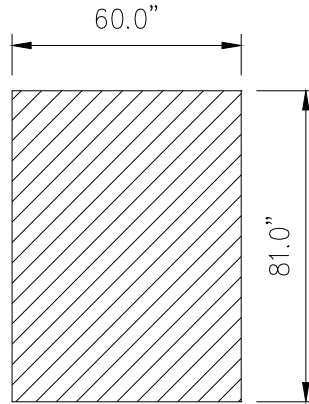


Figure 3.5 Cross-section of bent cap beams

During the hybrid simulation, the bridge deck, cap beams, and abutments are modeled analytically using Zeus-NL. The deck is shown to respond in the elastic range, and therefore the box girder is replaced with a built-up shape of equivalent moments of inertia and torsional stiffness (Figure D.1- Figure D.4). Details on this and other model parameters including material properties, abutment details, and modeling assumptions are described in full detail in Chapter 4 and Appendix D.

iii. Design of RC Piers

The three RC bridge piers all share the same cross-sectional properties (Figure 3.6a), and are of varying lengths. At full scale, the piers have a diameter of 4 ft., with longitudinal reinforcement provided by 28 #10 bars distributed evenly. Transverse reinforcement is a #5 continuous spiral stirrup. At the full scale, the pier heights are 28.5, 37.5, and 22.5 ft., respectively, when viewing from left to right in Figure 3.1. Note that it is the outer two piers that are constructed and tested at 1:3 scale, while the inner pier is tested at 1:20 scale. The 1:3 scale piers are therefore constructed with a diameter of 16", with 17 #4 longitudinal bars and a #3 spiral at 2" pitch and 3/4" cover (Figure 3.6b). Resulting heights are 9.5 and 7.5 ft. respectively for the left and right outer piers. Further information on the construction details and material properties of the 1:3 scale specimens is provided in Appendix A.3 .

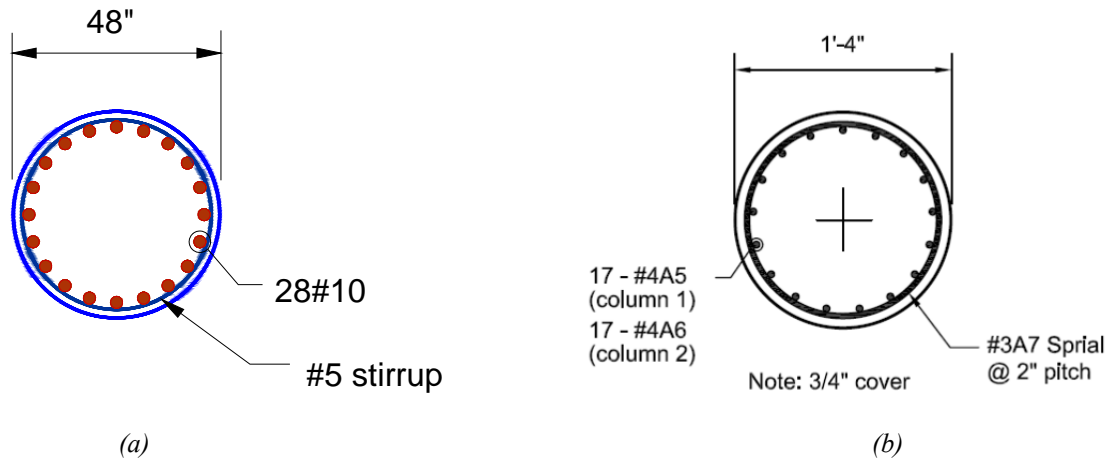


Figure 3.6 a) Cross-section of full-scale piers b) Cross-section of 1:3 scale piers

The inner pier is constructed at 1:20 scale due to its length and in order to accommodate facility space needs. Resulting dimensions are 22.5'' height and 2.4'' diameter. Details on the 1:20 scale inner pier, as well as justification for use of experimental data at this scale is provided later in this chapter.

3.2 Earthquake Input Motion

The applied earthquake record is a synthetically generated accelerogram representative of the seismic zone corresponding to Seattle, WA. The program SPECTRA is used to generate the response spectrum and SIMQKE is utilized to generate time history records. The site location is able to take advantage of the availability of Seattle seismic intensity data in generating the record. For the Seattle site, the short-period acceleration (0.2 sec) is 1.61 g and the 1.0-sec acceleration is 0.56 g for the maximum considered earthquake (MCE) corresponding to the 2,500-year return period. The record is applied as a sequence of imposed MCE records scaled to four performance levels corresponding to estimates of the states of structural response listed below. Estimates on scaling required to reach each performance level is based off of early modeling of the bridge in OpenSees. The design performance level is the third of four 10 second intervals of seismic loading applied to the bridge, and is therefore applied as 1(MCE). The first level is set to the cracking performance level, 0.08 MCE. The second level, at 10-20 seconds of the overall applied record, is the yielding performance level, at 0.3 MCE.

The final 10 seconds of the 40 second record reaches a peak ground acceleration of approximately 0.8g, and represents two times the MCE event. The four levels of excitation are shown in Figure 3.7a, with definition and response spectra for each level plotted in Figure 3.7b.

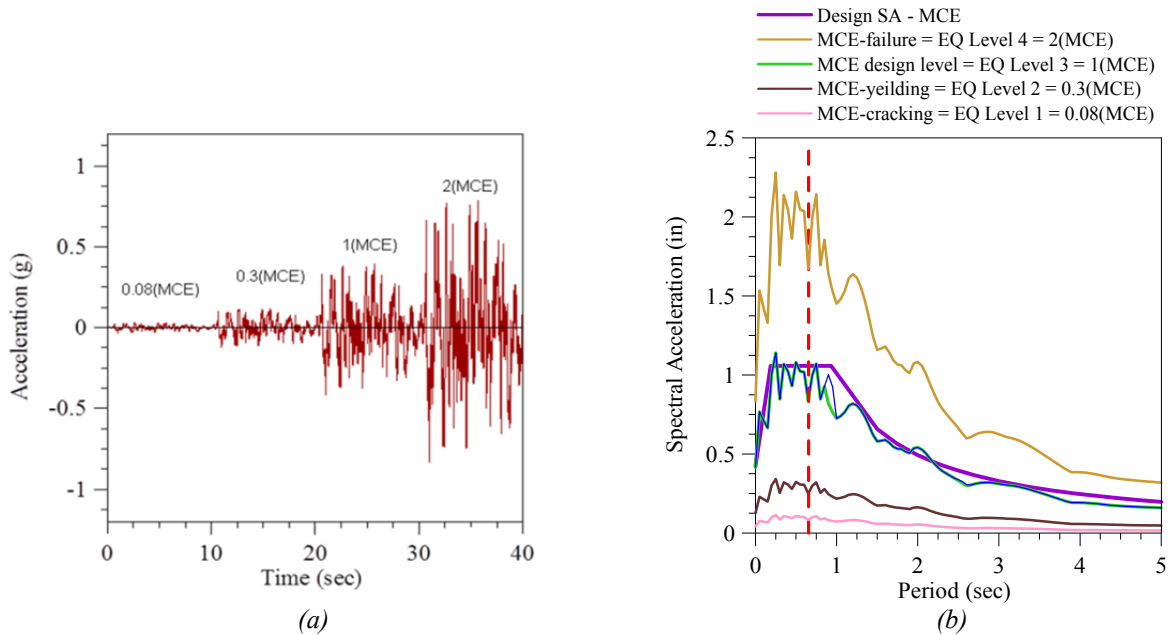


Figure 3.7 a) Levels of earthquake excitation applied b) Performance level definition and response spectra

In the hybrid testing of the curved RC bridge, multi-directional loading is applied. This is simulated through applying 100% of the 40 second record described above in the transverse direction of the bridge, while a 25% scaled version of the record is applied in the longitudinal direction (Figure 3.8). Here, the term multi-directional loading refers to the concept that accelerations are applied to the bridge system in two horizontal directions simultaneously. It is acknowledged that the load application described here differs in some ways from the two components of horizontal loading observed in the readings obtained from a natural record. The application of loading is provided to induce combined interaction effects to the piers, while loading the bridge primarily in the direction that will produce the most conservative results in relation to the stability of the system.

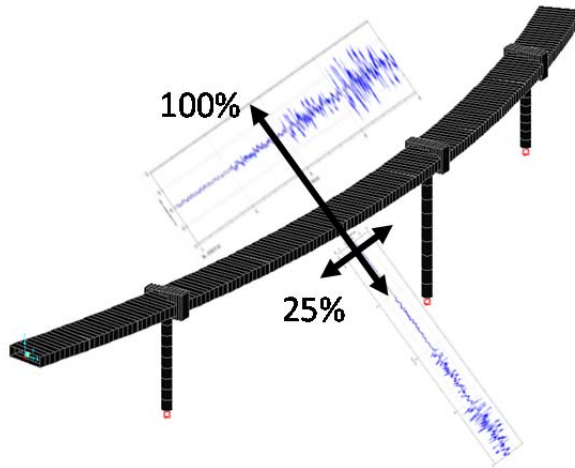


Figure 3.8 Application of multi-directional load

3.3 Hybrid Simulation Procedure

Hybrid simulation is the simulation of structural systems using any combination of computational and experimental testing methods to represent various components of the structure. Traditional experimental and computational approaches can be performed simultaneously through sub-structuring of the given system into separate modules of interest. Through the application of a simulation coordinator platform, communication is enabled between the experimental or computational modules of the structure being analyzed. This allows for increased flexibility in testing programs along with an improvement in the accuracy and efficiency previously available through traditional standalone experimental or computational testing programs (Kwon, Nakata, Elnashai, & Spencer, 2005).

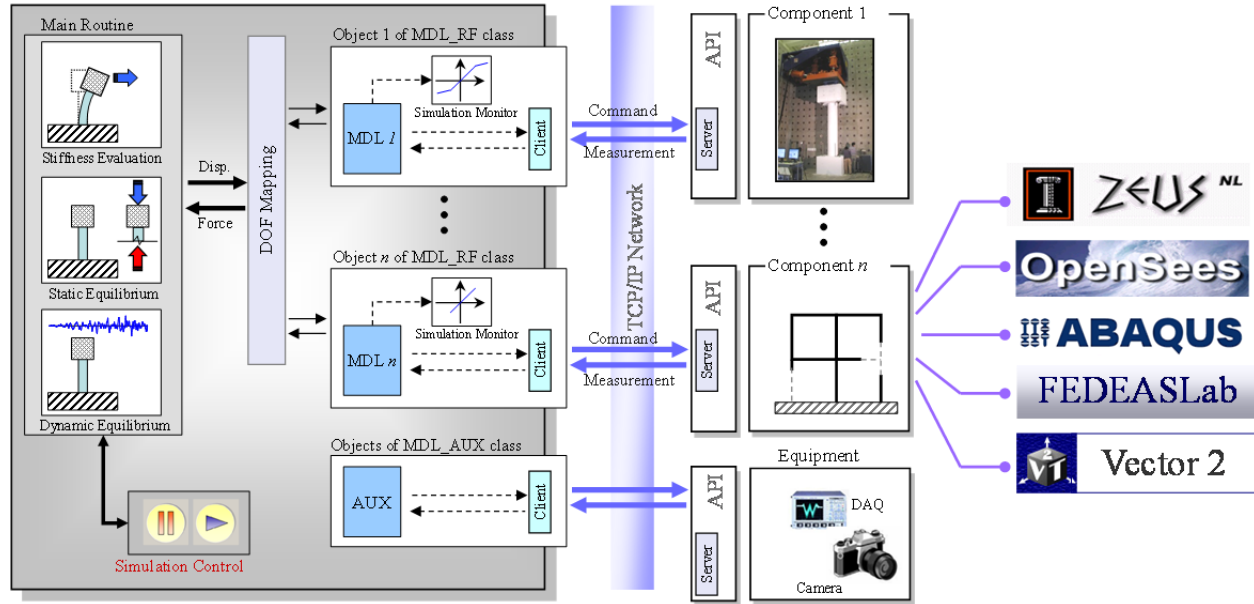


Figure 3.9 Illustration of UI-SimCor communication (Kwon et al. 2005)

In this testing program, hybrid analysis using experimental and analytical components is enabled through the use of the University of Illinois simulation coordinator (UI-SimCor). SimCor provides the communication between modules of an experiment that is necessary in order to perform hybrid analysis and testing. Communication of commands and responses between the various modules is diagrammed in Figure 3.9. Note that it is within the SimCor environment that coordinate transformation and scaling between commands and response for various modules occurs. To account for both unit transformation and geometry scaling factor, the relationship between commands and responses within the two modules is written as

$$d_{\text{scaled}} = \frac{U_L}{S} d_{\text{original}}, r_{\text{scaled}} = r_{\text{original}}, F_{\text{scaled}} = \frac{U_F}{S^2} F_{\text{original}}, M_{\text{scaled}} = \frac{U_F U_L}{S^3} M_{\text{original}} \quad (1)$$

where d , r , F , and M represent the translational and rotational deformations and actions, respectively. The subscripts *scaled* and *original* indicate responses after and prior to the scaling. S is the geometry scaling factor, U_L is the length unit transformation, and U_F is the force unit transformation. These commands and responses are passed to and from a control point that exists on both the analytical and experimental modules (Figure 3.10). This is the data point that deformations are measured at and

rotations are calculated about. Information regarding the actions measured or calculated in experimental or analytical modules is also fed back to SimCor in reference to this point. In addition to providing commands and responses for structural control points between these modules, SimCor also serves to trigger data acquisition devices such as the Krypton non-contact measurement system and cameras.

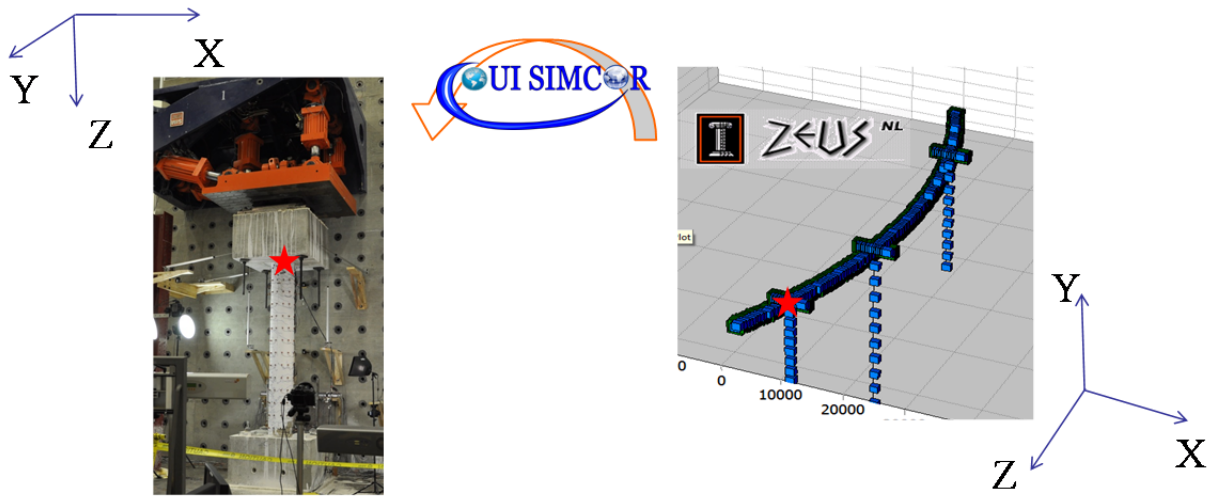


Figure 3.10 Illustration of control point and coordinate transformation via UI-SimCor

It should be noted here that this hybrid test is conducted pseudo-dynamically. This means that the earthquake acceleration was applied in a step-wise fashion and dynamic effects are accounted for numerically. A diagram detailing the hybrid test procedure for each time increment is illustrated below (Figure 3.11). The acceleration time history step is passed into UI-SimCor, which performs numerical time integration and sends displacement targets to the experimental and analytical components of the hybrid simulation. Forces are measured and calculated from the two components and read back into UI-SimCor. Any correction commands are then sent as necessary in order to balance the characteristic equation before proceeding to the next step in the earthquake time history and repeating this process for the next time step.

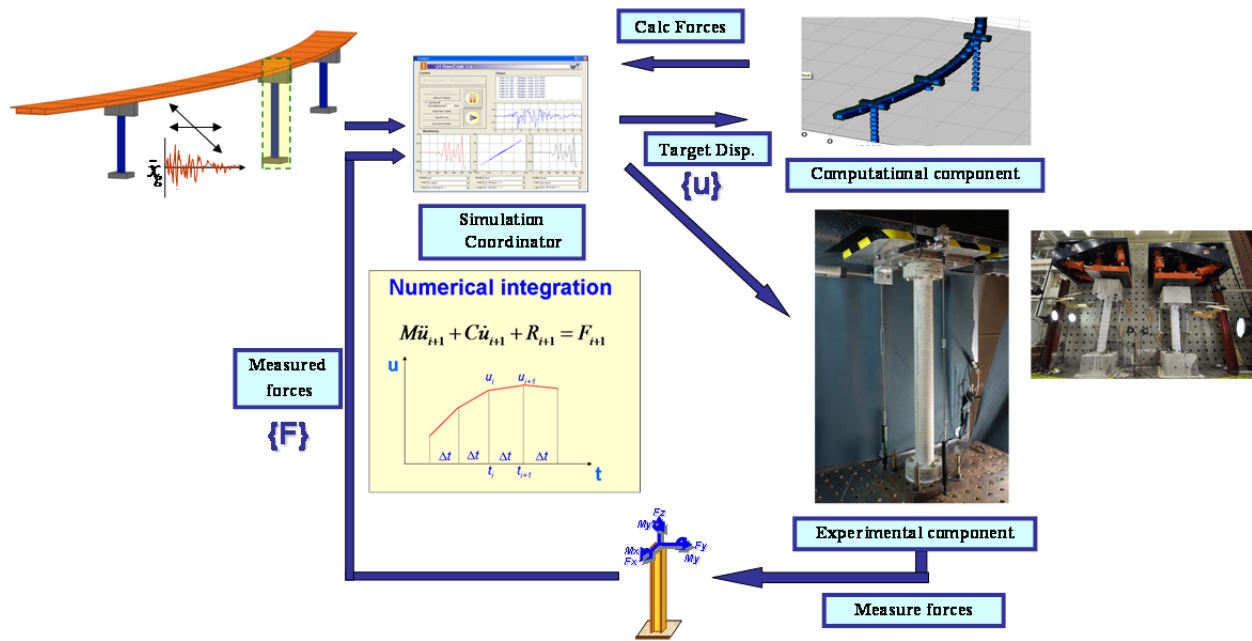


Figure 3.11 Step-wise routine of data flow in hybrid simulation

The advantages of hybrid testing over traditional purely experimental or purely numerical simulations are significant. The flexibility provided by the platform allows for structural components undergoing complex nonlinear hysteretic responses, such as the outer piers, to be conducted as large-scale experimental components. Meanwhile, components responding in their predictable range of linear-elastic response can be simulated numerically without losing accuracy or reliability in the simulation. Space and cost issues, such as those posed by the more slender flexurally-dominant inner pier, can be accommodated by shifting components to other facilities or analytical platforms. In this case, the inner pier is tested in a small-scale facility at the same site.

3.4 Advanced Capabilities and Experimental Methods

An advanced control scheme and hybrid simulation program is developed through a detailed series of analyses and small-scale experimental tests. Prior to the large-scale hybrid test, a series of simulations and experiments are conducted on small-scale piers. The level of combined actions resulting from geometrical asymmetry and complex loading are examined through an analytical

parametric study. Small-scale tests are subsequently performed to test control algorithms and to gain further information on general performance of piers after assessing similitude relationships. The findings from these tests guide the large-scale testing plan by producing capacity envelopes under individual actions and gaining qualitative understanding of complex interactions among axial, flexural, shear, and torsional loading. These results led to a successful large-scale hybrid test implemented in the MUST-SIM facility at the NEES laboratory of the University of Illinois.

i. Six Degree of Freedom Control Capabilities

The testing of the experimental components of this program is enabled by the unique six degree-of-freedom (6DOF) loading units and advanced controls software available at the Illinois MUST-SIM testing facility. The two 1:3 scale piers are tested using the large scale 6DOF Load and Boundary Condition Boxes (LBCBs). The inner pier at 1:20 scale is tested in a small-scale portable LBCB reaction frame at the same facility. The LBCBs can be moved about and fixtured to a large-scale L-shaped reaction wall. The LBCB control algorithm translates stroke of six linear actuators into three-dimensional global Cartesian space (Figure 3.12). As a result, a mixture of multiple DOF displacements and forces for testing structural components can be simultaneously employed.

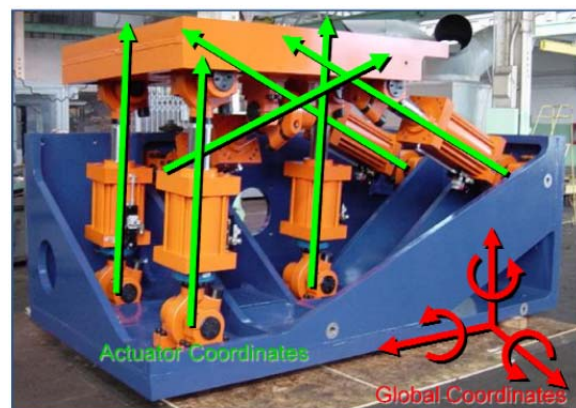
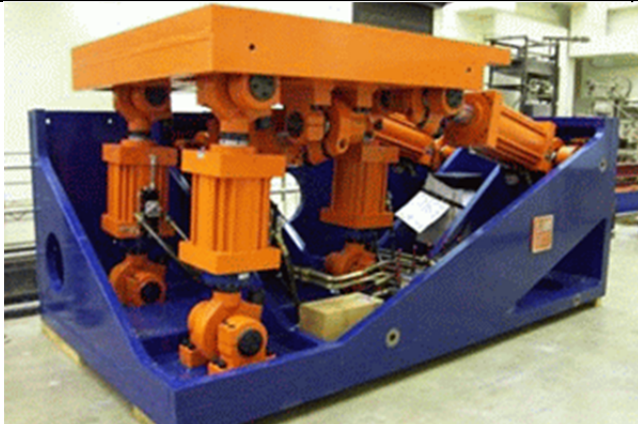
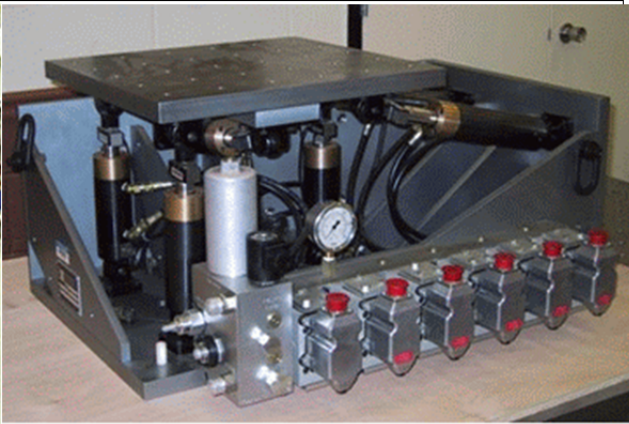


Figure 3.12 LBCB with actuator and global coordinates

The large-scale boxes contain three vertical actuators and one actuator in the out-of-plane (OOP) direction with stroke capacities of +/- 5 inches. The remaining two actuators run parallel to the wall face, and have a stroke of +/- 10 inches. Force capacity is 328 kips in compression, and 216 kips in tension. In terms of 6DOF global Cartesian force capacity, this amounts to 432/656 kips, 216/328 kips, and 648/984 kips in the x , y , and z directions for tension and compression, respectively. Small-scale LBCBs of 1:5 geometric scale are available for testing as well, and utilized on the inner pier in this study. Both large- and small-scale boxes are capable of generating approximately $\pm 11.8^\circ$, $\pm 16^\circ$, and $\pm 16^\circ$ in the r_x , r_y , and r_z rotations, respectively. The stroke and force capacities for the large and small-scale LBCB actuators are provided in Table 3.1. The unique capabilities of the LBCBs enables for realistic boundary conditions in all six degrees of freedom at the control point of the piers.

Table 3.1 Stroke and force capacities of LBCBs

Large-scale LBCB		Small-scale LBCB	
			
<i>Stroke Capacity</i>	<i>Force Capacity</i>	<i>Stroke Capacity</i>	<i>Force Capacity</i>
+/- 10'' (IP)	328 kips (C)	+/- 2'' (IP)	3 kips (C)
+/- 5'' (OOP / Vertical)	216 kips (T)	+/- 1'' (OOP / Vertical)	3 kips (T)

ii. Compensation for Deformations in Test Setup

Using the loading units described above, a number of displacements or forces can be applied to the test specimen, resulting in better understanding of structural behavior. However, when using these

complex LBCBs, it is critical to be able to control and monitor displacements with a high degree of accuracy. This is a non-trivial objective for many reasons. For example, the load capacity of LBCB boxes is high enough to induce significant deformations in surrounding non-specimen components, due to the finite stiffness of the loading units and reaction frame. The connections between the LBCB, specimen, strong wall, and strong floor may also introduce deformation or slippage that can result in incorrect calculated deformations and stiffness of specimens if neglected.

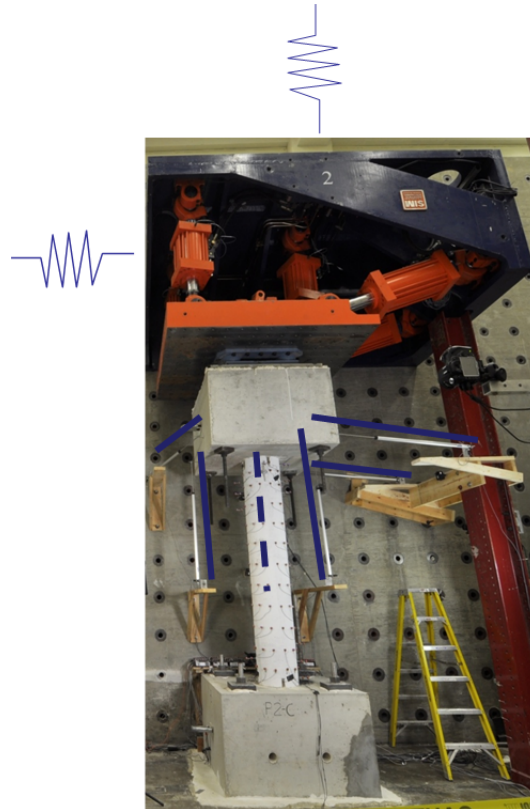


Figure 3.13 External control sensors for deformation correction procedure

Therefore, an alternative approach is used in place of relying on the readings of displacement transducers located inside of the individual LBCB actuators. External displacement sensors are connected to the specimen in order to improve the accuracy of monitoring the control point of the specimen. The control point is the shared point between experimental and analytical modules of the hybrid test, and is the target of the applied displacement and force commands in the experimental components. Six linear displacement sensors are needed for each of the piers in order to obtain accurate measurements of the control point in 3D space (Figure 3.13).

To do so, the ‘free’ end of the LVDT sensors are directly connected to the specimen and the ‘fixed’ ends are connected to solid brackets mounted to the reaction wall. Due to complicated geometry, the conversion from the measured displacements of linear external sensors to the Cartesian space of the LBCB platform is not straightforward. To fully capture 6DOF displacements, one LVDT must be in the first axis, two in the second axis, and three in the third axis. These LVDTs can be skewed if necessary, as long as they are primarily in the direction of the aforementioned axes. A set of equations must be developed to convert from Cartesian to the sensor space as follows:

$$\mathbf{x}_{i,\text{new}}^{\text{free}} = \mathbf{T}_1 \mathbf{T}_2 \mathbf{T}_3 \mathbf{x}_{i,\text{original}}^{\text{free}} + \begin{bmatrix} x^{\text{cp}} \\ y^{\text{cp}} \\ z^{\text{cp}} \end{bmatrix} \quad (2)$$

$$d_i = \|\mathbf{x}_{i,\text{new}}^{\text{free}} - \mathbf{x}_i^{\text{fixed}}\| - \|\mathbf{x}_{i,\text{original}}^{\text{free}} - \mathbf{x}_i^{\text{fixed}}\|$$

where

$$\mathbf{T}_1 = \begin{bmatrix} 1 & 0 & 0 \\ 0 & \cos(\theta_x^{\text{cp}}) & -\sin(\theta_x^{\text{cp}}) \\ 0 & \sin(\theta_x^{\text{cp}}) & \cos(\theta_x^{\text{cp}}) \end{bmatrix}, \mathbf{T}_2 = \begin{bmatrix} \cos(\theta_y^{\text{cp}}) & 0 & \sin(\theta_y^{\text{cp}}) \\ 0 & 1 & 0 \\ -\sin(\theta_y^{\text{cp}}) & 0 & \cos(\theta_y^{\text{cp}}) \end{bmatrix}, \mathbf{T}_3 = \begin{bmatrix} \cos(\theta_z^{\text{cp}}) & -\sin(\theta_z^{\text{cp}}) & 0 \\ \sin(\theta_z^{\text{cp}}) & \cos(\theta_z^{\text{cp}}) & 0 \\ 0 & 0 & 1 \end{bmatrix} \quad (3)$$

$\mathbf{x}^{\text{cp}} = [x^{\text{cp}} \quad y^{\text{cp}} \quad z^{\text{cp}} \quad \theta_x^{\text{cp}} \quad \theta_y^{\text{cp}} \quad \theta_z^{\text{cp}}]^T$ is a given displacement vector described in terms of the 6 DOFs at the control point; $\mathbf{x}_{i,\text{original}}^{\text{free}}$ and $\mathbf{x}_i^{\text{fixed}}$ are the initial free-pin and fixed-pin coordinates of the i -th LVDT; $\mathbf{x}_{i,\text{new}}^{\text{free}}$ is the updated free-pin coordinates of the i -th LVDT; and d_i is the differential displacement of the i -th LVDT after the specimen moves. This conversion from Cartesian space to LVDT sensor space in Eq. (2) is straightforward. In contrast, the inverse conversion, from the sensor space to the Cartesian space, is a highly nonlinear problem that requires a nonlinear solver to obtain the displacements at the control point. To prevent a convergence issue, a number of conditions can be added. These are represented by

$$\|\mathbf{x}_{i,\text{new}}^{\text{free}} - \mathbf{x}_{j,\text{new}}^{\text{free}}\| = \|\mathbf{x}_{i,\text{original}}^{\text{free}} - \mathbf{x}_{j,\text{original}}^{\text{free}}\|, \quad i, j = 1 \sim n \quad (4)$$

where n is the number of LVDTs being used. Because all free pins travel in rigid-body motion, the distance from one pin to another is constant. This is of course assuming that rigid body motion holds for the oversized top cap of the piers, where the free ends of the sensors are attached.

With the ability to read and translate control point deformations measured by these six external sensors to and from the Cartesian displacements, the deformation correction algorithm can be applied to send corrected commands to the specimen. When displacements outside of the specimens occur, the hydraulic actuators and their internal sensors cannot accurately represent the true deformations realized by the specimens, despite the fact that the readings from the loading units indicate that the target displacements have been achieved. In order to account for these external deformations, an iterative process is performed to correct for these undesired displacement differentials. By combining Eq. (2) and (4), the actual displacement of the specimen can be read. The command to the actuators of the LBCB boxes is then adjusted at the end of a time step, as shown in

$$\mathbf{x}_{l,k+1}^{\text{cmd}} = \mathbf{x}_{l,k}^{\text{cmd}} + (\mathbf{x}_l^{\text{target}} - \mathbf{x}_{l,k}^{\text{cp}}) \quad (5)$$

where $\mathbf{x}_{l,k}^{\text{cmd}}$ and $\mathbf{x}_{l,k+1}^{\text{cmd}}$ represent the commands at the iterative k -th and $(k+1)$ -th correction steps of the l -th time step, and $\mathbf{x}_l^{\text{target}}$ and $\mathbf{x}_{l,k}^{\text{cp}}$ indicate the target displacement and current position of the control point, respectively. In many cases, this process needs to be applied multiple times within a single time step. With a predefined tolerance limit set, the iterative process will continue until

$$|y_l^{\text{target}} - y_{l,k}^{\text{cp}}| \leq m, y \in \mathbf{x} = \{x \quad y \quad z \quad \theta_x \quad \theta_y \quad \theta_z\}, m \in \{\delta_x \quad \delta_y \quad \delta_z \quad \delta_{\theta_x} \quad \delta_{\theta_y} \quad \delta_{\theta_z}\} \quad (6)$$

where the δ terms indicate the tolerance specified for each DOF. In Eq. (6), each controlled DOF must satisfy the above condition in order to exit the iterative algorithm. If overshooting of the original target displacement is observed, Eq. (5) may have a correction factor applied by the user that automatically reduces the correction amount by a certain factor within each correction step. After the achieved displacement satisfies the tolerance, a small amount of error smaller than the given tolerance will still exist. A preliminary adjustment value, which is determined from the difference between the achieved and target displacements at the end of a given time step, is then compensated for in the next time step before further correction steps are applied. By combining these two features, a complete form of the correction procedure can be represented by

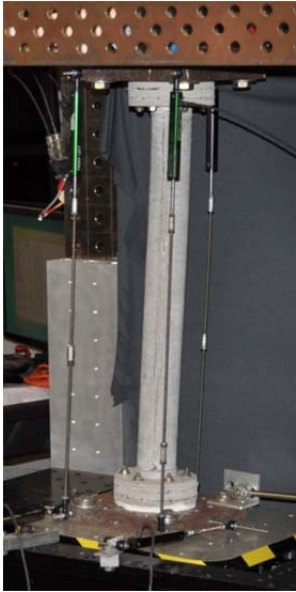
$$\begin{aligned}\mathbf{x}_{l,0}^{\text{cmd}} &= \mathbf{x}_l^{\text{target}} + \alpha (\mathbf{x}_{l-1}^{\text{target}} - \mathbf{x}_{l-1}^{\text{cp}}), \quad \alpha = 0 \text{ or } 1 \\ \mathbf{x}_{l,k+1}^{\text{cmd}} &= \mathbf{x}_{l,k}^{\text{cmd}} + \beta (\mathbf{x}_l^{\text{target}} - \mathbf{x}_{l,k}^{\text{cp}}), \quad \beta = 0 \sim 1\end{aligned}\tag{7}$$

where $\alpha = 1$ indicates the use of preliminary adjustment values, and β is the correction factor, both of which can be manually adjusted at each time step.

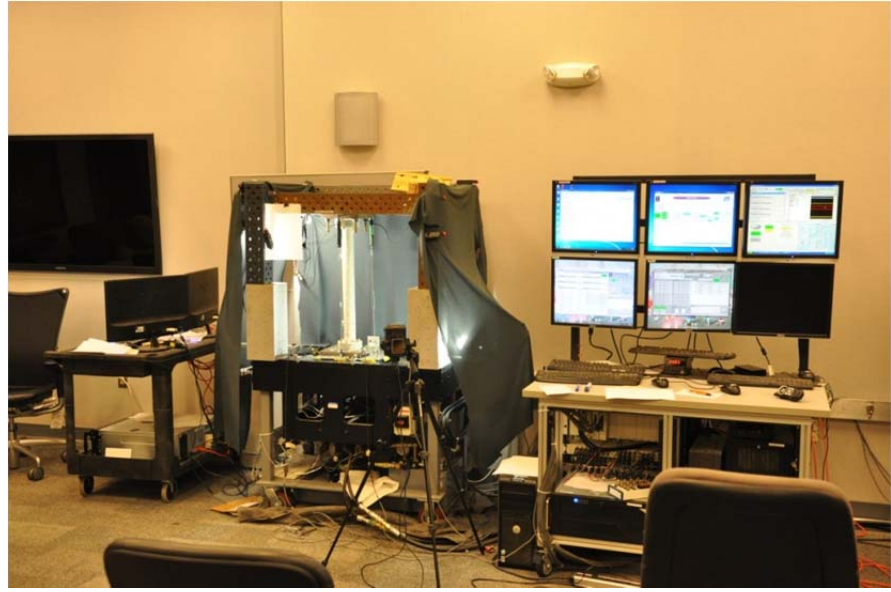
Using this approach, the positioning/force control achieves the response targets through a number of iterative correction steps. These steps appropriately account for the elastic deformation and slip that have the potential to occur in the experimental components of the hybrid testing. Together, the use of 6DOF external sensor displacement monitoring and the deformation correction algorithm provides the most realistic and precise representation of stiffness values and structural behavior that can be achieved through the use of experimental equipment and materials with finite stiffnesses.

iii. Justification of Small-Scale Testing

In discussing the suitability of this hybrid test for use in realistic model calibration, the reasons for implementing a 1:20 scale specimen to represent the inner pier must be explained, described in detail, and justified. Due to its aspect ratio and relative height compared to the two outside piers, it was not possible to test all three piers at 1:3 scale. This is due to height restrictions of the reaction wall at the NEES MUST-SIM laboratory. Secondly, due to other space needs for additional large-scale testing for other projects, it was determined necessary to allow for other tests to be conducted using the third large-scale LBCB parallel to the efforts of the hybrid test described here. The resulting small-scale test setup is shown in Figure 3.14. The 1:20 scale pier is connected to the small-scale LBCB reaction frame and instrumented with six external sensors for deformation correction calculations.



(a)



(b)

Figure 3.14 a) Small-scale specimen with external sensors b) Small-scale test setup

The constructed dimensions of the small-scale pier include a length of 22.5 inches and diameter of 2.4 inches. Details of the reinforcement and caps are provided in Appendix A.2 . The scaled down longitudinal reinforcement consists of 3-48 threaded rods to achieve the desired reinforcement ratio with an appropriate number and distribution of rods. These rods are annealed at 1000°F in order to achieve the target stress-strain response of the 1:3 scale longitudinal steel. Transverse reinforcement is provided by annealed wire of 0.0348 inch diameter. A micro-concrete mix is prepared using appropriately scaled and graded aggregate, along with Type III cement to achieve the desired characteristics, including an early-age compressive strength of approximately 5 ksi.

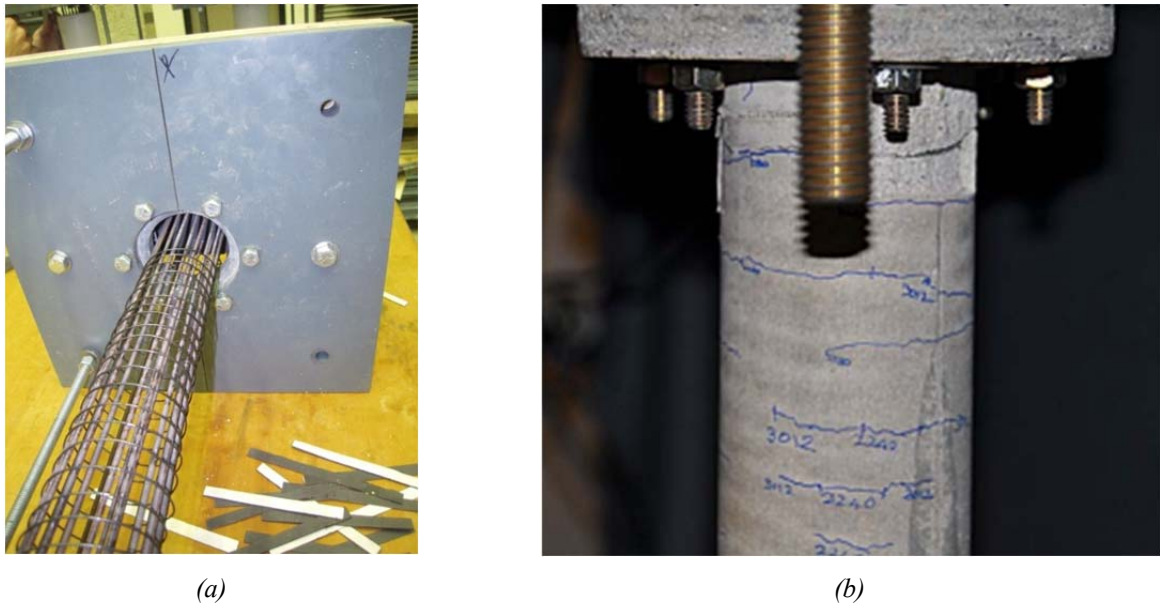


Figure 3.15 a) Reinforcement cage and cap formwork b) Small-scale flexural cracks

Piers are cast using PVC and wood formwork. Micro-concrete is poured and consolidated using a vibrating table, and specimens are cured for 7 days prior to form removal. The reinforcement cage prior to enclosure of formwork is shown in Figure 3.15a. Additional details regarding fabrication, formwork, mix design, and casting methods are provided in Appendix A.2 . The specimens are capped with hydrocal to remove potential stress concentrations from developing at the caps when connected for testing. The specimens are considered ready for testing any time after reaching their 14 day strength, with minimal strength gain occurring after this time.

Comparisons from large-scale and small-scale piers for past programs provides a great deal of certainty in the ability of the small-scale testing program to accurately represent the global response of this inner pier at 1:20 scale. This certainty is aided by the fact that the pier response is primarily dominated by flexure, even with the influence of multi-directional loading and curved geometry (Figure 3.15b). The similitude relationships for developing a level of repeatability and certainty in these small-scale test specimens are based on extensive studies by (Holub, 2005). A methodology for consistent and accurate small-scale fabrication of reinforced concrete piers was developed in this and other previous work performed by the author at the Illinois NEES site. In this study, a very similar method was adopted to previous fabrication procedures, with changes made only to accommodate for minor differences in specimen geometry and reinforcement ratio.

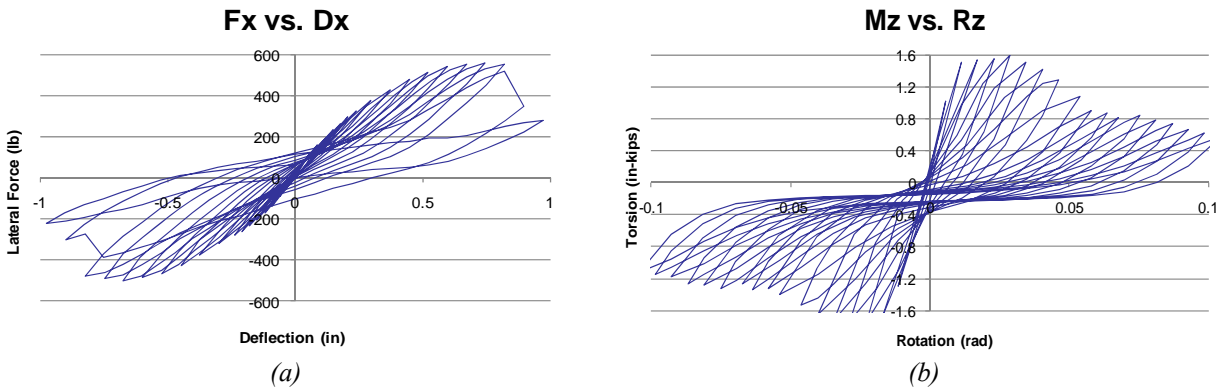


Figure 3.16 Envelope testing of 1:20 scale pier a) lateral b) torsional

Small-scale testing was utilized in development of the hybrid 6DOF test and also served to develop a mature small-scale testing program for preparation of future hybrid tests. Multiple specimens were produced and tested in the small-scale facility in order to ensure repeatability. Initial evaluation included envelope testing of the piers in pure lateral loading and pure torsional loading (Figure 3.16). The resulting relationships under individual actions were used in test setup considerations that led to additional small-scale hybrid testing before moving into the large-scale facility. First, an individual 1:20 scale pier identical to the one used in the final hybrid test including 1:3 scale piers was the only component modeled experimentally. Then, a full hybrid test with all three piers of varying aspect ratios tested at 1:20 scale was conducted (Figure 3.17). This served to confirm 6DOF control capabilities, and informed decisions on instrumentation location, loading algorithms, and test setup for the final simulation.



Figure 3.17 Two pier setup from small-scale hybrid simulation

Additionally, since the final large-scale hybrid simulation utilizes the same 1:20 scale center pier as the full small-scale hybrid simulation, the responses of this identical component from these two tests is compared. Figure 3.18 demonstrates the lateral displacement and rotation responses of this middle pier in the transverse translational and out-of-plane rotational degrees of freedom. The coordinate system used for comparison is that of the Zeus-NL full-scale model, where x is the transverse direction perpendicular to the primary direction of the bridge deck, and z is the longitudinal direction parallel to the primary direction of the bridge span. Therefore, r_z is the out-of-plane rotation of the top of the pier. The responses match very well all the way through the design-level excitation (which occurs from 20-30 seconds), and do not differ significantly until the small-scale specimen softens slightly more than the large-scale specimen at the end of this range. Still, the qualitative response matches very well even after this point. Additionally, the varying responses are also affected by the influence of the full system-level behavior which differs some due to the use of the two large-scale piers in the latter simulation. The results presented in this figure support the claims that repeatability can be achieved for these carefully constructed and tested small-scale specimens, particularly up to the design-level excitation.

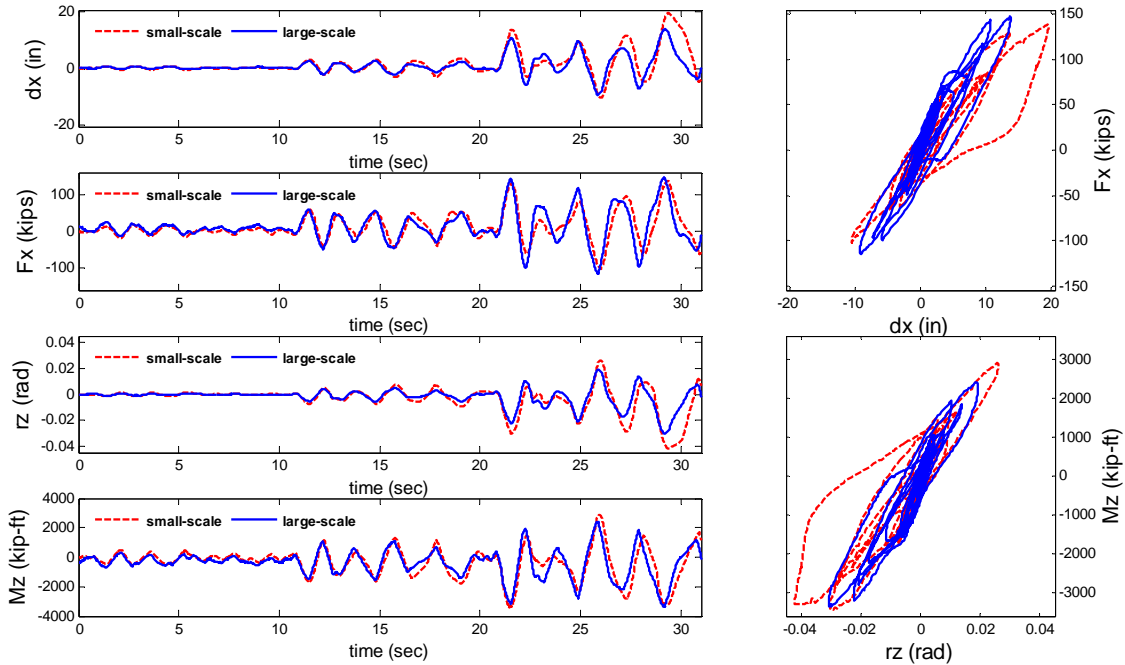


Figure 3.18 Comparison of middle 1:20 scale pier between small- and large-scale hybrid simulations

iv. Post-record structural capacity assessment

Following the completion of the hybrid simulation under the earthquake time history, a series of tests were performed to assess the remaining capacities of the piers (Figure 3.19). These tests included assessing various combinations of torsional, lateral, and axial capacities of the two large-scale piers. Combined lateral and torsional actions were imposed with boundary conditions set to examine both single and double curvature of the piers. These tests were conducted to the extent that the piers reached a plastic response in the torsional direction. Axial load at large lateral drift levels was varied to assess higher levels of flexural capacity. Finally, axial capacity in both compression and tension was evaluated to the extent that the piers lost all structural integrity. The residual capacities of the piers are used in determining upper-limit definitions of the failure limit state and for post-peak behavior parameters during model calibration.

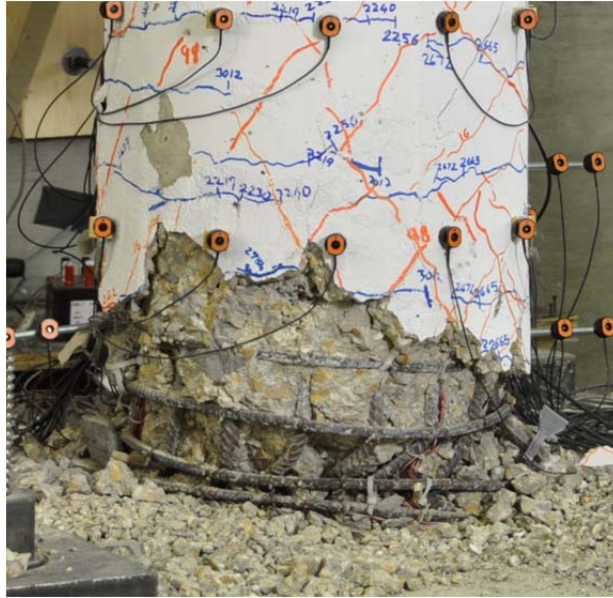


Figure 3.19 Post-earthquake capacity testing

3.5 Dense Data Acquisition

High quality and dense data acquisition methods are essential for producing the data necessary to fully represent the structural response observed during the hybrid test introduced in this study.

Examining the types and quality of the data obtained is particularly important when considering the role this data plays in the model calibration procedure described in Section 4.2 . Instrumentation that is inherently built into the loading platforms includes load cells and displacement transducers in each of the individual linear actuators of the LBCBs. The force and displacement measurements from these instruments are converted to global 6DOF actions and deformations. An overview of the additional external instrumentation is provided here, with descriptions following.

- 152 embedded steel strain gages
- 16 concrete surface strain gages
- 6 out-of-plan translation measurements
- 6 displacement measurements monitoring slip/uplift
- 12 displacement control sensors connected to the correction algorithm described above
- 200 Krypton LED data points
- 12 D-SLR cameras for crack pattern images

The overall instrumentation setup of the two piers is shown in Figure 3.20. Additional details, including drawings and photos of instrumentation layout, are located in Appendices A and B.

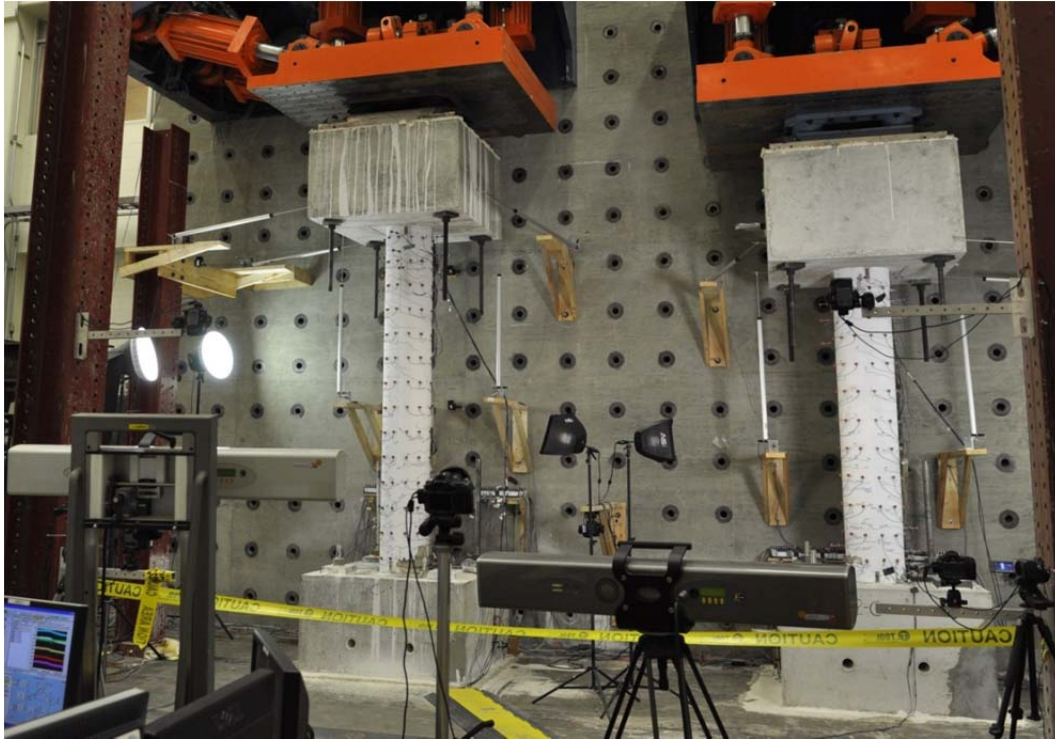


Figure 3.20 Broad view of instrumentation setup

i. Traditional Instrumentation

Traditional instrumentation discussed here includes strain gages, load cells, and linear displacement transducers. These instruments are either a part of the loading units, embedded in the specimens, applied to the surface of the piers, or are connected between the specimen and a stationary reference frame. Locations for embedded steel strain gages of the longitudinal and transverse reinforcement are provided in Appendix B.2 . Concrete surface strain gages are placed at the base and top of each of the piers, in the four locations above the embedded longitudinal gages. String potentiometers are connected to the back face of each of the piers to monitor out of plane displacements, while transducers are connected to the bottom caps to monitor for potential slip and uplift. Finally, the

external sensors utilized in the deformation correction algorithm described above are connected as shown in Appendix B.1 and B.2 .

ii. Advanced Non-Contact Instrumentation

Advanced non-contact instrumentation measuring three-dimensional displacements of specified points on a structural member can be post-processed to develop various strains, 6DOF deformations, and curvature of the instrumented specimen. These features allow for the investigation of both global and local behavior, including identifying strains associated with and capable of predicting cracking and concrete spalling. Additionally, the data provides understanding of the distributed response across the length of the member, in addition to the global actions and deformations at the boundary conditions. In each case, non-contact instrumentation data can be calculated and represented visually to yield further detailed understanding of the nonlinear behavior of structures.

The non-contact instrumentation systems utilized in this test are the Krypton K600 measurement system, as well as twelve D-SLR cameras. The Krypton camera uses light emitting diode (LED) targets to track points on the specimen in three dimensional space. The accuracy of these measurements is approximately 0.0004 inches (0.01 mm). The camera is capable of localizing a maximum of 256 LED target positions within a measurement volume of 600 ft³ (17 m³). This accuracy, combined with the number of targets that can be accommodated on the surface of the piers (Figure B.12) allows for high resolution 3D data of the deformation behavior of the piers to be obtained.



Figure 3.21 Krypton K600 cameras

A separate K600 camera was used for each of the 1:3 scale piers (Figure 3.21). Pier 1 utilized 120 targets, as shown in Figure B.13. Pier 2, the shorter pier, utilized 80 (Figure B.14). Targets were mounted on the surface of the piers, as well as on threaded rods embedded into the specimen at the top and bottom of each of the piers. This second set of targets served two purposes. First, they allowed for an improved measurement in the curvature of the piers close to the pier-cap interface. Secondly, the embedded rods ensured that deformation and curvature measurements would continue to be obtained even at later points in the earthquake time history when higher levels of deformation result in spalling of concrete in these regions.

As Krypton measurements only generate relative displacement histories of the LED target positions in 3D space, it is useful to convert this position data into the 6DOF deformations utilized in other aspects of the hybrid simulation. This allows for the full utilization of this non-contact instrumentation data in conjunction with other measurements. In order to make this conversion, a group of LEDs is assumed to move in rigid-body motion that has the following relationship:

$$\mathbf{x}_k = \mathbf{T}_1 \mathbf{T}_2 \mathbf{T}_3 \mathbf{x}_0 + [d_x \quad d_y \quad d_z]^T \quad (8)$$

where

$$\mathbf{T}_1 = \begin{bmatrix} 1 & 0 & 0 \\ 0 & \cos(\theta_x) & -\sin(\theta_x) \\ 0 & \sin(\theta_x) & \cos(\theta_x) \end{bmatrix}, \mathbf{T}_2 = \begin{bmatrix} \cos(\theta_y) & 0 & \sin(\theta_y) \\ 0 & 1 & 0 \\ -\sin(\theta_y) & 0 & \cos(\theta_y) \end{bmatrix}, \mathbf{T}_3 = \begin{bmatrix} \cos(\theta_z) & -\sin(\theta_z) & 0 \\ \sin(\theta_z) & \cos(\theta_z) & 0 \\ 0 & 0 & 1 \end{bmatrix} \quad (9)$$

and d_x , d_y , and d_z are translational displacements, and θ_x , θ_y , and θ_z , are rotational deformations. To solve this geometric problem, a least-squares solver can be used. In this case, at least three LEDs are required in order to perform the 6DOF displacement conversion, with increasing precision with increasing data points. It is noted that this problem only contains six variables, and that six values can be obtained from the displacement histories of two Krypton targets. However, considering the data of two LEDs may result in incorrect calculation of associated rotations. By specifying an appropriate group of LEDs, 6DOF displacements can be generated with respect to the region of these targets.

D-SLR cameras are mounted around the test setup in order to produce a history of crack development and propagation. Sample photos from each of the camera locations at the 5 second intervals throughout the test are provided in Digital Appendix C.2 . Each of the cameras, Krypton and D-SLR, are triggered by UI-SimCor at the same time that step data is sampled for all of the other traditional data acquisition methods. These photos and Krypton data can be used to develop stop-motion style videos of the response of the piers during the test. Synchronizing these videos with global and local structural response data provide improved understanding of the response of the piers. These and other visualization techniques are discussed in the following section.

iii. Visualization of test data

Visualization of test data is an extremely helpful tool for gaining more complete understanding of the structural response of structures and their components. In this study, visualization of test data is primarily accomplished through coupling camera-type data from the Krypton or D-SLR non-contact data acquisition systems with plots or other graphical representations of response data. The Krypton data set can be used to visually examine global and local response behavior. Development and propagation of cracks in D-SLR photos can be superimposed with embedded strain gage data in order to identify shifts in load carrying capacity across the piers by identifying localized yielding and failure. Similarly, many plots or graphical representations of global response data can be displayed

alongside photos in a step-wise manner to develop understanding of the mechanics and phenomena associated with the measured actions and deformations.

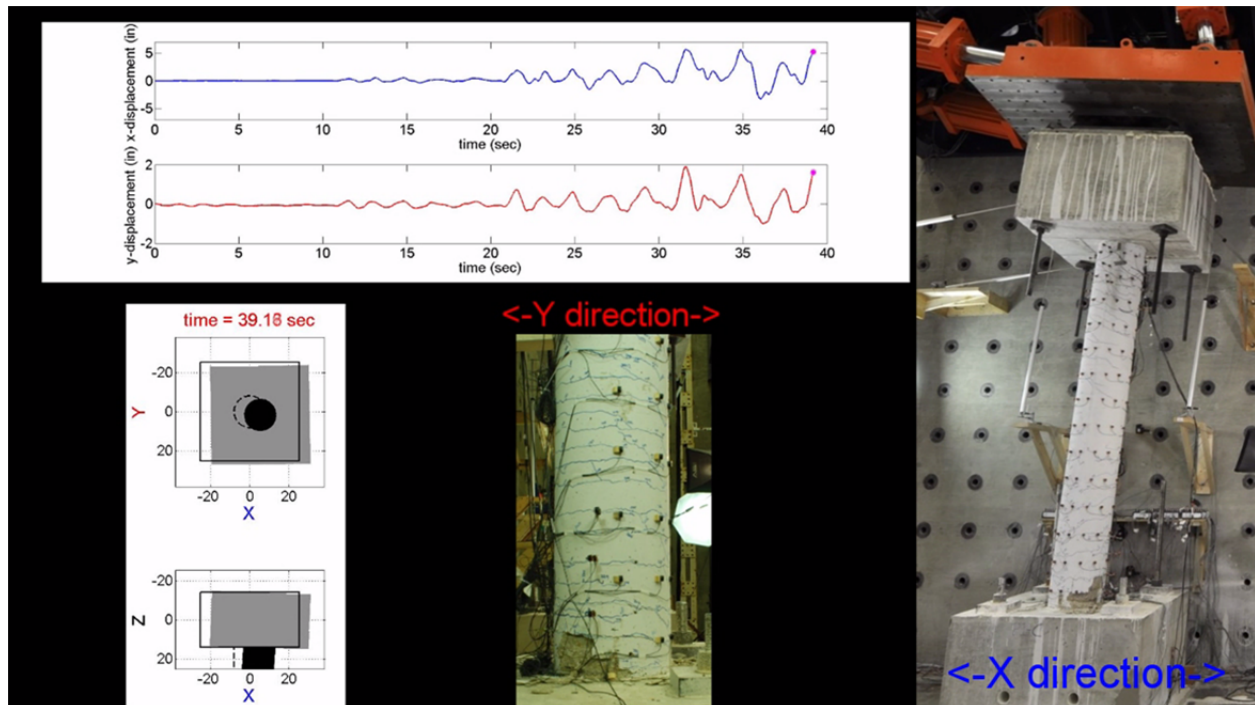


Figure 3.22 Visualization of deformations in piers

Additional methods for data visualization include creating views not captured by Krypton or D-SLR imaging through constructing and animating geometries based off of global response data. An example of this includes a view of the cross-section of the pier that allows for simultaneous visualization of lateral deformations and twist (Figure 3.22). One important procedure that is particularly helpful when considering the influence of structural behavior of the RC piers on the bridge system response is mapping of local strains to global deformations. Following model calibration, global response measurements, such as displacement ductility, are used to indicate performance levels of the bridge. The limit state threshold values that define the boundaries of these performance levels are based off of analysis of test data. Visualization of these results helps to determine what a particular level of global deformation indicates in terms of local cracking of concrete, yielding of longitudinal bars, or other relevant responses.

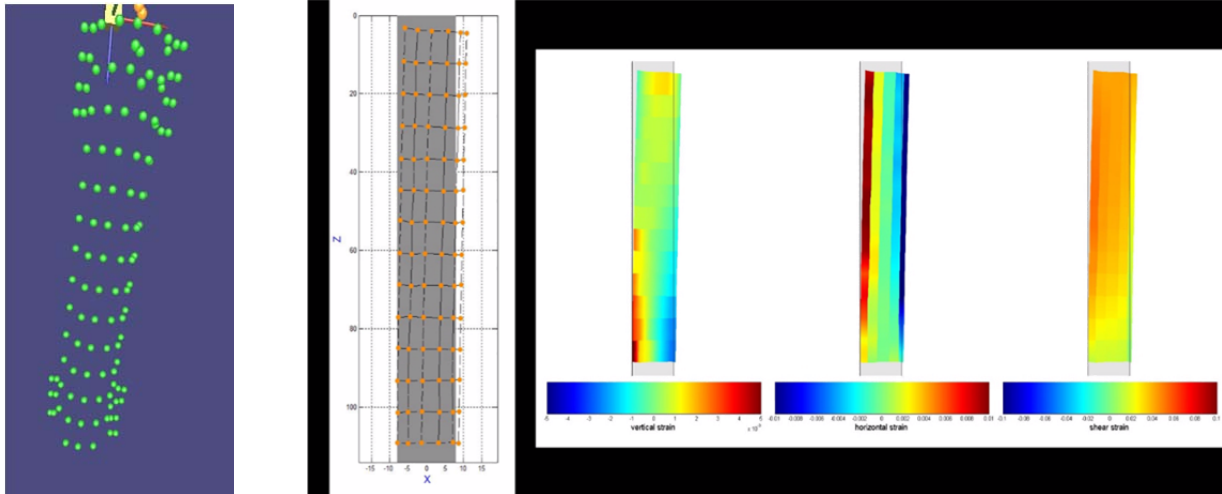


Figure 3.23 Visualization of deformations and strains in piers

The use of Krypton data is particularly helpful in this regard. Overall displacement of targets, as well as relative displacement between targets, allows for the same set of data points to generate visualization tools that yield information on both global and local response. The color-temperature mapping of vertical, horizontal, and shear strains on the surface of the pier (Figure 3.23) enable for seamless visualization of these parameters. The procedure for developing these plots is outlined below.

Plane strains can be calculated from the Krypton data once the uniformly spaced grid of LEDs is aligned with the direction of loading. Each set of four LEDs forms a number of elements derived from interpolating the four measurements into meshes, as shown in Figure 3.24.

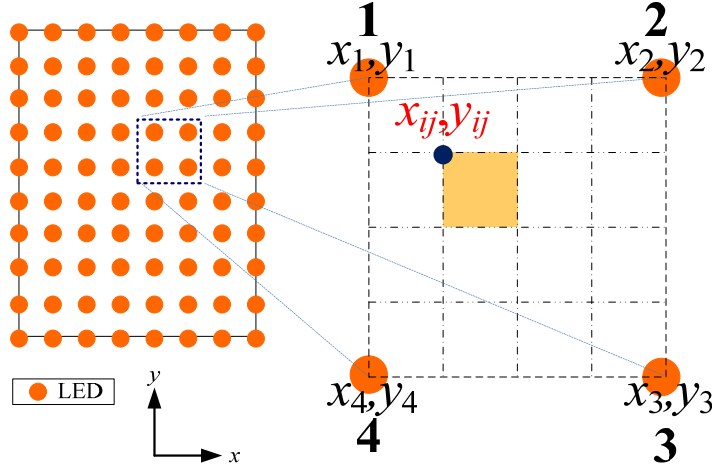


Figure 3.24 Grid of LEDs for interpolation of mesh

The nodes of these meshes are derived from a quadratic form similar to that of the Q4 element utilized in FEA approaches, as shown in

$$\begin{cases} x_{ij} = [(1-m)(1-n) & m(1-n) & mn & (1-m)n][x_1 & x_2 & x_3 & x_4]^T \\ y_{ij} = [(1-n)(1-m) & m(1-n) & mn & (1-m)n][y_1 & y_2 & y_3 & y_4]^T \end{cases} \quad (10)$$

where m and n range between 0 and 1 and indices i and j indicate the element number. The spacing in the x and y directions of the mesh can be different if required. The normal strains in an element are illustrated in Figure 3.25 and are calculated by

$$\varepsilon_{x,k} = \frac{l_{x,k} - l_{x,0}}{l_{x,0}}, \quad \varepsilon_{y,k} = \frac{l_{y,k} - l_{y,0}}{l_{y,0}} \quad (11)$$

where

$$l_{x,k} = \frac{1}{2} \sqrt{(x_{ij,k} + x_{i(j+1),k} - x_{(i+1)j,k} - x_{(i+1)(j+1),k})^2 + (y_{ij,k} + y_{i(j+1),k} - y_{(i+1)j,k} - y_{(i+1)(j+1),k})^2} \quad (12)$$

$$l_{y,k} = \frac{1}{2} \sqrt{(x_{ij,k} + x_{i(j+1),k} - x_{(i+1)j,k} - x_{(i+1)(j+1),k})^2 + (y_{ij,k} + y_{i(j+1),k} - y_{(i+1)j,k} - y_{(i+1)(j+1),k})^2} \quad (13)$$

In Eq. (11), index 0 indicates the initial step, and k indicates the k -th step.

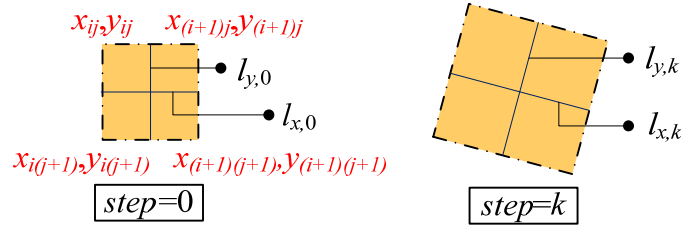


Figure 3.25 Calculation of normal strain values

Shear strain is then derived by the following formulation:

$$\gamma_{xy,k} = \frac{x_{ij,k} + x_{(i+1)j,k} + x_{(i+1)(j+1),k} + x_{i(j+1),k}}{4l_{y,0}} + \frac{y_{ij,k} + y_{(i+1)j,k} + y_{(i+1)(j+1),k} + y_{i(j+1),k}}{4l_{x,0}} - \frac{x_{ij,0} + x_{(i+1)j,0} + x_{(i+1)(j+1),0} + x_{i(j+1),0}}{4l_{y,0}} - \frac{y_{ij,0} + y_{(i+1)j,0} + y_{(i+1)(j+1),0} + y_{i(j+1),0}}{4l_{x,0}} \quad (14)$$

Calculation of shear strain is also displayed in Figure 3.26. In each case, for normal strain and shear strain, the resulting strain values can be interpreted as the strains at the center point of an element, and the approximation that they also represent a constant strain value across the entire element can be made.

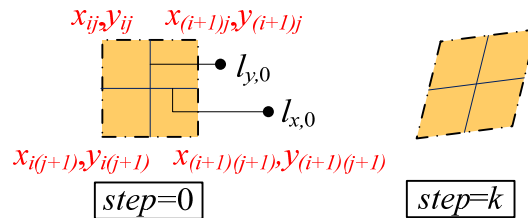


Figure 3.26 Calculation of shear strain values

Ultimately, this derived data enables local strains from the piers to be mapped to the performance limit states of the bridge in terms of global response. Strains plots derived from Krypton data can also be compared to discrete strain values measured along the longitudinal rebar (Figure 3.27). Examination of these temperature plots further contributes to understanding of the formation and

propagation of cracks, occurrence of spalling, and other local and global phenomena observed throughout the simulation.

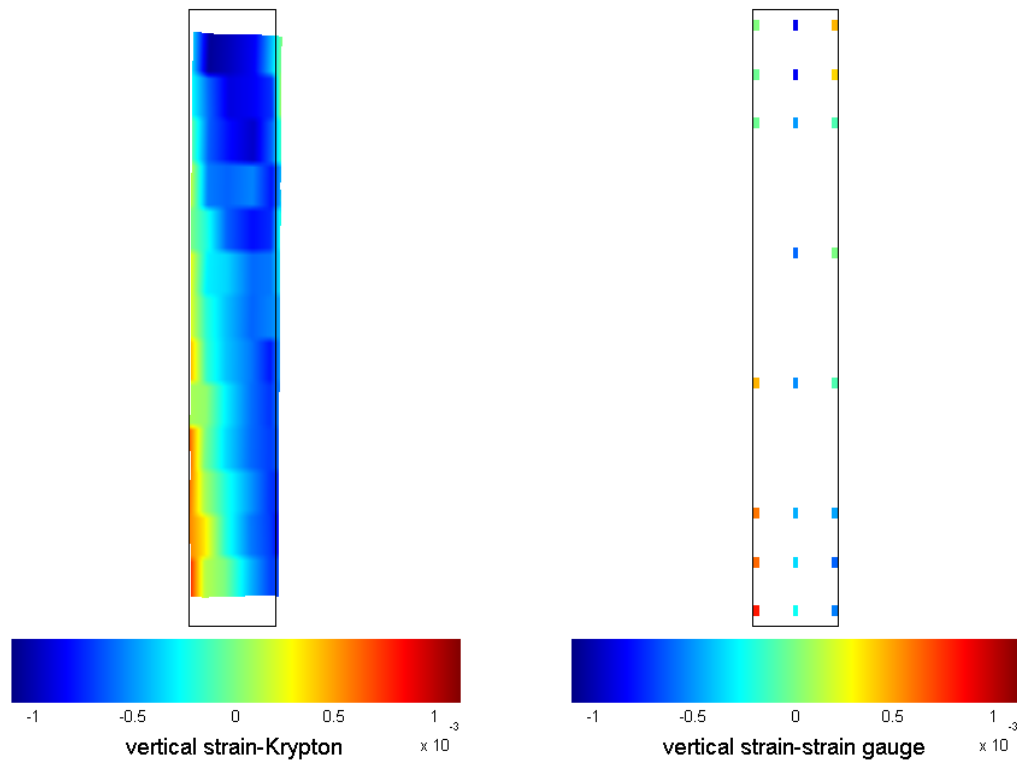


Figure 3.27 Comparison of krypton-derived and embedded gage vertical strain data

3.6 Test Results

The results from the hybrid simulation and capacity testing of the RC bridge piers are now summarized. The data set obtained from the instrumentation plan described above is heavily utilized in the model calibration procedure described in Section 4.2 . This data includes global response data obtained at the control point of each pier, which indicates the overall bridge response characteristics. Assessment of bridge response places particular focus on global deformations in terms of lateral drift of the piers. Additionally, hinge moment-rotation and moment-curvature relationships, as well as torque-twist behavior of the piers are examined. Response histories of these deformations and actions are provided in Appendix C.1 along with images to illustrate resulting crack patterns.

Additionally, the discrete and distributed instrumentation data presented in Appendix C.2 serves to illustrate the effect of combined actions on the piers, as well as the resulting local responses. A summary of longitudinal strain responses of embedded strain gages is provided in Figure C.21 through Figure C.28. Plots are grouped by the upper and lower half of each face of the two piers. The height level of each sensor is indicated in Figure B.10 and the correct reference for pier face labels is displayed in Figure B.18. 6DOF responses across the height of the piers are calculated from Krypton non-contact instrumentation as described above. Examples of this derived data are provided in Figure C.29 through Figure C.34.

Global response data obtained through corrected LBCB data is mapped to local strain gage data to determine the meaning of global parameters in terms crack formation, yielding, and local phenomena. The use of Krypton data for this purpose allows for the simultaneous examination and illustration of the global and local responses of the piers. Finally, a series of key events throughout the hybrid test are selected based off of local and global responses, as well as notes taken throughout the simulation regarding visual observations made. Summaries of structural response of each pier are provided for these key events in Appendix C.4 These results supplement the global and local response data already presented for each DOF of the two large-scale piers. Examination of changes in behavior of the bridge piers at these key data points in the earthquake record reveal a great deal about the response of the piers and the overall bridge subjected to combined actions.

iv. Summary of Results

Highlights of the global results from the hybrid experimental test are provided below:

- Pier 1 deformation response is controlled by predominantly flexural behavior, while Pier 2 exhibits some contribution to deformations and actions from shear response
- Extensive hinge formation in the piers, particularly Pier 1, leads to softening of the piers and period elongation
- The resulting period elongation shifts the dynamic response during the application of the final seismic scaling level
- Stiffness degradation, again particularly for Pier 1, causes greater deformation response demands than was obtained in analytical models
- Several flexural cracks exceeding 1.5mm (0.06 in) are observed on the lower region of face B for Pier 1
- Flexural stiffness and capacity both appear to have been reduced in the large-scale piers due to the influence of torsional softening

- Response shape of the piers in the transverse direction of the bridge is single curvature, while in-plane stiffness of the deck creates restraints that push the piers into double curvature in the longitudinal direction
- Transverse lateral drift at yield for the three piers is approximately 2%, 1%, and 3% respectively.
- Ultimate drift reached in each pier during hybrid simulation is 5.5%, 3.3%, and 6.7% respectively.
- Application of vertical load creates non-negligible rotations and moments at the top interface of the pier
- Torsional loading contributes significantly to formation and propagation of cracks for both piers, regardless of varying degrees of flexural response
- Higher torsion-to-bending ratios are observed in the outer bridge piers closest to the abutments, as compared to the inner pier
- Both flexural and torsional capacity are lower than anticipated due to the result of combined loading

The description of load and control capabilities for the hybrid test supports the use of the data set for model calibration based on the response of this curved four-span bridge. Hybrid simulation has allowed the data set to reflect the influence of the full system-level bridge response on the behavior of the RC bridge piers. Unique loading capabilities allow for control of any combination of deformations and actions in 6DOF for the curved bridge. Complex control and correction algorithms allow for very reliable data on the stiffness of the specimens in each direction. Extensive data acquisition systems have produced dense data that can be easily visualized to obtain conceptual understanding of the structural response, which aids in the development of the experimentally-based model. A great deal of certainty surrounding the data set has therefore been established, justifying use for model calibration that captures the influence of combined actions and full-system response. This high quality data set enables reliable assessment of the influence of curvature, complex loading, and modeling assumptions on seismic vulnerability of RC bridges.

CHAPTER 4: ANALYTICAL ENVIRONMENT

This Chapter provides a summary of the models and procedures employed in the analytical environment in order to produce structural response data for use in the statistical analysis described in Chapter 5. First, a detailed description is provided of the analytical Zeus-NL model utilized for the curved bridge structure. The parameters discussed for this initial model are utilized in the numerical component of the hybrid simulation. Following this description, a detailed overview is provided of the rigorous calibration procedure of the analytical model based on the experimental data set described in Chapter 3 and Appendix C. This procedure adjusts for initially incorrect modeling assumptions affecting stiffness degradation, hysteretic damping, and local mechanisms. The effects of these initial shortcomings are noted, and a series of nonlinear springs are introduced into the Zeus-NL model in order to represent the behavior of the bridge observed in the hybrid simulation.

Following model calibration for three levels of seismic loading, straight bridge models with identical calibrated and non-calibrated parameters to the curved models are developed. A series of nonlinear time history analyses are then performed on these models for a variety of earthquake loading conditions. An outline of the analytical cases to be examined in this study is provided later in Table 4.2. This table details the individual parameters that are varied in order to determine their impact on the seismic vulnerability of RC bridge structures. These variable parameters include bridge curvature, complexity of load application considerations, and the inclusion of the model calibrations introduced in this chapter.

A series of analyses are then performed using a suite of carefully selected earthquake records varying in spectral content, site condition, and magnitude. These analyses are performed under various levels of loading and boundary conditions. Analyzing the response under different uni-directional and multi-directional loading cases reveals the influence of neglecting out-of-plane, vertical, and combined loading. These parameters are varied for curved and straight bridges, each with and without model calibration applied. The results of this analytical study are used to demonstrate the influence of these parameters on the change in bridge performance, and thus seismic vulnerability.

4.1 Initial Un-Calibrated Model

Prior to small-scale testing, the three piers were modeled numerically, along with the superstructure and abutments, using Zeus-NL. This was done in order to gain a preliminary idea of the various phenomena likely to occur in the final test, in order to direct decisions regarding controls and data acquisition plans. The use of the model was valuable in obtaining qualitative understanding of the response of the bridge under complex loads, as well as to anticipate challenges in controlling the experimental specimens within the hybrid platform introduced in Chapter 3.

In this analysis, as in the hybrid test, the deck and transverse beams were assumed to remain in the elastic range during the analysis. This is a typical assumption for box girder-type bridges with rigid superstructures. Additionally, the strains at critical locations along the deck and transverse beams are monitored throughout early analyses to reveal that the strains did not exceed the rupture strain of concrete. Hence, inelasticity and failure are assumed to occur only at the piers and abutments. Therefore, most of the modifications made in order to update and improve the performance of the model are conducted with respect to the piers and their end connections to the foundation and superstructure.

For the purpose of comparison, the original model used to prepare for the hybrid test is referred to as the un-calibrated model from this point forward. Although the abutment and bridge superstructure characteristics of this un-calibrated model are identical to the analytical module employed in the hybrid simulation, the differences between the experimental and analytical response of the piers significantly affect the global system response. This is anticipated, particularly portions of the applied record where the piers reach greater damage levels. Therefore, the structural response data presented in Chapter 3 and described in greater detail in Appendix C is used to update and calibrate various components of the un-calibrated analytical model. In addition to assessing the impact of complex geometry and loading conditions on the vulnerability of RC bridge piers, the effects of these improvements to the performance of the analytical model are selected as one of the parameters affecting fragility functions of RC bridges.

It should be noted that the effectiveness of splitting up a structure into various models using the UI-SimCor hybrid simulation platform has been proved to have a negligible effect on structural response of the system. Prior to experimental hybrid simulation, two analytical tests were performed to

validate the use of the hybrid platform and analytical modules in the full hybrid simulation. The first analysis was of the entire structure built and analyzed in one Zeus-NL model. The second included all of the same analytical components, separated into three modules for use in a purely analytical hybrid test performed through SimCor. The deformation response of the inner pier obtained from both the whole and hybrid models is provided in Figure 4.1. The results demonstrate that hybrid simulation sub-structuring is not a cause for the differences observed between the purely analytical response of the model and the hybrid test data (Appendix D.2).

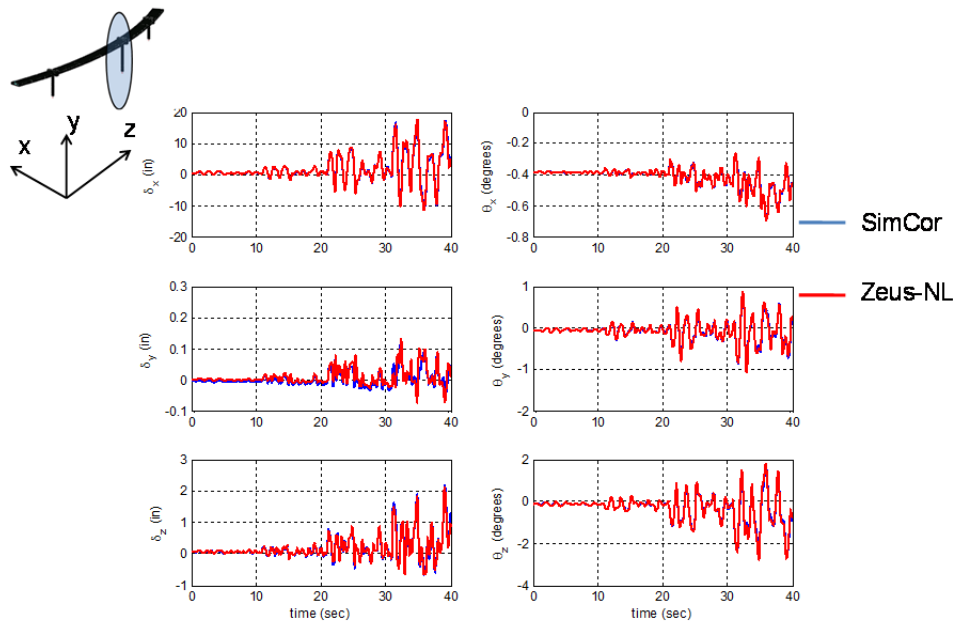


Figure 4.1 Analytical proof-of-concept for hybrid simulation of curved bridge

i. Modelling Assumptions

The following assumptions were made in the initial uncalibrated model. The results of these assumptions are further discussed in Section 4.2 as model calibration methods are introduced to account for the undesired consequences of these assumptions:

- a) Elastic response of deck and bent caps

Assumptions regarding the elastic response of the deck and bent caps are shown to be relatively accurate through a series of preliminary studies conducted on the superstructure components of the bridge. As discussed, the strains at critical locations along the deck and transverse beams are

monitored in an OpenSees analysis of the bridge subjected to the same loading as the hybrid simulation. The strains in the superstructure are shown to have remained in the elastic region for this analysis. This was therefore a validated assumption, and no calibrations were performed in response to this aspect of model behavior.

b) Rigid body motion and fixed condition at pier-cap interface

An assumption that the interface between the pier and cap behaves as a rigid body with fixed end conditions introduces errors into the analytical model. As would be expected, the interface does not have infinite stiffness, and in fact develops significant cracking and softening due to the moments that develop. This is even the case in the transverse direction of the bridge where the stiffness of the deck provides less rotation restraint of the pier than in the longitudinal direction. This assumption will contribute to an overestimation of stiffness and force values, and all other parameters aside, will underestimate the displacement and rotation levels reached during the loading history.

c) Fixation at the base of pier

In a similar vein of thought, the assumption of perfect fixation at the base of the pier provides an overestimation of the stiffness, and therefore an overestimation of the base actions generated due to seismic loading. This contributes to a higher stiffness and lower associated displacement and rotation values than the experimental test, all other things equal. This is due to cracking at the interface of the pier and the footing, as well as yield penetration and the eventual formation of plastic hinges.

d) Linear torque-twist response of pier cross-section

Perhaps one of the most incorrect assumptions made in the original uncalibrated model was in the modeling of the torque-twist behavior of the RC cross-section. The linear-elastic relationship utilized in the model was approximated from studies of the pure torque-twist response of the cross-section. Examination of the response data reveals that the influence of strains due to other shear, flexural, and axial loading effects create a vastly different and more complex non-linear response. As a result, the torque-twist relationship of the uncalibrated model excessively overestimates the stiffness in the torsional direction and fails to capture the observed stiffness

degradation. Not only does this result in an un-conservative assessment of the torsional rotations expected in the pier, the influence of torsional softening on lateral deformations of the pier is also not appropriately captured.

e) Rayleigh damping of only 0.5% added to account for non-hysteretic damping effects

It is anticipated that not all sources of damping are appropriately captured in an analytical model, and therefore distributed damping is applied to the initial model to account for these sources. However, the uncalibrated analytical model proved to be incapable of capturing the true level of hysteretic damping effects in the bridge. This damping occurs as a result of nonlinear behavior and damage to the piers. The assumption that this damping would be captured in the model resulted in a consistent overestimation of forces and displacements, particularly at higher levels of loading. This assumption significantly affected the perceived behavior of the structural system. If the limitation to the model was not identified through comparison to experimental data, the resulting behavior of the bridge system would have significantly overestimated the seismic response of the bridge.

Modifications made to the initial uncalibrated model in order to adjust for the effects of these assumptions are described later in this chapter. Significant improvements include capturing hysteretic damping, modeling stiffness degradation of piers at connection joints, and appropriately representing nonlinear torque-twist behavior. The option of implementing the calibrated and uncalibrated model is selected as a parameter investigated to assess its influence on perceived seismic vulnerability of RC bridge systems.

ii. Shear Key with Gap Model

A shear key with gap model was developed to represent behavior of the bridge abutments. The boundary conditions of the analytical bridge model at these locations are provided below. The abutment-deck interface is simulated by two non-linear spring models described in detail in Appendix D.1 . The first spring model simulates the gap between the bridge deck and the abutment and can therefore account for pounding effects during earthquake shaking. The second spring model depicts the hysteretic response of the shear key element of the abutment. The two spring models are

connected in series to yield the overall response displayed in Figure 4.2. Full details on parameters of the gap and shear key models can be viewed in Appendix D.1 .

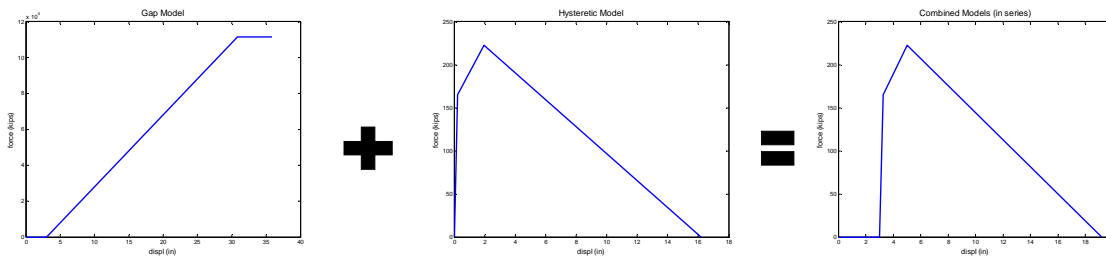


Figure 4.2 Shear key and gap models connected in series

iii. Preliminary Analytical and Experimental Response

Variations between analytical and experimental response for Pier 1 in all degrees of freedom can be viewed in Appendix D.2 . These results compare the corrected experimental data with the numerical results from the initial uncalibrated model. The results demonstrate the potential for significant improvement in model calibration. Experimental and analytical responses of each pier in the transverse direction are fairly consistent, with the main distinctions being larger actions and deformations, as well as a higher stiffness value in the model than was observed in the experimental test. This can easily be accounted for through straightforward changes to damping and nonlinear stiffness parameters based off of the experimental results. When rotational actions and deformations at the base of the piers are examined in this transverse out-of-plane direction, the same general relationship is observed. This indicates that some of the over-estimation of stiffness of the global response of the bridge piers is due to inaccuracies in the model’s ability to capture the properties of the base of the pier, in addition to the overall pier itself.

Examination of the piers in the longitudinal direction reveals an even starker contrast in stiffness. It should be kept in mind that the stiffness of the deck contributes to the response of the piers in the longitudinal direction. This rotational restraint of the deck drives the piers into double curvature. This distinct difference between anticipated and observed stiffness in the longitudinal displacement and in-plane rotation degrees of freedom is largely due to the inaccuracy in assuming a perfectly rigid

connection between the pier and deck. Cracking and nonlinearity at this interface do exist, and the resulting overestimation of stiffness in the analytical model highlights the error of this assumption.

Variation in torsional stiffness between the analytical and experimental results was the most significant inconsistency in terms of the accuracy of stiffness values assumed in individual degrees of freedom. The reason for this shortcoming is the modeling of the torsional response assumed in the element definitions utilized in Zeus-NL. It is concluded that significant reduction in stiffnesses obtained from pure torque-twist response are necessary in order to account for the torsional relationship that results from combined actions. In addition to observing stiffness degradation due to increased damage, there was torsional softening observed under increased levels of load combination that contributes significantly to this behavior.

4.2 Model Calibration

The model calibration is performed through rigorous comparison of corrected experimental test data with the results of the uncalibrated numerical model analyzed for the same seismic loading. Direct comparisons are made at the local and global response levels, utilizing data directly measured and derived from experimental instrumentation. These comparisons are made at each level of loading, and the majority of calibration techniques are rooted in the results of the final three levels of loading applied during the hybrid simulation. A unique set of model parameters are developed for each desired limit state, resulting in three curved bridge models with varying characteristics. Each of these models is uniquely capable of capturing the structural responses for a given severity of event. In the cases for moderate and severe seismic loading, the lower amplitudes of seismic record are still applied to the numerical models in the nonlinear time history analyses when comparing results at higher loads. Through doing so, both the experimental and analytical bridges are subjected to the same loading history, and the appropriate comparisons can be made at the desired level of loading currently being considered for calibrated.

i. Model Calibration Methods

A series of steps are taken in model calibration that produce a vast improvement of the response of the analytical models at all levels of seismic loading. These changes include adjusting for assumptions made in the uncalibrated model regarding behavior at the pier-cap interface, torsional response, and the ability to capture hysteretic damping effects. Adjustments are made to account for these assumptions first, before producing separate models with varying parameters for use with different levels of seismic loading.

The first step taken to perform model calibration of the response of the RC piers involves examination of the behavior at the pier-base and pier-cap interfaces. The uncalibrated model assumes rigid body behavior and fixities at these interfaces. Cracking observed in the hybrid simulation clearly indicates that there is flexibility at these locations, resulting in reduced stiffness and increased ductility that needs to be adjusted for in the calibrated model. In order to determine the stiffness degradation behavior at these locations, the 6DOF deformations derived from Krypton data at the ends of the piers are compared to the measured deformations of the base and cap (Figure 4.3). Recall that the base was instrumented to monitor slip and uplift, and was shown to remain stationary throughout the test. The 6DOF motions of the top cap are accurately measured by the deformation correction sensors as discussed in test setup and instrumentation.

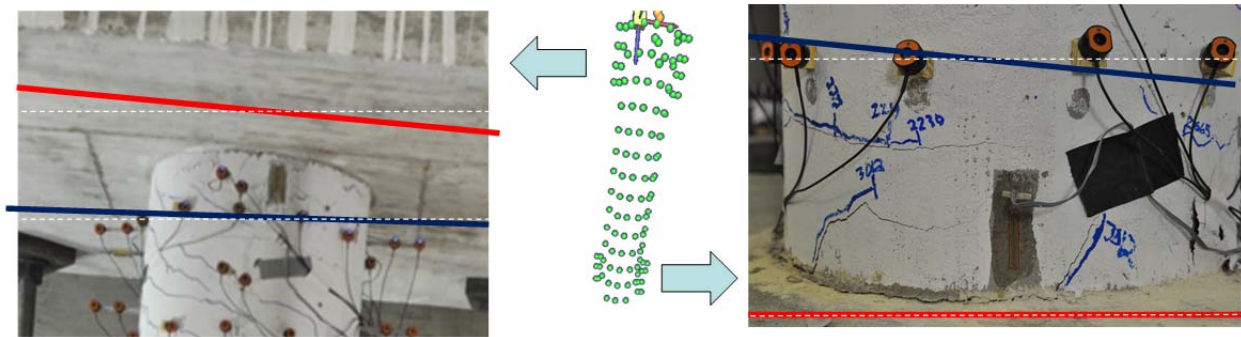


Figure 4.3 Comparison of 6DOF Krypton data (blue) with 6DOF Cap deformations (red)

The difference in displacement values between the derived krypton data and base and cap deformations are plotted against Cartesian force responses measured at the control point and

calculated at the base of the pier from LBCB data. These plots reveal the degrading stiffness at these locations, as displayed in Figure E.1-Figure E.8. Nonlinear rotational springs are then developed in all three rotational directions to account for this behavior. The procedure for development of these rotational spring parameters is presented later in this section.

Next, the torsional response is addressed. As was discussed in the modeling assumptions, the torsional stiffness of the uncalibrated model was based off of pure torque-twist response of the RC cross-section. After adjustment for the torsional softening at the pier-cap interface, the resulting torsional response of the pier itself is examined and a nonlinear torsional spring is developed. It should be noted that the transverse displacement response of the analytical model improved with the appropriate adjustment of the torsional response. The influence of this nonlinear torsional spring and its implications on combined interaction effects for the piers is discussed shortly.

Finally, the last broad-level improvement made across each model is an exploration of the aforementioned inability of the computational software to capture hysteretic damping effects due to the nonlinear response of the bridge piers. As was discussed in the model assumptions, the inability to model hysteretic damping effects results in an overestimation of force and displacement amplitudes. A parametric study is conducted where distributed Rayleigh damping is increased for the structural elements of the model to account for this shortcoming. The damping is subsequently adjusted for each level of seismic loading, as described later in this section.

With these changes implemented, the analytical model is compared to that of the hybrid simulation test data at every stage of the applied loading, as well as for the entire load history (Figure E.10-Figure E.21). This is done to display the significant improvements made through the methods described above. Additionally, these results are used to assess the secondary changes to parameters that are necessary for further calibration of specific degrees of freedom and at varying levels of seismic loading. Plots are developed for the 10-20, 20-30, and 30-40 second regions of the hybrid simulation, corresponding to 0.3, 1.0, and 2.0 MCE scaling levels of the record. These are referred to as slight, moderate, and severe levels in the plots. The results are assessed in order to determine how to develop models that accurately capture the bridge and pier response under these three categories of load level.

Upon further inspection of this first phase of calibration, additional modifications are made to stiffness parameters and degradation behavior in each degree of freedom and at each load level.

Significant additions include development of lateral spring models to represent the remaining variations in stiffness of the elements of the pier under combined actions. Though these effects are secondary to the initial phase of model calibration, they result in significant improvements. Additional details regarding various methods of model calibration and the respective influence on structural response is provided below. The degree to which each model parameter influences structural response is discussed.

a) Rotational Spring Model

Rotational spring models are developed for all three rotational degrees of freedom at the top and bottom of each pier. These include two flexural springs at each end of the pier, which are developed from responses in the transverse and longitudinal directions. Results are combined to create a uniform flexural rotational spring for application at the top and bottom of an individual pier. This is appropriate given the symmetry of the piers, and because the nature of this behavior at the interface is independent of the level of flexural loading experienced. As a result, a singular flexural rotational spring is developed for each pier. In addition, a torsional rotational spring is developed for application at the top and bottom of each pier, again with the same parameters defined at each end. For the torsional rotational spring, the same model is applied for each pier as this behavior is independent of pier height.

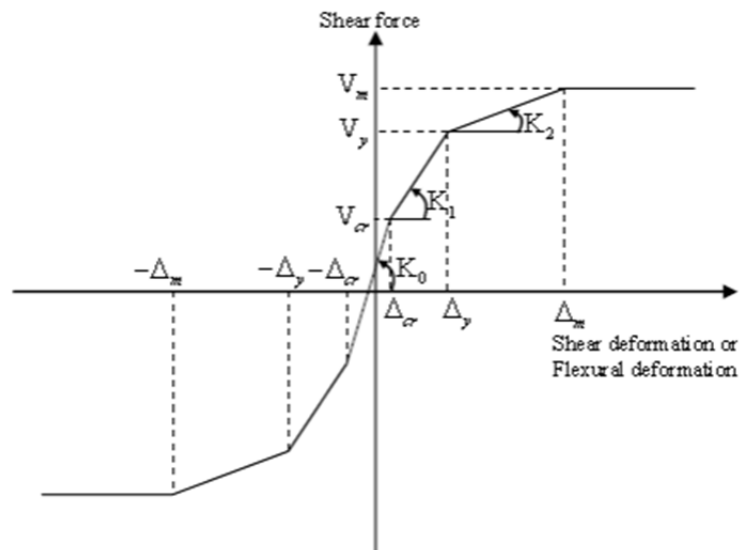


Figure 4.4 Hysteretic flexure model under constant axial force

Parameters for the spring models come from the procedure described above involving derived Krypton data and Cartesian loads and deformations (Figure E.1-Figure E.8). Spring models are developed from the backbone curve of the action-deformation relationships at the base and top pier-cap interfaces. The resulting rotational model captures the stiffness and strength degradation effects at increasing levels of loading. The model employed for this calibration is a variation of the hysteretic flexure model for constant axial load available in Zeus-NL (Figure 4.4). Slight modifications are made to the source code in order to enable to include the effects of a nonlinear unloading curve. The various parameters of the above curve are provided in Figure E.9. The example provided in Figure 4.5 is of the development of the rotational spring model for the out-of-plane flexural response of Pier 1. The improvement in the global transverse direction following implementation of the resulting flexural rotational spring models is then presented in Figure 4.6.

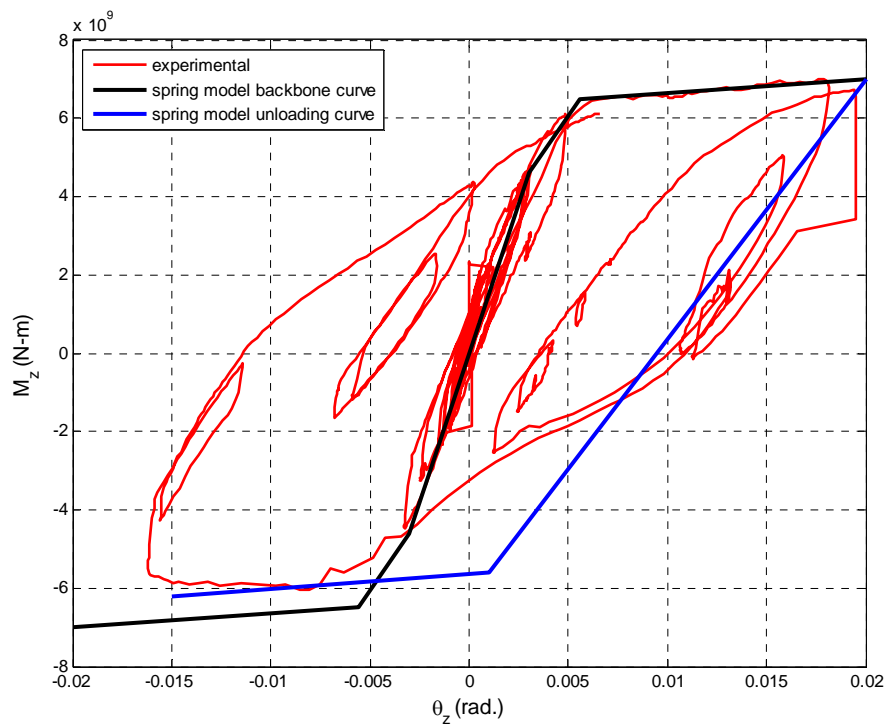


Figure 4.5 Development of rotational spring model from experimental data

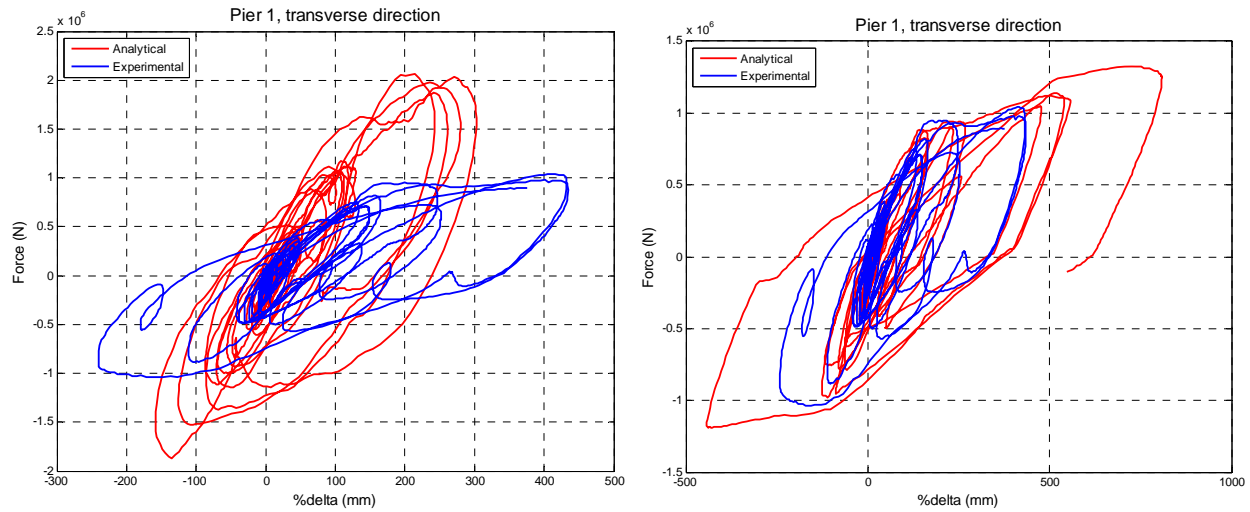


Figure 4.6 Transverse response of Pier 1 before (*left*) and after (*right*) implementation of flexural spring

b) Torsional Model

As introduced previously, the torsional stiffness of the uncalibrated model was based off of anticipated pure torque-twist response of the RC cross-section. In addition to the development of rotational springs to represent the torsional stiffness degradation at the pier-cap interfaces, a nonlinear torsional spring is developed to model the reduction in stiffness and accelerated degradation of the pier due to combined effects. A quadrilinear rotational spring model is used for this spring as well. Parameters are developed from examination of experimental response after removing the effects of the pier-cap interface behavior.

The immediate improvement in torsional response of the piers that results from these adjustments can be seen in Figure 4.7. It should be noted that in addition to the improved torque-twist relationship highlighted here, that there is a significant improvement in the agreement between analytical and experimental displacements and rotations in other degrees of freedom. This observation confirms that in addition to the previously stated observation that lateral actions result in torsional softening, the reverse effect holds true as the shift in load due to torsional softening then leads to increased levels of lateral displacement.

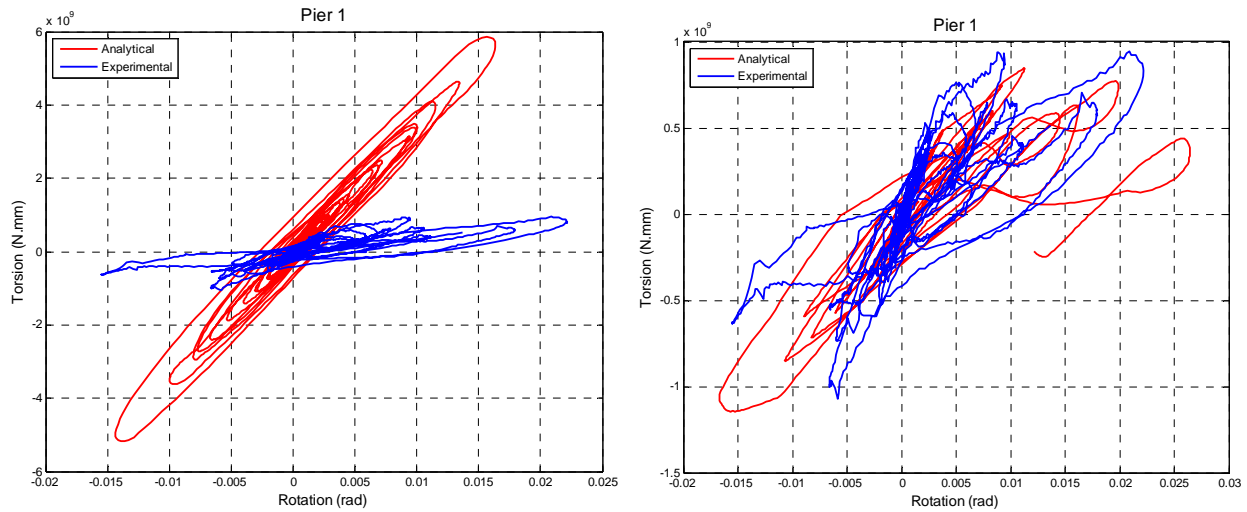


Figure 4.7 Torsional response of Pier 1 before (left) and after (right) implementation of torsional spring

This phenomenon highlights the importance of considering the influence of combined actions on the complex response of a structure. This interdependency also illustrates that neglecting the response in one degree of freedom can have implications on the behavior of the structure in other directions. Therefore, even in cases where response in a particular degree of freedom is known to control the overall behavior of a structure, the importance of appropriately simulating the response in the other seemingly less-critical directions, whether analytically or experimentally, is still necessary in order to achieve accurate results in the critical degree of freedom in question.

c) Damping

With only the above modifications to the analytical model, it was observed that there were still instances where the analytical model response was higher than that of the experimental results. Since both actions and deformations exceeded those of the experimental data, stiffness values of the specimens or errors in assumptions surrounding boundary conditions could not be the only contributing factors to this behavior. Instead, these conditions are indicators of the previously discussed issue of the model not fully capturing the hysteretic damping that occurs due to nonlinear response of the structure and its components. This is backed up by the observation that this trend of higher analytical actions and deformations increases in over the length of the calibration record,

resulting in the greatest differences at the most significant load levels. This is natural due to the increase in nonlinear response at higher levels of loading. It is acknowledged, therefore, that the Zeus-NL model employed was not capable of capturing all of the nonlinear hysteretic damping, and therefore the distributed Rayleigh damping for the bridge is increased in order to decrease the analytical actions and deformations throughout the loading history. A parametric study is performed to identify the appropriate levels of Rayleigh damping to be used in each model to obtain responses that most agree with the experimental results for each loading level.

d) Yield Penetration Model

The effects of yield penetration are accounted for in the softening of the joint model as discussed and presented above. The softening and increase in ductility at the plastic hinge zones adjacent to the footing and cap of the pier are accounted for through a combination of the effects of the rotational and lateral spring models developed. It is noted that these effects could have been partially accounted for through the approach presented in (Priestley & Park, 1987), where an increase in effective length of the piers is proposed. Instead the development of spring models are implemented since they are necessary for representing other aspects of the pier behavior not captured in the initial uncalibrated model.

e) Shear Spring Model

Examination of the structural response in each lateral direction revealed that a small component of the displacements at higher loads is due to shear deformation in the piers. This is somewhat significant in the longitudinal direction, though nearly negligible in the transverse direction of the bridge. This is because of the rotational restraint provided by the stiffness of the bridge deck in this direction. This drives the piers into double-curvature, effectively reducing dominance of pure flexure in the response. A shear spring model could potentially be included in the calibration procedure to produce some slight improvements at higher levels of seismic loading. However, computational costs would have to be weighed. A hysteretic shear spring model could be calibrated according to the force-displacement relationships from the experimental data in the longitudinal direction of the

bridge. The model could likely be developed as outlined in (Lee & Elnashai, 2001). This is discussed in Section 6.2 as a potential component of future work.

f) Variations in Constitutive Properties

A great deal of care was taken in the initial input of the appropriate constitutive relationships for steel and concrete materials. Experimental testing of rebar coupons and concrete cylinders is performed prior to the experimental test, as presented in Appendix A.3 . Critical parameters calculated from these tests are used to define the material properties employed in the analytical model. This is completed in the development of the uncalibrated model, so no changes are made to constitutive properties in the calibration procedure presented here. In any case, it should be noted that research has shown that the material properties contribute to variability in structural response very little compared to input motion characteristics (Kwon & Elnashai, 2006).

ii. Calibrated Models Employed

Following the above calibration methods and procedures, the most critical components of the calibration are assessed for each level of seismic loading. The associated improvements in structural response that are achieved with each development are weighed against the computational cost of implementing a more complex calibrated model. It is determined that the most significant improvements for all models include the influence of the rotational springs developed at the base of the piers, the improvements to the nonlinear torque-twist response of the pier itself, and an appropriate increase in distributed damping to account for the inability to fully capture the hysteretic damping at higher levels of nonlinear response.

In addition, minor improvements are achieved through the development of lateral springs in the transverse and longitudinal directions of each pier to account for any remaining variation in stiffness observed after correcting for the above assumptions. Finally, shear deformation in the transverse direction is shown to be negligible, and shear-springs developed in this degree of freedom have little to no effect on any global response. The only remaining degree of freedom unaltered by the calibration procedure is the vertical direction. This is because the analytical model correctly

represents the appropriate axial strength and stiffness. Therefore, in order to appropriately model the bridge response, the following set of nonlinear springs are required for each pier, with stiffness parameters varying by pier in the non-torsional degrees of freedom:

- Three torsional springs for each pier (two identical springs at the top and bottom of each pier to account for the stiffness degradation at the pier-cap interface, and one spring with different parameters to account for the nonlinear torque-twist response of the pier)
- Four rotational springs for flexure (two identical springs at the top and bottom in each flexural direction to account for stiffness degradation at the pier-cap interface)
- Two lateral springs adjusting for the variation in nonlinear stiffness response of the piers themselves

The simultaneous implementation of 9 nonlinear springs for each pier results in a very computationally expensive analysis. Therefore, efforts are made to produce a smaller set of equivalent nonlinear springs capable of representing an approximation of the effective stiffness of the nonlinear springs developed above. This procedure results in one lateral spring in each direction, transverse and longitudinal, as well as one effective torsional spring. The effective stiffness of a lateral spring in the simplified model is therefore calculated as follows

$$\frac{1}{k_{eq}} = \frac{1}{k_a * L} + \frac{1}{k_b * L} + \frac{1}{k_c} + \frac{1}{k_d} \quad (15)$$

where k_a is the rotational spring modeling pier-base cap rotation, k_b is the rotational spring modeling pier-top cap rotation, k_c and k_d are lateral springs representing any additional numerical model calibration for pier response, and L is the length of the pier that is utilized to convert rotational springs to an equivalent lateral spring stiffness. Through this procedure, the fully calibrated pier models undergo transformation to a simplified spring model as shown in Figure 4.8.

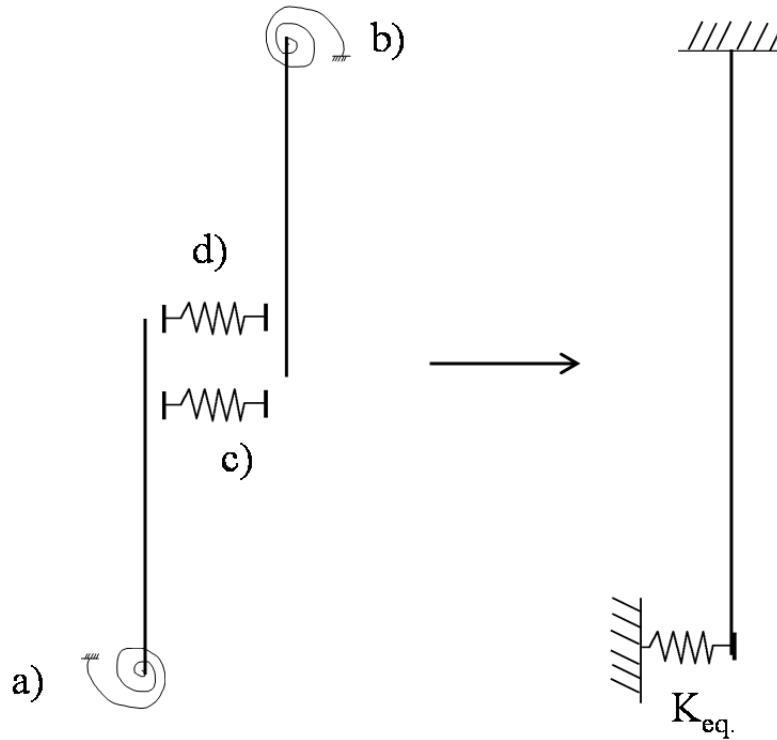


Figure 4.8 Conversion from fully calibrated to simplified equivalent spring model

The simplified equivalent spring model in the transverse and longitudinal directions undergoes the procedure as shown above, with one or two lateral springs depending on the calibration case. The equivalent torsional spring is likewise developed (with no length term present) from the three torsional springs defined for the top and bottom cap interfaces, as well as the nonlinear torsional response of the pier. It should be noted that since the stiffness values of the nonlinear spring models vary according to deformation, the deformations at which the equivalent lateral springs change stiffness values is an approximation. These points are based off of contributions from each of the components at their respective deformation levels. Rotations and associated displacements are combined to yield quadrilinear equivalent spring models. The results of this procedure is a simplified model with three equivalent nonlinear springs which is determined to be appropriate for use under slight and moderate levels of ground motion. This decision is made to save computational time and resources, since each analysis runs approximately five times faster using the simplified model.

However, it is determined that the use of equivalent springs in simplified models is not appropriate for performing analyses under severe earthquake loading. A much less desirable match between

numerical results and experimental data is observed for the final scaling of the hybrid simulation record. This is partially due to the increased dispersion between the deformations at which stiffness is reduced, coupled with the limited number of degrees of nonlinearity in the quadrilinear equivalent spring models. Due to the inability of the equivalent model to accurately approximate stiffness degradation at the appropriate deformation levels for various DOFs, the fully calibrated model is employed for the severe levels of loading. This decision is also justified by the importance of the resulting fragility analysis at the severe limit state, which is often associated with life safety. Since the highest levels of loads and deformations occur in this classification of loading, the most precise model for generating structural response data for statistical analysis is naturally desirable.

The final result of the calibration procedure is three calibrated models for each seismic design level. The slight and moderate models are simplified through the use of equivalent springs, and only differ in distributed damping levels. The severe model includes the direct application of all the nonlinear springs developed in the above methods, and is therefore more computationally expensive. Examples of the numerical results and comparison with experimental results for these respective levels of loading are provided in Appendices E.3 and E.4

4.3 Suite of Earthquake Records

Through a careful set of selection criteria, three suites of natural records are developed for performing structural assessment in Zeus-NL. Natural records are selected rather than generating synthetic records or scaling existing records in order to match a specific response spectrum. It is not desired in this study to overly bias the response of the curved bridge by tuning the demand to the natural bridge response. Therefore, a large set of natural earthquake records are selected so that a sufficient number of records for performing accurate statistical analysis of structural response data can be obtained without scaling. A wide range of input motions with varying properties are applied to the three calibrated models to generate structural response parameters for use in fragility analysis. This is important, as the uncertainty associated with input ground motion is shown to have a more significant impact on the vulnerability of structures than many structural capacity-related parameters (Kwon & Elnashai, 2006).

Records are selected primarily from the Next Generation Attenuation (NGA) strong motion database (PEER, 2010). The NGA database contains 3182 natural records from 104 shallow crustal events. In addition to records selected from the NGA database, a series of severe strong motions from the 2011 Tohoku event in Japan are obtained through K-NET (NIED, 2013).

i. Natural Ground Motion Selection Criteria

Initially, records obtained from the NGA database are sorted into separate bins according to pairings of magnitude and distance as displayed in Table 4.1. This procedure is a more discretized version of the method presented in (Shome, Cornell, Bazzurro, & Carballo, 1998). The slight, moderate, and severe categories have 8, 6, and 4 bins respectively. Each bin is limited to a maximum of 50 natural records in order to maintain a feasible analytical program, since a nonlinear time history analysis is performed for each record within all three categories, once for each of the sixteen geometry, calibration, and loading cases.

Table 4.1 Record Selection Bins

		Distance (d)		
		Near-field ($d \leq 14\text{km}$)	Mid-field ($14\text{km} < d \leq 38\text{km}$)	Far-field ($38\text{km} < d$)
Magnitude (M)	$5.0 \leq M < 5.25$	Slight 1		x
	$5.25 \leq M < 5.5$	Slight 2		x
	$5.5 \leq M < 5.75$	Slight 3		x
	$5.75 \leq M < 6.0$	Slight 4		x
	$6.0 \leq M < 6.25$	Moderate 1	Slight 5	
	$6.25 \leq M < 6.5$	Moderate 2	Slight 6	
	$6.5 \leq M < 6.75$	Moderate 3	Slight 7	
	$6.75 \leq M < 7.0$	Moderate 4	Slight 8	
	$7.0 \leq M < 7.5$	Severe 1		Moderate 5
	$7.5 \leq M < 7.75$	Severe 3	Severe 2	Moderate 6
	$7.75 \leq M$	Severe 4		

Careful analysis of the records in each bin is performed to identify outliers with respect to spectra, site conditions, and acceleration and displacement parameters. Natural records located in bins belonging to the slight or moderate categories with stronger ground motion intensity parameters are

moved into a higher category. Records located at soft or hard soil conditions are noted for use to ensure that each category includes a distribution of site conditions, in addition to the appropriate levels of ground motion intensity.

Examination of the above bins developed from the NGA database revealed a shortage of severe records. Only three events of greater than M 7.5 are available, with none exceeding M 8.0. Therefore, a series of 100 of the most significant records collected from the 2011 Tohoku event are selected from K-NET. Figure 4.9 displays the effect of including these records with those previously selected into the severe bins from the NGA database. The parameters of the Tohoku records alone are provided in Figure F.28 to Figure F.30 and Table F.4. Following this procedure, and with the inclusion of the Tohoku ground motions, the resulting three suites of earthquake records are defined as follows:

- a) Slight Records – 301 natural records detailed in Figure F.1-Figure F.9 and Table F.1
- b) Moderate Records – 205 natural records detailed in Figure F.10-Figure F.18 and Table F.2
- c) Severe Records – 403 natural records detailed in Figure F.19-Figure F.33 and Table F.3 and Table F.4

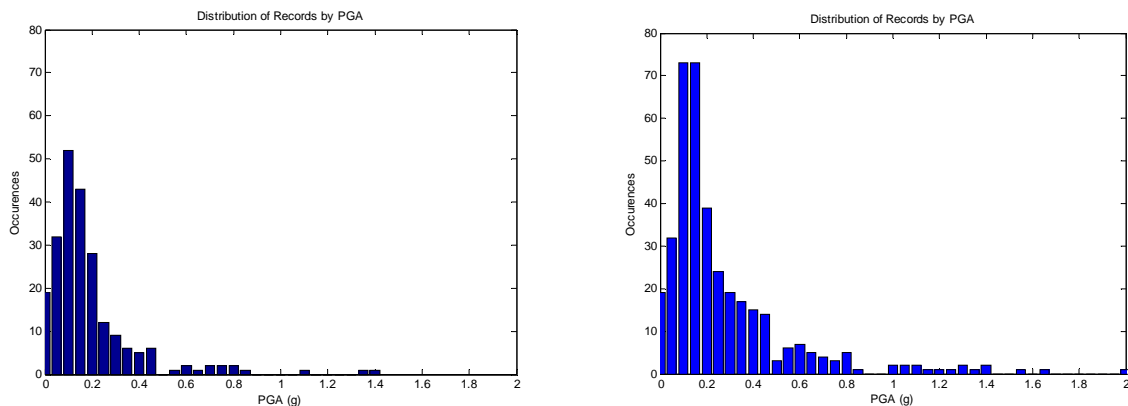


Figure 4.9 Increase in severe suite with the addition of Tohoku records

These categories were selected to loosely represent a set of generic 75-, 475-, and 2500-year return period events. Each suite is then utilized to develop vulnerability relationships representing the slight, moderate, and severe limit state threshold values, respectively, as defined in Section 4.5 . An

example of the transition from magnitude- and distance-defined bins to the aggregated suites described above is displayed in Figure 4.10. Peak ground displacement parameters at each level are provided as an example of the varying properties within each bin. It should be noted that each of the higher categories still maintain records with lower intensity measurements if the natural records originally met the magnitude- and distance-defined parameters for bins in that category. This is an important feature to retain, as attenuated far-field ground motions from a large magnitude event differ in spectral content from nearer events of smaller magnitude. Ground motion parameters for the full suite of earthquake records are provided in Figure F.34-Figure F.45. Data files of seismic records are provided in Digital Appendix F.

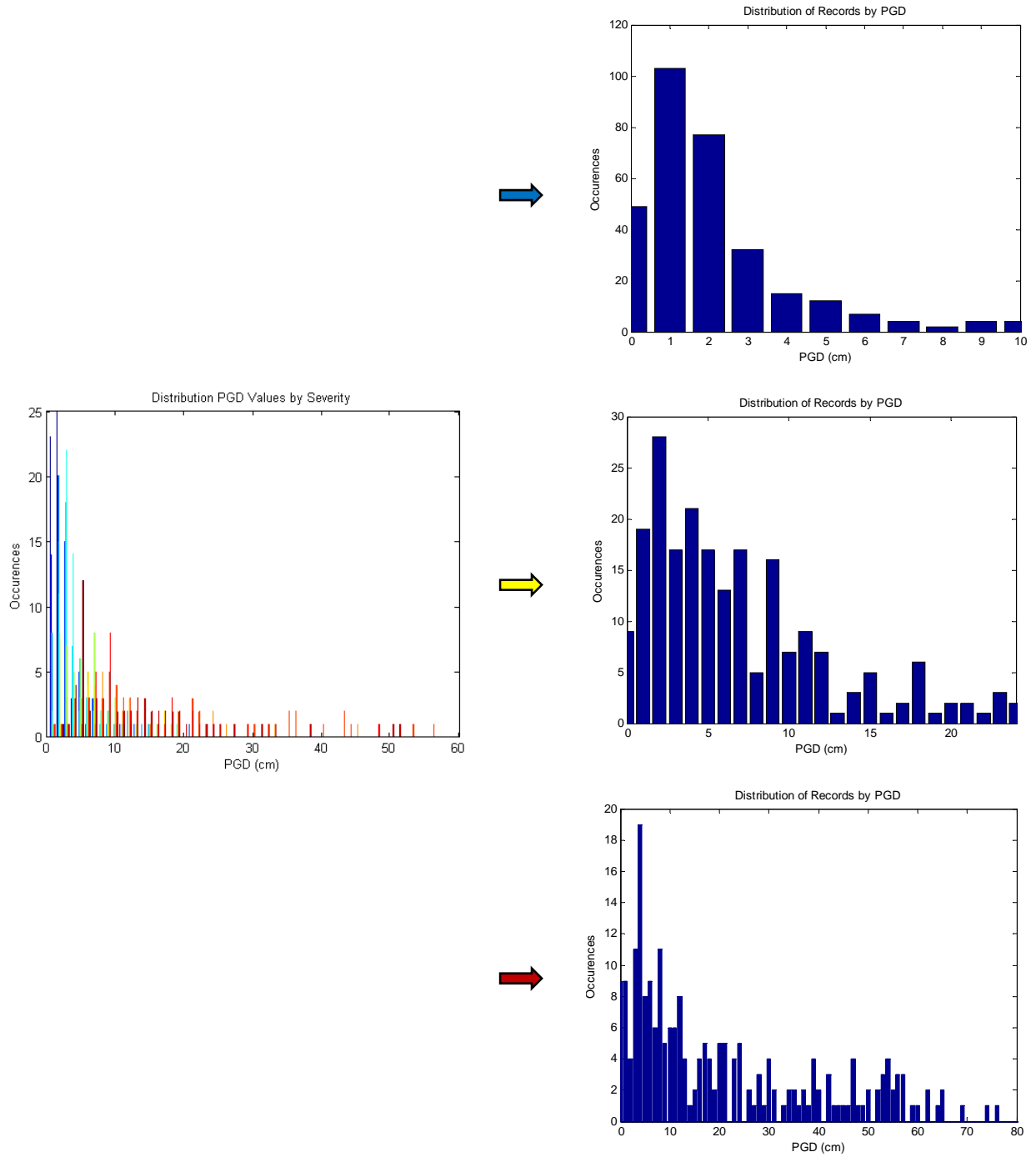


Figure 4.10 PGD values plotted by bin and seismic level categories

ii. Properties and Characteristics of Set

A great deal of care was taken to ensure that the natural records are capable of representing a wide range of possible scenarios. Variation in soil site condition is carefully selected in order to not bias the vulnerability relationships toward any specific site (Figure 4.11). A wide range of response spectra characteristics are also selected. This helps to create a set of structural response data that is not biased due to an unreasonable level of amplification in the response spectra.

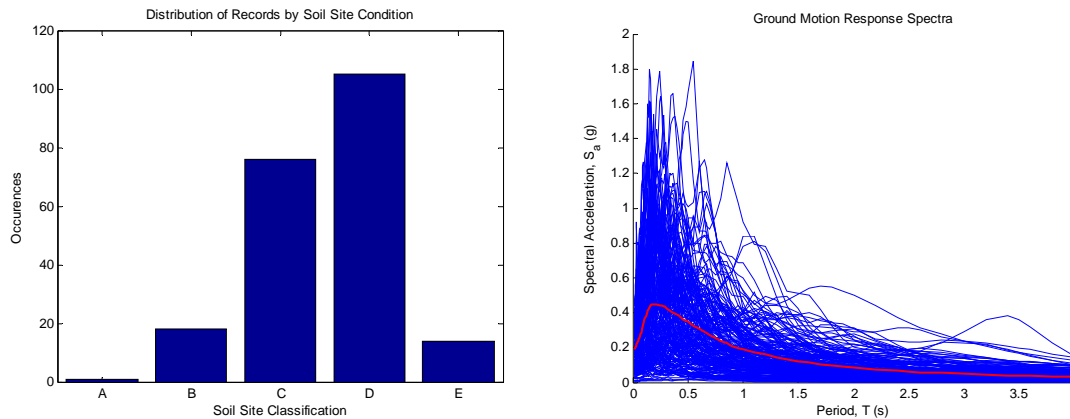


Figure 4.11 Distribution of Soil Site Classification (*left*) and Spectra (*right*) for Moderate Suite

Other characteristics examined are peak response parameters, ratios of peak parameters for orthogonal horizontal directions, and ratios of peak parameters of vertical to horizontal directions of loading. These traits are assessed to inform decisions when performing analyses for varying directions and levels of seismic loading. An example of the peak parameter data for the full suite of records is displayed in Figure 4.12. A summary of these characteristics for each category and for the overall suite of records can be viewed in the figures displayed in Appendix F.

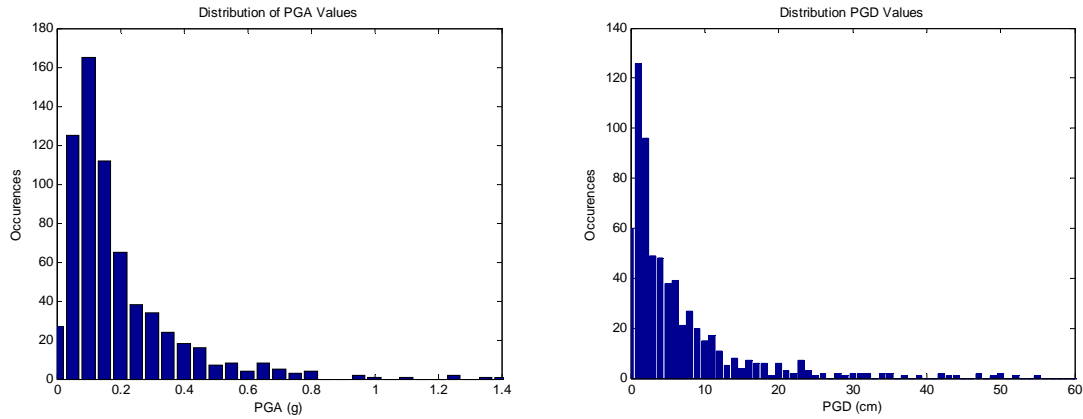


Figure 4.12 All NGA Records – PGA and PGD Distributions

Each natural record has three orthogonal accelerograms, including two horizontal and one vertical component. The two perpendicular accelerograms recorded in the natural record of an event are arbitrarily selected such that the N-S component of a natural record is always applied in the transverse direction of the bridge, and the E-W component is always applied in the longitudinal direction of the bridge. The analysis of the ratios of the two components of horizontal loading across all records is provided in (Figure 4.13). Regardless of whether the two horizontal components are compared as N-S and E-W components or as fault-parallel and fault-normal components, there is minimal statistical bias toward higher amplitudes in any one direction applied to the bridge. This is because the ratio of peak ground motion parameters are very evenly distributed between dominance of one horizontal component over the other. There is perhaps a very slight tendency toward higher fault-normal components. However, the records are applied to the bridge in their N-S and E-W component sense. This method of uniformly applying horizontal components allows for the most realistic distribution of accelerations in each seismic loading event and do not bias the resulting structural response.

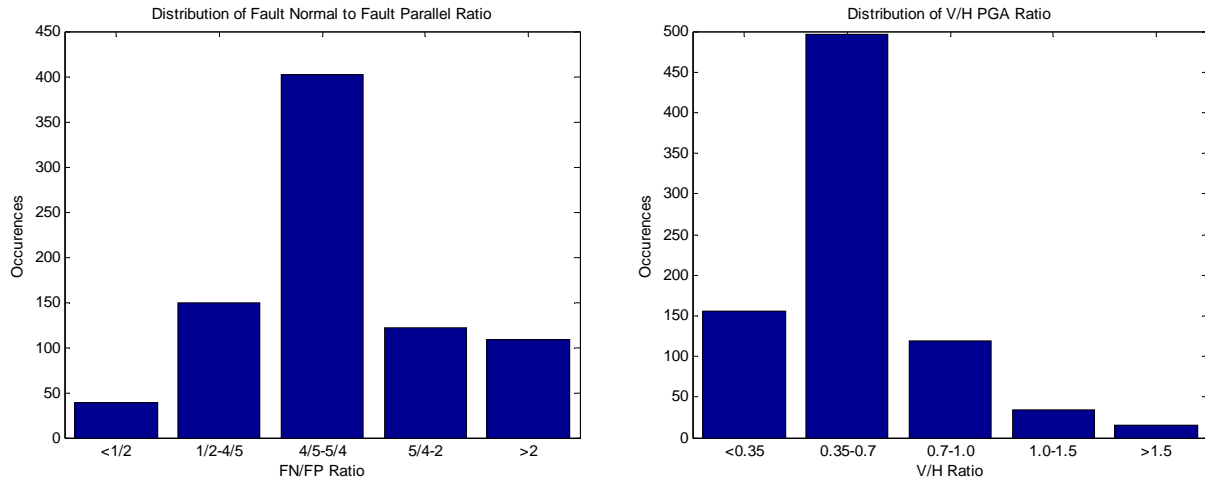


Figure 4.13 Ratio of orthogonal horizontal (*left*) and vertical to horizontal (*right*) peak parameters

4.4 Set of Analytical Cases Examined

The full set of cases examined for influence on seismic vulnerability is provided below. Table 4.2 illustrates the matrix of sixteen cases for which fragility relationships are developed at each limit state level. The cases vary in terms of calibration, geometry, direction(s) of excitation, and magnitude of excitation. The first three of these characteristics are outlined in Table 4.2, with each of these sixteen cases analyzed under three suites of earthquake records to develop vulnerability relationships for slight, moderate, and extensive limit states under each case. Bridge geometry is classified as either curved or straight. Calibration parameter is either un-calibrated or calibrated according to the procedure presented in this chapter. For each of the four geometry and calibration scenarios, four different uni-directional or multi-directional earthquake loading cases are applied. These are Uni-directional Longitudinal (UD-L), Uni-directional Transverse (UD-T), Bi-directional (BD) loading of these first two horizontal directions, and finally Tri-directional (TD) loading, which includes both horizontal components, as well as vertical excitation. A detailed description of the parameters which compose these cases is then provided below.

Table 4.2 Matrix of analysis cases for vulnerability assessment

	Bridge Geometry	
Calibration Parameter	<i>Straight</i>	<i>Curved</i>
<i>Un-Calibrated</i>	UD-L/UD-T/BD/TD	UD-L/UD-T/BD/TD
<i>Calibrated</i>	UD-L/UD-T/BD/TD	UD-L/UD-T/BD/TD

i. For Assessing Influence of Curved Geometry

The original model used in the hybrid simulation would be classified as the un-calibrated curved bi-directional case, with slight variations to the relative amplitude of the bidirectional loading, as discussed further in this section. The first differentiating factor examined is the influence of the bridge curvature on the combined actions observed in the bridge piers. In order to study this effect, two straight bridge models of the same overall length are constructed using the same parameters as the calibrated and uncalibrated curved models. All material and element properties of the model are the same between the two cases, with only the location of structural nodes varying such that the bridge geometry changes in shape and slightly in overall distance spanned.

This slightly elongated straight bridge is selected over the alternative option of developing a straight bridge formed from a projection of the curved bridge. This alternative case would have resulted in a straight bridge that spans the same overall length in physical space. However, this would have also resulted in shortening of the individual spans between piers, and modifications to the distributed loading on the deck would be necessary in order to maintain the same level of axial load transferred to each bent. Instead, the elongated straight bridge spans a slightly greater distance, though with all other parameters that would affect pier response under the same lateral load case kept constant. At the time, the unknown relationship between varying axial force and pier response also contributed to this decision.

ii. For Assessing Influence of Multi-directional Loading

The next parameter that is considered is the direction and/or combination of loading that the bridge is subjected to. For reference, the terms transverse and longitudinal correlate to the global Cartesian

axes of x and z in the analytical space, and x and y in the LBCB space, respectively. Longitudinal loading therefore represents loading along the length of the deck, such that in the straight bridge case the loading direction is parallel to the span of the bridge. In the curved case, it is along the global axis that is most parallel to the span of the bridge. Transverse direction then, is loading perpendicular to the direction that the bridge deck spans in the straight case, and along the axis most perpendicular to the bridge in the curved case.

As would be imagined, the response of these two uniaxial loading cases is greatly influenced by the orientation of the box-girder. The deck effectively restrains rotations at the top of the piers along the longitudinal axis of loading. This longitudinal restraint corresponds to what is referred to herein as the in-plane rotation of the bridge piers. In contrast, the bridge piers are significantly freer to deform in the transverse direction, and to rotate in the associated out-of-plane direction.

As discussed above, the two horizontal components from a natural record are arbitrarily selected in such a way as to avoid biasing the structural response, as described in Section 4.3 . A complete summary of these ratios and spectra of each record component presented by seismic level can be found in APPENDIX F. Again, it has been shown that there is no statistical bias toward higher amplitudes in any one direction. Therefore, the method of uniformly applying horizontal components in the Bi-directional and Tri-directional loading cases allows for the most realistic distribution of relative magnitudes in the two varying directions of bridge response.

iii. For Assessing Influence of Modelling Assumptions

There are several different calibrated models developed in this study, which were fully discussed in Section 4.2 . However, for each level of earthquake loading a case is only considered as being either un-calibrated or calibrated. This is because the different calibration procedures employed vary according to the level of seismic loading, not by geometry or loading direction applied. Therefore, there are three calibrated analytical models, but for each level of loading there is only the option of using the calibrated or uncalibrated model. Again, the uncalibrated model uses the parameters laid out in Section 4.1 for the initial hybrid test. The calibrated models for the slight, moderate, and severe analyses cases, as well as the procedure used to obtain these models, are described above in Section 4.2 .

4.5 Structural Analyses

Nonlinear time history analyses are performed through batch processing of the 48 cases developed from the varying model and seismic loading parameters. The numerous cases and records amounts to approximately 15,000 nonlinear time history analyses performed in the analytical environment of Zeus-NL. Due to the significant amount of required computational power, as well as the immense size of output data files from each individual analysis, a simplified and partially-automated method for assessing structural performance is developed.

A set of limit state threshold values are defined which are capable of capturing various local structural response mechanisms through the use of a minimal number of global parameters. These particular global parameters are selected and monitored after an output file for a given nonlinear time history analysis is generated. The values of these parameters are monitored and recorded from each analysis and are compared to threshold values defined for each of the three limit states as described below. The resulting data is then used to develop the fragility relationships as described in Section 5.1 .

i. Limit State Definitions

The origin of the limit state definitions comes from the hybrid simulation described in CHAPTER 3:. The performance of the curved bridge system can be separated into four performance regions for each 10 second interval of the 40 second earthquake record applied to the curved bridge (Table 4.3). The levels of earthquake scaling were selected in order to drive the bridge into each of the limit states described here. However, the structural performance points that indicate where the bridge passes from one state of response occur sometime after the breakpoint between each two levels of scaling of the earthquake motion. It is the definition of this point that must be identified for developing a parameter to indicate performance levels of the piers, and thus overall performance of the bridge.

Table 4.3 Limit state definitions based on hybrid simulation load levels

	None-Slight	Slight-Moderate	Moderate-Heavy	Heavy-Collapse
Earthquake Scaling	0.08 MCE	0.3 MCE	1.0 MCE	2.0 MCE
Record Portion	0-10 sec	10-20 sec	20-30 sec	30-40 sec
Structural Parameters	Cracking	Yielding	Peak load	Loss of load capacity
Societal Limit State Definition	Serviceability	Moderate Down-Time	Economic Loss	Life Safety

These structural limits correspond to exceedance of each of the three societal limit states of serviceability, economic loss, and life safety, respectively. The three limit state threshold values need to be identified from the analysis of the hybrid response data in order to define the four performance levels of the bridge. The structural definition of these limit states is based on both local and global parameters, and for the sake of comparison in the vulnerability assessment, these parameters are mapped to one another. This mapping of local to global structural parameters allows for a simple and straightforward comparison of exceedance when the series of nonlinear time history analyses are performed.

Table 4.4 Limit state threshold value definitions

	LS1	LS2	LS3
Threshold Value	Slight	Moderate	Severe
Structural Parameters	Concrete rupture strain, initial reduction of stiffness, cracking observed	Yield of reinforcing bars, reduction of global stiffness response	Concrete crushing strains, spalling observed, loss of load carrying capacity
Societal Limit State Definition	Serviceability	Economic Loss	Life Safety

The following parameters are examined in order to define limit state threshold values: local strains from embedded gages and external sensors; cracking and spalling observed visually during the test; reduction in stiffness values in hysteretic response of piers; ductility levels achieved; and loss of load carrying capacity observed. The characteristics utilized to identify each limit state are listed in Table 4.4.

The first step in identifying limit state threshold values involves an automated procedure that sorts through the data acquired in the hybrid simulation. External and internal sensors, as well as global response measurements collected in the data acquisition system are examined numerically. The data is sorted through to identify steps in the simulation where local strains exceed rupture, yielding, and concrete crushing strains ($\epsilon_c = +0.0005$, $\epsilon_s = +0.002$, and $\epsilon_c = -0.004$ respectively). The corrected global hysteretic responses of the piers are plotted in several degrees of freedom, and the steps of the hybrid simulation where these identified strains occur are then plotted on each of the hysteretic responses. Next, notes from the test that indicate the visual observation of phenomena such as cracking and spalling are added to the hysteretic responses as well. An example of these various definitions for the severe limit state plotted against the transverse displacement for Pier 2 is displayed in Figure 4.14. The multiple definitions for each proposed limit state are plotted against translations and rotations in each of the two primary directions of loading from the hybrid simulation. These plots can be viewed in Figure G.1 through Figure G.24.

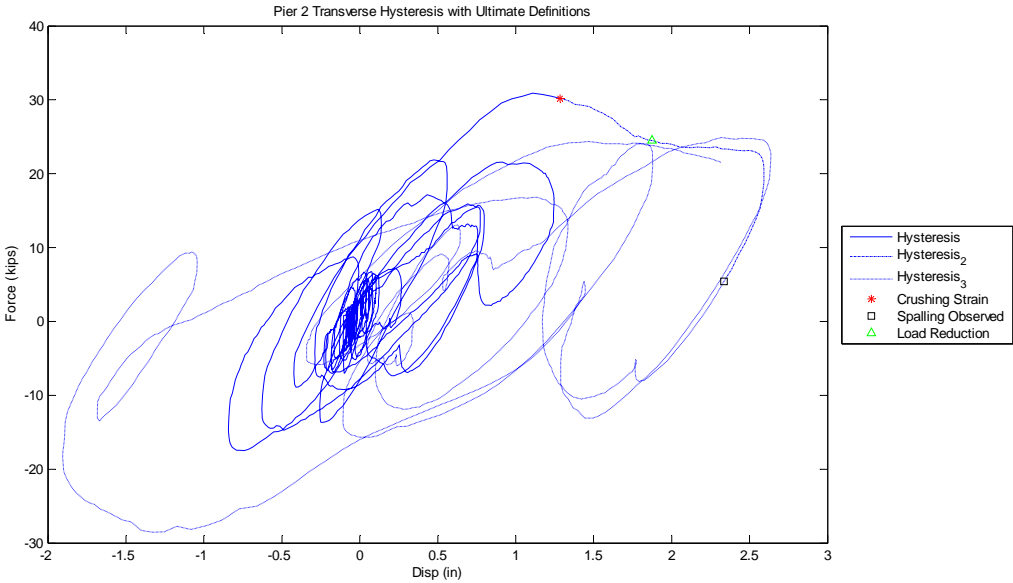


Figure 4.14 Pier 2 Transverse Displacement Ultimate Definition

Finally, the limit states are examined visually and compared to numerical results for other records. Modifications are made as necessary to account for observations of global changes in stiffness, ductility, and strength parameters. Therefore, the automation of instrumentation data and observation of global parameters combines to yield a set of displacement and force values in the transverse and longitudinal direction of the bridge that indicate exceedance of a limit state. Deformations are presented in terms of displacement, drift level, and ductility ratios. Lateral forces not utilized in identifying exceedance of a threshold value due to the sensitivity of force parameters to variations in damping of the structural system. The resulting deformation-based limit state threshold values are compared to the results of several nonlinear time history analyses under different seismic records. This served to confirm that the relationship between the local parameters used to generate global deformation limit state threshold values holds under varying load cases.

Table 4.5 Limit State Threshold Values in Transverse DOF

	Pier 1			Pier 2		
	Crack	Yield	Ult	Crack	Yield	Ult
dx (mm)	26.7	63.5	121.9	9.1	38.1	72.4
dx (in)	1.05	2.50	4.80	0.36	1.50	2.85
drift (%)	0.3%	0.7%	1.4%	0.1%	0.6%	1.1%
ductility ratio	0.42	1.00	1.92	0.24	1.00	1.90

Table 4.6 Limit State Threshold Values in Longitudinal DOF

	Pier 1			Pier 2		
	Crack	Yield	Ult	Crack	Yield	Ult
dx (mm)	27.4	61.0	133.4	13.0	26.7	41.9
dx (in)	1.08	2.40	5.25	0.51	1.05	1.65
drift (%)	0.3%	0.7%	1.5%	0.2%	0.4%	0.6%
ductility ratio	0.45	1.00	2.19	0.49	1.00	1.57

The resulting limit state threshold values are first presented in terms of the full-scale simulation results in English and SI units, % drift, and in terms of ductility ratio for the transverse (Table 4.5)

and longitudinal (Table 4.6) directions of the piers. It should be noted here that the slight longitudinal displacement limit state can appear relatively high. This is due to the significant actions resulting from the gravity loading of the bridge. Pier 1 specifically has the greatest asymmetry about it in terms of the relative lengths of each adjacent span. As a result, vertical loading of the bridge deck creates approximately 12mm of longitudinal displacement prior to the application of dynamic loading. Therefore, the threshold limit state is also increased according to this initial offset. It is possible that some early cracking will appear in the longitudinal direction due to static gravity loading, though this is not determined to indicate a significant change in the performance of the overall system.

ii. Structural Response Data

The following values are recorded for each pier under the three levels of seismic loading applied (Table 4.7). Output files from the batch analyses performed for each case include 18 values for each seismic record. These are recorded for each nonlinear time history analyses in the given suite, and serve as indicators for identifying if the bridge has exceeded a particular damage limit state threshold value. In each case, the absolute value of actions and deformations is taken before identifying maxima achieved within a given analysis. As a result, the output data allows for direct comparison to limit state threshold values, which are defined to be symmetric due to the symmetry of the structural specimens. It is acknowledged that differing responses are observed in the positive and negative directions, though these are due to the demand, not the capacity of the specimens. The only slight exception might be noted for the influence of static load in the longitudinal direction of Pier 1. Here, the magnitude of deformation under static loading is significant compared to the deformations reached in the slight level of loading. Apart from this case, the assumption of symmetric behavior in identifying probabilities of exceedance for a given limit state does not fail to capture responses in any degree of freedom. The full set of structural response data is provided in Digital Appendix G.

Table 4.7 Output data for each nonlinear time history analysis

Quantity	Trans. Disp.		Long. Disp.		Trans. Force		Long. Force		Tors. Rot.		Tors. Mom.		Pier 1 Vertical Load			Pier 2 Vertical Load		
	P1	P2	P1	P2	P1	P2	P1	P2	P1	P2	P1	P2	Mean	Min	Max	Mean	Min	Max
Data Col.	1	2	3	4	5	6	7	8	9	10	11	12	13	14	15	16	17	18

It should be noted that an additional study is conducted with the final six vertical load values collected for each pier. Comparisons are made across cases to identify the variance in vertical load

for a given geometry and loading condition. It is acknowledged that relationship between local and global responses, and thus the drift levels observed at the exceedance of a particular local limit state, have the potential to vary under different axial loading scenarios. The range of vertical loads observed under multi-directional loading of a particular bridge geometry, with and without vertical ground accelerations, is used to identify the range of axial load that can be expected in a pier throughout a seismic event. These values presented in Table 4.8 come from the results collected from the severe suite of earthquake records. The resulting variation in vertical loads is associated with a maximum range of 6% of the axial capacity of the piers. This is relatively evenly biased toward an increase and reduction in vertical load on the piers, and is therefore approximated as $\pm 3\%$ axial capacity. The associated variation in deformations under this vertical loading history is inherently captured in the Zeus-NL model subjected to bi-directional horizontal and tri-directional loading. The structural response data therefore contains the effects of vertical loading on the lateral and rotational action-deformation relationships. Therefore, any effects on structural response that might be introduced into the analysis due to vertical load variation are reflected in the vulnerability relationships developed from this data.

Table 4.8 Variation in vertical loading during simulations

	Bi-directional		Tri-directional	
	Pier 1	Pier 2	Pier 1	Pier 2
Average Vertical Load (kN)	4882	2316	4883	2315
Minimum Vertical Load (kN)	4803	2257	3667	1179
Maximum Vertical Load (kN)	5000	2393	6122	3539
Range (kN)	197	136	2455	2360
Approximate Range (+/-%)	2.0%	2.9%	25.1%	51.0%

Each of the 16 combinations of geometry, model calibration, and loading scenarios has now had three nonlinear time-history analyses performed in Zeus-NL, once for each suite of earthquake records. These records were selected carefully to vary in spectral content, site condition, and relative magnitude of various components. Therefore, the key structural response parameters collected are suitable for the development vulnerability relationships that are not biased to any structure or site conditions. These curves, developed and discussed in the following chapter, allow for the

examination of the influence of varying load combinations applied to calibrated and uncalibrated models of curved and straight bridges.

CHAPTER 5: BRIDGE FRAGILITY RELATIONSHIPS

In this chapter, the format and procedure for developing vulnerability relationships for RC bridges with various parameters is provided. Fragility curve generation is a form of statistical analysis performed on the structural response data obtained through the analyses described in CHAPTER 4. The resulting responses are used to generate standard two-parameter lognormal fragility curves. These relationships are able to represent the inherent uncertainty in bridge capacity and ground motion demand. The format of the relationships presents the probability of exceeding the defined limit state threshold values (obtained in Section 4.5 relative to a given ground motion intensity (GMI) parameter. The primary GMI parameter examined in this study is selected to be the peak ground acceleration (PGA). Investigation of the use of peak ground displacement (PGD) as the GMI parameter were conducted as well, and are not recommended for assessment and comparison purposes for the example bridge typology. This is due to the high levels of dispersion and lack of a consistent relationship between PGD and bridge response. Vulnerability relationships for a long-span bridge or otherwise long-period structure might display greater sensitivity to displacement intensity measures due to the influence of static displacements if directivity effects were accounted for in seismic loading. Peak ground motion parameters are selected over spectral quantities because they lend themselves to a more straightforward procedure when conducting risk assessment. This is due to the relative ease of obtaining these parameters directly from seismic records. It is acknowledged though that the selection of peak parameters over spectral parameters has the potential to result in higher levels of dispersion in the resulting fragility curves. This is due to the varying levels of response amplification of the bridge for different records with the same PGA and different spectral content.

By comparing the fragility curves derived for cases with the various differing parameters outlined in Table 4.2, the individual and combined influence of complex system-level behavior on the vulnerability of RC bridges can be assessed through examining these curves. A set of correction factors are then proposed to approximate the statistical influence of the individual factors of geometric, loading, and model calibration parameters. In lieu of performing additional analyses, these factors could be implemented to modify the parameters of existing fragility curves already developed for a specific application. With further development, it may be possible in the future for researchers to utilize fragility curves currently available in the literature to assess seismic

vulnerability for a wider range of complex bridge and loading scenarios than the existing curves were originally applicable for.

It is acknowledged at this point that no new advancements in the field of statistical analysis or fragility generation techniques are presented here. A simple and straightforward methodology for developing fragility curves from the response data is utilized instead. It is important to note therefore, that development of risk assessment techniques is not the main objective of this study. Instead, focus is placed on the quality of the capacity and demand models developed through rigorous model calibration based off of high quality experimental data and careful selection of records. The greatest strength of the research program presented here lies in the fact that the fragility relationships are developed in such a way that they capture combined interaction effects on system-level bridge response. Then, the primary objective becomes utilizing these curves to identify the impact of geometrical, loading, and modeling parameters on seismic vulnerability assessment.

5.1 Fragility Generation Procedure

i. Fragility Curve Format

Modeling of structural capacity and seismic demand both have varying degrees of uncertainty associated with them. The uncertainties considered are both epistemic, due to lack of knowledge, missing information, or errors in modeling, and aleatory, due to the fact that many of the factors which affect the resulting relationships are inherently random. If the uncertainties conform to either a normal or log-normal distribution, then following the central limit theorem, the resulting outcome from combining these uncertainties is lognormally distributed. Therefore, the resulting relationship between exceedance of a limit state and a ground motion intensity parameter can be expressed by a log-normal cumulative distribution function (P) as shown below. This curve is defined by a median value and a normalized logarithmic standard deviation. This curve function can be expressed in the following form:

$$\mathbf{P(Exceedance}_i\mathbf{|GMI)} = \Phi \left[\frac{1}{\beta_i} \ln \left(\frac{GMI}{LS_i} \right) \right] \quad (16)$$

where GMI is the ground motion intensity parameter (PGA for the remainder of this discussion), LS_i is the median value (the ground motion intensity at which the 50th percentile of exceedance for the i^{th} limit state occurs), and Φ is the probability density function of the normal distribution. β_i is the normalized log-normal standard deviation, obtained from regression analysis of the exceedance values of the response data for each limit state, similar to (Hwang, Liu, & Chiu, 2001) and (Wen & Ellingwood, 2005). This parameter is also referred to as the coefficient of variation (CV) and represents the dispersion in potential response that is associated with the resulting fragility curve. A higher coefficient of variation will reduce the slope of the fragility curve, indicating a greater dispersion of ground motion intensity values over which a range of probability of exceedance values for a given limit state will span.

ii. Resulting Curves and Parameters

The resulting fragility curves for varying cases are provided below, with the three structurally-based limit states defined as the slight, moderate, and severe limit state threshold values. Again, distinctions are made between calibrated and uncalibrated structural models, as well as curved and straight bridge geometries. Seismic loading of the natural records is applied in one of four uni- or multi-directional cases. These include transverse only (perpendicular to the main span of the bridge deck), longitudinal only (along the main span of the bridge deck), both transverse and longitudinal combined bi-directional loading, and finally tri-directional loading with the addition of the vertical component. The resulting fragility curve parameters for all 48 cases are provided in Table H.2 through Table H.5.

The procedure performed in this work, including careful execution of the hybrid simulation, model calibration, and record selection produces a set of fragility relationships that are accurately based in experimental data. Thus, there is the potential for application of these relationships in impact assessment studies, as long as the use of the curves is limited to this bridge typology. Still, the resulting fragility relationships presented in this chapter are to be considered primarily in the context of evaluating the influence of these parameters on structural response. A total of sixteen plots, one for each geometry, calibration, and loading scenario, are provided in Appendix H.1. Each plot contains one curve for each of the three limit state definitions, as shown in the example for curved calibrated models subjected to uni-directional longitudinal loading (Figure 5.1). In the following

figures, the slight, moderate, and severe limit states will be represented by green, red, and black traces, respectively. They will also naturally appear in this same order from left to right. Legends are provided to indicate which of the 48 curves is displayed in each plot. Table H.1 provides a key to the notation used to identify the cases compared in each of the figures presented in this chapter and in APPENDIX H.

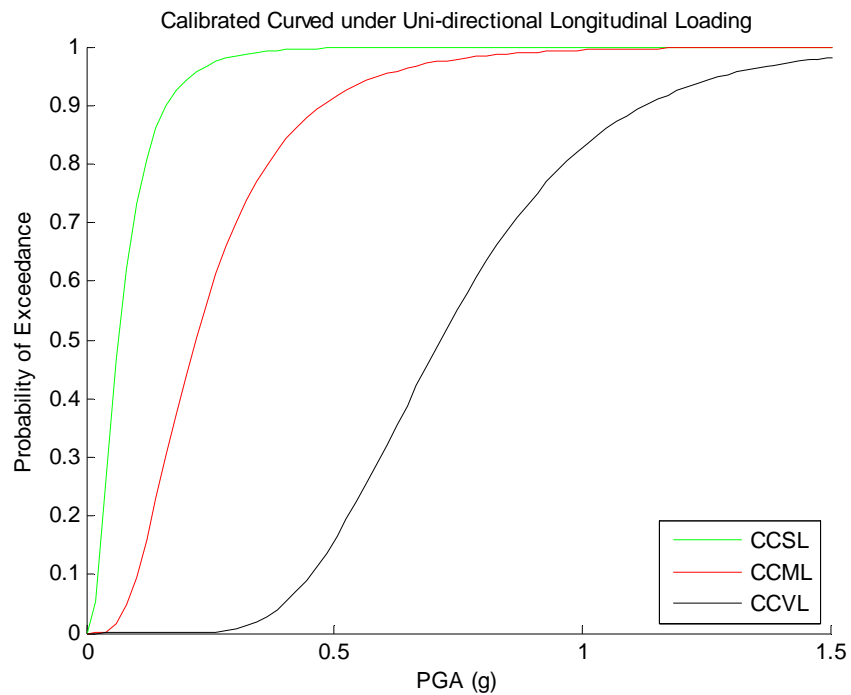


Figure 5.1 Calibrated Curved model subjected to Uni-Directional Longitudinal loading

Through the comparison of these vulnerability functions performed below, an increased understanding of the effects of various bridge conditions and modeling decisions on structural response can be assessed. The impact of these observed or perceived changes in seismic vulnerability, and the resulting potential influence on loss estimation methods can then be determined. These results are important because they reveal the degree to which the results of a study can be impacted based off of various assumptions made in terms of geometry, loading, and modeling. These effects should be considered by researchers when making decisions regarding future experimental and analytical seismic assessment studies.

5.2 Impact of Varying Parameters on Bridge Vulnerability

Below, the individual and combined effects of varying bridge parameters are compared through plots of fragility curves for each case. Geometry, model calibration, and directions of load application are considered. In each case, two parameters are kept constant, while the effects of varying the third are studied. In the cases where geometry and model calibration are evaluated, all three limit state curves are displayed. For the purpose of assessing the influence of varying the directions and combinations of loading, only one limit state is plotted at a time in order to allow for easier inspection of results. Upon review of individual effects, specific combinations of these cases are then compared to assess the combined influence considering multiple parameters at the same time.

i. Individual Effects

In each of the following discussions, a selection of cases is presented to evaluate the influence of an individual parameter. In the order assessed, these are bridge geometry, seismic load application, and model calibration. The resulting variations in vulnerability relationships due to the change in this parameters is only known to hold for the reinforced concrete bridge typology and initial uncalibrated model assumptions presented in this paper. However, the potential for extending results to other bridge classes could possibly be made in a qualitative sense for changes observed in vulnerability due to global geometry conditions alone. Still, future work is required to make this assessment due to the varying conditions that may indicate performance levels for different bridge classes.

a) Bridge Curvature

Plots of the fragility curves developed for comparing curved and straight bridges vulnerability are presented below for 2 of the 8 total parameter combinations of model calibration and loading direction (Figure 5.2 and Figure 5.3). The cases shown below are for the calibrated models only. Results for the remaining cases, including for uncalibrated models, can be viewed in Appendix H.2 . Fragility curves for all three limit states are presented in each plot.

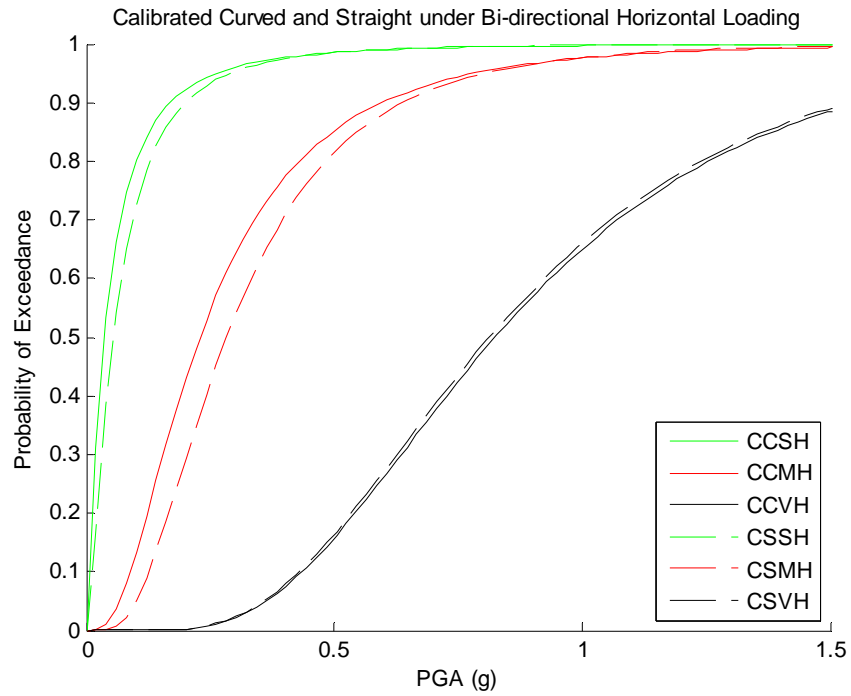


Figure 5.2 Calibrated Curved and Straight bridges subjected to Bi-Directional loading

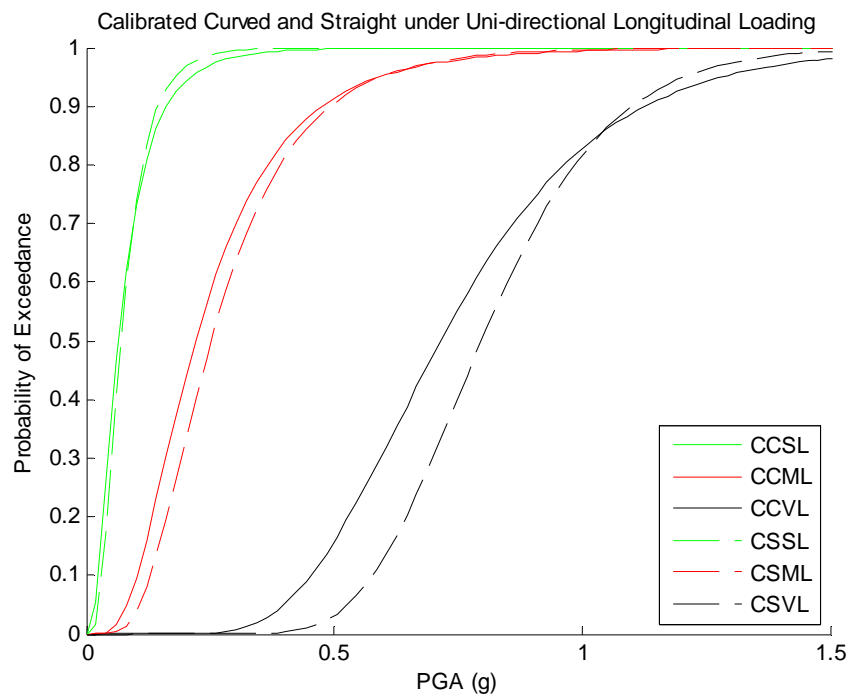


Figure 5.3 Calibrated Curved and Straight bridges subjected to Uni-Directional Longitudinal loading

The influence of the curvature of the bridge is consistent across most of the cases assessed in this study. For a given limit state, degree of model calibration, and direction of input loading, a curved bridge is typically shown to be more vulnerable. This is indicated by having a greater likelihood of exceeding a given limit state at a lower level of ground motion intensity than a straight bridge with identical model and loading parameters. This is expected, and is the result of softening of the response in various degrees of freedom due to combined actions. The curved bridge is subjected to greater levels of torsional load applied to piers that are experiencing similar levels of axial, flexural, and shear deformations as their counterparts in the straight bridges. This phenomenon was observed at multiple stages of data analysis from the hybrid test, and was also confirmed at several points in the calibration process.

It should also be noted that the dispersion associated with the vulnerability of the curved bridges is generally higher than that of the straight bridges. This is most notably observed when two fragility curves for the same limit state intersect. The solid lines, representing the probability of limit state exceedance for curved bridges, are more sloped than the traces of the straight bridges, and if the median values of the fragility parameters are close enough, the traces will intersect. This is likely due to the increased complexity of the responses, and the varying degree of combined interaction effects that result under different records. This is shown to be true for multi-directional loading cases in the following section. Therefore it is natural to conclude that the influence of different levels of loading in each primary direction also have the potential to increase the dispersion of structural response, particularly at higher load levels in the region of the severe limit state values.

Exceptions to the trend of increasing vulnerability for curved bridges include some comparisons of the severe limit state (Figure 5.2), as well as the slight-longitudinal limit state (Figure 5.3). The trend discussed above does not always hold at the severe limit state because the shift in vulnerability is due to the influence of early precipitation of certain mechanisms in the curved bridge. At higher levels of demand, these mechanisms may fully develop regardless of the different levels of combined actions that are influenced by bridge geometry. Therefore the observed response for curved and straight bridges may be similar at the severe loading case. The influence of the hybrid simulation and abutment models on curves developed from longitudinal loading is discussed in the next section. In general though, the relationship of higher seismic vulnerability for curved bridges holds true. In any case, the overall impact demonstrates the importance of considering the effects of bridge curvature in

seismic assessment of RC bridges, namely the measurable increase in vulnerability to seismic loading observed in most cases.

b) Multi-Directional Loading

Plots of the fragility curves that display the influence of considering varying combinations of seismic loading are presented below. The loading parameters examined are uni-directional transverse, uni-directional longitudinal, bi-directional horizontal, and tri-directional loading. Each plot displays the influence of the loading parameter for only one limit state in order to minimize the number of curves on an individual plot. Three plots are provided below, one for each limit state for the calibrated curved bridge model subjected to varying loading cases (Figure 5.4 - Figure 5.6). Comparisons for each of the remaining combinations of bridge geometry and model calibration are provided in Appendix H.3 .

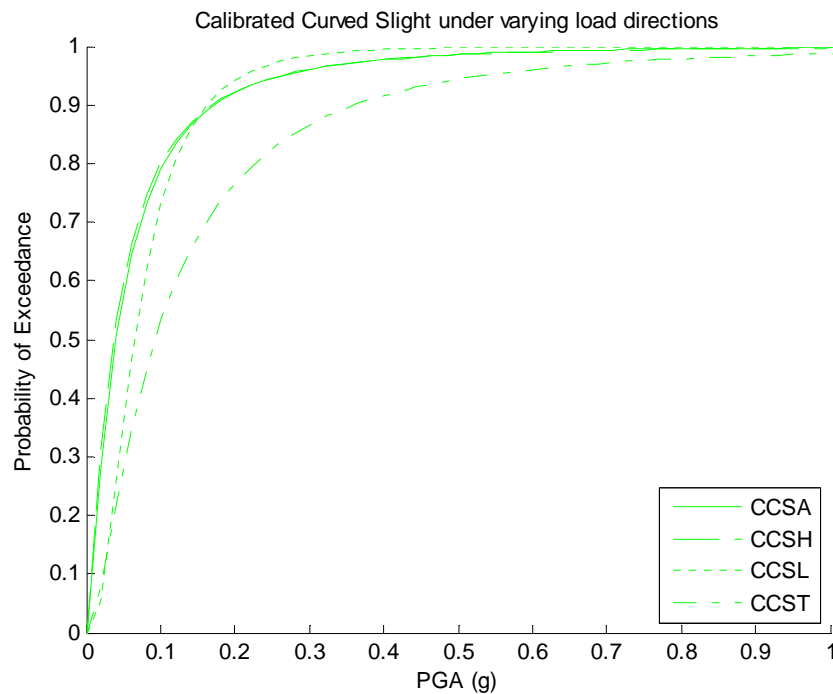


Figure 5.4 Calibrated Curved Bridge - Slight limit for varied loading

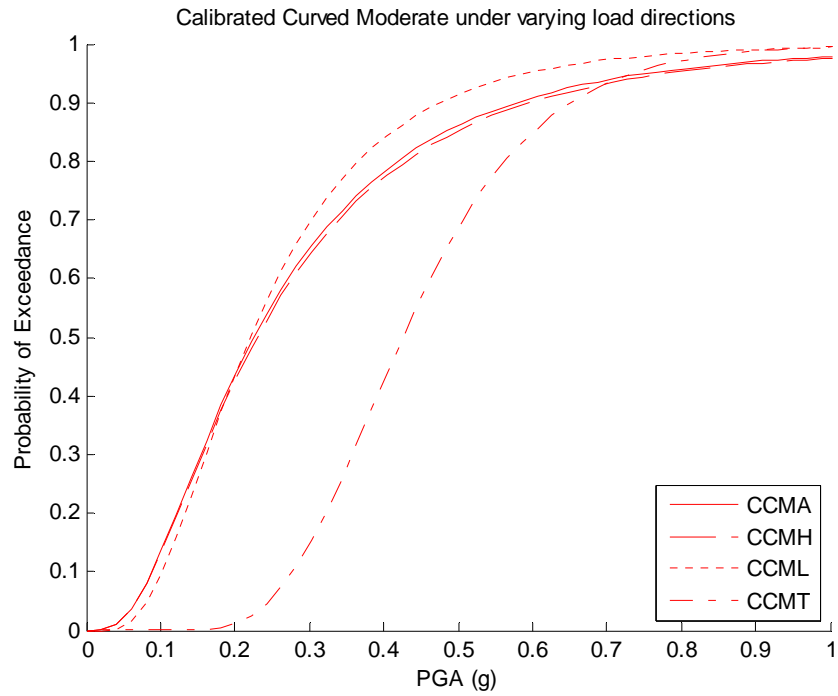


Figure 5.5 Calibrated Curved Bridge - Moderate limit for varied loading

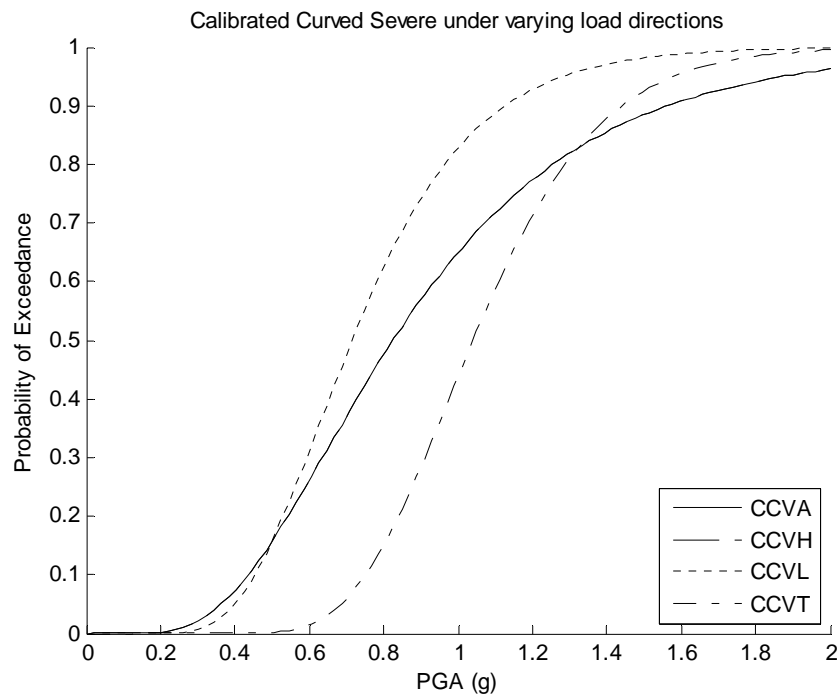


Figure 5.6 Calibrated Curved Bridge - Severe limit for varied loading

The impact of varying combinations of applied loading on bridge vulnerability is shown to be fairly consistent across all of the cases assessed in this study. For a given limit state, bridge geometry, and degree of model calibration, uni-directional transverse loading of a bridge is always shown to exhibit the lowest probability of exceeding a given limit state at a particular ground motion intensity than the curves developed under multi-directional loading for this same case. This can be observed by comparing the dotted and dashed trace in each of the figures to the solid or dashed curves. This is expected, and is again attributed to the higher levels of combined actions that result from multi-directional loading on a bridge of any geometry. The softened response and potential for additive stresses and strains at certain points of the structure yields this increase in vulnerability.

An important note is now provided regarding the unique behavior and resulting fragility relationships developed for bridges subjected to longitudinal loading only. In many of the figures presented, bridges subject to uni-directional longitudinal loading appear to exhibit higher vulnerability than even the multi-directional loading cases. This is potentially due to several factors. First of all, the restraints in the longitudinal direction of the bridge will result in local mechanisms occurring at lower deformation levels than those same limit states defined for the transverse direction of pier response. Since the abutment model in the longitudinal direction includes a gap element which exhibits very low stiffness until the shear key is engaged, these displacements can be realized earlier under longitudinal loading. In a similar way, high longitudinal displacements are realized when the shear key capacity is exceeded, which is only observed when the bridge is subjected to high levels of longitudinal loading. Each of these influences is amplified for straight bridges, where the longitudinal application of loading is directly in line with the shear key and gap elements. Abutment models are not addressed in the calibration procedure because the same models are used in the hybrid simulation. Discussion of how to view longitudinal response in terms of overall bridge behavior is identified as an area where further investigation is required.

It should also be noted that there was very little difference in the vulnerability relationships for bi-directional and tri-directional loading cases. This indicates that an increased variation in axial load, at least within the ranges observed in this study, had a minimal effect in the lateral deformations of the bridge piers that were used to define structural performance levels. In many cases, the fragility curves for these two cases are nearly identical.

Finally, an increase in the degree of seismic loading is shown to result in a significant increase in the dispersion of the vulnerability relationships developed. Throughout the plots presented, the bi-

directional and tri-directional loading cases have shallower curves, indicating greater dispersion. This is due to the increased complexity of the response, as well as the varying ratios of transverse and longitudinal loading associated with any particular record. As discussed above, the influence is greater in cases with curved geometry that are already subject to higher uncertainties under a given load due to greater degrees of complex load interaction effects. The rapid changes in stiffness characteristics in the longitudinal direction result in the lowest level of dispersion for curves generated under this loading condition, as indicated by the relative steepness of these curves.

The overall conclusion to be drawn from these results focuses on the importance of considering multi-directional loading in structural assessment. Direct comparison of transverse and multi-directional loading indicates significant changes in seismic vulnerability functions. Researchers performing uni-directional loading of structures such as an RC bridge of this type, should be aware of the un-conservative results that they may report to obtain. This is because it is very likely that the loading and boundary conditions selected in a study with only uniaxial loading will neglect the combined interaction effects that will realistically be experienced in the field.

c) Modeling Assumptions

Plots of the fragility curves developed for comparing calibrated and uncalibrated models are presented below for 2 of the 8 parameter combinations of bridge geometry and loading direction (Figure 5.7 and Figure 5.8). These two cases are for the curved calibrated and uncalibrated models only. Results for the remaining curved and straight bridge cases can be viewed in Appendix H.4 . Fragility curves for all three limit states are presented in each plot.

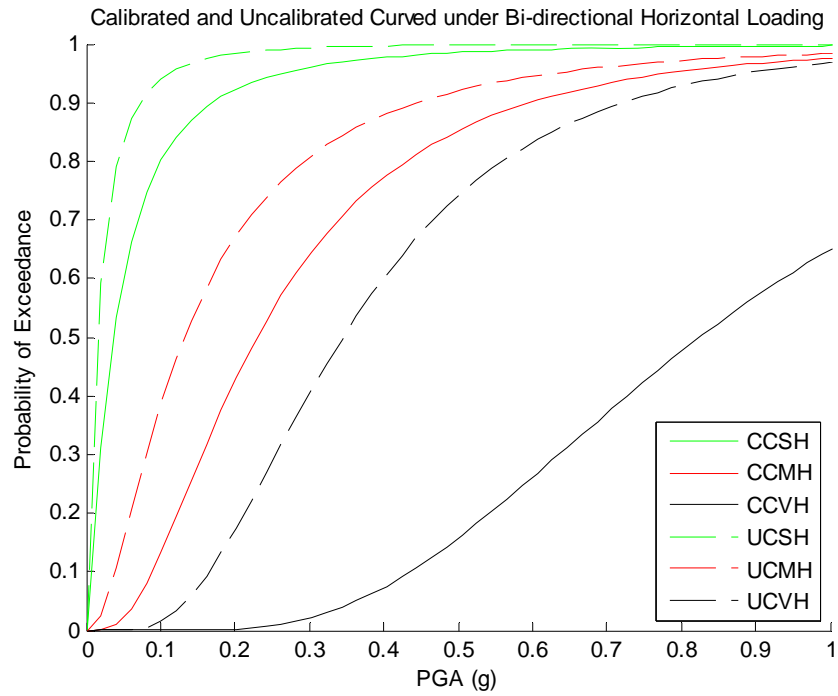


Figure 5.7 Calibrated and Uncalibrated Curved bridge subjected to Bi-Directional loading

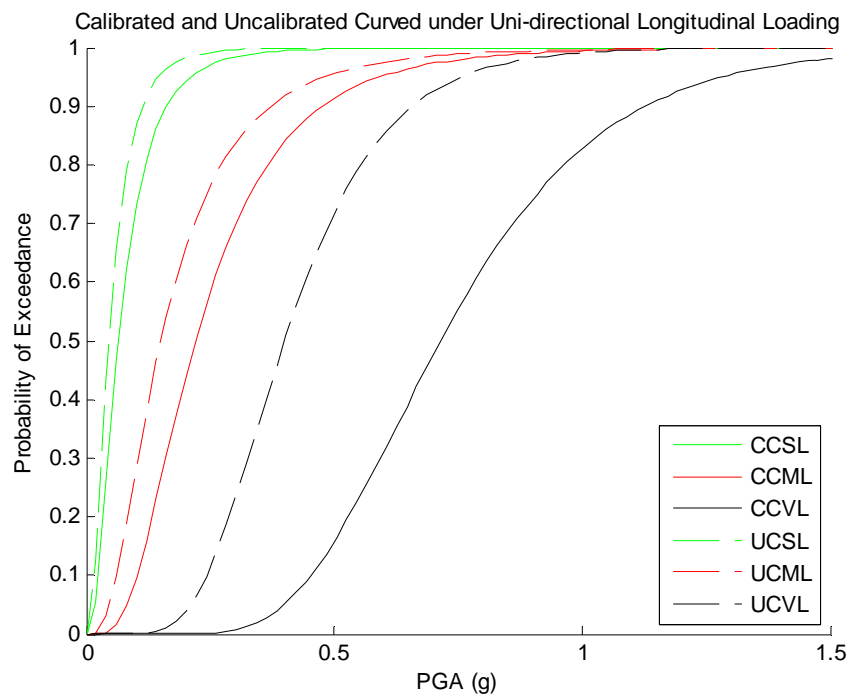


Figure 5.8 Calibrated and Uncalibrated Curved bridge subjected to Uni-Directional Longitudinal loading

The influence of model calibration is the same across all of the cases assessed in this study. For each limit state, geometry, and direction of input loading, the calibrated bridge models are shown to have higher vulnerability. This is exhibited in lower probabilities of exceedance for a given limit state at each level of ground motion intensity than the corresponding uncalibrated models. Upon initial observation, this may seem counterintuitive since much of the model calibration procedure details the application of springs to correctly model stiffness degradation. With lower stiffness resulting in higher displacements at a given level of loading, one might expect higher displacements in the calibrated model than the uncalibrated model. However, these components of the model calibration took place following a significant adjustment in structural damping to bring analytical results of the model closer to those of the experimental response. As can be seen in the displacement time histories of Figure D.16 - Figure D.23, the peaks of the uncalibrated analytical response were consistently as much as twice that of the peak displacements in the experimental data.

The reduction in stiffness of the calibrated models therefore does not outweigh the initial overestimation of displacement (and force) parameters resulting from the inability of the uncalibrated model to appropriately capture hysteretic damping effects. As a result, in this study, the assumptions initially made in the analytical model contributed to an overestimation of the vulnerability of the structure. This was due to incorrect expectations regarding potential sources for damping and the capability of the numerical model to effectively represent these sources. It should be noted that the incorrect modeling assumptions made in this study may differ significantly from those in other studies and result in underestimating seismic vulnerability. Carefully developed computational models may require fewer calibrations when compared to experimental results. However, the procedure should still be conducted in order to validate results obtained in seismic assessment procedures rooted in numerical simulation.

Finally, it is noted that the dispersion associated with the vulnerability of the calibrated bridge models is lower than that of the uncalibrated models. This is natural, given that the model calibration procedure involved increased damping of the calibrated model, which also reduces peaks that result in greater dispersion of results. Again, it is noted that the nature of the initial analytical modeling assumptions, as well as the degree of model calibration, have the potential to change the relative influence of model calibration on seismic assessment results. Regardless, the observed relationships highlight the importance of performing model calibration to develop realistic relationships for

performing seismic vulnerability assessment. The nature of the influence of various assumptions and features of a model may change. In any case, however, calibration of analytical models to high quality experimental data will improve reliability for vulnerability assessment through accurately accounting for incorrect assumptions and incomplete model features.

ii. Combined Effects

Upon review of the individual influences of geometry, loading, and modeling assumptions on fragility relationships, it is determined that a critical combination of conditions should be examined. The combined result that varying multiple parameters has on vulnerability of reinforced concrete bridges of this typology is therefore presented below. The case investigates changes in geometry and loading for calibrated models only. Figure 5.9 presents a comparison between vulnerability curves for a straight bridge subjected to uni-directional loading and a curved bridge subjected to multi-directional loading. The results of varying each of these parameters simultaneously are presented for each limit state definition. This comparison is selected to illustrate the extent to which experimentally-based models could still produce unreliable vulnerability relationships if incorrect assumptions are made in the geometry and loading conditions applied in experimental and analytical testing programs.

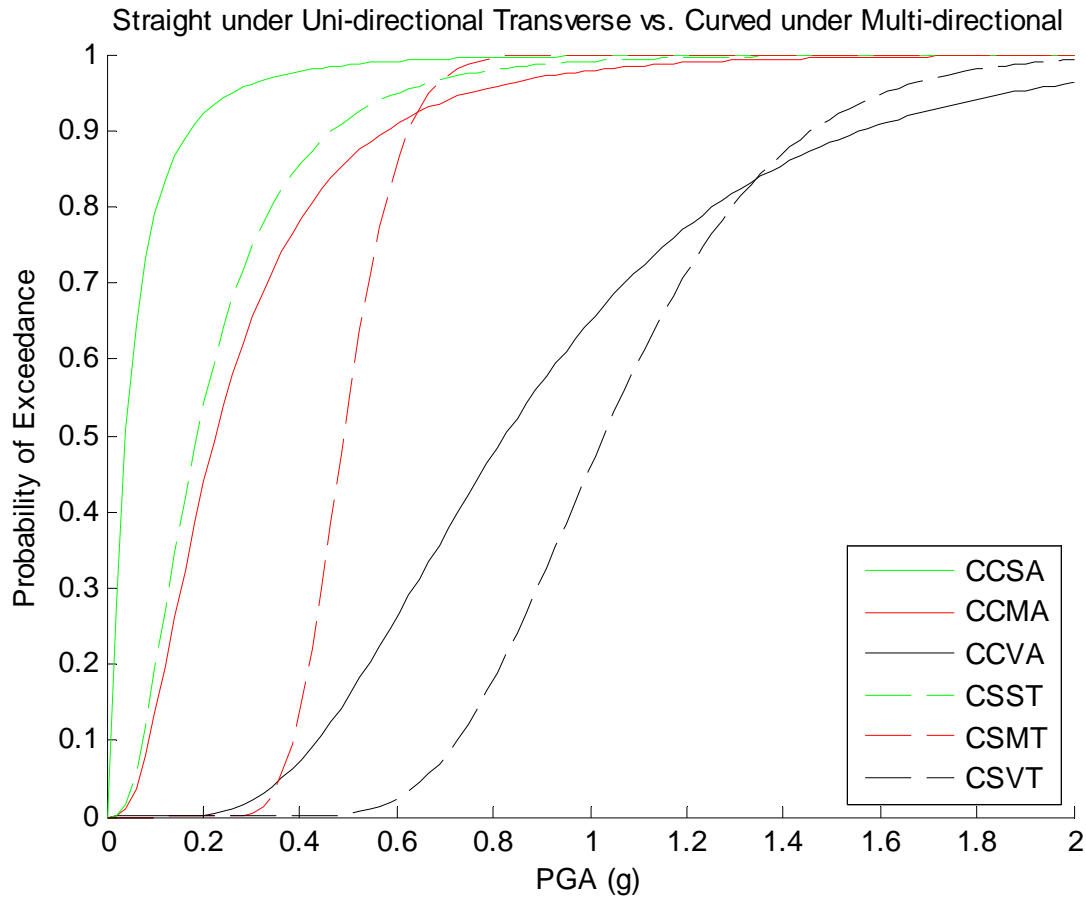


Figure 5.9 Combined influence of geometry and combined loading on seismic vulnerability

For the sake of comparison, the straight bridge subjected to uni-directional loading, represented by the dashed curves) will be referred to as the simple case. The solid lines, representing the curved bridge subjected to multi-directional loading, will be referred to as the complex case. The significant increase in seismic vulnerability that is observed in moving from the simple to complex case is due to increasing the propensity for the overall geometry and loading combination to exhibit greater levels of combined actions. This is most significant at the slight and moderate limit states, as was discussed in the analysis of the severe fragility curve parameters for varying geometries. Additionally, the complex case exhibits significantly higher levels of dispersion, which increase with increasing levels of seismic input.

The results presented above continue to reinforce the importance of considering the consequences of applying simplified loading cases to 2D regular structures. Experimental and analytical assumptions

and simplifications result in the absence of these combined effects, which are shown to significantly influence seismic vulnerability. If no attempt is made to represent irregularities or asymmetries in any way, seismic assessment of bridge systems based on oversimplified results will yield a significant underestimation of consequences for a realistic earthquake scenario.

5.3 Methodology for Simulating Complex Bridge Effects

Having examined and isolated the varying influence of geometry, loading, and modeling on the vulnerability functions of a curved RC bridge, the question of how the community might be able to employ this knowledge is addressed. A straightforward method is proposed for appropriately modifying fragility curve parameters to account for these various effects. In order to employ this concept, a user would have to identify which case their experimentally or analytically derived fragility curves falls into. If the relationship does not capture a certain characteristic such as curved geometry or multi-directional loading, then the user could apply a modification factor to the fragility curve parameters developed for a seed case to generate vulnerability relationships for a variety of other cases which have the ability to more accurately capture the influence of more complex seismic scenarios than were initially accounted for in the original study that produced the seed curve.

A similar procedure is developed and proposed in (Choe, Gardoni, & Rosowsky, 2010) to simulate the effects of deterioration of RC bridge columns, specifically the corrosion of reinforcing steel, on fragility functions. A set of fragility increment functions were developed for varying environmental and material conditions. The proposed procedure involves multiplying the initial fragility of the non-deteriorated, or “pristine,” columns by these functions. In the work presented in the following section, only a set of simple factors are developed for three parameters. These parameters are introduced and described below, and correspond to each of the variables considered in the above assessment of fragility relationships. The limited applicability of these specific factors to the field of seismic risk analysis is then stated along with the additional work required before realistic application of this procedure to seismic assessment frameworks could be achieved.

i. Modification Parameter Development

A proposed method for the development of modification factors is now provided. These factors are developed by examining the change in the two fragility relationship parameters, the median and CV values, when only one of the model parameters of geometry, loading, or calibration is varied. The change in median and CV values are checked across all combinations of cases where only that specific model parameter changes. The influence is first defined as the direct change in the value of the parameter. Next, the change is examined as a percentage increase or decrease of a baseline case. For the purposes of this comparison, it is natural to select the most basic variation of each parameter as the baseline case. For example, the influence of geometry on the vulnerability parameters will be presented in terms of the impact on the fragility curve function that is observed in moving from straight to curved geometry. Likewise, loading cases will be evaluated as the influence of moving from uni-directional transverse to the more complex tri-directional case. Finally, the impact of model calibration will be evaluated with the uncalibrated model serving as the baseline for evaluation of the impact of the modeling parameter.

Table 5.1 Relative shift and proportional change in fragility parameters

Factor	Shift in Median	% Change in Median	Shift in CoV	% Change in CoV
Geometry	-0.04	-24.30	0.15	23.73
Calibration	0.07	87.74	-0.19	-22.01
Loading	-0.14	-53.37	0.30	82.09

Table 5.1 displays the average resulting scaling factors for median and coefficient of variation fragility parameters. Plots of the distribution of these parameters across all cases for the slight and moderate limit states are provided in Appendix H.5 . An example of the proportional change in median and dispersion values resulting from a change of bridge curvature are provided in Figure 5.10. The notable exclusion from this plot and from the average scale factor values is the slight uncalibrated case where exceedance occurs immediately, resulting in miniscule median and CV values not suitable for use in a calculation of percentage change from a starting value. Factors obtained from the severe records are not presented here due to the higher degree of uncertainty associated with these fragility relationships. This is due in part to the limited number of seismic records which result in exceedance of this limit state, as well as the highly nonlinear behavior of the bridge when it has reached this performance level.

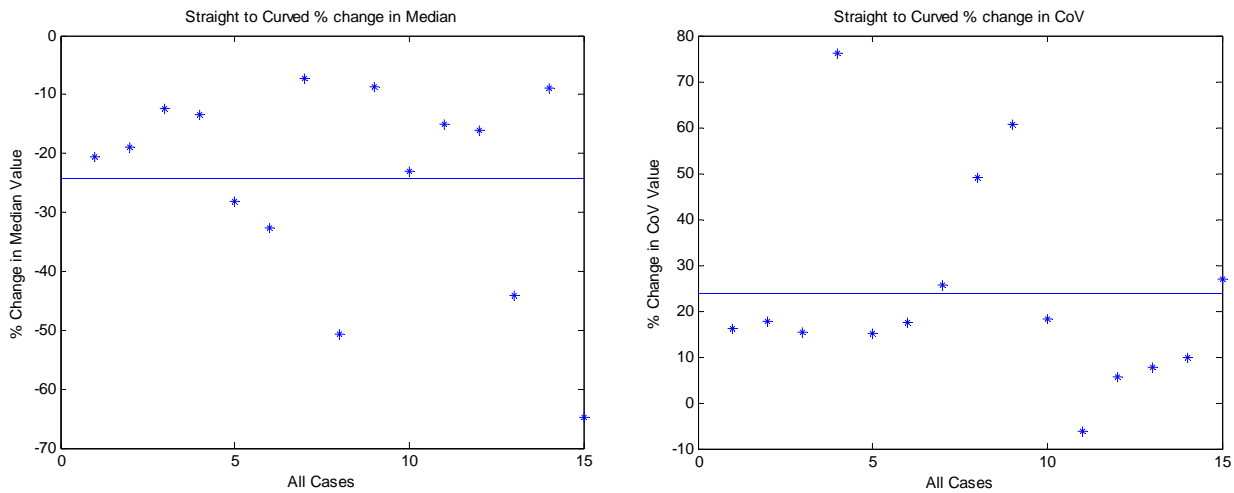


Figure 5.10 Percent change in median (*left*) and CV (*right*) values resulting from bridge curvature

The resulting influence in terms of changes to fragility curve parameters is fairly uniform. The conclusions that can be drawn from these values are the same as those observed visually in the above discussion of the curves themselves. That is, that moving from straight models subjected to uniaxial loading to curved models subjected to multi-directional loading results in higher vulnerability (lower median value) and higher dispersion (higher coefficient of variation). Conversely, consideration of calibrated models compared to uncalibrated models yields lower vulnerability (higher median value) and lower dispersion (lower coefficient of variation). In the cases where there are outliers in the methodology of applying factors as a percentage change, conditions exist such that application of a direct change in the parameter is more representative of the actual influence in vulnerability parameters.

ii. Applying Modification Parameters in Impact Assessment Framework

It is acknowledged that a more significant database of results from high quality experimental tests and calibrated numerical analyses is needed in order to ensure a degree of confidence in this proposed method for updating fragility parameters. A wider variety of bridge curvatures should be included in order to improve the ability of the geometric design factor to appropriately account for

the introduction of combined actions due to the irregularity of the structure. Similarly, analyses for a wide range of angles of incidence for the same suites of earthquake records are needed to assess the potential effects on the complex loading factor developed. Finally, a set of modeling assumptions and their varying effect in terms of structural response need to be developed. As varying assumptions have the ability to result in either over-conservative or under-conservative fragility relationships, the modeling effect factor is perhaps the factor that would be most challenging to realistically develop and employ. A great deal would have to be known about the relative influence of each testing or modeling decision, in order to appropriately select which components of a modeling effect factor to apply in adjusting fragility curve parameters. Additional information and further studies are necessary to investigate the influence of various aspects of geometry and loading direction as well.

The actual modification factors presented in this paper are therefore not suggested for use in developing new fragility curves for use in impact assessment or loss estimation studies. Too little is known about the influence of the class of RC bridge and the bridge typology addressed in this study on these factors. In addition, the combined influence of model calibration for generation of the modeling effect factor includes multiple changes, none of which have been isolated in terms of their impact on vulnerability functions. Therefore, a more exhaustive parametric study for each factor, with the inclusion of data from other high-fidelity simulations, would be required to validate or contribute to the formulation of these factors such that they could be applied with some degree of confidence.

There is certainly potential for further development and implementation of the first two modification factors regarding geometry and combination of loading. With additional sources to support the relative influence on fragility curves identified in this study, these parameters could be used in a straightforward manner to directly modify the curve parameters of previously defined vulnerability relationships. These factors would likely become a component of more complex functions that would be capable of accounting for and applying appropriate weights to multiple uncertainties in demand and capacity modeling. A validated set of functions would be an extremely useful tool within the field, given the expansion to the applicability of existing fragility relationships that could be achieved. Numerous curves for bridges under varying conditions could be developed without performing any additional reliability analyses. Bayesian updating could then be utilized to conduct continual improvements to the parameters employed in such a framework. This concept is discussed in the future work section in the following chapter.

CHAPTER 6: CONCLUSIONS

Chapter 6 presents conclusions of the findings in this study as well as recommended areas of future work. The components of the research presented here are summarized, with main findings provided throughout the summary of the study. The achievements of the hybrid simulation and validity of the resulting data set for use in model calibration is highlighted. Model calibration, record selection, and limit state definition procedures are discussed in light of their impact on structural response. The response data obtained from analyses of bridge cases with varying geometry, loading, and modeling parameters is assessed. The resulting effects of combined actions on seismic assessment and associated bridge fragility curve parameters are discussed. These results are presented within the context of bridge system-level performance. The implications of these results on decisions made regarding geometry and loading conditions for future testing and modeling of bridges for seismic assessment are addressed.

Suggested areas of future work are then proposed. First, a set of additional parameters that could also be assessed through a similar procedure to determine their influence on seismic vulnerability are presented. Then, potential improvements to the methods and procedures described in this work are discussed. These include extensions and improvements in the areas of model calibration, limit state definitions, fragility curve format, as well as the proposed use of Bayesian updating of the presented fragility relationships. Finally, recommendations for potential areas of future research with more broad impact are provided. These include additional discussion of the application of Bayesian updating for application of the results presented here to other results in the literature, as well as the development of modification factors into functions that could expand the applicability of existing curves in the literature. Finally, recommendations for potential design considerations in members susceptible to combined actions including torsion are presented.

6.1 Main Findings

The level of complexity and precision that is achieved in the hybrid test presented in Chapter 3 is uniquely capable of realistically capturing the system-level response of RC bridges. This includes the

following features which support the use of this data set to calibrate models for use in seismic assessment methods.

- Preliminary studies indicate the influence of bridge irregularity on levels of combined actions in piers, including torsion. Pier heights and spacing are selected to increase torsional demand, while still maintaining a bridge geometry which could feasibly be required by site conditions in the field.
- The 6DOF loading and control capabilities of the NEES MUST-SIM facility enable precise control and accurate measured responses of the specimens in any combination of deformations and actions. This enables researchers to provide realistic combinations of loading and boundary conditions without making assumptions in any degree of freedom.
- Errors are introduced in many experimental testing programs that assume infinite stiffness within the loading units and connections of their test setup. A correction algorithm in the hybrid simulation accounts for deformations that occur outside of the specimen, thus obtaining more reliable data on the stiffness of specimens in each direction.
- Hybrid simulation allows for the data obtained to represent the full system-level response, appropriately reflecting the interaction between the piers, superstructure, and abutments. This enables the pier responses to be subjected to the combined actions that result from the curved deck, as well as the irregularity introduced through uneven spans and pier heights.
- Interaction effects between components of bridge systems are not typically accounted for in other experimental studies, and piers are rarely controlled in all six degrees of freedom.
- The structural response results of this test demonstrate the important influence of combined actions on response of bridge piers, particularly the influence of torsion on lateral action and deformation response.
- Non-contact instrumentation data is processed to provide numerical and visual descriptions of the nonlinear behavior. This improves conceptual understanding of the complex response of RC bridge piers subjected to combined actions, and provides additional information for performing model calibration.
- The high level of certainty surrounding this data set is established to justify the use of this data for developing calibrated models capable of capturing the influence of combined actions and system-level response.

Model calibration is performed to obtain a high degree of agreement between numerical results and the experimental data set. Corrections for assumptions made in the initial uncalibrated model are

adjusted for through the inclusion of several nonlinear springs. It is proposed that the careful calibration of models is most essential in cases where irregularities in geometry and the application of multi-directional loading result in combined actions in structural components.

- The initial assumption of fixed end conditions and rigid body motion at the pier-cap interface proves inaccurate and overestimates the flexural stiffness of the pier response. Nonlinear rotational springs are provided in the flexural and torsional degrees of freedom at the top and bottom of each pier to appropriately model the stiffness degradation and hinge formation at these locations.
- There is a severe reduction in stiffness and accelerated stiffness degradation in the torsional response under combined loading when compared to pure torque-twist response. A nonlinear torsional spring is developed and implemented, resulting in improved matching of lateral displacements in the calibrated model as well.
- The numerical model was shown to be incapable of fully capturing hysteretic damping. Actions and deformations in the analytical model are therefore overestimated, particularly at higher levels of load. Distributed Rayleigh damping is provided to account for these damping effects, and effectively reduces these responses.
- Initial and degrading stiffness behavior is adjusted in each degree of freedom using the derived 6DOF data coupled with global pier response. Adjustments in the stiffness of each degree of freedom typically impacted other degrees, displaying some influence of combined actions and particular influence of torsional response on lateral actions.
- Other adjustments made in model calibration reveal that significant reductions in stiffness occur in the torsional response. Softening in the torsional degree of freedom is also shown to in turn influence the lateral deformation and load capacities, indicating the significant influence of interaction effects.

Limit state definitions are carefully developed from the experimental data set. An automated procedure identifies strain indicators for local mechanisms and plots this data against global pier response. Visual observation of cracking and spalling, as well as examination of stiffness degradation at various stages of the simulation are also noted. Together, these results are used to develop a relationship for mapping local actions to global deformation response. Limit state threshold values are set according to these global deformations, and are capable of representing exceedance of the defined slight, moderate, and severe limit states developed in this study.

A comprehensive suite of natural seismic records is selected for use in nonlinear time history analysis. Great care is taken to remove any statistical bias for site condition, response spectra, and effects of loading direction applied. This suite of records is carefully developed to ensure a high resolution of data for use in fragility analysis without the need for developing synthetic accelerograms or scaling natural records. The resulting sets of natural records are selected to conduct a comprehensive set of analyses for each calibrated model in order to develop reliable fragility curve parameters at each limit state.

A series of nonlinear time history analyses are performed on the set of bridge cases that range in geometry, calibration, and loading parameters. Statistical analysis is performed to develop fragility curves for three limit states over sixteen combinations of bridge cases. The limited range of applicability of the fragility curve relationships for use in loss estimation and design are noted as well. This is due to the curves being developed from testing and analysis of a specific bridge typology. Therefore, the uncertainties associated with the capacity and demand models implemented in their development are not fully quantified. On this note, improvements to expand the utility of the vulnerability relationships beyond the comparison purposes described below are proposed in the future work described later in this Chapter. A comparison of the resulting vulnerability functions still allows for the influence of each of these parameters to be individually assessed as summarized below.

- A curved bridge is shown to have a measurable increase in seismic vulnerability when compared to a straight bridge with all other characteristics being the same. A greater level of dispersion is also indicated for curved bridges, likely due to varying degrees of combined actions for different seismic records.
- Moving from uni-directional transverse to multi-directional loading also results in an increase in seismic vulnerability and an increase of dispersion, as represented in the associated fragility curve parameters. This is also attributed to the influence of combined actions.
- The influence of model calibration in this study resulted in a decrease in seismic vulnerability due to the inability of the uncalibrated model to model hysteretic damping. In other studies, different assumptions in the analytical model could result in either an increase or a decrease in the perceived vulnerability of a bridge prior to performing model calibration.
- The development of modification factors which capture the probabilistic influence of complex geometry and combined loading conditions are proposed as well. Presenting these

changes for slight and moderate curves as a percent change in fragility relationships parameters provides a fairly uniform factor observed across each case. Future work is suggested to assess and improve the utility and reliability of this method.

- A standardized modification factor representing bridge calibration is not recommended due to the wide variance in potential influence of the calibration procedure on the associated fragility function.

In light of these results, the following considerations must be made by researchers conducting experimental testing or numerical simulations of RC bridges. These are important because decisions made regarding simplifications or exclusion of complex parameters will severely limit the applicability of the results. This is shown to hold true for the RC bridge type presented in this work, and the concepts are transferable to some degree for seismic assessment research of other structures as well.

- The consideration of irregular geometry and multi-directional loading will significantly affect the resulting structural response when compared to regular geometry subjected to uni-directional loading.
- Researchers performing uni-directional loading of structures such as a RC bridge of this type, should be aware of the un-conservative results that they will obtain in terms of reported structural performance. This is because the loading and boundary conditions selected in such a study neglect the combined interaction effects that result from realistic multi-directional loading that is experienced in the field.
- Likewise, if simplifications are made to the geometry of the simulated structure, seismic assessment of the system will result in an underestimation of the vulnerability of these types of structures, since the potential for combined actions due to irregularities is reduced.
- Assumptions made in experimental testing, including the behavior of reaction frames and loading units, as well as the realism of boundary conditions, should be carefully assessed and monitored. Whenever possible, the resulting errors should be corrected during testing or accounted for in post-processing of data.
- Interdependency between torsional and lateral response indicates that neglecting the response in one degree of freedom can have detrimental effects on the accuracy of the responses measured in other directions of the structure.

- Therefore, even in cases where a researcher is only interested in observing response in a particular degree of freedom that is known to control the overall behavior of a structure, it is important to appropriately simulate the response in other degrees of freedom. This is necessary to achieve accurate results in the desired degree of freedom, particularly when combined actions are anticipated.
- The use of a hybrid simulation platform can assist experimental research by applying realistic loading conditions to physical specimens that accurately reflect the response of the overall system subjected to seismic loading.
- Analytical studies involving complex geometries with the potential for exhibiting combined actions should be calibrated to experimental data sets which are known to have captured the resulting effects of damping as well as stiffness and capacity degradation of the members.

6.2 Future Work

The first and most obvious area for future work involves conducting a similar procedure to what is presented in this research with an expanded set of parameters to study. There are numerous additional variables of bridges that likely have a significant influence on seismic performance.

Additional bridge parameters that might be proposed for investigation of their influence on seismic assessment include:

- Varying span lengths, defined by the ratios of the two adjacent spans on each side of a pier
- Pier heights, defined by the overall range in heights as well as the maximum difference in two adjacent piers
- Degree of skew, since skewed bridges were not considered in this study
- Degree of curvature, where the minimum radius of curvature is typically defined according to the imposed speed limit
- Angle of approach of the seismic record, to assess if application of bidirectional loading at various orientations to the bridge results in any influence on vulnerability
- Pier cross sections, to distinguish between the effects of combined actions on circular and rectangular cross sections, which some information in the literature has already revealed
- Number of lanes, and the influence of deck width and vertical loading on bridge response

- Presence of collector or distributor ramps, or other components providing some sort of stiffening effect to the structure
- Seismic design considerations such as location or age of the structure, as well as deterioration and exposure to multiple seismic events or multiple hazards

Expansion of the work presented here can be executed to increase the accuracy of bridge-specific vulnerability relationships by developing base curve sets for other bridge categories, as well as modification factors for these additional parameters. Sets of curves for other bridge types can be developed using a similar procedure, and will be most effective if they can be rooted in high quality experimental testing programs that account for complex full-system response.

Potential improvements to the methods and results presented in this work are now discussed. These include improvements to model calibration, limit state definitions, fragility curve format, and Bayesian updating of fragility relationships.

The model calibration methods employed in this work were selected in order to adjust for the most significant disparity in model behavior and experimental data. Model calibration was focused on achieving similar global displacement responses in order to compare with defined limit state threshold values in these directions. For the slight and moderate cases, simplified effective springs were employed to approximate the responses of the more computationally expensive calibrated model components. Further work should be done to investigate obtaining a more accurate response in each action and deformation, while maintaining a model that does not become too complex to feasibly run a large series of analyses.

Four areas are identified for improvement to the models used in this study to develop response data for fragility assessment. The first involves future work to calibrate the abutment models to experimental data. The use of results presented in (Silva, Megally, & Seible, 2003), as well as future testing for 6DOF response of abutments could be used to perform this calibration. This is crucial as the abutment models were shown to have a significant effect on the longitudinal response of the bridges, and an experimentally based model would increase the degree of reliability of the fragility relationships developed for loading scenarios including longitudinal components. This is most critical for its influence on the straight bridges, where the geometry and loading of the bridge is collinear with the idealized load-deformation response of the numerical model of the abutment.

Secondly, future development of a shear spring to represent the effects of shear deformation on the overall lateral response is proposed. Shear deformations were shown to be negligible in the transverse direction of the bridge. However, in the longitudinal direction, boundary conditions result in a greater contribution of shear deformation, particularly at higher levels of loads. The measured response in the longitudinal direction of the piers could be used to develop a nonlinear shear spring model for future implementation. The shear spring could be included directly, or the behavior could be included in development of an effective spring. This procedure is already performed for lateral springs representing stiffness degradation of the pier in the simplified models.

Previous RC models elsewhere in the literature have also been shown to underestimate deformation response due to neglecting the effects of combined flexure-shear interaction (Lee & Elnashai, 2001). In addition to underestimating total deflection, it is shown that neglecting to account for shear deformation can lead to overestimating energy dissipation capacity, because flexural deformation is overestimated. A shear spring model developed as presented in (Lee & Elnashai, 2001) would therefore be capable of appropriately accounting for this combined flexure-shear interaction. Development of this model would be significant for future studies that include piers with smaller aspect ratios. In these cases, neglecting the effects of shear would result in significant errors in assessing the ductility, stiffness degradation, and period elongation of the piers.

The next area of model calibration for which additional work could be performed to improve the assessment of bridge response is in the vertical degree of freedom of the piers. As discussed in the analysis of the resulting fragility curve parameters, there was little effect observed in the analytical study of the calibrated bridge model due to the presence of vertical accelerations. It is acknowledged that the models utilized in this study may not accurately capture the influence of varying vertical load on performance of bridges. This is because the hybrid simulation did not include vertical accelerations, and therefore the model was not calibrated in this degree of freedom. Additionally, the assumption of elastic response in the superstructure is based off of the loading applied in the hybrid simulation. The application of high vertical accelerations could potentially result in inelasticities in the deck. The significant influence of vertical accelerations on pier response is well documented in (Kim, Holub, & Elnashai, 2011). Therefore, it is recommended that results from the literature as well as additional testing on the influence of vertical loads on the resulting seismic vulnerability of the bridge systems be considered to perform further model calibration in this degree of freedom.

The final area of future work in model calibration is an improvement of the method for capturing hysteretic damping effects. The increase of distributed Rayleigh damping is only a broad approximation used to reduce the actions and deformations of the model response to the same range as the experimental data. Discrete damping at the locations of nonlinear behavior, specifically the hinges of the piers, would be a preferred method for use in developing the most accurate assessment of structural response. Existing work performed by (Kappos, Manolis, & Moschona, 2002) for a four-span bridge includes a finite element model of piers with spring-dashpot-mass components that are also capable of capturing soil-structure interaction effects. The addition of rotational dashpots at the top and bottom of each pier is proposed to accurately represent discrete hysteretic damping in the bridge. These models will capture the influence of soil-structure interaction, opening and closing of cracks, yielding of rebar, and friction due to slippage at the ends of the piers on the damping of the bridge system. This direct representation of the pier hinge behavior and associated hysteretic damping effects will improve model performance for more reliable seismic assessment.

The next area for proposed future work and improvements of the methods developed in this study is a more comprehensive set of limit state definitions. For the sake of simplicity, local mechanisms were mapped to global limit state parameters, which were used to indicate the exceedance of a particular limit state. However, a more elegant approach would be the development of a damage index capable of appropriately weighting various factors that influence overall bridge response. In the work presented here, cracking and yielding of the piers are mapped to displacements using the same parameters in the longitudinal and transverse directions. Although these result in appropriately distinct drift levels that indicate local mechanisms in each direction, the effects of those mechanisms are not considered independently. It is very possible that yielding in the longitudinal direction does not create the same instability in the bridge as yielding in the transverse direction.

In addition, the behavior of other connections and restraints, such as the shear key and gap elements of the abutments, are not directly taken into account in the limit state definitions. The influence of these components on the response of the piers, particularly in the longitudinal direction, is captured. However, potential failure of a component outside of the bridge pier is possible and should result in an increase in vulnerability of the overall bridge system. On a similar note, a study on redistribution of forces and susceptibility to progressive failure should be assessed. This would confirm or disprove the validity of the conservative assumption that the failure or loss of load capacity in one pier effectively indicates a failure of the overall bridge. Finally, the influence on structural response

associated with other parameters such as pier curvature, loss of cover, excessive crack widths, and slip or rupture of bars should be considered. Development of a damage index that provides an appropriate weighting factor to each of these components in order to indicate that the bridge system has entered a particular performance level is therefore recommended.

The ground motion intensity measurement selected for development of the fragility curves parameters in this study is PGA. This was determined in order to improve the utility of these curves for users who could examine peak-ground parameters obtained directly from the earthquake records in order to assess the probabilistic value of exceedance for a given bridge. The shortcomings of this method are acknowledged, including the fact that the curves will exhibit greater dispersion. Therefore, future work to map probability of reaching limit states against spectral parameters, particularly S_a and S_d parameters could provide for more clear comparison of the influence of various parameters. This is because capturing the influence of the spectral response will yield less dispersion and greater sensitivity to the selected GMI parameter.

The final potential area for future work to incrementally improve the results of this study is the use of Bayesian updating to validate and improve the fragility relationships presented. This is possible through digesting additional experimental data as it becomes available. A Bayesian updating procedure similar to that presented in (Choe, Gardoni, & Rosowsky, 2007) is proposed for updating of the vulnerability functions and associated modification factors developed in this work. Only the use of high-quality experimental tests of RC bridges should be included, in order to maintain the ability of the data to capture the complex effects observed in these results.

It is noted that additional efforts in the research community to conduct comprehensive experimental testing programs to examine complex behavior where knowledge is currently lacking will provide new data for the advancement of various seismic assessment methods. This occurs on one of two fronts. These tests can improve understanding of structural phenomena, thus improving analytical model capabilities and capacity models in vulnerability assessment studies. Secondly, fragility curves developed directly from these studies can be used to update existing vulnerability relationships for similar bridge types. The use of the curves developed in this study for this purpose is the first area of future work proposed for broader implications to research efforts distinct from the work presented above.

6.3 Future Work with Broad Impact

Bayesian updating is proposed for the improvement of existing fragility functions through the use of the relationships developed in this study. It has also been shown that hybrid simulation using appropriately calibrated bridge models provides an economic and efficient means of improving the reliability of fragility functions through Bayesian updating (Li, Spencer, & Elnashai, 2013) . The approach can be used to improve the ability of existing fragility functions to capture complex system-level interaction effects without conducting additional reliability analyses. The procedure would enable the updating of existing fragilities in the literature, and provide an open avenue for continual improvements in accuracy with increasing levels of data available from high-quality experiments and simulations. Additionally, this will extend the influence of the fragility relationships developed in this work, by incorporating the data developed in this study into fragility relationships used for an entire class of bridge. This allows for a wider impact of the highly calibrated and realistic results that would otherwise be confined to represent a much narrower subsection of the existing bridge inventory.

Additional work proposed for further development and improvement of the fragility relationships produced in this study is now presented. As discussed above, the range of applicability for the curves developed in this study is currently limited in terms of applicable bridge typologies. It is proposed that the calibrated analytical models developed in this study can be used to assess the influence of changes in geometry, materials, and other physical bridge characteristics that affect the demand model used to develop vulnerability relationships. Through this effort, several of the parameters discussed at the opening of Section 6.2 can be explored without requiring a comprehensive experimental testing program. The initial assessment of the effects of some of these parameters can then be assessed.

The extent of the uncertainties associated with the demand and capacity models implemented in this study to develop vulnerability relationships should also be explored. As presented in Section 5.1 , the uncertainties associated with the fragility curve generation procedure are both epistemic, due to lack of knowledge, missing information, or errors in modeling, and aleatory, due to the fact that many of the factors which affect the resulting relationships are inherently random. It has been demonstrated that the uncertainty associated with input ground motions has a more significant impact on the vulnerability of structures than many structural capacity-related parameters (Kwon & Elnashai,

2006). However, the demand and capacity models utilized in this study can be examined, sources of uncertainty can be statistically quantified, and the results of the structural analyses described in Section 4.5 can be analyzed to develop an accurate representation of the uncertainty associated with the fragility curves developed in this study. It is proposed that these uncertainties be presented in terms of confidence intervals. Visually, this would result in upper and lower bounds of the 90% confidence interval plotted on each side of a given fragility relationship. This improved representation of the uncertainties associated with the curves developed in this study enables appropriate application of the results presented here for use by engineers and disaster response professionals.

Finally, the potential implementation of the geometric and load combination modification factors developed from the assessment of changes in the fragility curve parameters is also explored as a means to improve fragility relationships. To do so will require additional sources from studies on a wide array of structures. This would be necessary in order to validate the relative influence observed in fragility relationships identified in this study, and to identify the extent to which these influences extend for other classes of bridges. The modification factors are proposed for use in a straightforward manner to directly modify the curve parameters of previously defined vulnerability relationships. In order to be appropriately developed, these factors would be developed into a set of more comprehensive functions capable of accounting for many uncertainties in demand and capacity modeling. Factors could only be developed for parameters that result in similar effects across many cases of a given type of structure. An example of a parameter where broad application would not be possible is the calibration factor developed in this study. There are too many different assumptions and decisions that could be made for an uncalibrated or calibrated model. Therefore, a change in this parameter could result in any number of changes to fragility curve parameters for relationships developed from distinct experimental and analytical studies.

Development of reliable factors for specific parameters that are shown to have similar effects on vulnerability across broad classes of a given structure would be a very powerful tool. Within the literature, there are significant experimental and analytical results that have been developed for a specific structure typology or event. Often these results do not fully capture the levels of complexity and realism discussed in this work. If the effects of these considerations can be accounted for statistically, it could allow for improvements to existing relationships and result in curves that capture more complex effects. Fragility relationships for additional structures and scenarios not

initially considered could be generated simply through applying modification factors to the curve parameters. The possibility of conducting Bayesian updating to validate and improve these factors based off of additional studies should be explored as a means of using these factors with some degree of reliability. Thus, the effects of geometry, loading, and potentially other parameters could be modified for the extensive existing literature in order to enable a vast expansion of existing curves without performing additional reliability analyses.

In addition to the assessment of vulnerability of existing structures, it is important to consider if there are any design recommendations that come out of the results of this study. One area for future investigation concerns the level of transverse reinforcement recommended for RC bridge piers in seismic regions. The influence of combined actions has been shown to amplify the progression of damage in RC bridge columns. Guidelines and requirements for sufficient transverse reinforcement already exist to resist shear and torsion in RC members. The results of this study, in conjunction with data collected in the CABER program on combined actions for bridge piers, enables future work to be performed to assess the precise effects of transverse reinforcement on susceptibility to damage under combined actions.

Recent studies, including the work presented in (Prakash & Belarbi, 2010) and (Hindi & Browning, 2011) have highlighted the influence of transverse reinforcement on torsional response. These include innovative transverse reinforcements such as interlocking and cross-spiral reinforcement, respectively. It is shown that an increase in transverse reinforcement can delay the progression of damage under combined bending and torsion by shifting the pier response to flexure-dominant behavior. Designs that are capable of achieving higher performance levels under combined loading, including torsion, would improve resilience of infrastructure. Future work needs to be performed to identify the most readily acceptable method of providing this reinforcement, and to determine geometric conditions of a bridge that should result in additional transverse reinforcement being recommended to avoid early precipitation of failure under combined actions including torsion. Such recommendations could be made based off of the degree of asymmetry or curvature associated with the geometry of the bridge, and would severely reduce the risk of early precipitation of failure mechanisms that result from combined interaction effects.

Finally, an important area of future research with potential for significant impact in the field of seismic engineering is a study of the impact of multiple earthquakes on infrastructure. This is specifically of interest for structures such as bridges, which are designed and constructed with the

intention of long service lives. Long service life, in addition to the potential for aftershock events, means it is very likely that a bridge in a seismic region will experience loading from multiple events over varying time intervals within its design life. Assessments should be performed to determine the influence of damage from previous seismic loading on the capacity and demands expected in future events. Capacity will be reduced due to damage to the structure, while demand may increase or decrease as a result of the natural period of the bridge shifting from that of the original undamaged structure. This shift in natural period, coupled with the potential for different spectral content of separate seismic events, results in the change in demand response. In essence, a damaged bridge behaves distinctly different from the same bridge in pristine condition. When subjected to additional unique earthquake loads, its response, due to these shifts in demand and capacity, may vary significantly. The influence of these changes on system-level response and seismic vulnerability under multiple events is significant. For bridges, the case of aftershocks occurring while disaster response efforts are underway in response to an initial event is of high consequence and should be examined further.

In the above conclusions, the results of this research are summarized, with key findings provided. Model calibration is performed for RC bridges based on the advanced hybrid simulation presented in this work. Focus is placed on the individual and combined influence of geometry, loading, and model calibration parameters on system-level behavior and RC bridge vulnerability. Recommendations are provided to researchers for considering the effects of various testing and modeling decisions on the impact of combined actions and resulting seismic response of irregular structures and combined loading scenarios. The effects of these combined actions are presented in the form of fragility curve parameters.

Suggestions for future research and improvements to the work presented here are made. These include the proposed development of modification factors for application to existing curves to accounting for additional geometric and loading conditions of structures. Bayesian updating is also recommended for the verification and improvement of vulnerability relationships presented here, and for achieving greater impact through incorporating these results into existing relationships for broader bridge classes. The hybrid simulation data set, calibrated models, and vulnerability relationships presented are shown to be capable of accurately representing the influence of combined actions on system-level RC bridge performance. Future work for improvement of the methods developed and presented here, as well as suggestions for achieving broad impact in the field of

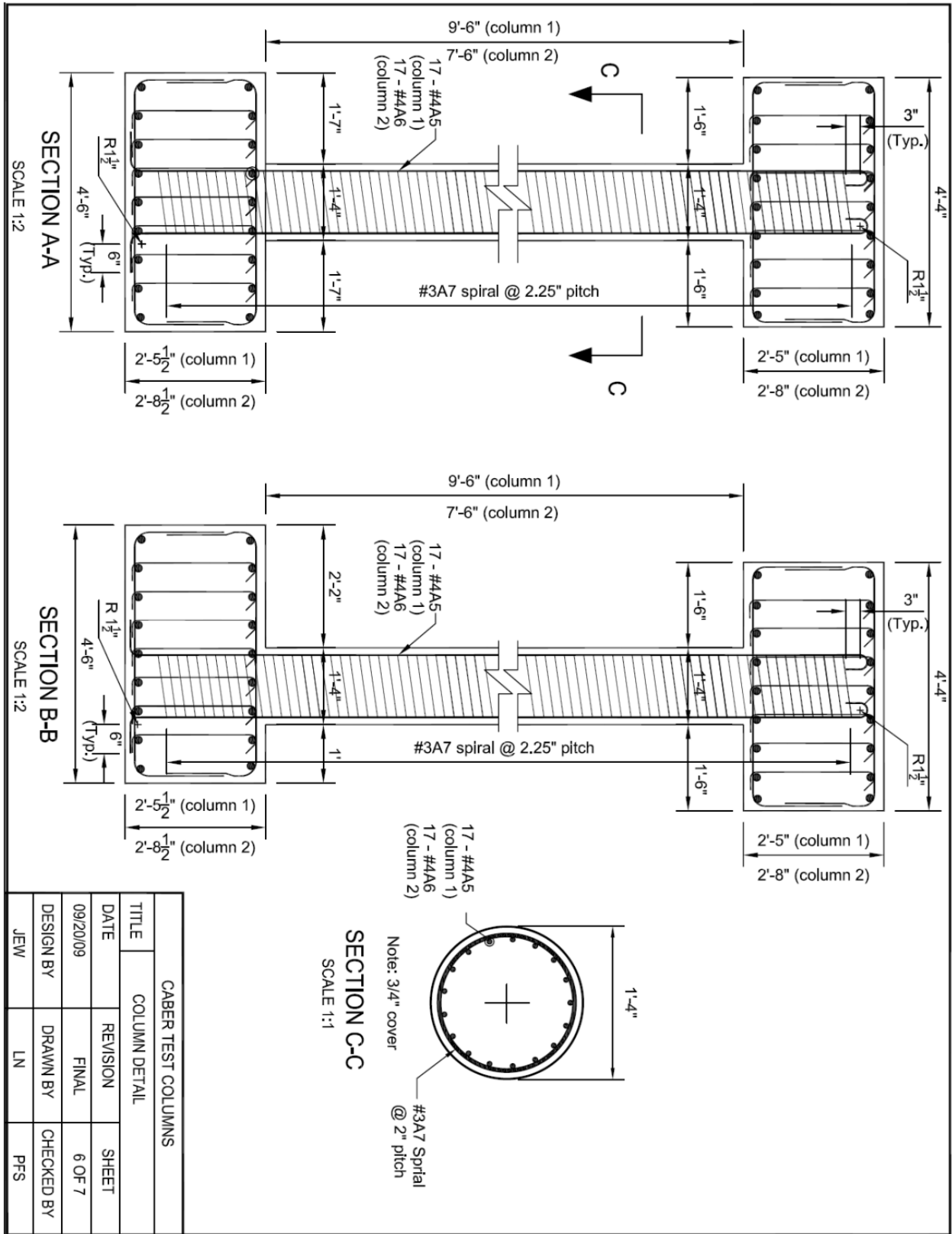
seismic assessment and design of bridges is also presented. Therefore, the work performed advances the current understanding of the influence of combined actions and provides several tools and recommendations for performing seismic assessment of complex RC bridge systems subjected to realistic loading scenarios.

APPENDIX A. HYBRID SIMULATION TEST PREPARATION

Construction drawings, and material properties for the experimental test specimens utilized in the hybrid simulation test are provided below.

A.1 Large-Scale Specimen Design and Fabrication

The following figures are provided as a reference to the large-scale specimen design and fabrication. This includes dimensions and reinforcement details for both large 1:3 scale piers, as well as their square concrete cap and footing used in the experimental hybrid simulation.



CABER TEST COLUMNS			
TITLE	COLUMN DETAIL		SHEET
DATE	REVISION	FINAL	6 OF 7
09/20/09			
DESIGN BY	DRAWN BY	CHECKED BY	
JEW	LN	PFS	

Figure A.1 Column details of 1:3 scale bridge piers

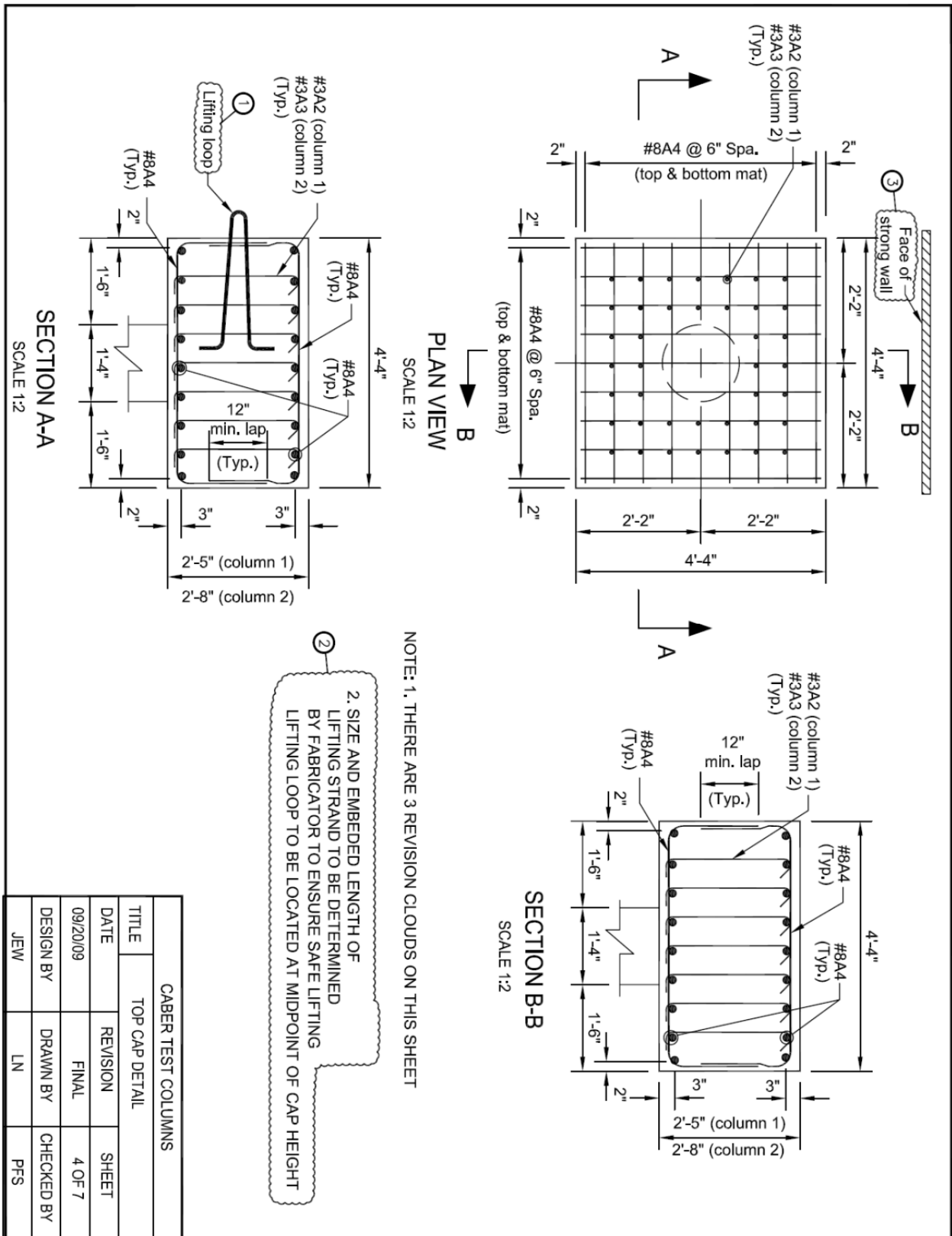


Figure A.2 Top cap details of 1:3 scale bridge piers

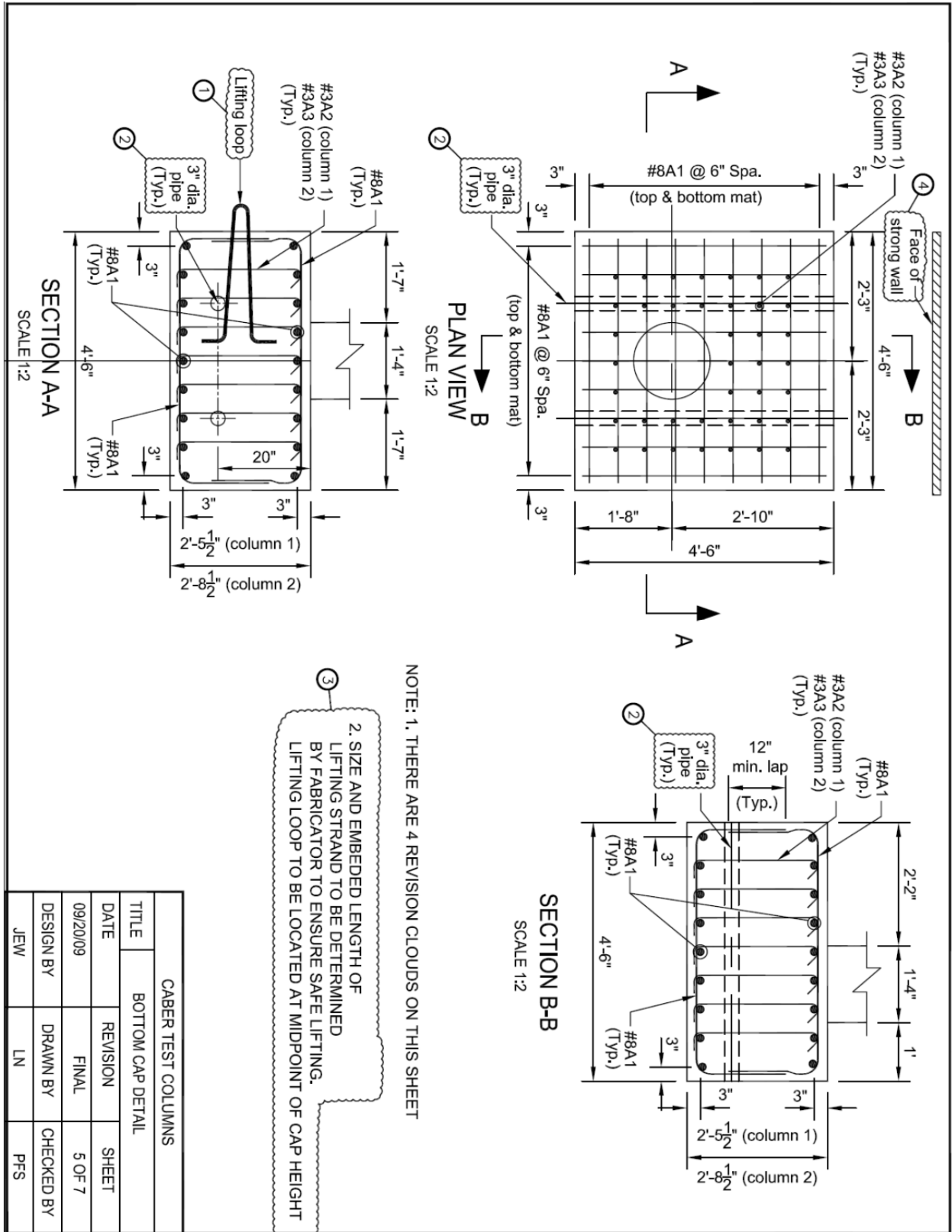


Figure A.3 Bottom cap details of 1:3 scale bridge piers

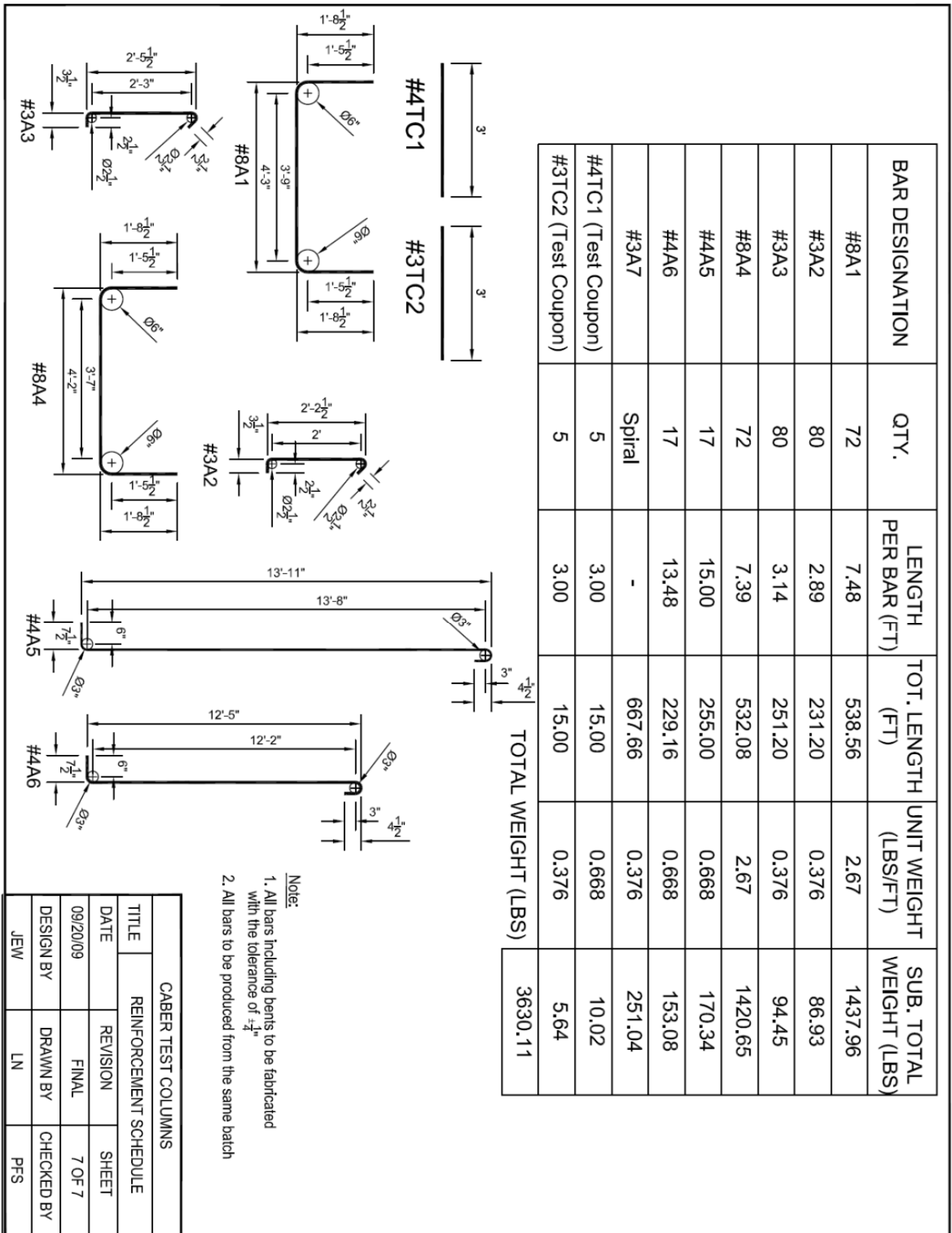


Figure A.4 Reinforcement details of 1:3 scale bridge piers



Figure A.5 Reinforcement cages of 1:3 scale piers

A.2 Small-Scale Specimen Design and Fabrication

The following figures are provided as a reference to the small-scale specimen design and fabrication. This includes dimensions and reinforcement details for the single small 1:20 scale pier, as well as its circular caps used in the small-scale experimental hybrid simulation. Also provided are highlights of the fabrication and construction techniques, including formwork, placing of reinforcement, and casting of concrete.

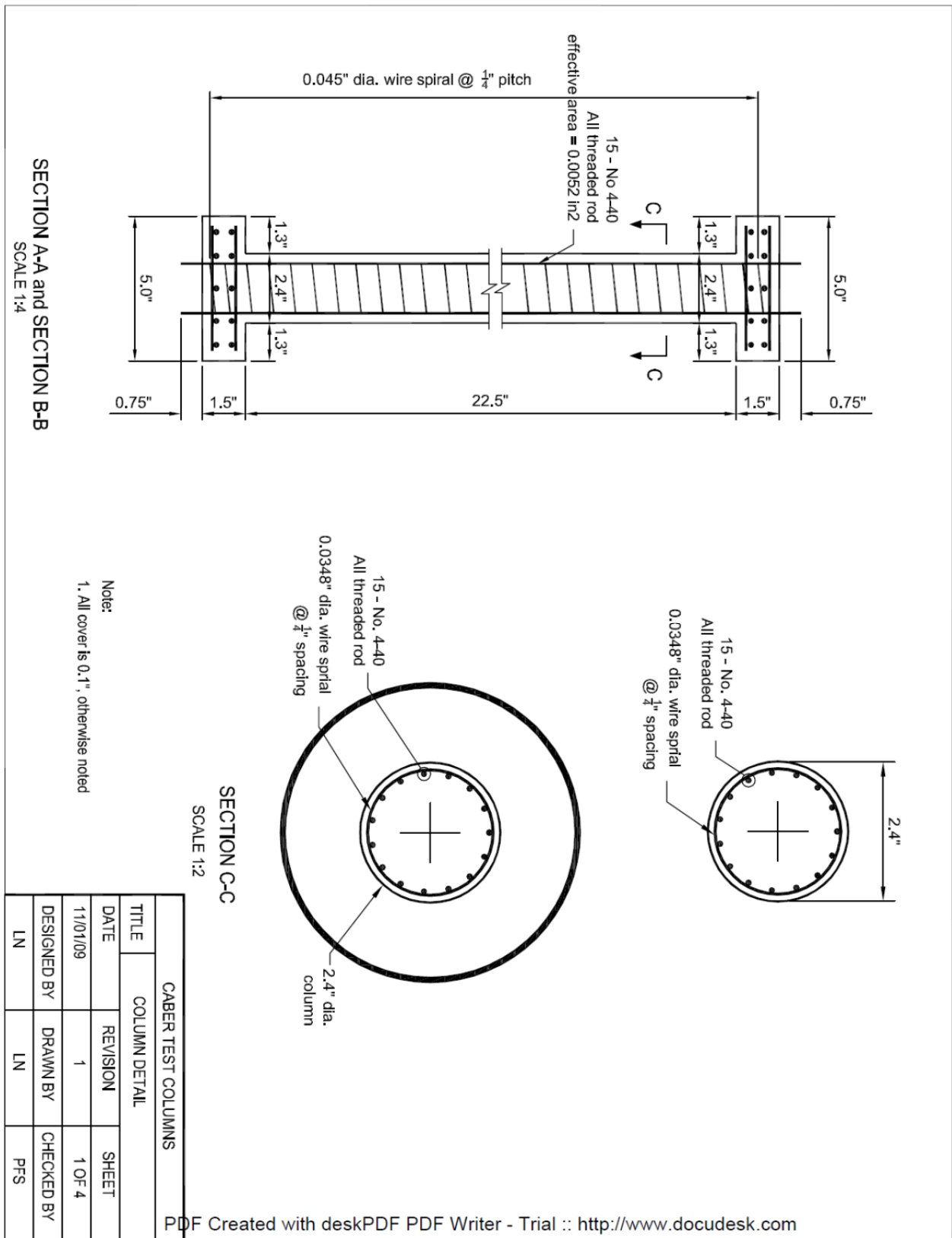
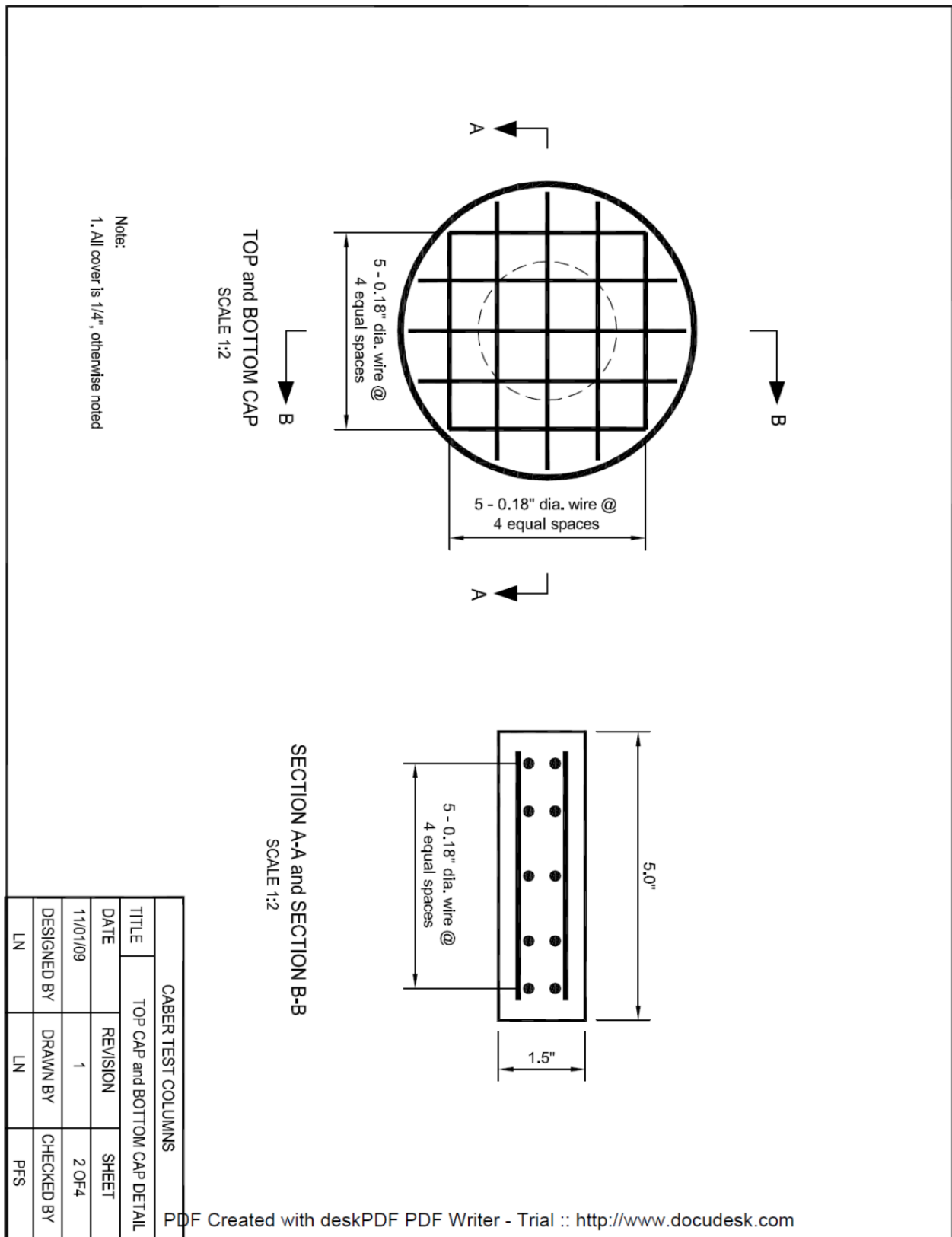


Figure A.6 Column details of 1:20 scale bridge pier



PDF Created with deskPDF PDF Writer - Trial :: <http://www.docudesk.com>

Figure A.7 Cap details of 1:20 scale bridge pier

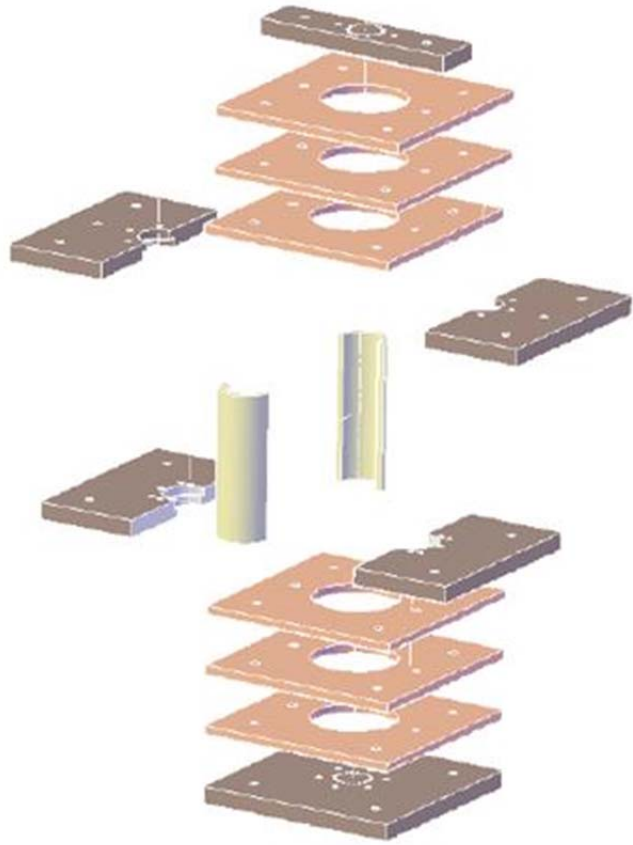


Figure A.8 Exploded view of formwork for small-scale fabrication



Figure A.9 Small-scale reinforcement cage and cap formwork



Figure A.10 Casting small-scale specimens

A.3 Material Properties

The following figures are provided as a reference to the constitutive properties of materials utilized in the hybrid simulation test. This includes stress-strain behavior of four longitudinal reinforcing bars and three concrete compression test cylinders. Additionally, photos of the associated failures of the bars and cylinders are included. Also provided are cylinder break histories for the various pours for the caps and piers of the two 1:3 scale specimens, as well as the mix design history, provided by Prestressed Engineering Corp. Digital Appendix A includes data from the materials properties tests. A list of files and folders included in the digital appendices is also provided in APPENDIX I.



Figure A.11 Necking and rupture of 1:3 scale longitudinal reinforcing bars

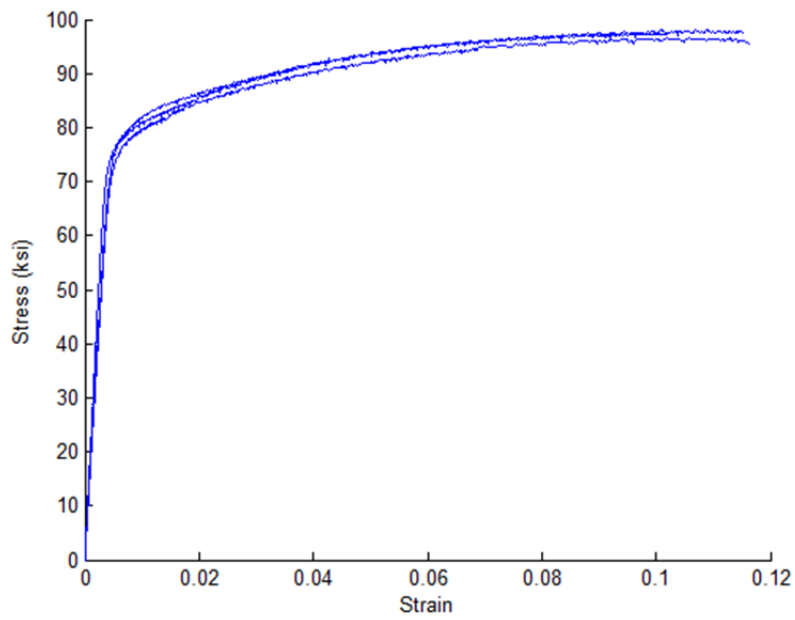


Figure A.12 Constitutive properties of 1:3 scale longitudinal reinforcement

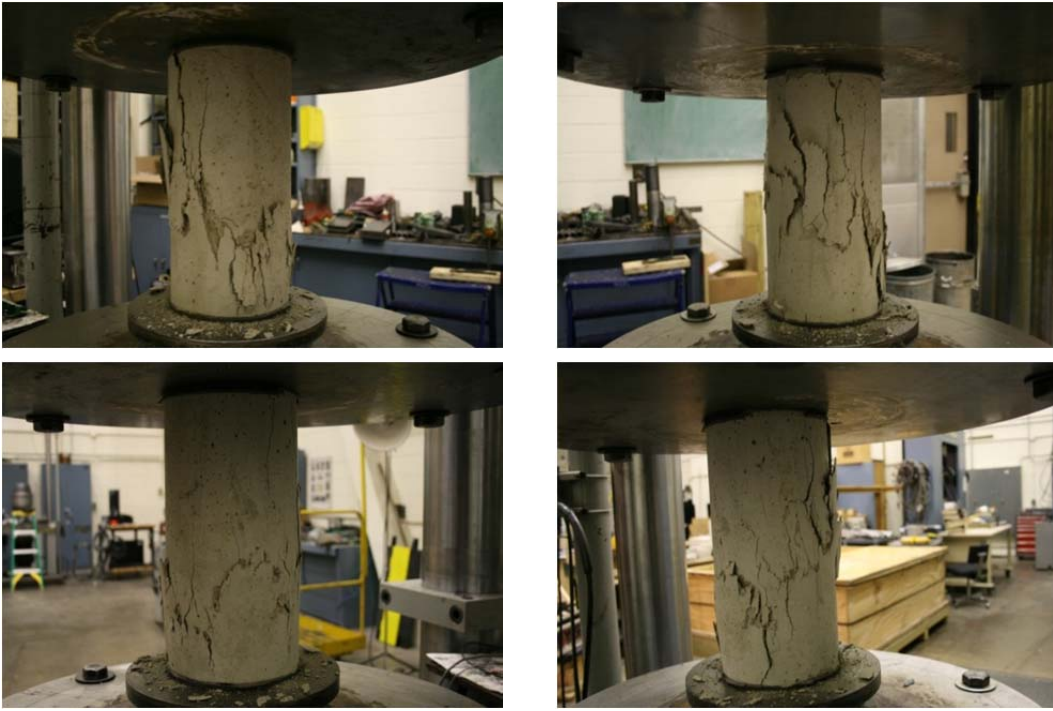


Figure A.13 Concrete cylinder compression test example

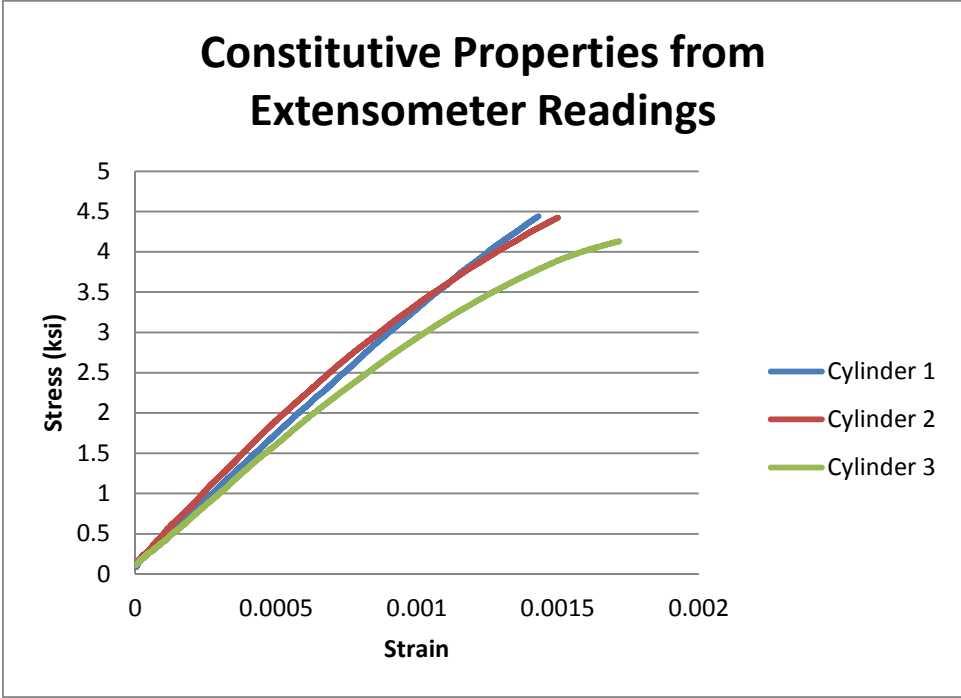


Figure A.14 Extensometer readings for concrete stiffness evaluation

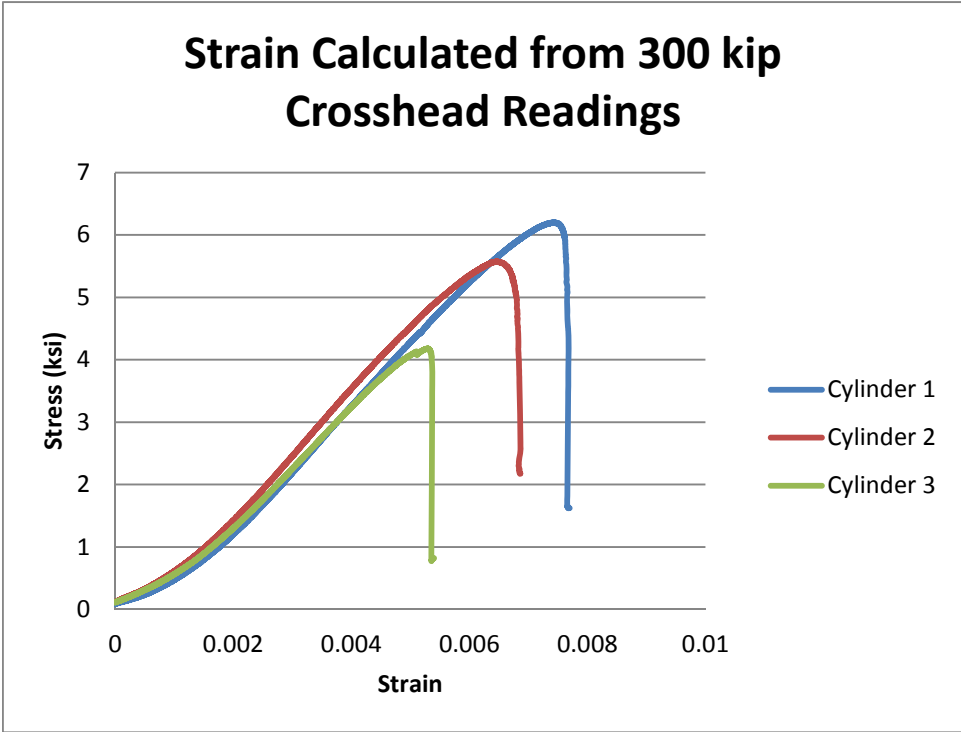


Figure A.15 Constitutive properties of concrete calculated from compression tests

Table A.1 Test cylinder history from Prestressed Engineering Corp.

CAST DATE & TIME	SET I.D.	MIXER <small>Old or New</small>	JOB NUMBER	SEQ. #	STRENGTH TEST DATE & TIME	STRENGTH (PSI)	TEST AGE	Days/ Hours	CONCRETE MIX DESIGNATION	STRENGTH REQUIREMENT	BREAK STATUS	PRODUCTION BED or FORM
							(auto)	(auto)			(auto)	(optional)
12/1/09 1:13 PM	A	NEW	209260	1	12/8/09 6:54 PM	6515	7	Days	575	5000 6000	FINAL	COLUMNS
12/1/09 1:13 PM	A	NEW	209260	1	12/8/09 6:59 PM	6985	7	Days	575	5000 6000	FINAL	COLUMNS
12/1/09 1:13 PM	A	NEW	209260	1	12/8/09 7:06 PM	6660	7	Days	575	5000 6000	FINAL	COLUMNS
12/1/09 1:13 PM	A	NEW	209260	1	1/5/10 11:34 AM	7591	35	Days	575	5000 6000	FINAL	COLUMNS
12/1/09 1:13 PM	A	NEW	209260	1	1/5/10 11:34 AM	7531	35	Days	575	5000 6000	FINAL	COLUMNS
12/1/09 1:13 PM	A	NEW	209260	1	1/5/10 11:34 AM	7499	35	Days	575	5000 6000	FINAL	COLUMNS
12/1/09 1:13 PM	A	NEW	209260	1	1/26/10 1:50 PM	7242	56	Days	575	5000 6000	FINAL	COLUMNS
12/1/09 1:13 PM	A	NEW	209260	1	1/26/10 1:55 PM	7515	56	Days	575	5000 6000	FINAL	COLUMNS
12/3/09 12:00 AM			209260	2	12/11/09 10:52 AM	6037	8	Days		5000 6000	FINAL	TEST COLUMN
12/3/09 12:00 AM			209260	2	12/11/09 10:58 AM	5944	8	Days		5000 6000	SAVE	TEST COLUMN
12/3/09 12:00 AM			209260	2	12/11/09 11:03 AM	6252	8	Days		5000 6000	FINAL	TEST COLUMN
12/3/09 12:00 AM			209260	2	1/5/10 11:52 AM	7186	33	Days		5000 6000	FINAL	TEST COLUMN
12/3/09 12:00 AM			209260	2	1/5/10 11:52 AM	7104	33	Days		5000 6000	FINAL	TEST COLUMN
12/3/09 12:00 AM			209260	2	1/5/10 11:52 AM	7121	33	Days		5000 6000	FINAL	TEST COLUMN
12/3/09 12:00 AM			209260	2	1/27/10 10:00 AM	6366	55	Days		5000 6000	FINAL	TEST COLUMN
12/3/09 12:00 AM			209260	2	1/27/10 10:00 AM	5903	55	Days		5000 6000	SAVE	TEST COLUMN
12/3/09 12:00 AM			209260	2	1/27/10 10:00 AM	6421	55	Days		5000 6000	FINAL	TEST COLUMN
12/8/09 5:46 PM	A	NEW	209260	3	12/15/09 11:43 AM	4597	7	Days	660	5000 6000	OUT	TEST COLUMN
12/8/09 5:46 PM	A	NEW	209260	3	12/15/09 11:43 AM	4615	7	Days	660	5000 6000	OUT	TEST COLUMN
12/8/09 5:46 PM	A	NEW	209260	3	12/15/09 11:43 AM	4582	7	Days	660	5000 6000	OUT	TEST COLUMN
12/8/09 5:46 PM	A	NEW	209260	3	1/5/10 12:08 PM	5257	28	Days	660	5000 6000	SAVE	TEST COLUMN
12/8/09 5:46 PM	A	NEW	209260	3	1/5/10 12:08 PM	5628	28	Days	660	5000 6000	SAVE	TEST COLUMN
12/8/09 5:46 PM	A	NEW	209260	3	1/5/10 12:08 PM	5370	28	Days	660	5000 6000	SAVE	TEST COLUMN
12/8/09 5:46 PM	A	NEW	209260	3	2/2/10 4:37 PM	6190	56	Days	660	5000 6000	FINAL	TEST COLUMN
12/8/09 5:46 PM	A	NEW	209260	3	2/2/10 4:42 PM	6371	56	Days	660	5000 6000	FINAL	TEST COLUMN
1/5/10 2:49 PM	A	OLD	209260	4	1/12/10 12:35 PM	5283	7	Days	575	5000 6000	SAVE	TEST COLUMNS
1/5/10 2:49 PM	A	OLD	209260	4	1/12/10 12:35 PM	5280	7	Days	575	5000 6000	SAVE	TEST COLUMNS
1/5/10 2:49 PM	A	OLD	209260	4	1/12/10 12:35 PM	5349	7	Days	575	5000 6000	SAVE	TEST COLUMNS
1/5/10 2:49 PM	A	OLD	209260	4	2/2/10 4:47 PM	7154	28	Days	575	5000 6000	FINAL	TEST COLUMNS
1/5/10 2:49 PM	A	OLD	209260	4	2/2/10 4:50 PM	7182	28	Days	575	5000 6000	FINAL	TEST COLUMNS
1/5/10 2:49 PM	A	OLD	209260	4	2/2/10 4:55 PM	7171	28	Days	575	5000 6000	FINAL	TEST COLUMNS
1/5/10 2:49 PM	A	OLD	209260	4	3/8/10 11:17 AM	6535	62	Days	575	5000 6000	FINAL	TEST COLUMNS
1/5/10 2:49 PM	A	OLD	209260	4	3/8/10 11:23 AM	6849	62	Days	575	5000 6000	FINAL	TEST COLUMNS
1/18/10 12:22 PM	A	OLD	209260	5	2/18/10 11:39 AM	5187	31	Days	575	5000 6000	SAVE	TEST COLUMNS
1/18/10 12:22 PM	A	OLD	209260	5	2/18/10 11:44 AM	5396	31	Days	575	5000 6000	SAVE	TEST COLUMNS
1/18/10 12:22 PM	A	OLD	209260	5	2/18/10 11:50 AM	5246	31	Days	575	5000 6000	SAVE	TEST COLUMNS
1/18/10 12:22 PM	A	OLD	209260	5	3/16/10 3:55 PM	5339	57	Days	575	5000 6000	SAVE	TEST COLUMNS
1/18/10 12:22 PM	A	OLD	209260	5	3/16/10 4:00 PM	5524	57	Days	575	5000 6000	SAVE	TEST COLUMNS
1/18/10 12:22 PM	A	OLD	209260	5	3/16/10 4:05 AM	5433	57	Days	575	5000 6000	SAVE	TEST COLUMNS
1/19/10 2:17 PM	A	OLD	209260	6	2/18/10 11:55 AM	6065	30	Days	575	5000 6000	FINAL	TEST COLUMNS
1/19/10 2:17 PM	A	OLD	209260	6	2/18/10 12:01 PM	5821	30	Days	575	5000 6000	SAVE	TEST COLUMNS
1/19/10 2:17 PM	A	OLD	209260	6	2/18/10 12:07 PM	5934	30	Days	575	5000 6000	SAVE	TEST COLUMNS
1/19/10 2:17 PM	A	OLD	209260	6	3/16/10 4:08 PM	6236	56	Days	575	5000 6000	FINAL	TEST COLUMNS
1/19/10 2:17 PM	A	OLD	209260	6	3/16/10 4:11 PM	6275	56	Days	575	5000 6000	FINAL	TEST COLUMNS
1/19/10 2:17 PM	A	OLD	209260	6	3/16/10 4:17 PM	6230	56	Days	575	5000 6000	FINAL	TEST COLUMNS

Table A.2 Concrete mix design from Prestressed Engineering Corp.

Material	Supplier	Description	Product Code	Specific Gravity	Absorption
Cement:	Buzzi Unicem USA, Inc 6097-02	Type III, Portland Cement	-	3.15	-
Coarse Agg.:	Riverstone Group 50992-01	CM13 Crushed Limestone	022CM1301AS	2.71	2.2
Fine Agg.:	Valley Sand & Gravel 51230-25	FA-01 Natural Sand	O27FM01	2.59	2.8
Water:	PEC -	On-site, IDOT Approved	-	1.00	-
Admix 1:	WRG 767-01	Darex II	42138	1.04	-
Admix 2:	WRG 767-01	ADVA Cast 575	43836	1.1	-
Admix 3:	WRG 767-01	Recover	43758	1.15	-
Admix 4:	WRG 767-01	DCI	43725	1.28	-
MIX Design:	BL575				
	Weight (LB) (SSD)	Absolute Volume			
Cement:	575	2.925			
Coarse Agg.:	1790	10.585			
Fine Agg.:	1240	7.673			
Water:	250	4.006	30.0	gallons	
(gallons ->)	30.0				
Admix 1:	10	0.010	w/c ratio =	0.434782609	
(Fl. Oz.)					
Admix 2:	50	0.052			
(Fl. Oz.)					
Admix 3:	-				
(Fl. Oz.)					
Admix 4:	-				
(Fl. Oz.)					
Entrained Air	6.5%	1.755			
	Yield:	27.007			
	Theoretical Unit Weight:	142.897838			

APPENDIX B. HYBRID SIMULATION TEST SETUP

Details of the large-scale test setup and instrumentation plan are provided, followed by small-scale test setup.

B.1 Large-Scale Test Setup

Plan and elevation views of the two 1:3 scale piers in place and connected to the LBCB units in the Illinois NEES MUST-SIM facility are provided below, along with drawings of the connector plates utilized an images illustrating the procedures used to prepare for conducting hybrid simulation.

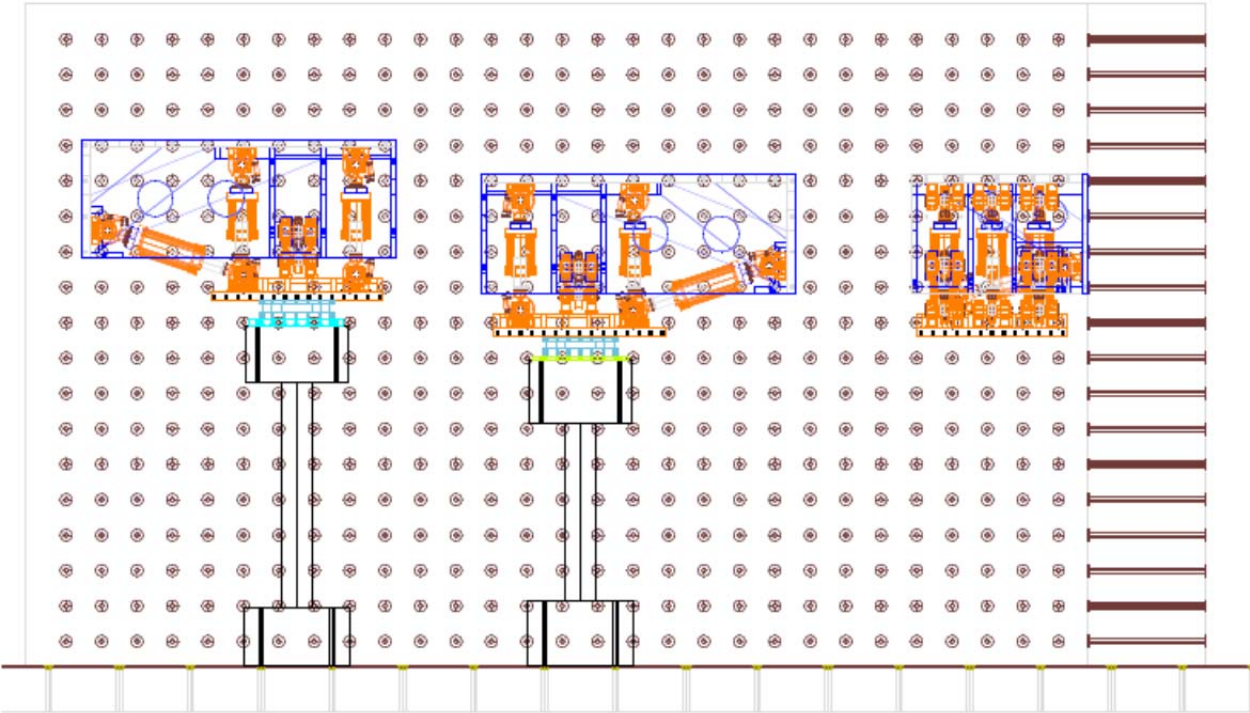


Figure B.1 Elevation view of large-scale experimental test setup

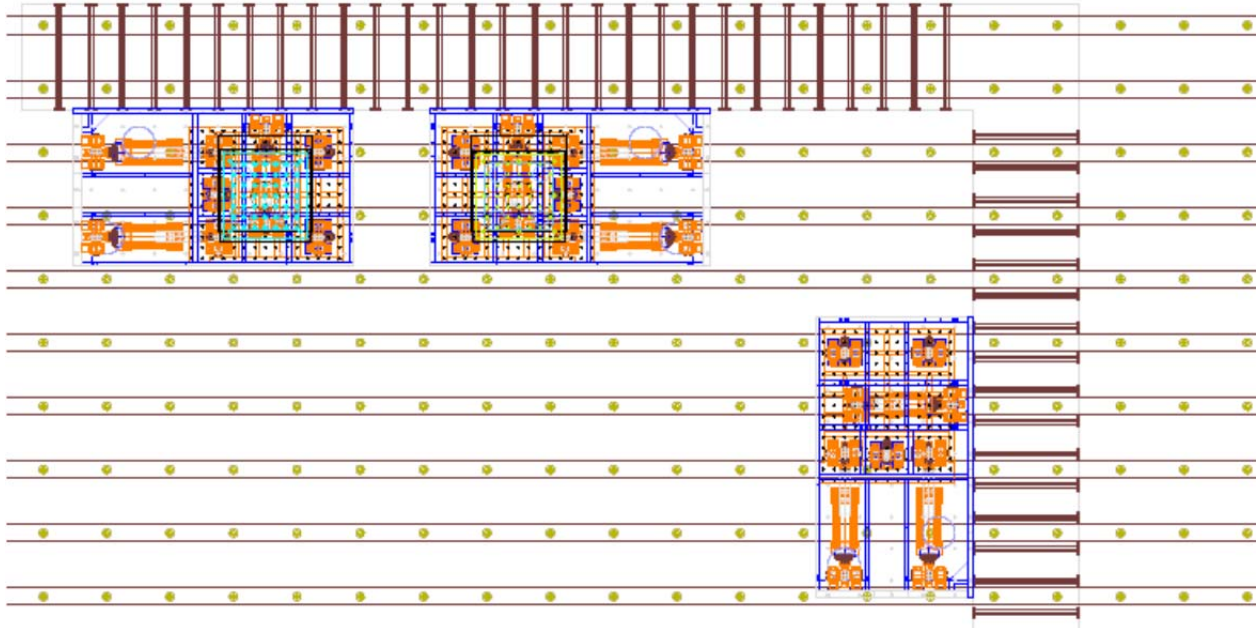


Figure B.2 Plan view of large-scale experimental test setup

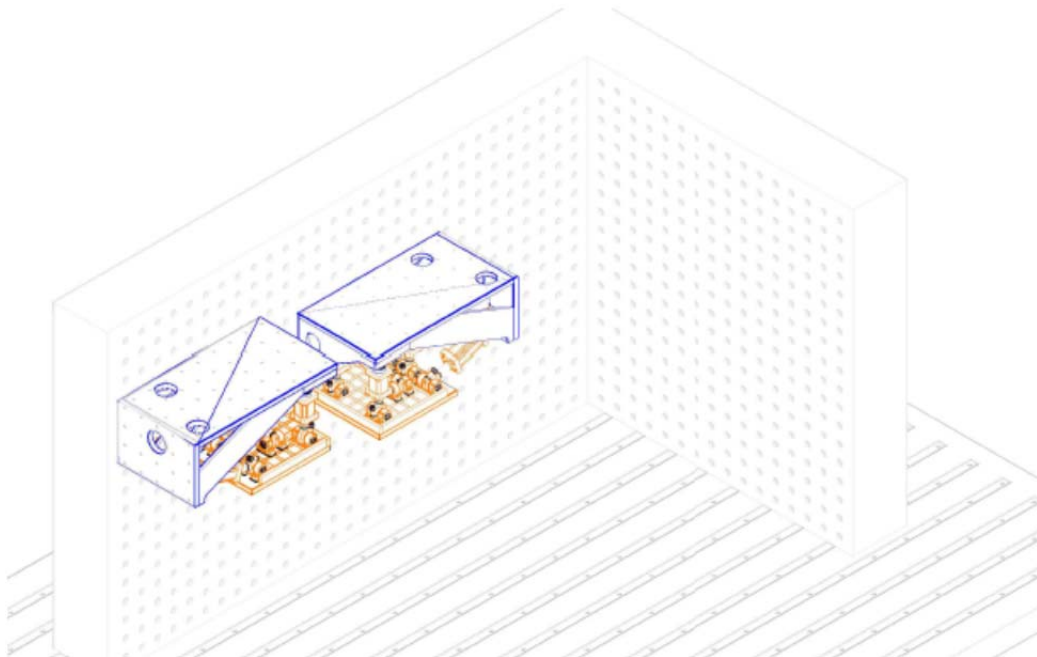


Figure B.3 Isometric view of loading units and reaction wall

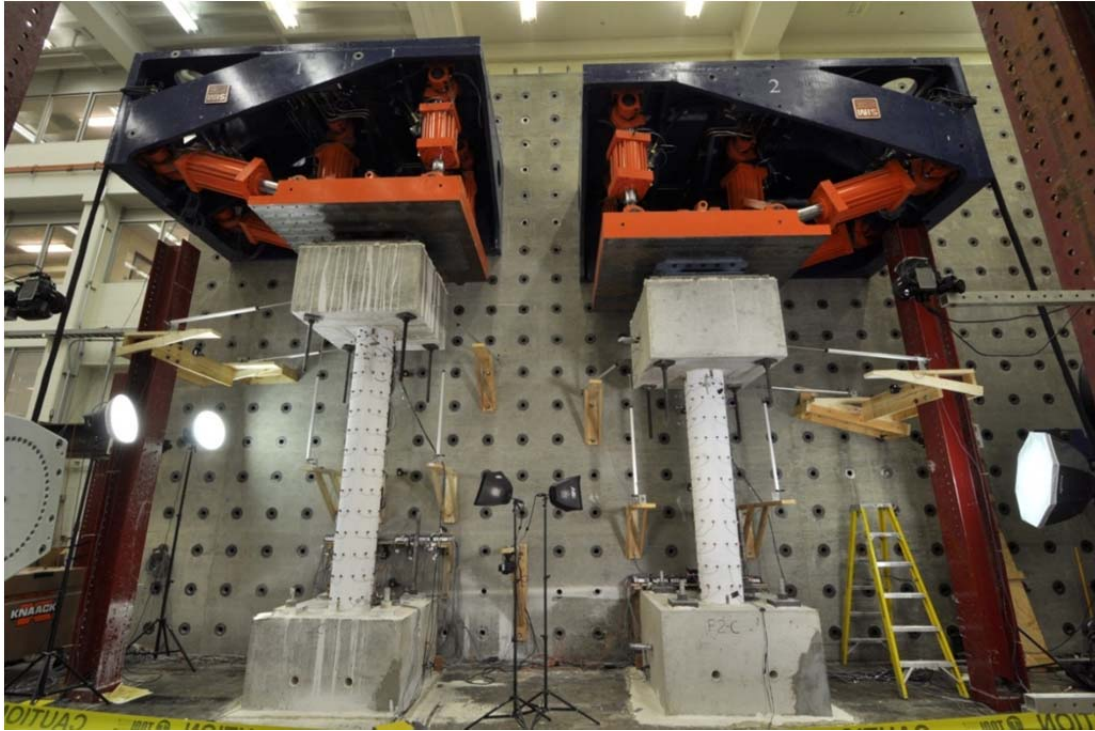


Figure B.4 Photo of test setup at beginning of hybrid simulation

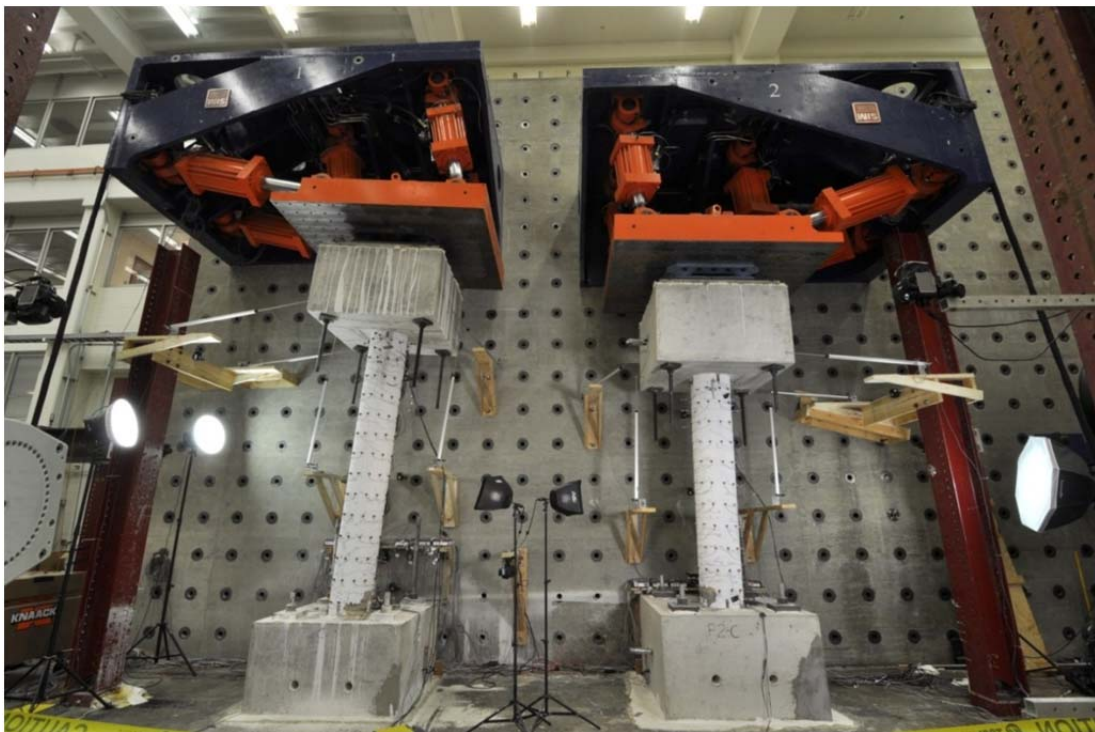


Figure B.5 Photo of test setup at end of hybrid simulation



Figure B.6 Test setup including controls and data acquisition

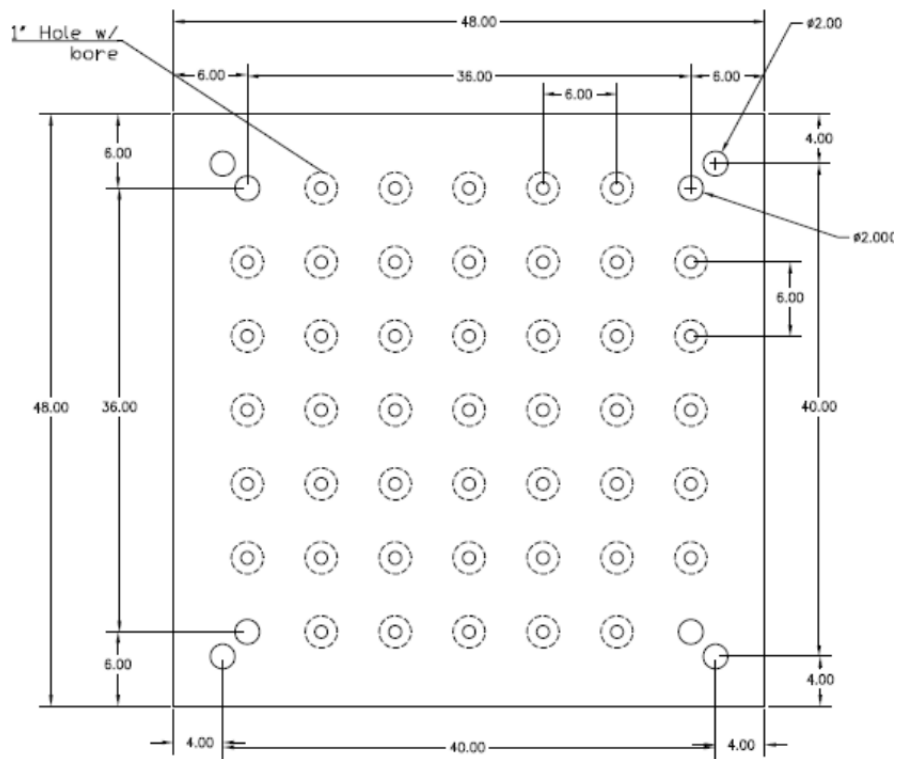


Figure B.7 Adaptor plate for connection to pier cap

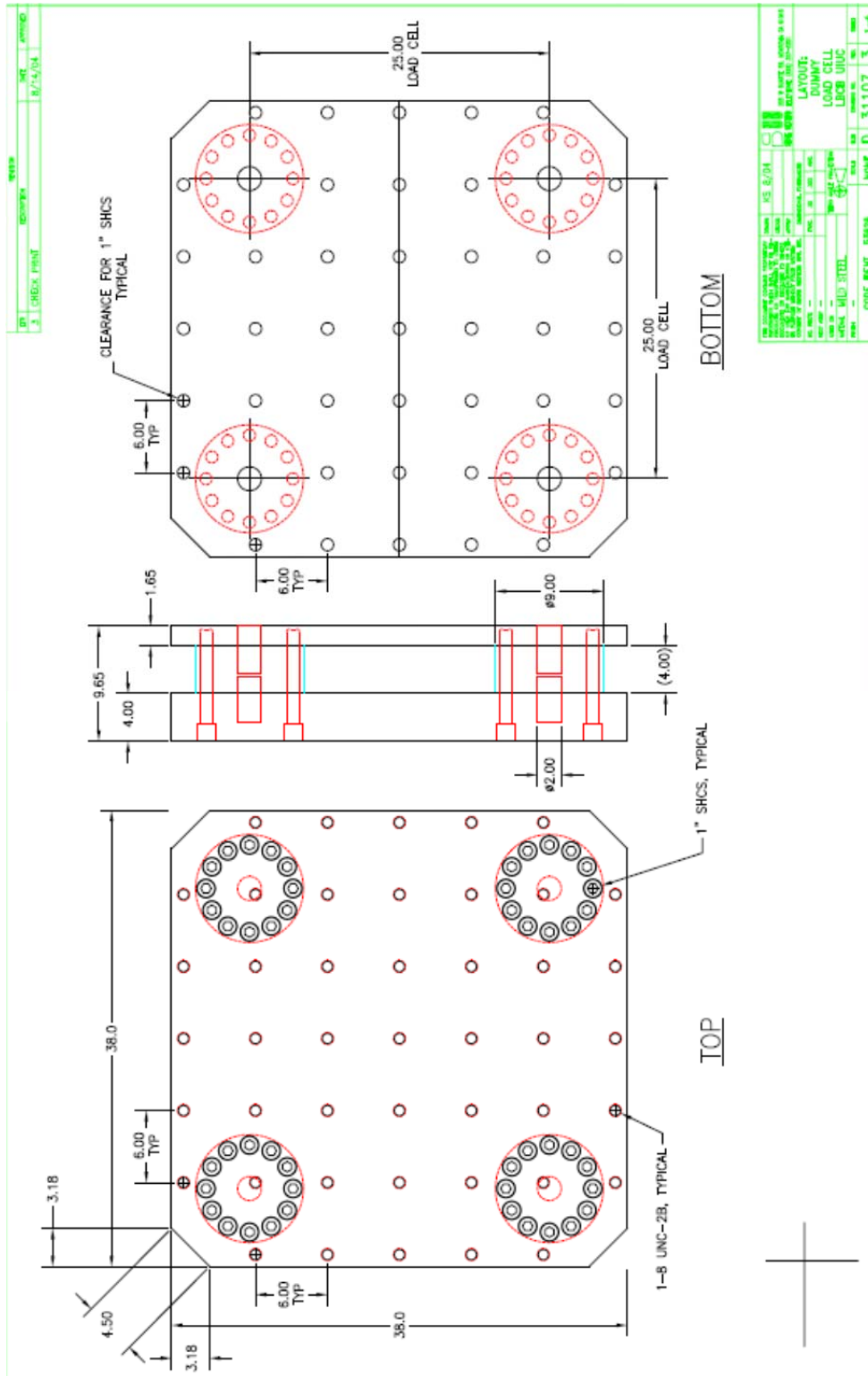


Figure B.8 Adaptor plate for connection to LCB

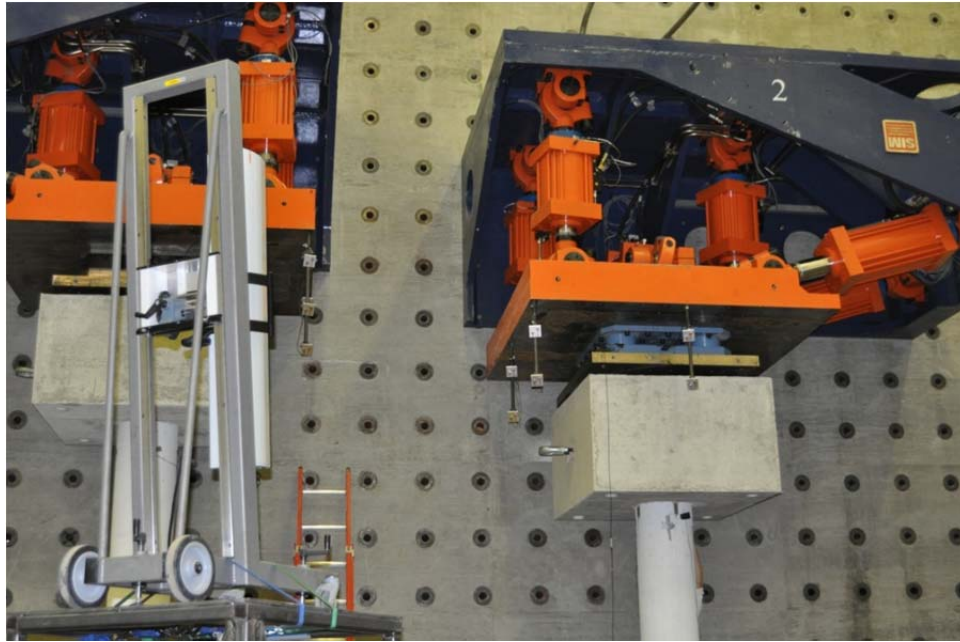


Figure B.9 Krypton camera during LCB-specimen alignment procedure

B.2 Instrumentation Plans

The following figures are provided as a reference to the instrumentation plans utilized to gather data for the hybrid simulation test. Components include locations and labeling of longitudinal and transverse embedded steel gages, Krypton non-contact LED targets, control sensors, and labeling notation to distinguish the face of the RC pier being discussed. It should be noted that Figure B.10 and Figure B.11 should be utilized to indicate the height level of strain gages in question, while Figure B.18 contains the correct labeling of pier faces in relation to the global LCB coordinate system.

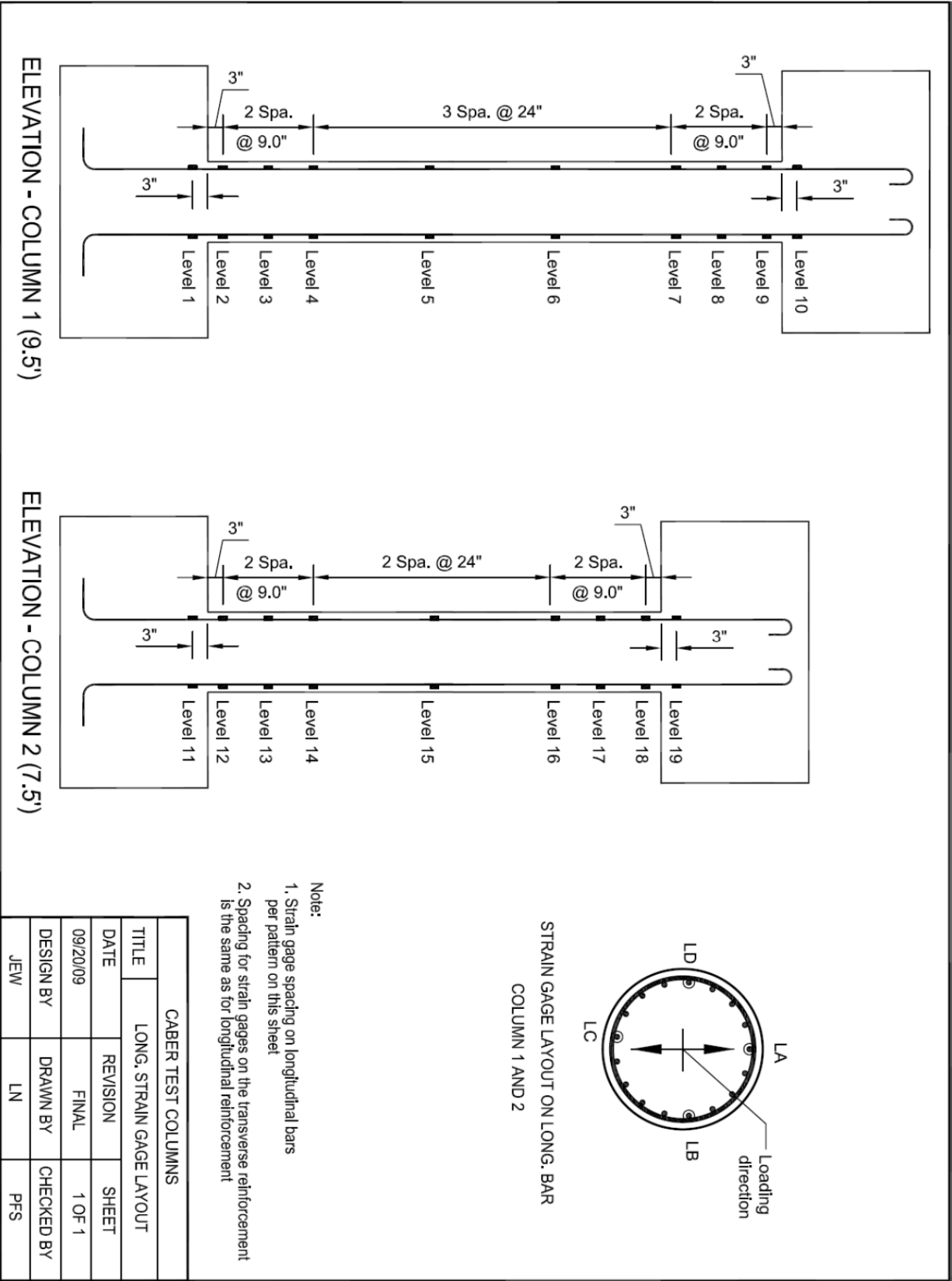


Figure B.10 Location of longitudinal steel strain gages embedded in 1:3 scale piers

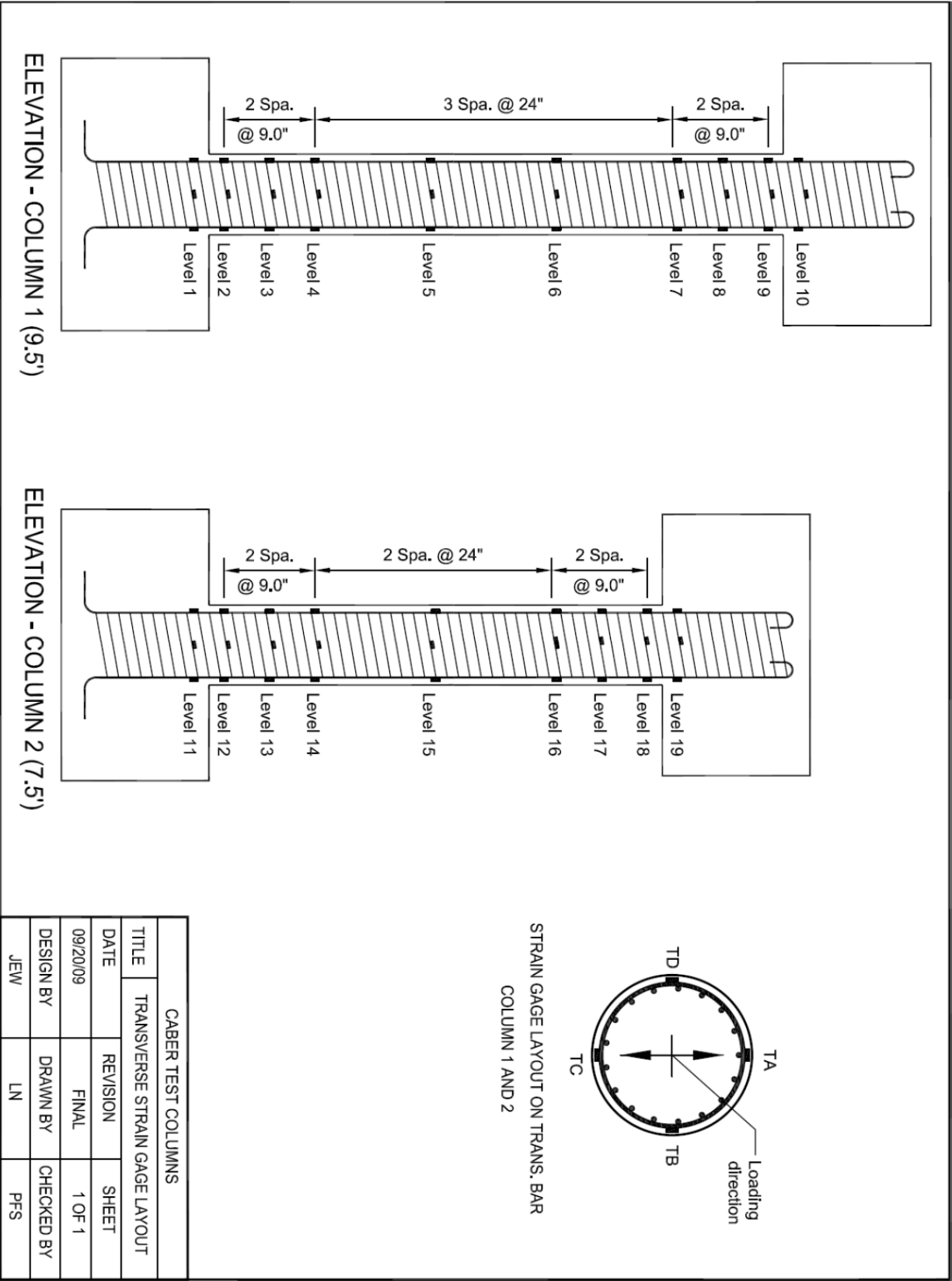


Figure B.11 Location of transverse steel strain gages embedded in 1:3 scale piers

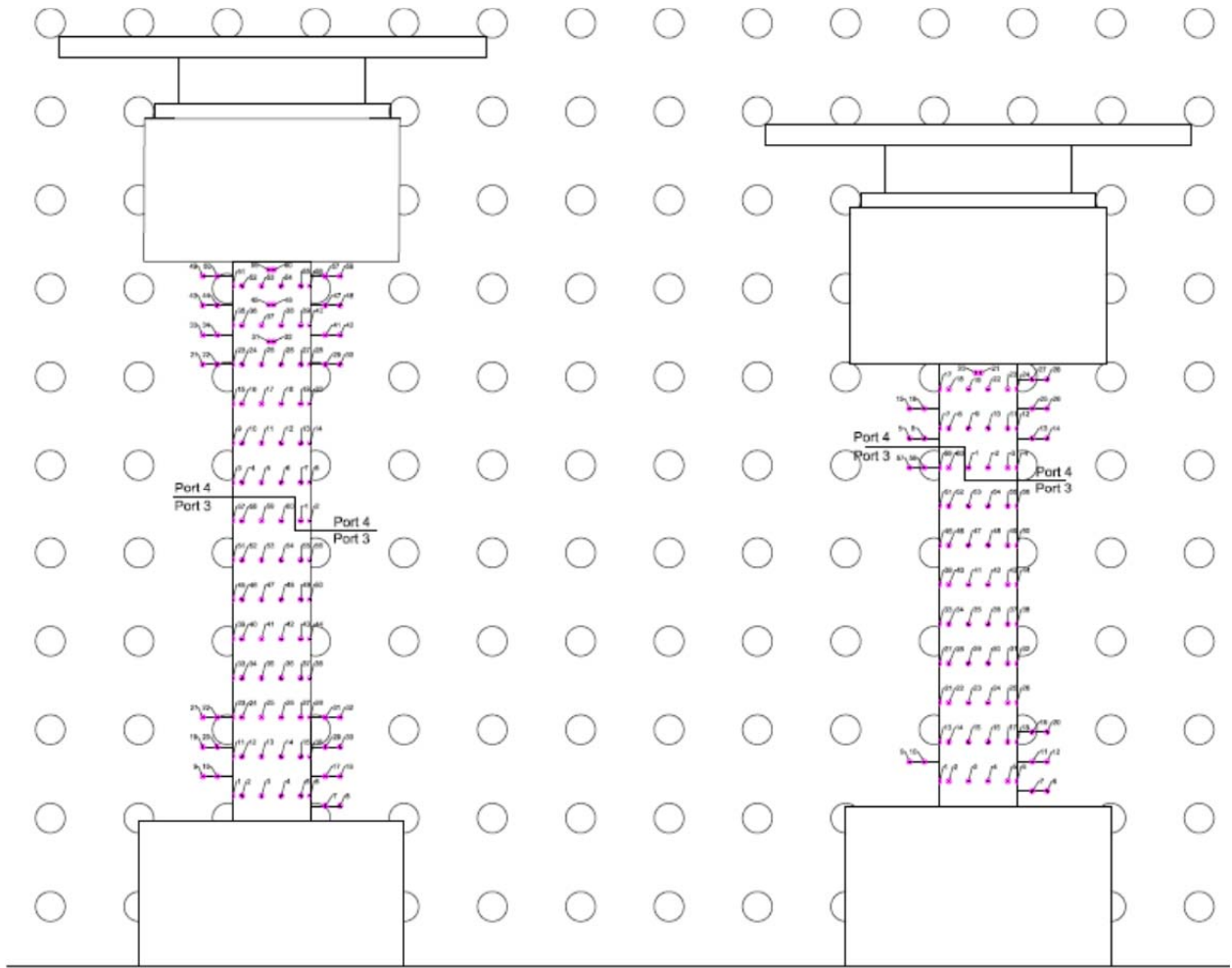


Figure B.12 Krypton target locations

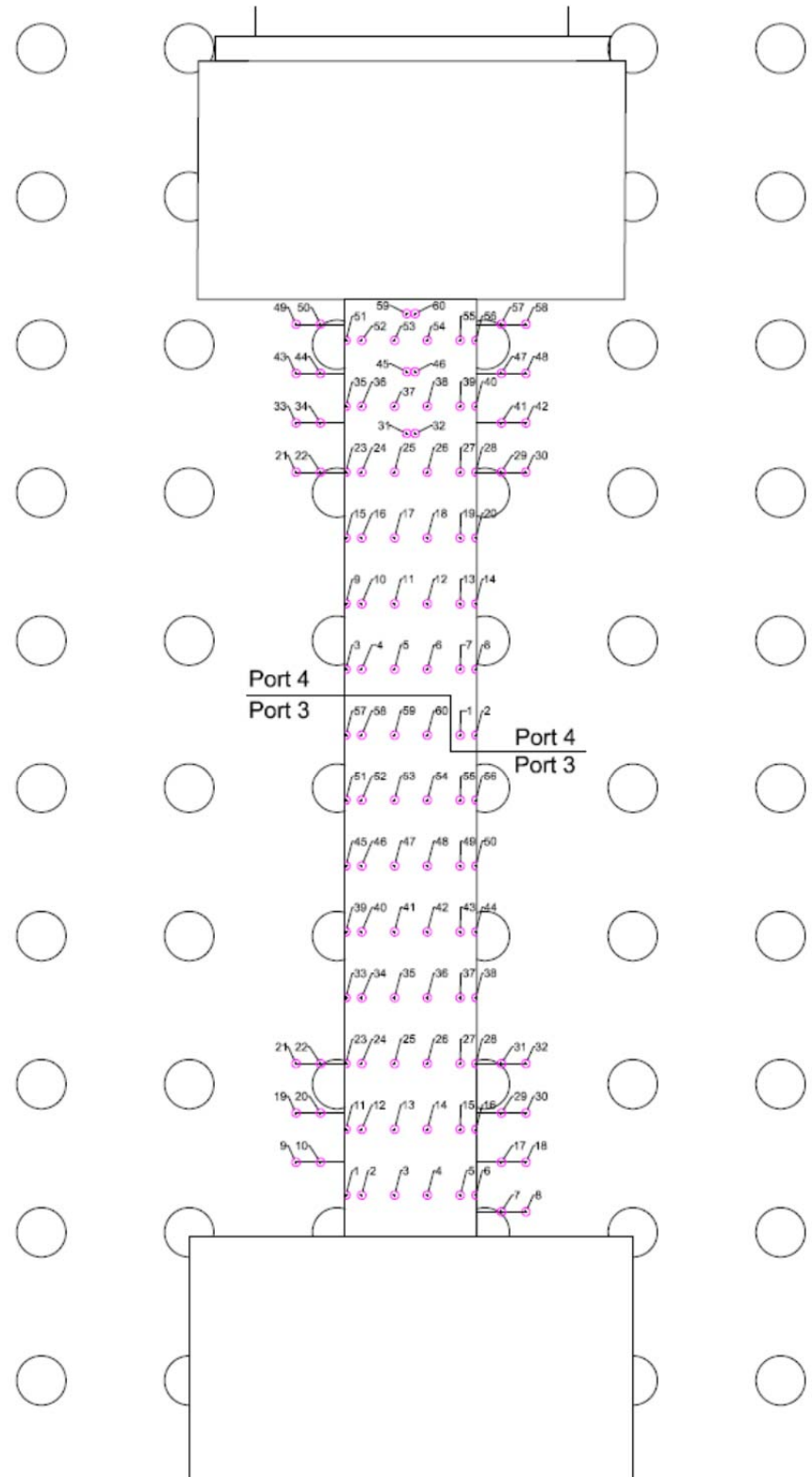


Figure B.13 Krypton targets - Pier 1

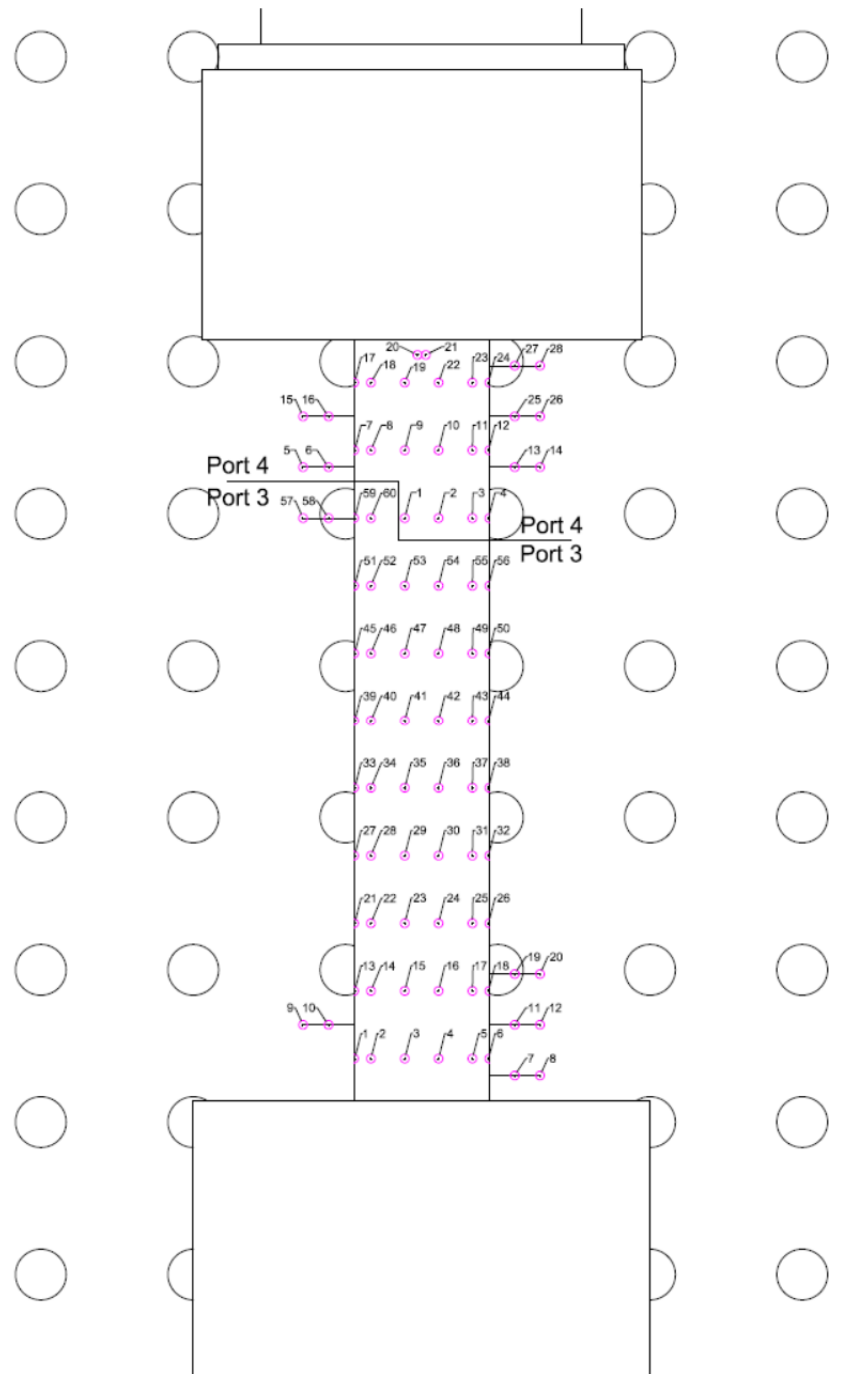


Figure B.14 Krypton targets - Pier 2

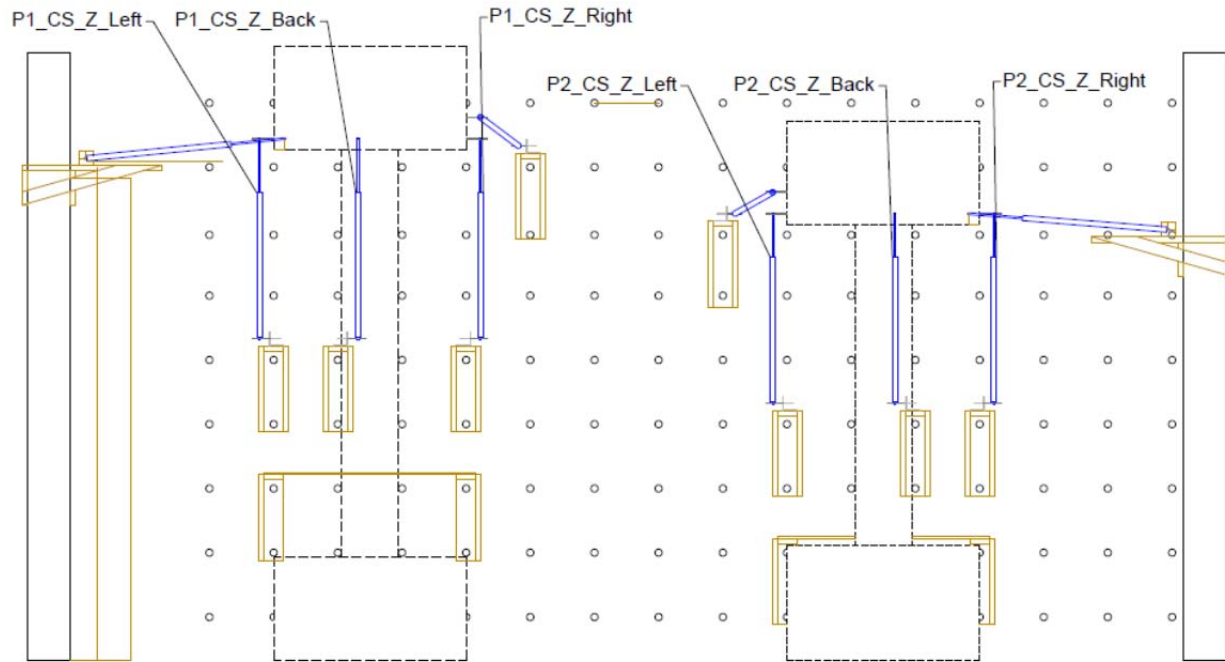


Figure B.15 Elevation view of control sensors

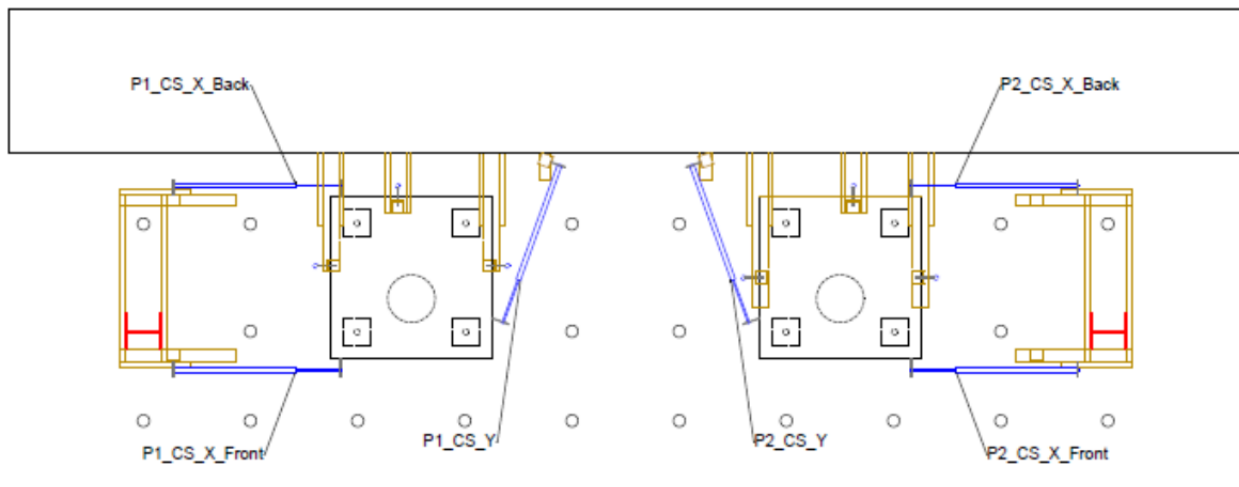


Figure B.16 Plan view of control sensors



Figure B.17 Embedded and surface strain gage boxes - Pier 1

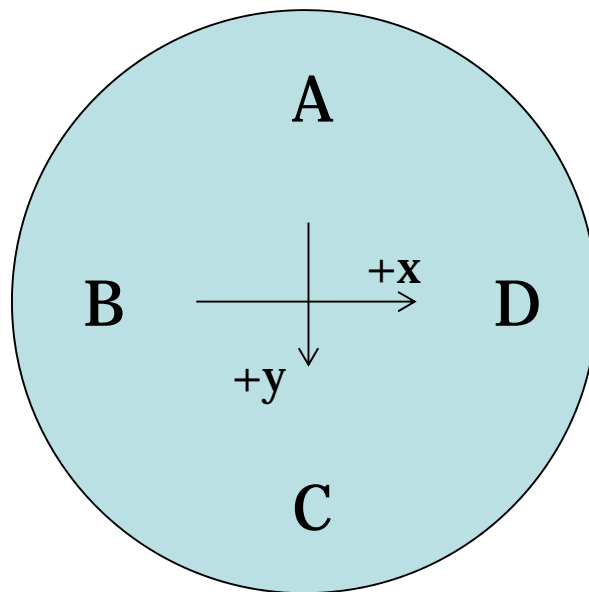


Figure B.18 Index of pier faces for strain gage identification

B.3 Small-Scale Test Setup

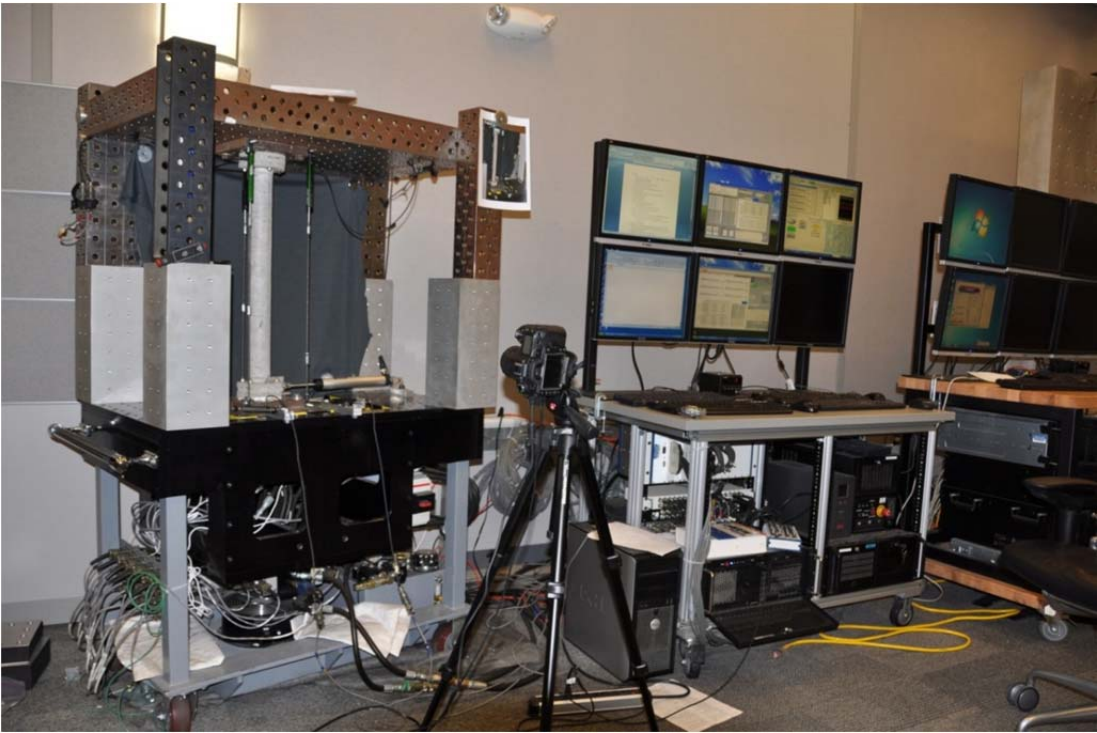


Figure B.19 Small-scale test setup with camera and controls

APPENDIX C. HYBRID SIMULATION RESULTS

Provided below is a summary of the global 6DOF response displayed as time histories and hysteretic responses in each degree of freedom, as well as measurements from instrumentation data. Finally, a methodology and format for selection and plotting of key events throughout the hybrid simulations is provided.

C.1 Global Response

Global 6DOF responses are displayed as time histories and hysteretic responses, along with photos of the associated cracking observed in each of the three specimens. Digital Appendix C includes associated global Cartesian action and deformation response data sets.

i. Pier 1 (1:3 Scale 9.5' Outside Pier)

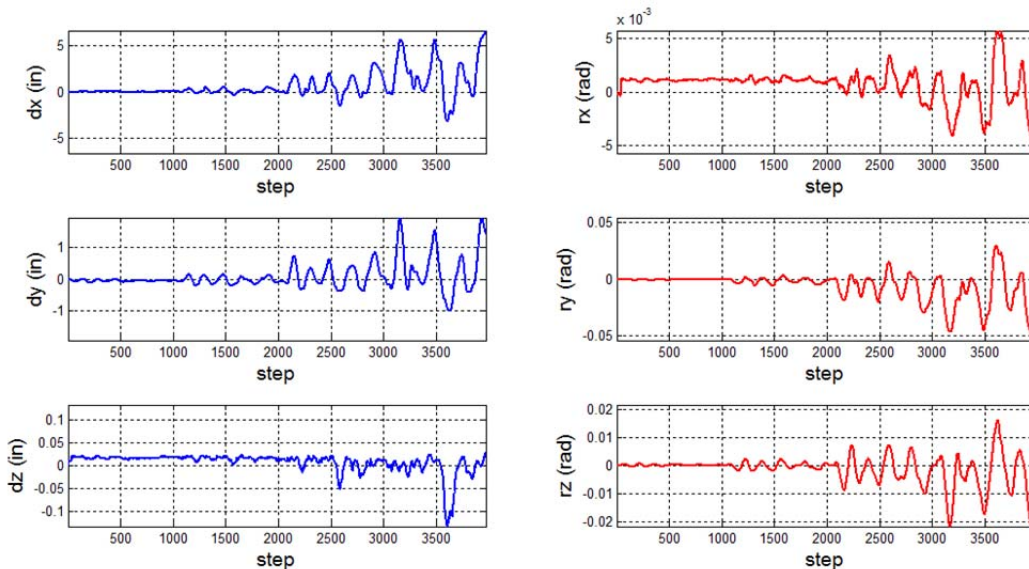


Figure C.1 Pier 1 deformation response time history

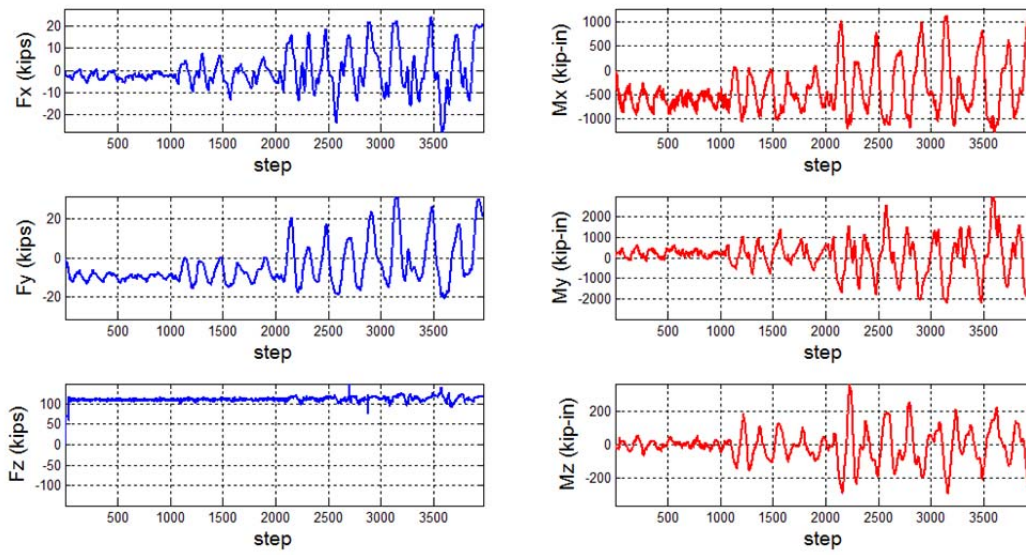


Figure C.2 Pier 1 load response time history

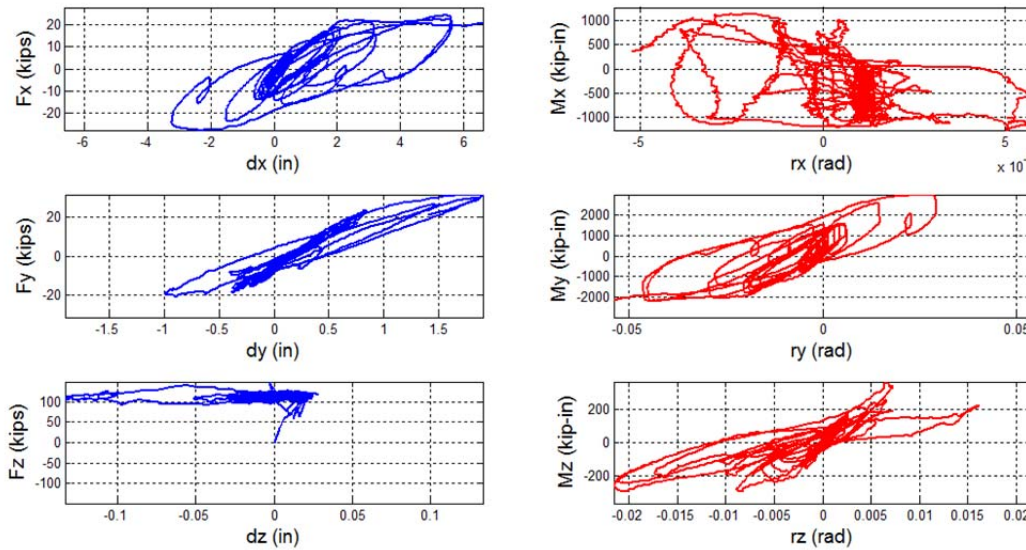


Figure C.3 Pier 1 hysteresis

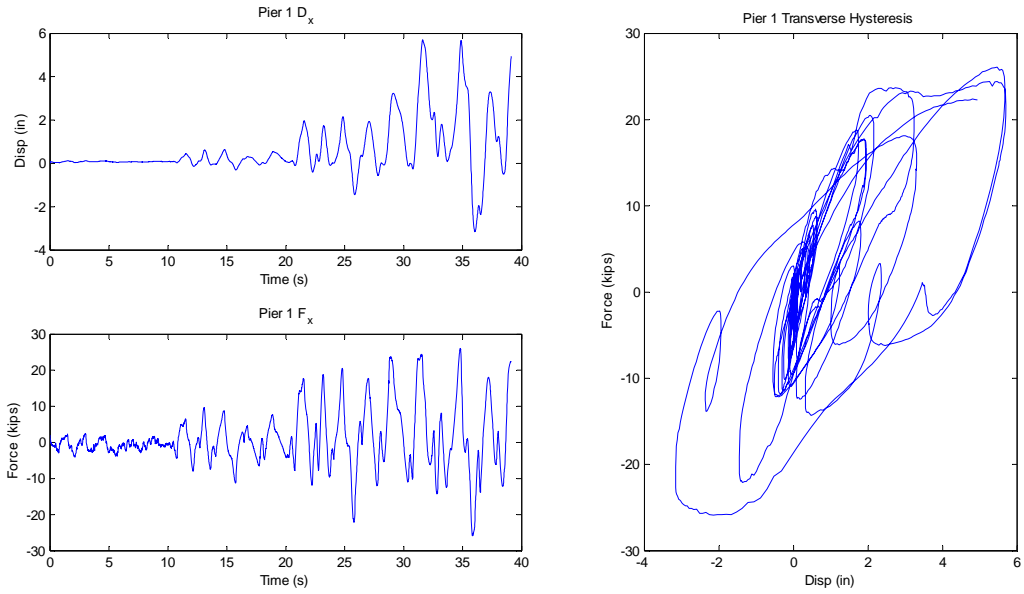


Figure C.4 Pier 1 Transverse Response

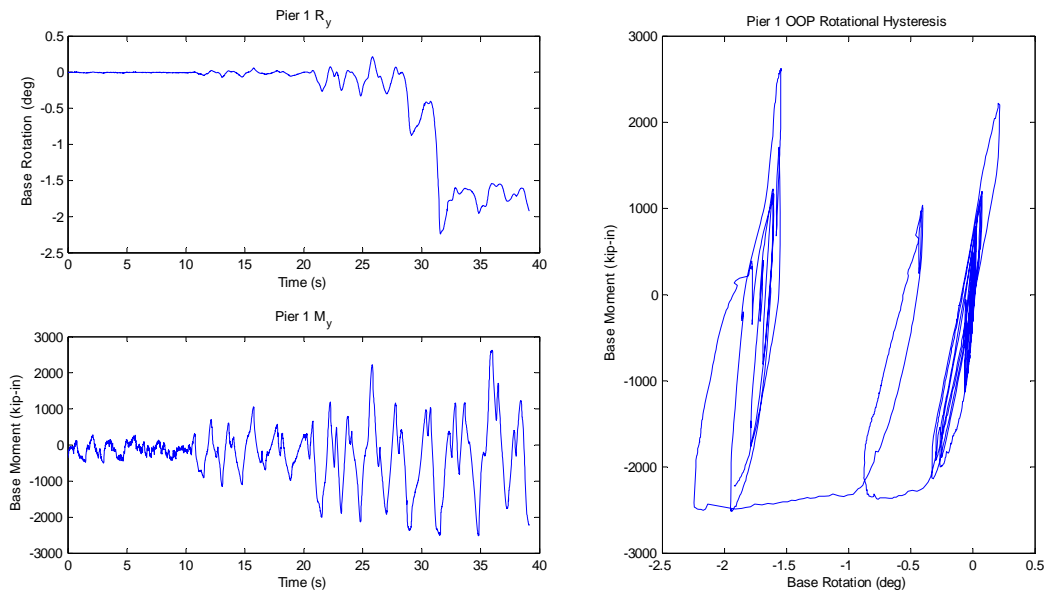


Figure C.5 Pier 1 Out-of-plane Response

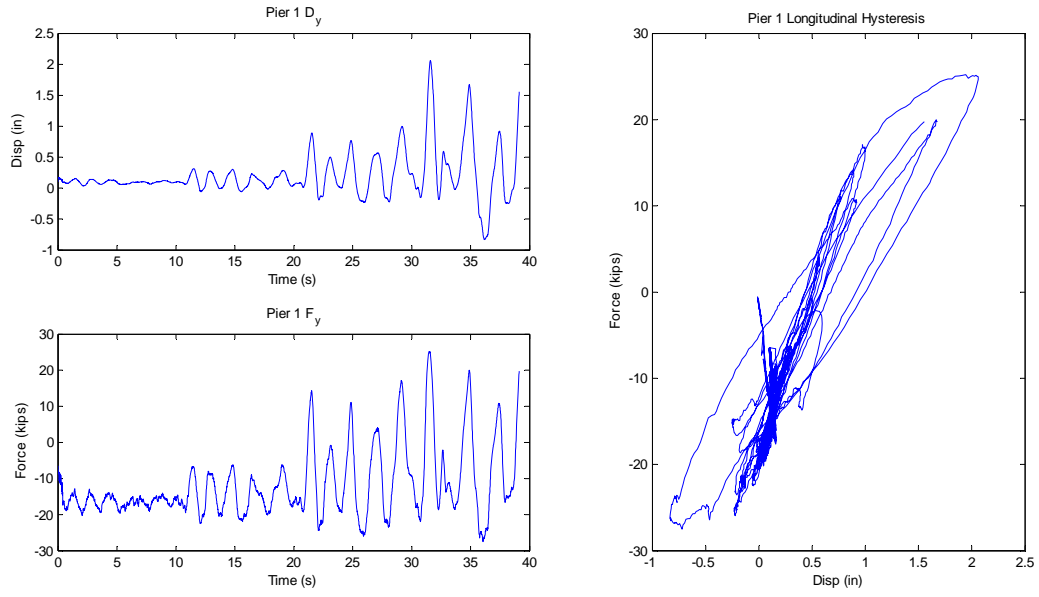


Figure C.6 Pier 1 Longitudinal Response

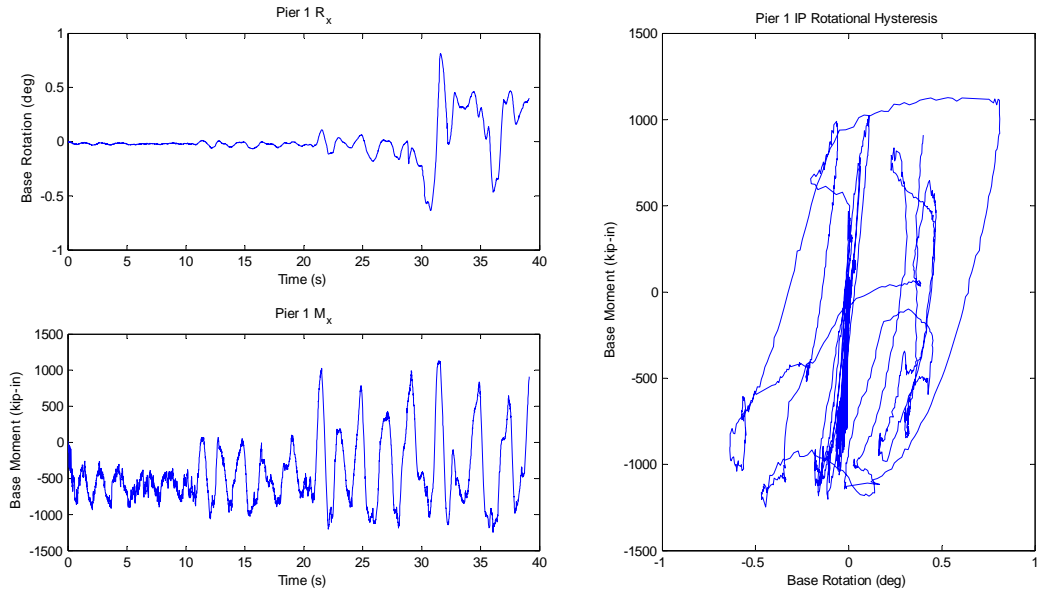


Figure C.7 Pier 1 In-plane Response



Figure C.8 Pier 1 Cracking Patterns

ii. Pier 2 (1:3 Scale 7.5' Outside Pier)

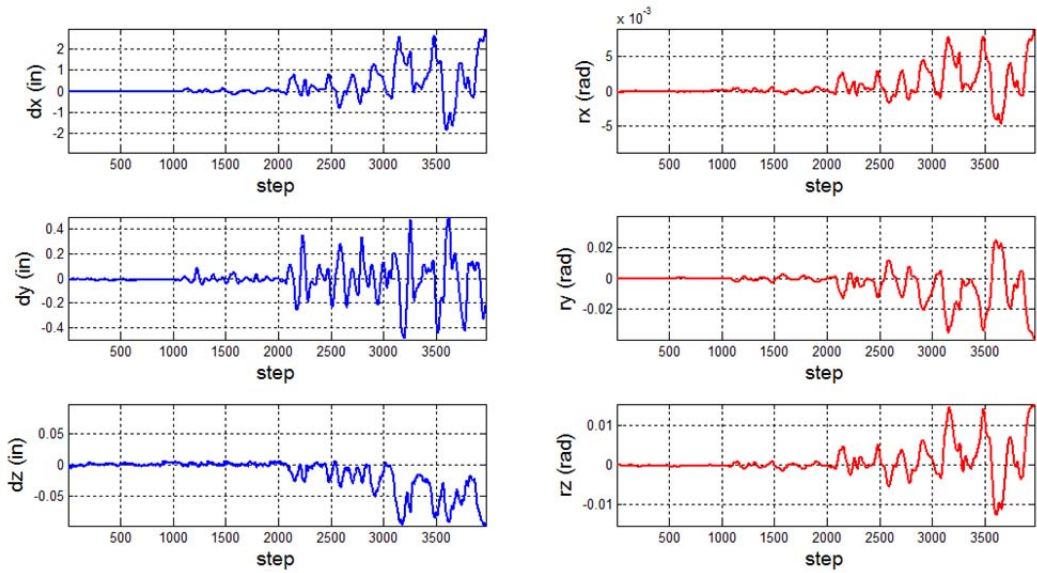


Figure C.9 Pier 2 deformation response time history

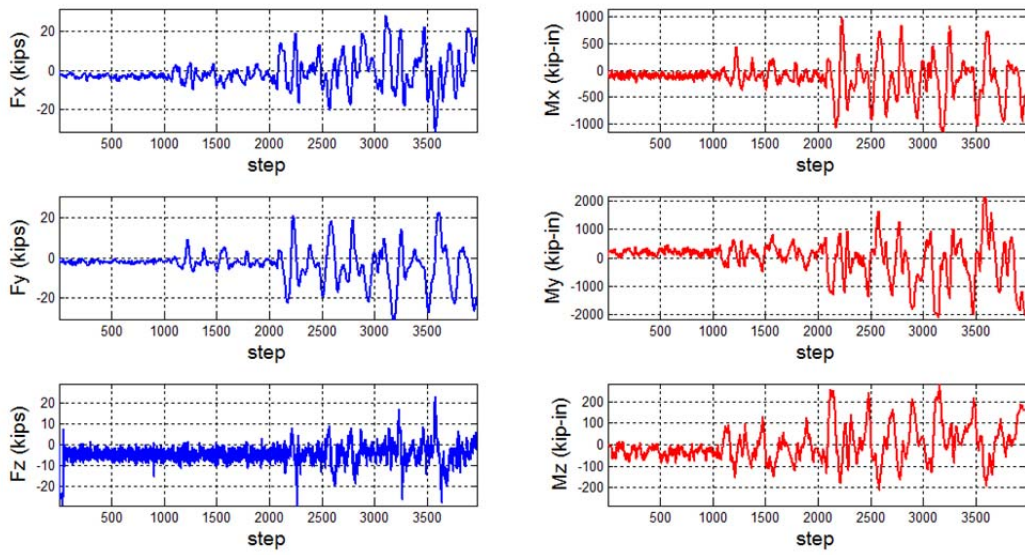


Figure C.10 Pier 2 load response time history

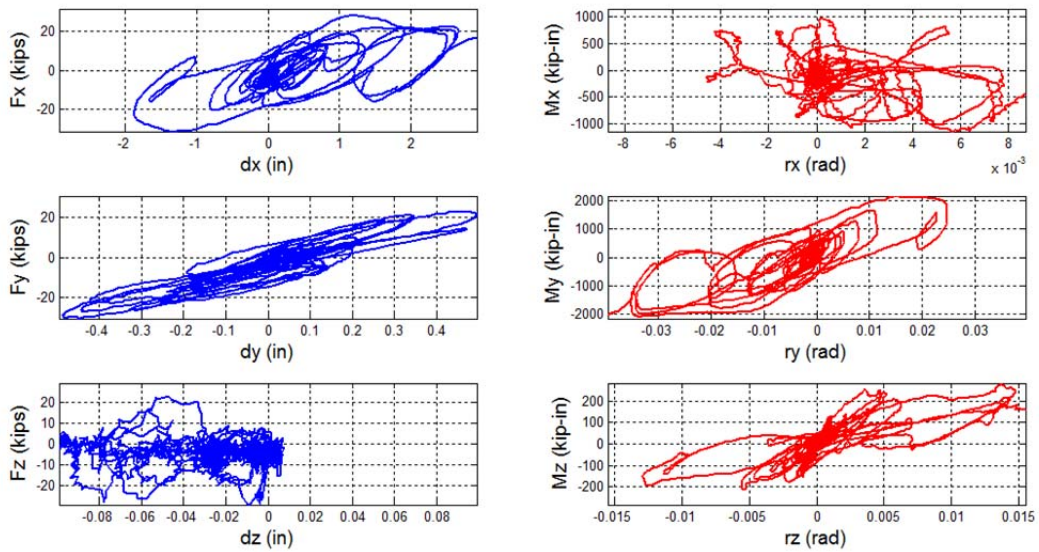


Figure C.11 Pier 2 hysteresis

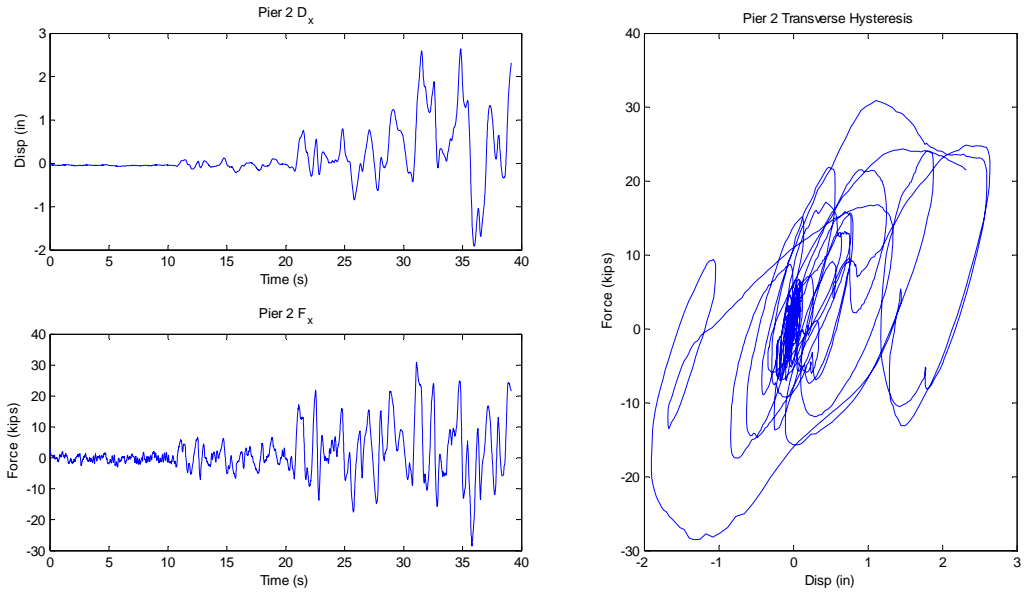


Figure C.12 Pier 2 Transverse Response

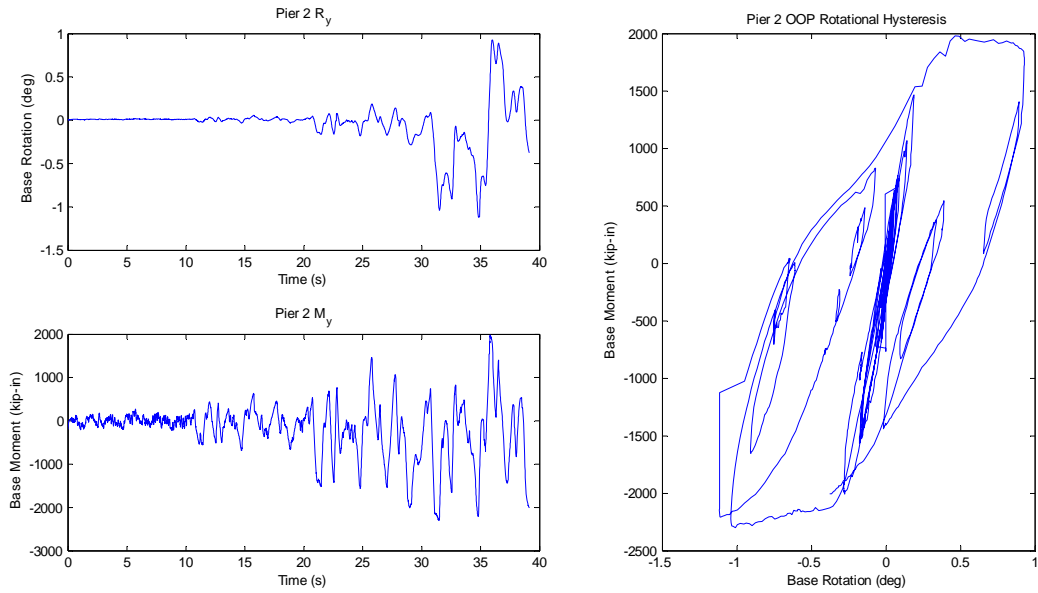


Figure C.13 Pier 2 Out-of-plane Response

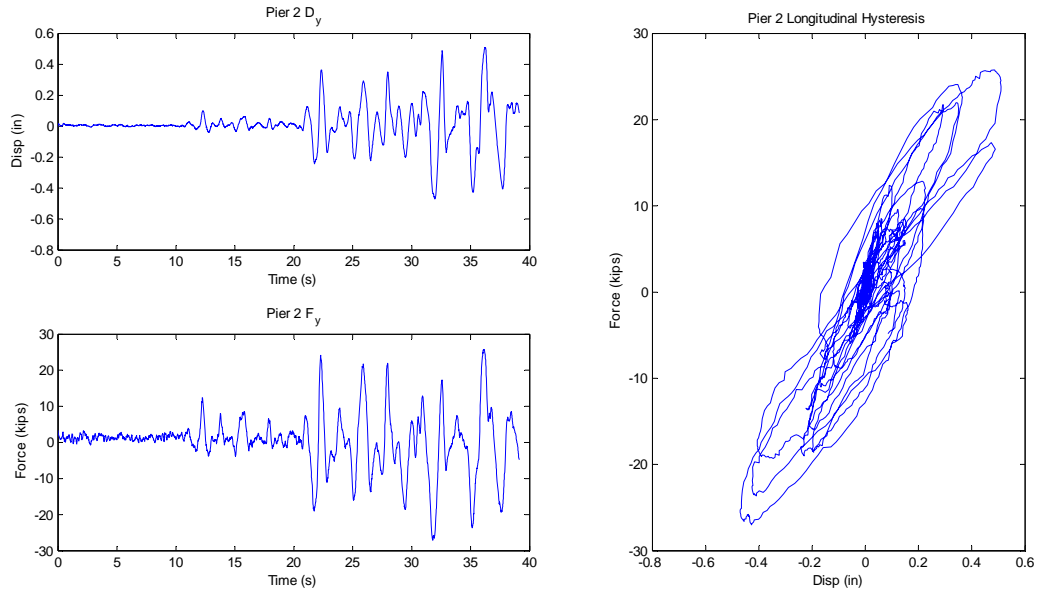


Figure C.14 Pier 2 Longitudinal Response

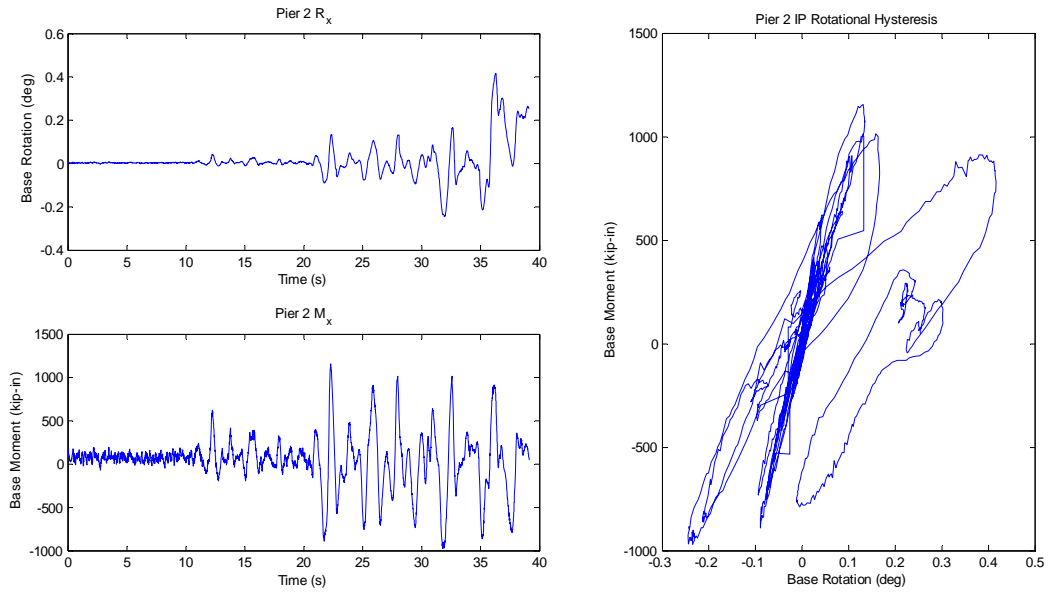


Figure C.15 Pier 2 In-plane Response

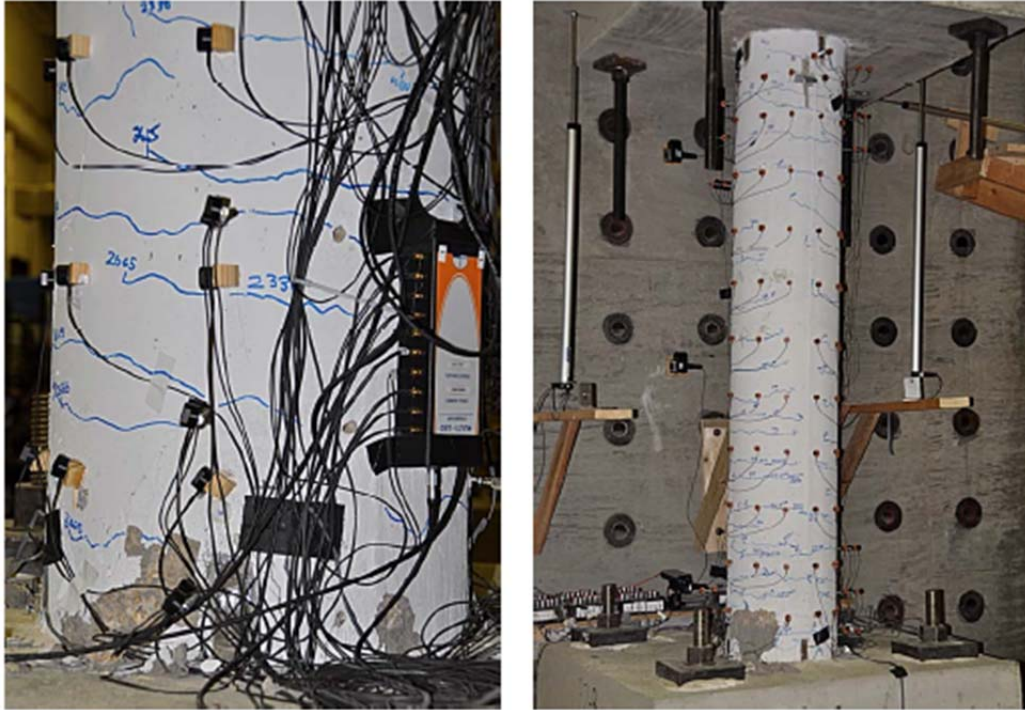


Figure C.16 Pier 2 Cracking Patterns

iii. Pier 3 (1:20 Small-Scale Inner Pier)

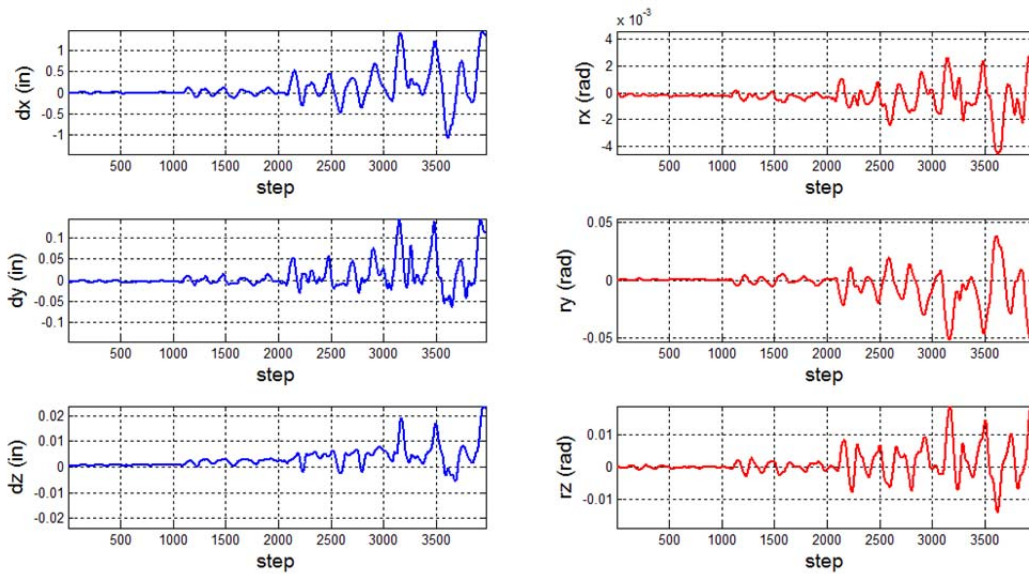


Figure C.17 Pier 3 deformation response time history

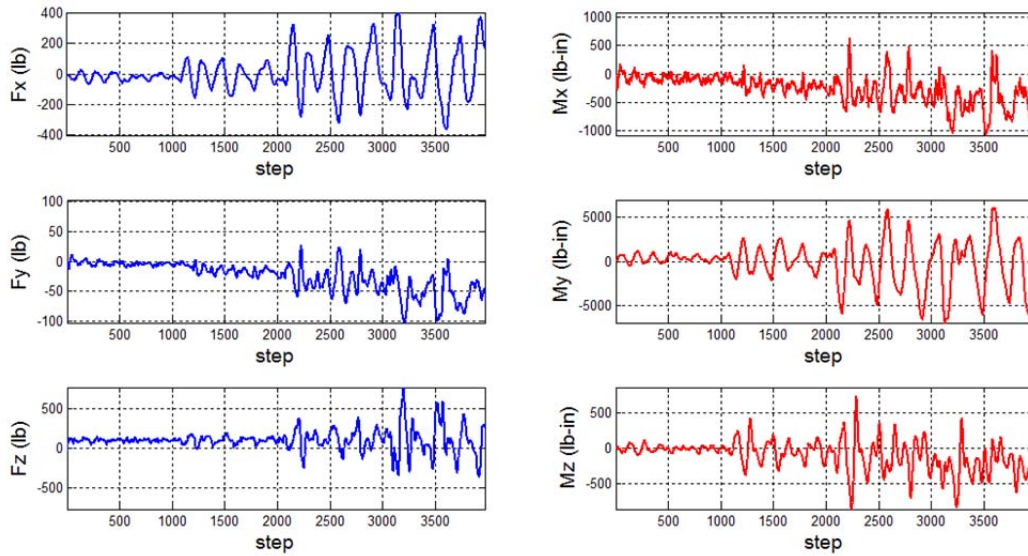


Figure C.18 Pier 3 load response time history

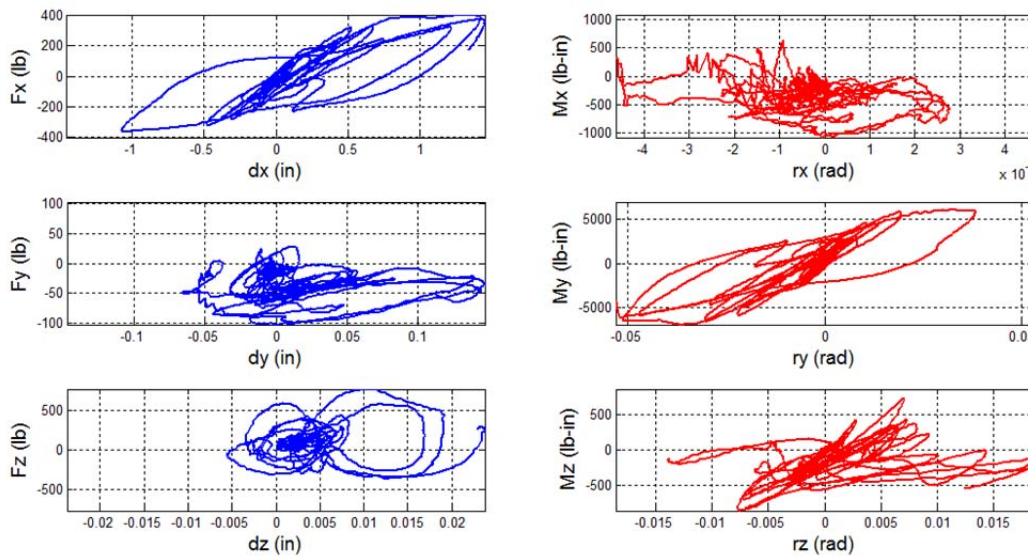


Figure C.19 Pier 3 hysteresis

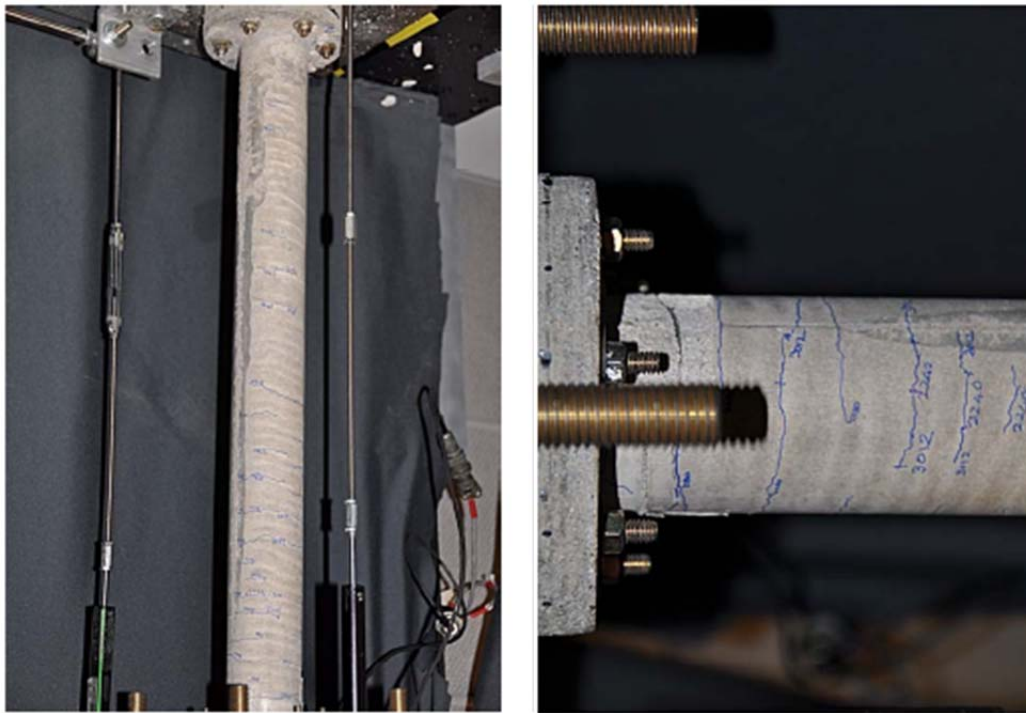


Figure C.20 Pier 3 Cracking Patterns

C.2 Data Acquisition Summary

Plots of the instrumentation data, including embedded steel strain gages and derived Krypton data are provided below. Digital Appendix C includes data sets for strain gages, individual Krypton LED and derived 6DOF Krypton motion data. Also included in digital Appendix C are plots of the full set of key event summary data.

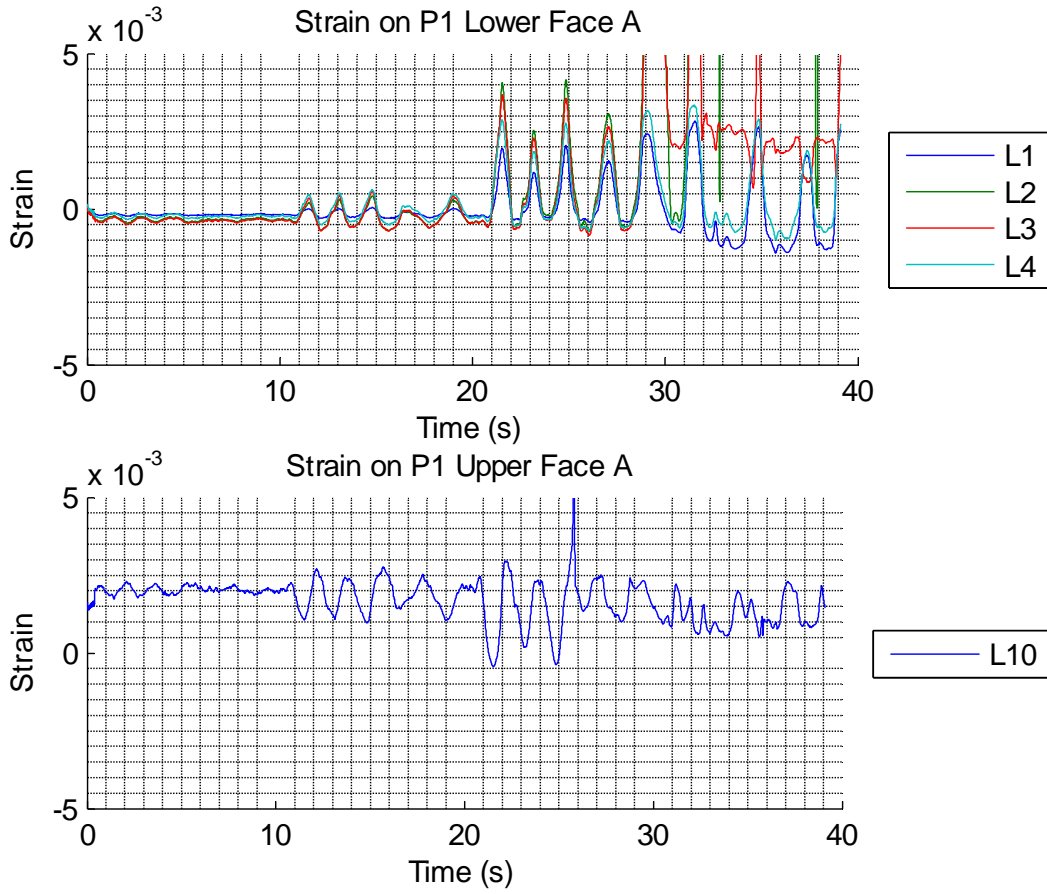


Figure C.21 Longitudinal Strains on Face A of Pier 1

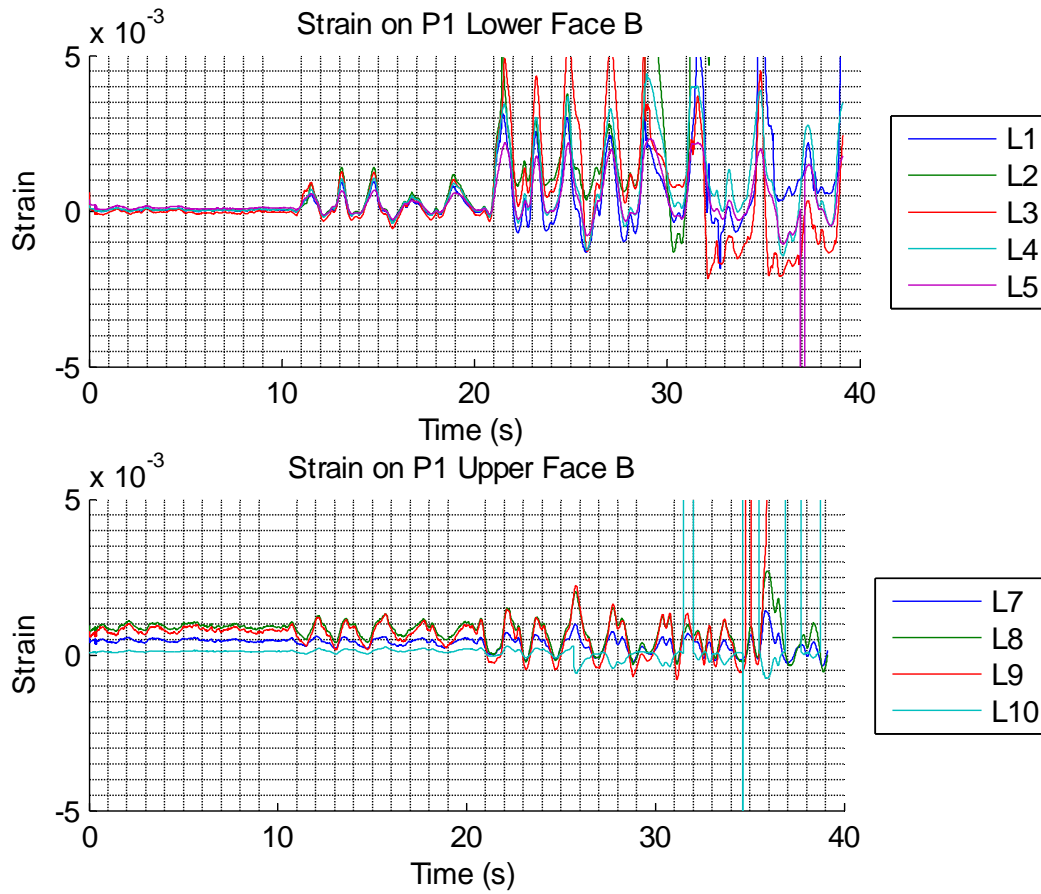


Figure C.22 Longitudinal Strains on Face B of Pier 1

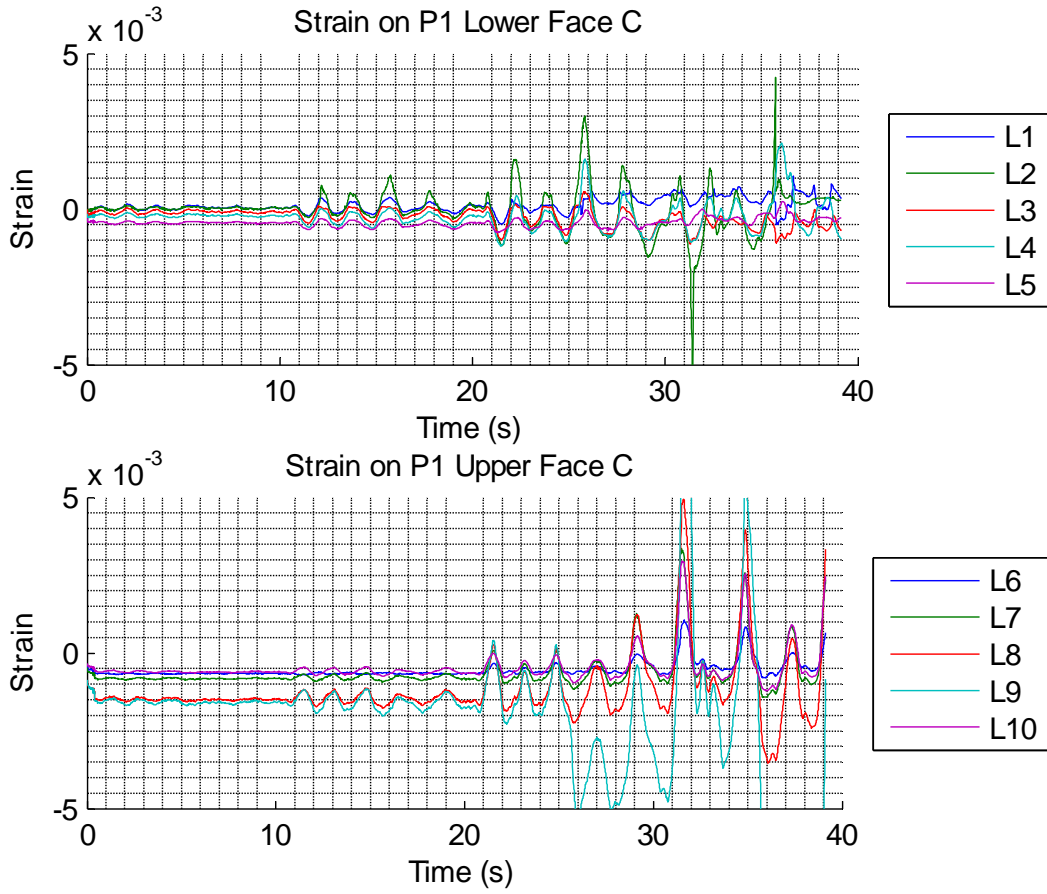


Figure C.23 Longitudinal Strains on Face C of Pier 1

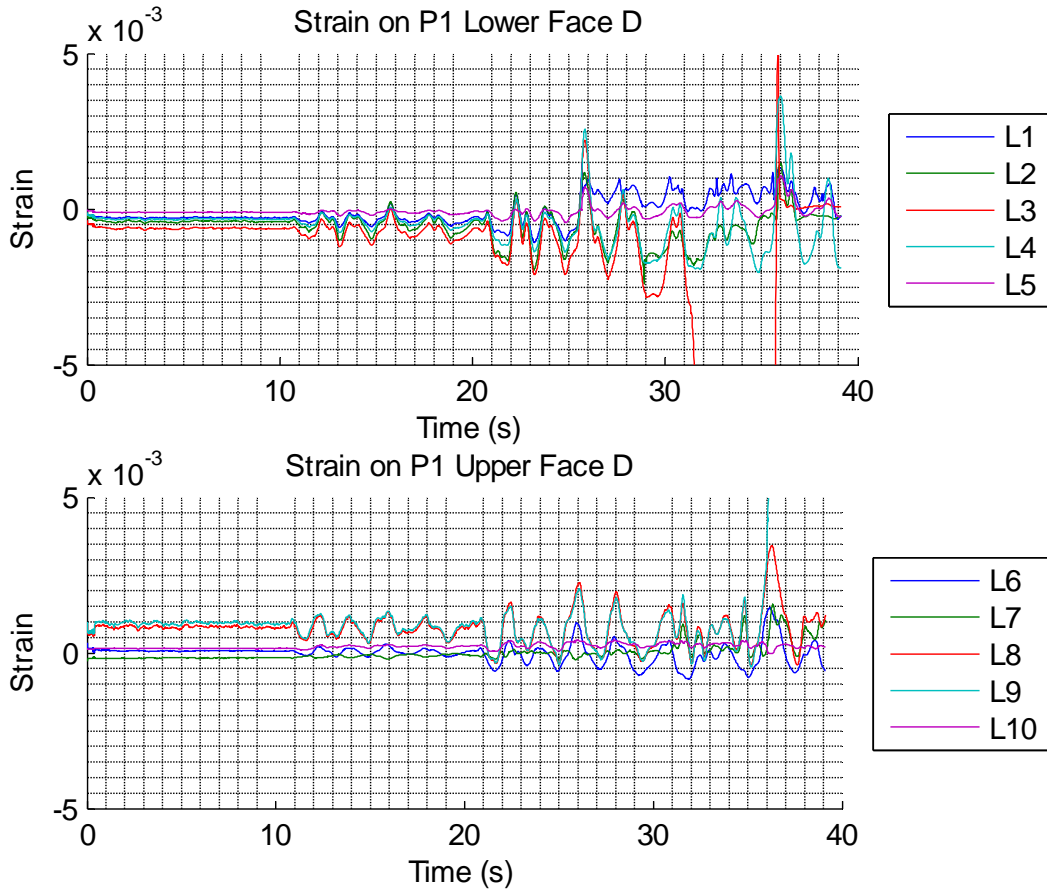


Figure C.24 Longitudinal Strains on Face D of Pier 1

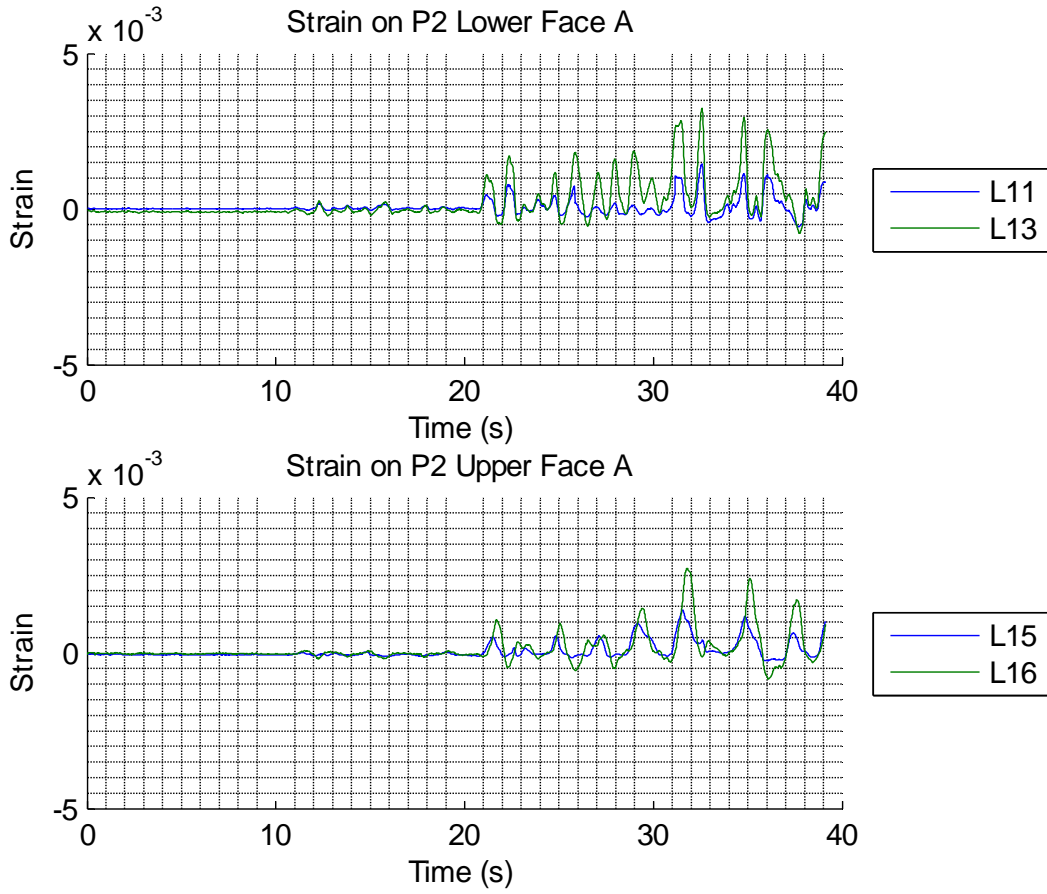


Figure C.25 Longitudinal Strains on Face A of Pier 2

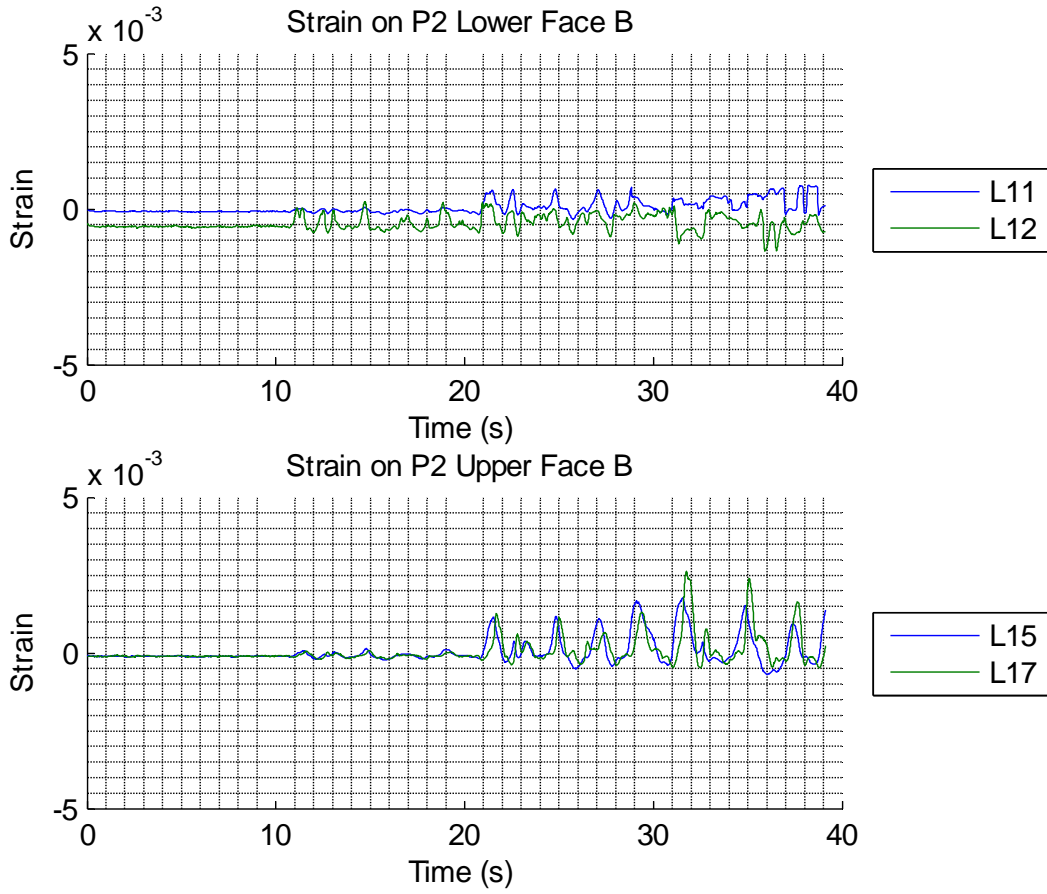


Figure C.26 Longitudinal Strains on Face B of Pier 2

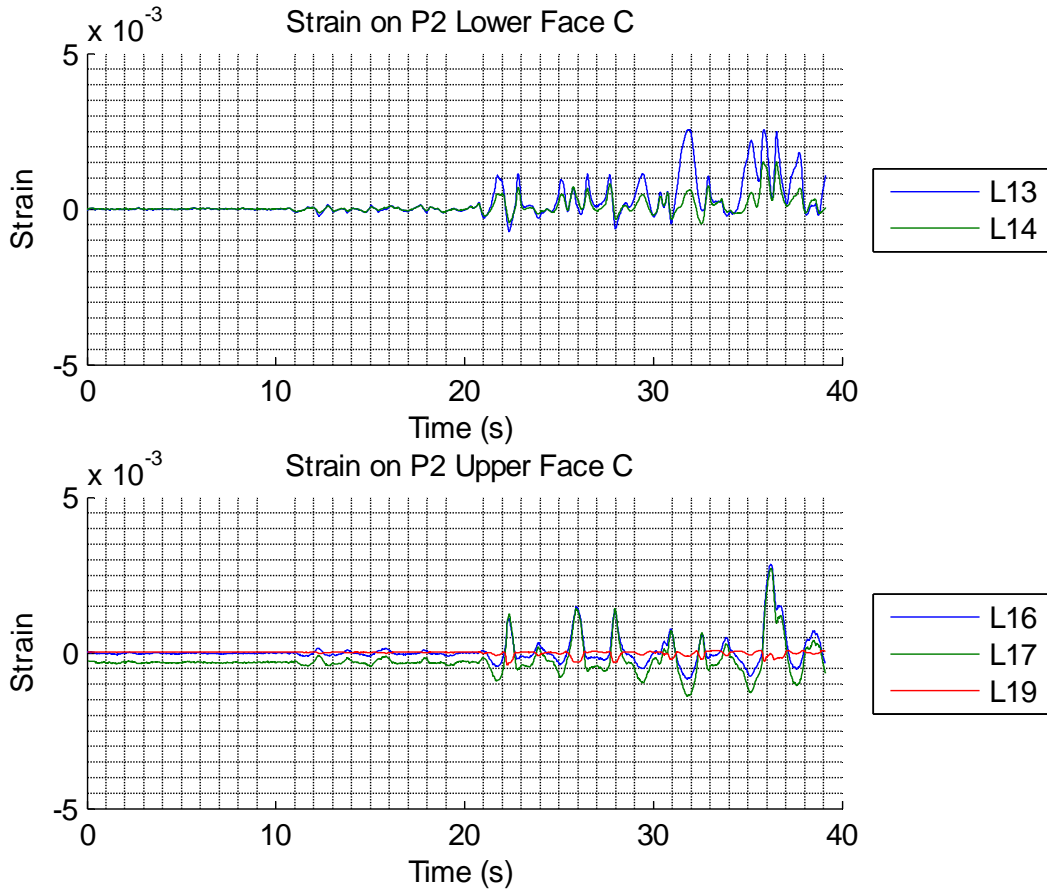


Figure C.27 Longitudinal Strains on Face C of Pier 2

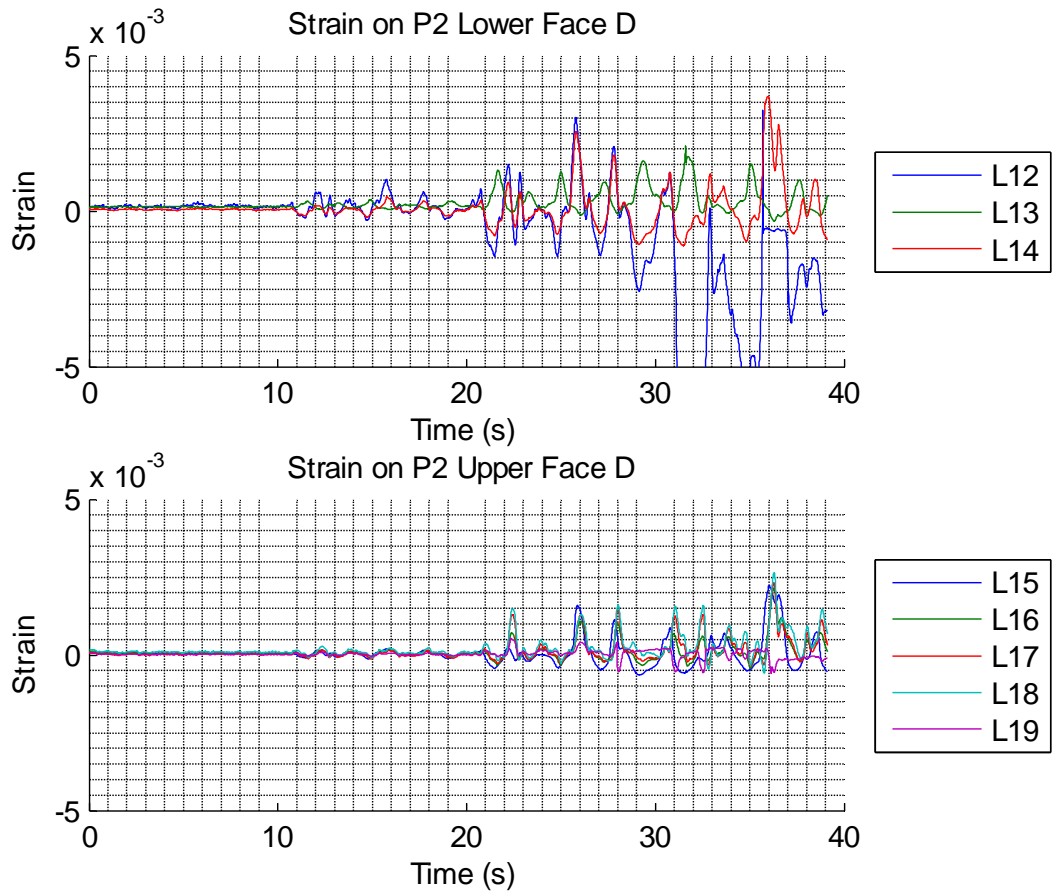


Figure C.28 Longitudinal Strains on Face D of Pier 2

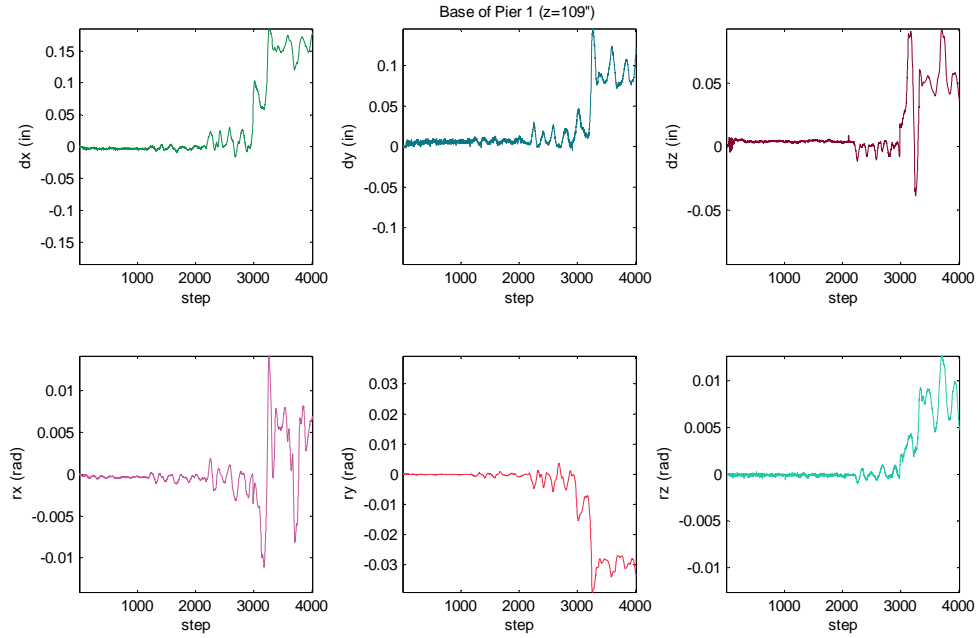


Figure C.29 Pier 1 Base Krypton 6DOF Movement

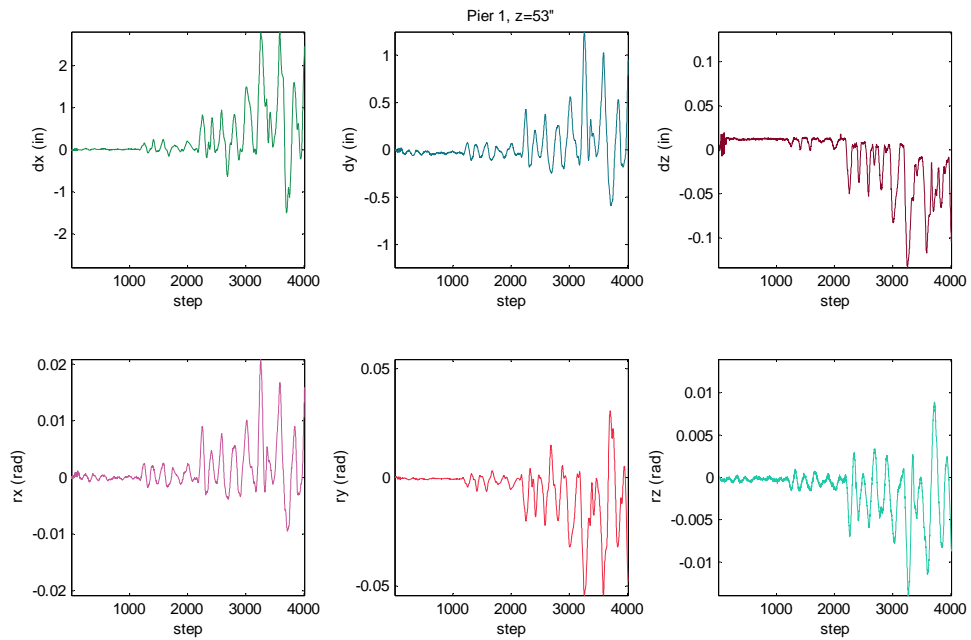


Figure C.30 Pier 1 Middle Krypton 6DOF Movement

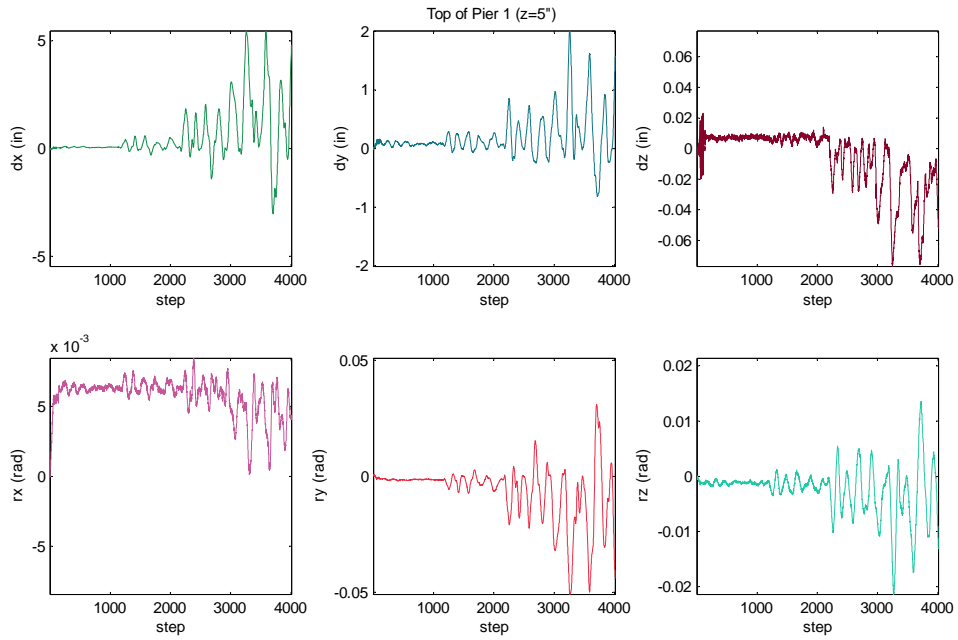


Figure C.31 Pier 1 Top Krypton 6DOF Movement

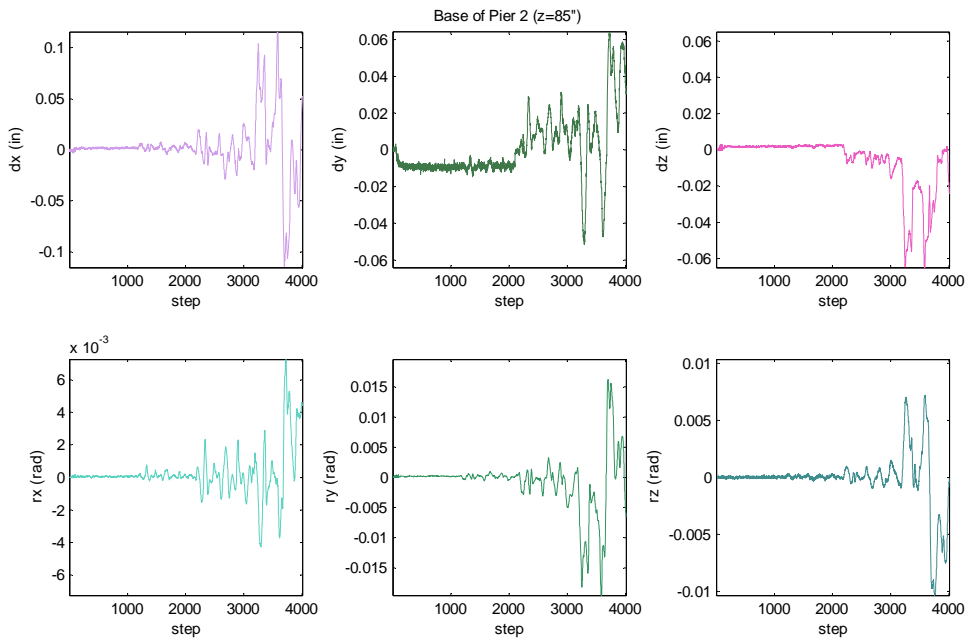


Figure C.32 Pier 2 Base Krypton 6DOF Movement

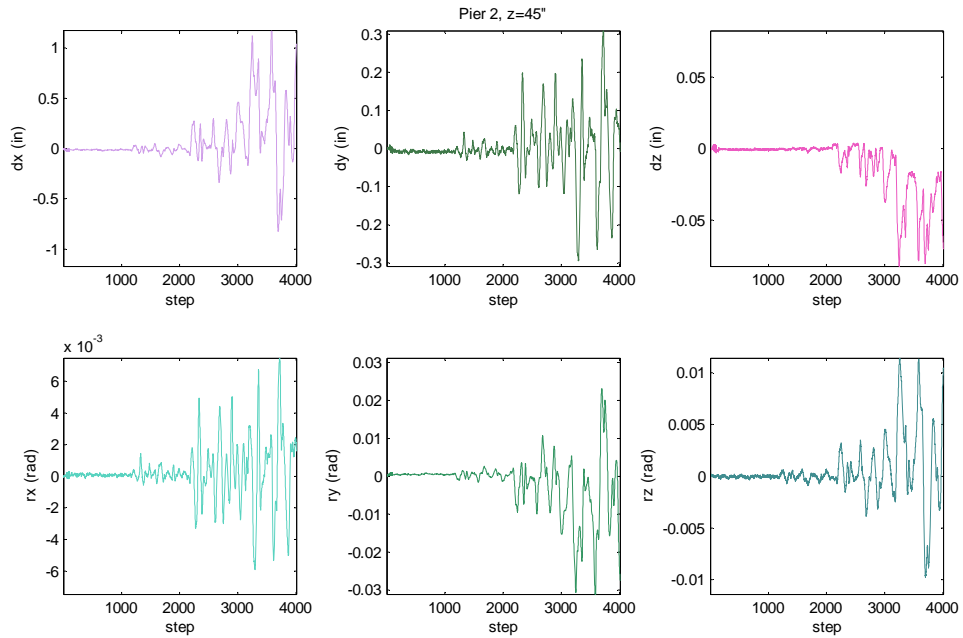


Figure C.33 Pier 2 Middle Krypton 6DOF Movement

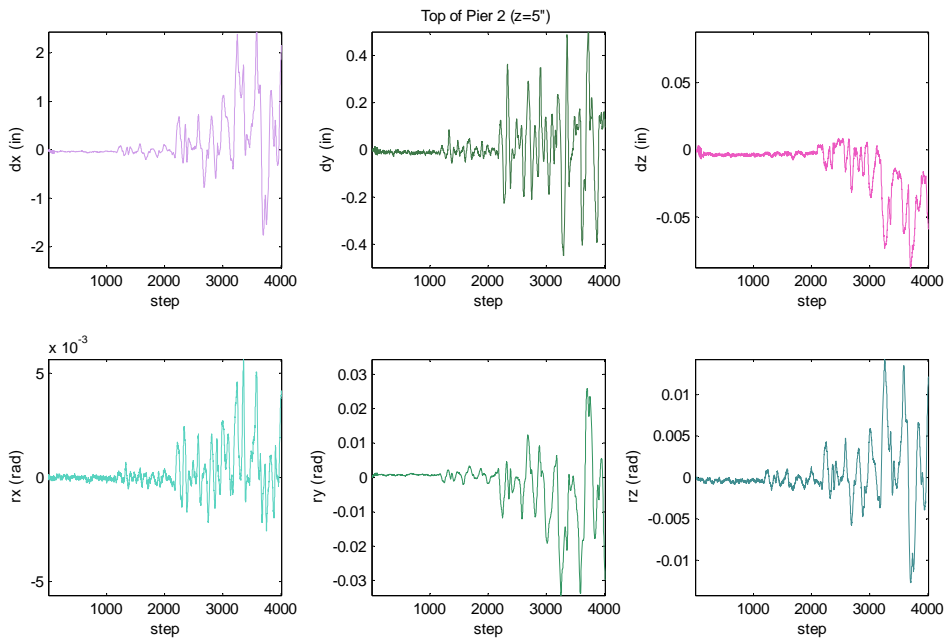


Figure C.34 Pier 2 Top Krypton 6DOF Movement

C.3 Description of Key Event Points

Key events are identified throughout the course of the hybrid simulation, and are presented in the following section. These events are identified through analyzing instrumentation data, global response data, and reviewing notes of physical phenomena observed throughout the seismic loading record. Various methods for isolating a step at which a significant event occurs include identifying key local and global maxima for deformations and actions. Additionally, the steps at which longitudinal rebar yield are noted. This is done due to the influence of this local phenomena on global response. Finally, events are created for cracking, spalling, and audible rupturing of concrete reinforcement at various stages of the test.

A template is created for presenting key aspects of the bridge response at a given event. This template is provided in Figure C.38 with labels explaining the various components of the structural response data presented throughout the plots of key events.

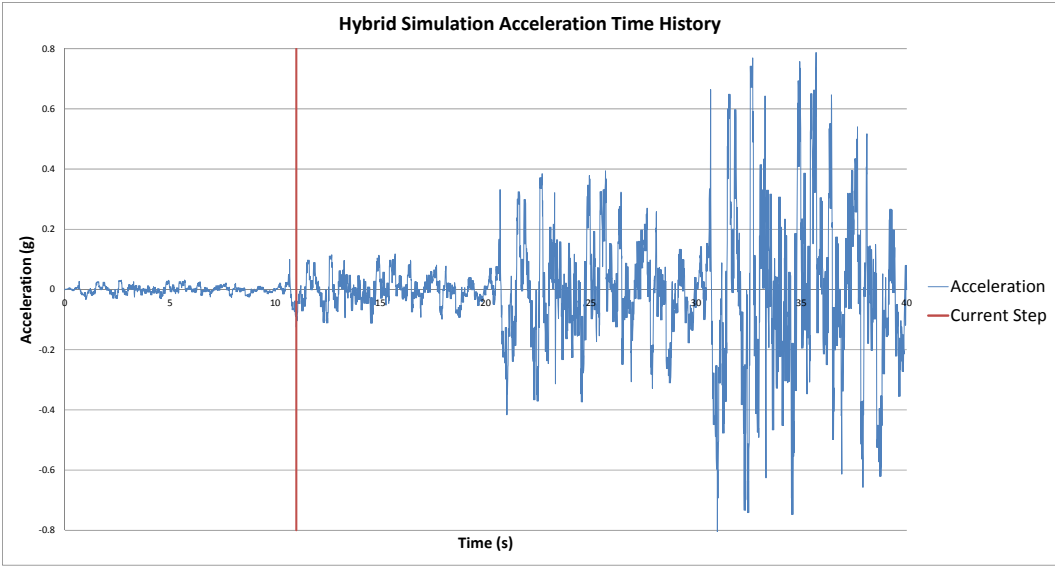


Figure C.35 Acceleration time history with current step marker

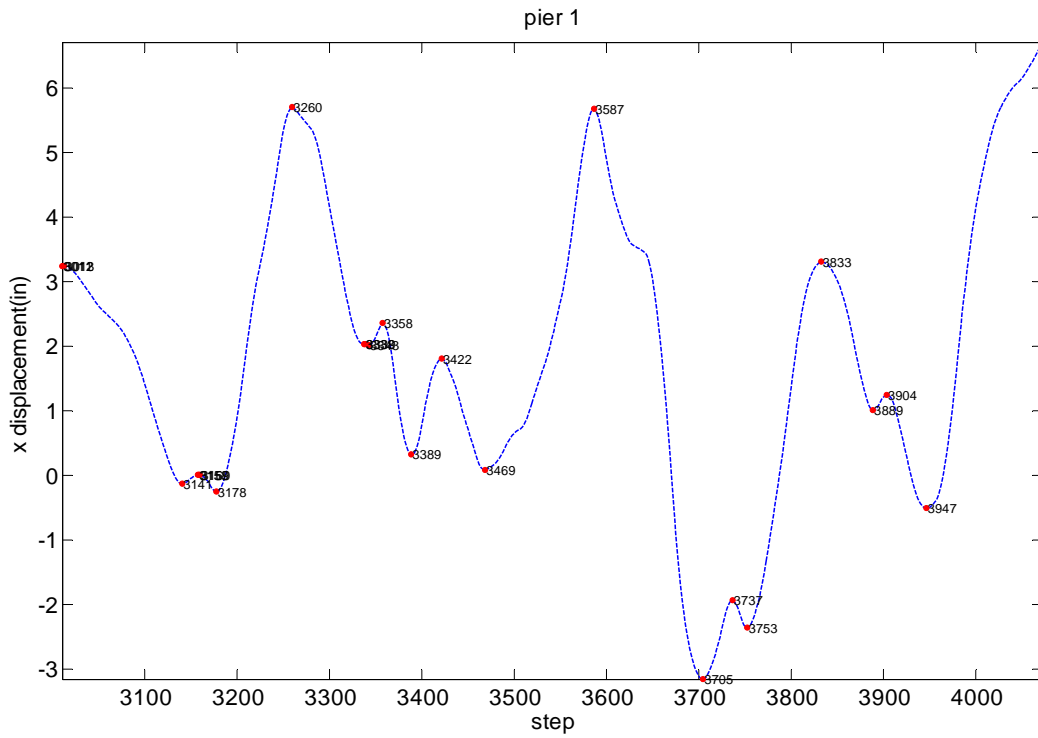


Figure C.36 Peak displacement responses at final seismic loading level - Pier 1

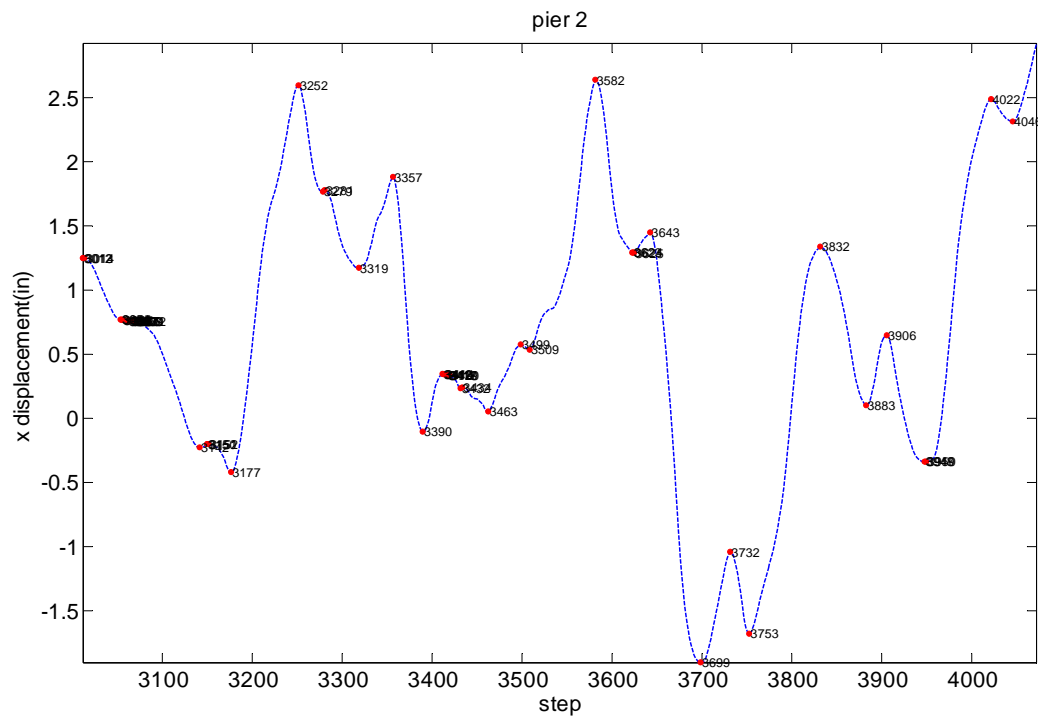


Figure C.37 Peak displacement responses at final seismic loading level - Pier 2

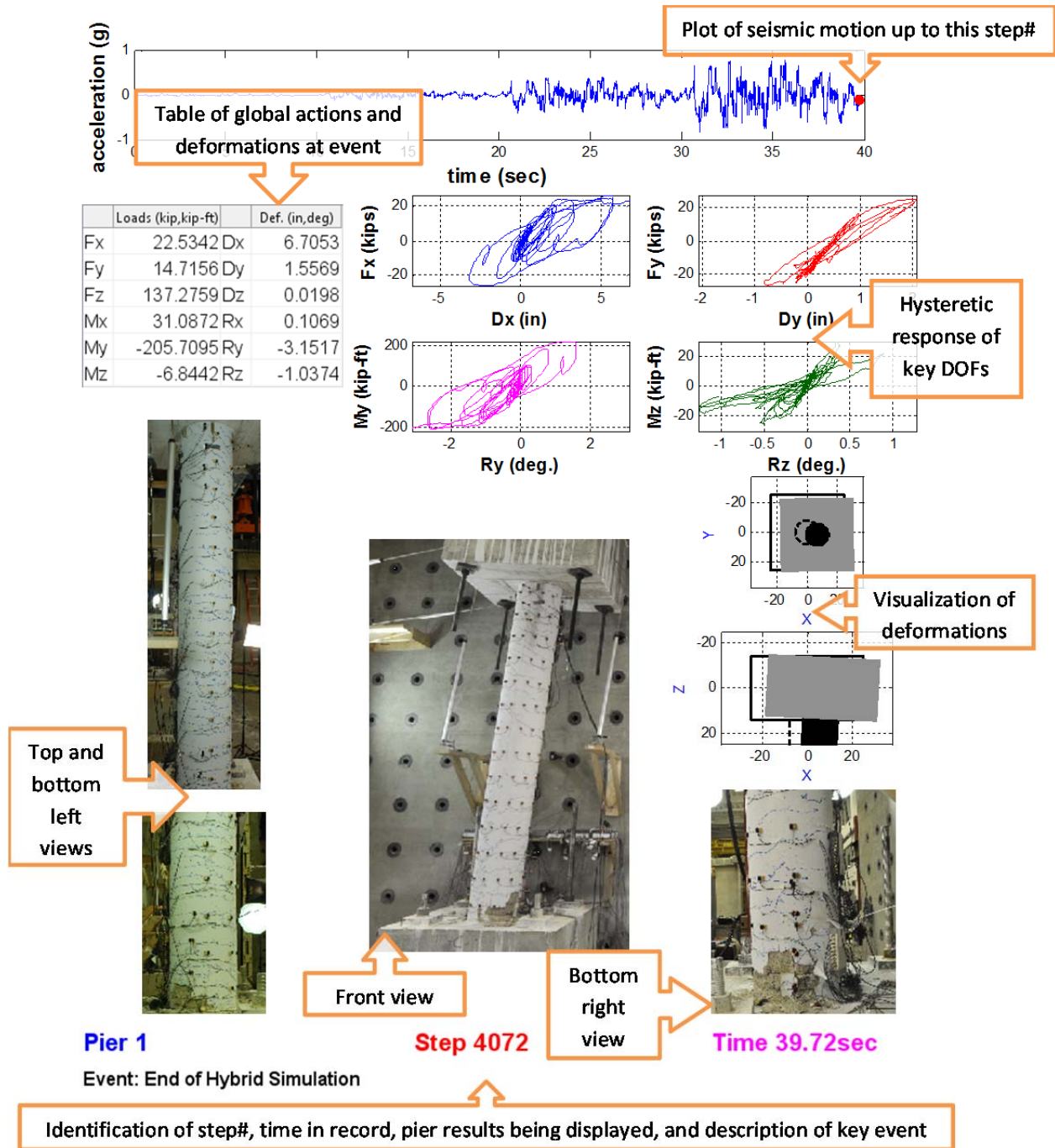
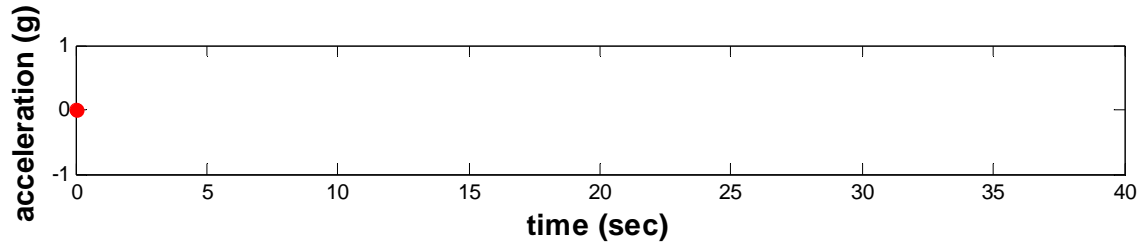


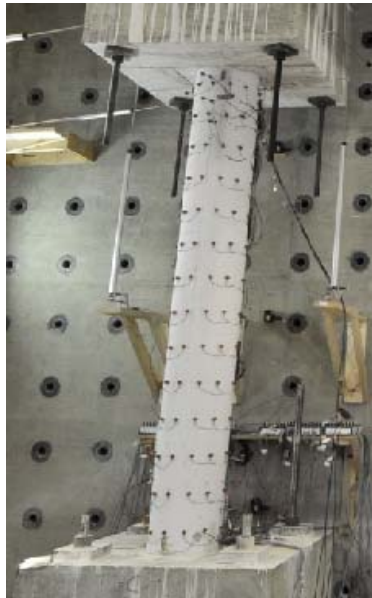
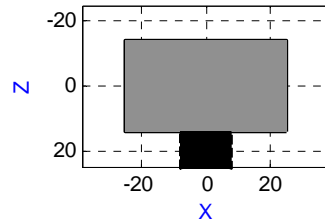
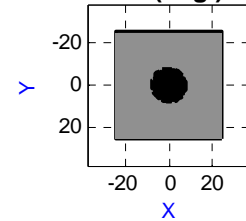
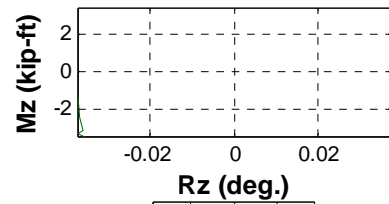
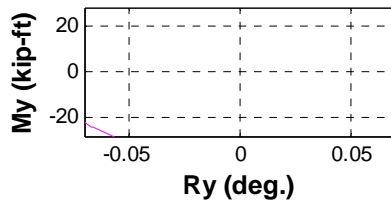
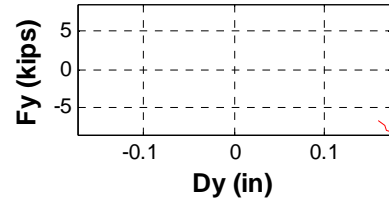
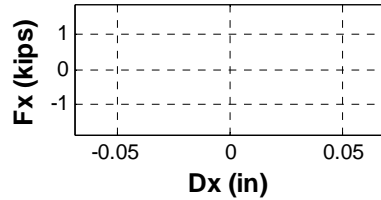
Figure C.38 Template of structural response at key events

C.4 Summary of Structural Response at Key Events

A summary of structural responses at select key events is provided in the following figures. A full set of all key events for which this data summary is provided can be found in Digital Appendix C. Structural response data is provided for peak global parameters of each pier, yielding of any longitudinal rebar, noteworthy events in the loading protocol, and significant observed cracking and spalling.



	Loads (kip,kip-ft)	Def. (in,deg)
Fx	0.7186 Dx	0.0688
Fy	-8.3630 Dy	0.1725
Fz	87.3290 Dz	-8.6042e...
Mx	-8.5643 Rx	0.3895
My	-22.1256 Ry	-0.0707
Mz	-3.4175 Rz	-0.0352



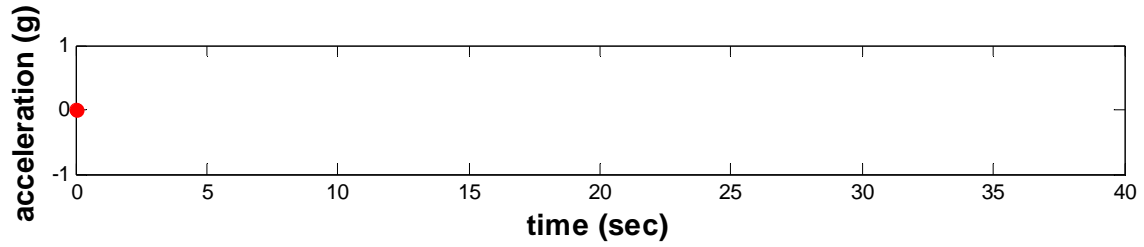
Pier 1

Step 105

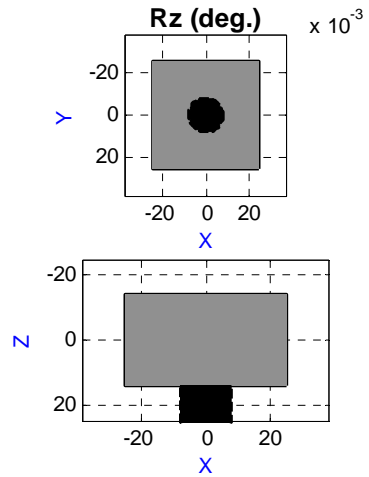
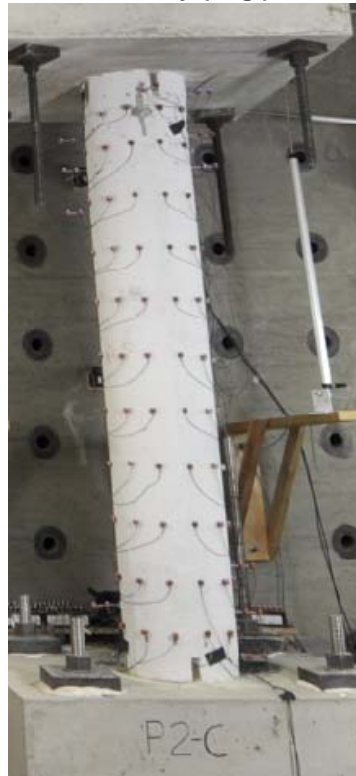
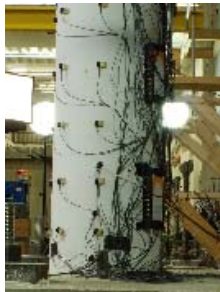
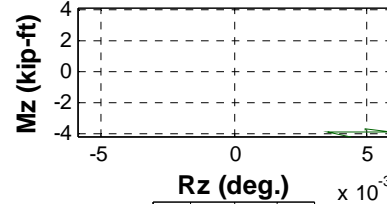
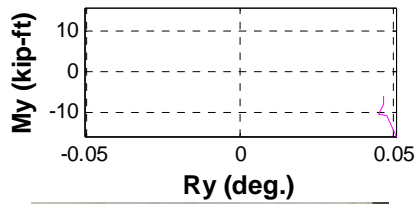
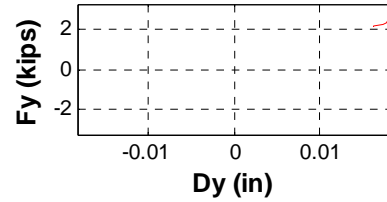
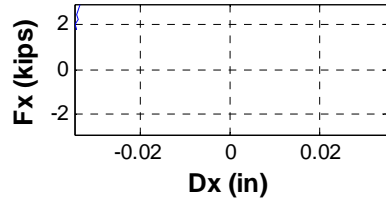
Time 0.05sec

Event: Beginning of Dynamic Loading

Figure C.39 Pier 1 Response at Step 105



	Loads (kip,kip-ft)	Def. (in,deg)
Fx	1.7335 Dx	-0.0343
Fy	2.1735 Dy	0.0164
Fz	35.9351 Dz	0.0044
Mx	10.0815 Rx	-0.0127
My	-5.9859 Ry	0.0466
Mz	-4.1464 Rz	0.0044



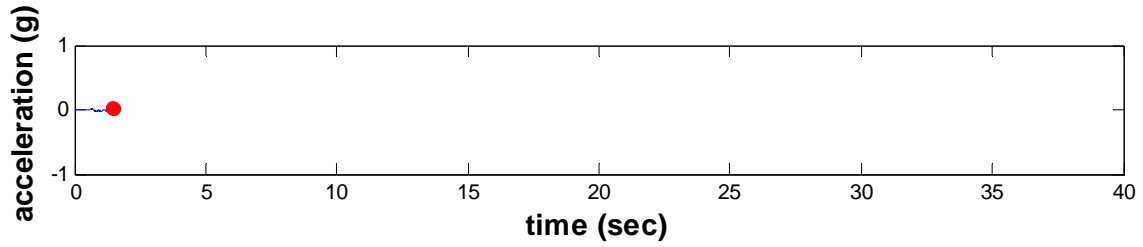
Pier 2

Step 105

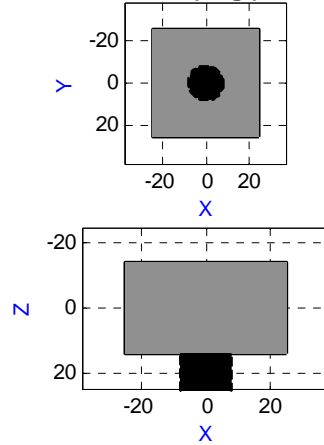
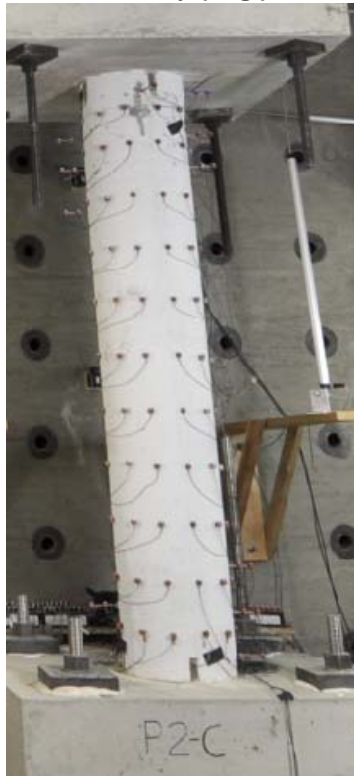
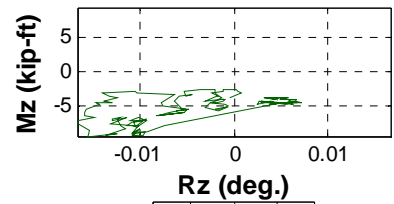
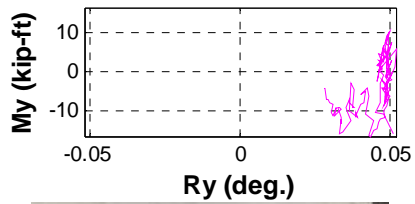
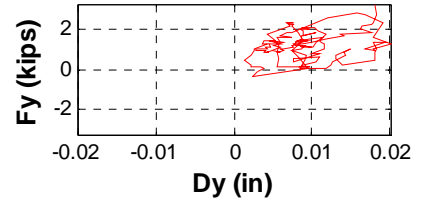
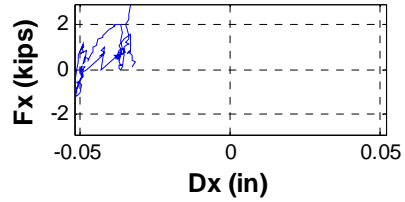
Time 0.05sec

Event: Beginning of Dynamic Loading

Figure C.40 Pier 2 Response at Step 105



	Loads (kip,kip-ft)	Def. (in,deg)
Fx	0.0735 Dx	-0.0329
Fy	0.9822 Dy	0.0049
Fz	53.5644 Dz	0.0052
Mx	6.6485 Rx	-0.0109
My	-4.3570 Ry	0.0283
Mz	-3.7297 Rz	-3.8606e...



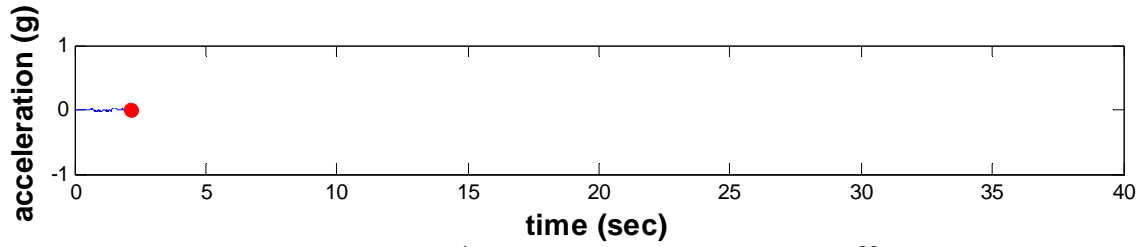
Pier 2

Step 248

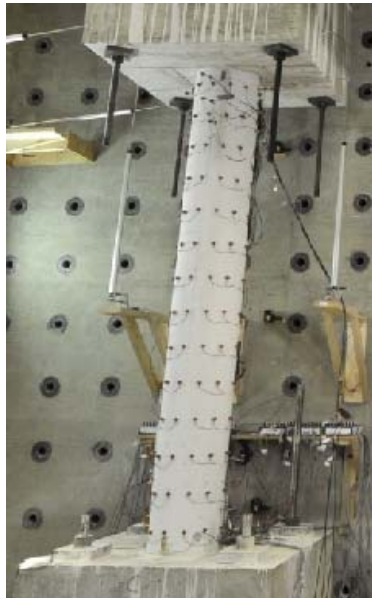
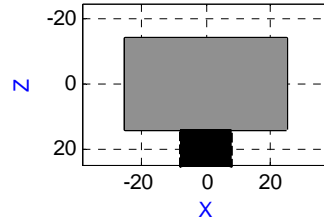
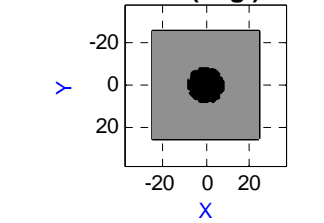
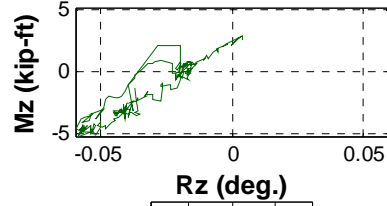
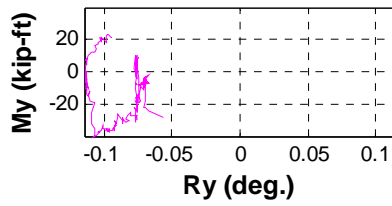
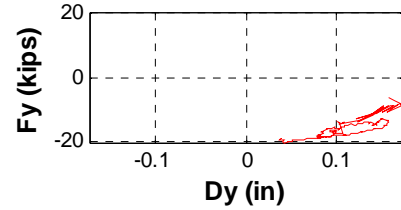
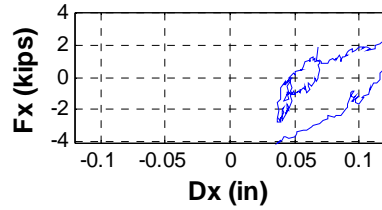
Time 1.48sec

Event: +dx Peak of 0.08(MCE) Record

Figure C.41 Pier 2 Response at Step 248



	Loads (kip,kip-ft)	Def. (in,deg)
Fx	-3.9173 Dx	0.0386
Fy	-18.8117 Dy	0.0399
Fz	125.4642 Dz	0.0035
Mx	-61.8278 Rx	0.4563
My	21.2264 Ry	-0.0945
Mz	2.5715 Rz	0.0038



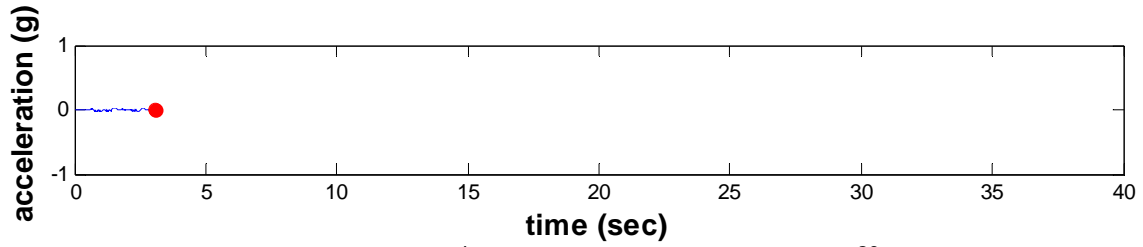
Pier 1

Step 313

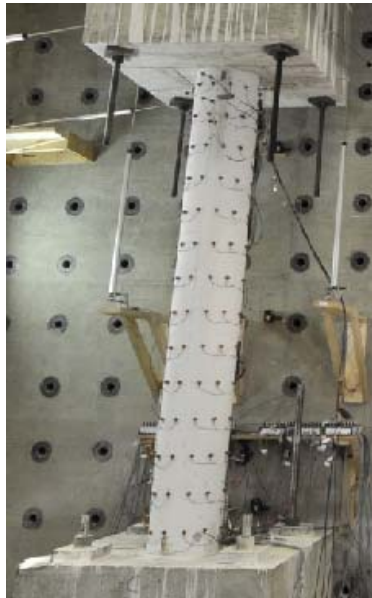
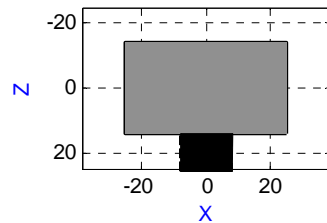
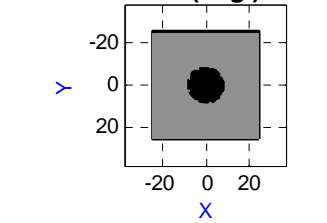
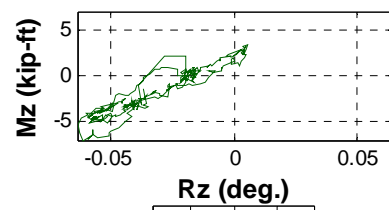
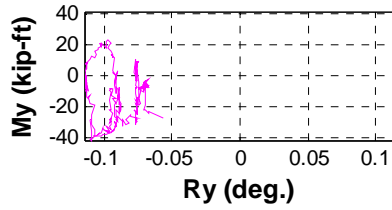
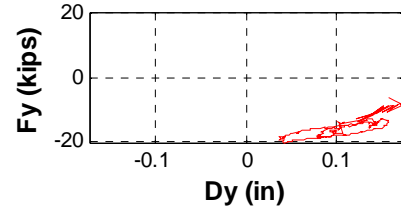
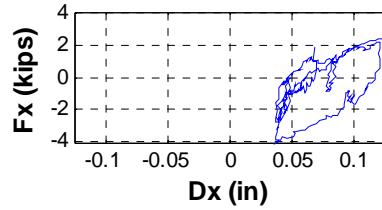
Time 2.13sec

Event: -dy Peak of 0.08(MCE) Record

Figure C.42 Pier 1 Response at Step 313



	Loads (kip,kip-ft)	Def. (in,deg)
Fx	1.3990 Dx	0.1246
Fy	-15.8792 Dy	0.1366
Fz	125.9091 Dz	0.0063
Mx	-49.8945 Rx	0.4695
My	-28.3962 Ry	-0.1105
Mz	-2.5921 Rz	-0.0448



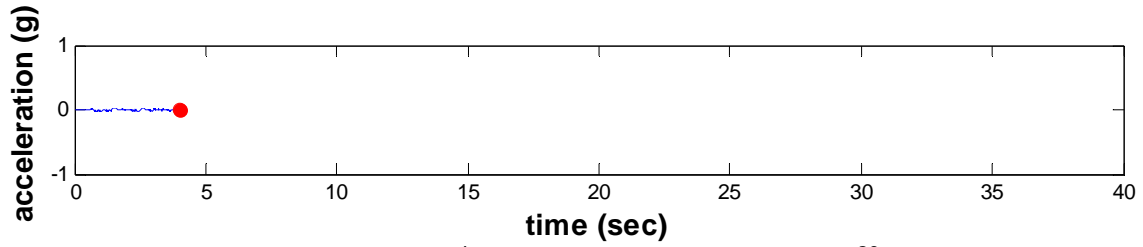
Pier 1

Step 406

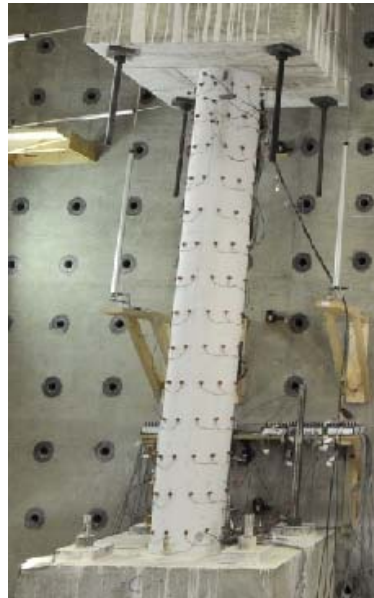
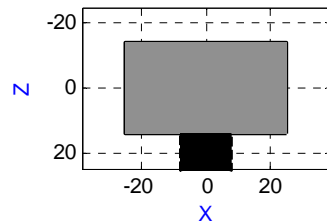
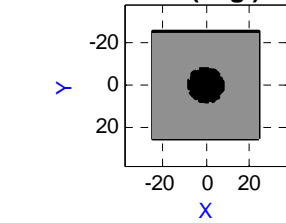
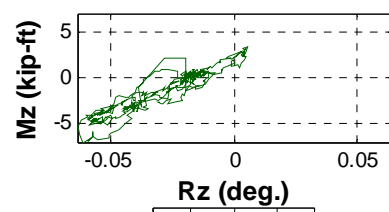
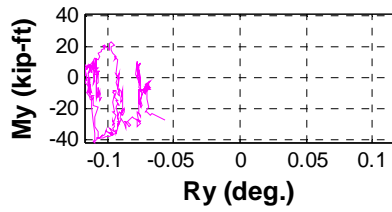
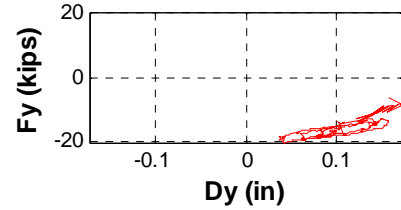
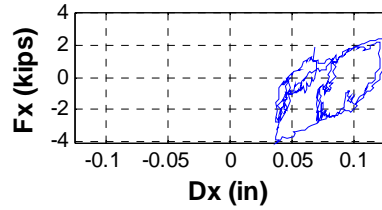
Time 3.06sec

Event: +dx Peak of 0.08(MCE) Record

Figure C.43 Pier 1 Response at Step 406



	Loads (kip,kip-ft)	Def. (in,deg)
Fx	-0.3806 Dx	0.0802
Fy	-15.3400 Dy	0.1034
Fz	127.7764 Dz	0.0064
Mx	-39.5886 Rx	0.4662
My	-12.7417 Ry	-0.1048
Mz	-2.7174 Rz	-0.0302



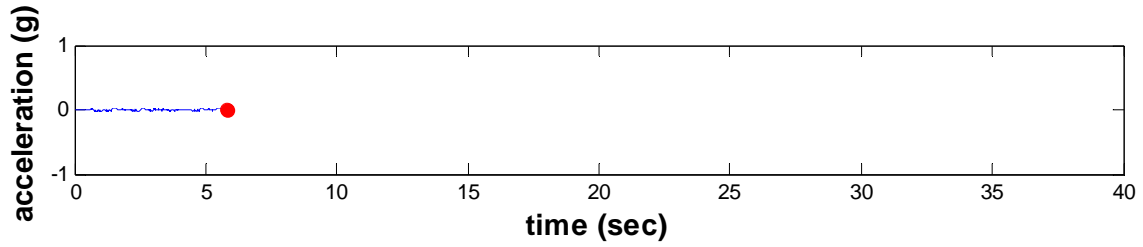
Pier 1

Step 500

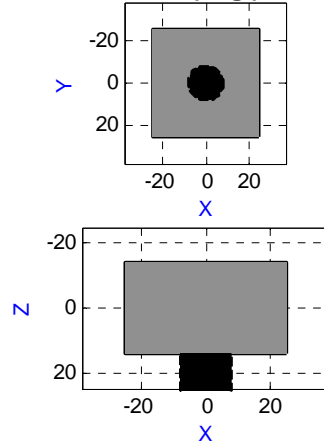
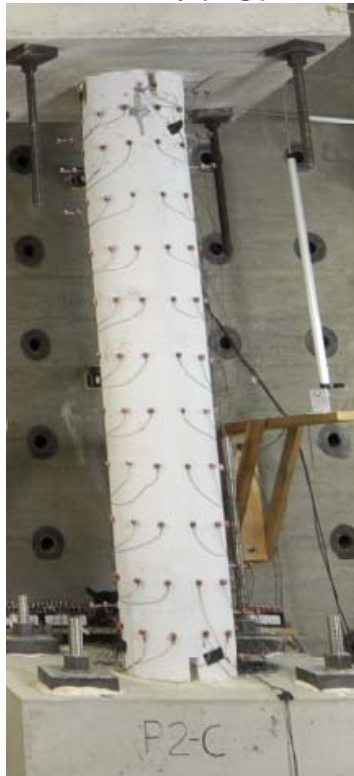
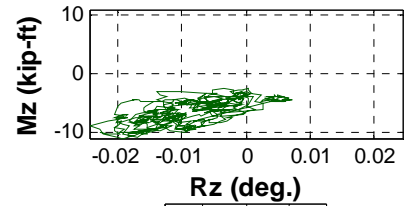
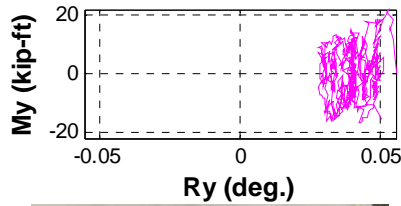
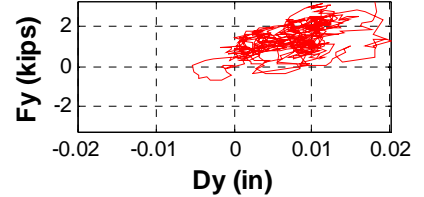
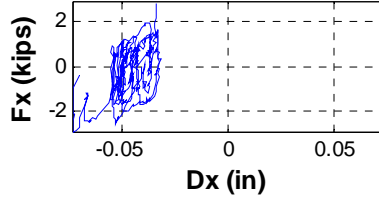
Time 4.00sec

Event: Concrete cracking at face A-B, level 7-8

Figure C.44 Pier 1 Response at Step 500



	Loads (kip,kip-ft)	Def. (in,deg)
Fx	-0.3874 Dx	-0.0701
Fy	1.5759 Dy	0.0031
Fz	59.1586 Dz	0.0082
Mx	7.4575 Rx	-0.0152
My	0.3966 Ry	0.0558
Mz	-10.1338 Rz	-0.0229



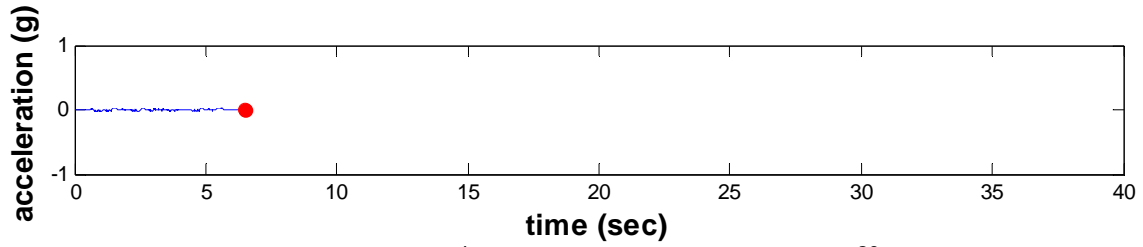
Pier 2

Step 680

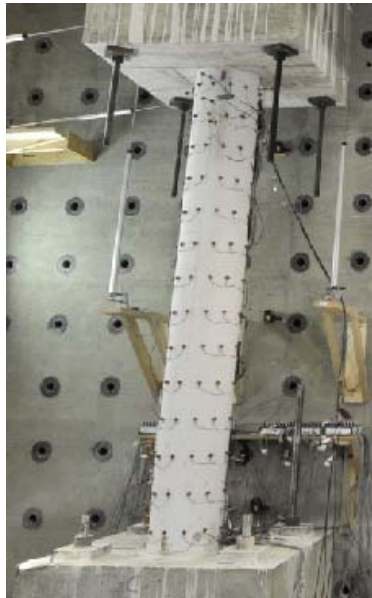
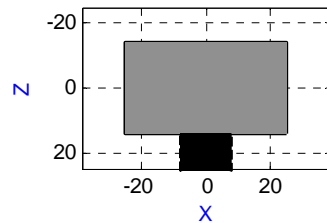
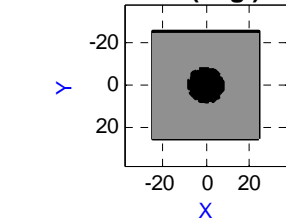
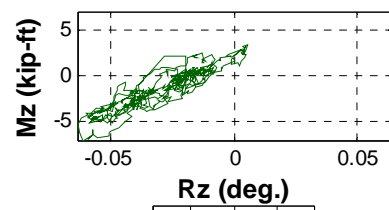
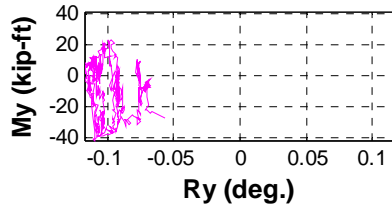
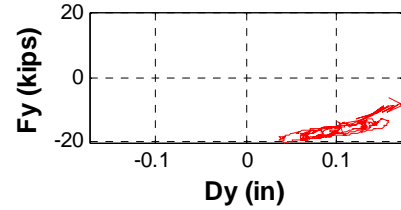
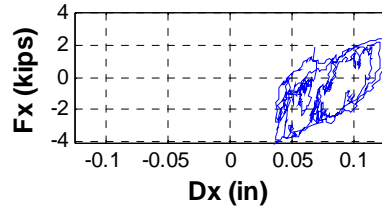
Time 5.80sec

Event: -dx Peak of 0.08(MCE) Record

Figure C.45 Pier 2 Response at Step 680



	Loads (kip,kip-ft)	Def. (in,deg)
Fx	-1.4460 Dx	0.0578
Fy	-16.9180 Dy	0.0968
Fz	123.2295 Dz	0.0080
Mx	-48.7459 Rx	0.4733
My	-5.9251 Ry	-0.0915
Mz	-1.2342 Rz	-0.0349



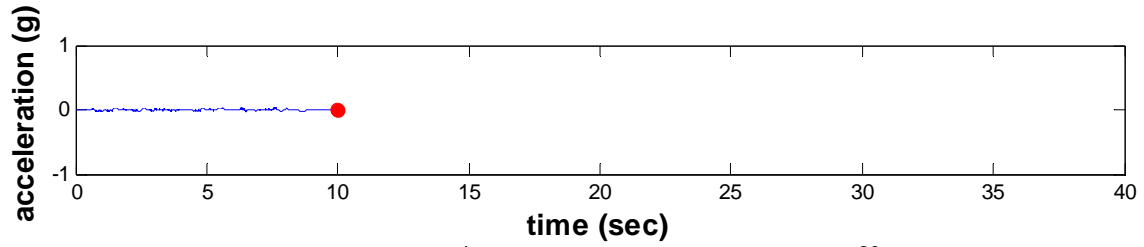
Pier 1

Step 750

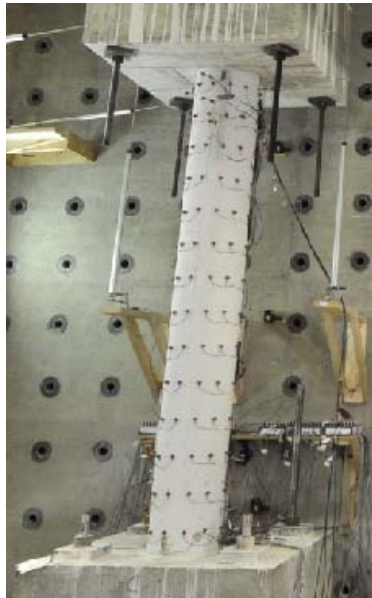
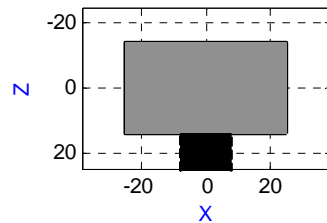
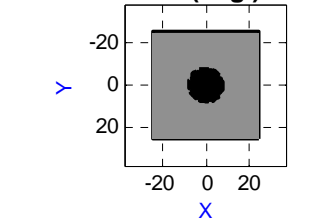
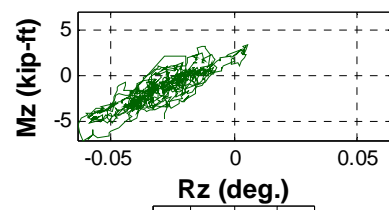
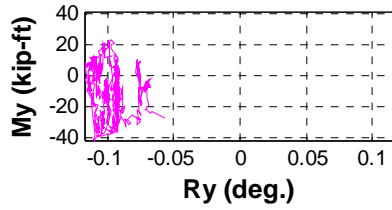
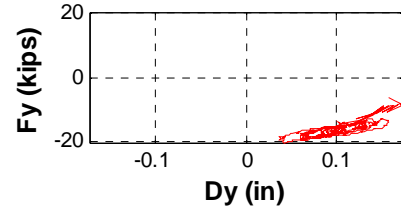
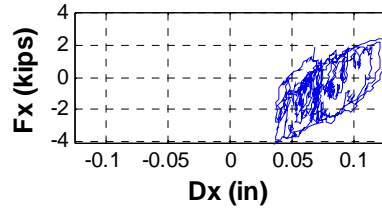
Time 6.50sec

Event: Cracks extended at face A-B, level 7-8

Figure C.46 Pier 1 Response at Step 750



	Loads (kip,kip-ft)	Def. (in,deg)
Fx	-0.4413 Dx	0.0820
Fy	-16.0184 Dy	0.1021
Fz	125.0742 Dz	0.0097
Mx	-49.0709 Rx	0.4690
My	-12.8067 Ry	-0.1017
Mz	-4.7286 Rz	-0.0286



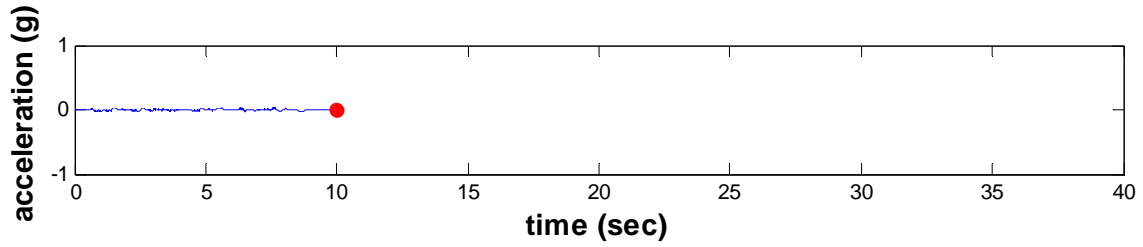
Pier 1

Step 1100

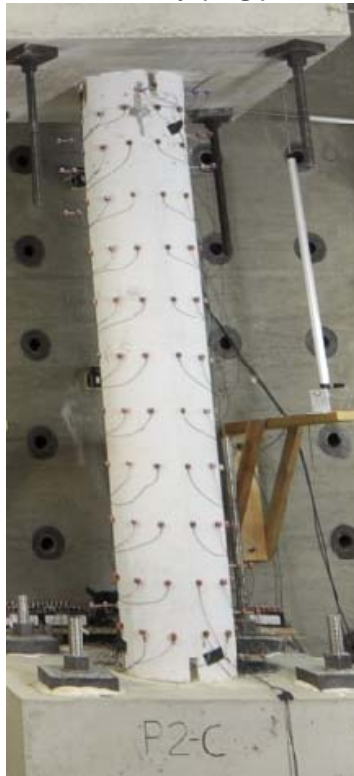
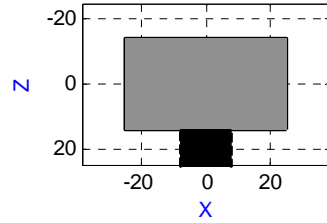
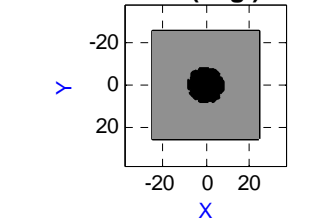
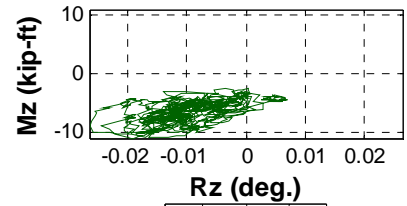
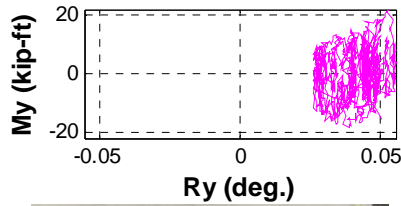
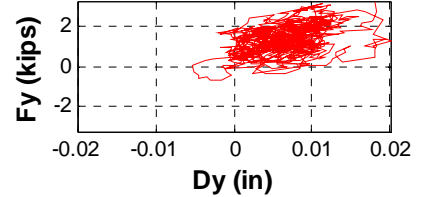
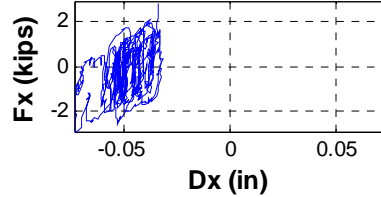
Time 10.00sec

Event: End of 0.08(MCE) Record

Figure C.47 Pier 1 Response at Step 1100



	Loads (kip,kip-ft)	Def. (in,deg)
Fx	-0.9523 Dx	-0.0440
Fy	0.8063 Dy	0.0018
Fz	55.1942 Dz	0.0101
Mx	1.0541 Rx	-0.0086
My	3.2180 Ry	0.0292
Mz	-8.2464 Rz	-0.0064



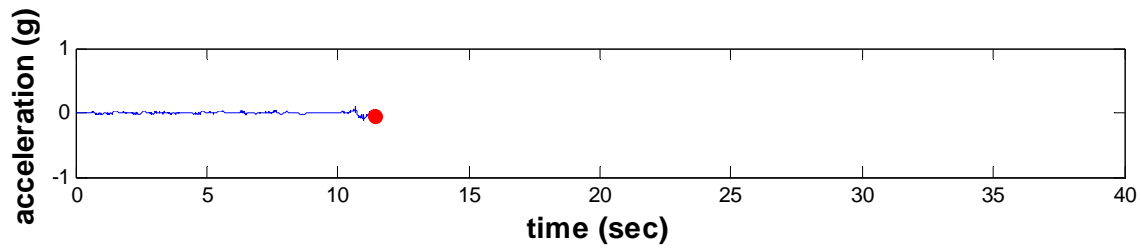
Pier 2

Step 1100

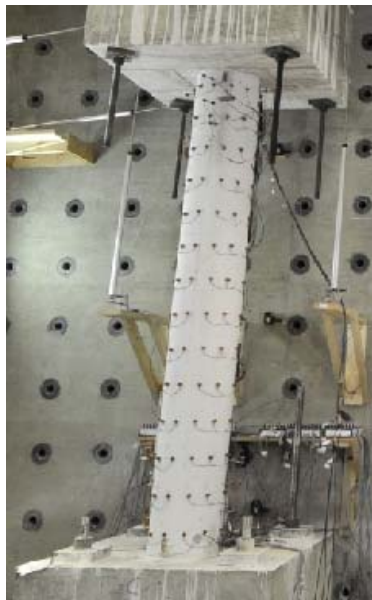
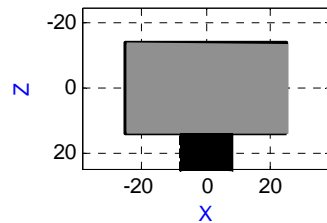
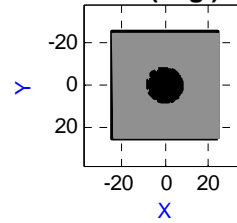
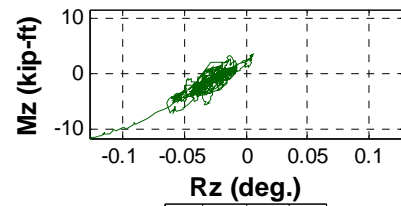
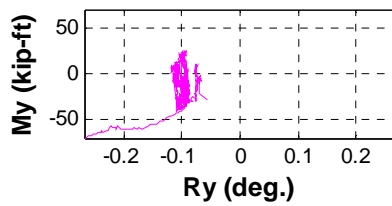
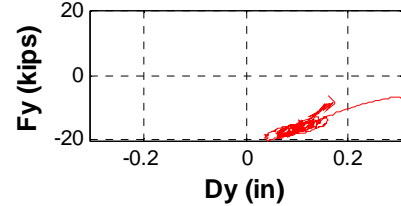
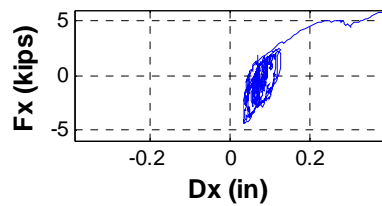
Time 10.00sec

Event: End of 0.08(MCE) Record

Figure C.48 Pier 2 Response at Step 1100



	Loads (kip,kip-ft)	Def. (in,deg)
Fx	5.9714 Dx	0.3888
Fy	-7.0703 Dy	0.3059
Fz	127.1317 Dz	0.0080
Mx	2.0842 Rx	0.4665
My	-71.2714 Ry	-0.2689
Mz	-11.7190 Rz	-0.1263



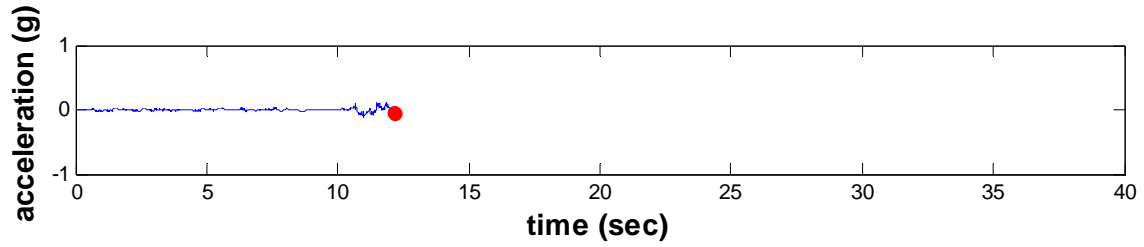
Pier 1

Step 1243

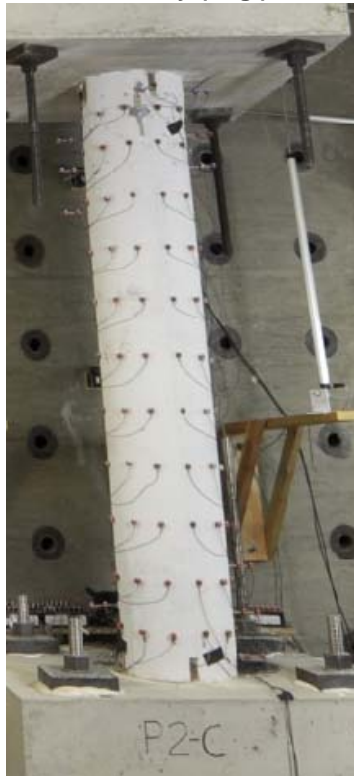
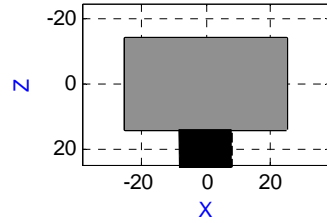
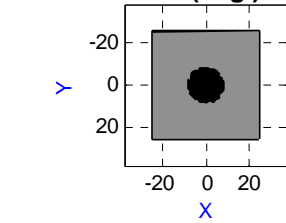
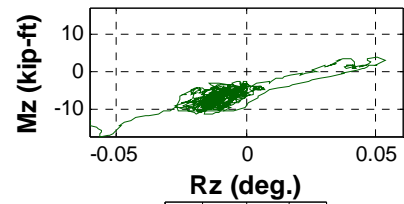
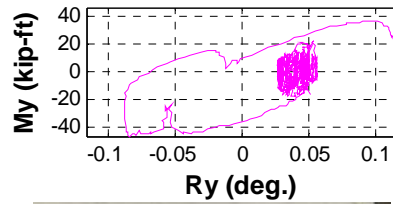
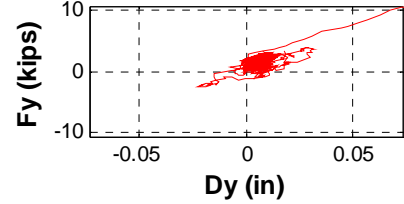
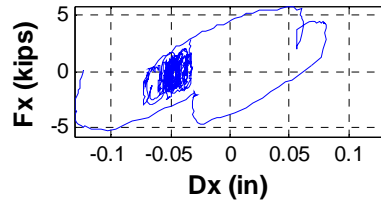
Time 11.43sec

Event: Concrete cracking at face B, level 2-4

Figure C.49 Pier 1 Response at Step 1243



	Loads (kip,kip-ft)	Def. (in,deg)
Fx	0.0850 Dx	-0.1236
Fy	10.7874 Dy	0.0730
Fz	58.8116 Dz	0.0085
Mx	46.2222 Rx	-0.0124
My	10.1825 Ry	0.1152
Mz	-12.8406 Rz	-0.0605



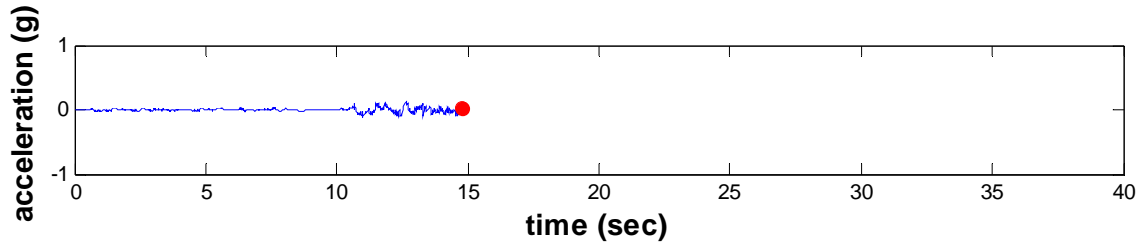
Pier 2

Step 1319

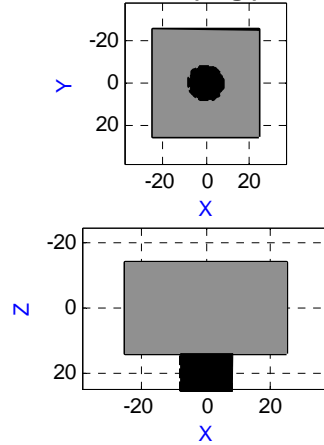
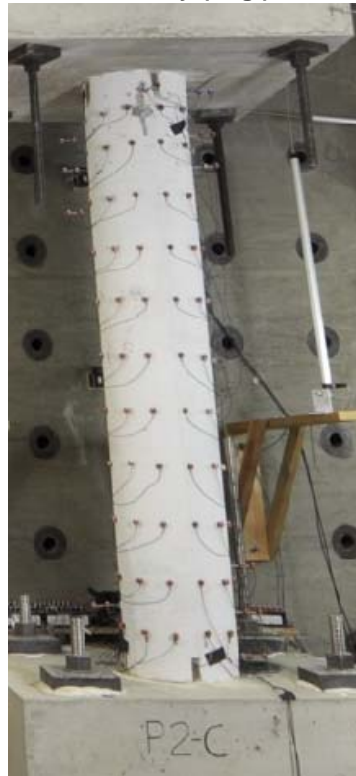
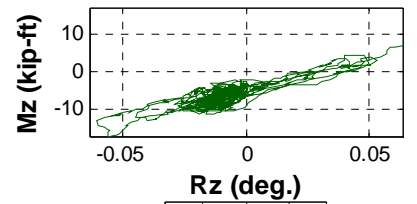
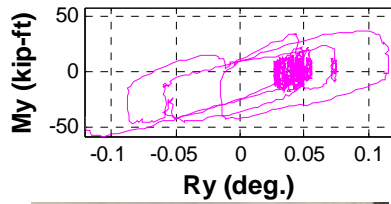
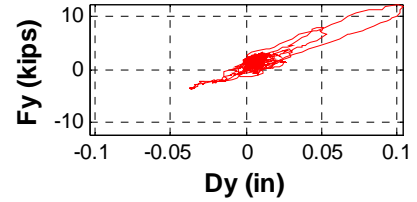
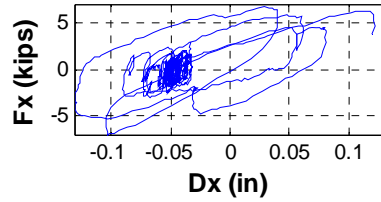
Time 12.19sec

Event: Torsional cracking

Figure C.50 Pier 2 Response at Step 1319



	Loads (kip,kip-ft)	Def. (in,deg)
Fx	3.7952 Dx	0.1199
Fy	1.4777 Dy	0.0260
Fz	55.1601 Dz	0.0071
Mx	11.0734 Rx	0.0252
My	-41.5151 Ry	-0.1213
Mz	6.9795 Rz	0.0638



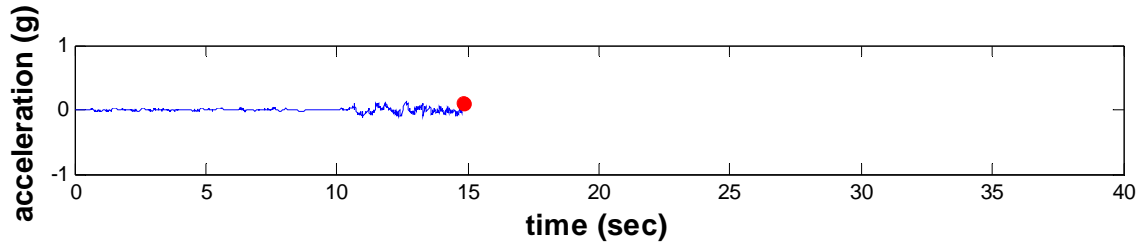
Pier 2

Step 1579

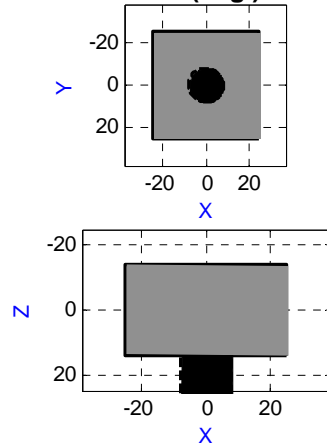
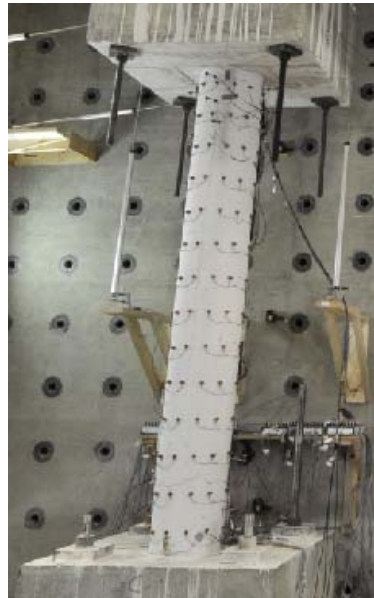
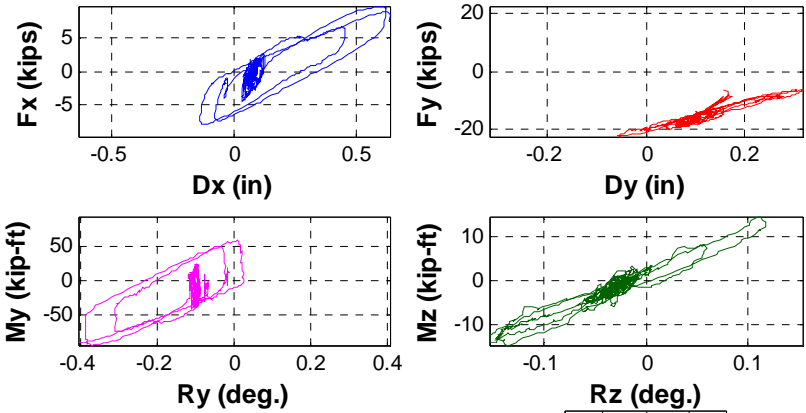
Time 14.79sec

Event: -Mz Peak of 0.3(MCE) Record

Figure C.51 Pier 2 Response at Step 1579



	Loads (kip,kip-ft)	Def. (in,deg)
Fx	7.2366 Dx	0.6307
Fy	-6.5508 Dy	0.3061
Fz	126.2444 Dz	0.0094
Mx	-4.6156 Rx	0.4574
My	-73.8047 Ry	-0.4045
Mz	-10.0397 Rz	-0.1351



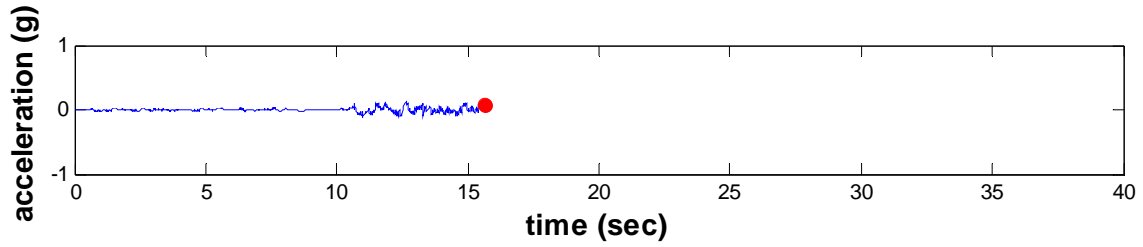
Pier 1

Step 1582

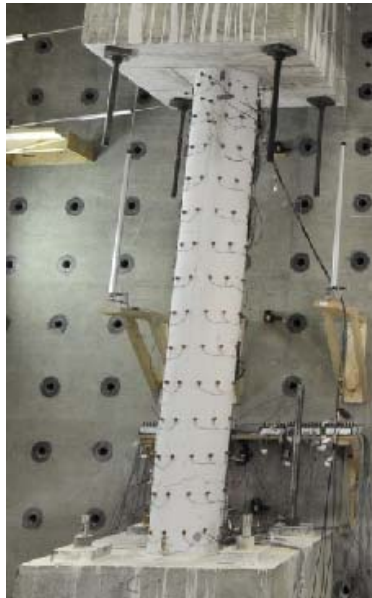
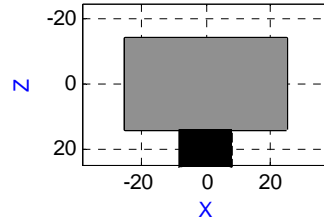
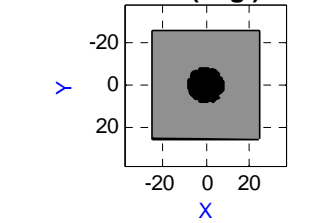
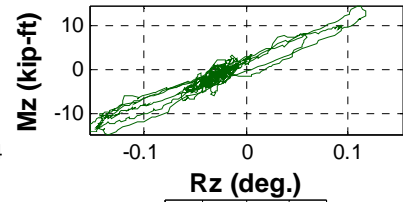
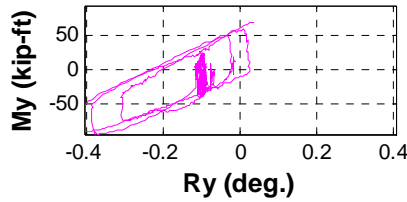
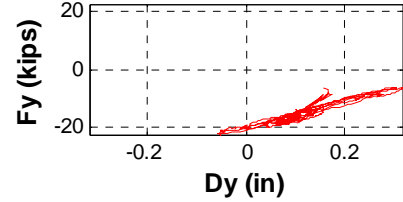
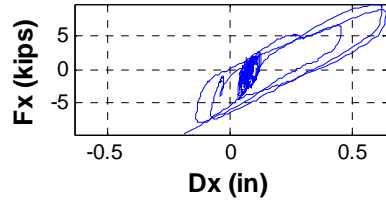
Time 14.82sec

Event: +dx Peak of 0.3(MCE) Record

Figure C.52 Pier 1 Response at Step 1582



	Loads (kip,kip-ft)	Def. (in,deg)
Fx	-9.5323 Dx	-0.1849
Fy	-21.6048 Dy	-0.0424
Fz	130.4766 Dz	-0.0035
Mx	-73.8398 Rx	0.4637
My	71.1773 Ry	0.0341
Mz	9.2955 Rz	0.0908



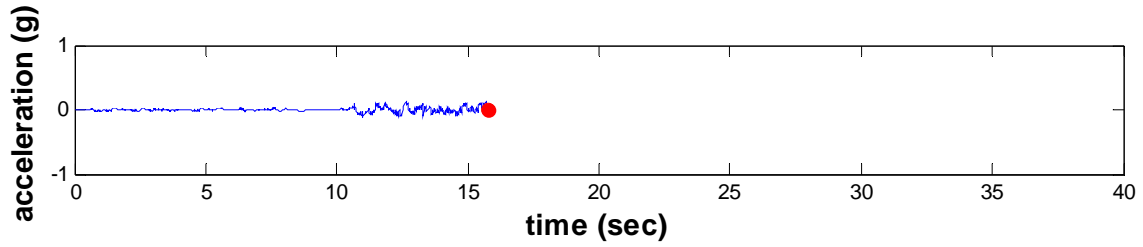
Pier 1

Step 1662

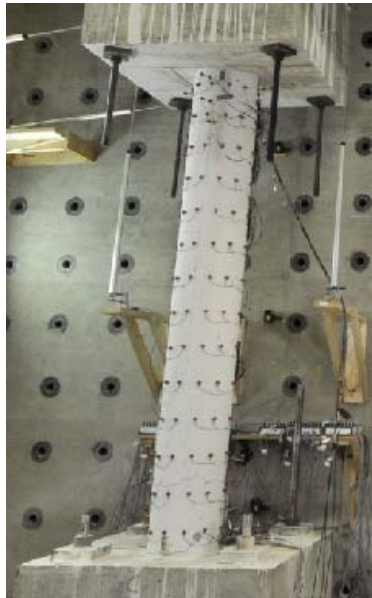
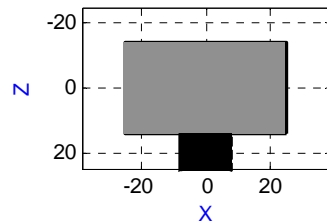
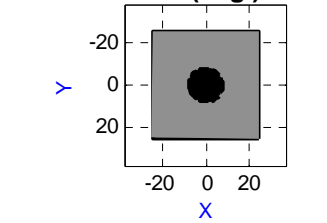
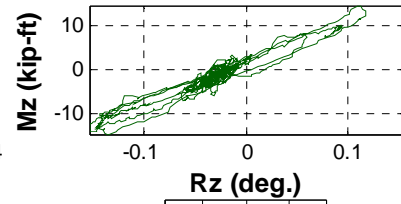
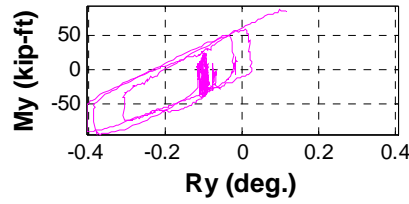
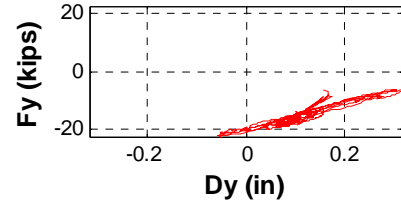
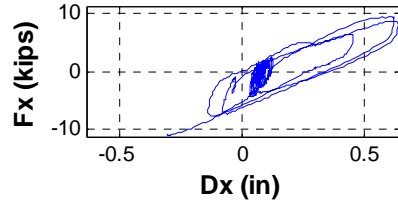
Time 15.62sec

Event: Yield of Longitudinal Reinforcement at face C, level 9

Figure C.53 Pier 1 Response at Step 1662



	Loads (kip,kip-ft)	Def. (in,deg)
Fx	-11.0177 Dx	-0.3037
Fy	-20.4810 Dy	-0.0168
Fz	121.6749 Dz	-0.0087
Mx	-68.1546 Rx	0.4846
My	87.7202 Ry	0.1160
Mz	7.5863 Rz	0.0773



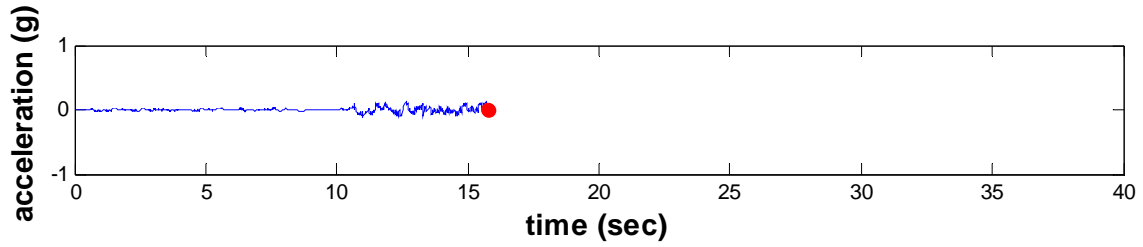
Pier 1

Step 1677

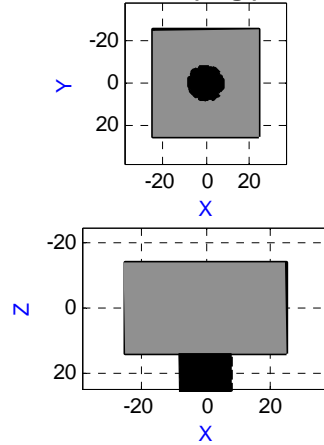
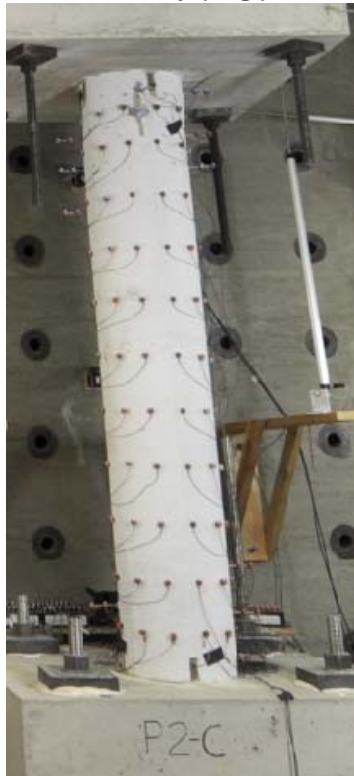
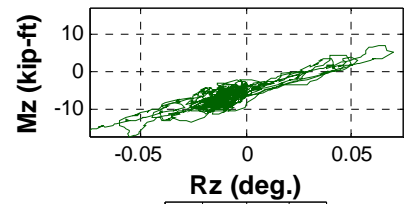
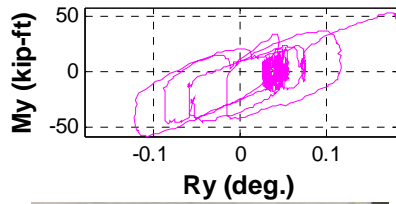
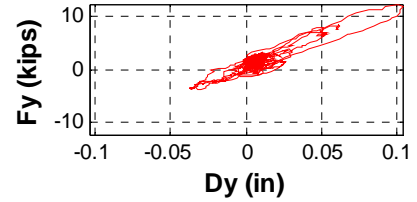
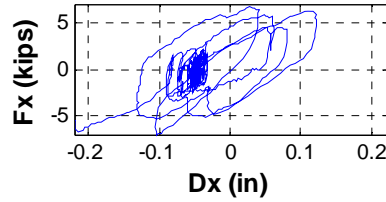
Time 15.77sec

Event: -dx Peak of 0.3(MCE) Record

Figure C.54 Pier 1 Response at Step 1677



	Loads (kip,kip-ft)	Def. (in,deg)
Fx	-5.4328 Dx	-0.2185
Fy	8.3782 Dy	0.0607
Fz	61.3422 Dz	0.0074
Mx	31.7635 Rx	-0.0236
My	45.2933 Ry	0.1796
Mz	-15.5408 Rz	-0.0750



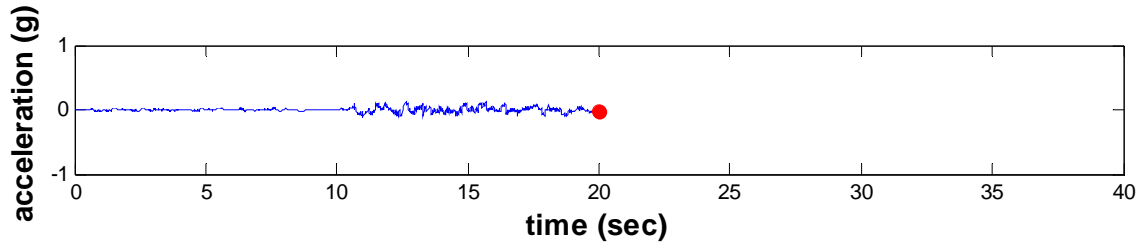
Pier 2

Step 1678

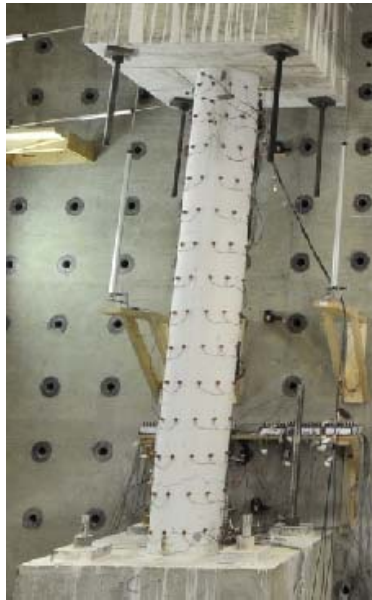
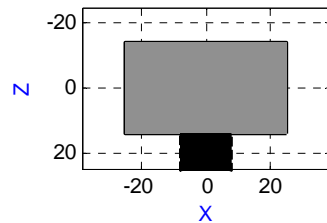
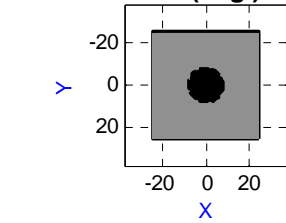
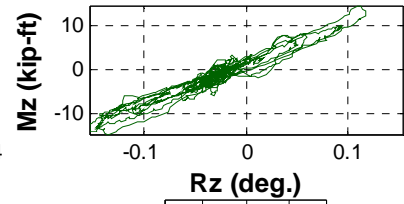
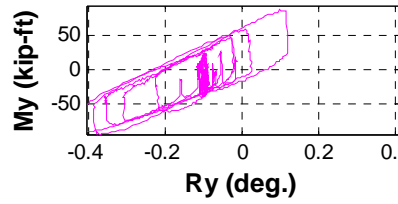
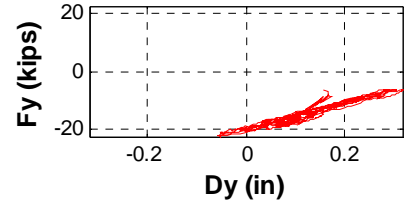
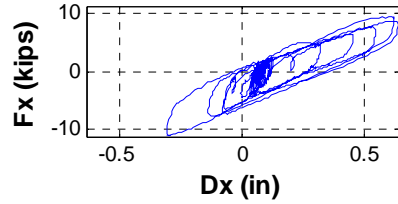
Time 15.78sec

Event: -dx Peak of 0.3(MCE) Record

Figure C.55 Pier 2 Response at Step 1678



	Loads (kip,kip-ft)		Def. (in,deg)	
Fx	-3.8734	Dx	0.0821	
Fy	-16.6169	Dy	0.0545	
Fz	126.5334	Dz	0.0048	
Mx	-54.2497	Rx	0.4566	
My	21.0937	Ry	-0.1284	
Mz	1.2341	Rz	0.0069	



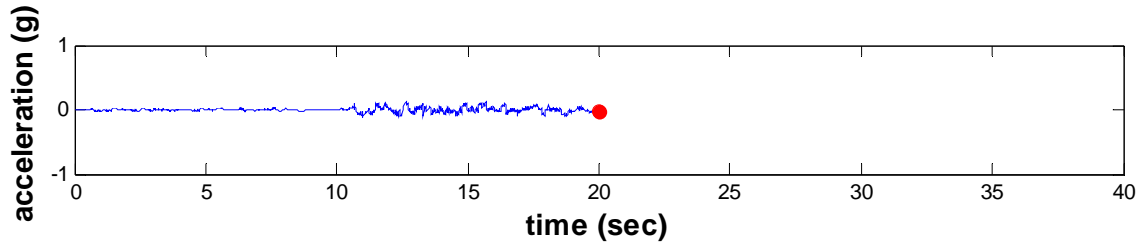
Pier 1

Step 2100

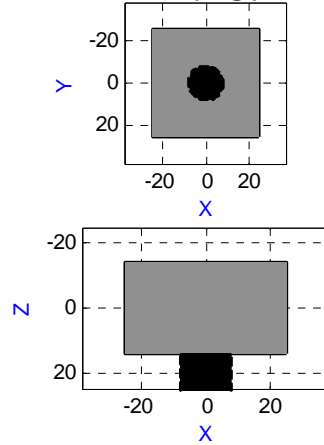
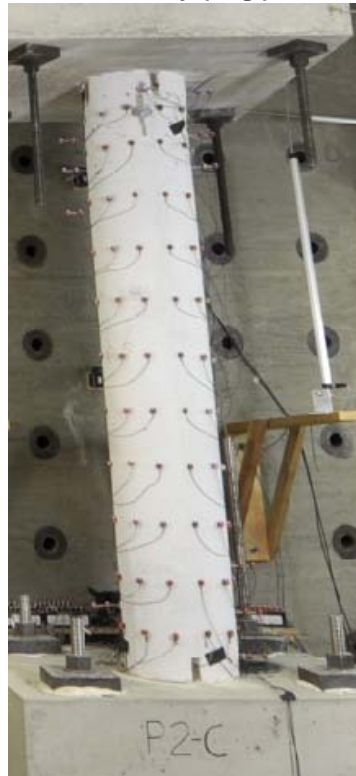
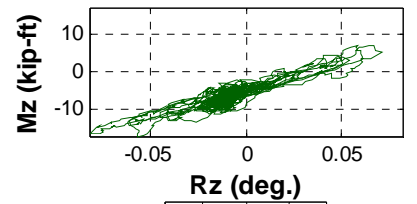
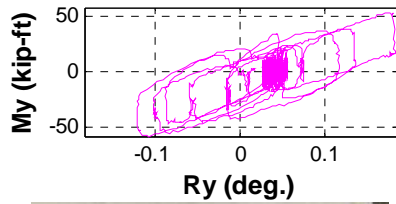
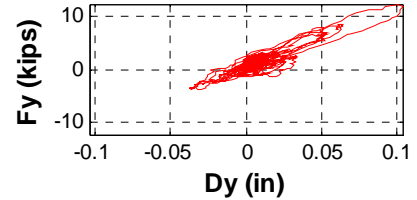
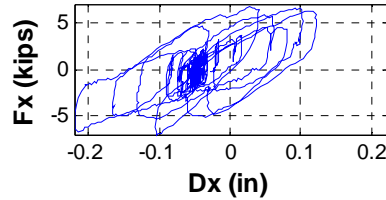
Time 20.00sec

Event: End of 0.3(MCE) Record

Figure C.56 Pier 1 Response at Step 2100



	Loads (kip,kip-ft)	Def. (in,deg)
Fx	-0.2654 Dx	-0.0281
Fy	2.5441 Dy	0.0153
Fz	58.3991 Dz	0.0117
Mx	9.1745 Rx	-0.0046
My	1.4529 Ry	0.0139
Mz	-6.1384 Rz	-0.0065



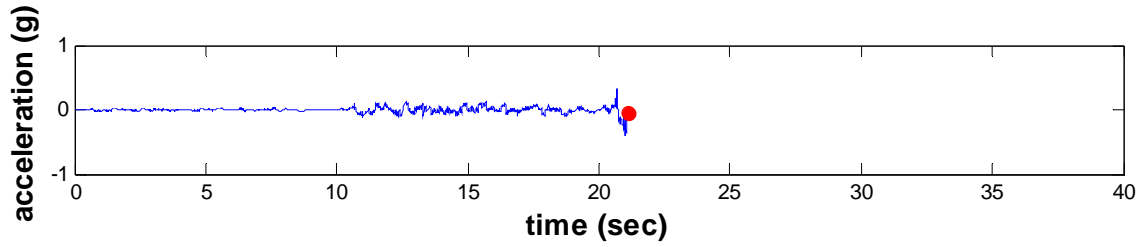
Pier 2

Step 2100

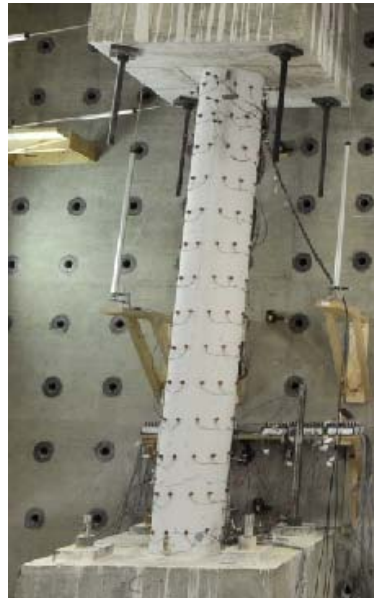
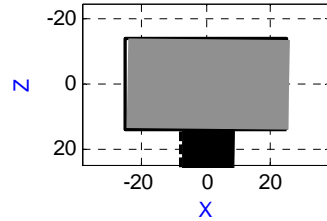
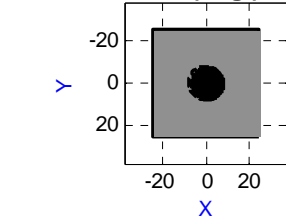
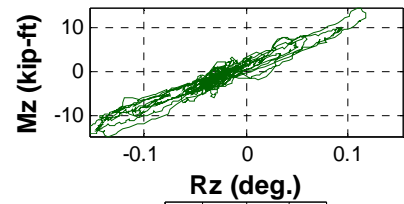
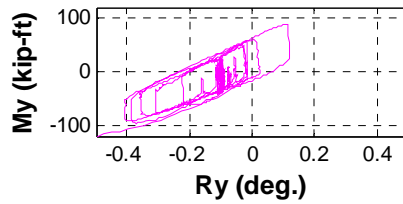
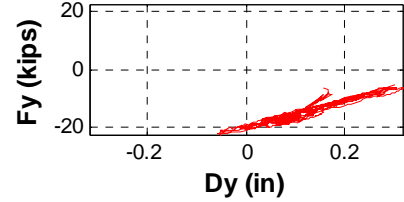
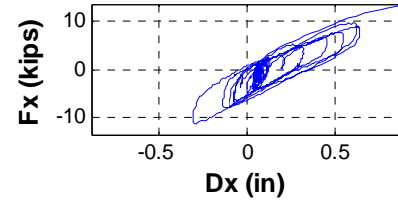
Time 20.00sec

Event: End of 0.3(MCE) Record

Figure C.57 Pier 2 Response at Step 2100



	Loads (kip,kip-ft)		Def. (in,deg)	
Fx	13.4814	Dx	0.8764	
Fy	-5.6077	Dy	0.3050	
Fz	121.8212	Dz	0.0026	
Mx	2.0177	Rx	0.4381	
My	-119.2181	Ry	-0.4980	
Mz	-5.7062	Rz	-0.0702	



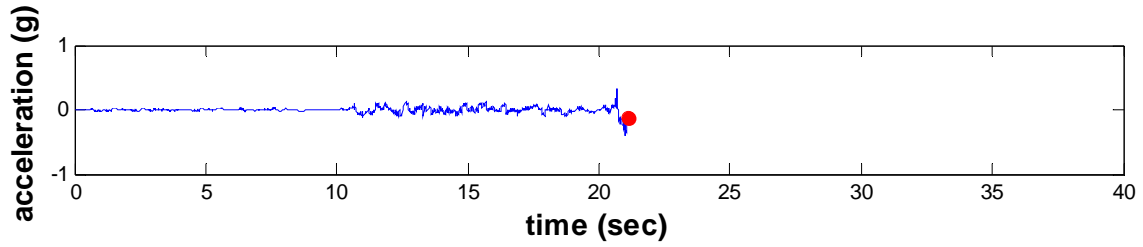
Pier 1

Step 2211

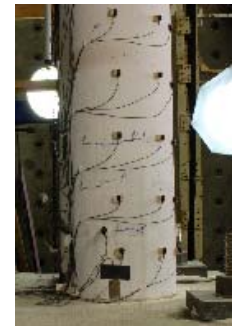
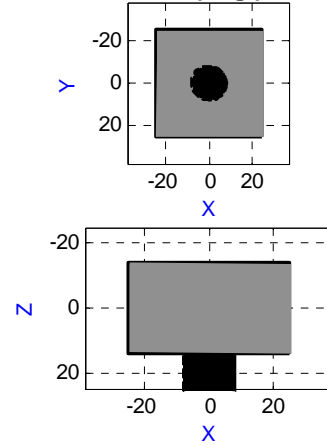
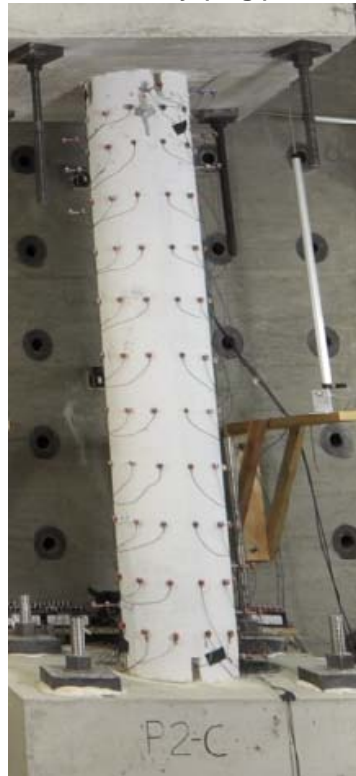
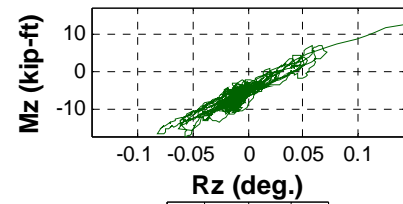
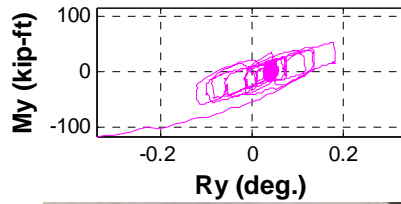
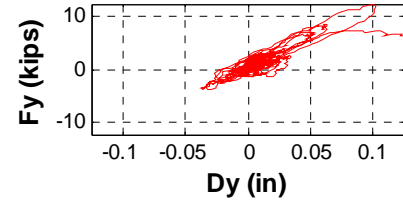
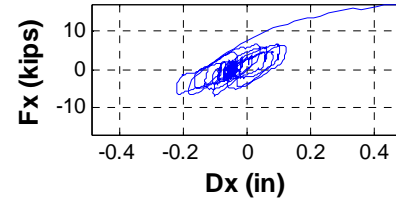
Time 21.11sec

Event: Yield of Longitudinal Reinforcement at face B, level 2

Figure C.58 Pier 1 Response at Step 2211



	Loads (kip,kip-ft)	Def. (in,deg)
Fx	16.8534 Dx	0.4879
Fy	6.0325 Dy	0.1257
Fz	57.9313 Dz	-0.0026
Mx	28.2679 Rx	0.0928
My	-114.6229 Ry	-0.3407
Mz	12.5408 Rz	0.1412



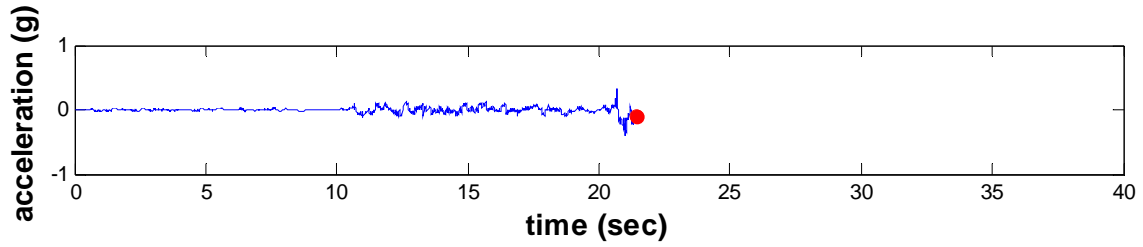
Pier 2

Step 2212

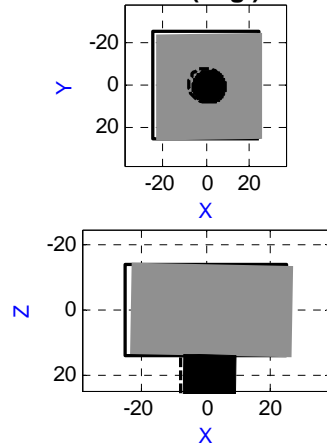
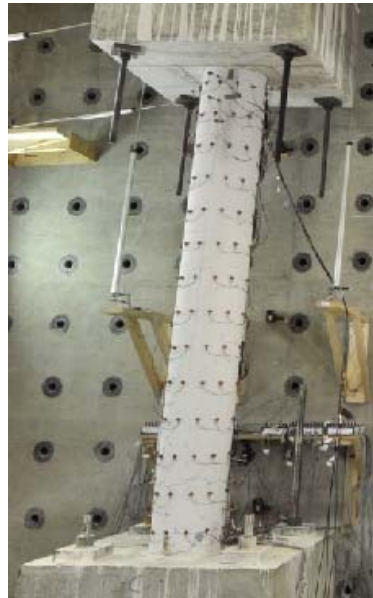
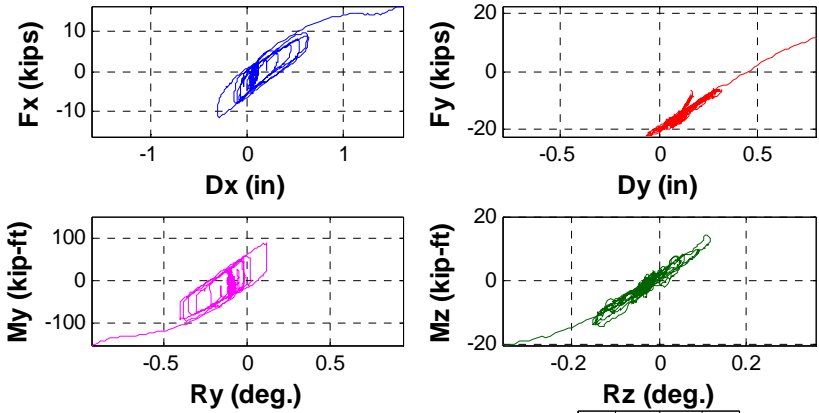
Time 21.12sec

Event: Concrete cracking and cracks extended at face A-B-C, level 12-15

Figure C.59 Pier 2 Response at Step 2212



	Loads (kip,kip-ft)	Def. (in,deg)
Fx	16.1499 Dx	1.6067
Fy	11.7379 Dy	0.7962
Fz	130.9592 Dz	0.0039
Mx	77.4764 Rx	0.4404
My	-153.6891 Ry	-0.9449
Mz	-20.1715 Rz	-0.3615



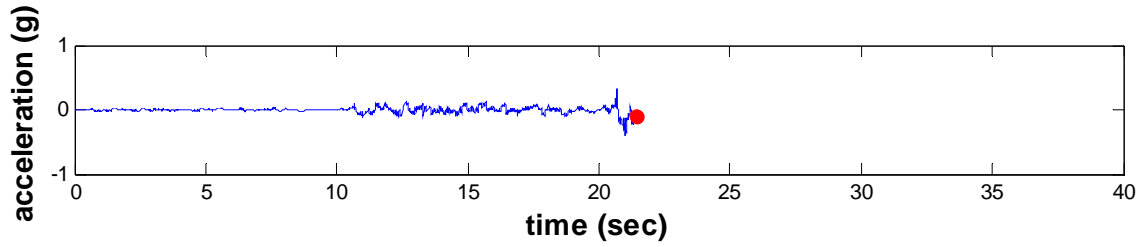
Pier 1

Step 2240

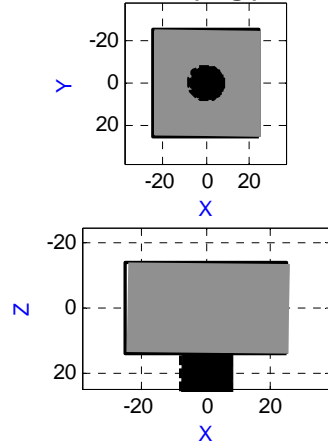
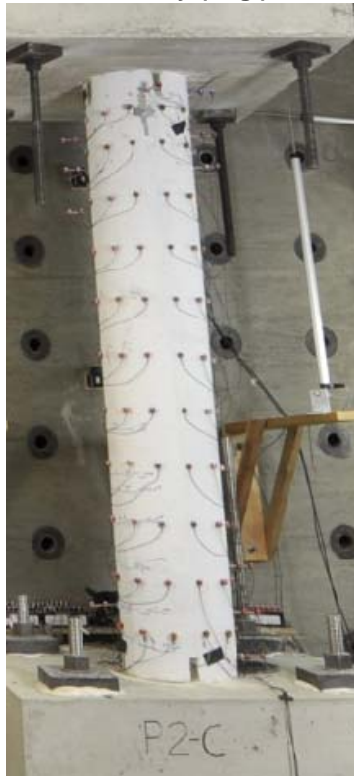
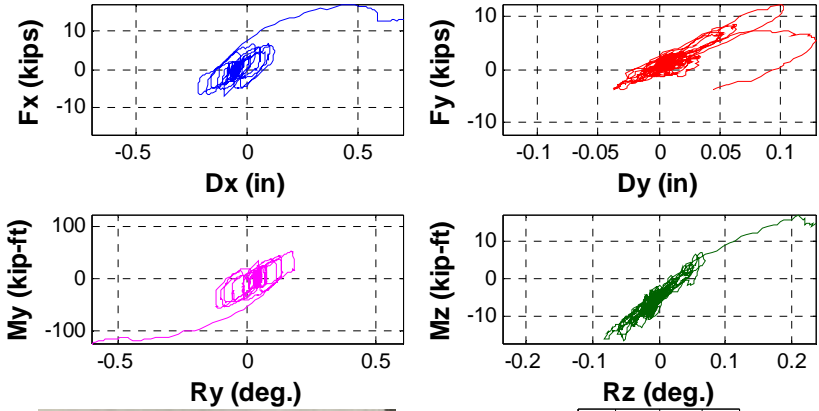
Time 21.40sec

Event: Inclined cracking at face B-C, level 2-3

Figure C.60 Pier 1 Response at Step 2240



	Loads (kip,kip-ft)	Def. (in,deg)
Fx	13.1649 Dx	0.7032
Fy	-3.8920 Dy	0.0447
Fz	60.4299 Dz	-0.0124
Mx	-4.6339 Rx	0.1256
My	-124.2723 Ry	-0.6038
Mz	14.9735 Rz	0.2369



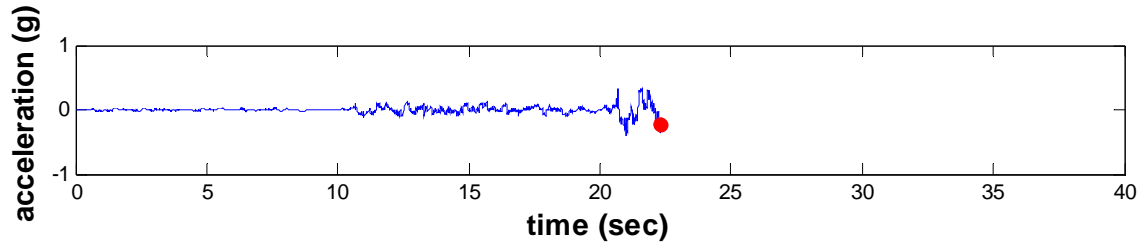
Pier 2

Step 2240

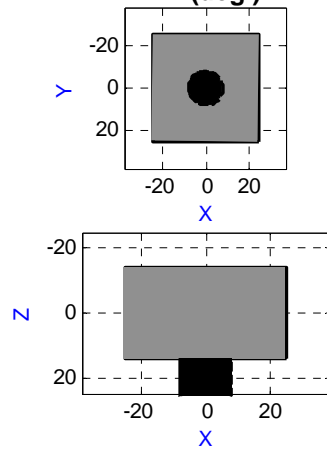
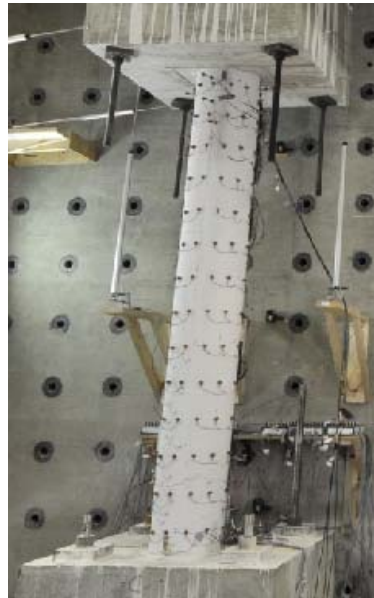
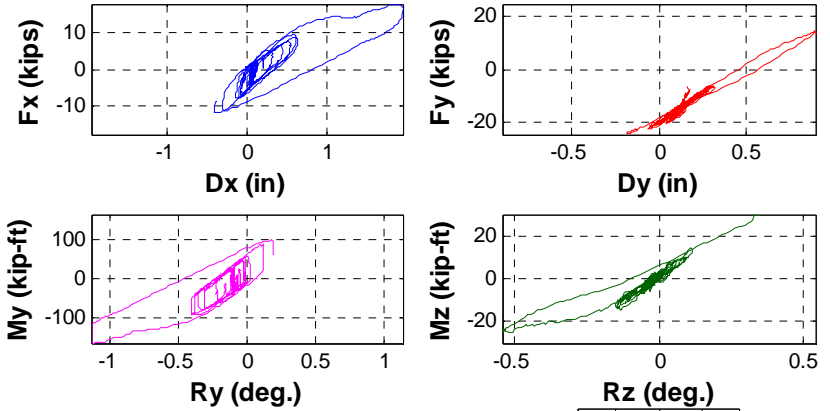
Time 21.40sec

Event: Flexural cracking at face B

Figure C.61 Pier 2 Response at Step 2240



	Loads (kip,kip-ft)	Def. (in,deg)
Fx	-8.4736 Dx	-0.3921
Fy	-22.1466 Dy	-0.1260
Fz	119.0786 Dz	-0.0231
Mx	-77.5986 Rx	0.4808
My	65.2172 Ry	0.1936
Mz	29.8328 Rz	0.3477



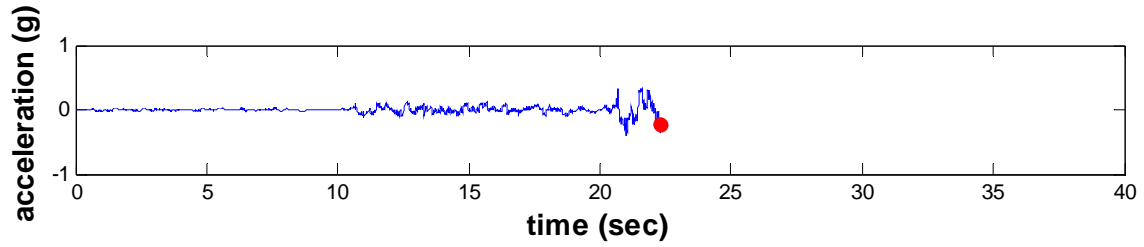
Pier 1

Step 2330

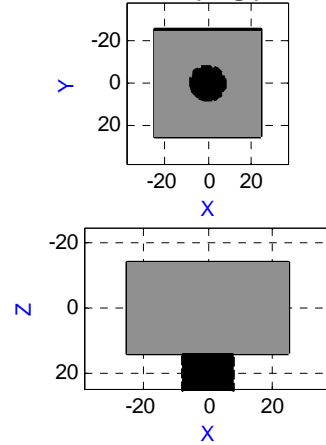
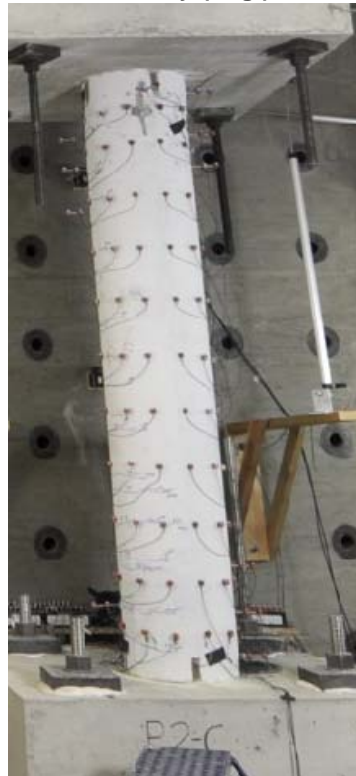
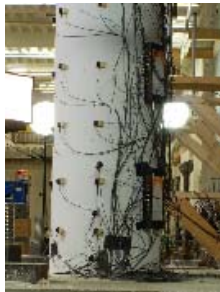
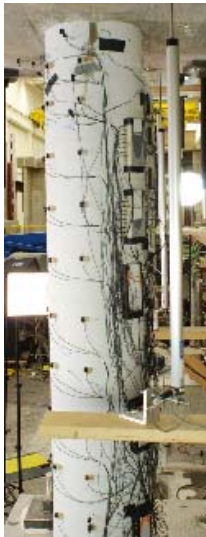
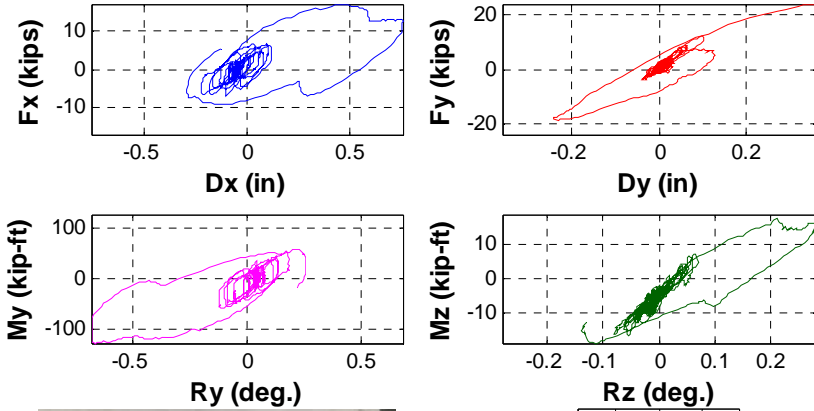
Time 22.30sec

Event: Flexural cracking at face C-D, level 4

Figure C.62 Pier 1 Response at Step 2330



	Loads (kip,kip-ft)	Def. (in,deg)
Fx	5.5260 Dx	-0.1300
Fy	24.0676 Dy	0.3575
Fz	66.3701 Dz	-0.0148
Mx	96.4951 Rx	0.0039
My	-15.5606 Ry	0.2174
Mz	-12.7519 Rz	-0.1298



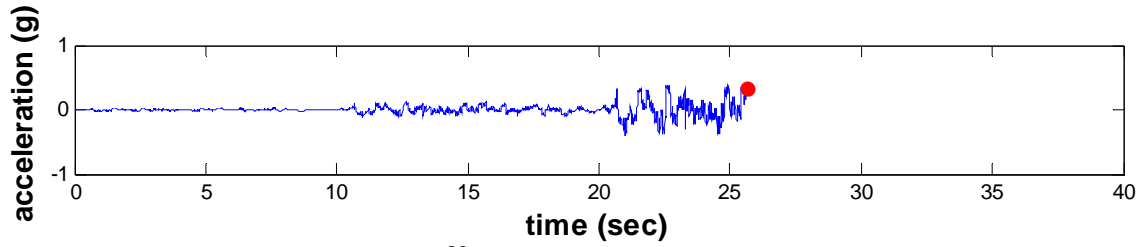
Pier 2

Step 2330

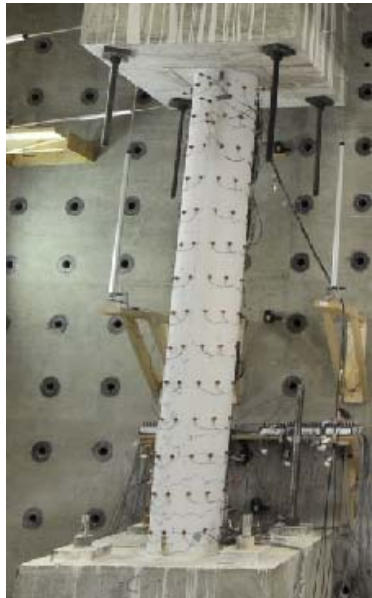
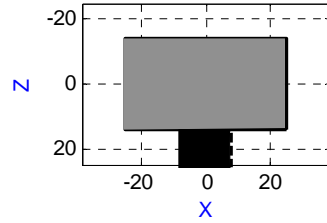
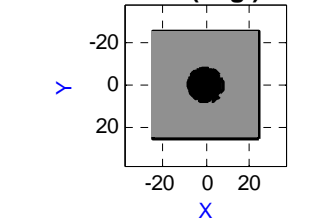
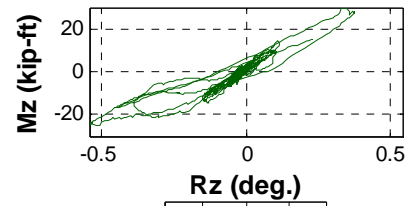
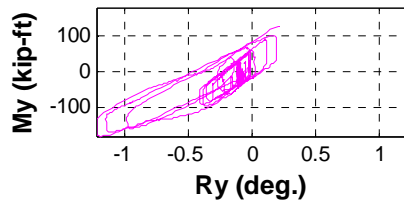
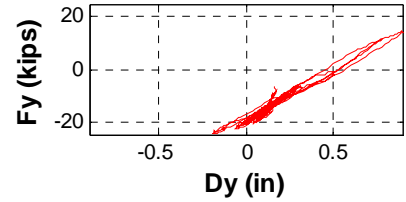
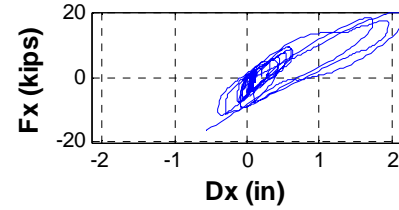
Time 22.30sec

Event: Flexural cracking at face D, level 14

Figure C.63 Pier 2 Response at Step 2330



	Loads (kip,kip-ft)	Def. (in,deg)
Fx	-16.4635 Dx	-0.5574
Fy	-24.2517 Dy	-0.1947
Fz	135.3343 Dz	-0.0294
Mx	-88.6658 Rx	0.4623
My	127.9265 Ry	0.2181
Mz	14.8923 Rz	0.2328



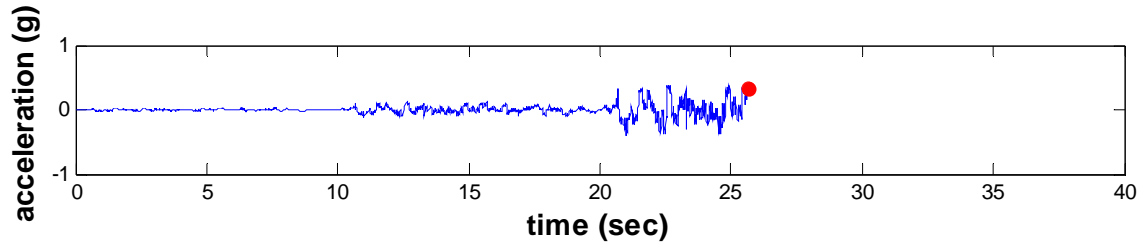
Pier 1

Step 2663

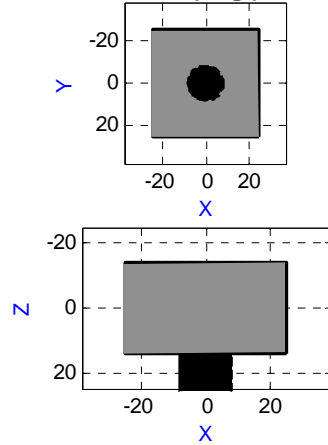
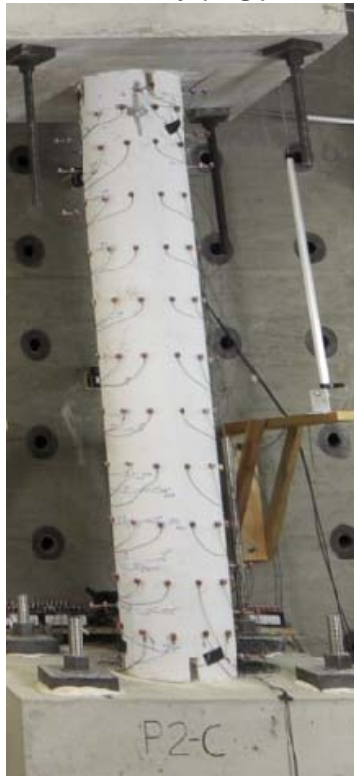
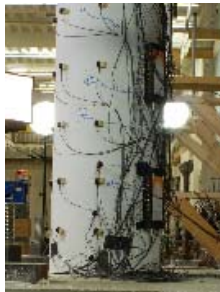
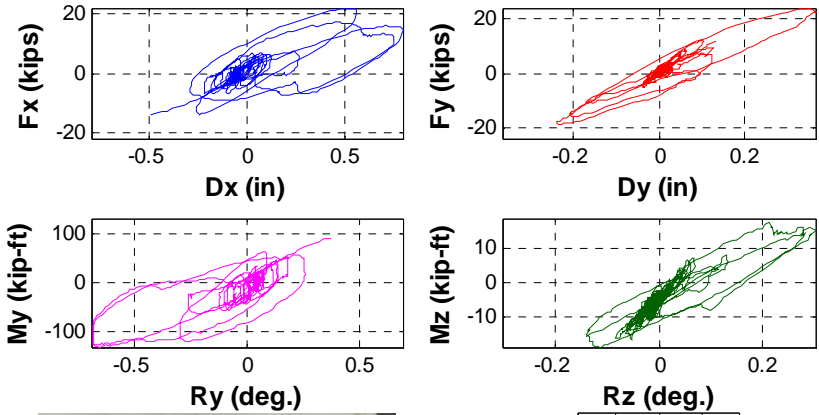
Time 25.63sec

Event: Yield of Longitudinal Reinforcement at face C, level 2

Figure C.64 Pier 1 Response at Step 2663



	Loads (kip,kip-ft)	Def. (in,deg)
Fx	-14.0541 Dx	-0.4956
Fy	11.5451 Dy	0.1304
Fz	67.5499 Dz	-0.0034
Mx	37.4398 Rx	-0.0547
My	90.9696 Ry	0.3652
Mz	-15.5477 Rz	-0.1406



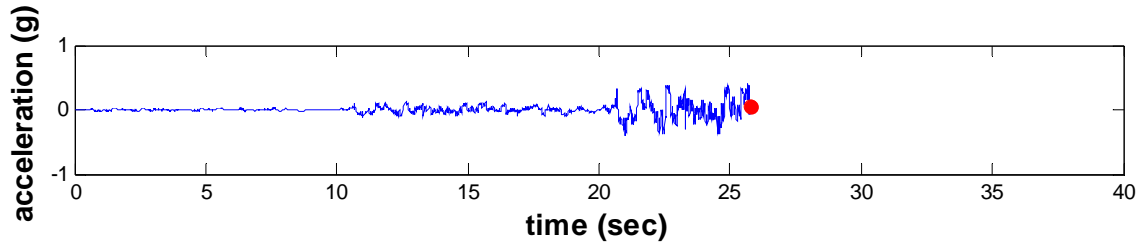
Pier 2

Step 2663

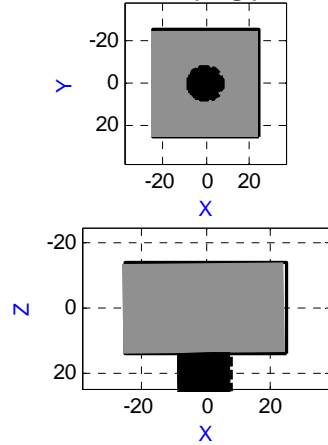
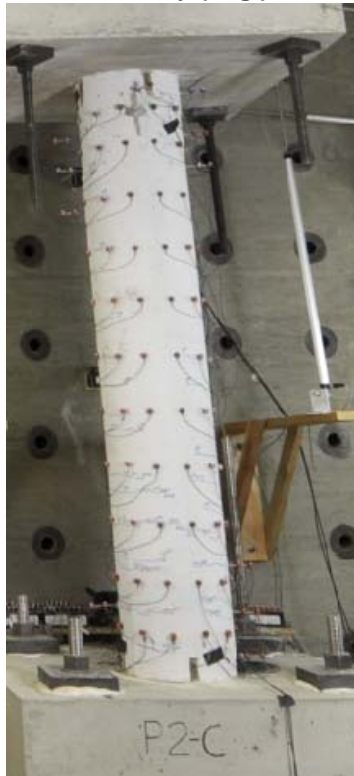
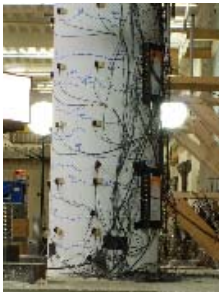
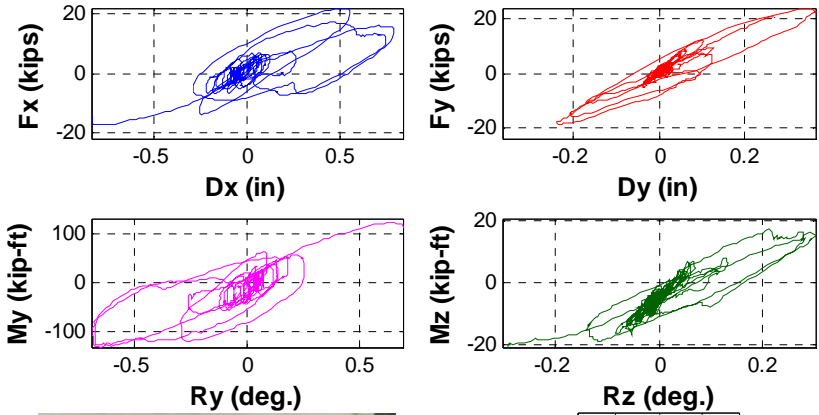
Time 25.63sec

Event: Yield of Longitudinal Reinforcement at face D, level 12

Figure C.65 Pier 2 Response at Step 2663



	Loads (kip,kip-ft)	Def. (in,deg)
Fx	-14.7367 Dx	-0.8415
Fy	20.9980 Dy	0.2697
Fz	63.5520 Dz	-0.0245
Mx	74.0489 Rx	-0.0986
My	113.0681 Ry	0.6935
Mz	-20.8362 Rz	-0.2911



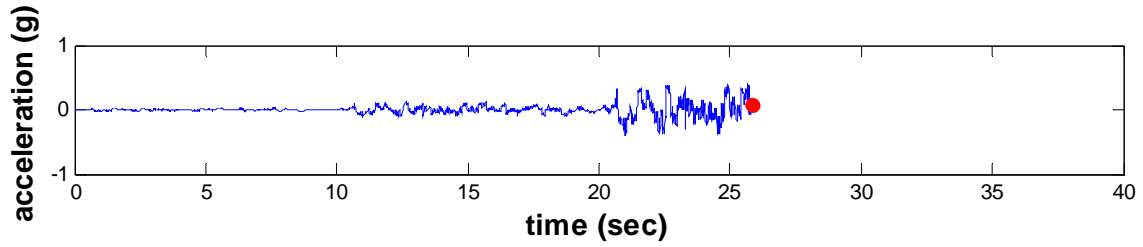
Pier 2

Step 2681

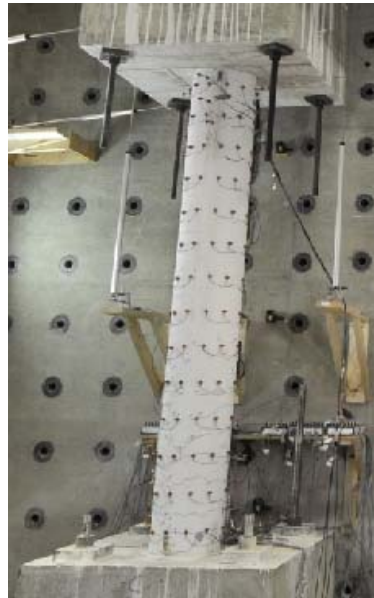
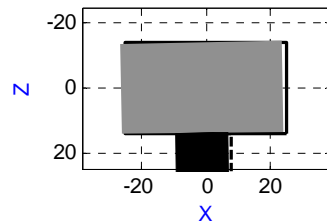
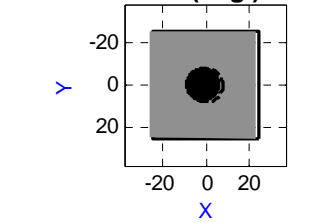
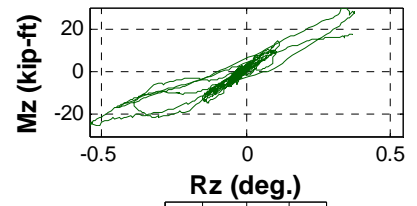
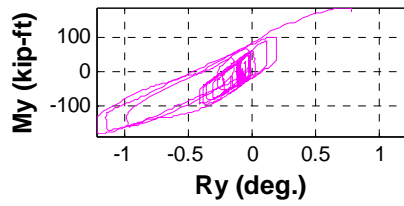
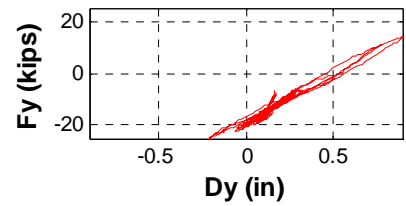
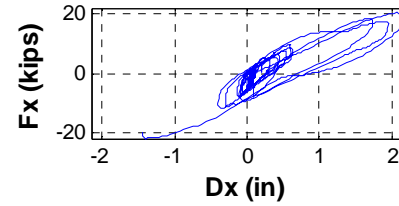
Time 25.81sec

Event: -dx Peak of 1.0(MCE) Record

Figure C.66 Pier 2 Response at Step 2681



	Loads (kip,kip-ft)	Def. (in,deg)
Fx	-20.4562 Dx	-1.4496
Fy	-24.8872 Dy	-0.2089
Fz	124.8361 Dz	-0.0615
Mx	-77.7793 Rx	0.5748
My	175.5176 Ry	0.7777
Mz	17.1740 Rz	0.3700



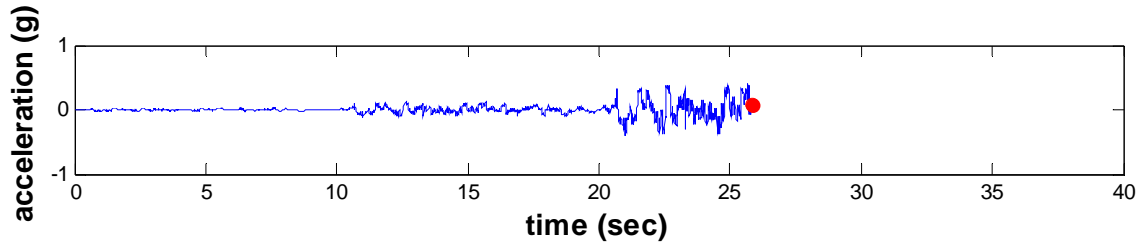
Pier 1

Step 2685

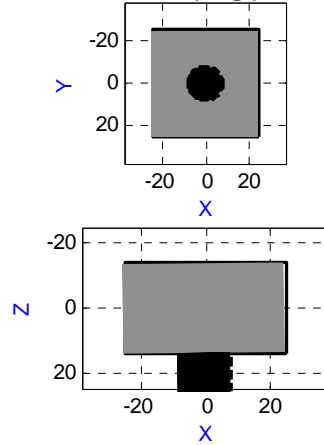
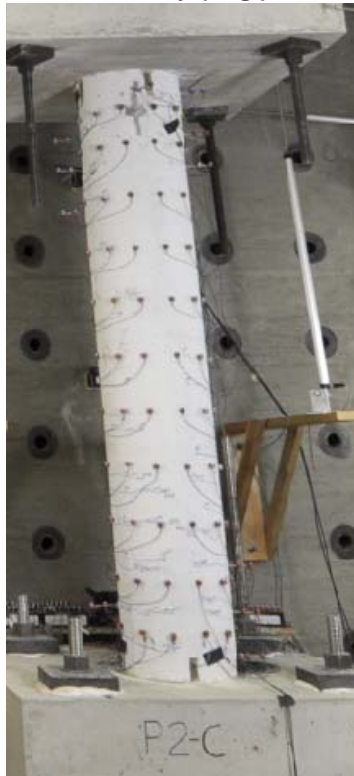
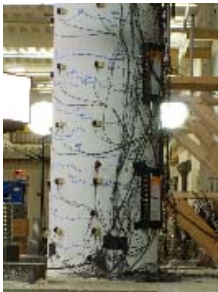
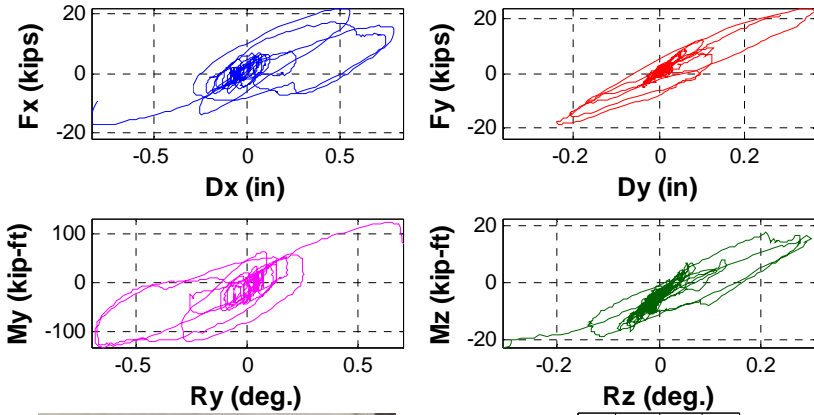
Time 25.85sec

Event: Cracks extended at face B-C, level 6-8

Figure C.67 Pier 1 Response at Step 2685



	Loads (kip,kip-ft)	Def. (in,deg)
Fx	-9.6990 Dx	-0.8091
Fy	21.1861 Dy	0.2867
Fz	58.0382 Dz	-0.0272
Mx	76.0108 Rx	-0.1015
My	79.0812 Ry	0.7072
Mz	-20.3374 Rz	-0.3087



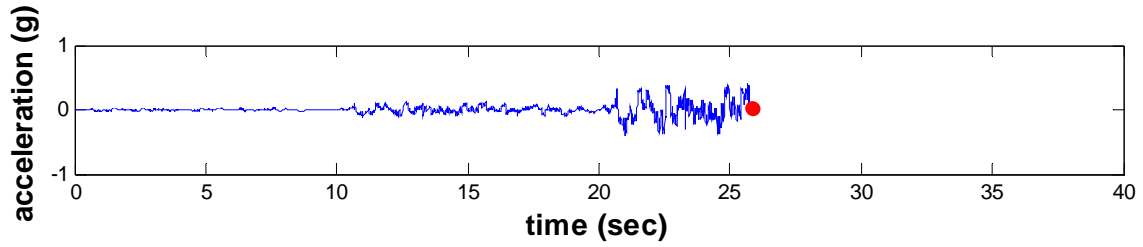
Pier 2

Step 2685

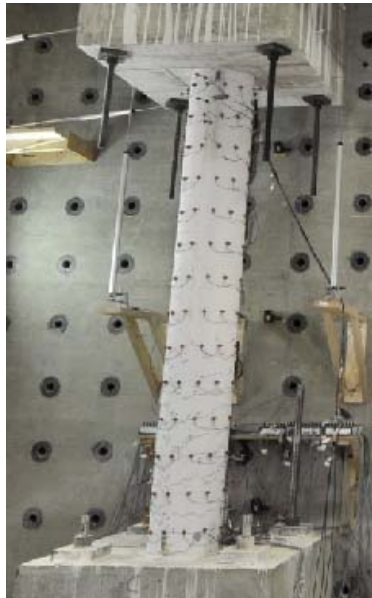
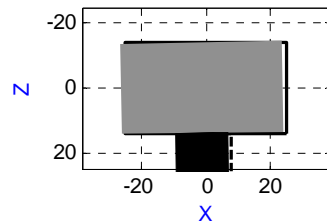
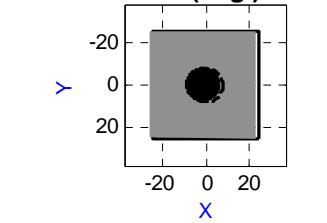
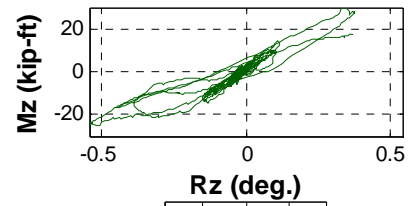
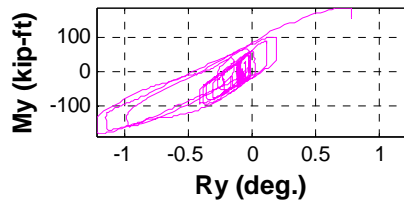
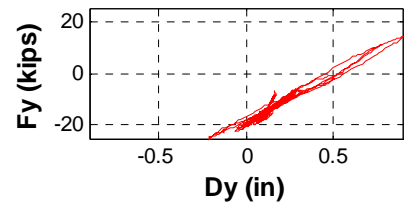
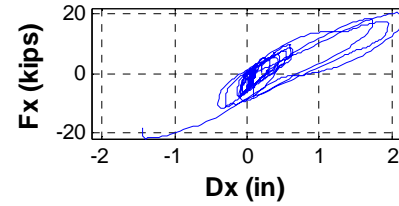
Time 25.85sec

Event: Torsional cracking at face C-D, level 12-18

Figure C.68 Pier 2 Response at Step 2685



	Loads (kip,kip-ft)	Def. (in,deg)
Fx	-18.6815 Dx	-1.4437
Fy	-24.5617 Dy	-0.2092
Fz	123.9556 Dz	-0.0620
Mx	-75.8783 Rx	0.5766
My	155.7900 Ry	0.7821
Mz	17.7289 Rz	0.3749



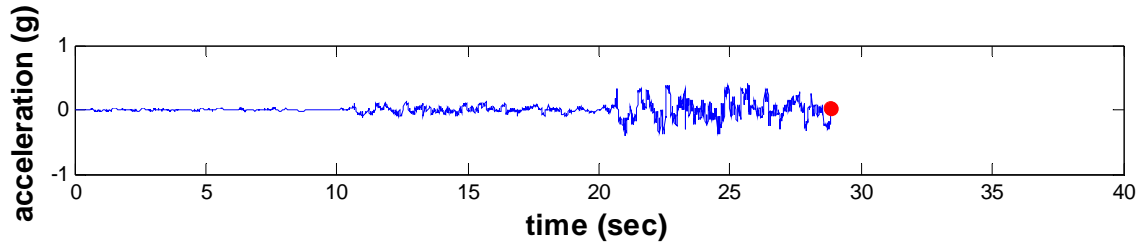
Pier 1

Step 2686

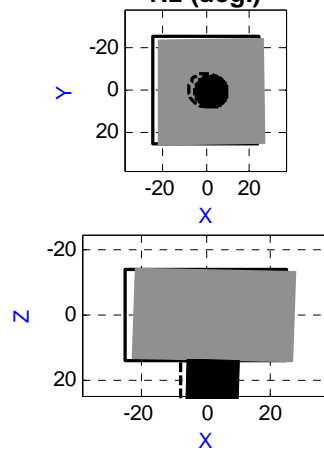
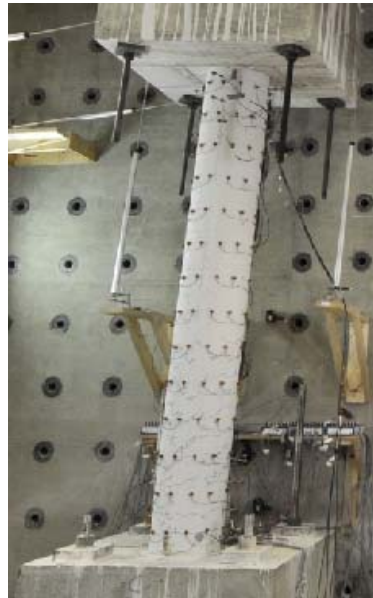
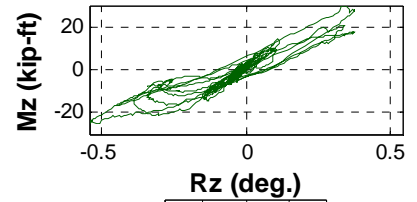
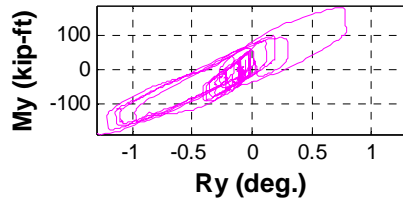
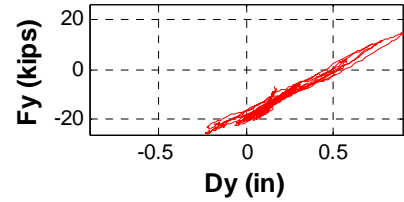
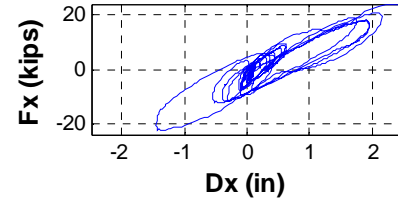
Time 25.86sec

Event: -dx Peak of 1.0(MCE) Record

Figure C.69 Pier 1 Response at Step 2686



	Loads (kip,kip-ft)		Def. (in,deg)	
Fx	23.4161	Dx	2.4943	
Fy	9.8161	Dy	0.7216	
Fz	129.2395	Dz	-0.0036	
Mx	51.5342	Rx	0.3685	
My	-189.9601	Ry	-1.3055	
Mz	-7.5963	Rz	-0.3418	



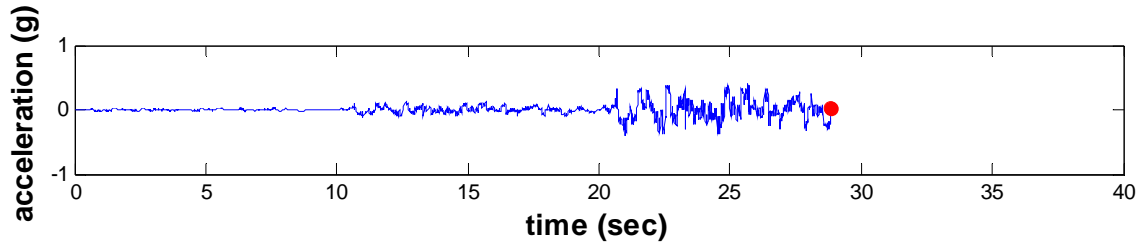
Pier 1

Step 2986

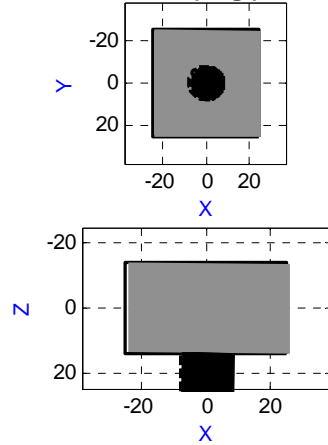
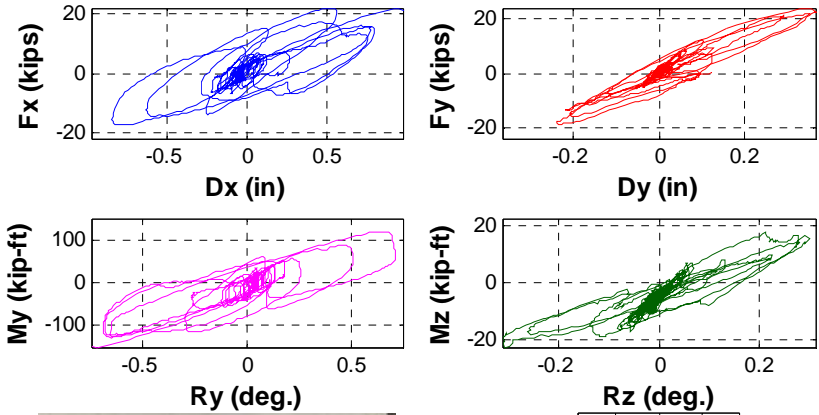
Time 28.86sec

Event: Widening of cracks at face B, level bottom interface

Figure C.70 Pier 1 Response at Step 2986



	Loads (kip,kip-ft)		Def. (in,deg)	
Fx	21.2349	Dx	0.9753	
Fy	0.1329	Dy	0.1247	
Fz	56.5552	Dz	-0.0270	
Mx	14.5080	Rx	0.1684	
My	-153.7767	Ry	-0.7454	
Mz	8.5522	Rz	0.2214	



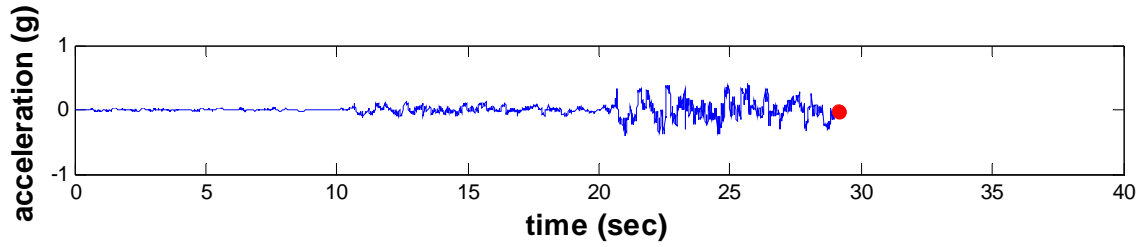
Pier 2

Step 2986

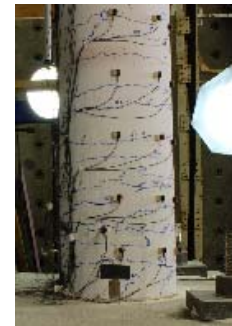
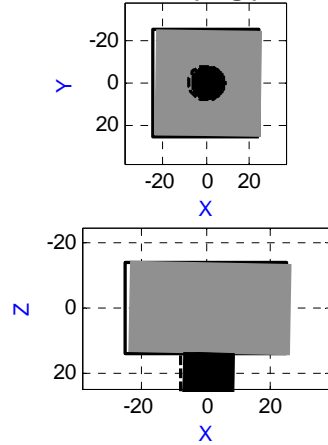
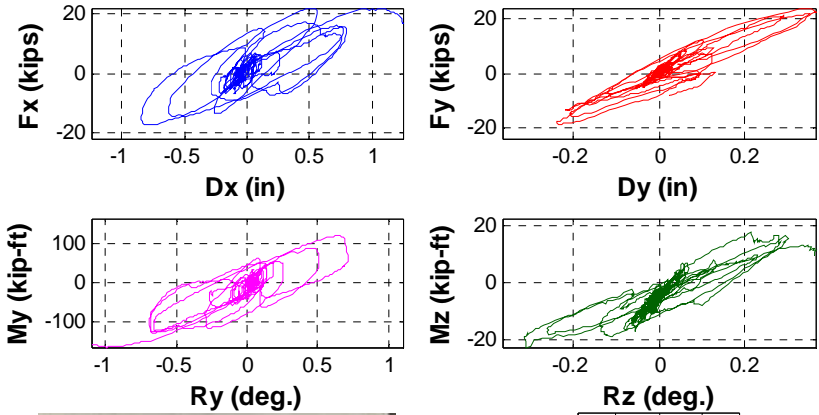
Time 28.86sec

Event: Widening of cracks at face B, level bottom interface

Figure C.71 Pier 2 Response at Step 2986



	Loads (kip,kip-ft)	Def. (in,deg)
Fx	16.5692 Dx	1.2431
Fy	-8.4067 Dy	0.0253
Fz	58.7746 Dz	-0.0432
Mx	-17.8349 Rx	0.2305
My	-159.2583 Ry	-1.1005
Mz	9.6345 Rz	0.3621



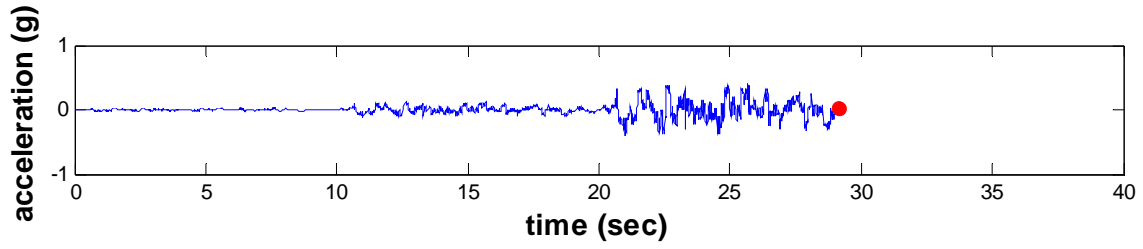
Pier 2

Step 3013

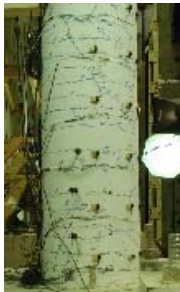
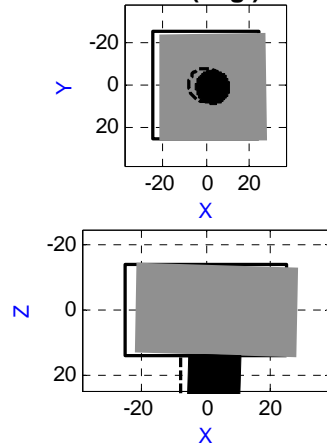
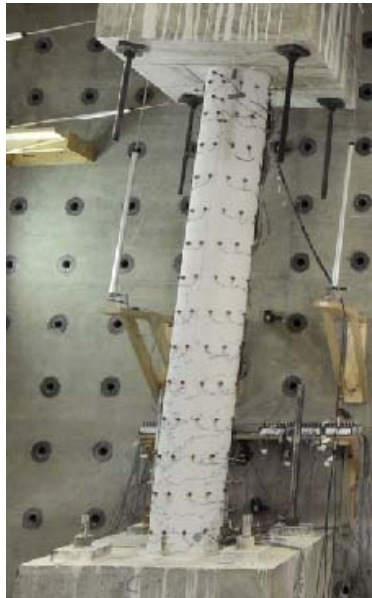
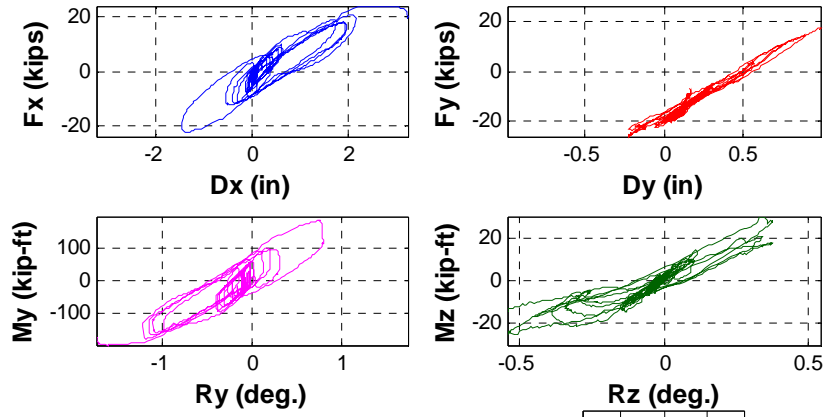
Time 29.13sec

Event: +dx Peak of 1.0(MCE) Record

Figure C.72 Pier 2 Response at Step 3013



	Loads (kip,kip-ft)		Def. (in,deg)	
Fx	19.3613	Dx	3.2361	
Fy	16.6630	Dy	0.9936	
Fz	132.9805	Dz	-0.0081	
Mx	80.3880	Rx	0.3310	
My	-175.8366	Ry	-1.7299	
Mz	-13.9727	Rz	-0.5447	



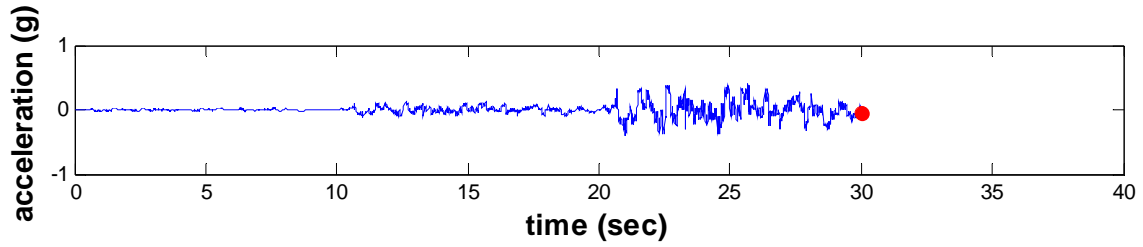
Pier 1

Step 3014

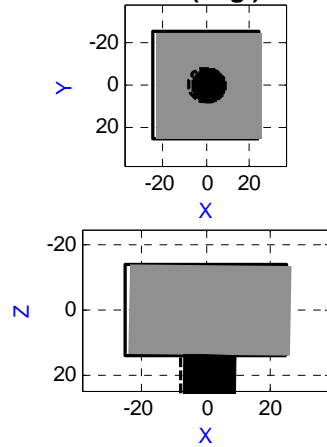
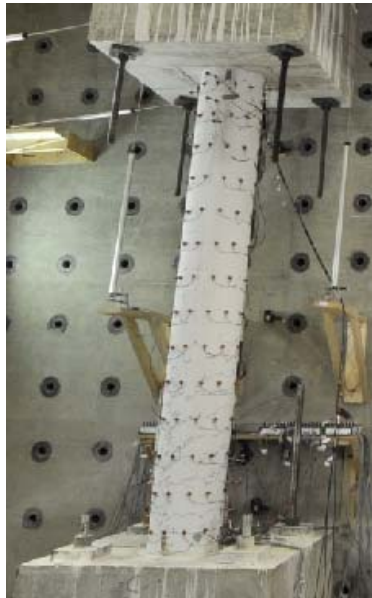
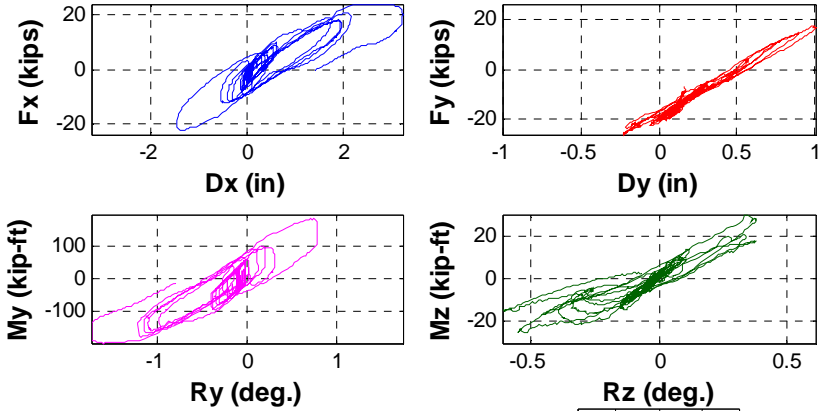
Time 29.14sec

Event: +dx Peak of 1.0(MCE) Record

Figure C.73 Pier 1 Response at Step 3014



	Loads (kip,kip-ft)	Def. (in,deg)
Fx	-0.3036 Dx	1.4132
Fy	-9.2609 Dy	0.2371
Fz	127.8636 Dz	0.0017
Mx	-35.3355 Rx	0.3544
My	-14.2484 Ry	-0.7987
Mz	2.2142 Rz	-0.0646



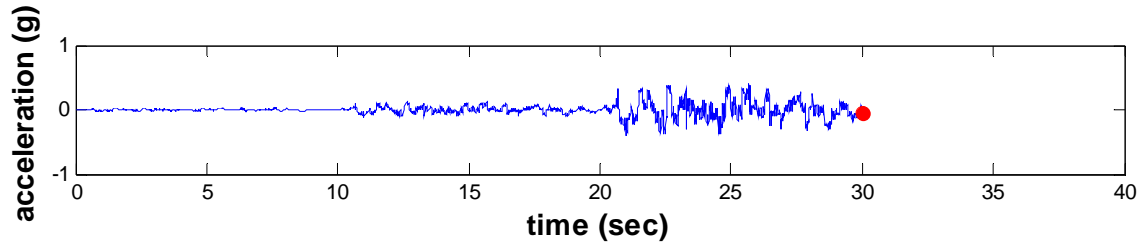
Pier 1

Step 3100

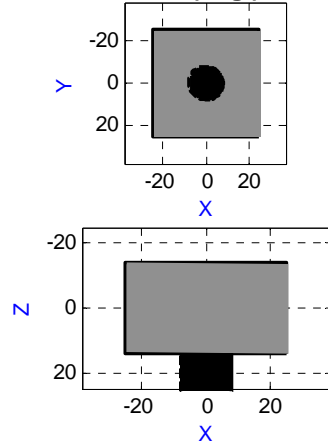
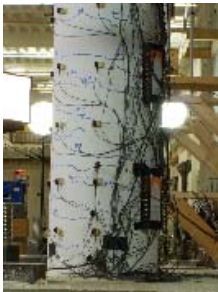
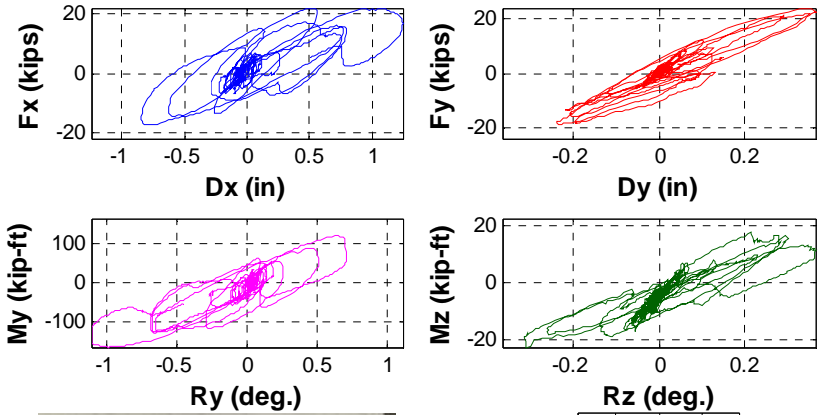
Time 30.00sec

Event: End of 1.0(MCE) Record

Figure C.74 Pier 1 Response at Step 3100



	Loads (kip,kip-ft)	Def. (in,deg)
Fx	5.0889 Dx	0.5039
Fy	6.0031 Dy	0.1504
Fz	60.2108 Dz	-0.0043
Mx	30.8262 Rx	0.1189
My	-54.2809 Ry	-0.4525
Mz	-0.6829 Rz	0.0889



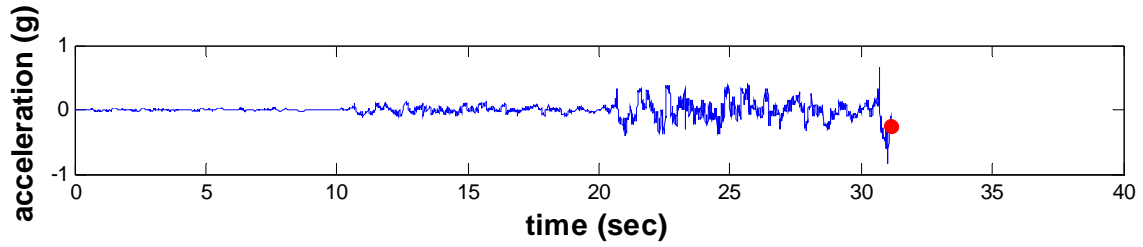
Pier 2

Step 3100

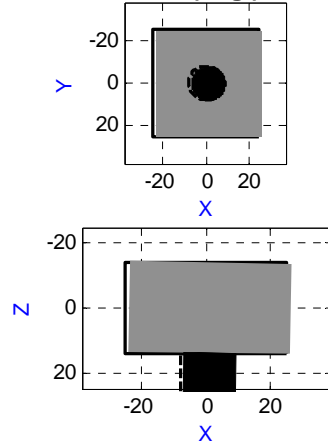
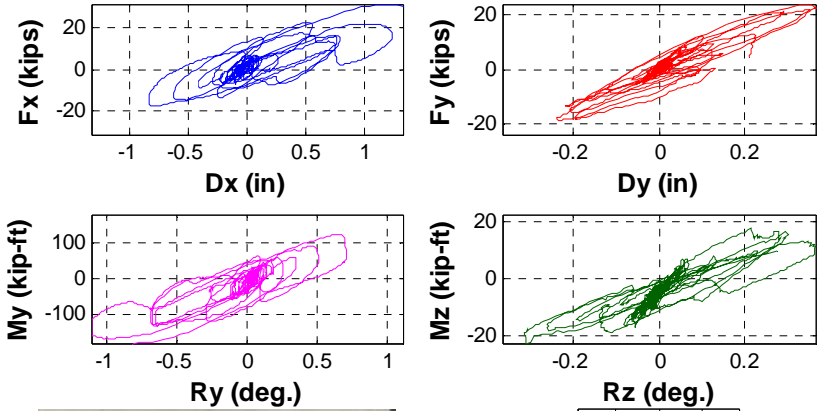
Time 30.00sec

Event: End of 1.0(MCE) Record

Figure C.75 Pier 2 Response at Step 3100



	Loads (kip,kip-ft)	Def. (in,deg)
Fx	30.1459 Dx	1.3318
Fy	4.5712 Dy	0.2127
Fz	61.3566 Dz	-0.0464
Mx	30.8435 Rx	0.1809
My	-178.5620 Ry	-0.8145
Mz	9.8615 Rz	0.2734



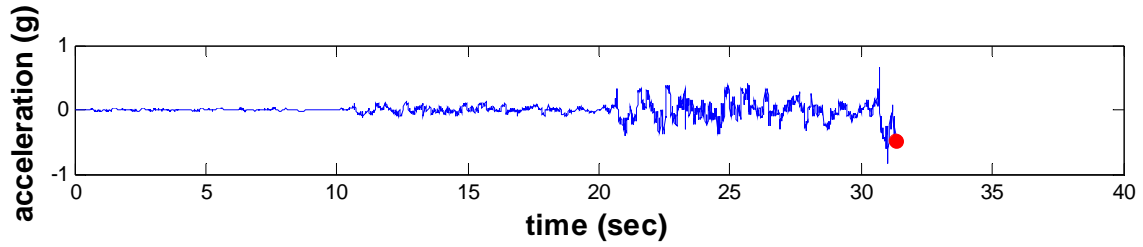
Pier 2

Step 3212

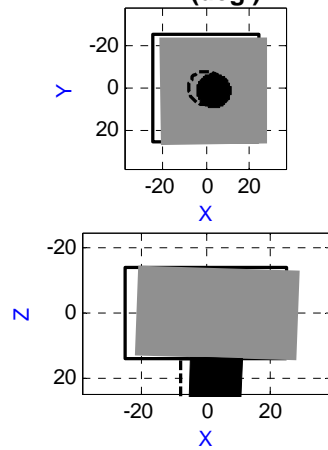
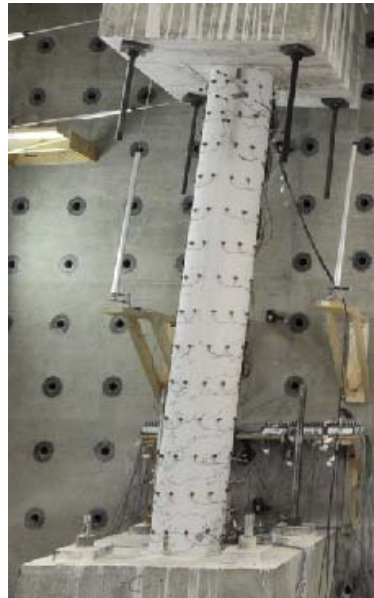
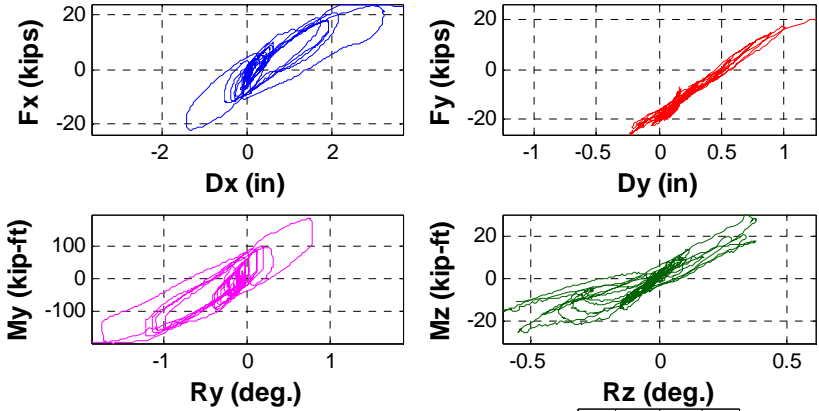
Time 31.12sec

Event: Audible cracking

Figure C.76 Pier 2 Response at Step 3212



	Loads (kip,kip-ft)		Def. (in,deg)	
Fx	22.7437	Dx	3.7002	
Fy	20.0696	Dy	1.2512	
Fz	136.3992	Dz	-0.0133	
Mx	86.0683	Rx	0.3368	
My	-195.8485	Ry	-1.8667	
Mz	-10.7058	Rz	-0.5526	



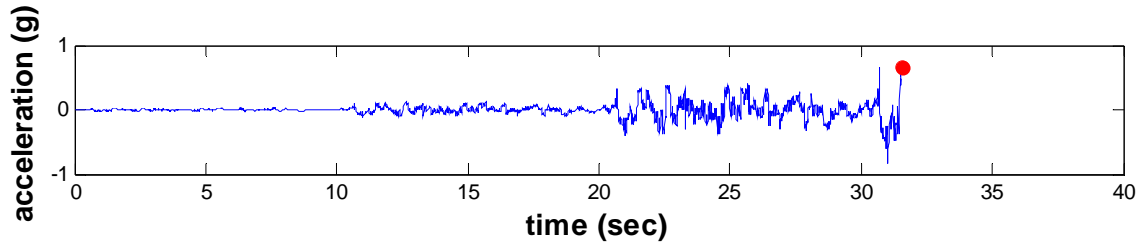
Pier 1

Step 3231

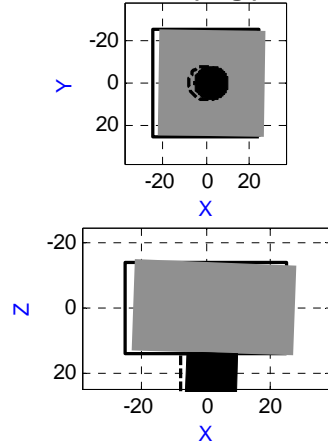
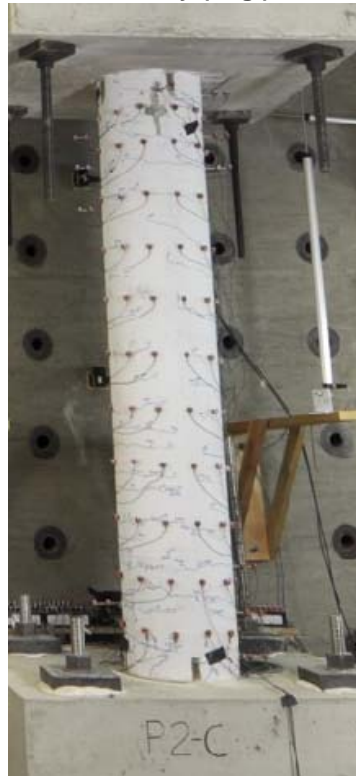
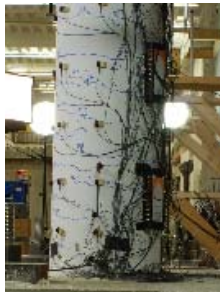
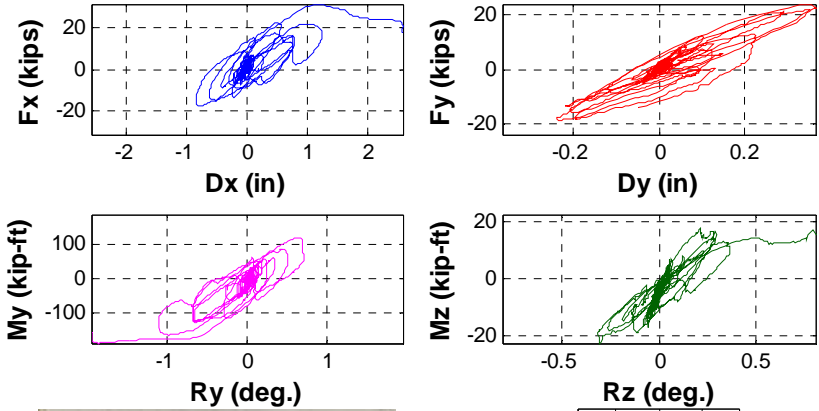
Time 31.31sec

Event: Yield of Longitudinal Reinforcement at face C, level 7

Figure C.77 Pier 1 Response at Step 3231



	Loads (kip,kip-ft)		Def. (in,deg)	
Fx	17.1217	Dx	2.5661	
Fy	-14.3884	Dy	-0.0465	
Fz	61.6673	Dz	-0.0842	
Mx	-24.2459	Rx	0.4344	
My	-158.7725	Ry	-1.9604	
Mz	15.4567	Rz	0.8041	



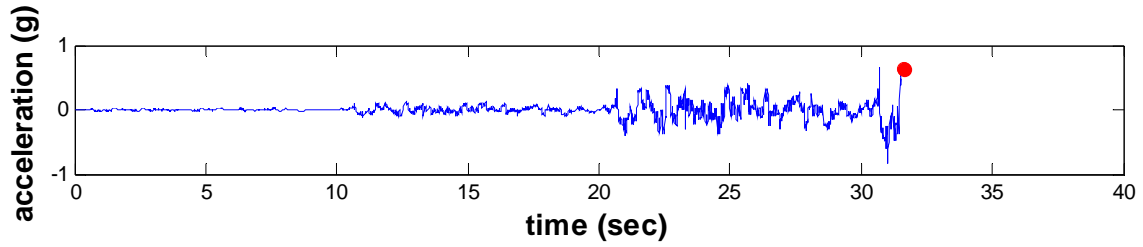
Pier 2

Step 3254

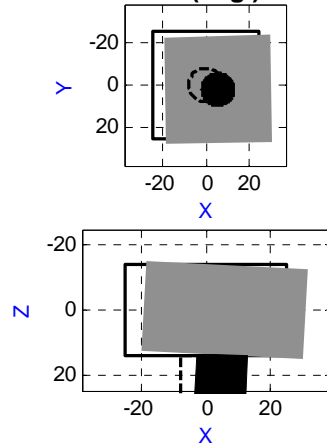
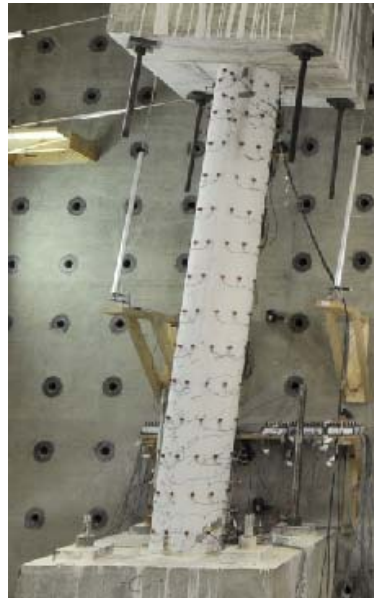
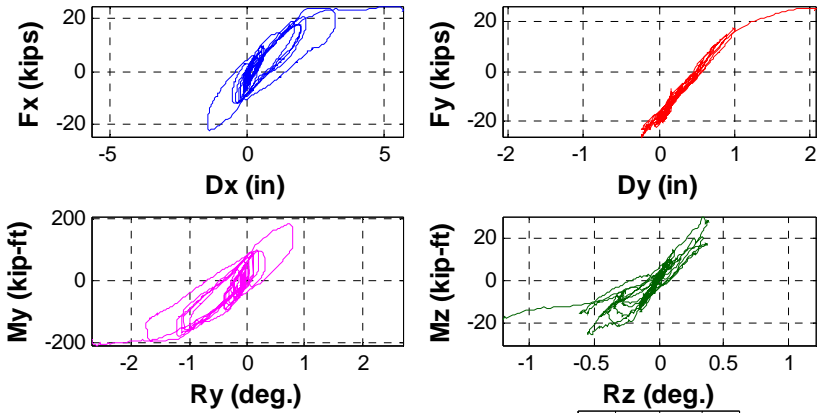
Time 31.54sec

Event: Yield of Longitudinal Reinforcement at face C, level 13

Figure C.78 Pier 2 Response at Step 3254



	Loads (kip,kip-ft)		Def. (in,deg)	
Fx	22.0563	Dx	5.6962	
Fy	24.2288	Dy	2.0456	
Fz	137.7677	Dz	-0.0116	
Mx	78.6853	Rx	0.2369	
My	-190.2793	Ry	-2.6945	
Mz	-18.1081	Rz	-1.2056	



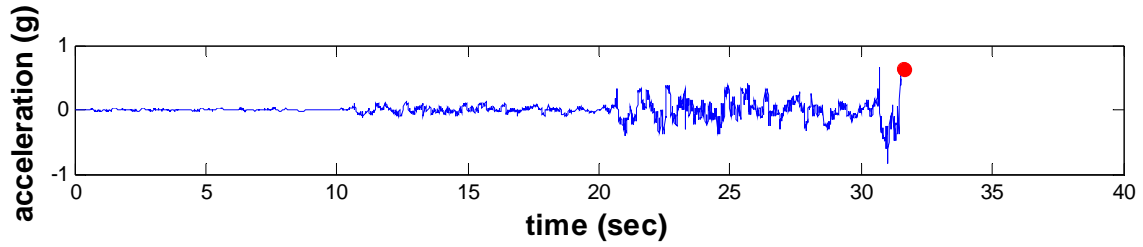
Pier 1

Step 3261

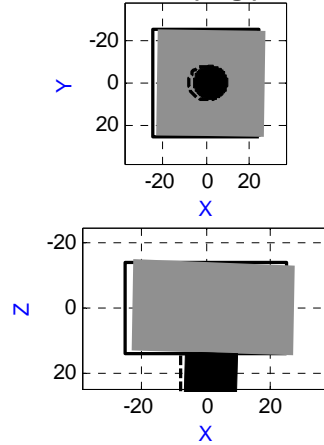
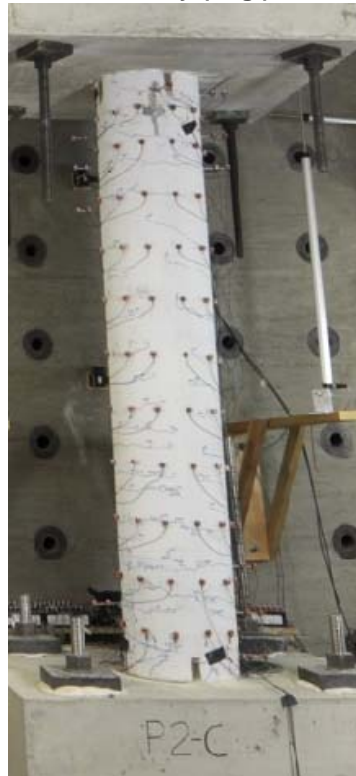
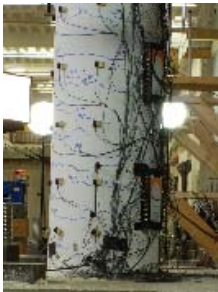
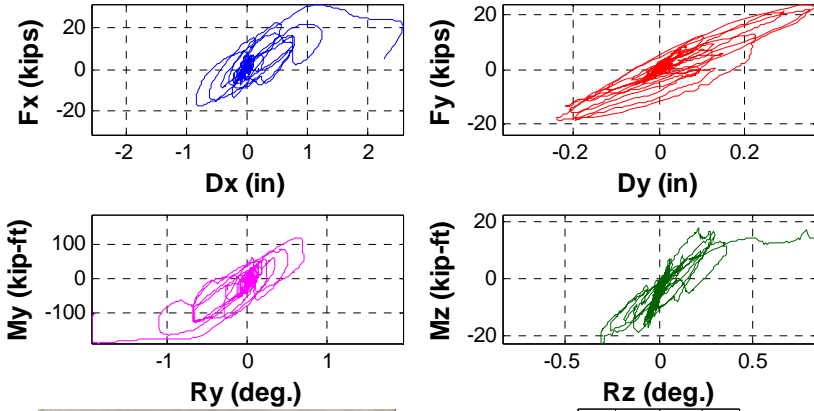
Time 31.61sec

Event: Spalling at face D

Figure C.79 Pier 1 Response at Step 3261



	Loads (kip,kip-ft)	Def. (in,deg)
Fx	5.3905 Dx	2.2813
Fy	-18.9411 Dy	-0.1974
Fz	51.0942 Dz	-0.0854
Mx	-44.7587 Rx	0.4141
My	-99.3977 Ry	-1.9075
Mz	13.7794 Rz	0.8408



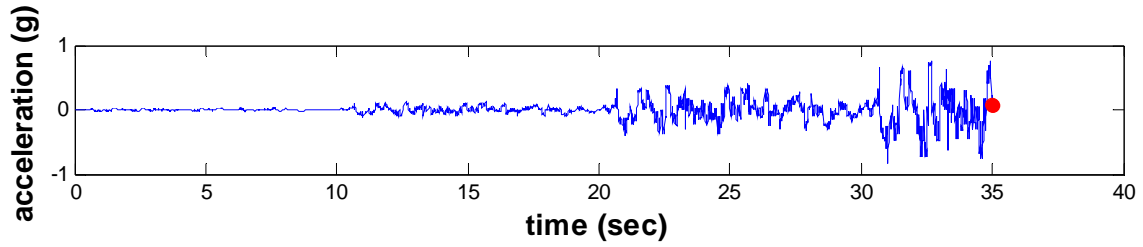
Pier 2

Step 3261

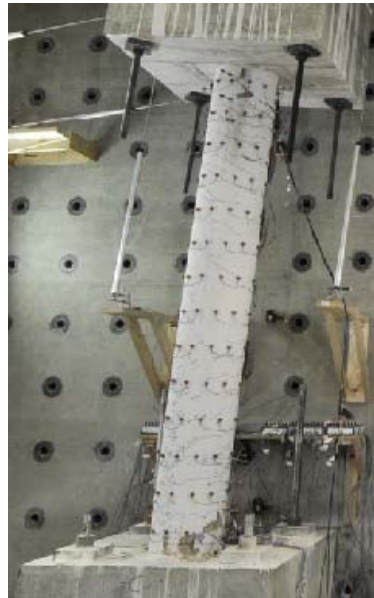
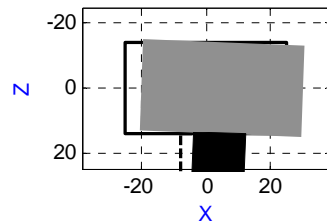
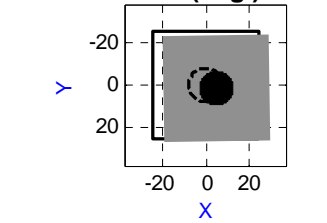
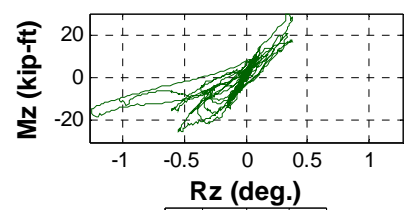
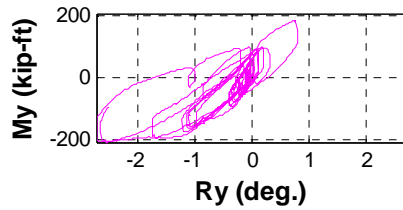
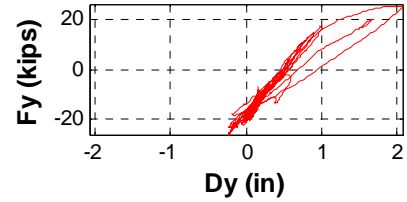
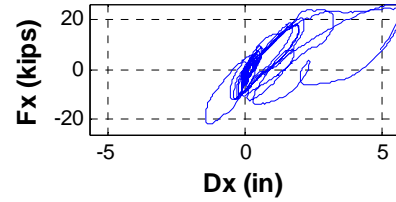
Time 31.61sec

Event: Spalling at face D

Figure C.80 Pier 2 Response at Step 3261



	Loads (kip,kip-ft)		Def. (in,deg)	
Fx	8.3591	Dx	4.9794	
Fy	16.6851	Dy	1.5176	
Fz	138.6605	Dz	9.4975e-...	
Mx	53.1427	Rx	0.1927	
My	-94.7744	Ry	-2.5062	
Mz	-10.0277	Rz	-1.0239	



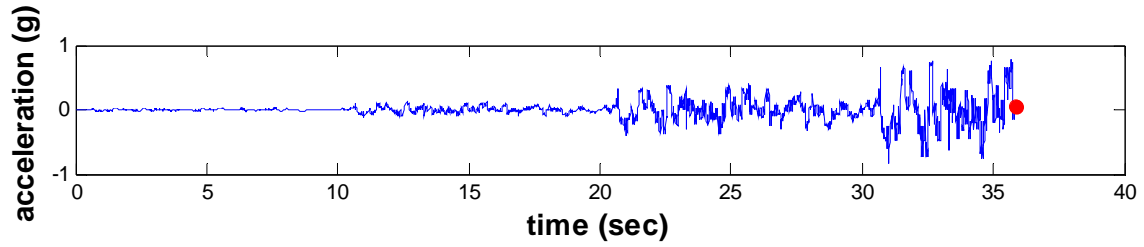
Pier 1

Step 3599

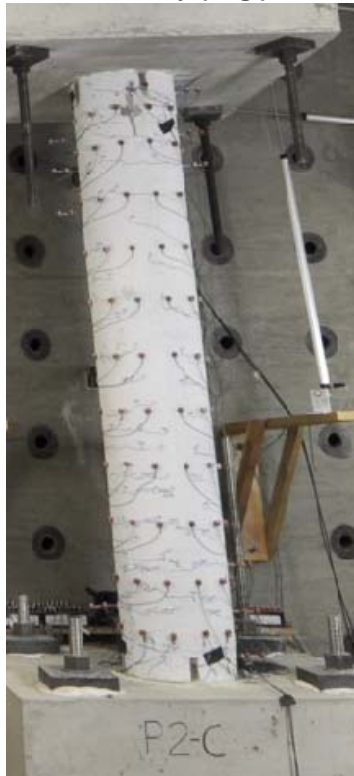
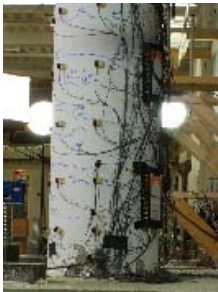
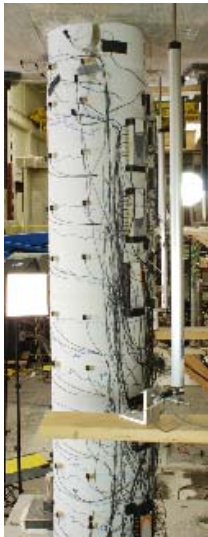
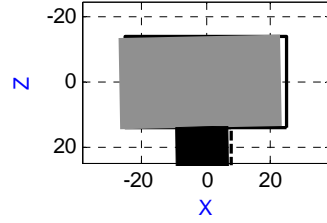
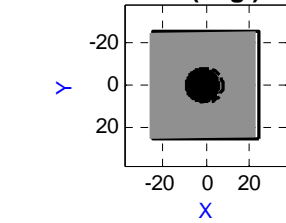
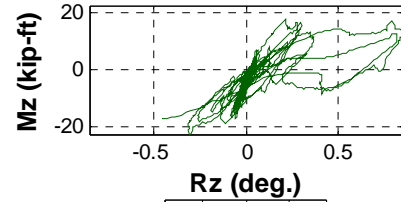
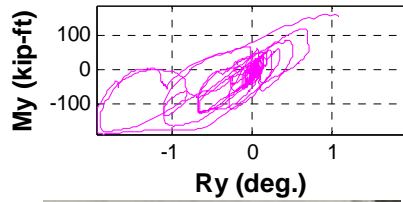
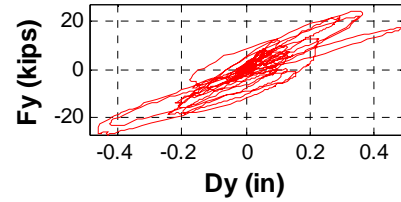
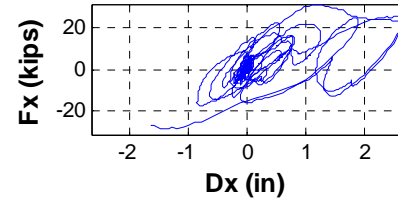
Time 34.99sec

Event: Spalling at face C-D

Figure C.81 Pier 1 Response at Step 3599



	Loads (kip,kip-ft)	Def. (in,deg)
Fx	-26.3102 Dx	-1.6228
Fy	12.6127 Dy	0.0996
Fz	76.4797 Dz	-0.0548
Mx	27.6548 Rx	-0.1908
My	161.8583 Ry	1.0791
Mz	-17.0988 Rz	-0.4508



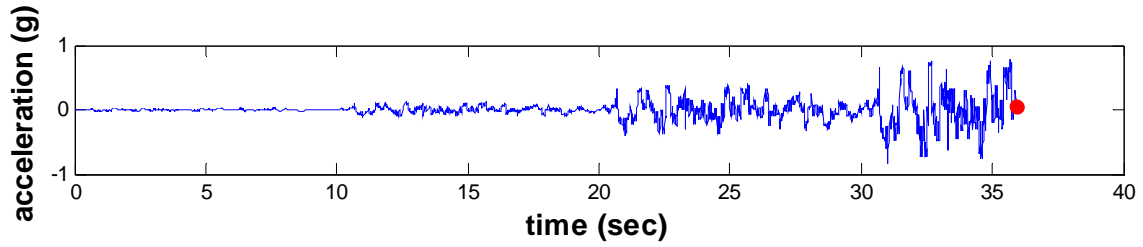
Pier 2

Step 3684

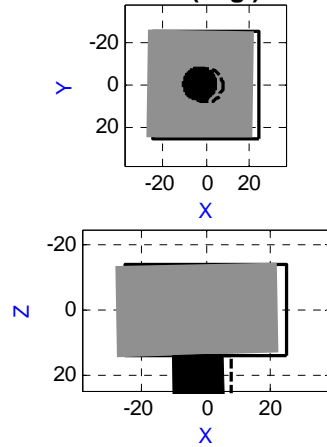
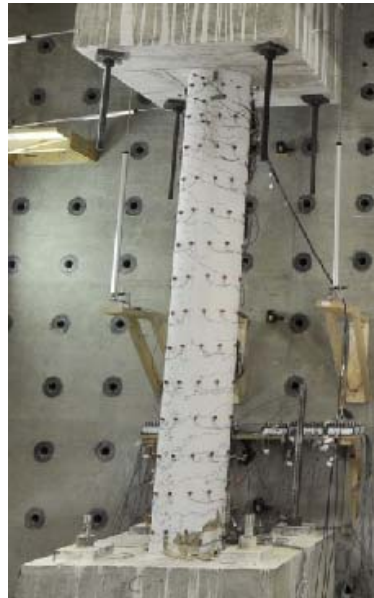
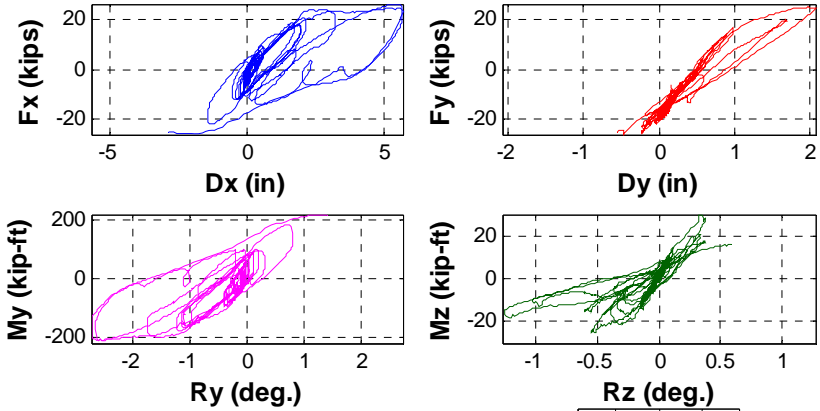
Time 35.84sec

Event: Audible cracking

Figure C.82 Pier 2 Response at Step 3684



	Loads (kip,kip-ft)	Def. (in,deg)
Fx	-25.0934 Dx	-2.8496
Fy	-25.2350 Dy	-0.5543
Fz	134.9177 Dz	-0.1241
Mx	-80.1358 Rx	0.6487
My	218.7088 Ry	1.3973
Mz	16.0133 Rz	0.5918



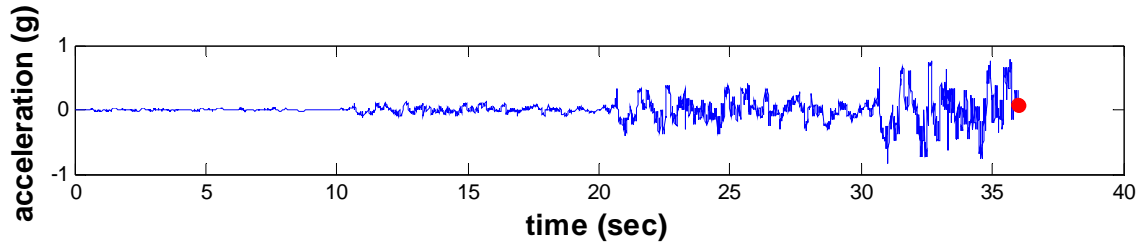
Pier 1

Step 3693

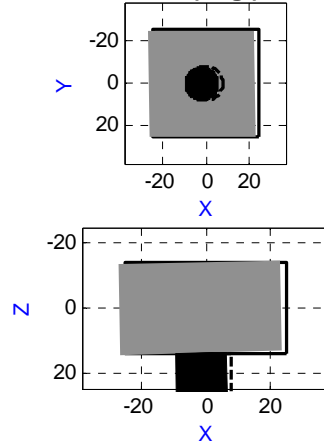
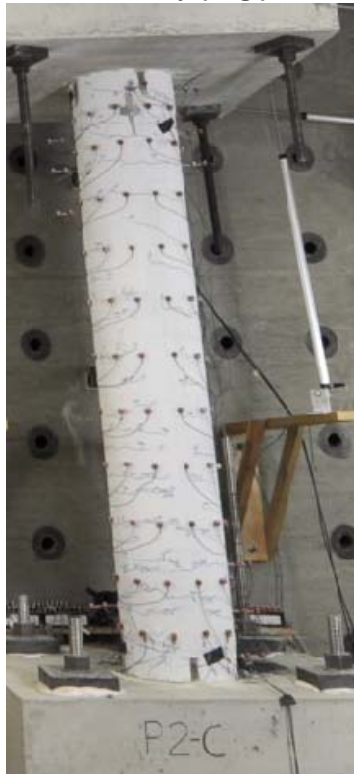
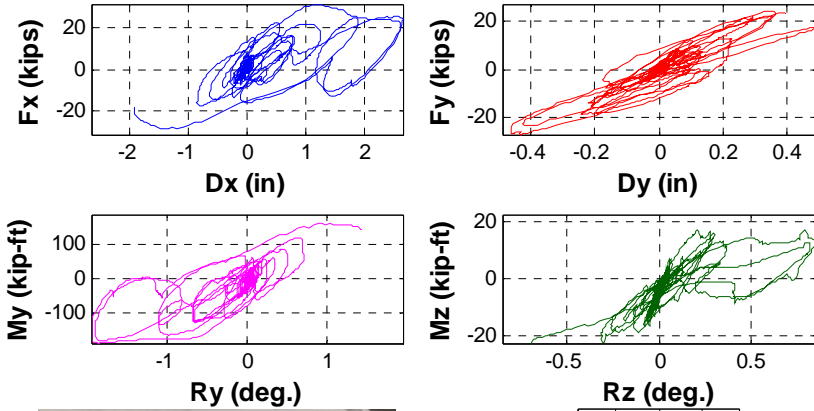
Time 35.93sec

Event: Yield of Longitudinal Reinforcement at face C, level 4

Figure C.83 Pier 1 Response at Step 3693



	Loads (kip,kip-ft)	Def. (in,deg)
Fx	-18.2713 Dx	-1.9063
Fy	23.5655 Dy	0.3933
Fz	60.6440 Dz	-0.0746
Mx	65.4721 Rx	-0.2367
My	147.1504 Ry	1.4393
Mz	-22.6477 Rz	-0.6898



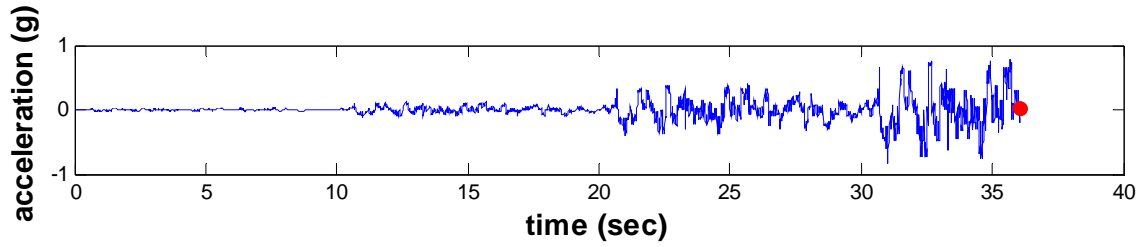
Pier 2

Step 3700

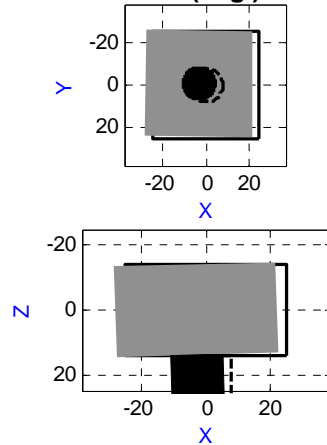
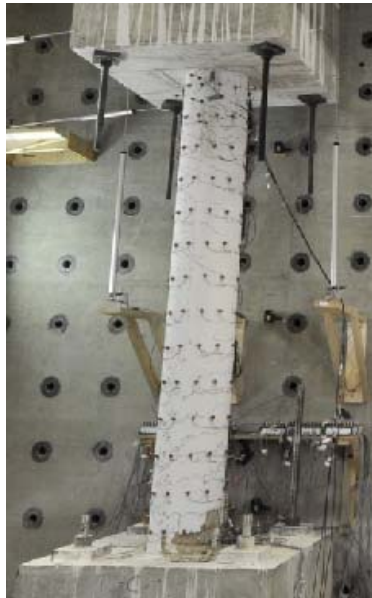
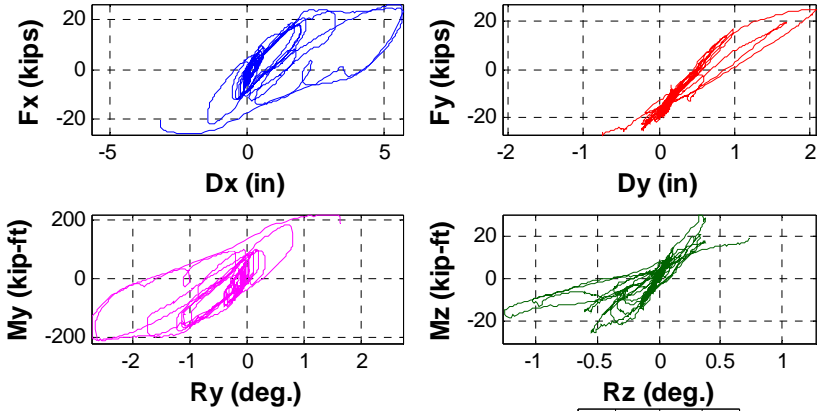
Time 36.00sec

Event: -dx Peak of 2.0(MCE) Record

Figure C.84 Pier 2 Response at Step 3700



	Loads (kip,kip-ft)	Def. (in,deg)
Fx	-20.2716 Dx	-3.1485
Fy	-26.8587 Dy	-0.7528
Fz	126.7026 Dz	-0.1424
Mx	-99.3364 Rx	0.7002
My	187.3325 Ry	1.6160
Mz	19.2585 Rz	0.7396



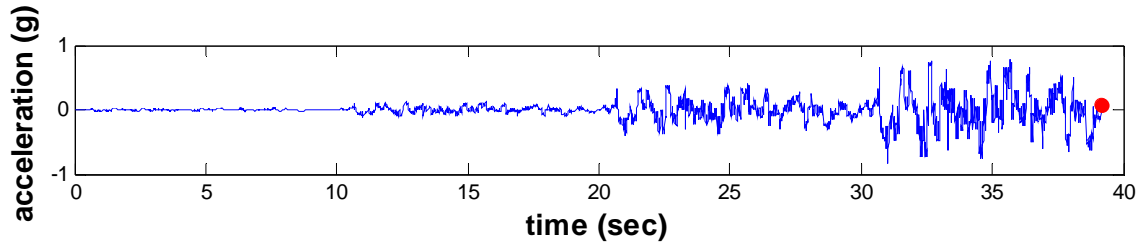
Pier 1

Step 3706

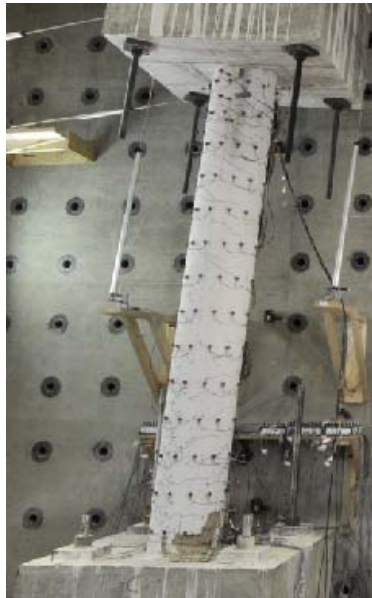
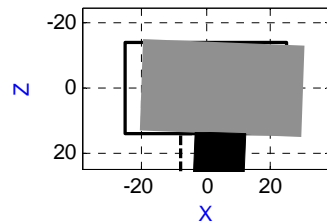
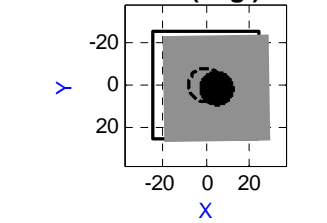
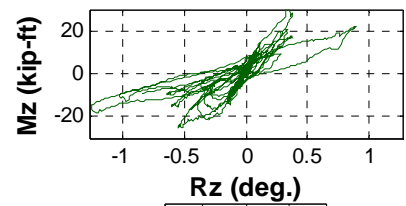
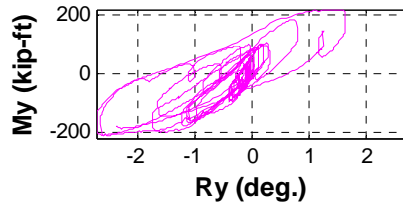
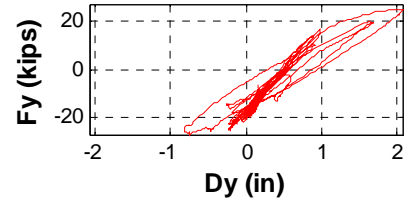
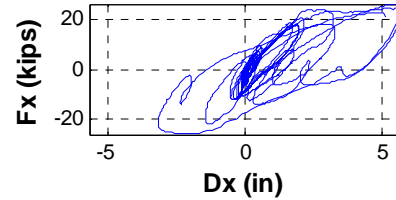
Time 36.06sec

Event: -dx Peak of 2.0(MCE) Record

Figure C.85 Pier 1 Response at Step 3706



	Loads (kip,kip-ft)		Def. (in,deg)	
Fx	21.2395	Dx	5.1283	
Fy	19.7574	Dy	1.6700	
Fz	132.8912	Dz	-0.0082	
Mx	71.2554	Rx	0.2462	
My	-179.5468	Ry	-2.3464	
Mz	-9.0376	Rz	-0.8432	



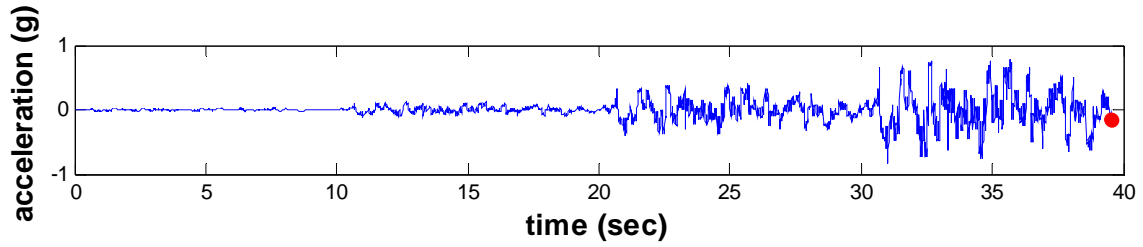
Pier 1

Step 4014

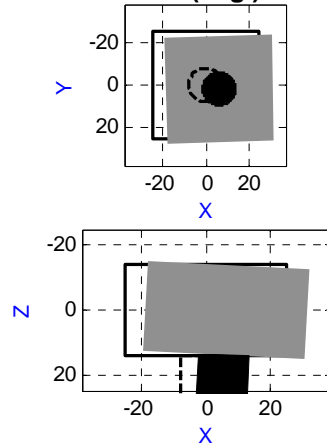
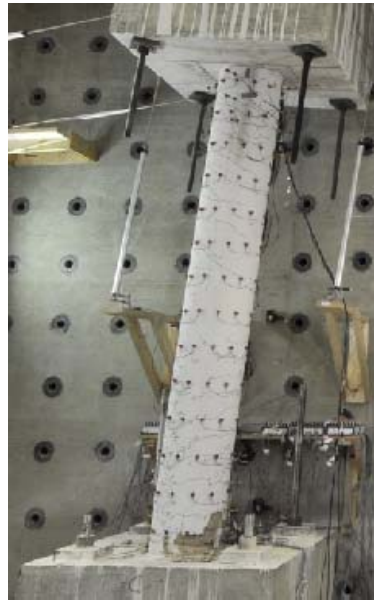
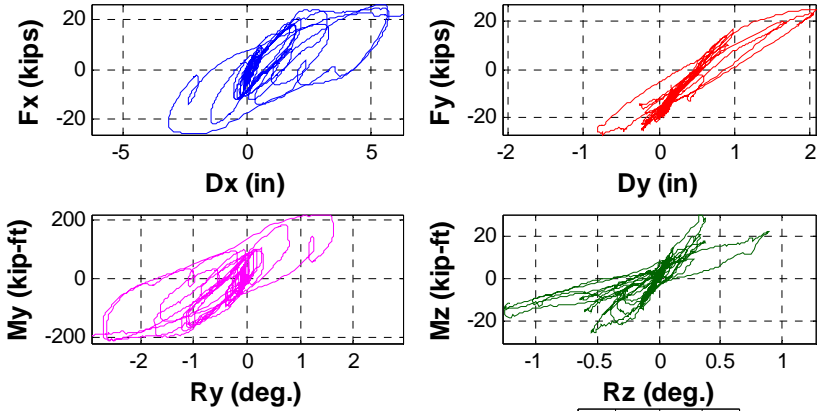
Time 39.14sec

Event: Audible pop and opening of 1.5mm crack at face A, level base

Figure C.86 Pier 1 Response at Step 4014



	Loads (kip,kip-ft)		Def. (in,deg)	
Fx	21.5364	Dx	6.2641	
Fy	18.6861	Dy	1.8204	
Fz	134.4481	Dz	0.0013	
Mx	52.3226	Rx	0.1402	
My	-196.0385	Ry	-2.9308	
Mz	-11.0420	Rz	-1.2132	



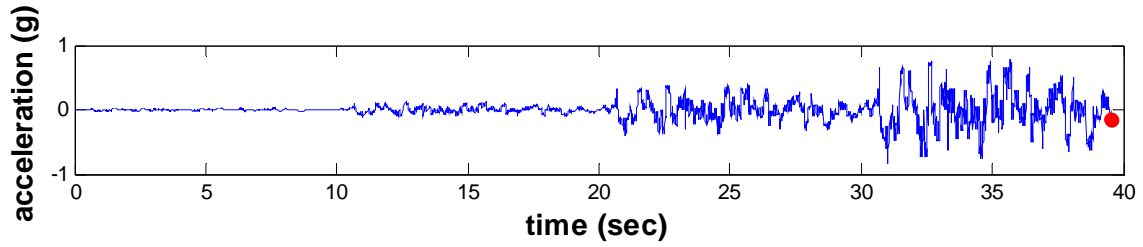
Pier 1

Step 4055

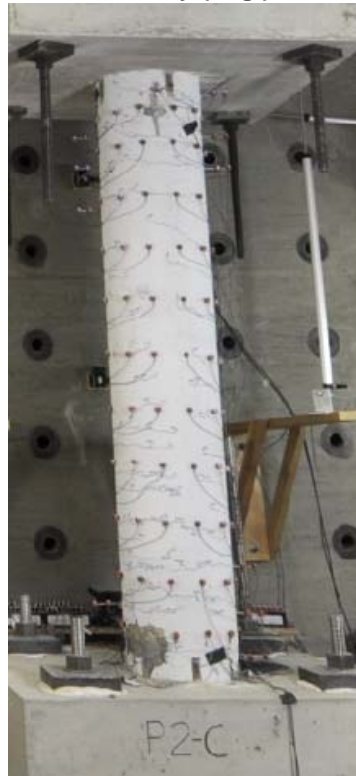
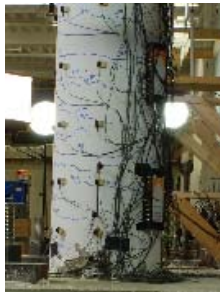
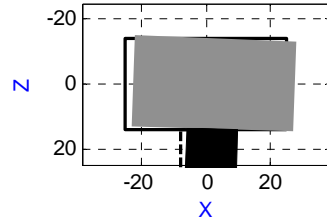
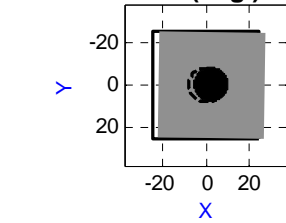
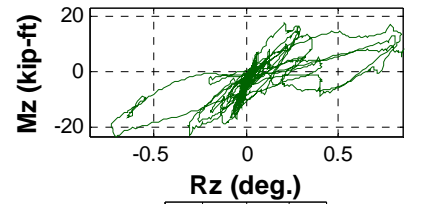
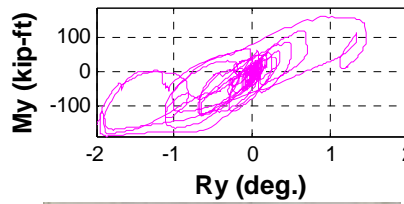
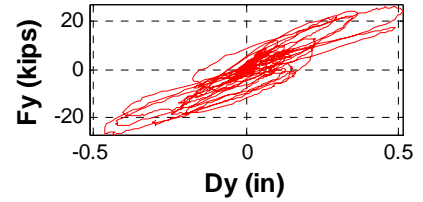
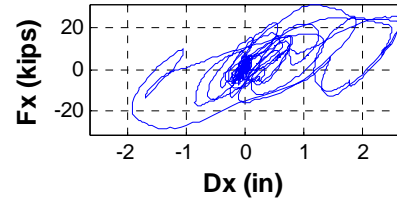
Time 39.55sec

Event: Audible cracking

Figure C.87 Pier 1 Response at Step 4055



	Loads (kip,kip-ft)		Def. (in,deg)	
Fx	12.0726	Dx	2.4424	
Fy	-21.3204	Dy	-0.2963	
Fz	59.8236	Dz	-0.0894	
Mx	-50.6525	Rx	0.4291	
My	-153.2226	Ry	-2.0101	
Mz	5.3888	Rz	0.8504	



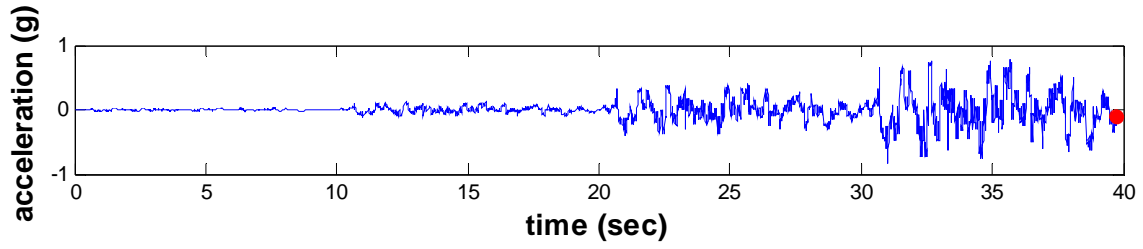
Pier 2

Step 4055

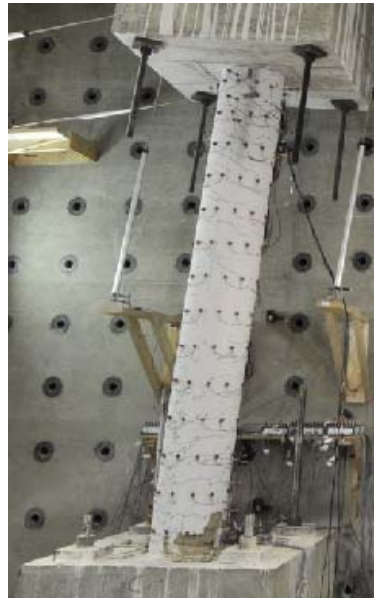
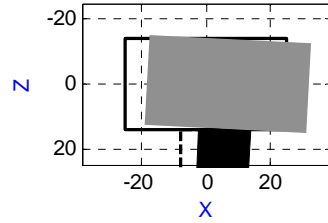
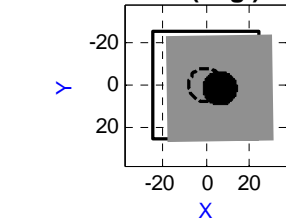
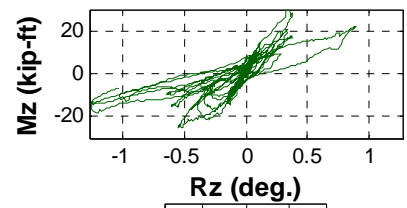
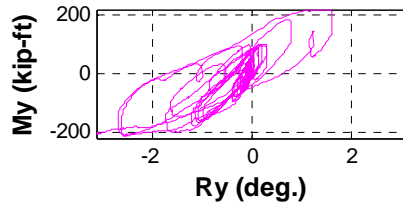
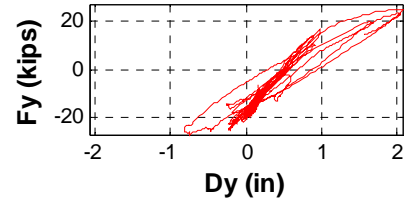
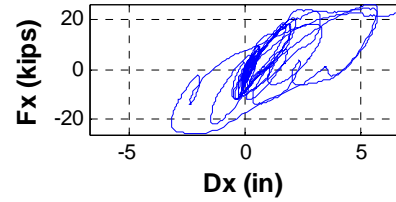
Time 39.55sec

Event: Audible cracking

Figure C.88 Pier 2 Response at Step 4055



	Loads (kip,kip-ft)		Def. (in,deg)	
Fx	22.5342	Dx	6.7053	
Fy	14.7156	Dy	1.5569	
Fz	137.2759	Dz	0.0198	
Mx	31.0872	Rx	0.1069	
My	-205.7095	Ry	-3.1517	
Mz	-6.8442	Rz	-1.0374	



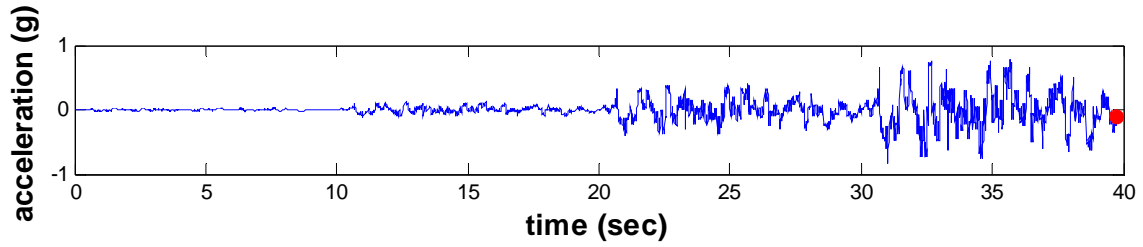
Pier 1

Step 4072

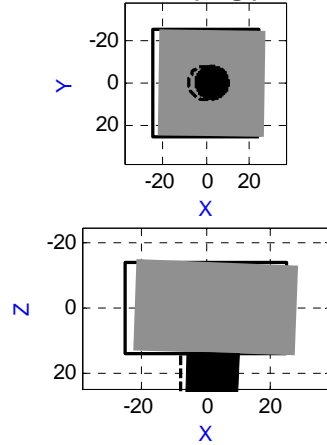
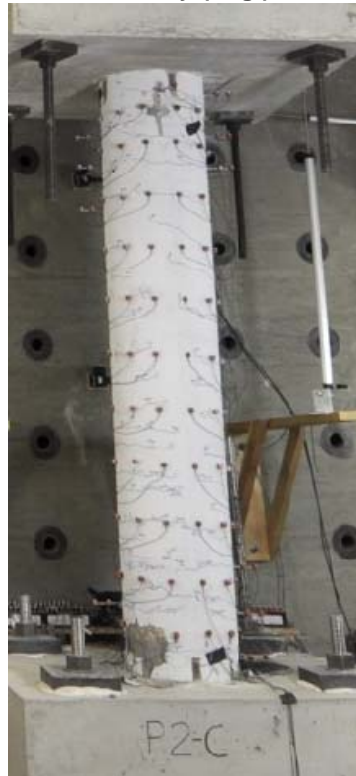
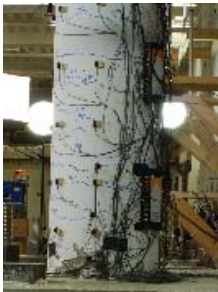
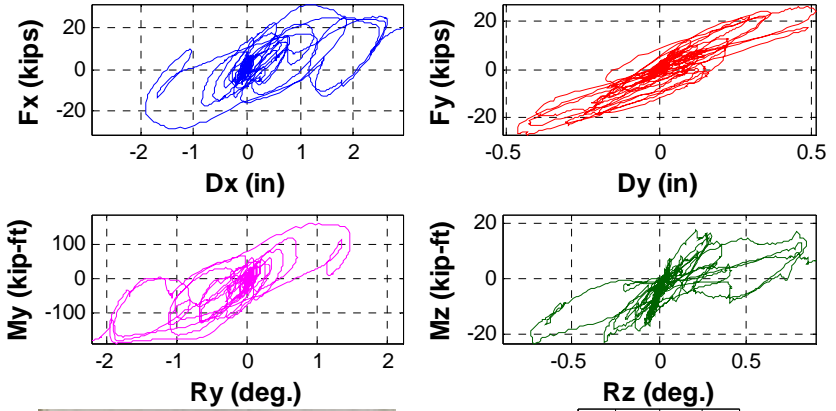
Time 39.72sec

Event: End of Hybrid Simulation

Figure C.89 Pier 1 Response at Step 4072



	Loads (kip,kip-ft)	Def. (in,deg)
Fx	20.0369 Dx	2.9219
Fy	-15.6754 Dy	-0.1832
Fz	61.6710 Dz	-0.0911
Mx	-20.7938 Rx	0.4938
My	-185.6476 Ry	-2.2309
Mz	6.2241 Rz	0.8953



Pier 2

Step 4072

Time 39.72sec

Event: End of Hybrid Simulation

Figure C.90 Pier 2 Response at Step 4072

APPENDIX D. OVERVIEW OF INITIAL ANALYTICAL MODEL

An overview of the details of the analytical model prepared in Zeus-NL is presented in this appendix. This model was used to assess the anticipated global response of the bridge. The deck described is used in the hybrid simulation, and the full Zeus-NL model including analytical piers and abutments is referred to as the initial uncalibrated model.

D.1 Model Details

Described below is the bridge deck geometry and method of modeling an equivalent cross-section in Zeus-NL, as well as steel and concrete models and details on the abutments, including shear key with gap model.

- **Bridge Deck**

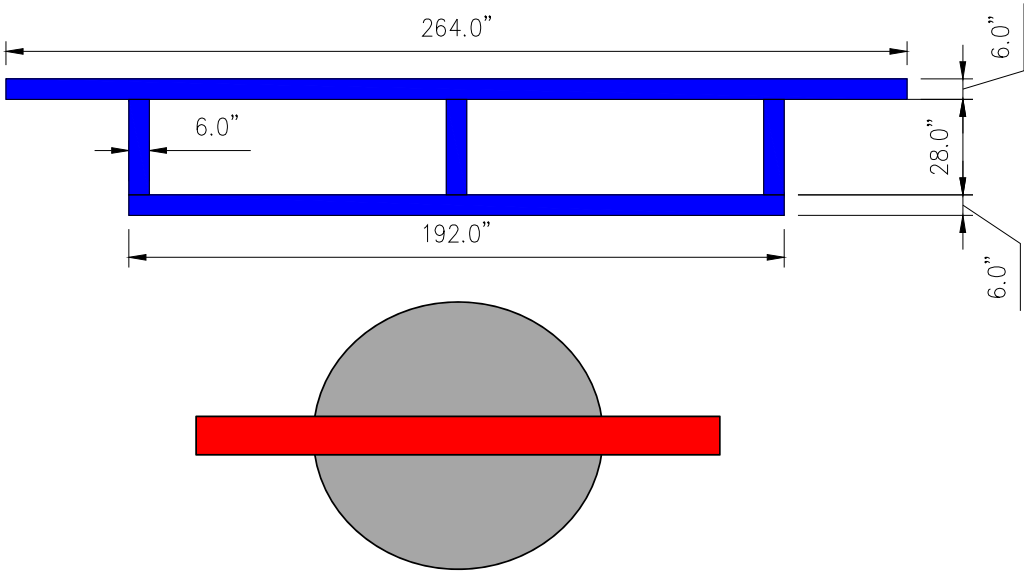


Figure D.1 Equivalent built-up section of deck model

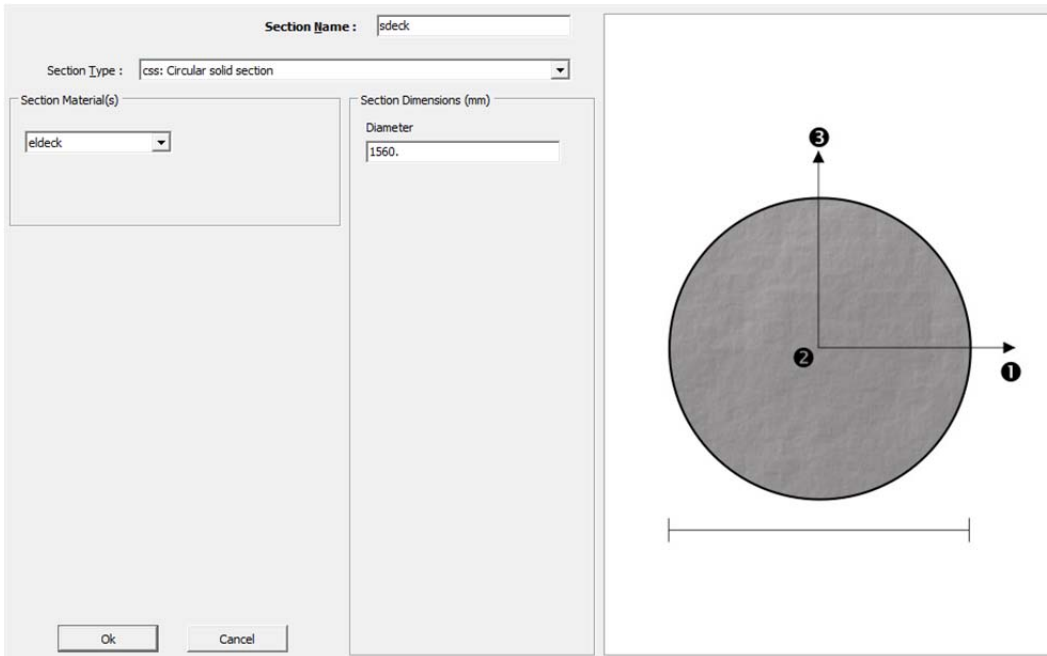


Figure D.2 Equivalent Deck Circular Section

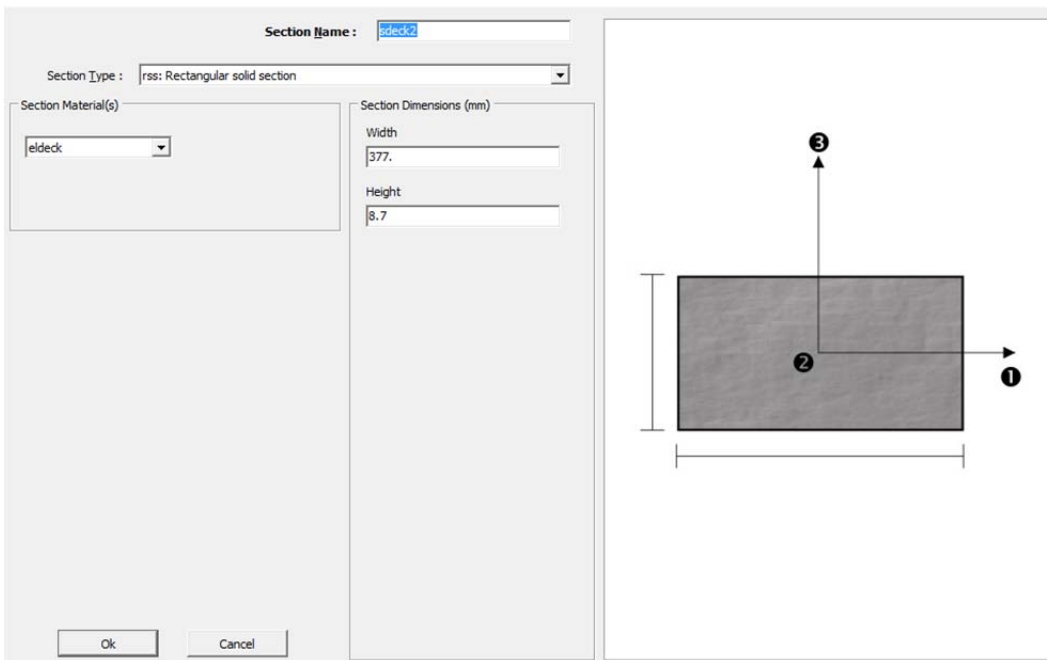


Figure D.3 Equivalent Deck Rectangular Section

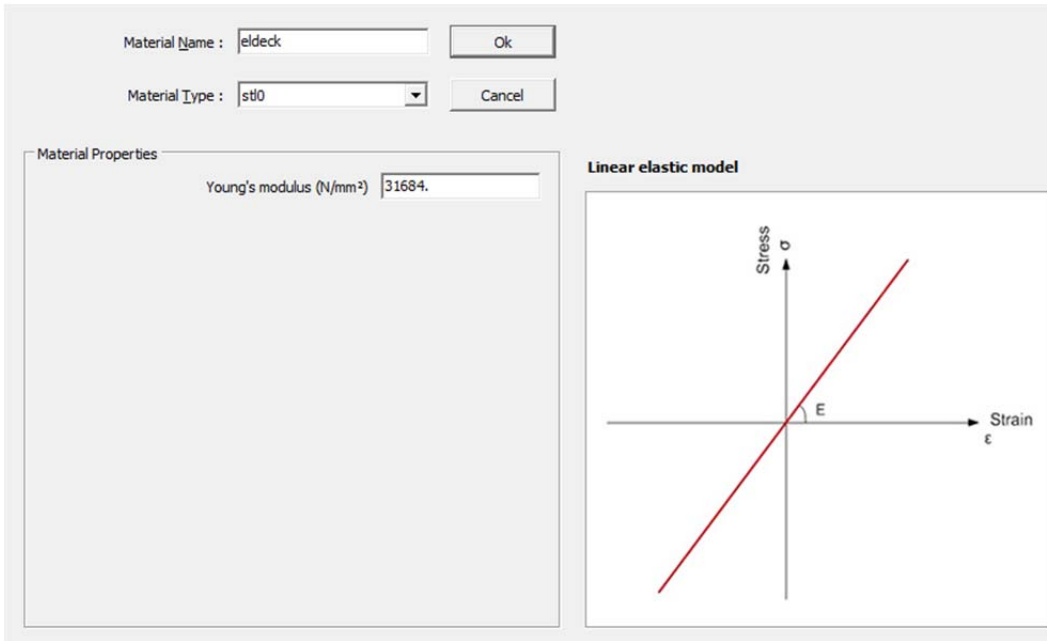


Figure D.4 Equivalent Deck Material Properties

- **Concrete Material Model**

- $f'_c = 6.5 \text{ ksi}$

- $f_t = 1.0 \text{ ksi}$

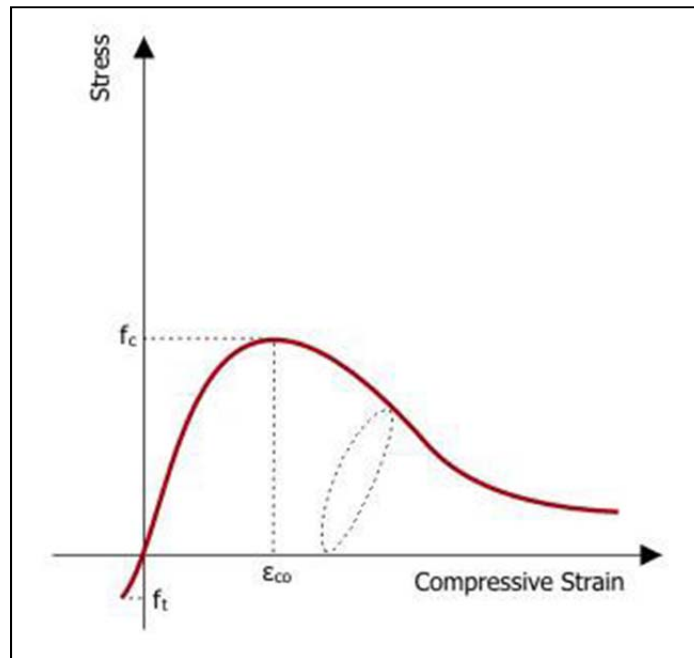


Figure D.5 – Concrete model - con2 (Mander et al.)

- **Steel Material Model**

- $E_s = 29000 \text{ ksi}$
- $f_y = 66 \text{ ksi}$
- $f_{ult} = 106 \text{ ksi}$

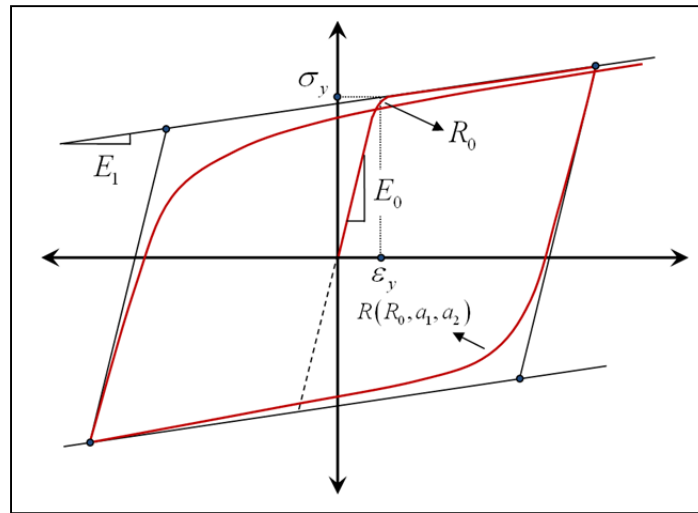


Figure D.6 Steel model - stl2 (Menegotto-Pinto)

- **Abutment Model**

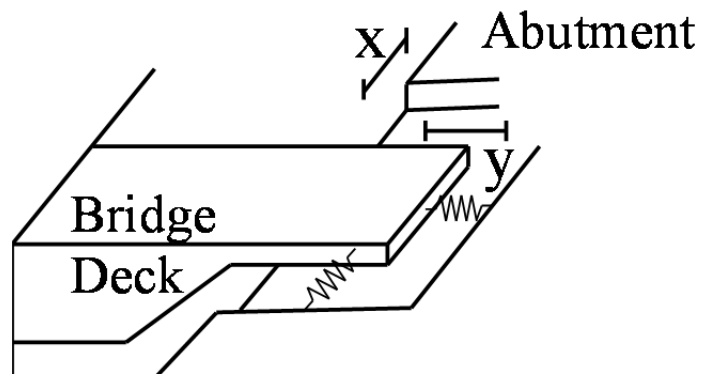


Figure D.7 Representation of abutment

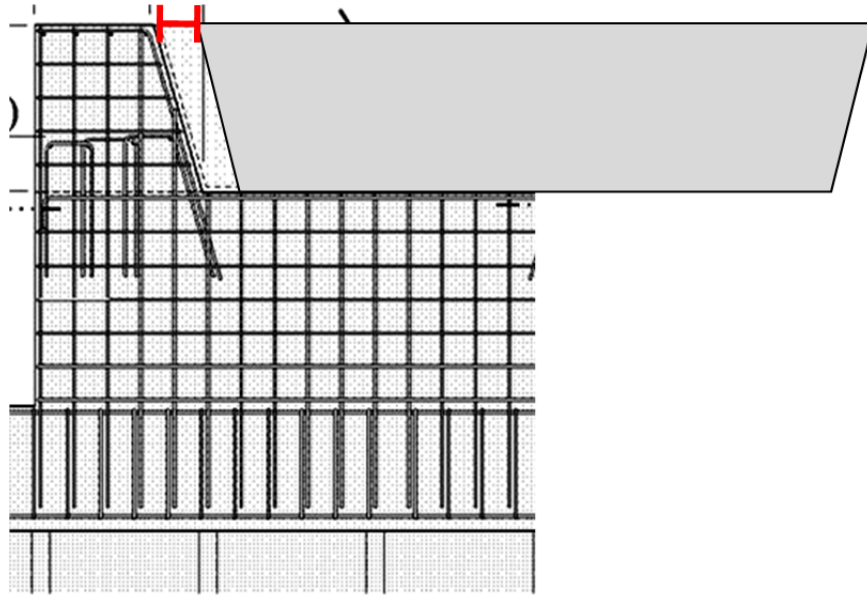


Figure D.8 Schematic of abutment gap

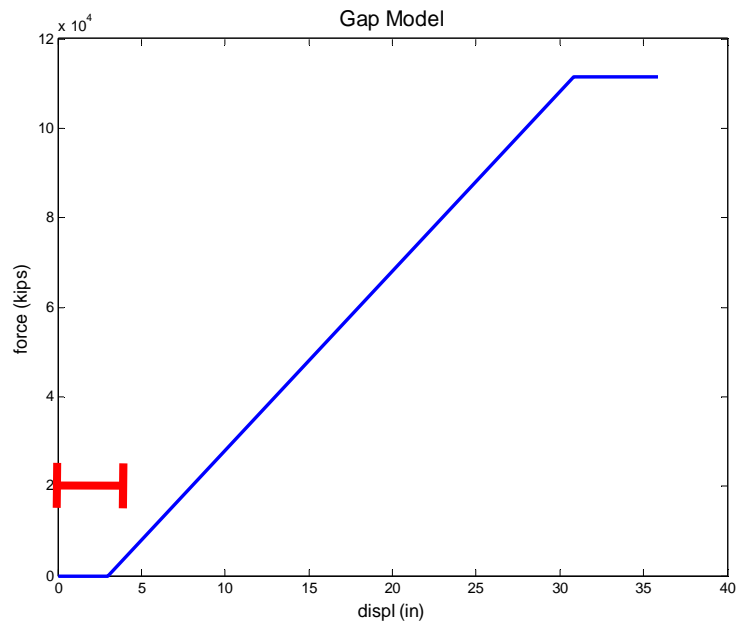


Figure D.9 Gap Model

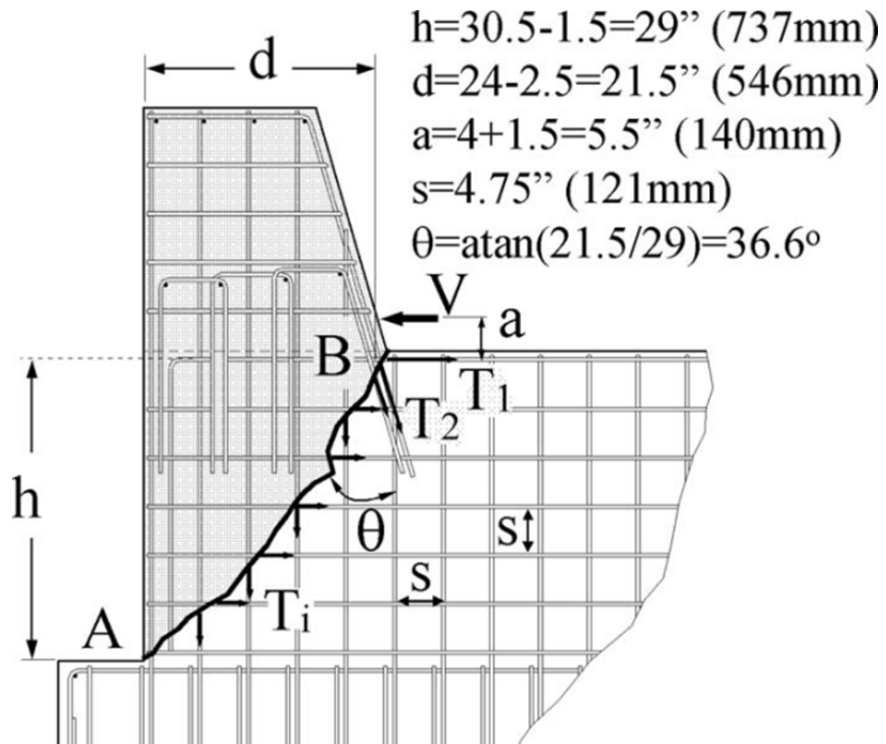


Figure D.10 Shear key model parameters

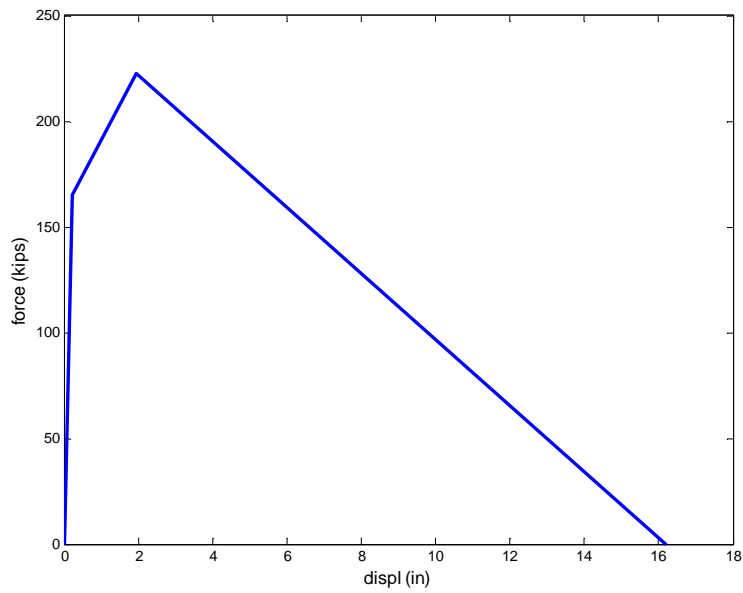


Figure D.11 Shear key model

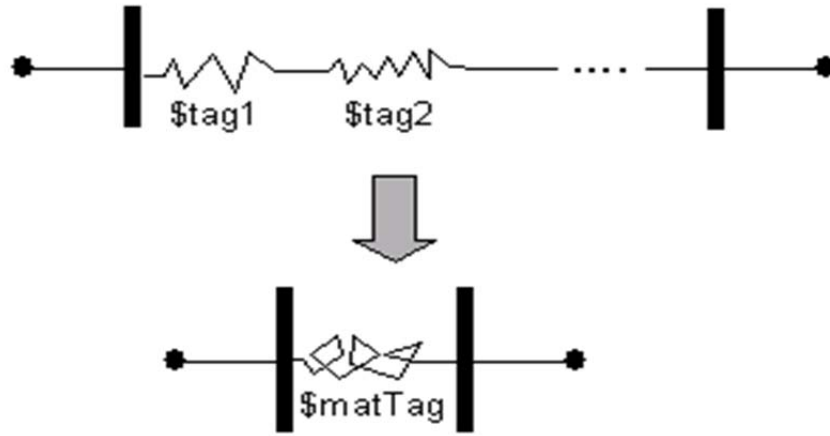


Figure D.12 Combined models in series

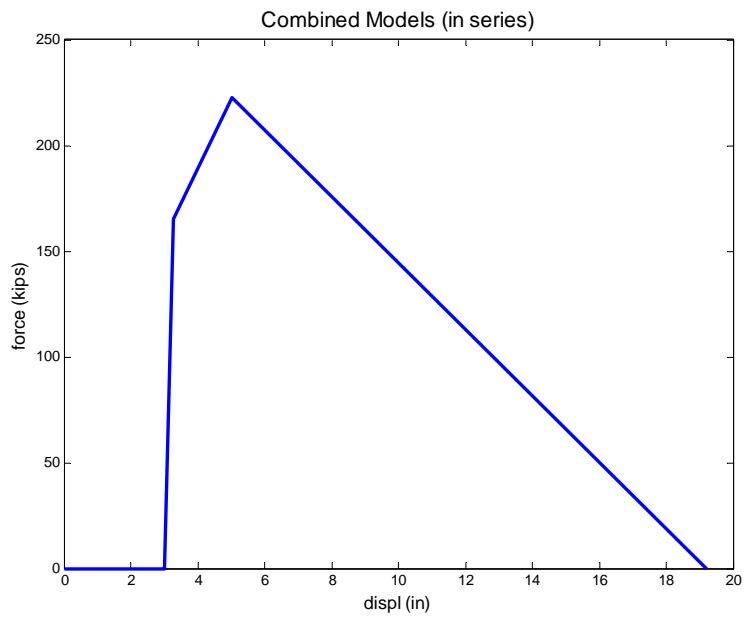


Figure D.13 Shear key with gap model combined in series

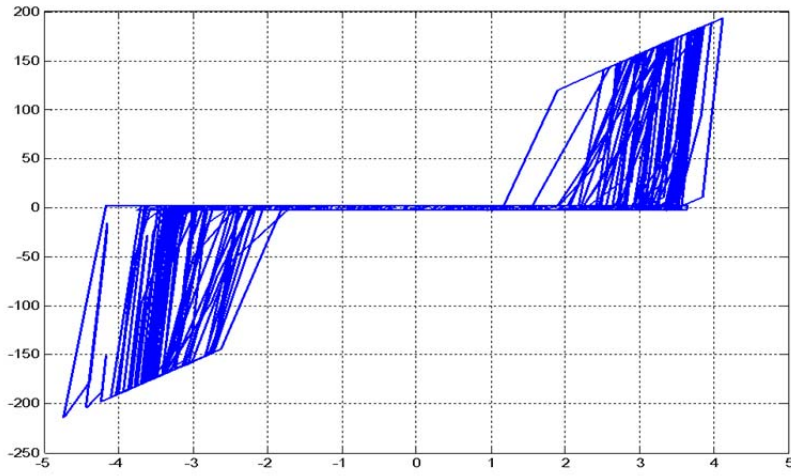


Figure D.14 Hysteretic response of shear key with gap model

- Overall Zeus-NL Model

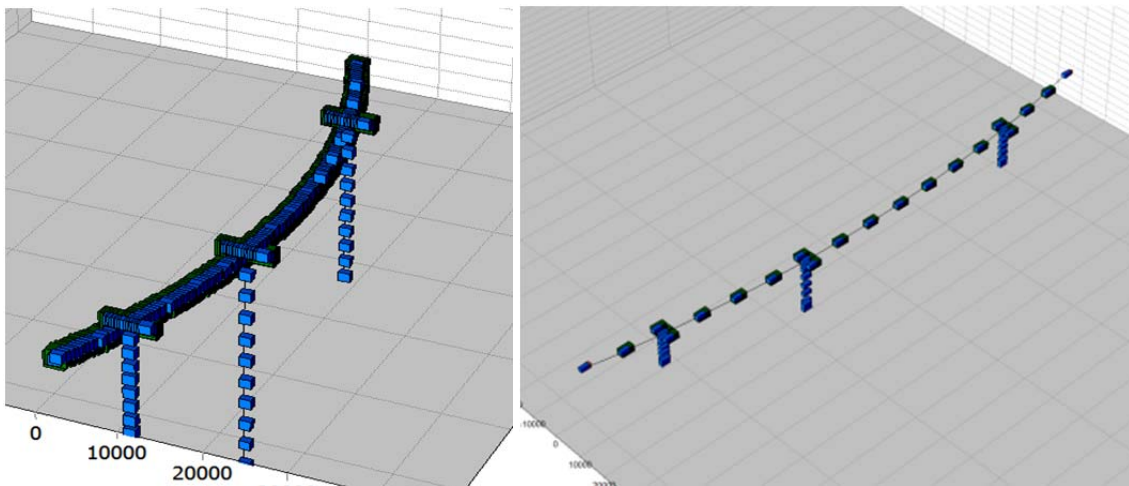


Figure D.15 Nodes, elements and masses of Zeus-NL model

D.2 Results of Preliminary Analysis

These results present the comparison of the uncalibrated analytical model described above with the experimental hybrid results that employed the same bridge deck and abutment models, while piers were tested experimentally. Therefore, the resulting errors observed are a result of assumptions and inadequacies in the performance of the bridge pier models. These plots are presented to highlight the promise toward achieving high quality calibration of the model using experimental hybrid data, and to identify the most significant areas for improvement in the existing uncalibrated model.

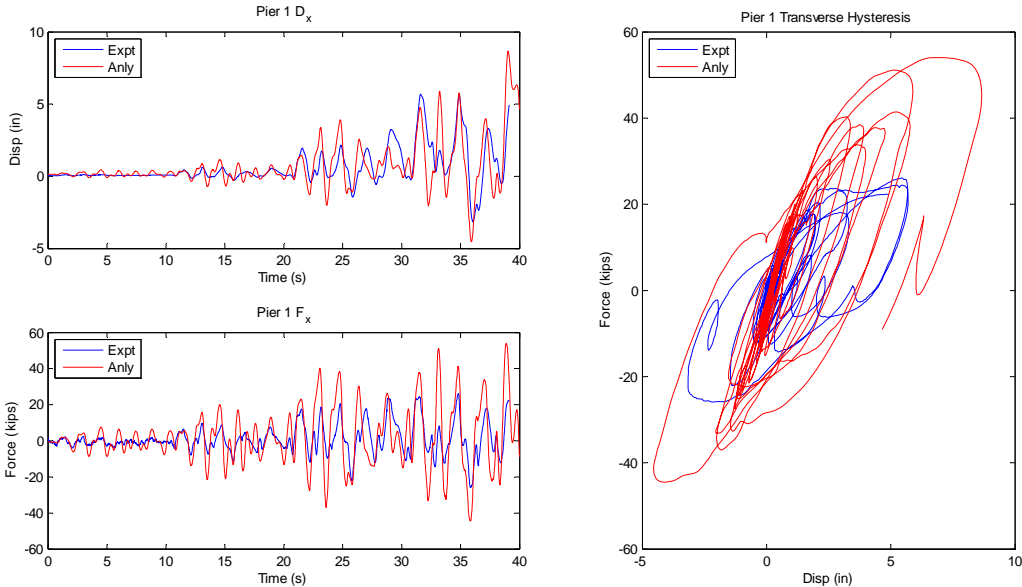


Figure D.16 Transverse comparison - Pier 1

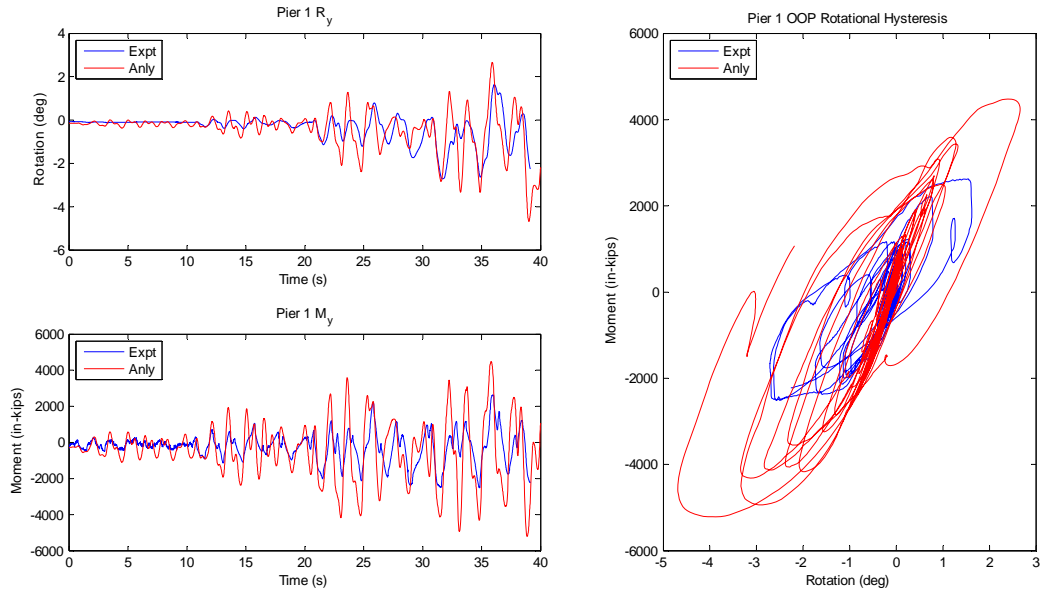


Figure D.17 Out-of-plane rotational comparison - Pier 1

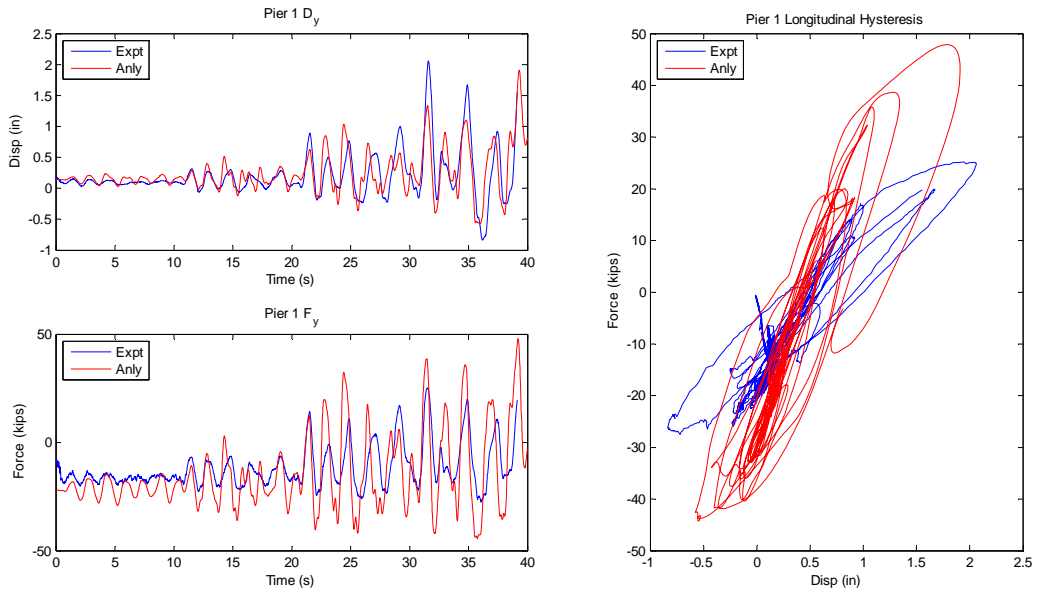


Figure D.18 Longitudinal comparison - Pier 1

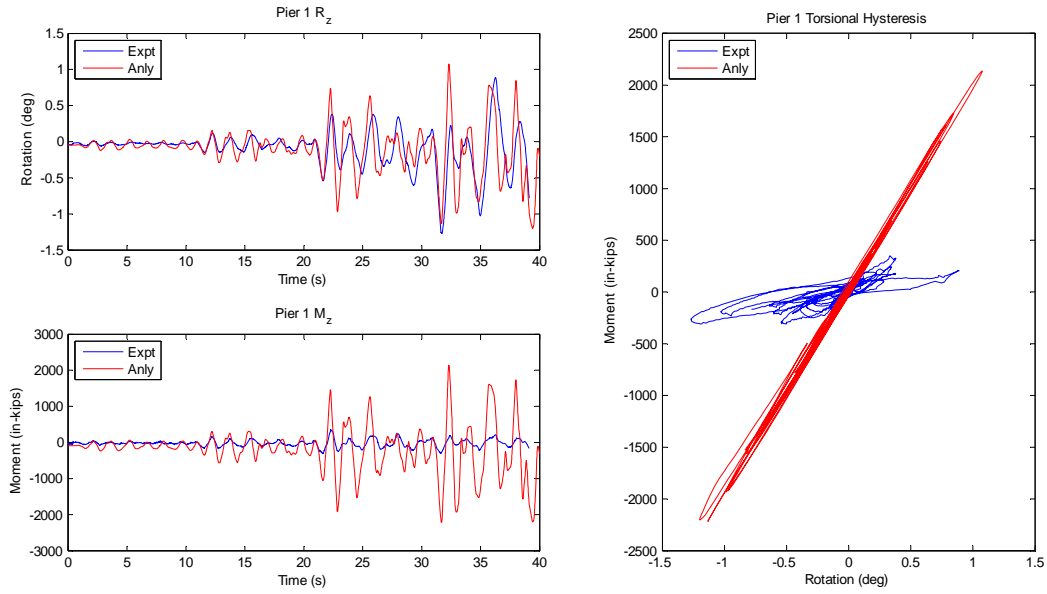


Figure D.19 Torsional comparison - Pier 1

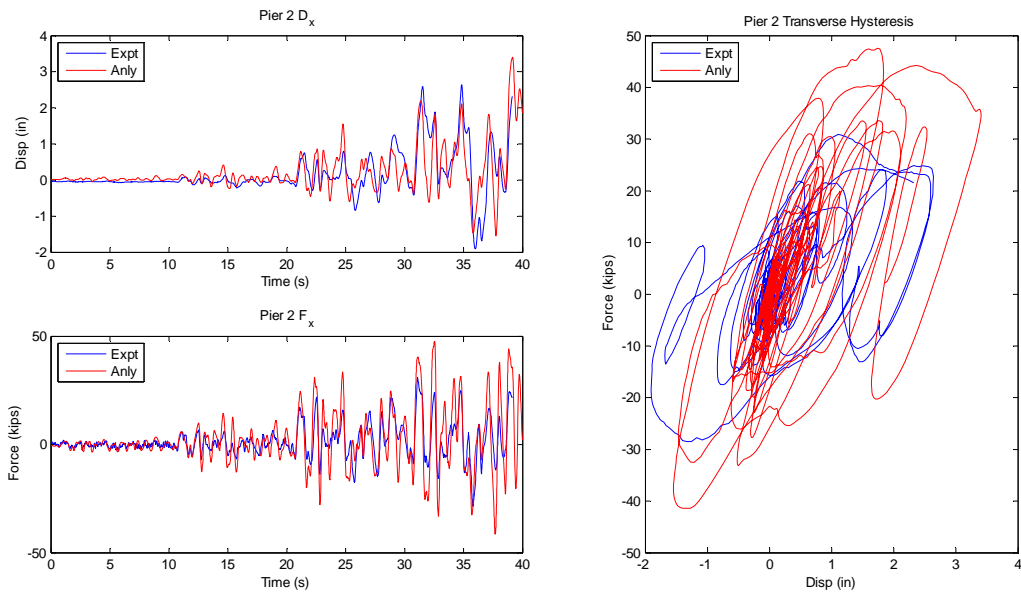


Figure D.20 Transverse comparison - Pier 2

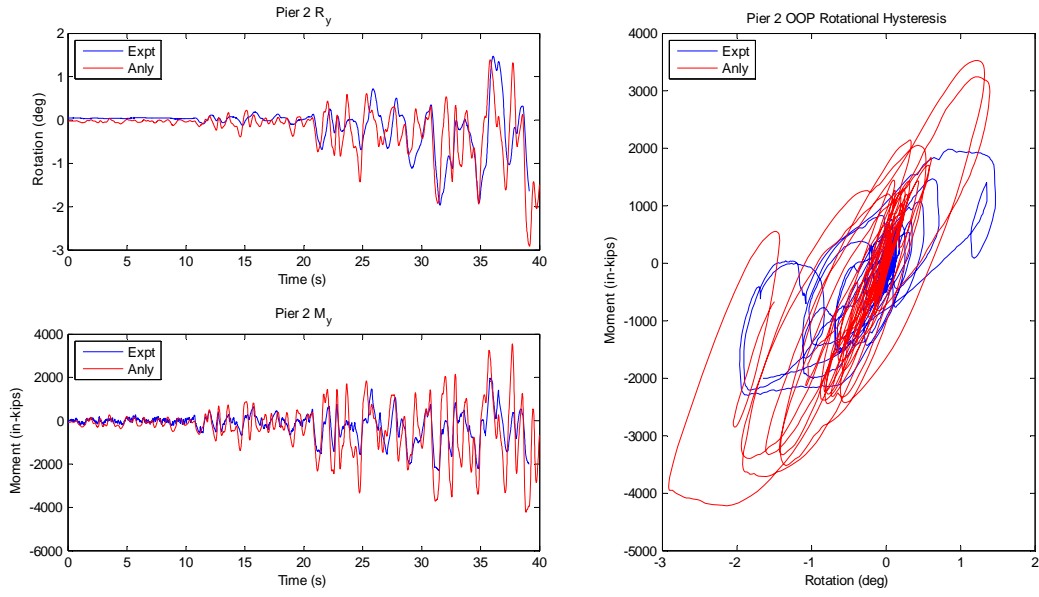


Figure D.21 Out-of-plane rotational comparison - Pier 2

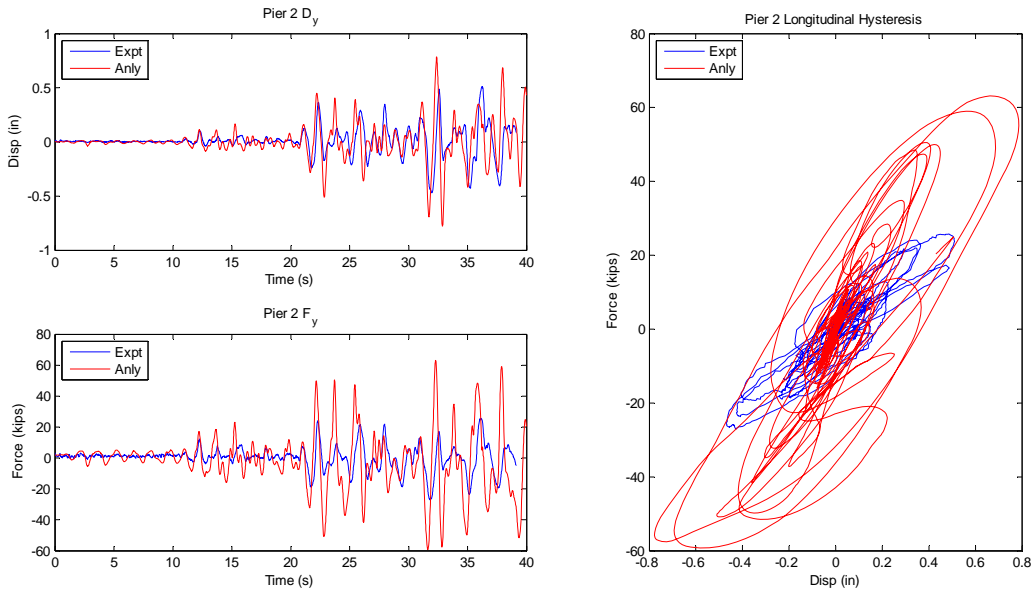


Figure D.22 Longitudinal comparison - Pier 2

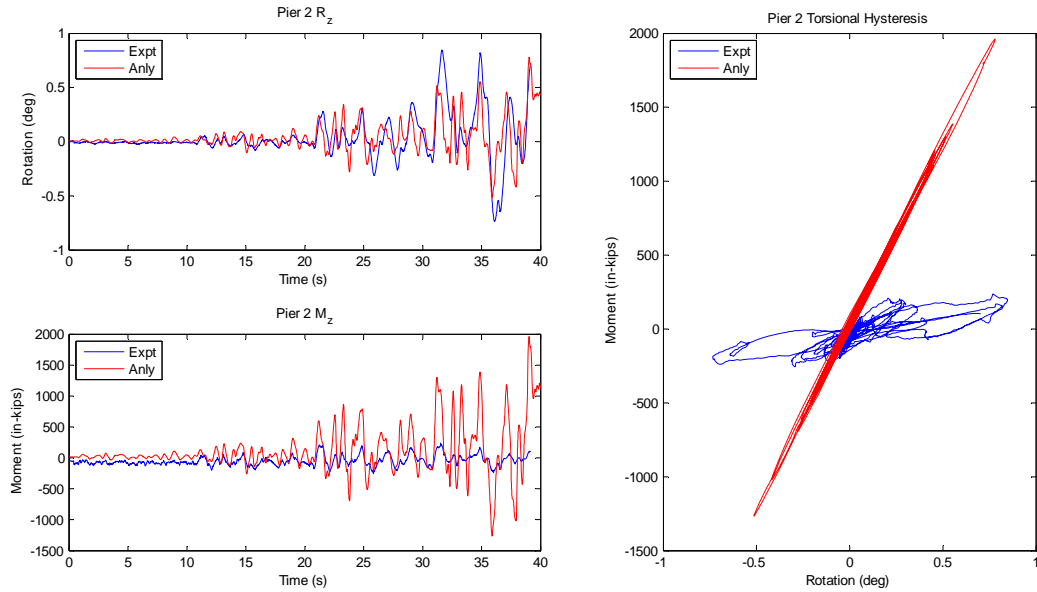


Figure D.23 Torsional comparison - Pier 2

D.3 Results with Adjustments for Hysteretic Damping

These results present the comparison of the experimental hybrid results to the uncalibrated analytical model with Rayleigh damping increased to provide 3% damping. This is an increase over the 1.2% damping provided in the results presented in the previous section. The increase is to account for hysteretic damping not captured in the initial uncalibrated model.

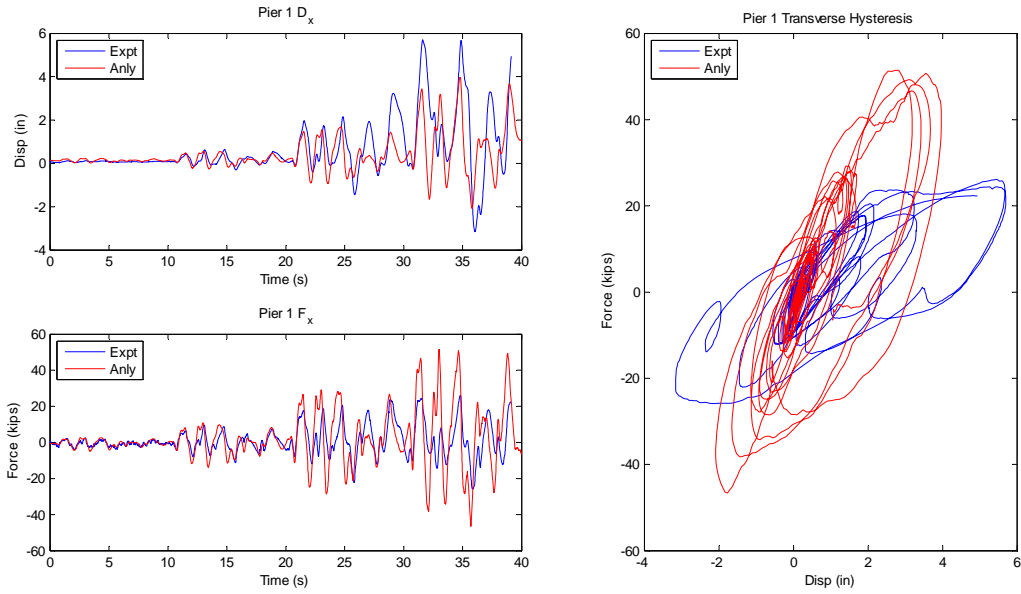


Figure D.24 Transverse comparison - Pier 1 (3% damping)

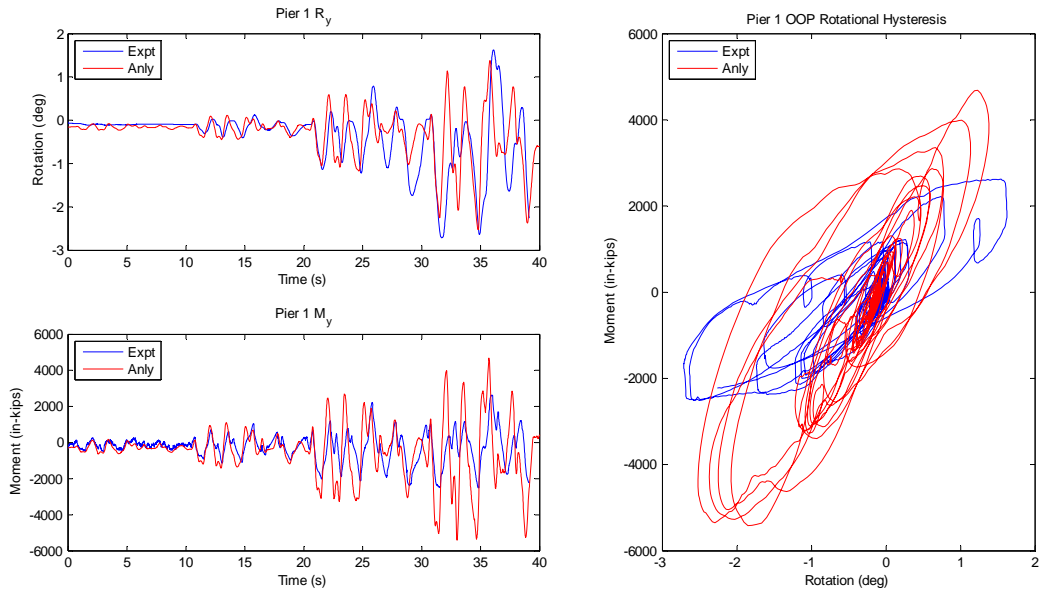


Figure D.25 Out-of-plane rotational comparison - Pier 1 (3% damping)

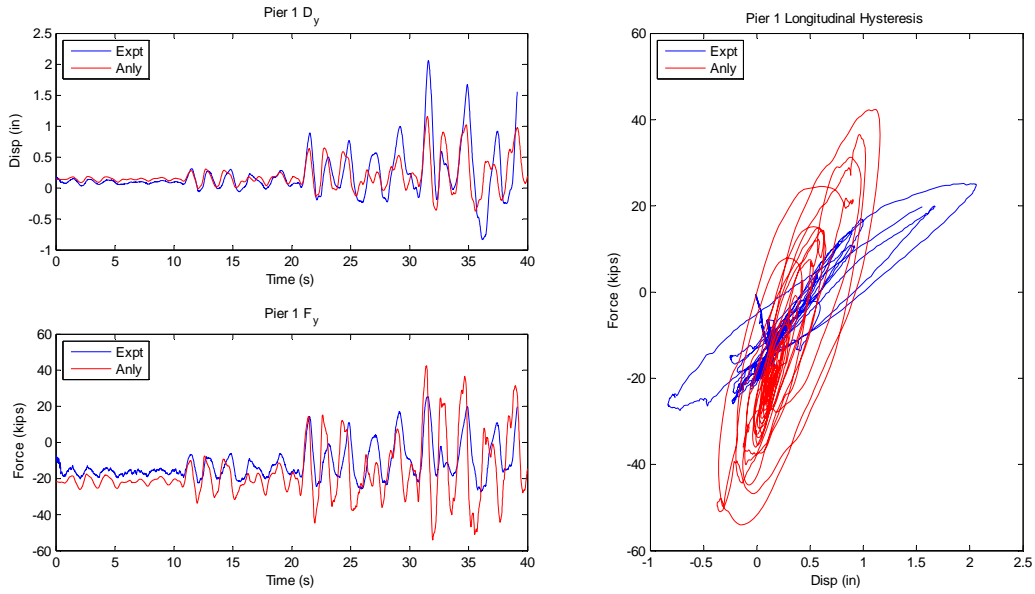


Figure D.26 Longitudinal comparison - Pier 1 (3% damping)

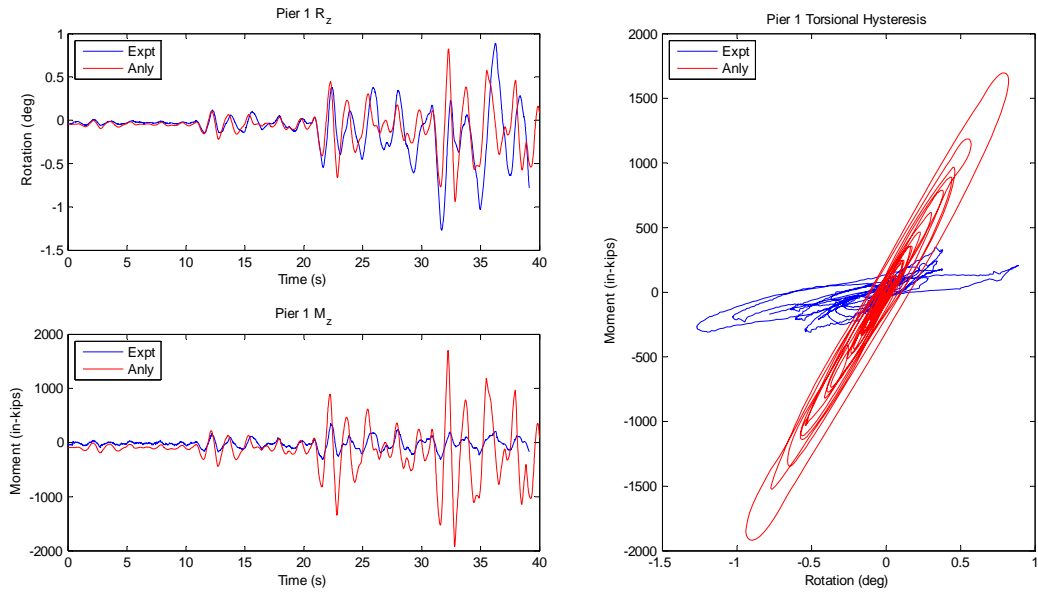


Figure D.27 Torsional comparison - Pier 1 (3% damping)

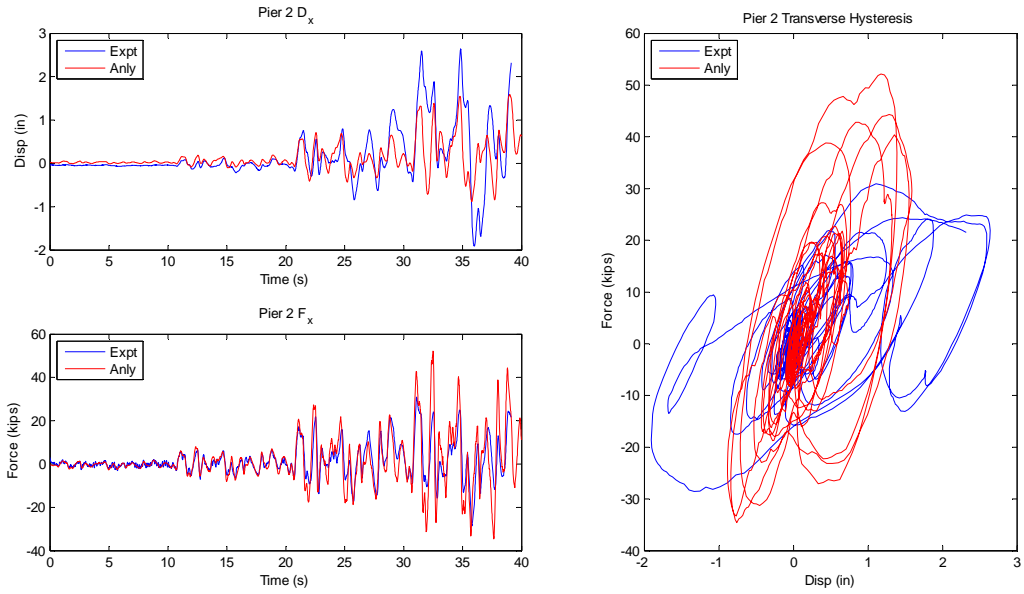


Figure D.28 Transverse comparison - Pier 2 (3% damping)

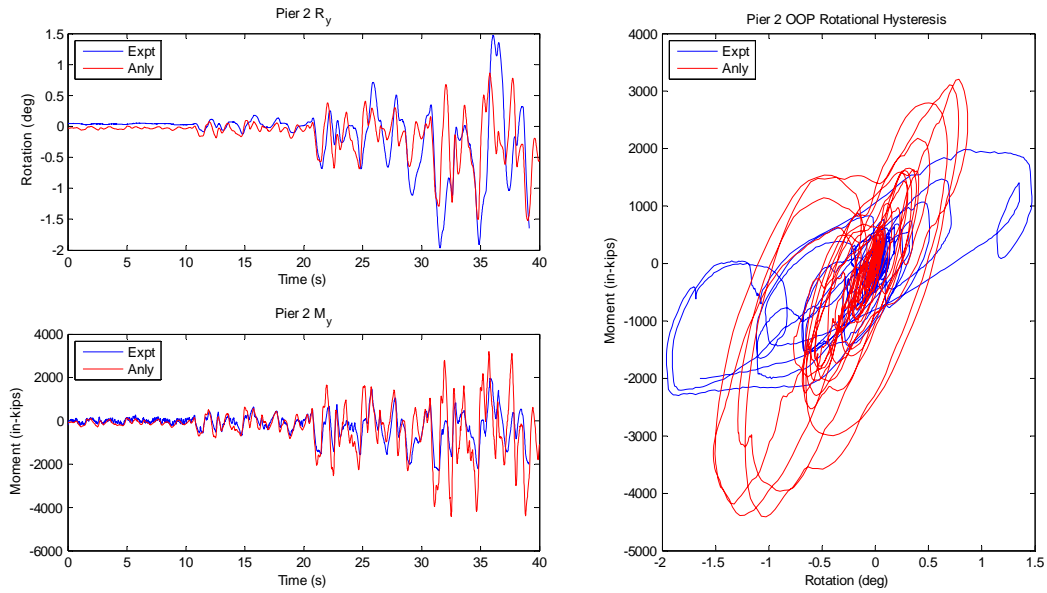


Figure D.29 Out-of-plane rotational comparison - Pier 2 (3% damping)

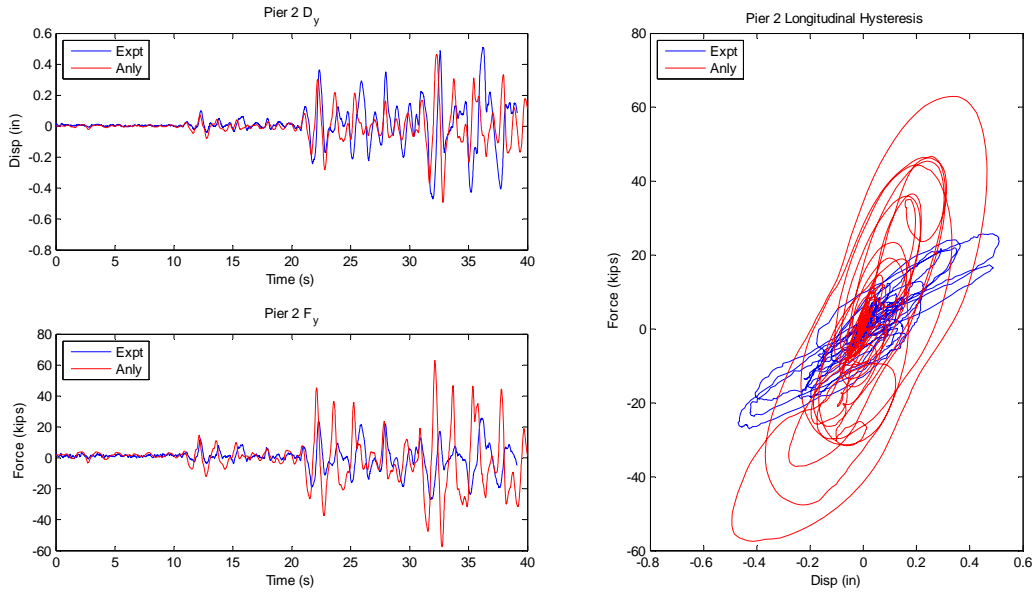


Figure D.30 Longitudinal comparison - Pier 2 (3% damping)

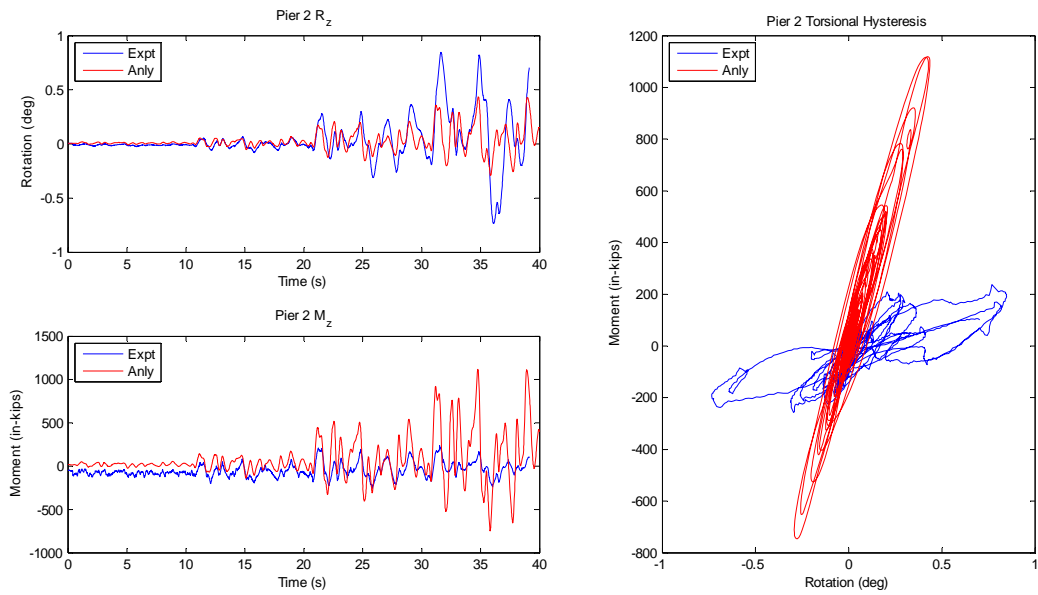


Figure D.31 Torsional comparison - Pier 2 (3% damping)

APPENDIX E. CALIBRATED MODEL DEVELOPMENT STAGES

Provided in the following sections of this appendix are the stiffness degradation behavior of the pier-cap interfaces used for making initial improvements to the model, the first generic model calibration iteration, and final calibrated model numerical data plotted against corresponding hybrid experimental data for demonstration of improvements in the behavior of the calibrated model.

E.1 Identifying Stiffness Degradation Behavior

In this section, the difference in derived 6DOF data from Krypton and 6DOF external sensor data of the caps is plotted against global actions to determine the stiffness degradation behavior of the pier-cap interfaces. Displacement jumps are due to loss of a Krypton target due to spalling concrete. The remaining response is approximated from the relative stiffness behavior at the pier-cap interface. The hysteretic flexure model used to model the rotational springs representing this behavior is presented.

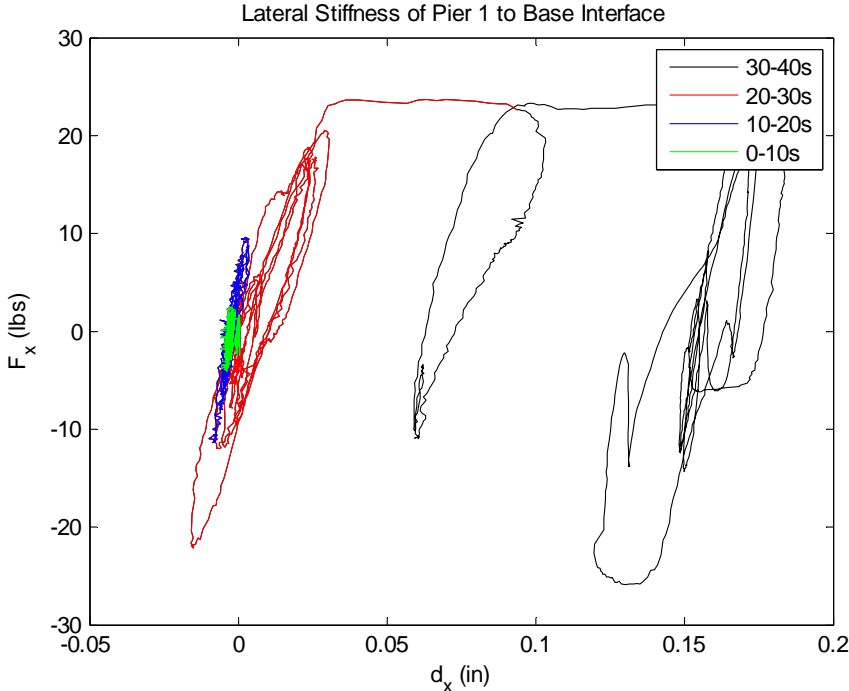


Figure E.1 Lateral Hysteresis for Examining Pier 1 Stiffness Degradation

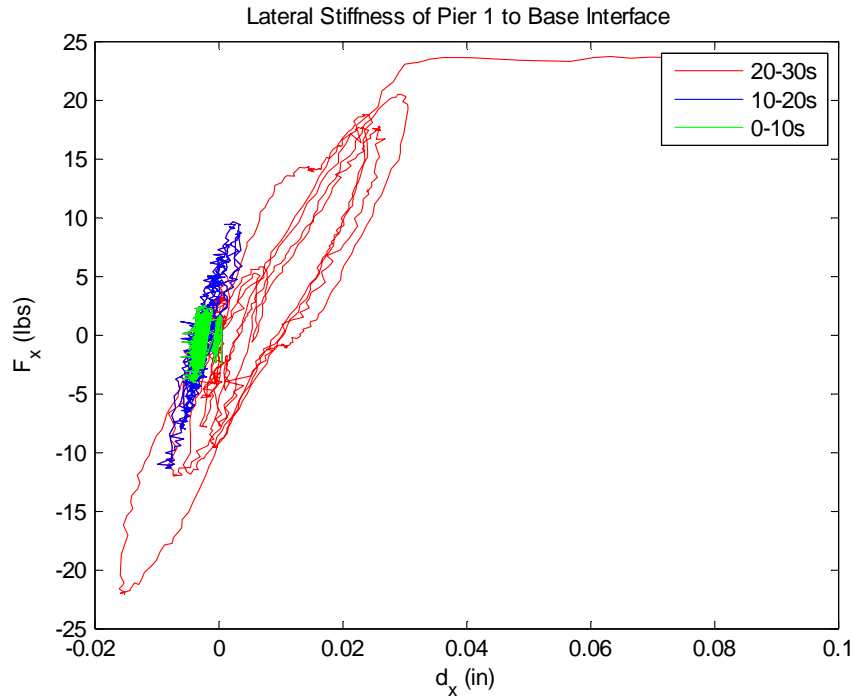


Figure E.2 Lateral Hysteresis for Examining Early Pier 1 Stiffness Degradation

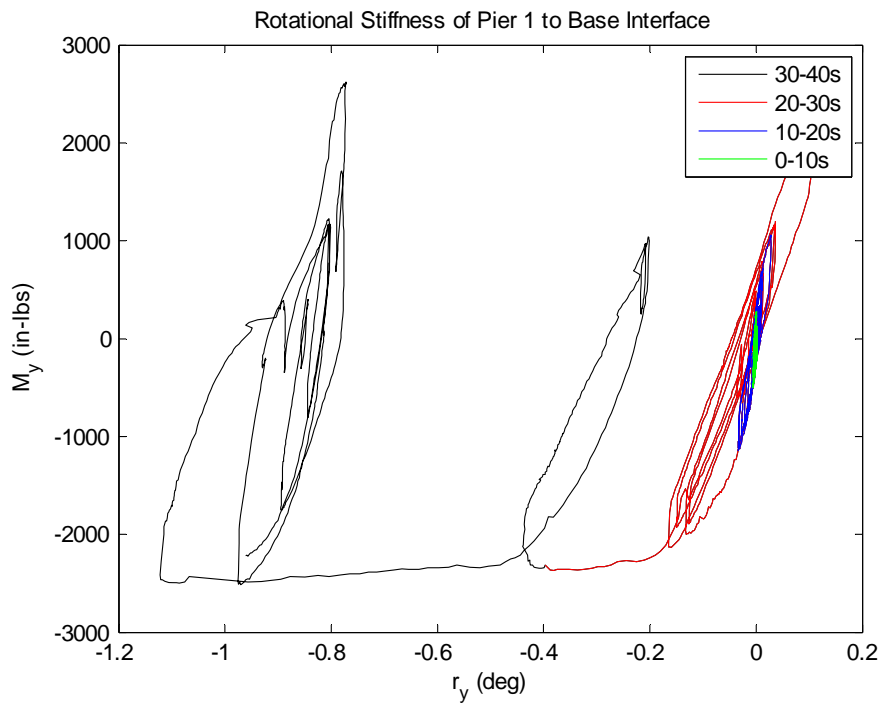


Figure E.3 Rotational Hysteresis for Examining Pier 1 Stiffness Degradation

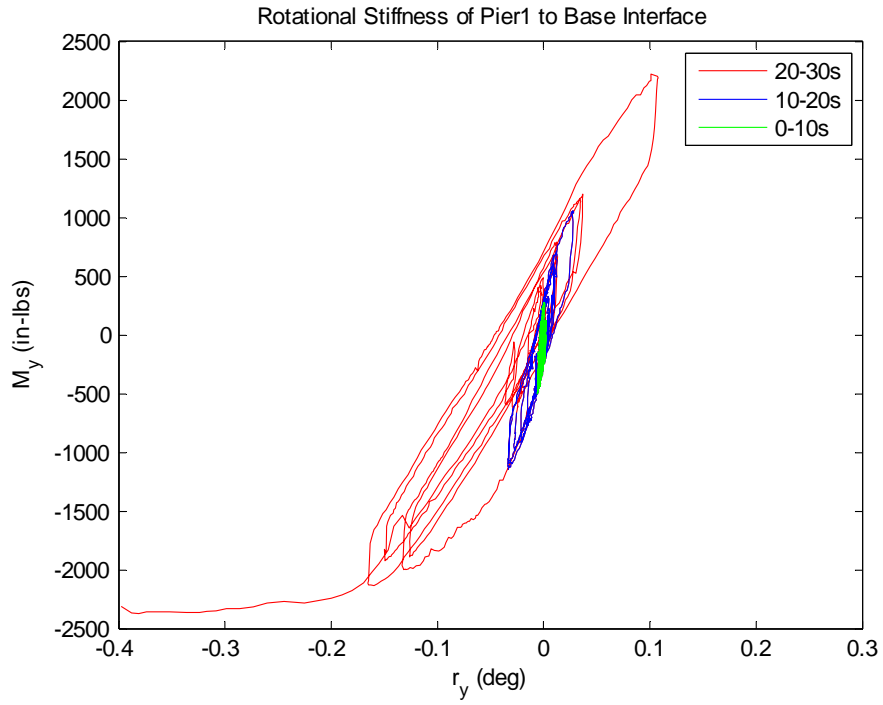


Figure E.4 Rotational Hysteresis for Examining Early Pier 1 Stiffness Degradation

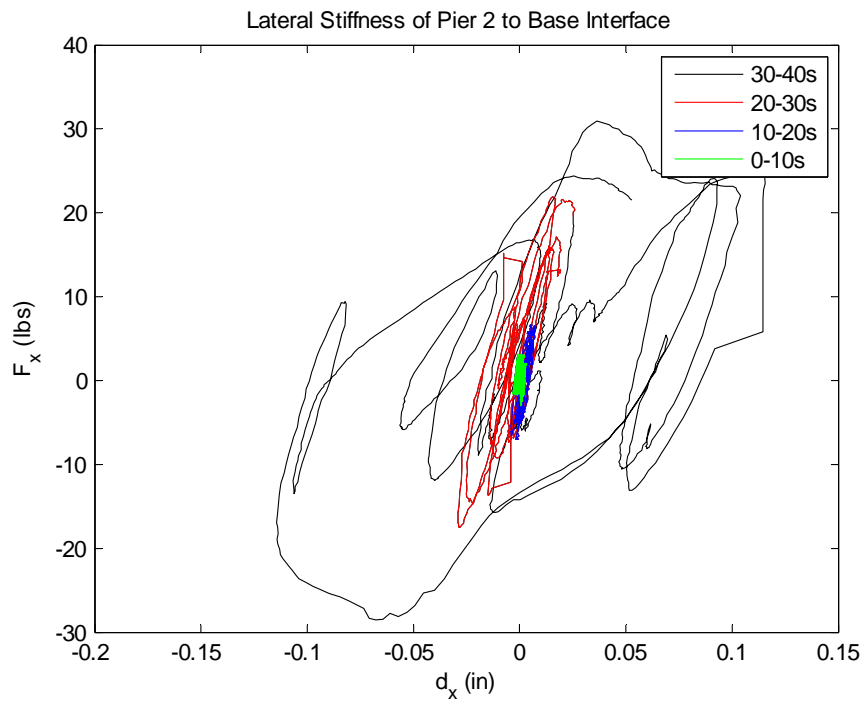


Figure E.5 Lateral Hysteresis for Examining Pier 2 Stiffness Degradation

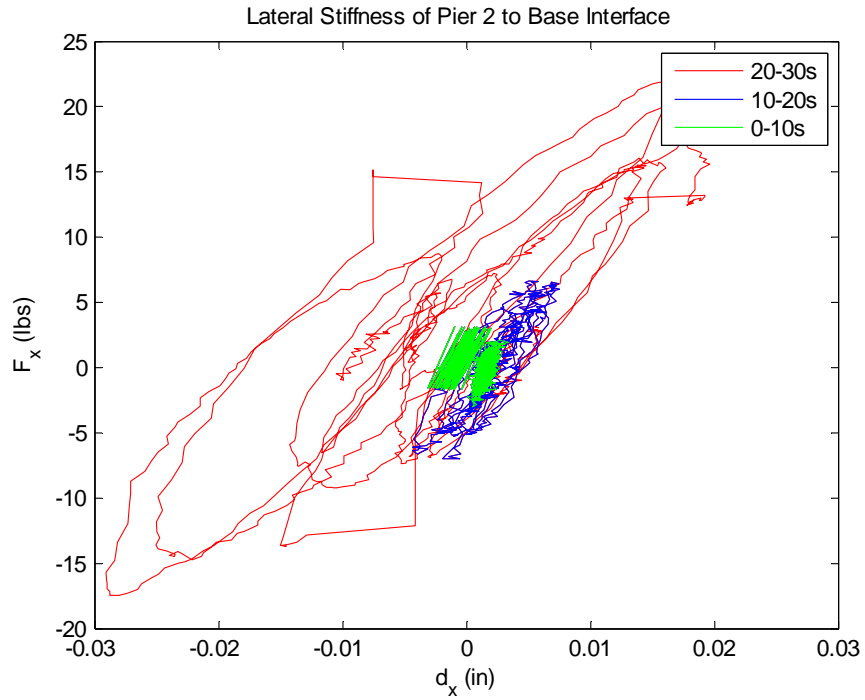


Figure E.6 Lateral Hysteresis for Examining Early Pier 2 Stiffness Degradation

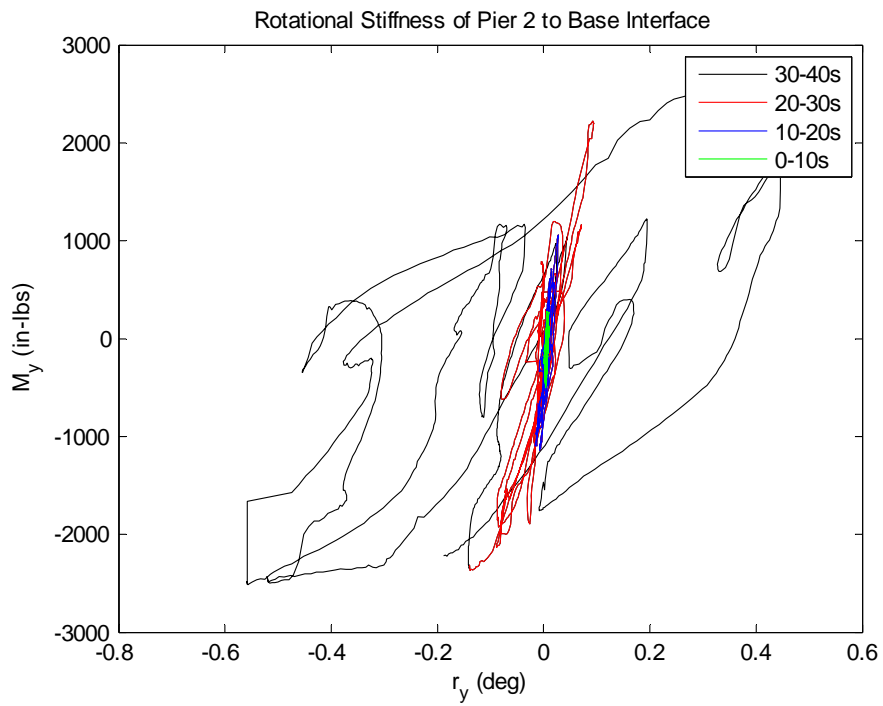


Figure E.7 Rotational Hysteresis for Examining Pier 2 Stiffness Degradation

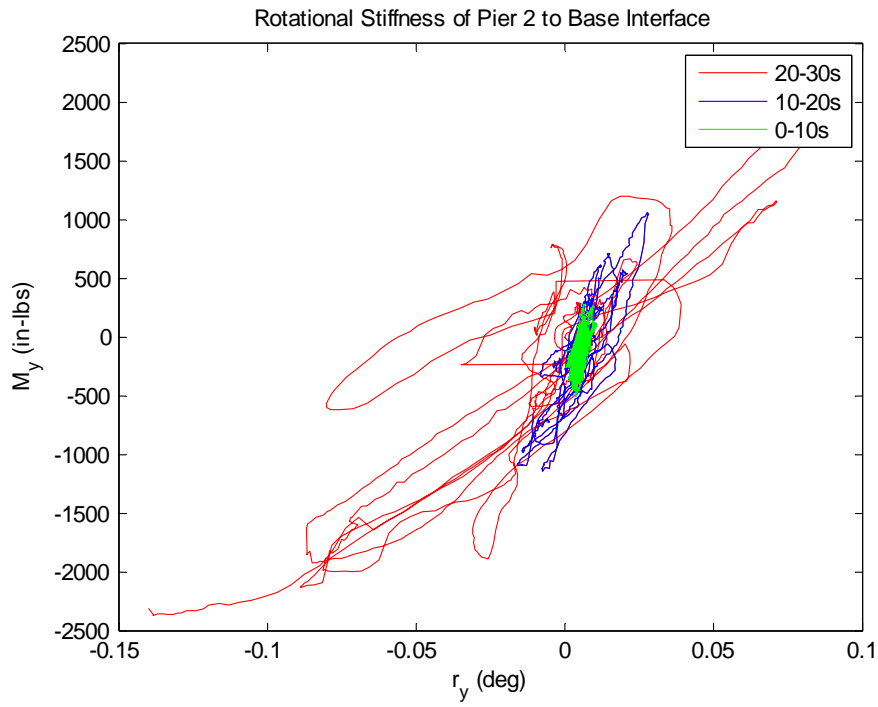
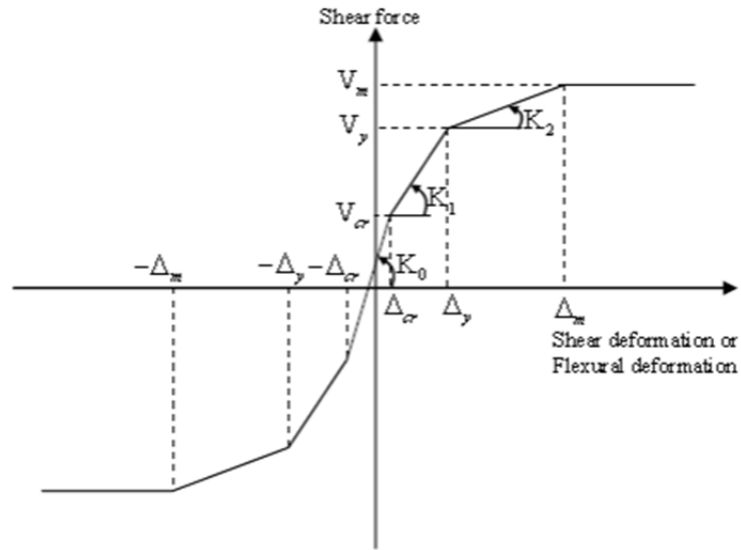


Figure E.8 Rotational Hysteresis for Examining Early Pier 2 Stiffness Degradation



- Initial flexural stiffness: K_0
- Flexural displacement at cracking: Δ_{cr}
- Shear force at cracking: V_{cr}
- Flexural stiffness after cracking: K_1
- Flexural displacement at yielding: Δ_y
- Shear force at yielding: V_y
- Flexural stiffness after yielding: K_2
- Flexural displacement at ultimate: Δ_m
- Shear force at ultimate: V_m
- Flexural stiffness after ultimate: 0.0

Figure E.9 Hysteretic flexure model under constant axial force spring model parameters

E.2 Sample Generic Calibration Results

The following comparisons between this iteration of the model calibration procedure and the experimental results is used to demonstrate the improvement that has been achieved through the inclusion of flexural rotational models and torsional models at the ends of the piers to model stiffness degradation of the pier-cap interfaces. In addition, the influence of a nonlinear torsional spring and an additional lateral spring are included. Following this calibration step for the overall model and full record, calibration procedures are performed for a given seismic input level and three separate calibrated models are developed, one for each limit state.

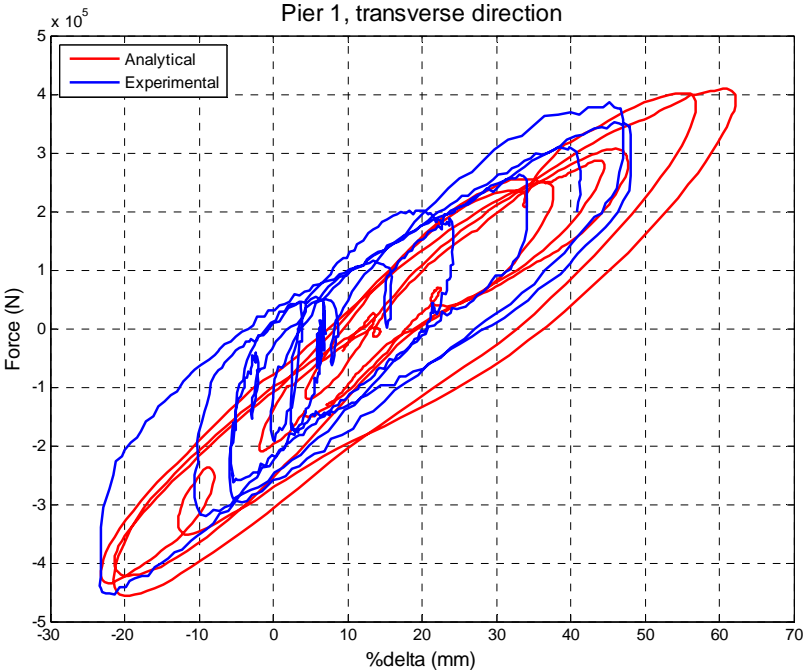


Figure E.10 Transverse Calibration - Slight Level

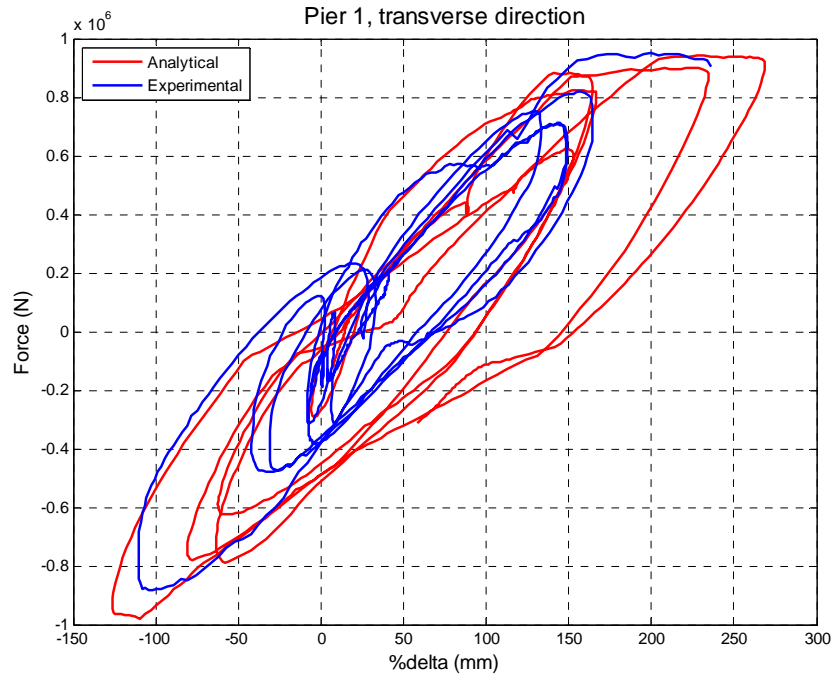


Figure E.11 Transverse Calibration - Moderate Level

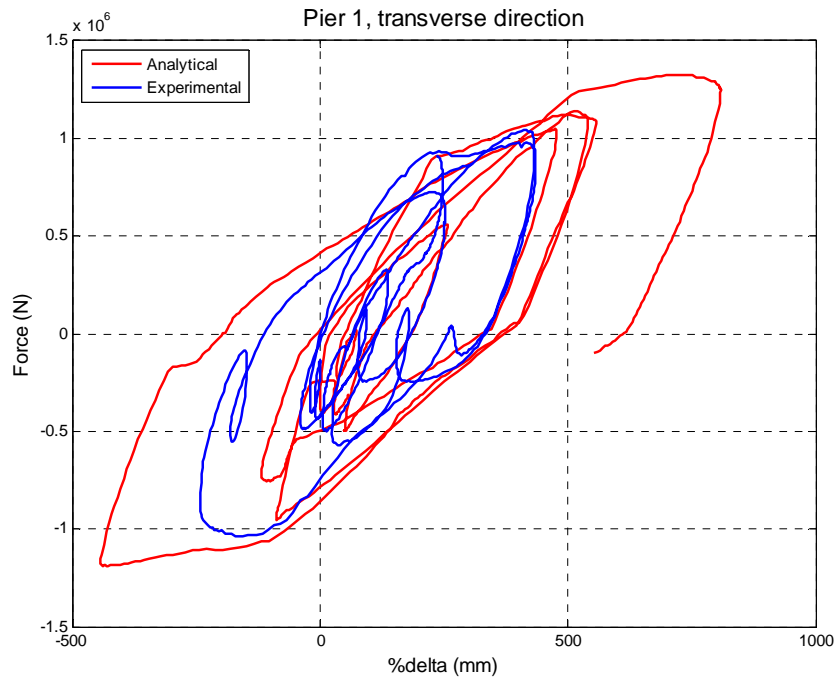


Figure E.12 Transverse Calibration - Severe Level

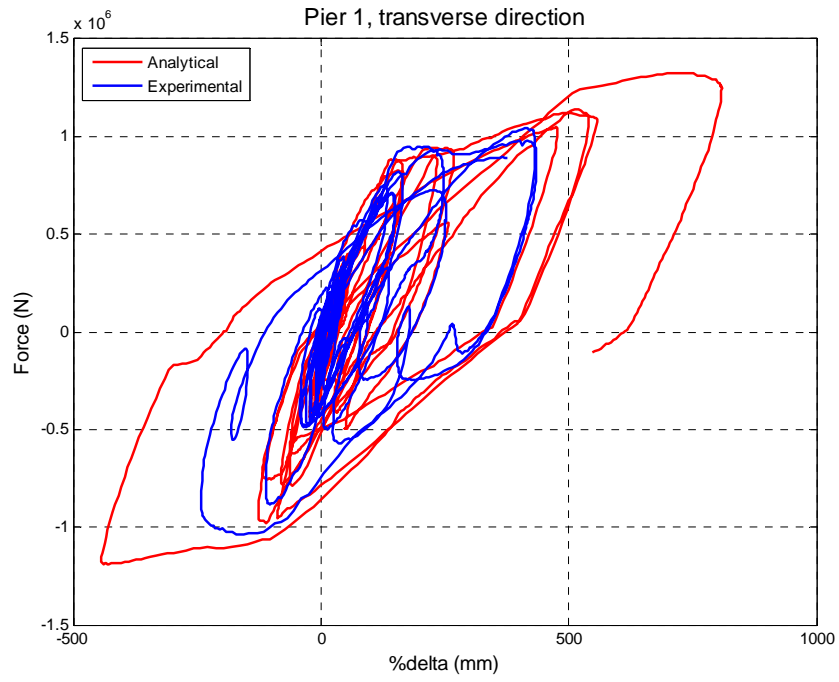


Figure E.13 Transverse Calibration - All Levels

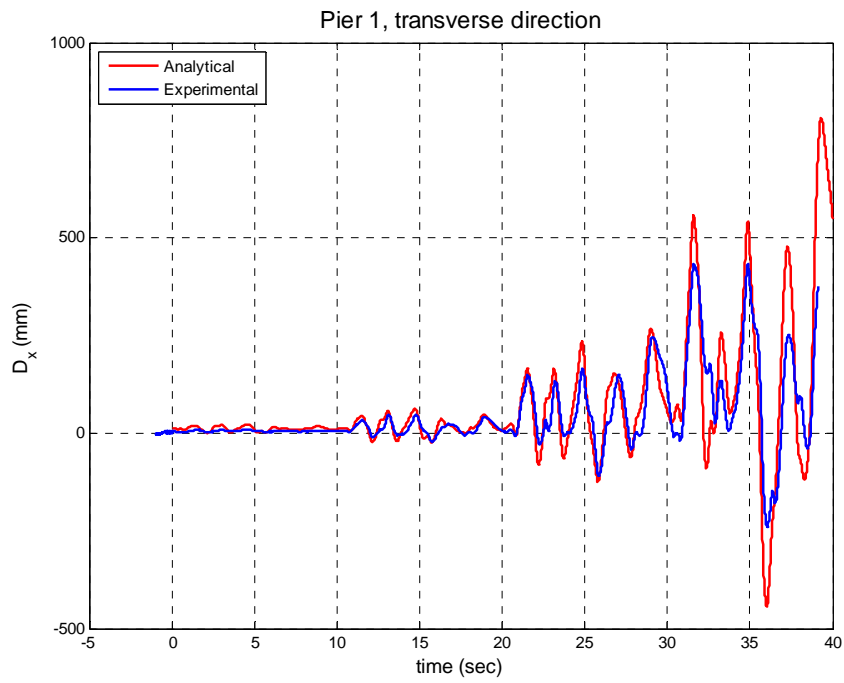


Figure E.14 Transverse Calibration - Displacement History

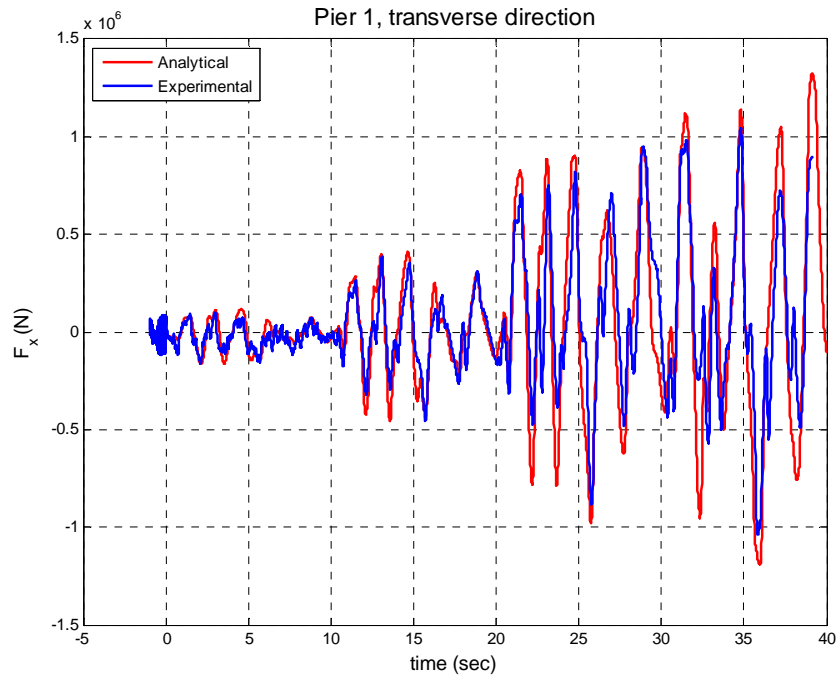


Figure E.15 Transverse Calibration - Force History

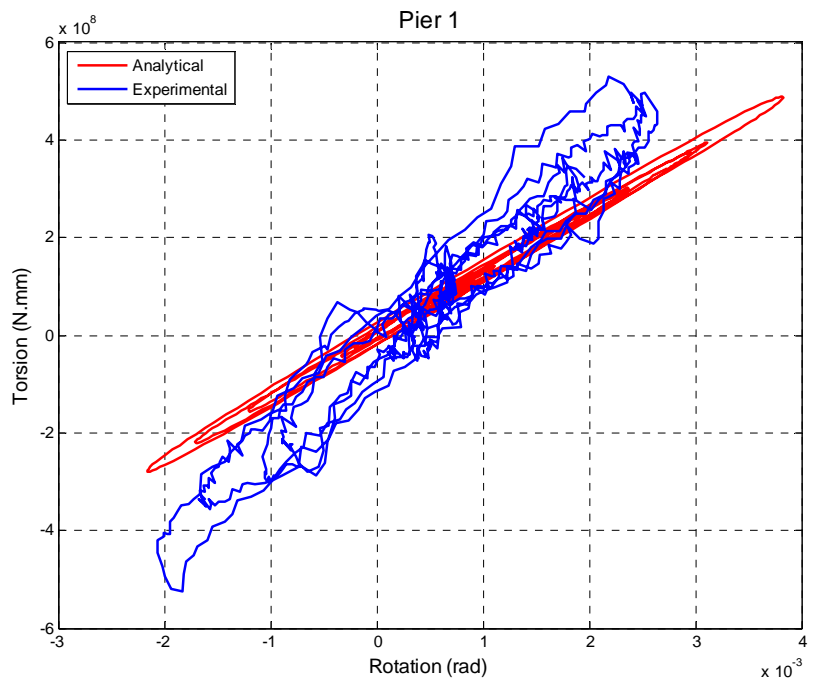


Figure E.16 Torsional Calibration - Slight Level

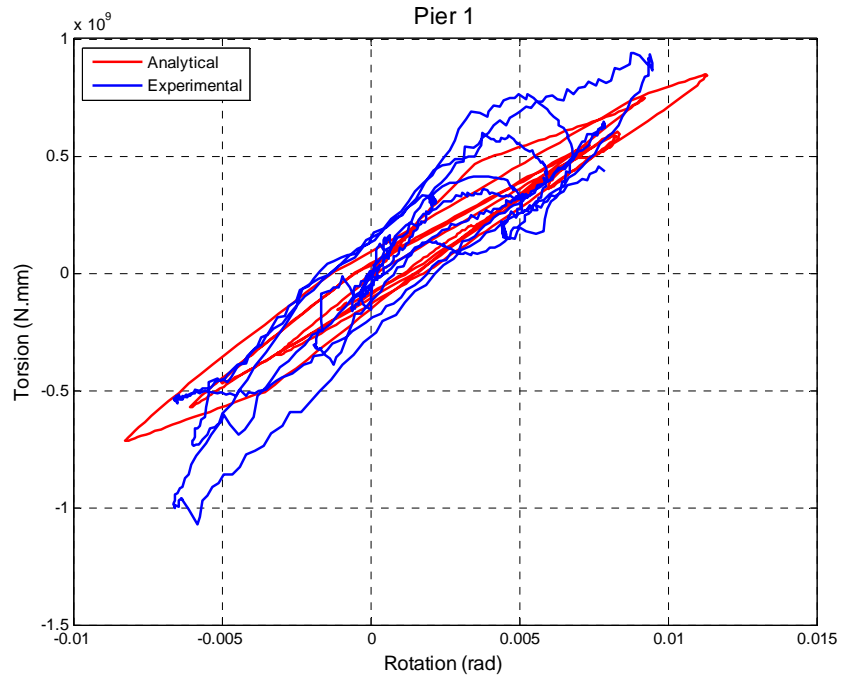


Figure E.17 Torsional Calibration - Moderate Level

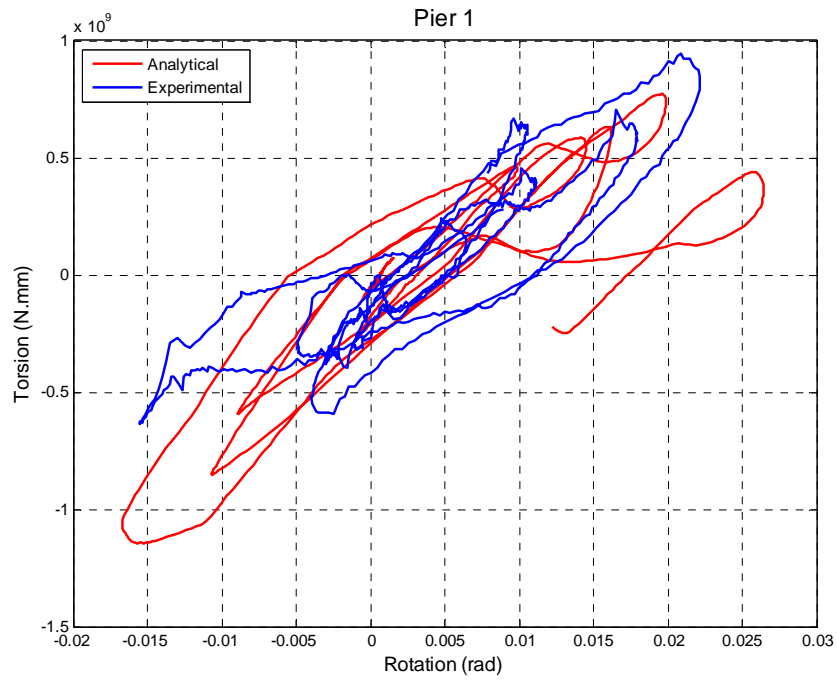


Figure E.18 Torsional Calibration - Severe Level

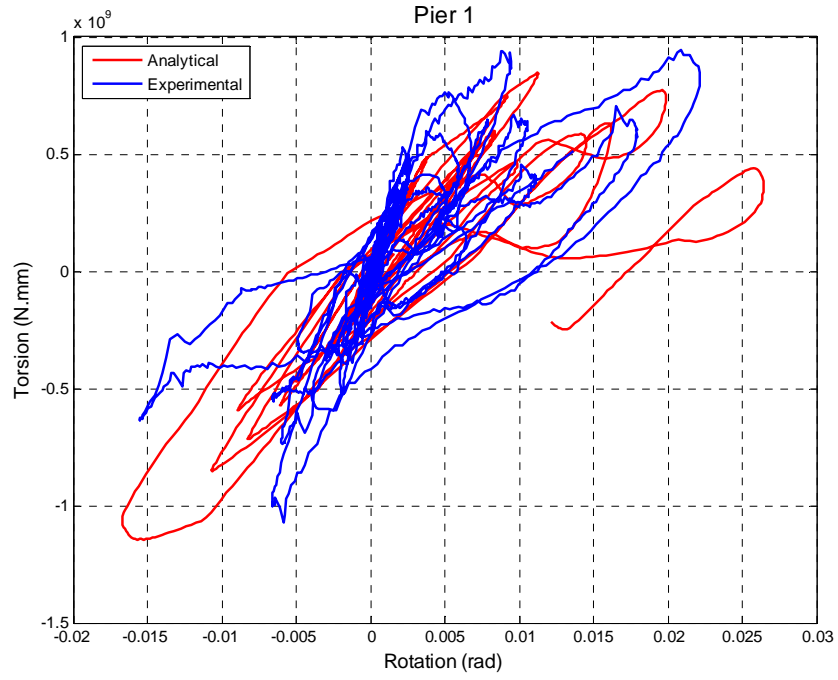


Figure E.19 Torsional Calibration - All Levels

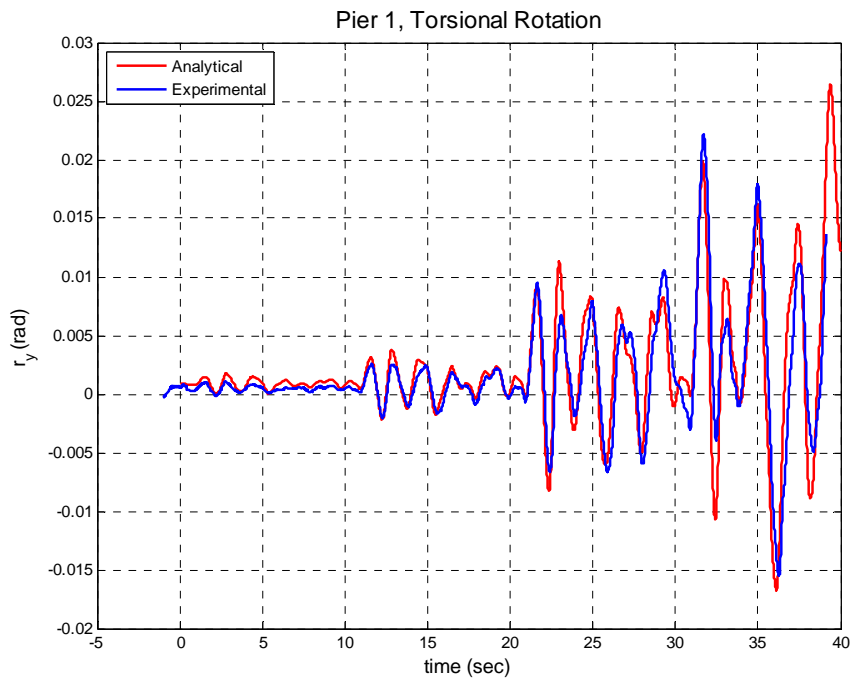


Figure E.20 Torsional Calibration - Rotation History

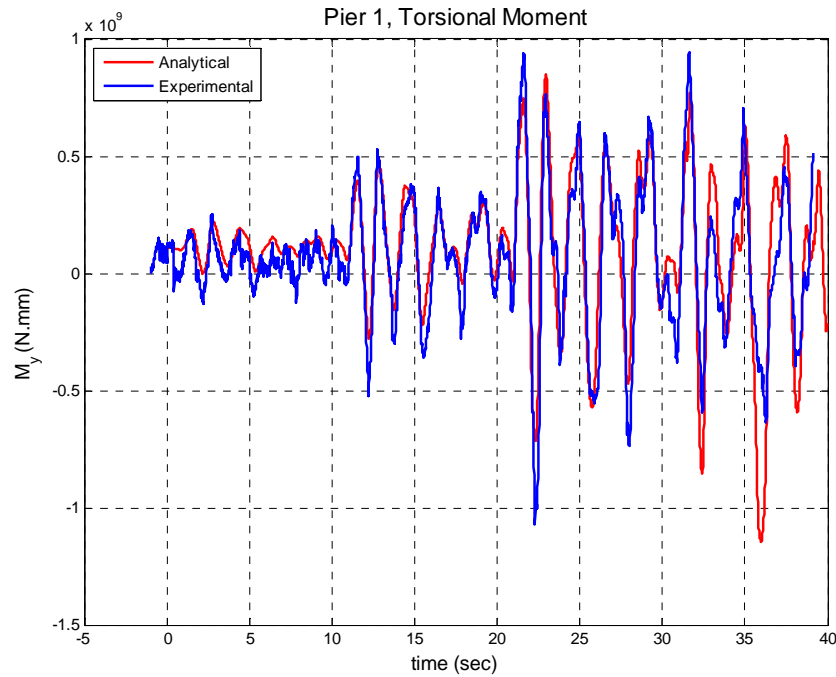


Figure E.21 Torsional Calibration - Moment History

E.3 Slight and Moderate Calibrated Models

This section displays the calibrated parameters for the models used to develop slight and moderate limit state definitions. Inaccuracies in the calibration displayed here are primarily the result of utilizing a simplified model with effective springs in order to reduce computational expenses. Note that displacement offsets that are visible in some of these figures are accounted for when comparing structural response data to limit state threshold values.

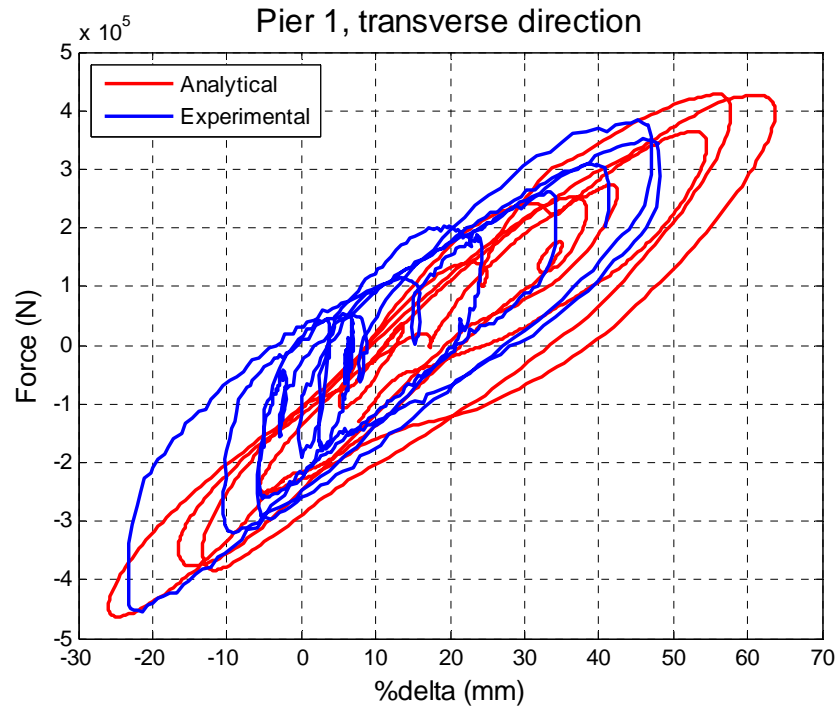


Figure E.22 Slight P1 Transverse Calibration

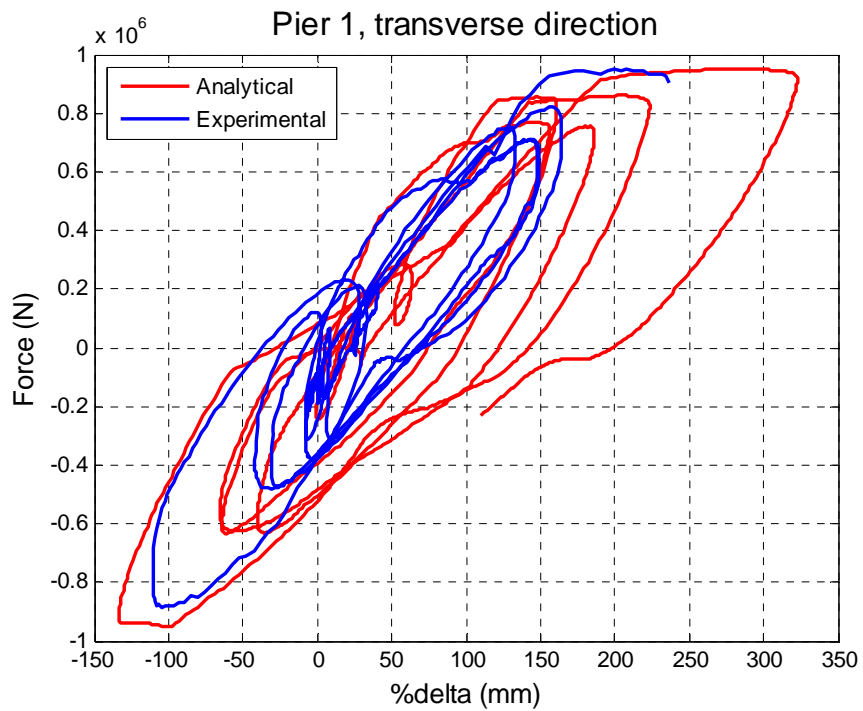


Figure E.23 Moderate P1 Transverse Calibration

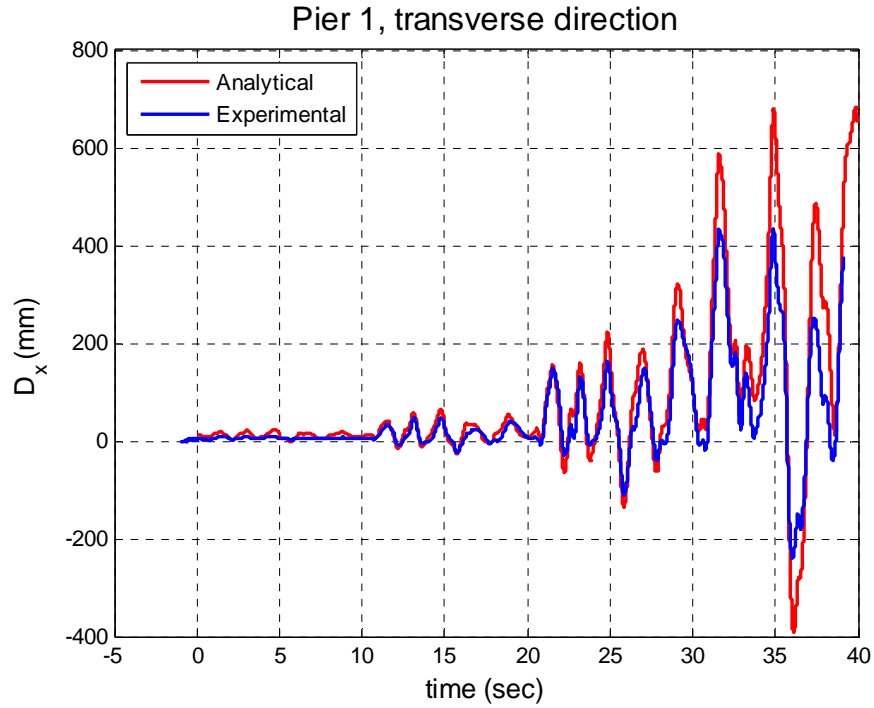


Figure E.24 Slight-Moderate P1 Transverse Displacement History

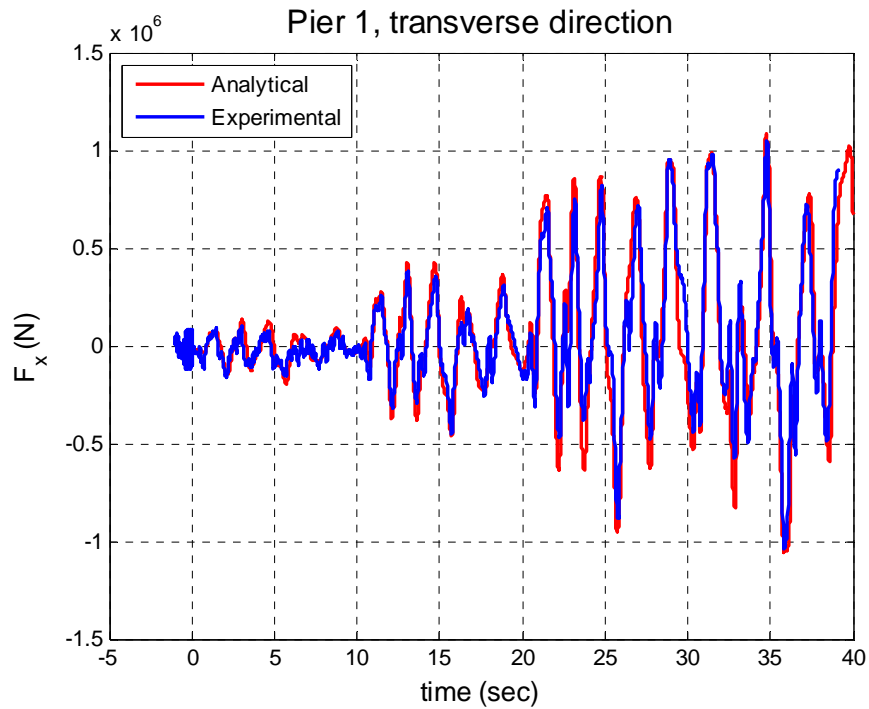


Figure E.25 Slight-Moderate P1 Transverse Force History

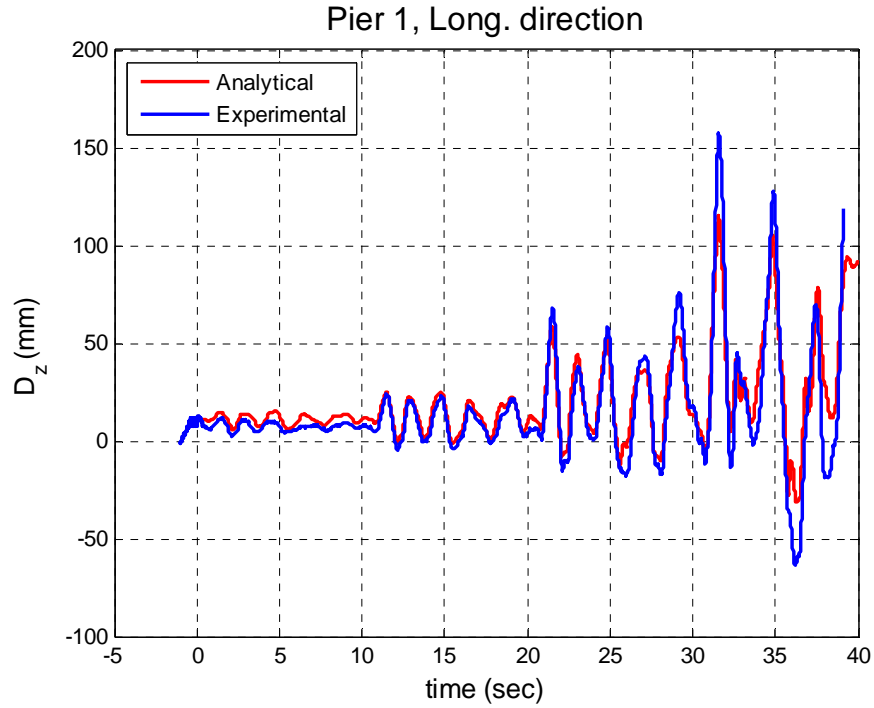


Figure E.26 Slight-Moderate P1 Longitudinal Displacement History

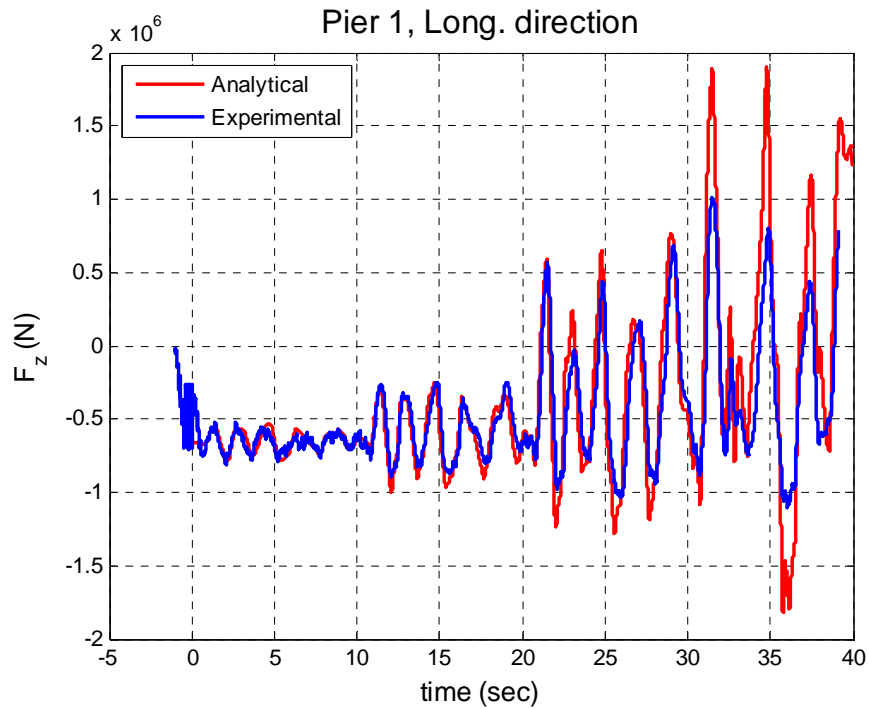


Figure E.27 Slight-Moderate P1 Longitudinal Force History

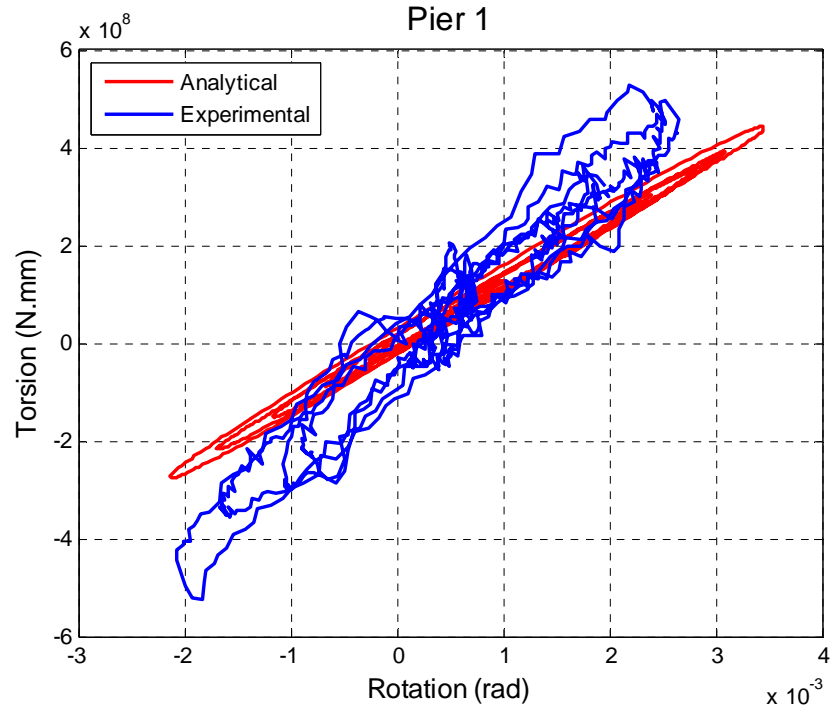


Figure E.28 Slight P1 Torsional Calibration

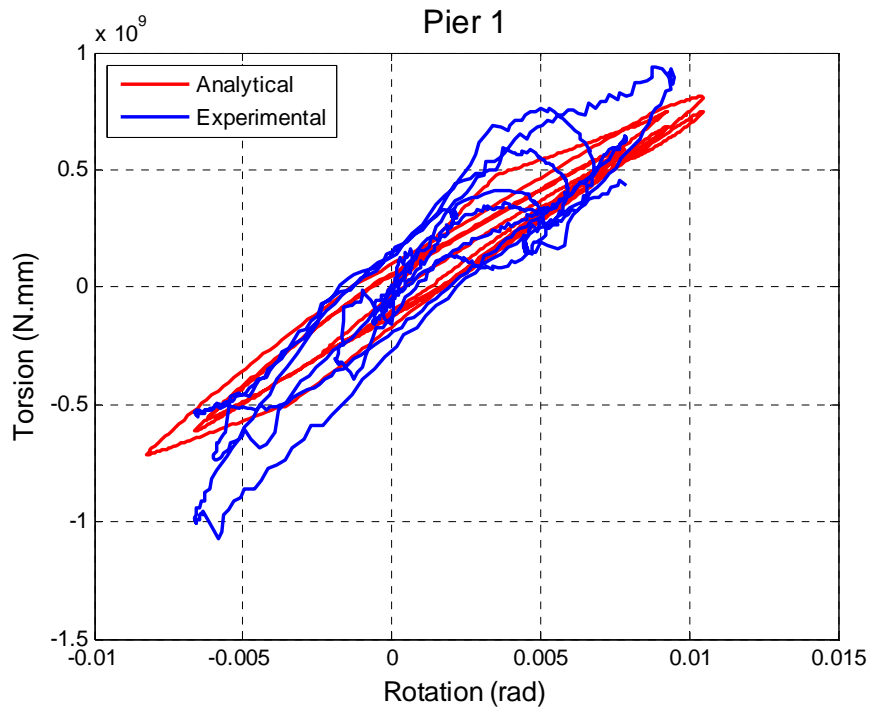


Figure E.29 Moderate P1 Torsional Calibration

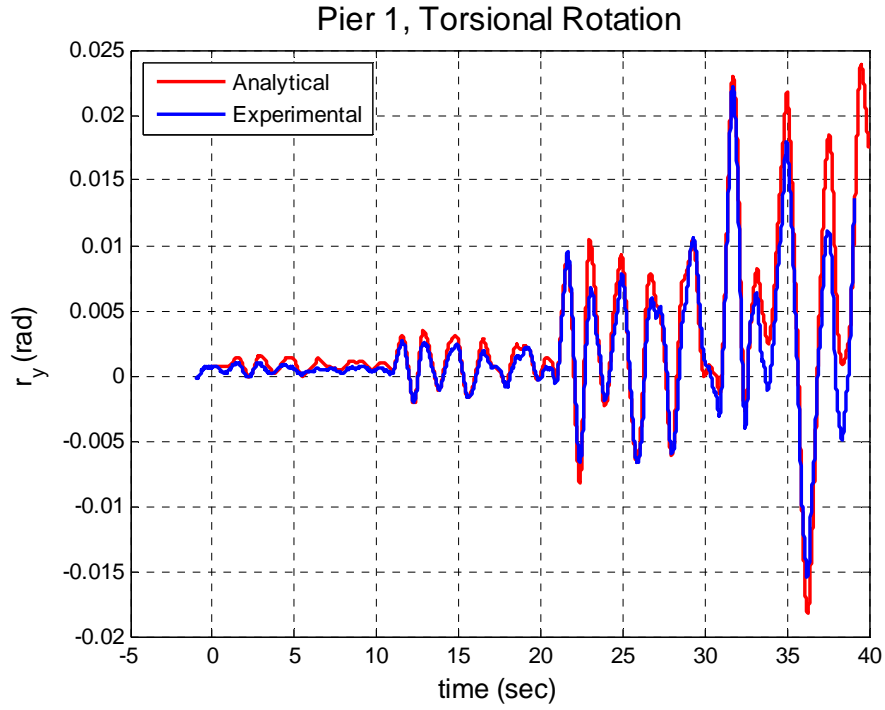


Figure E.30 Slight-Moderate P1 Torsional Rotation History

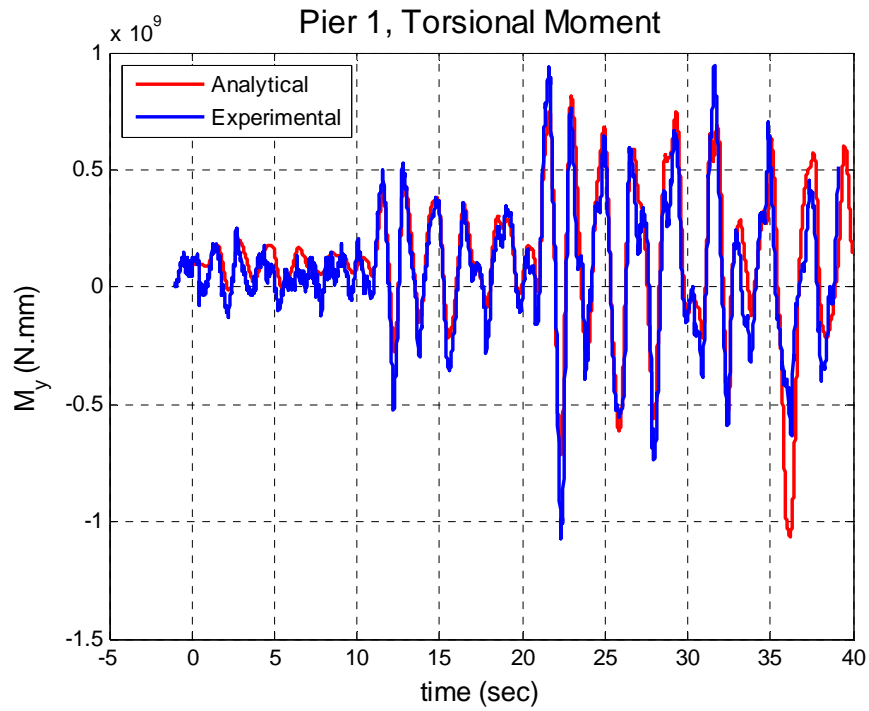


Figure E.31 Slight-Moderate P1 Torsional Moment History

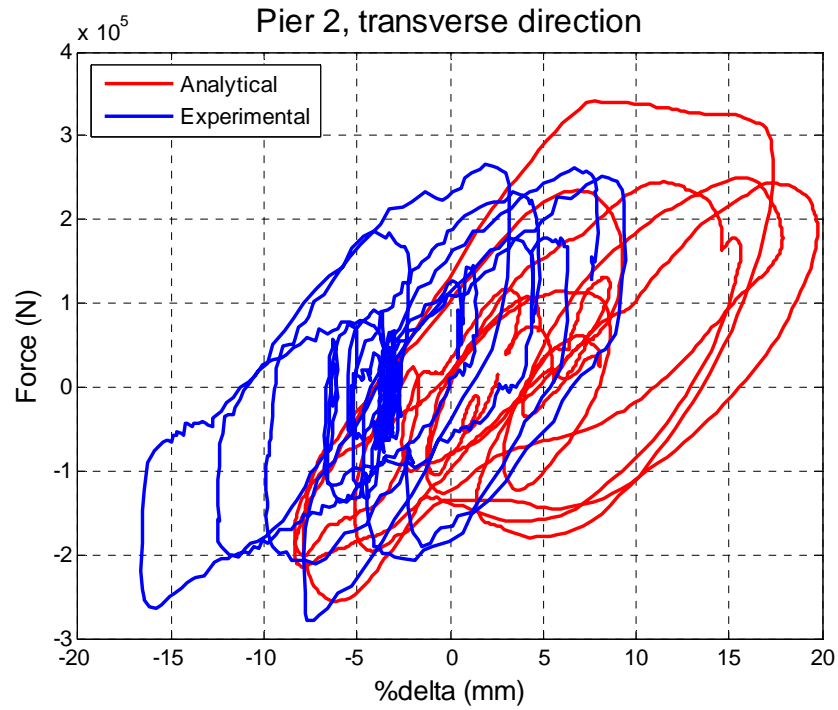


Figure E.32 Slight P2 Transverse Calibration

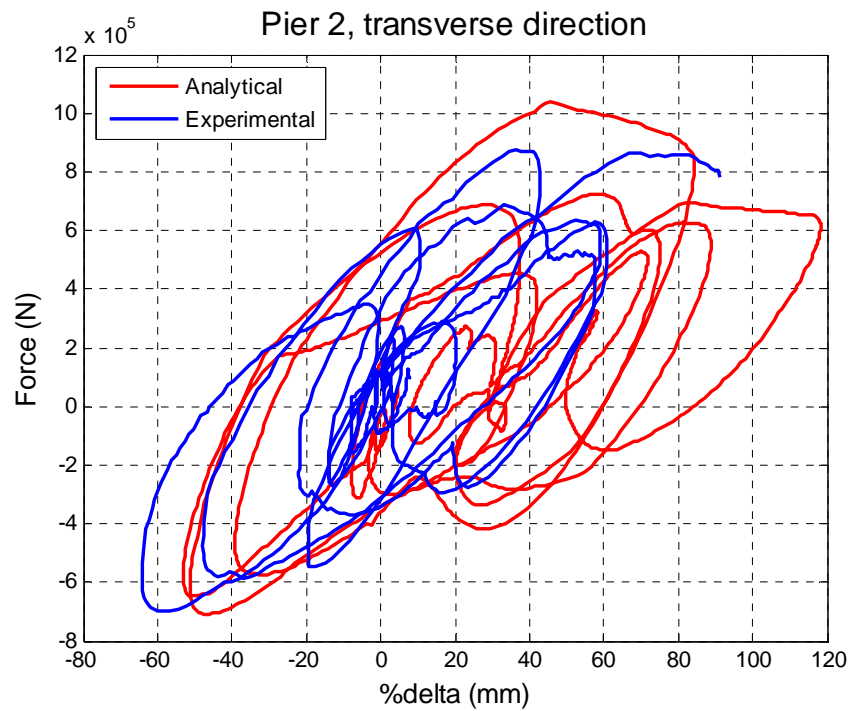


Figure E.33 Moderate P2 Transverse Calibration

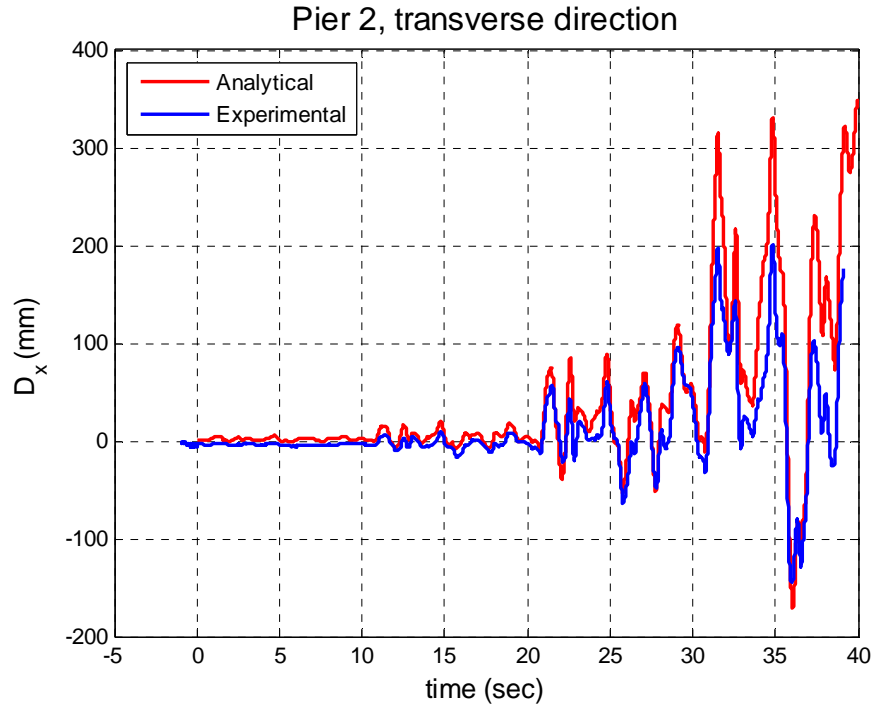


Figure E.34 Slight-Moderate P2 Transverse Displacement History

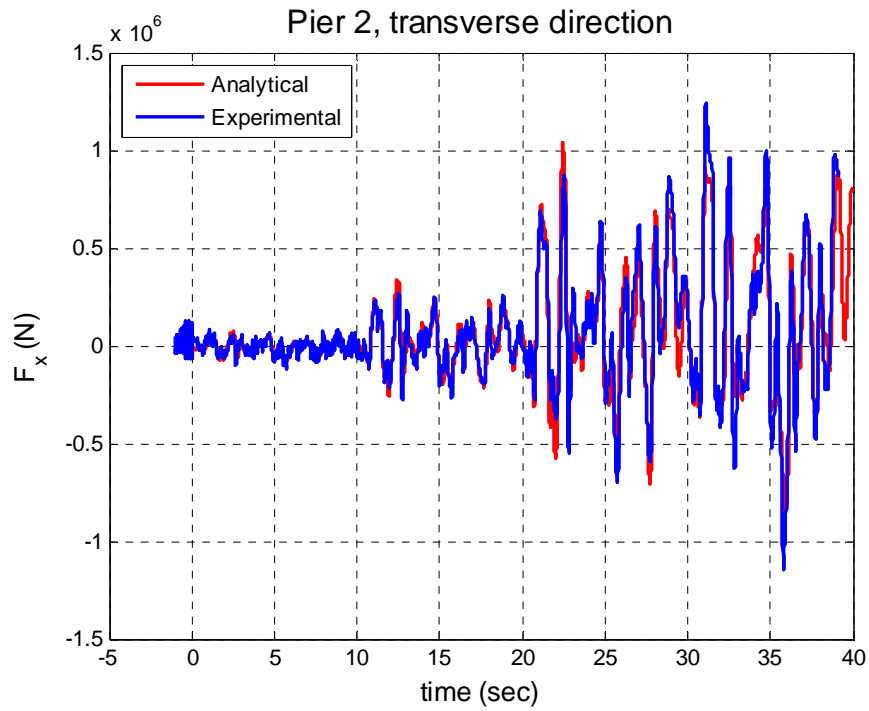


Figure E.35 Slight-Moderate P2 Transverse Force History

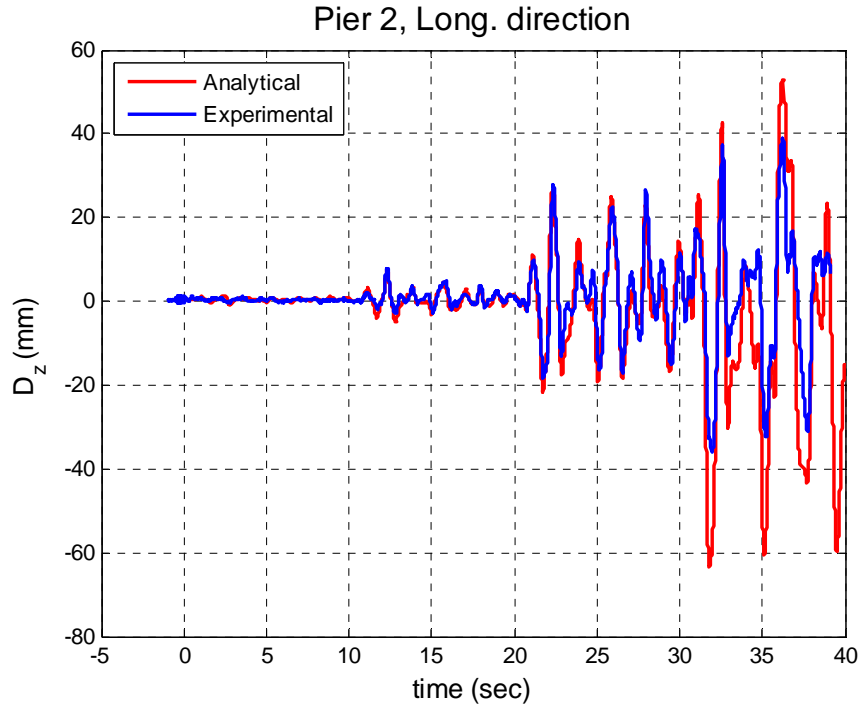


Figure E.36 Slight-Moderate P2 Longitudinal Displacement History

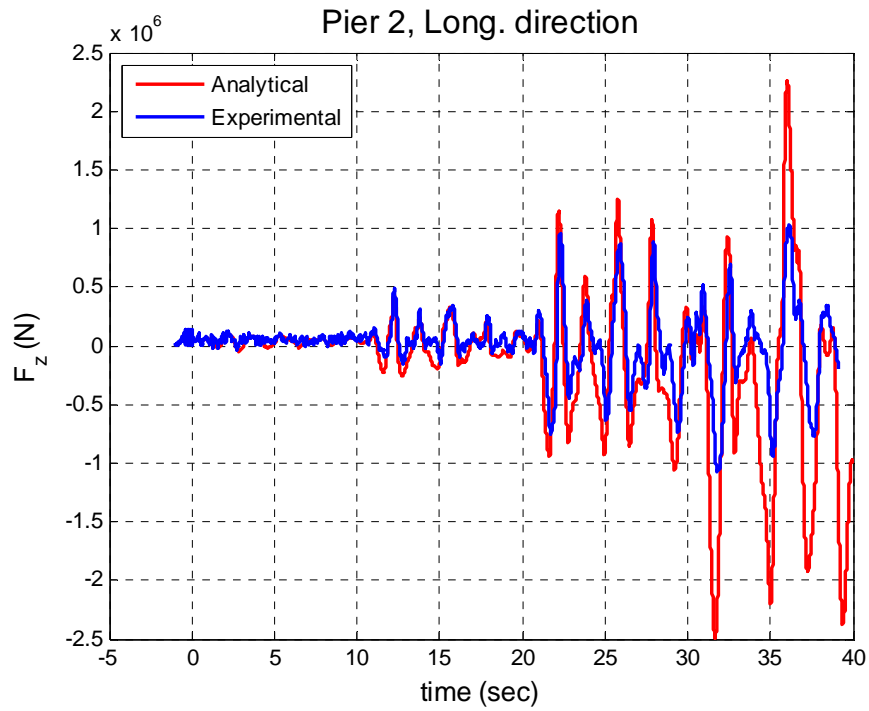


Figure E.37 Slight-Moderate P2 Longitudinal Force History

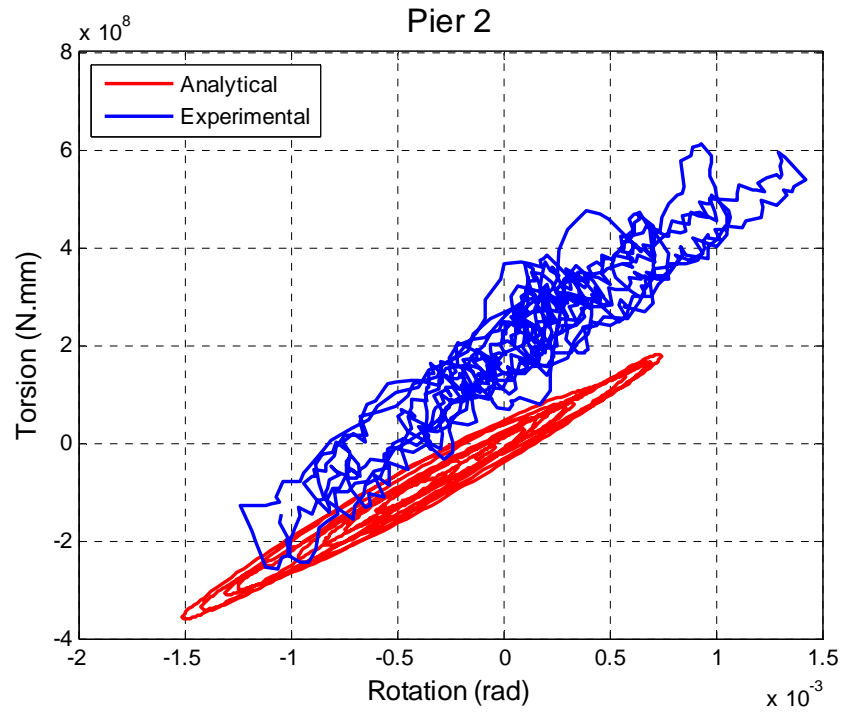


Figure E.38 Slight P2 Torsional Calibration

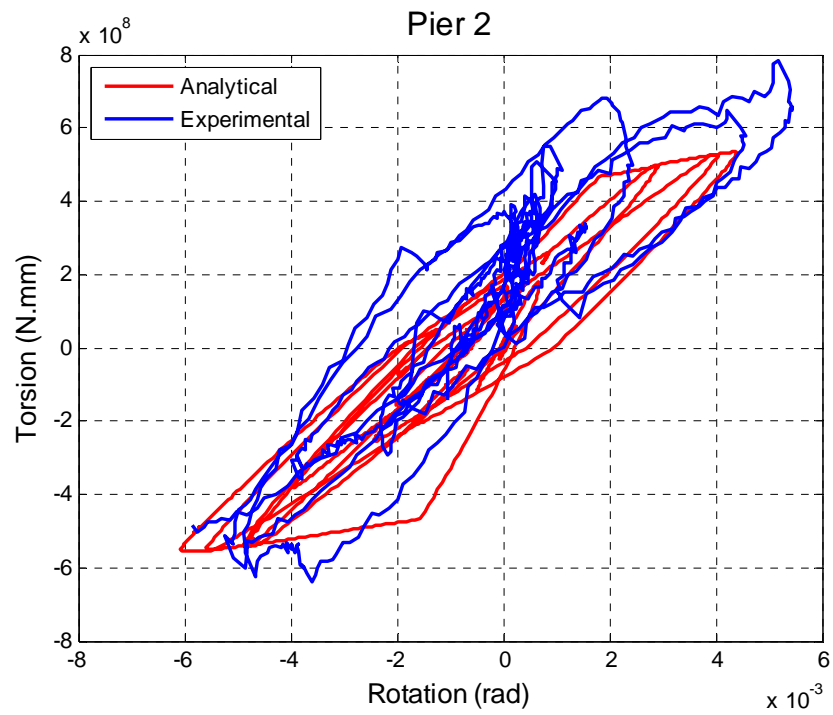


Figure E.39 Moderate P2 Torsional Calibration

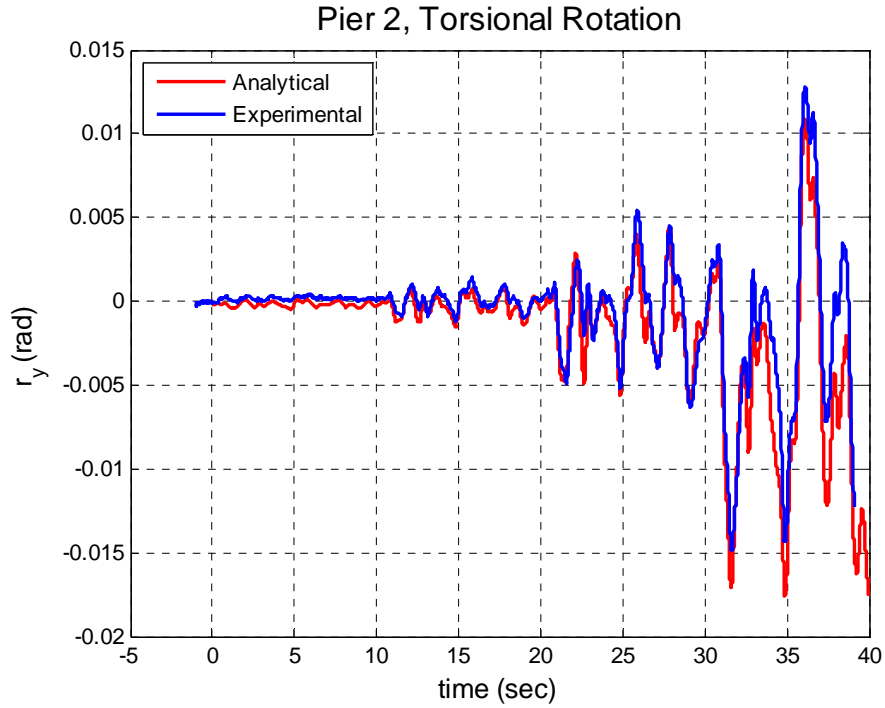


Figure E.40 Slight-Moderate P2 Torsional Rotation History

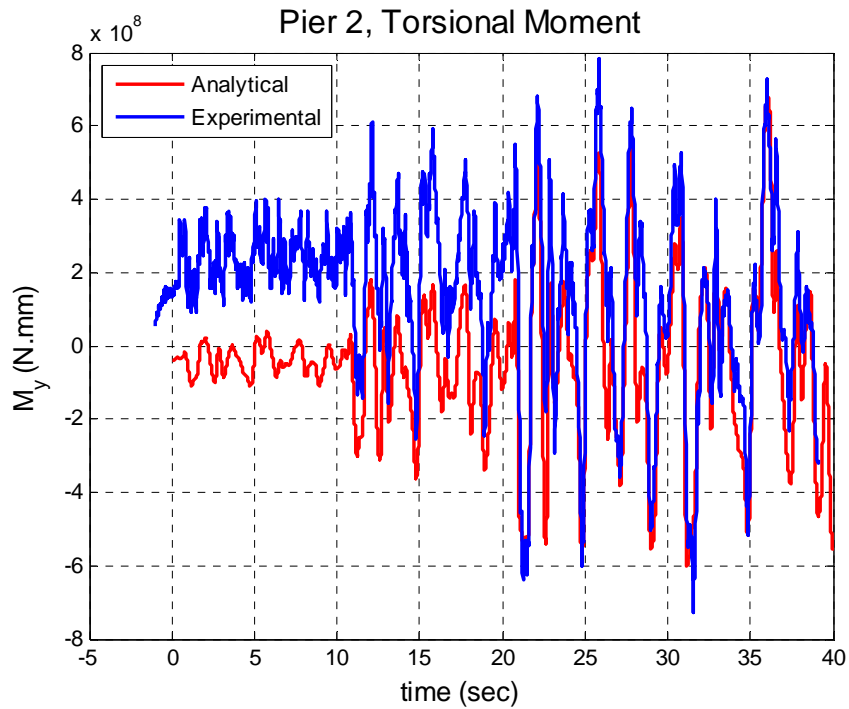


Figure E.41 Slight-Moderate P2 Torsional Moment History

E.4 Severe Calibrated Model

The severe calibrated model is presented below for use in developing this final limit state. Inaccuracies are identified to be the result of the influence of shear deformation at higher load levels. This has little effect on the results due to the strong agreement in the degrees of freedom considered as indicators of overall bridge performance. Additionally, the analytical model contains a slightly longer hysteresis for response of the bridge beyond the conclusion of the hybrid simulation.

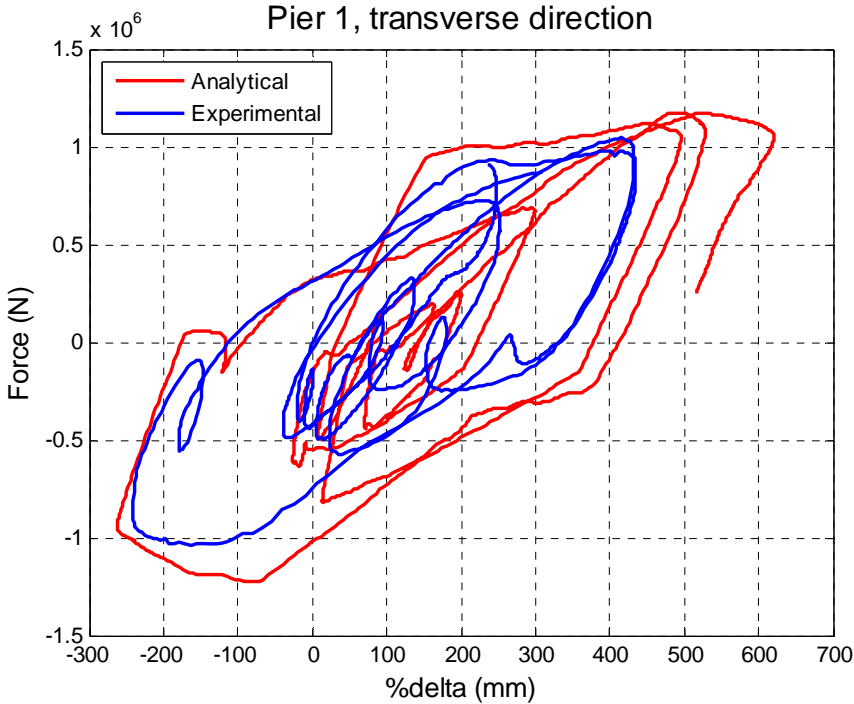


Figure E.42 Severe P1 Transverse Calibration

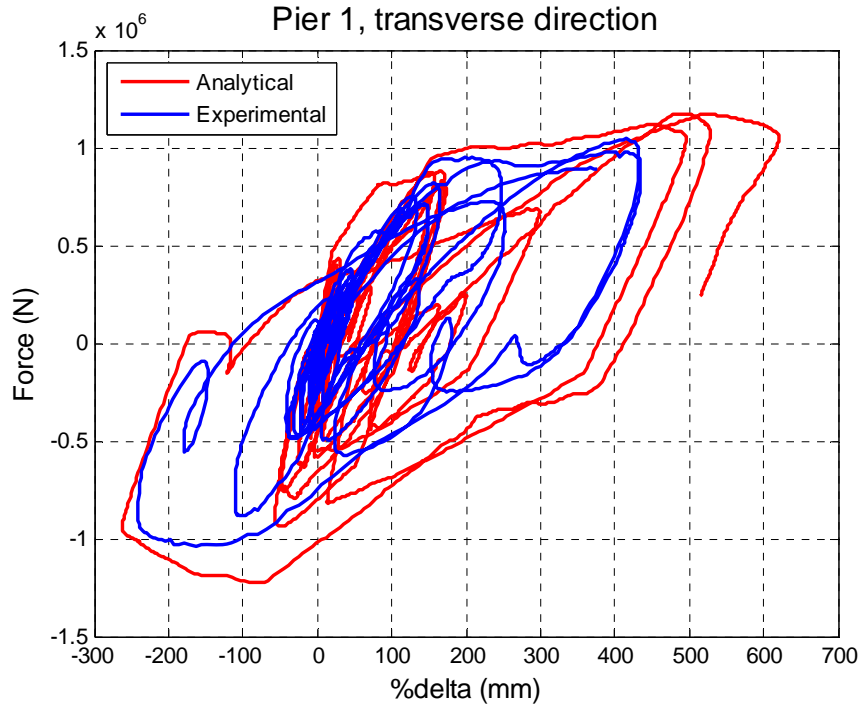


Figure E.43 Severe P1 Full Transverse Calibration

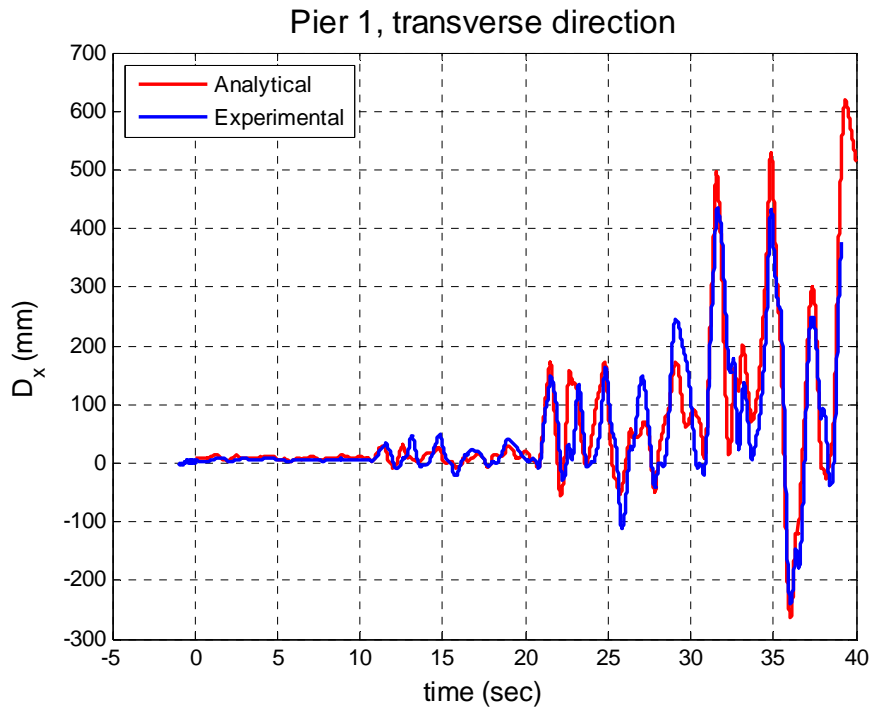


Figure E.44 Severe P1 Transverse Displacement History

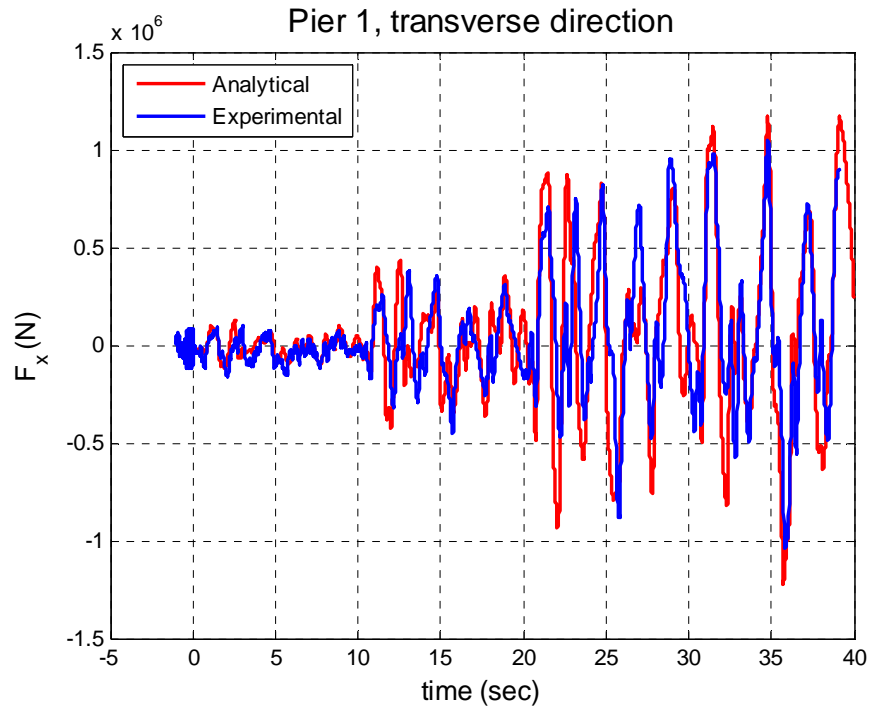


Figure E.45 Severe P1 Transverse Force History

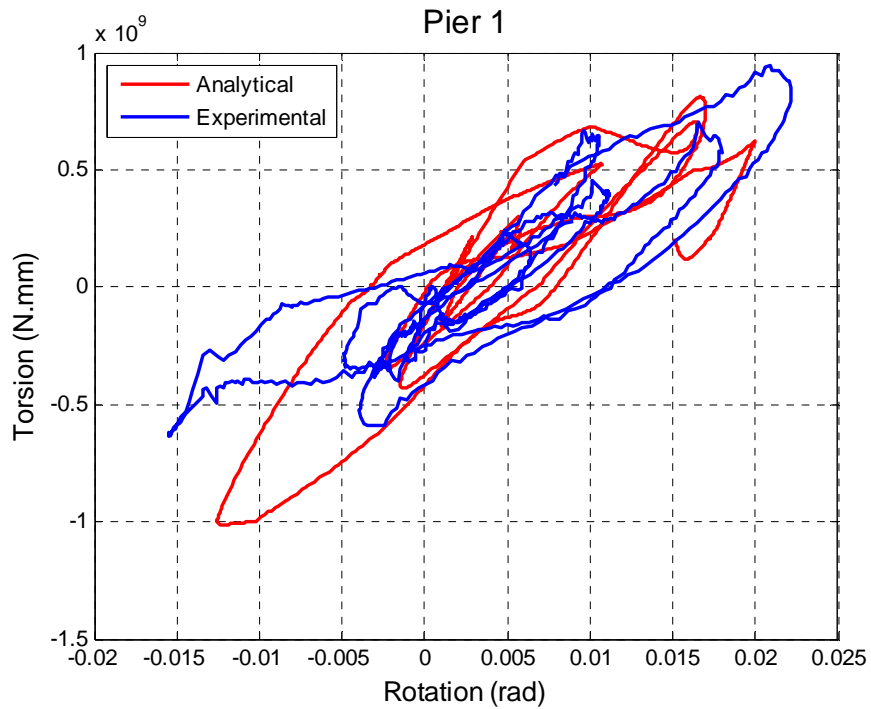


Figure E.46 Severe P1 Torsional Calibration

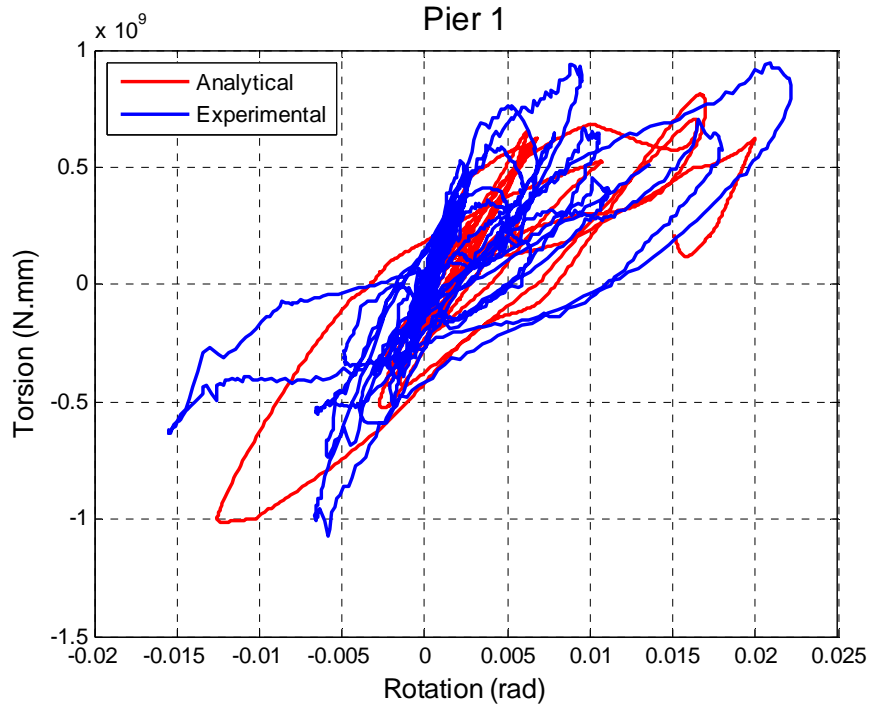


Figure E.47 Severe P1 Full Torsional Calibration

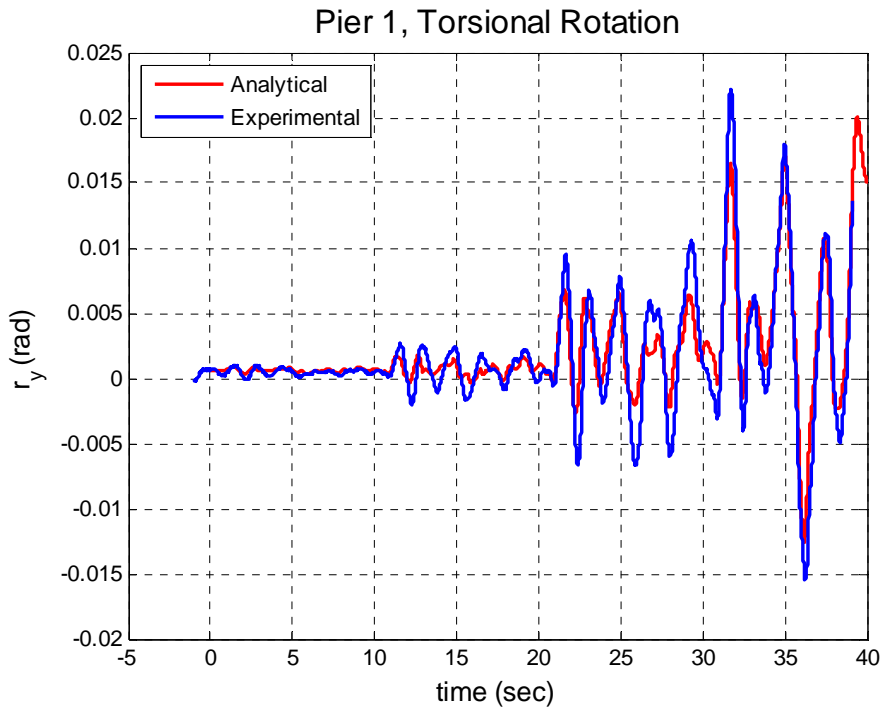


Figure E.48 Severe P1 Torsional Rotation History

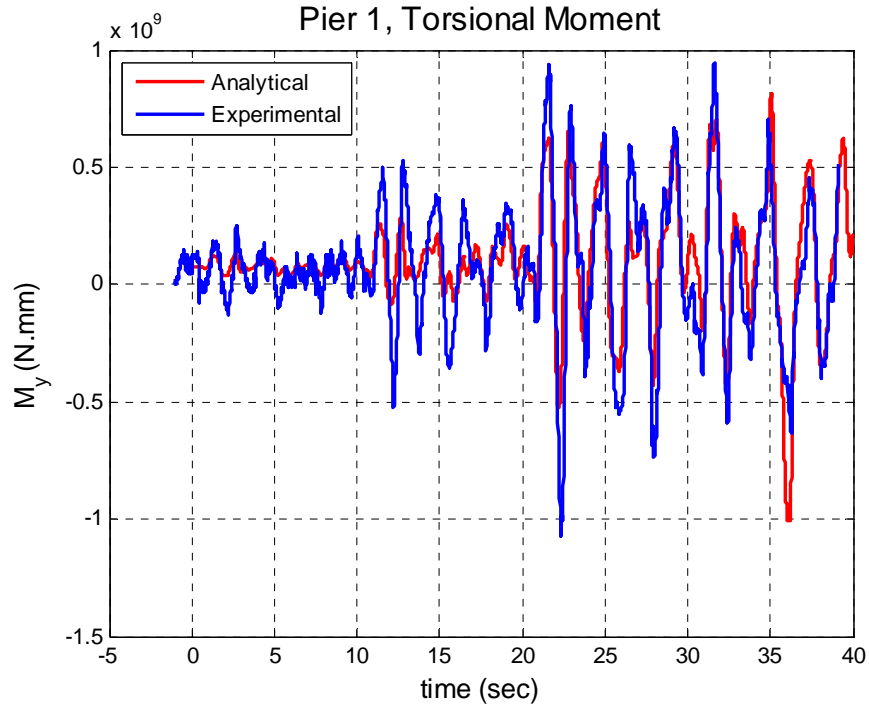


Figure E.49 Severe P1 Torsional Moment History

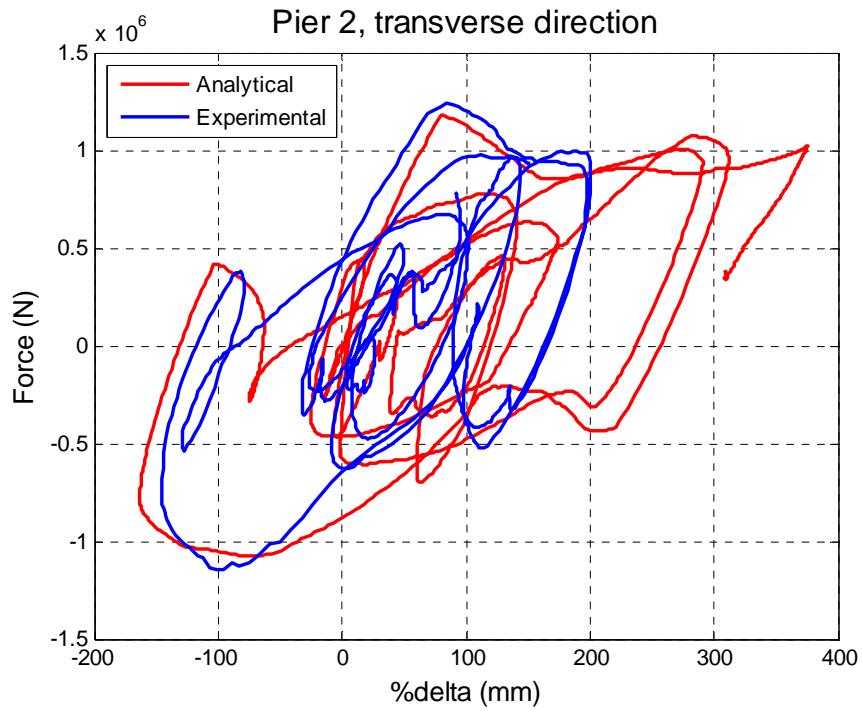


Figure E.50 Severe P2 Transverse Calibration

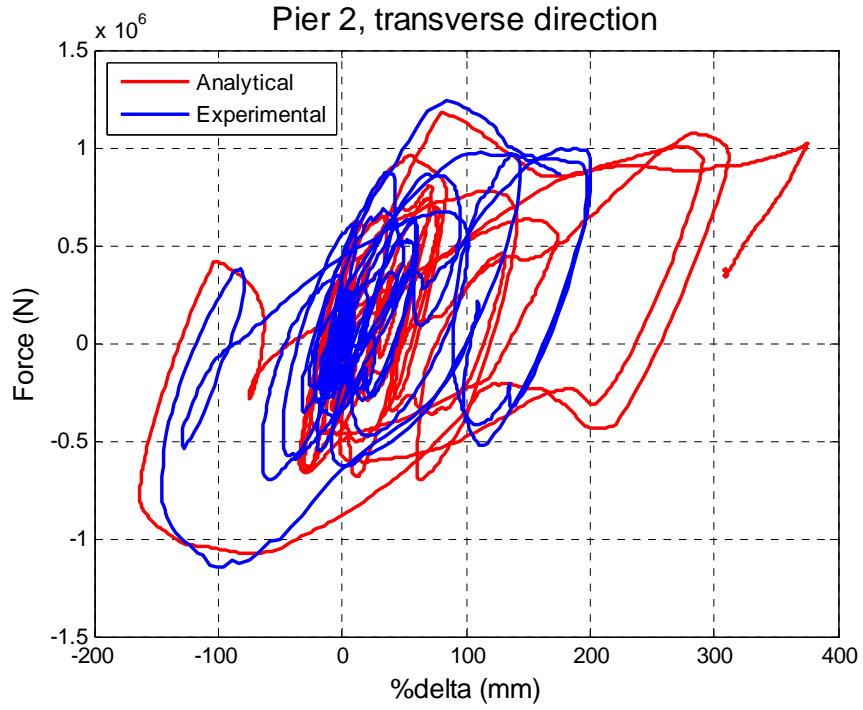


Figure E.51 Severe P2 Full Transverse Calibration

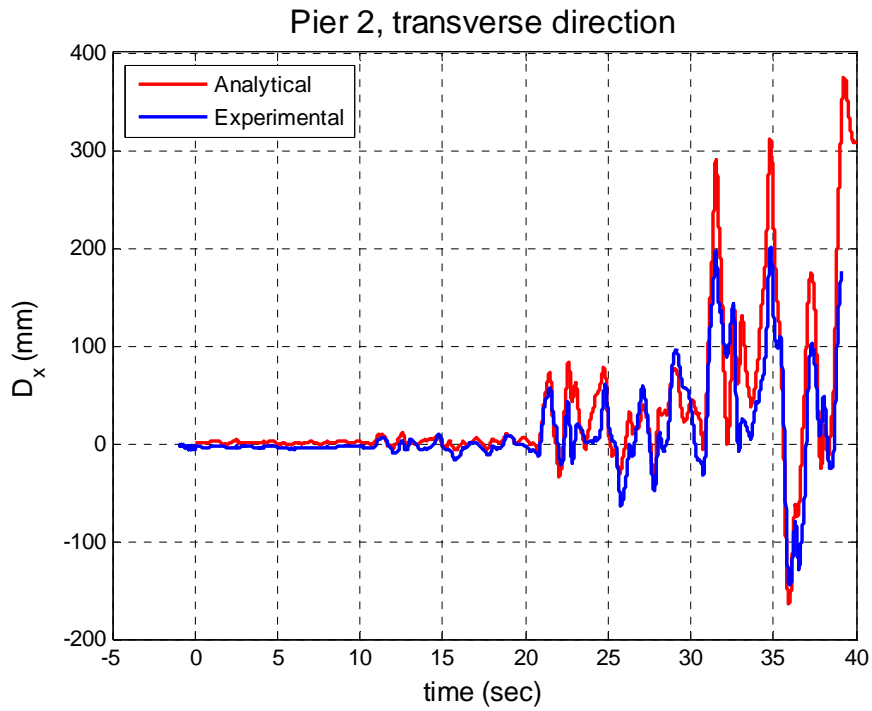


Figure E.52 Severe P2 Transverse Displacement History

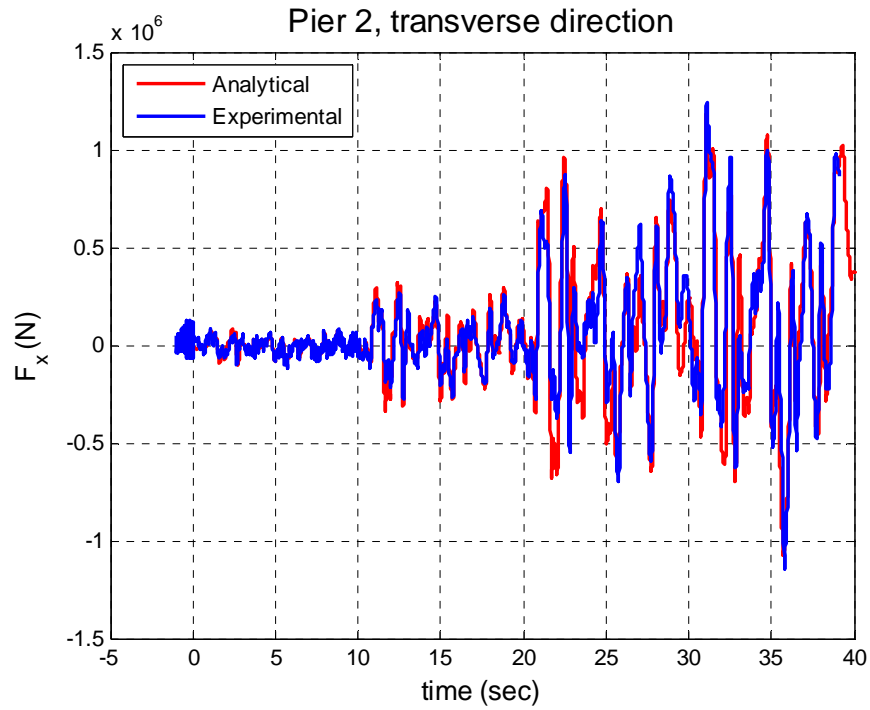


Figure E.53 Severe P2 Transverse Force History

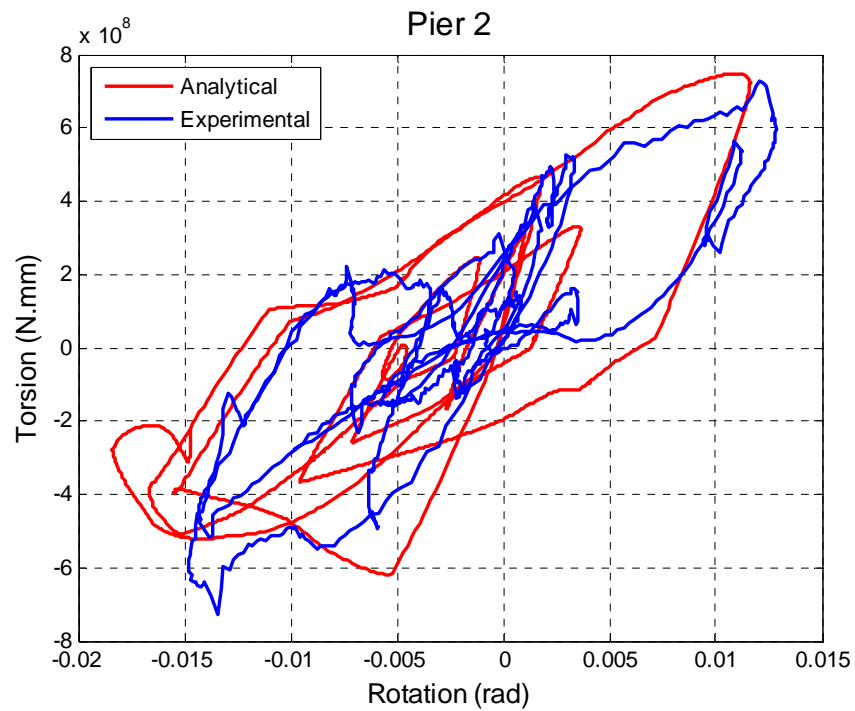


Figure E.54 Severe P2 Torsional Calibration

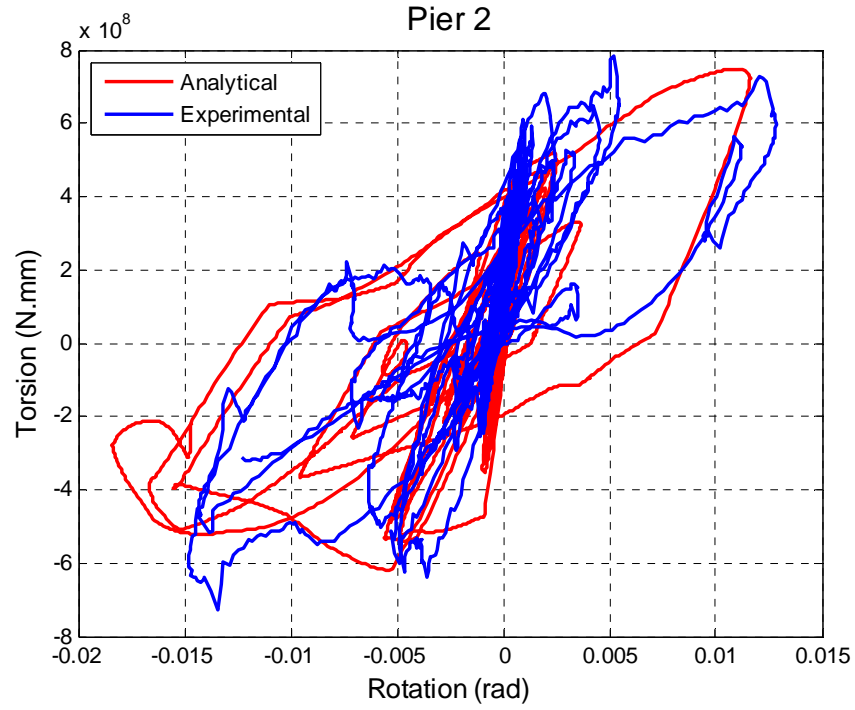


Figure E.55 Severe P2 Full Torsional Calibration

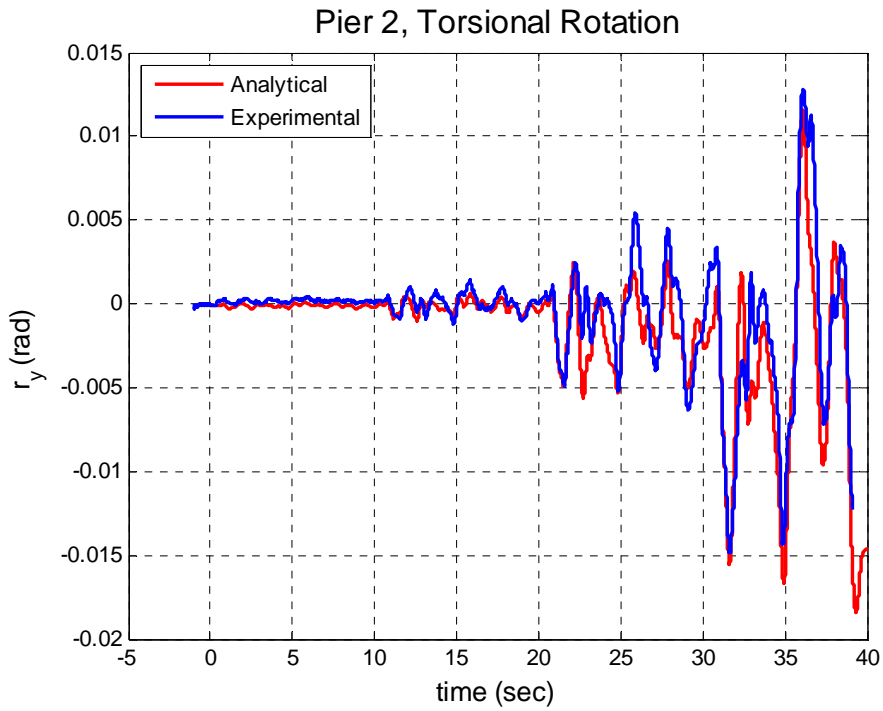


Figure E.56 Severe P2 Torsional Rotation History

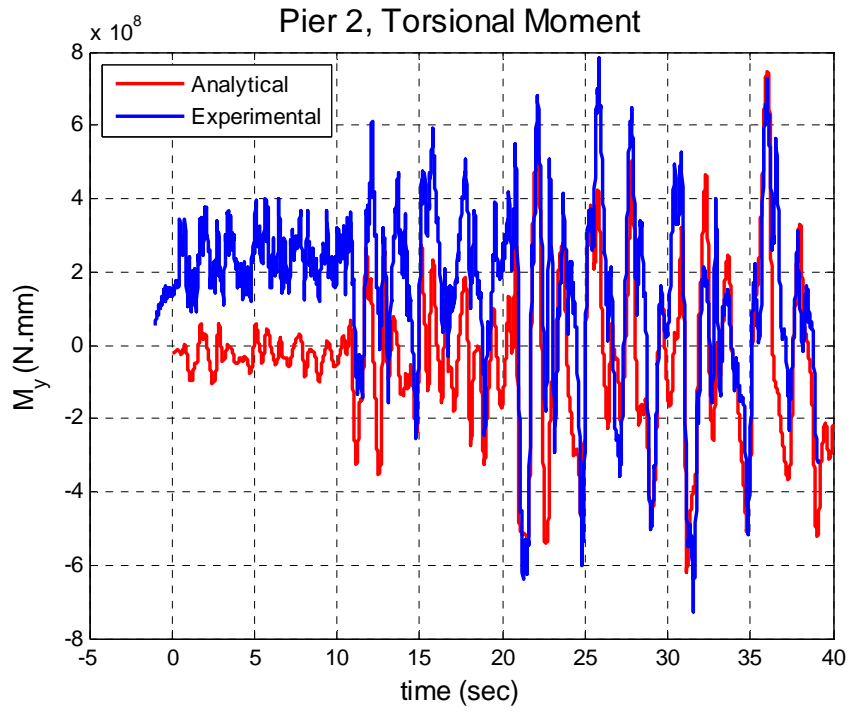


Figure E.57 Severe P2 Torsional Moment History

APPENDIX F. SUITE OF SEISMIC RECORDS

This appendix presents a comprehensive study of the natural records selected for use in performing nonlinear time history analyses for each of the calibrated models. Thus, the records are sorted into three bins, to be applied to each of the three calibrated models, and ultimately to yield the parameters of the vulnerability relationship for the given limit state threshold. For each suite, the spectra of the ground motion and its components, as well as distribution of soil site condition, peak ground parameters, and relative ratios of horizontal and vertical to horizontal peak parameters are provided. Plots are presented for each suite, and for the overall set of over 900 natural records. It should be noted that the severe suite of records includes records from two distinct sources, as presented in the tables following the summary plots that present additional details and parameters of the records.

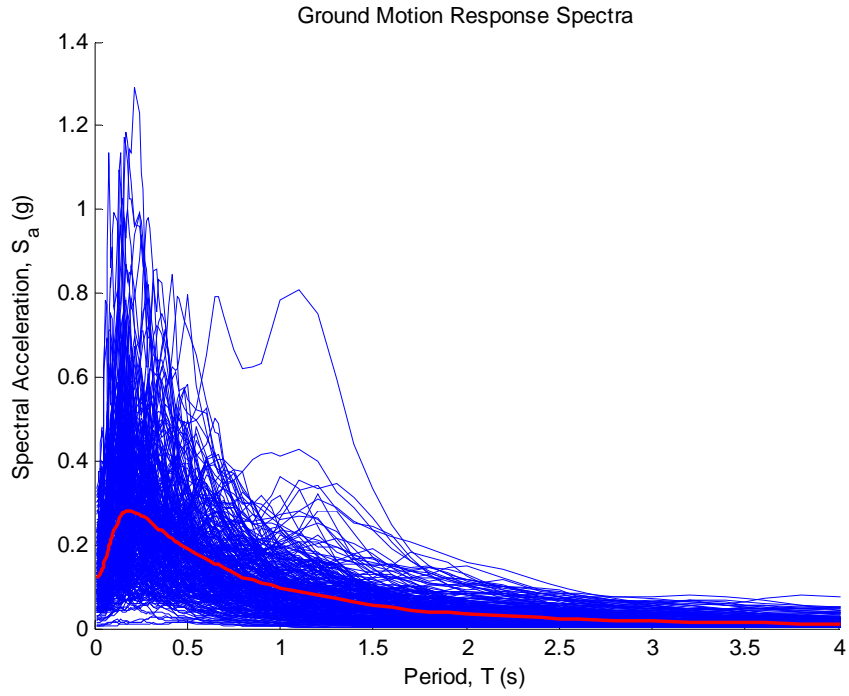


Figure F.1 Slight Suite - Ground Motion Response Spectra

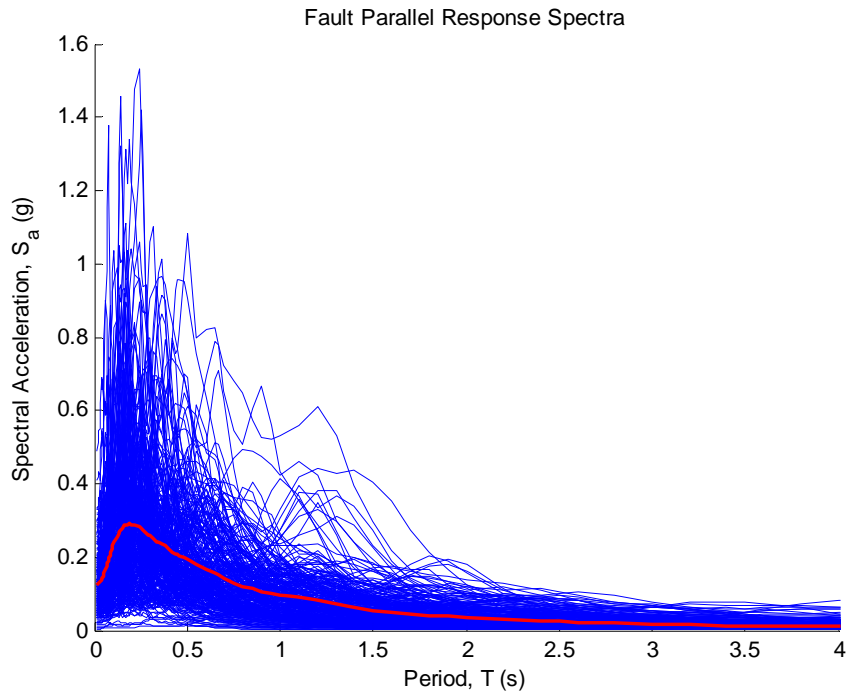


Figure F.2 Slight Suite - Fault Parallel Response Spectra

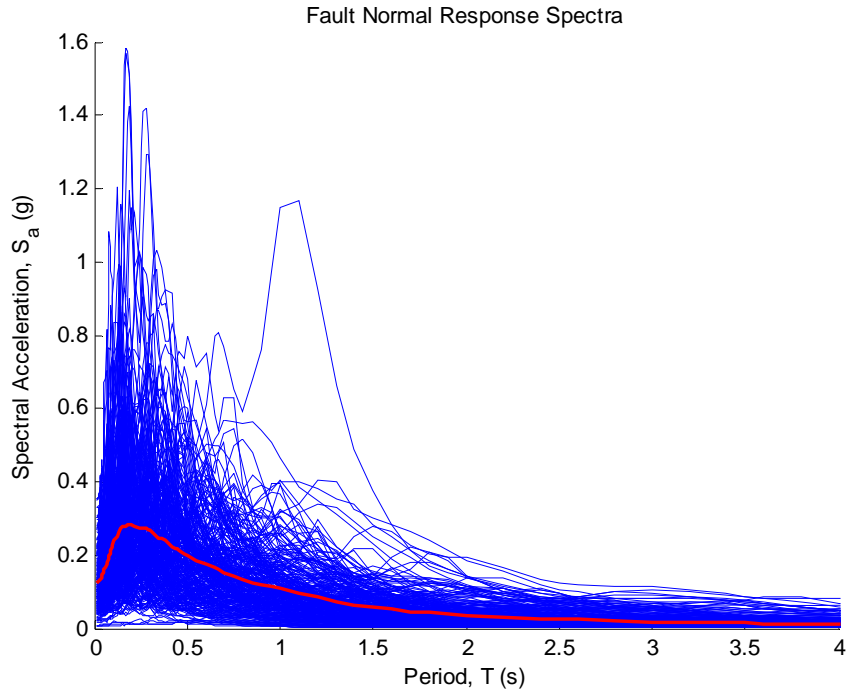


Figure F.3 Slight Suite - Fault Normal Response Spectra

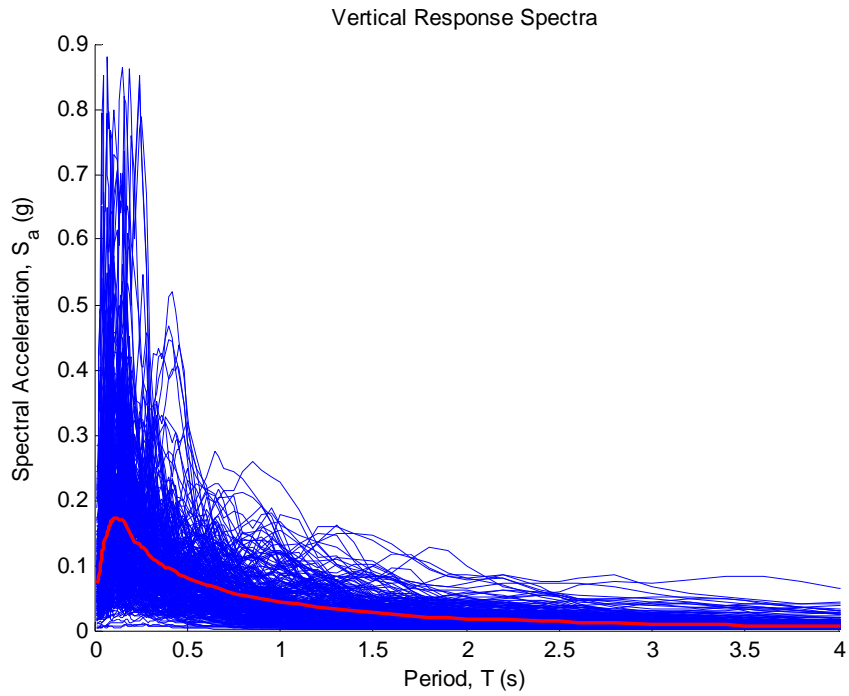


Figure F.4 Slight Suite - Vertical Response Spectra

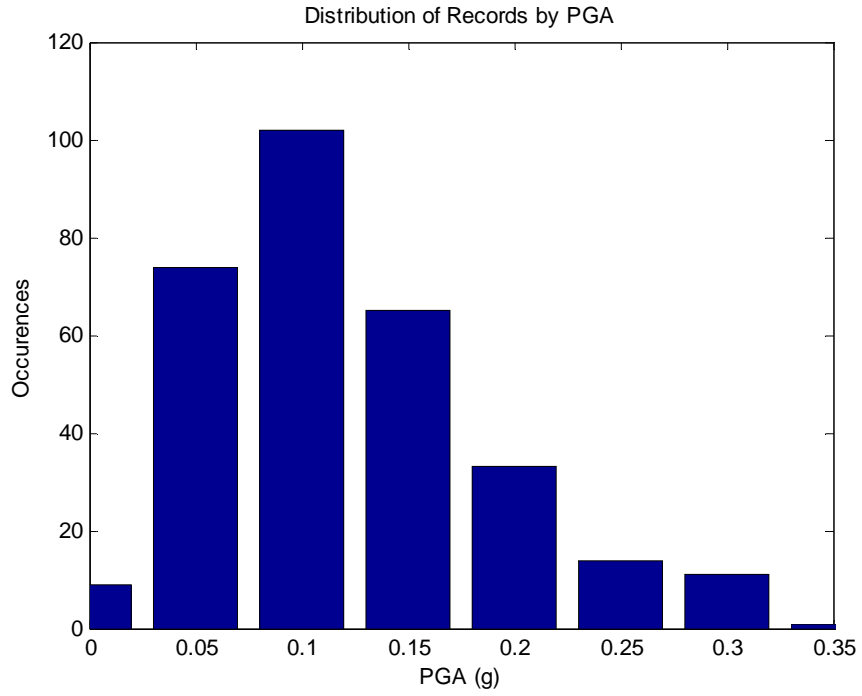


Figure F.5 Slight Suite - PGA Distribution

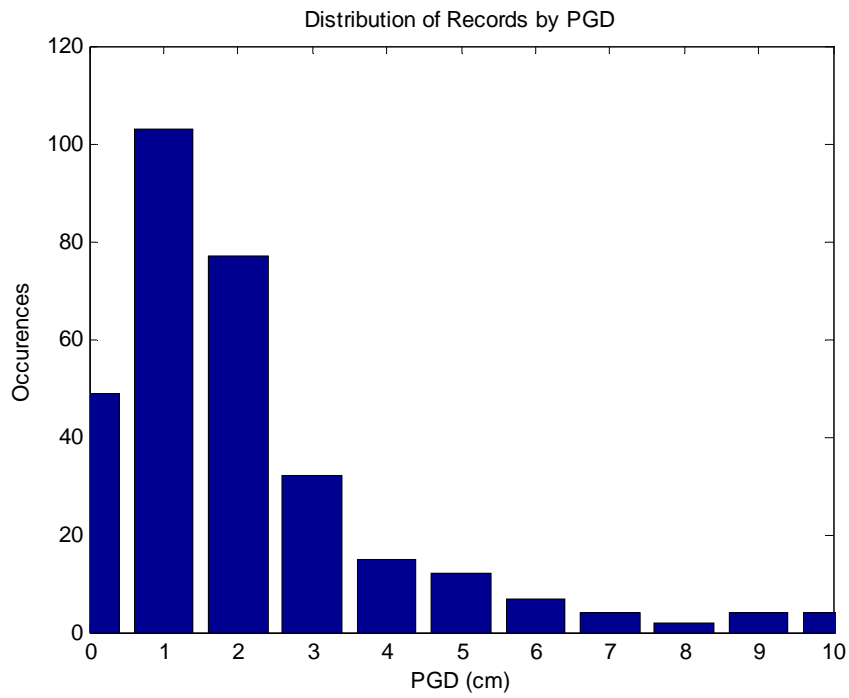


Figure F.6 Slight Suite - PGD Distribution

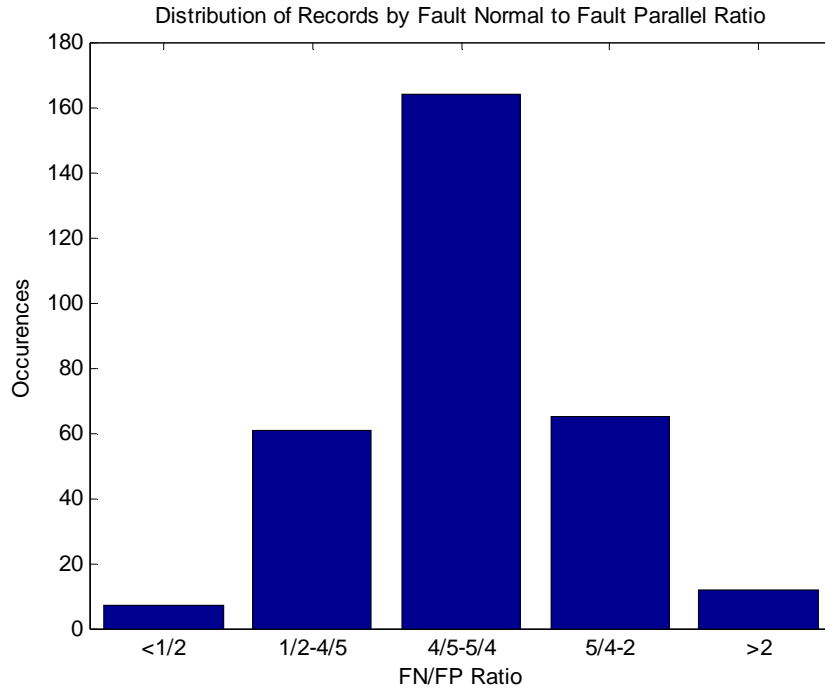


Figure F.7 Slight Suite - Horizontal Peak Parameter Ratios

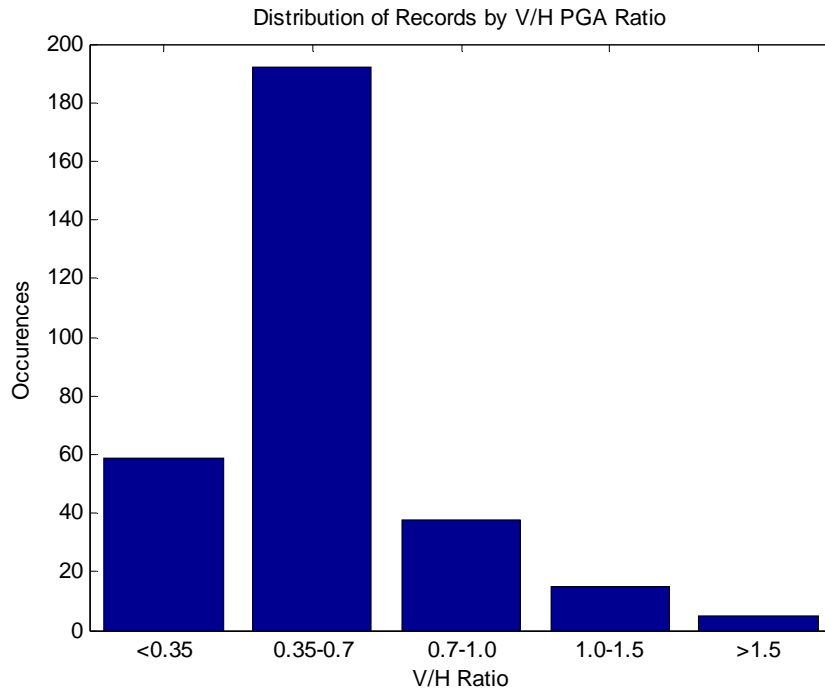


Figure F.8 Slight Suite - Vertical to Horizontal Peak Parameter Ratios

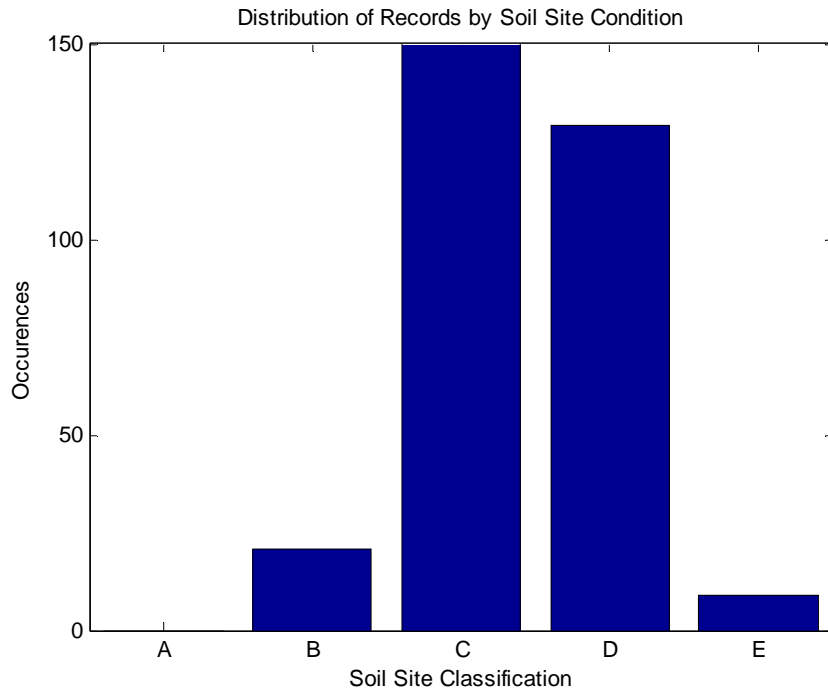


Figure F.9 Slight Suite - Soil Site Distribution

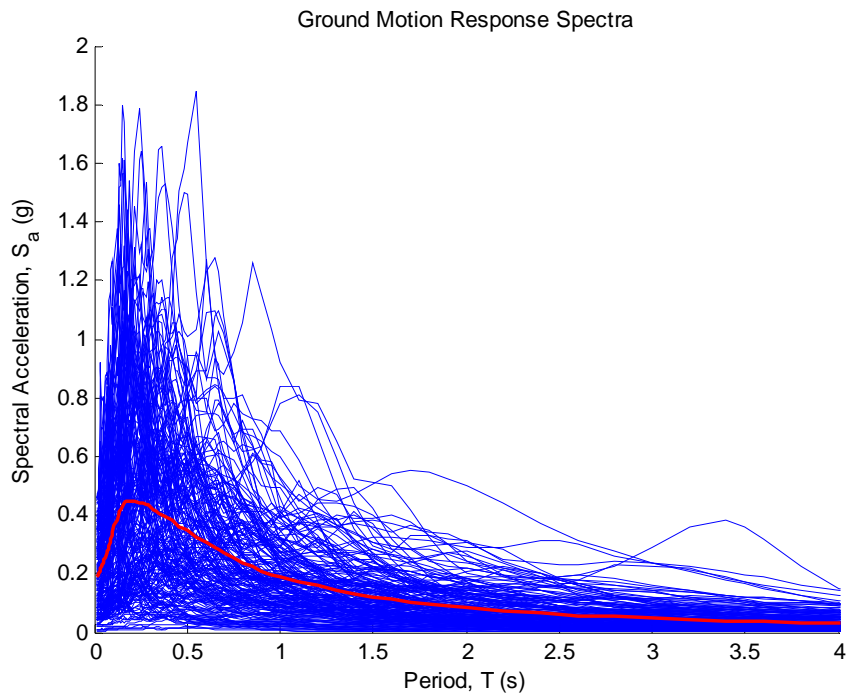


Figure F.10 Moderate Suite - Ground Motion Response Spectra

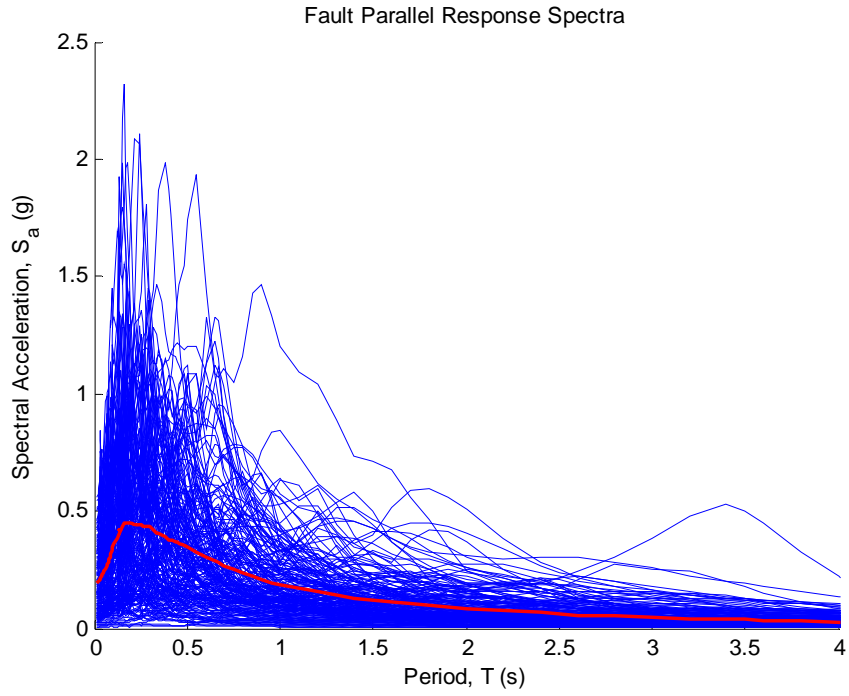


Figure F.11 Moderate Suite - Fault Parallel Response Spectra

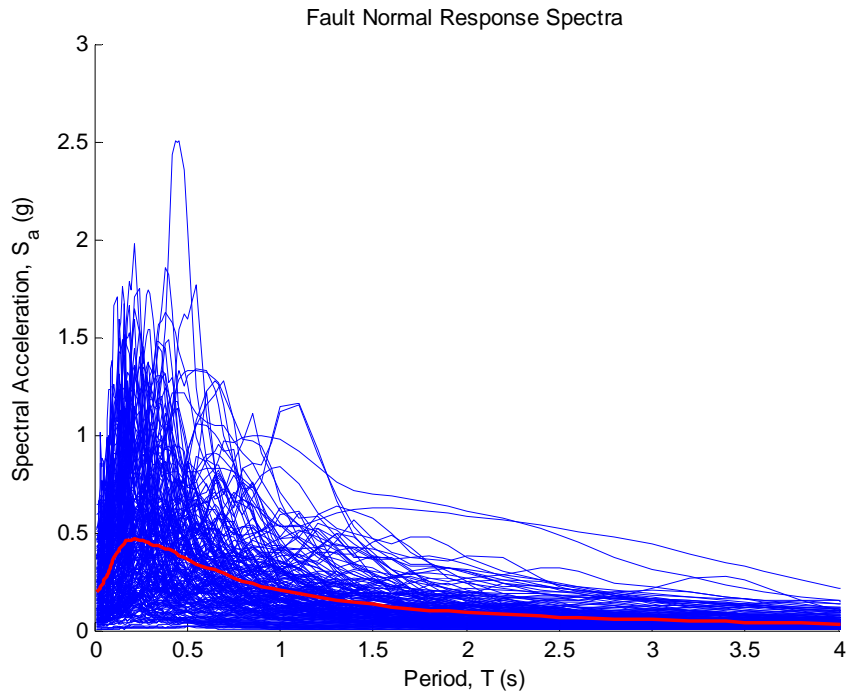


Figure F.12 Moderate Suite - Fault Normal Response Spectra

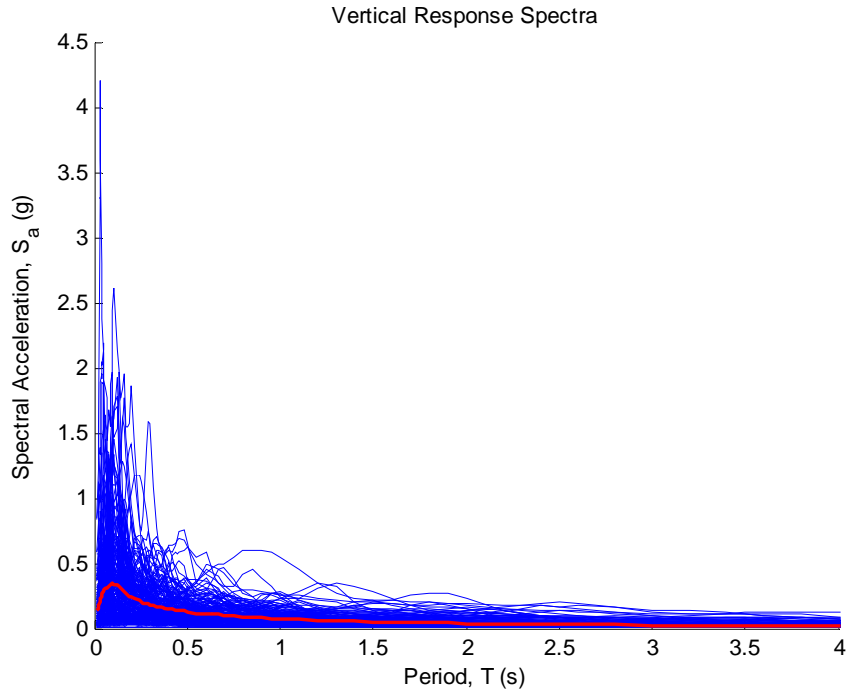


Figure F.13 Moderate Suite - Vertical Response Spectra

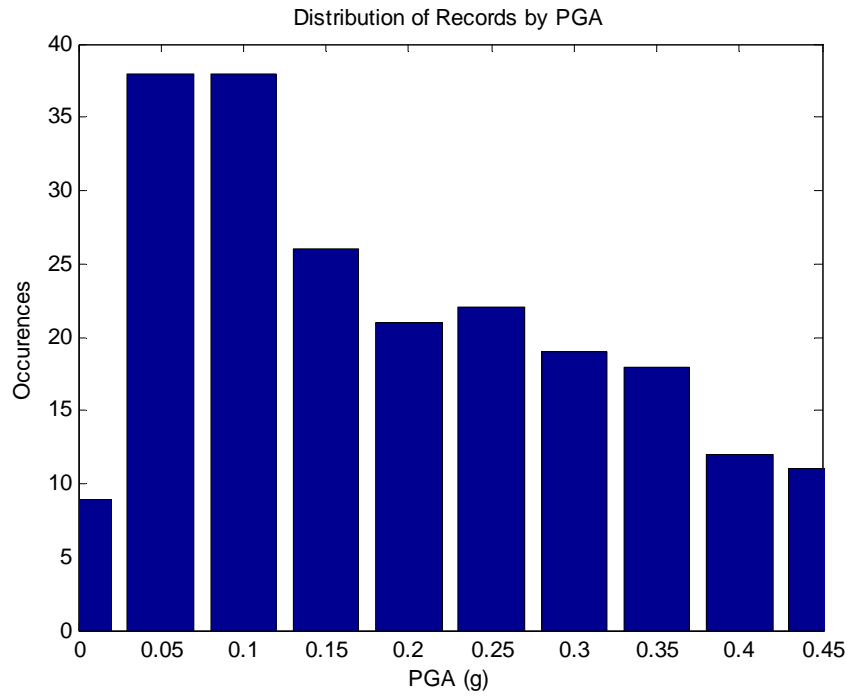


Figure F.14 Moderate Suite - PGA Distribution

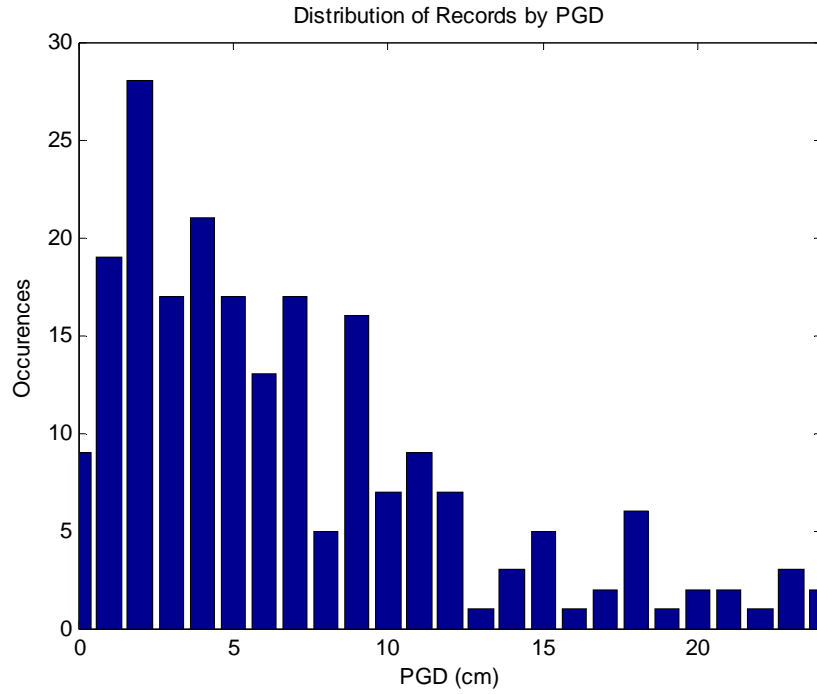


Figure F.15 Moderate Suite - PGD Distribution

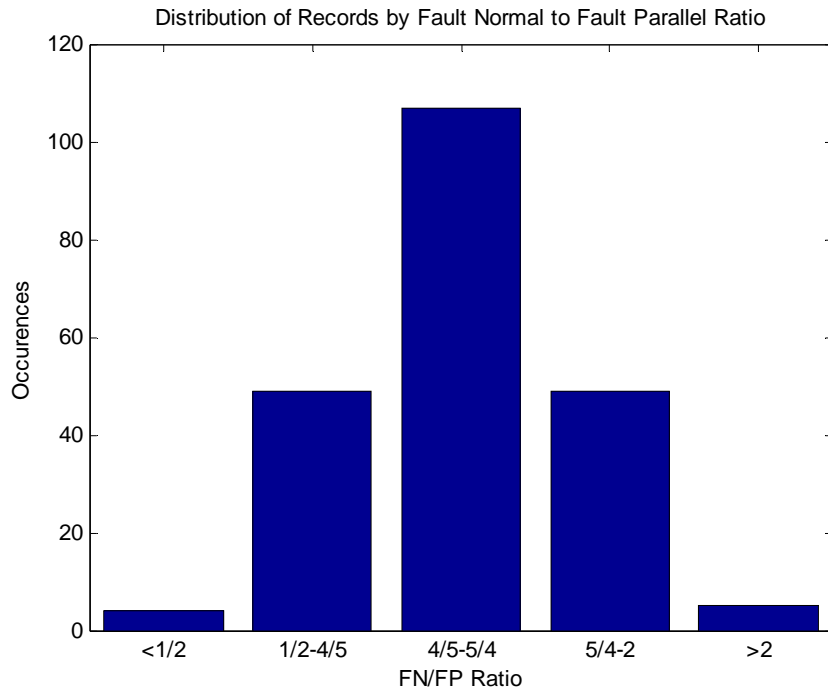


Figure F.16 Moderate Suite - Horizontal Peak Parameter Ratios

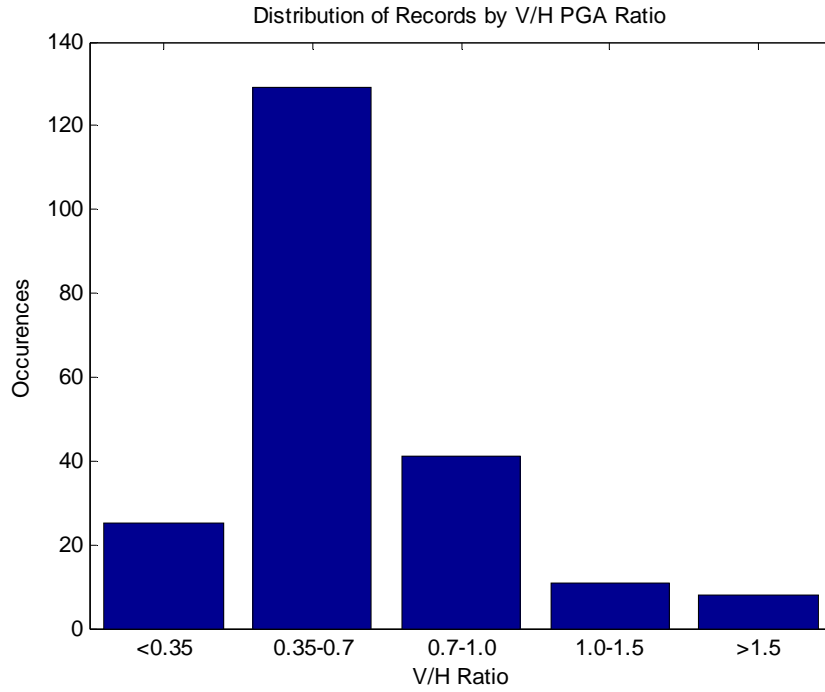


Figure F.17 Moderate Suite - Vertical to Horizontal Peak Parameter Ratios

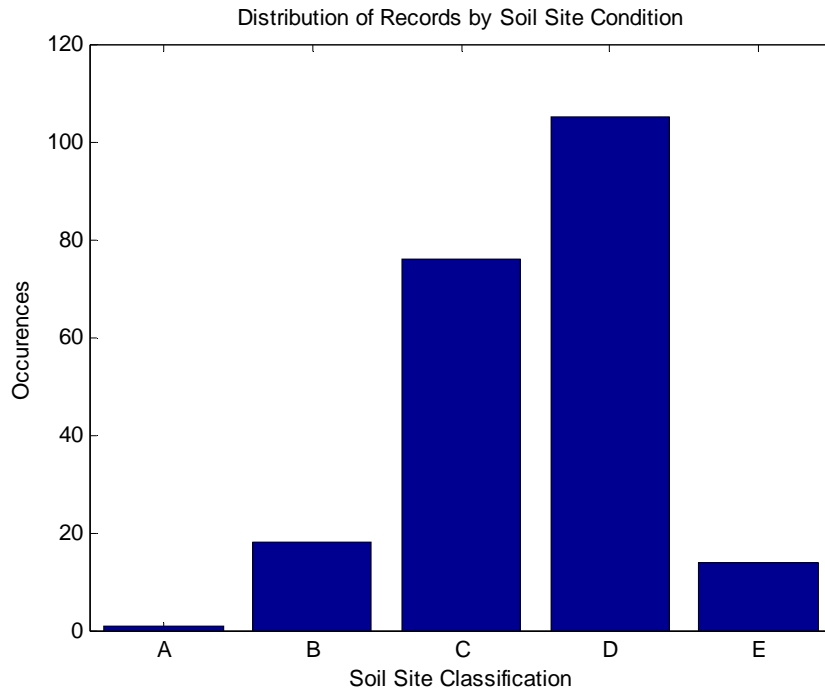


Figure F.18 Moderate Suite - Soil Site Distribution

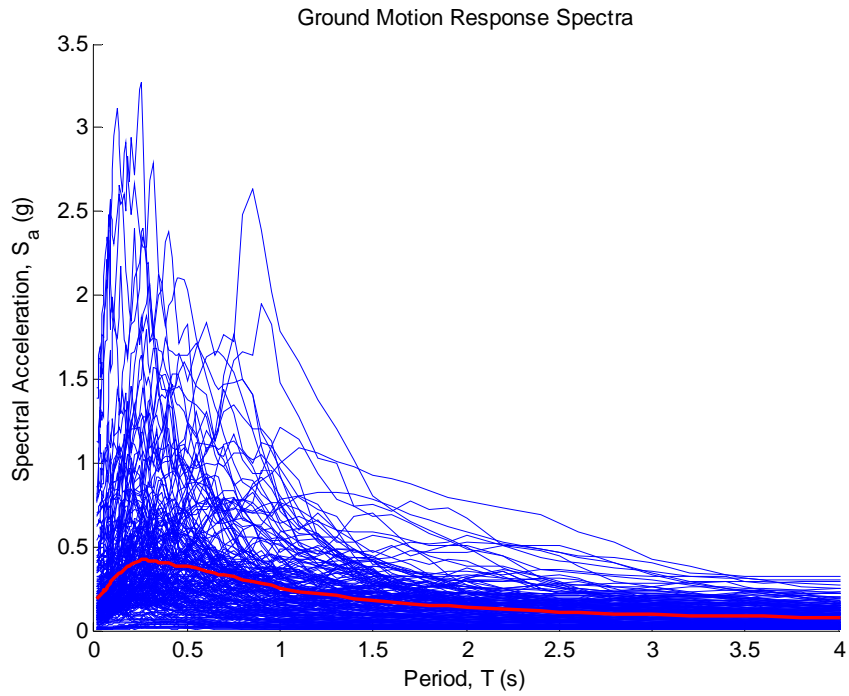


Figure F.19 Severe NGA Suite - Ground Motion Response Spectra

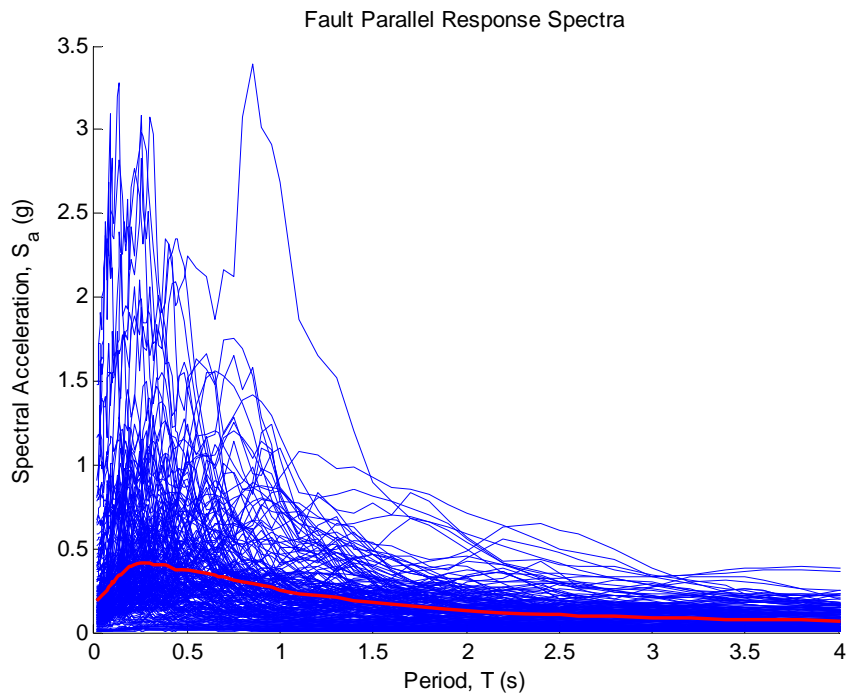


Figure F.20 Severe NGA Suite - Fault Parallel Response Spectra

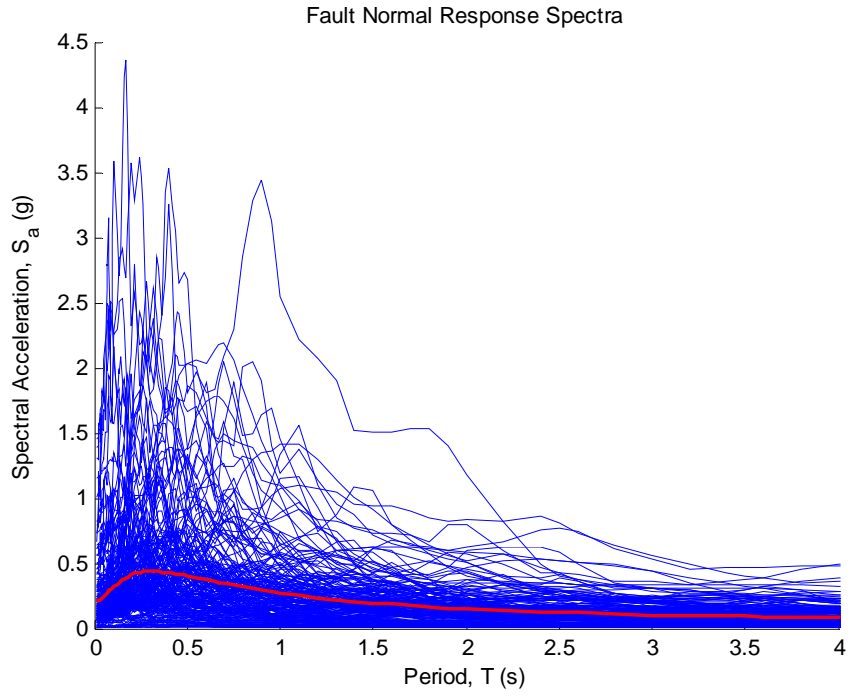


Figure F.21 Severe NGA Suite - Fault Normal Response Spectra

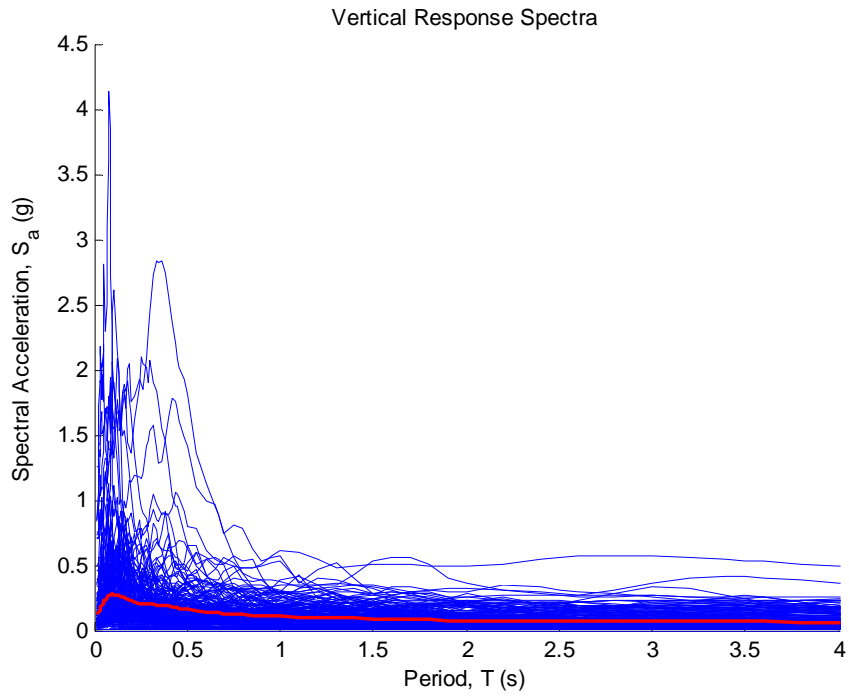


Figure F.22 Severe NGA Suite - Vertical Response Spectra

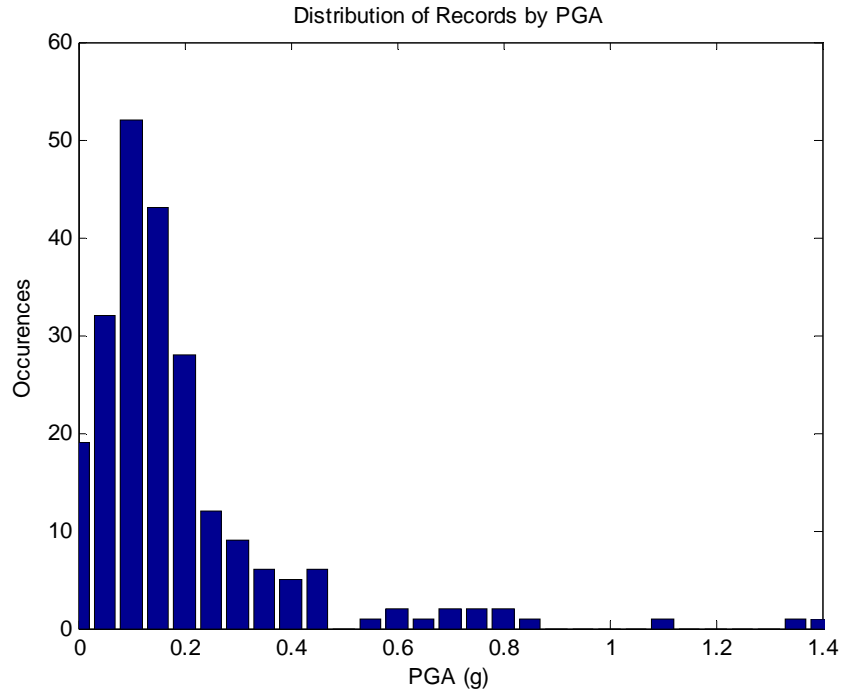


Figure F.23 Severe NGA Suite - PGA Distribution

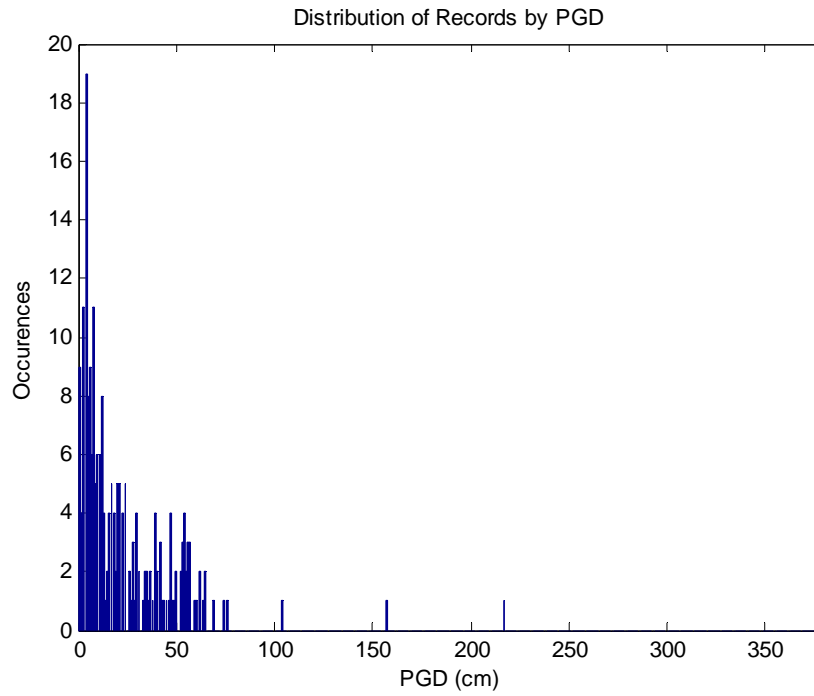


Figure F.24 Severe NGA Suite - PGD Distribution

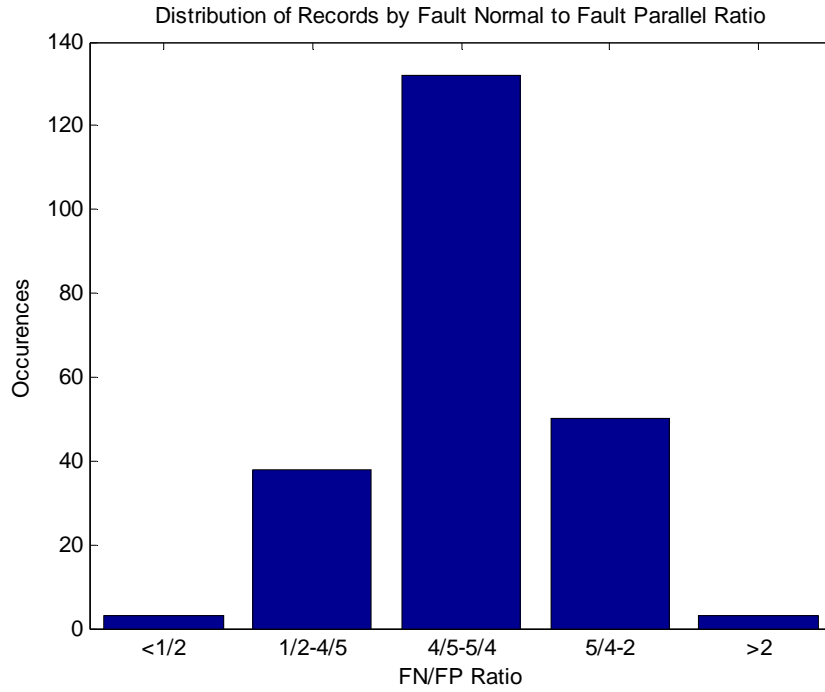


Figure F.25 Severe NGA Suite - Horizontal Peak Parameter Ratios

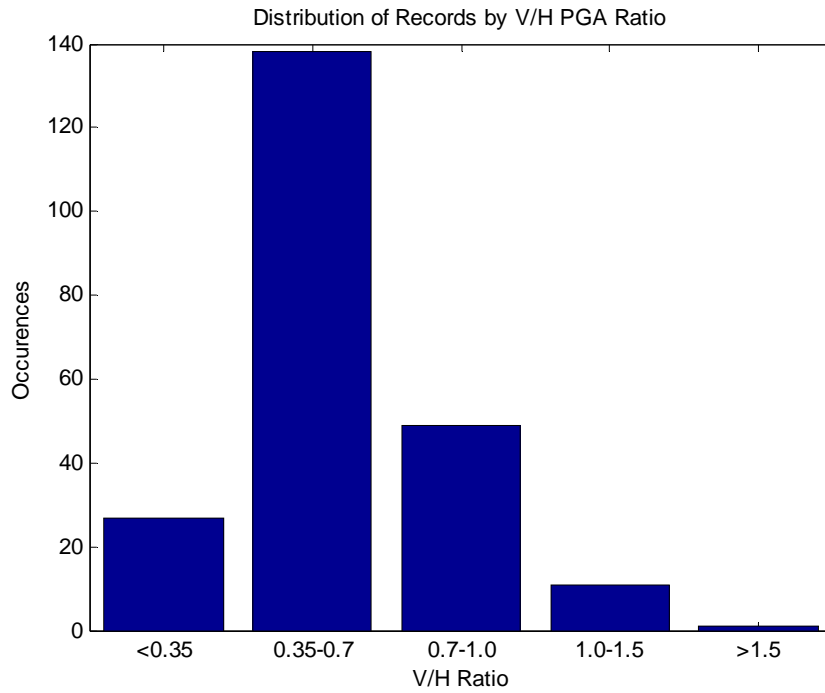


Figure F.26 Severe NGA Suite - Vertical to Horizontal Peak Parameter Ratios

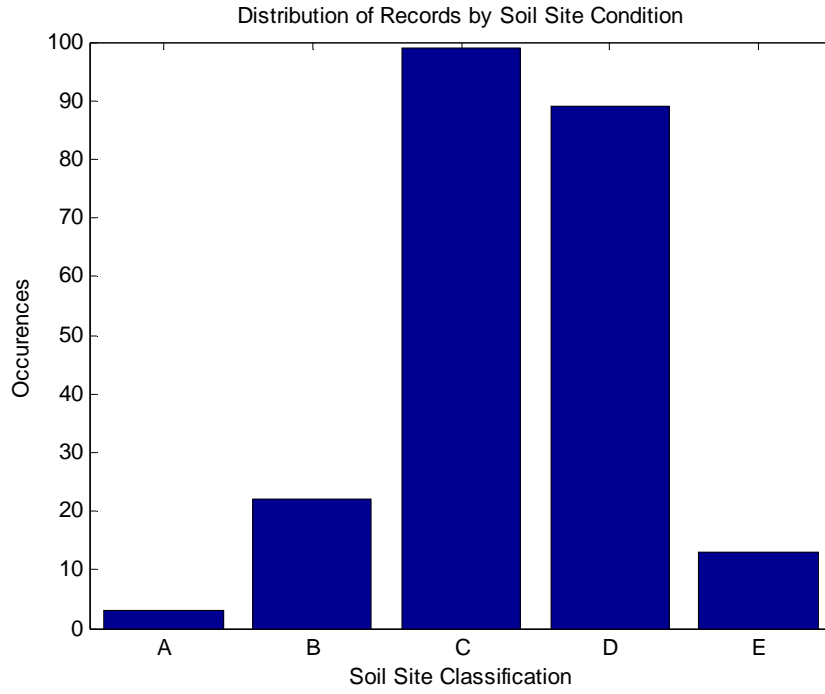


Figure F.27 Severe NGA Suite - Soil Site Distribution

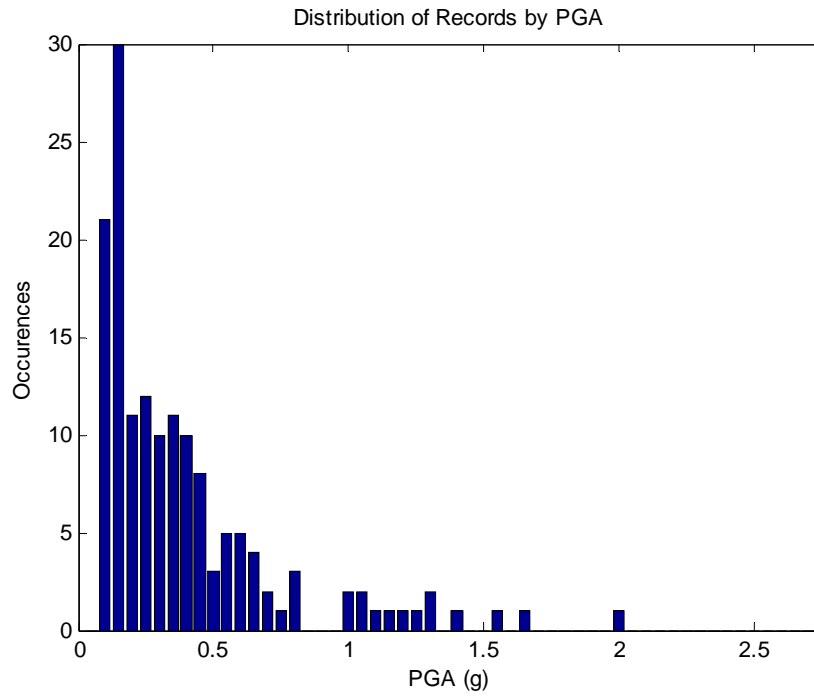


Figure F.28 Tohoku Records - PGA Distribution

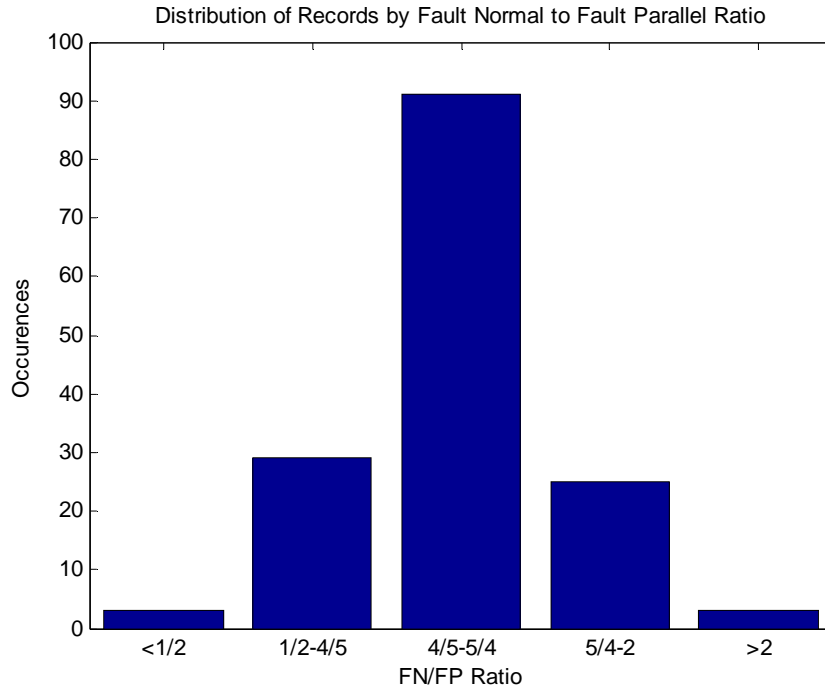


Figure F.29 Tohoku Records - Horizontal Peak Parameter Ratios

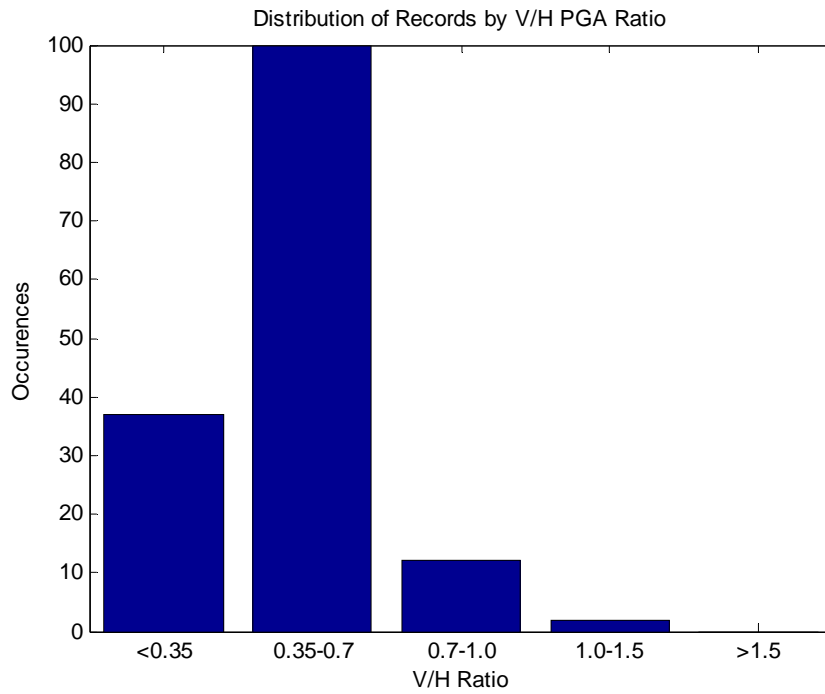


Figure F.30 Tohoku Records - Vertical to Horizontal Peak Parameter Ratios

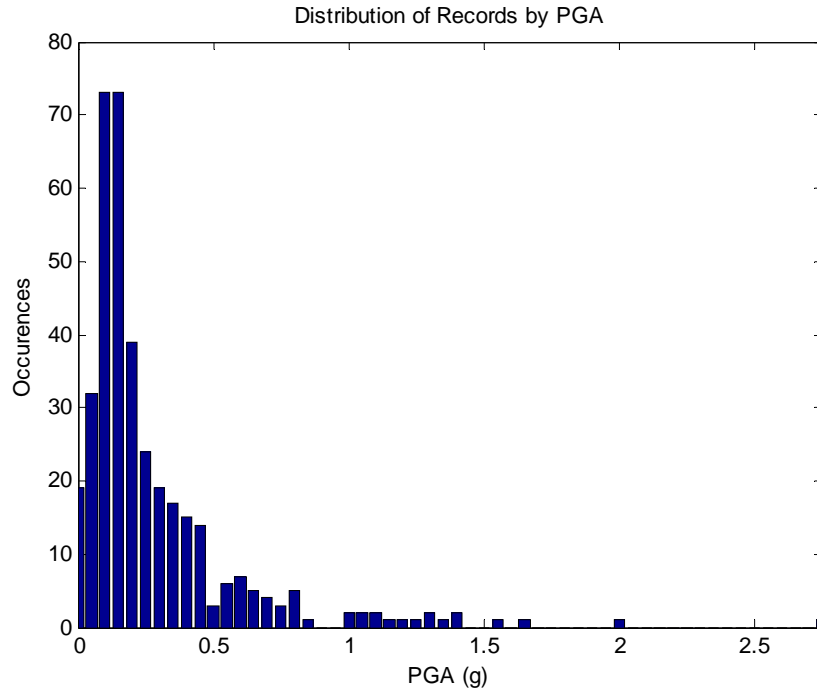


Figure F.31 Severe Suite - PGA Distribution

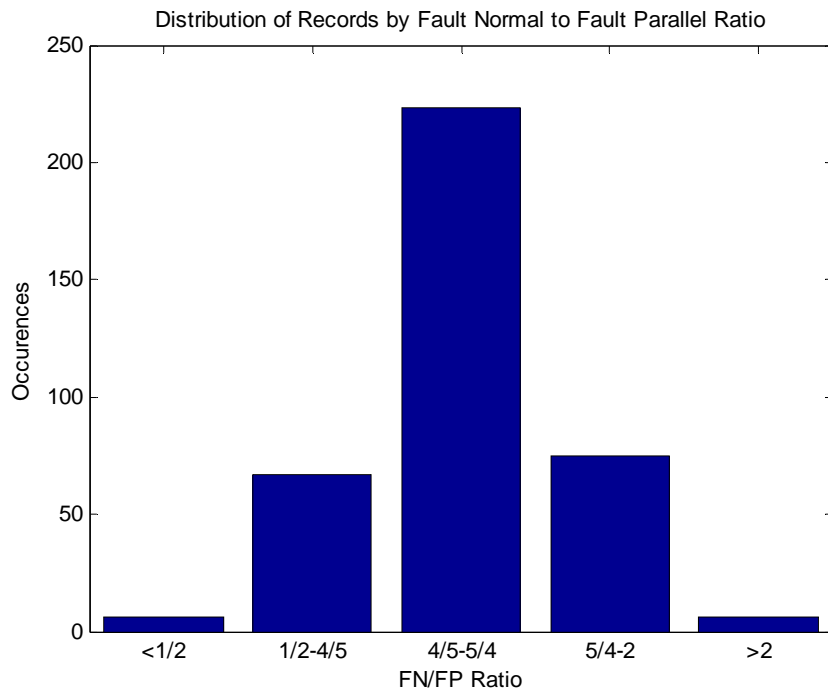


Figure F.32 Severe Suite - Horizontal Peak Parameter Ratios

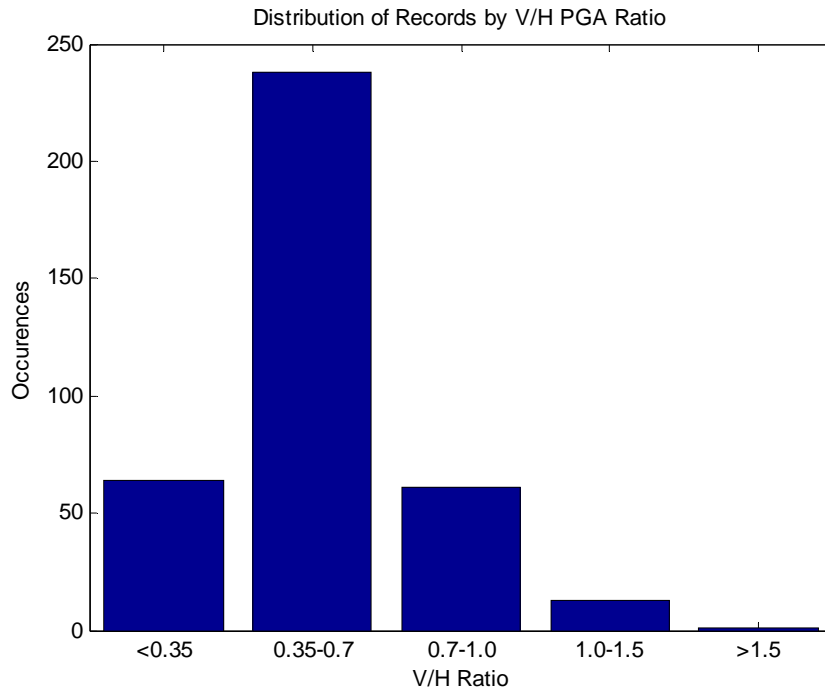


Figure F.33 Severe Suite - Vertical to Horizontal Peak Parameter Ratios

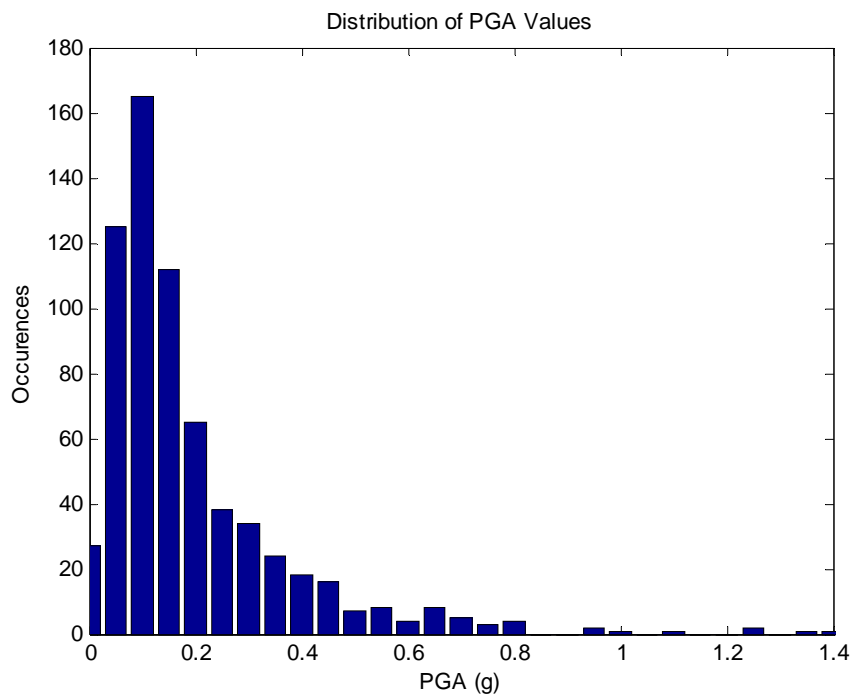


Figure F.34 All NGA Records - PGA Distribution

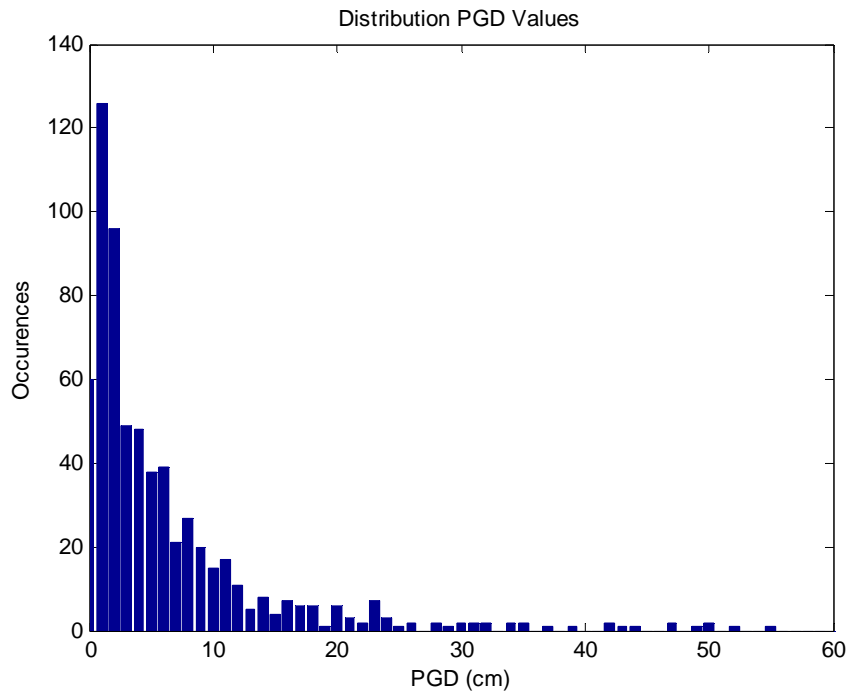


Figure F.35 All NGA Records - PGD Distribution

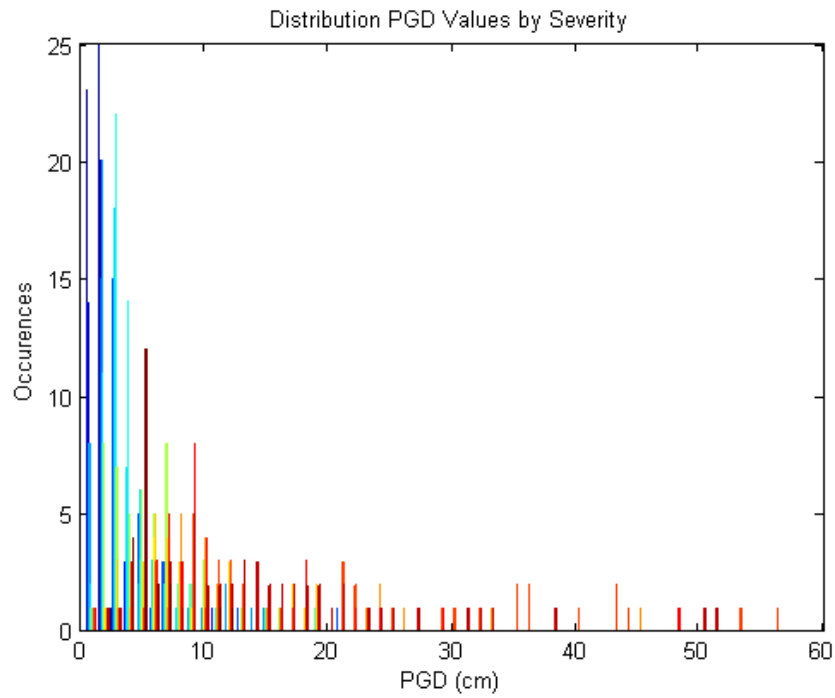


Figure F.36 All NGA Records - PGD Distribution by Bin

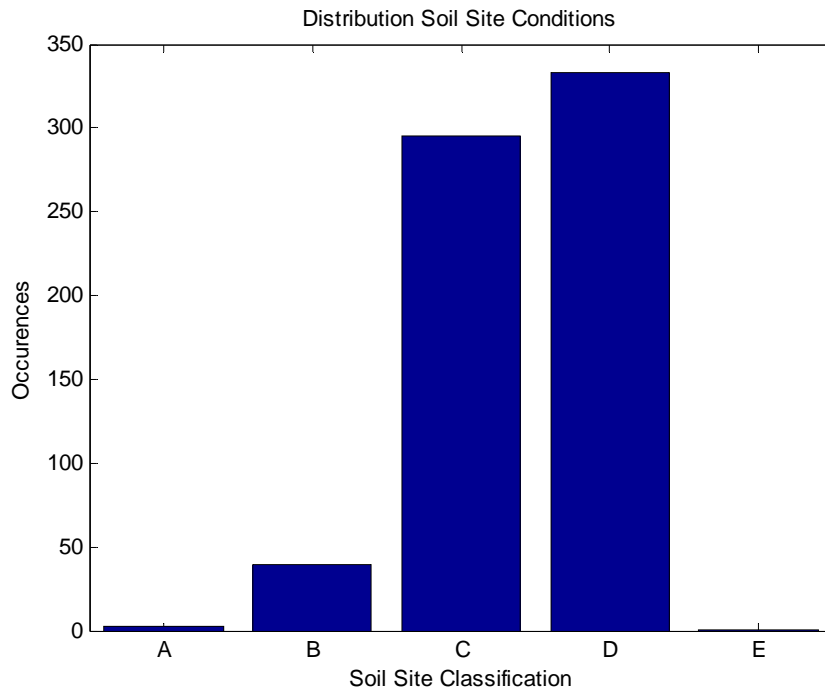


Figure F.37 All NGA Records - Soil Site Distribution

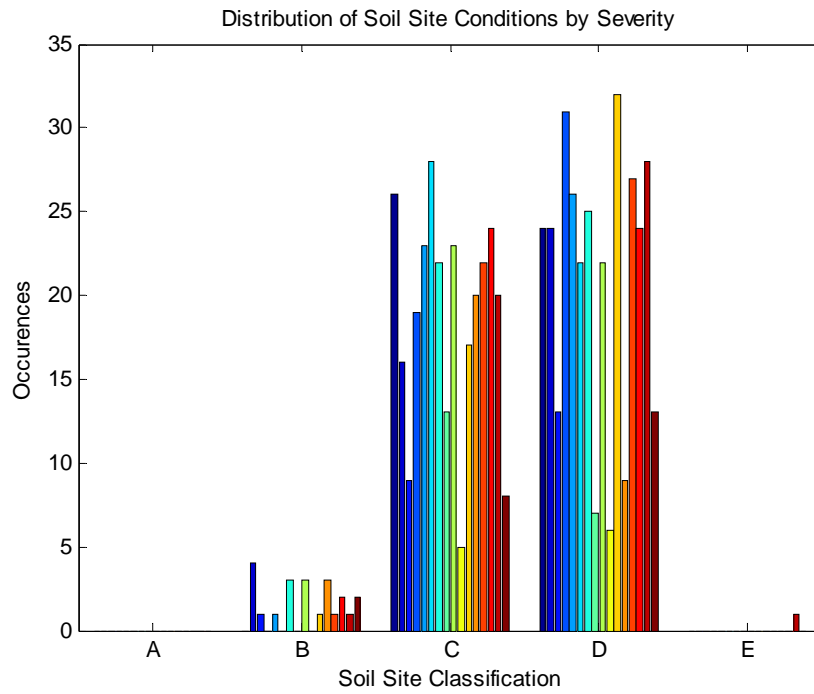


Figure F.38 All NGA Records - Soil Site Distribution by Bin

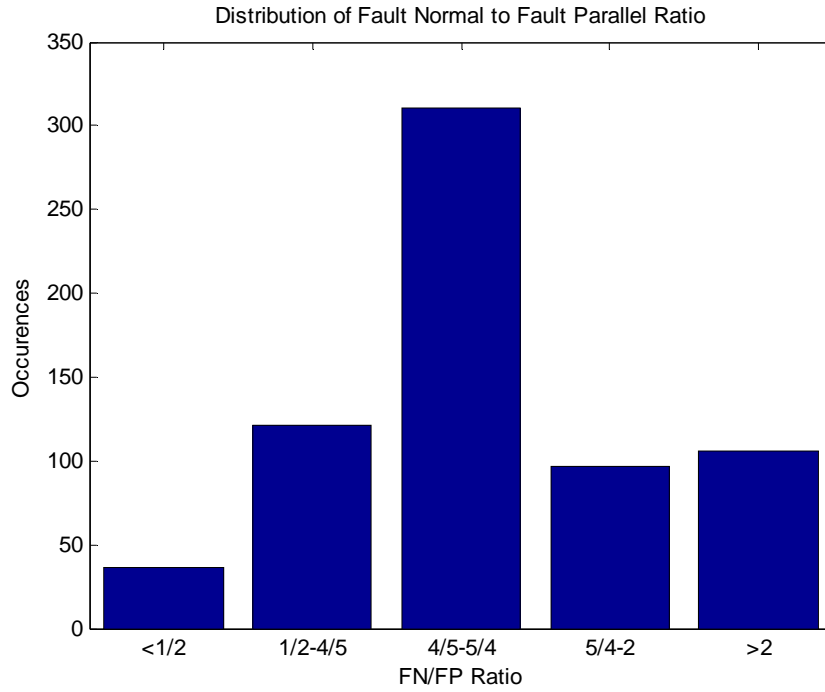


Figure F.39 All NGA Records - Horizontal Peak Parameter Ratios

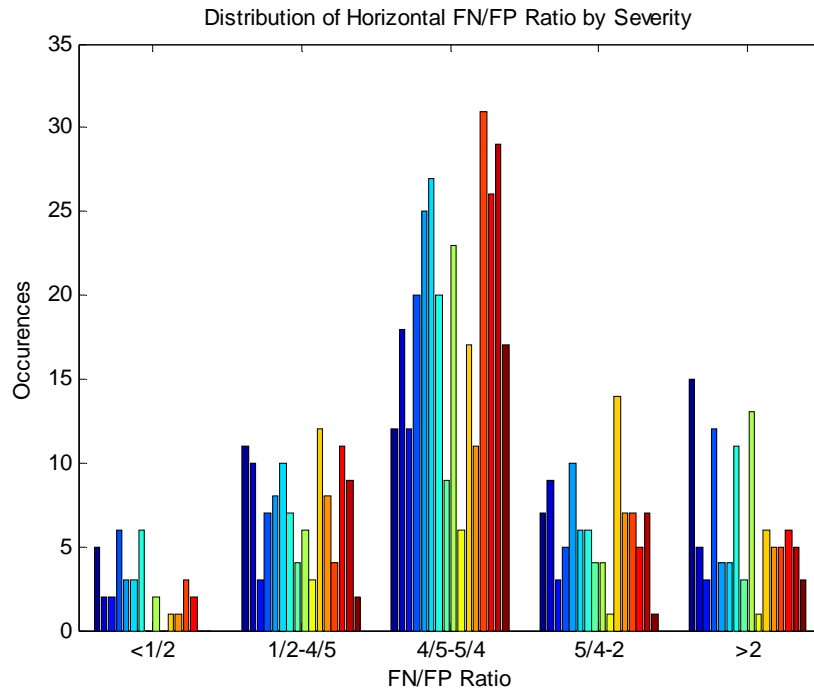


Figure F.40 All NGA Records - Horizontal Peak Parameter Ratios by Bin

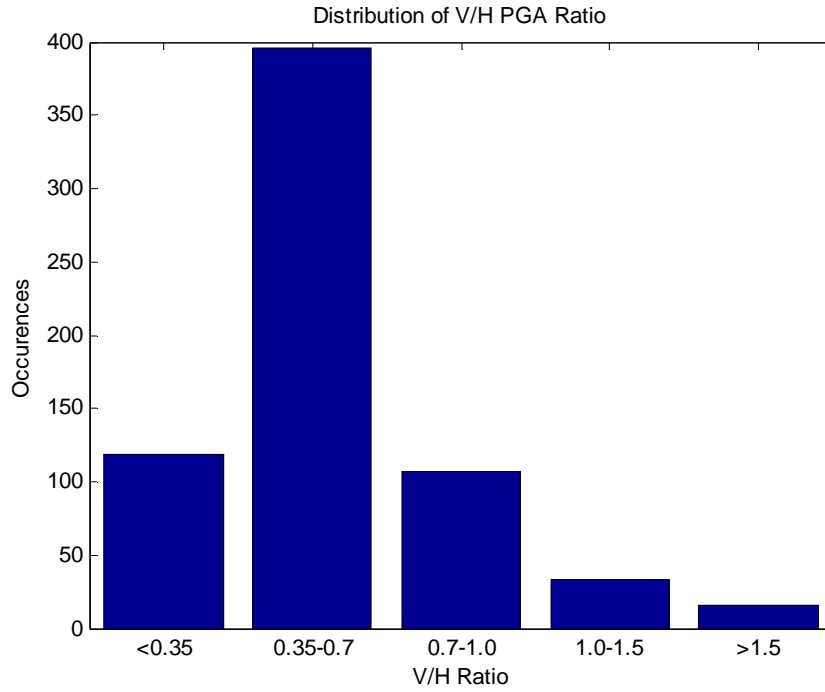


Figure F.41 All NGA Records - V/H Peak Parameter Ratios

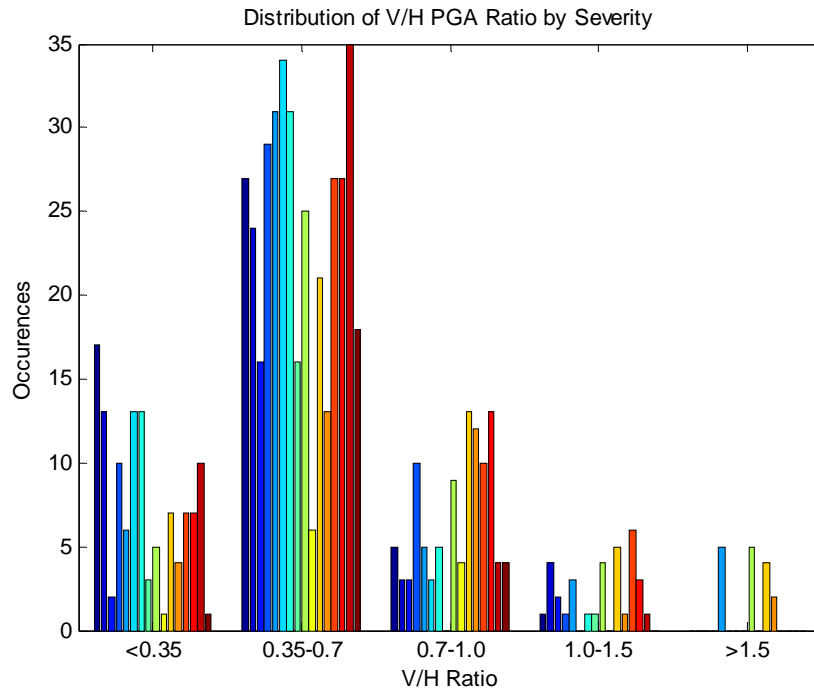


Figure F.42 All NGA Records - V/H Peak Parameter Ratios by Bin

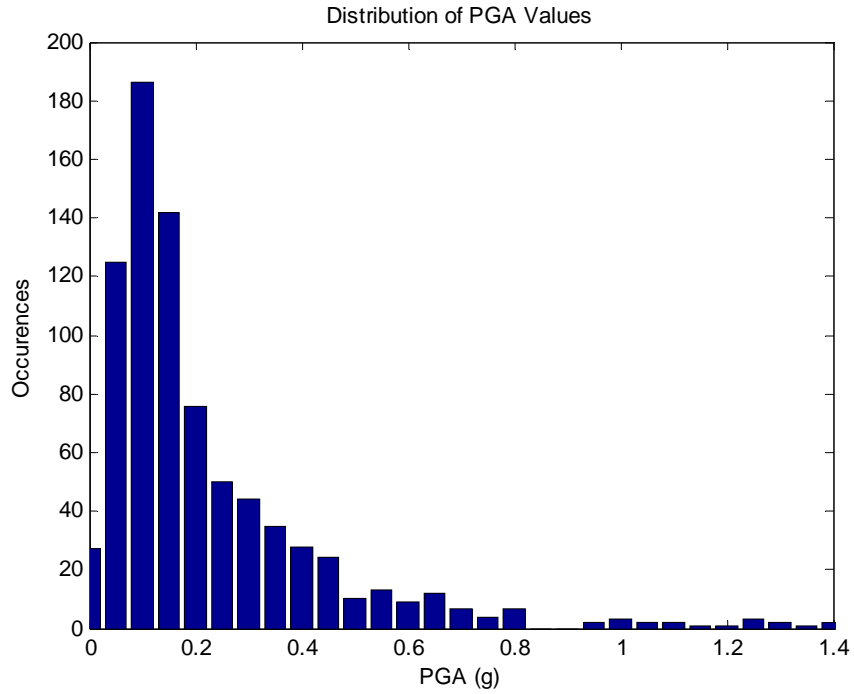


Figure F.43 All Records - PGA Distribution

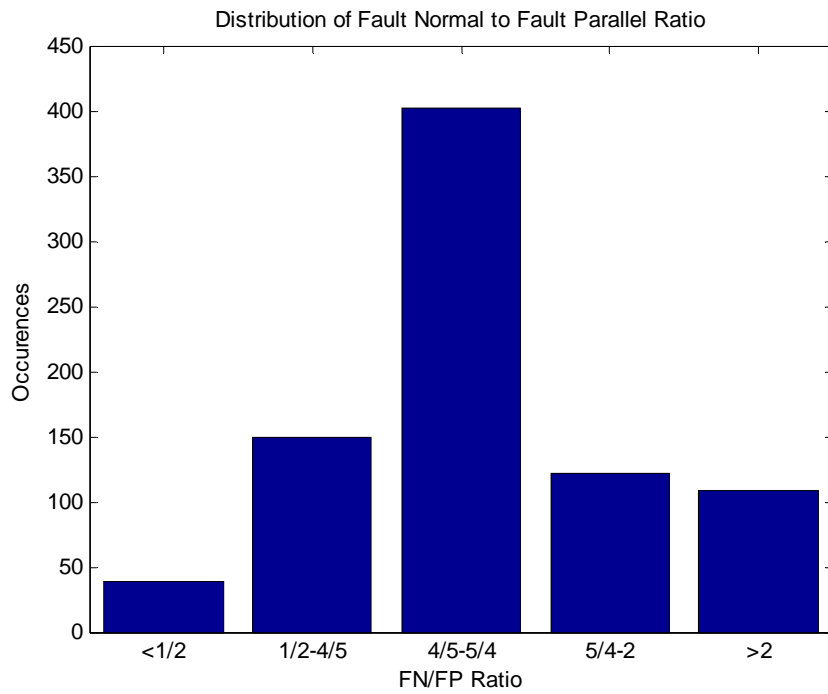


Figure F.44 All Records - Horizontal Peak Parameter Ratios

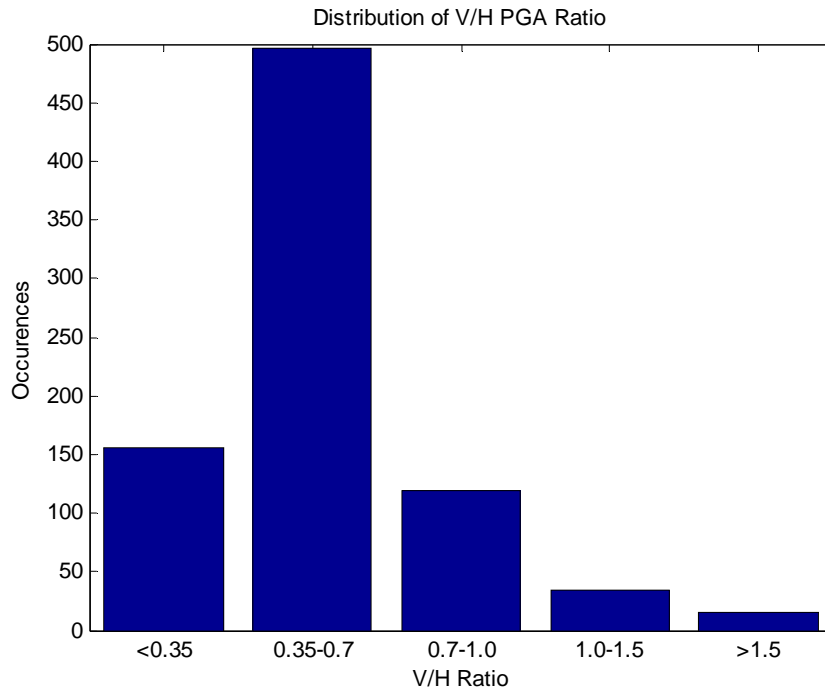


Figure F.45 All Records - V/H Peak Parameter Ratios

Table F.1 Details of Slight Suite of Earthquake Records

NGA Sequence #	Event Name	Year	Station	Magnitude	Fault Mechanism	Closest Distance (km)	Vs30 (m/s)
23	San Francisco	1957	Golden Gate Park	5.28	Reverse	[11.0]	874
45	Lytle Creek	1970	Devil's Canyon	5.33	Reverse-Oblique	[20.1]	685
50	Lytle Creek	1970	Wrightwood - 6074 Park Dr	5.33	Reverse-Oblique	[12.4]	486
63	San Fernando	1971	Fairmont Dam	6.61	Reverse	30.2	685
81	San Fernando	1971	Pearblossom Pump	6.61	Reverse	39	529
87	San Fernando	1971	Santa Anita Dam	6.61	Reverse	30.7	685
93	San Fernando	1971	Whittier Narrows Dam	6.61	Reverse	39.5	299
97	Point Mugu	1973	Port Hueneme	5.65	Reverse	[17.7]	298
122	Friuli- Italy-01	1976	Codroipo	6.5	Reverse	33.4	275
130	Friuli- Italy-02	1976	Buia	5.91	Reverse	11	339
132	Friuli- Italy-02	1976	Forgaria Cornino	5.91	Reverse	14.8	412
133	Friuli- Italy-02	1976	San Rocco	5.91	Reverse	14.5	660
145	Coyote Lake	1979	Coyote Lake Dam (SW Abut)	5.74	Strike-Slip	6.1	597
146	Coyote Lake	1979	Gilroy Array #1	5.74	Strike-Slip	10.7	1428
154	Coyote Lake	1979	San Juan Bautista- 24 Polk St	5.74	Strike-Slip	19.7	371
155	Norcia- Italy	1979	Bevagna	5.9	Normal	[31.4]	1000
156	Norcia- Italy	1979	Cascia	5.9	Normal	[4.6]	660
157	Norcia- Italy	1979	Spoletto	5.9	Normal	[13.4]	339
186	Imperial Valley-06	1979	Niland Fire Station	6.53	Strike-Slip	36.9	208
188	Imperial Valley-06	1979	Plaster City	6.53	Strike-Slip	30.3	345
191	Imperial Valley-06	1979	Victoria	6.53	Strike-Slip	31.9	275
193	Imperial Valley-07	1979	Bonds Corner	5.01	Strike-Slip	[13.0]	223
195	Imperial Valley-07	1979	Calexico Fire Station	5.01	Strike-Slip	[13.3]	231
198	Imperial Valley-07	1979	El Centro Array #10	5.01	Strike-Slip	[10.6]	203
199	Imperial Valley-07	1979	El Centro Array #11	5.01	Strike-Slip	[15.3]	196
200	Imperial Valley-07	1979	El Centro Array #2	5.01	Strike-Slip	[18.8]	189
201	Imperial Valley-07	1979	El Centro Array #3	5.01	Strike-Slip	[16.3]	163
202	Imperial Valley-07	1979	El Centro Array #4	5.01	Strike-Slip	[12.1]	209
203	Imperial Valley-07	1979	El Centro Array #5	5.01	Strike-Slip	[11.2]	206
205	Imperial Valley-07	1979	El Centro Array #7	5.01	Strike-Slip	[10.3]	211
206	Imperial Valley-07	1979	El Centro Array #8	5.01	Strike-Slip	[11.0]	206
207	Imperial Valley-07	1979	El Centro Differential Array	5.01	Strike-Slip	[10.7]	202
208	Imperial Valley-07	1979	Holtville Post Office	5.01	Strike-Slip	[10.7]	203
214	Livermore-01	1980	San Ramon - Eastman Kodak	5.8	Strike-Slip	[17.2]	271
215	Livermore-01	1980	San Ramon Fire Station	5.8	Strike-Slip	[18.1]	271
219	Livermore-02	1980	Del Valle Dam (Toe)	5.42	Strike-Slip	[15.7]	339
221	Livermore-02	1980	Livermore - Fagundas Ranch	5.42	Strike-Slip	[11.8]	339
222	Livermore-02	1980	Livermore - Morgan Terr Park	5.42	Strike-Slip	[14.1]	713
223	Livermore-02	1980	San Ramon - Eastman Kodak	5.42	Strike-Slip	[18.3]	271
225	Anza (Horse Canyon)-01	1980	Anza - Pinyon Flat	5.19	Strike-Slip	[17.4]	725
226	Anza (Horse Canyon)-01	1980	Anza - Terwilliger Valley	5.19	Strike-Slip	[12.7]	685
227	Anza (Horse Canyon)-01	1980	Anza Fire Station	5.19	Strike-Slip	[17.6]	339
233	Mammoth Lakes-02	1980	Convict Creek	5.69	Strike-Slip	9.5	339
234	Mammoth Lakes-02	1980	Long Valley Dam (Upr L Abut)	5.69	Strike-Slip	16.9	345
236	Mammoth Lakes-03	1980	Convict Creek	5.91	Strike-Slip	[12.5]	339
237	Mammoth Lakes-03	1980	Long Valley Dam (Downst)	5.91	Strike-Slip	[18.1]	345
238	Mammoth Lakes-03	1980	Long Valley Dam (L Abut)	5.91	Strike-Slip	[18.1]	345
239	Mammoth Lakes-03	1980	Long Valley Dam (Upr L Abut)	5.91	Strike-Slip	[18.1]	345
241	Mammoth Lakes-04	1980	Long Valley Dam (Downst)	5.7	Strike-Slip	[14.4]	345

Table F.1 (cont.)

242	Mammoth Lakes-04	1980	Long Valley Dam (L Abut)	5.7	Strike-Slip	[14.4]	345
243	Mammoth Lakes-04	1980	Long Valley Dam (Upr L Abut)	5.7	Strike-Slip	[14.4]	345
248	Mammoth Lakes-06	1980	Convict Creek	5.94	Strike-Slip	[12.2]	339
284	Irpinia- Italy-01	1980	Auletta	6.9	Normal	9.6	1000
285	Irpinia- Italy-01	1980	Bagnoli Irpinio	6.9	Normal	8.2	1000
286	Irpinia- Italy-01	1980	Bisaccia	6.9	Normal	21.3	1000
287	Irpinia- Italy-01	1980	Bovino	6.9	Normal	46.2	275
290	Irpinia- Italy-01	1980	Mercato San Severino	6.9	Normal	29.8	350
291	Irpinia- Italy-01	1980	Rionero In Vulture	6.9	Normal	30.1	530
295	Irpinia- Italy-02	1980	Auletta	6.2	Normal	29.9	1000
296	Irpinia- Italy-02	1980	Bagnoli Irpinio	6.2	Normal	19.6	1000
297	Irpinia- Italy-02	1980	Bisaccia	6.2	Normal	14.7	1000
303	Irpinia- Italy-02	1980	Sturno	6.2	Normal	20.4	1000
314	Westmorland	1981	Brawley Airport	5.9	Strike-Slip	15.4	209
315	Westmorland	1981	Niland Fire Station	5.9	Strike-Slip	15.3	208
317	Westmorland	1981	Salton Sea Wildlife Refuge	5.9	Strike-Slip	7.8	191
318	Westmorland	1981	Superstition Mtn Camera	5.9	Strike-Slip	19.4	362
320	Mammoth Lakes-10	1983	Convict Creek	5.34	Strike-Slip	[6.5]	339
321	Mammoth Lakes-11	1983	Convict Creek	5.31	Strike-Slip	[7.7]	339
326	Coalinga-01	1983	Parkfield - Cholame 2WA	6.36	Reverse	44.7	185
335	Coalinga-01	1983	Parkfield - Fault Zone 10	6.36	Reverse	31.6	438
336	Coalinga-01	1983	Parkfield - Fault Zone 11	6.36	Reverse	28.5	376
337	Coalinga-01	1983	Parkfield - Fault Zone 12	6.36	Reverse	29.3	339
339	Coalinga-01	1983	Parkfield - Fault Zone 15	6.36	Reverse	29.4	376
340	Coalinga-01	1983	Parkfield - Fault Zone 16	6.36	Reverse	27.7	339
341	Coalinga-01	1983	Parkfield - Fault Zone 2	6.36	Reverse	39	339
342	Coalinga-01	1983	Parkfield - Fault Zone 3	6.36	Reverse	37.2	371
343	Coalinga-01	1983	Parkfield - Fault Zone 4	6.36	Reverse	34.6	339
344	Coalinga-01	1983	Parkfield - Fault Zone 6	6.36	Reverse	32.9	438
345	Coalinga-01	1983	Parkfield - Fault Zone 7	6.36	Reverse	31.2	371
346	Coalinga-01	1983	Parkfield - Fault Zone 8	6.36	Reverse	29.9	376
347	Coalinga-01	1983	Parkfield - Fault Zone 9	6.36	Reverse	31.7	438
348	Coalinga-01	1983	Parkfield - Gold Hill 1W	6.36	Reverse	36.1	339
349	Coalinga-01	1983	Parkfield - Gold Hill 2E	6.36	Reverse	33.1	339
350	Coalinga-01	1983	Parkfield - Gold Hill 2W	6.36	Reverse	37	376
351	Coalinga-01	1983	Parkfield - Gold Hill 3E	6.36	Reverse	30.1	371
356	Coalinga-01	1983	Parkfield - Stone Corral 2E	6.36	Reverse	36.4	376
357	Coalinga-01	1983	Parkfield - Stone Corral 3E	6.36	Reverse	34	376
358	Coalinga-01	1983	Parkfield - Stone Corral 4E	6.36	Reverse	31.6	376
360	Coalinga-01	1983	Parkfield - Vineyard Cany 1W	6.36	Reverse	29.1	376
362	Coalinga-01	1983	Parkfield - Vineyard Cany 2W	6.36	Reverse	30.4	339
363	Coalinga-01	1983	Parkfield - Vineyard Cany 3W	6.36	Reverse	32.2	297
364	Coalinga-01	1983	Parkfield - Vineyard Cany 4W	6.36	Reverse	34.5	376
369	Coalinga-01	1983	Slack Canyon	6.36	Reverse	27.5	685
371	Coalinga-02	1983	Anticline Ridge - Palmer Ave	5.09	Reverse	[11.6]	376
374	Coalinga-02	1983	Burnett Construction	5.09	Reverse	[17.4]	352
375	Coalinga-02	1983	Coalinga-14th & Elm (Old CHP)	5.09	Reverse	[16.4]	339
376	Coalinga-02	1983	Harris Ranch - Hdqtrs (temp)	5.09	Reverse	[15.5]	271
377	Coalinga-02	1983	LLN (temp)	5.09	Reverse	[11.3]	438
379	Coalinga-02	1983	Oil City	5.09	Reverse	[12.6]	376

Table F.1 (cont.)

380	Coalinga-02	1983	Oil Fields - Skunk Hollow	5.09	Reverse	[10.7]	376
381	Coalinga-02	1983	Oil Fields Fire Station	5.09	Reverse	[10.8]	376
382	Coalinga-02	1983	Palmer Ave	5.09	Reverse	[11.4]	376
383	Coalinga-02	1983	Pleasant Valley P.P. - yard	5.09	Reverse	[12.4]	257
384	Coalinga-02	1983	SGT (temp)	5.09	Reverse	[13.2]	376
385	Coalinga-02	1983	SUB (temp)	5.09	Reverse	[12.3]	270
386	Coalinga-02	1983	Skunk Hollow	5.09	Reverse	[10.6]	376
387	Coalinga-02	1983	Sulphur Baths (temp)	5.09	Reverse	[19.9]	617
388	Coalinga-02	1983	TRA (temp)	5.09	Reverse	[14.1]	247
389	Coalinga-02	1983	VEW (temp)	5.09	Reverse	[11.8]	376
391	Coalinga-03	1983	Burnett Construction	5.38	Reverse	[13.4]	352
392	Coalinga-03	1983	Coalinga-14th & Elm (Old CHP)	5.38	Reverse	[12.6]	339
393	Coalinga-03	1983	Sulphur Baths (temp)	5.38	Reverse	[13.3]	617
394	Coalinga-04	1983	Anticline Ridge Free-Field	5.18	Reverse	[10.9]	376
395	Coalinga-04	1983	Anticline Ridge Pad	5.18	Reverse	[10.9]	376
396	Coalinga-04	1983	Burnett Construction	5.18	Reverse	[14.7]	352
397	Coalinga-04	1983	Coalinga-14th & Elm (Old CHP)	5.18	Reverse	[13.8]	339
399	Coalinga-04	1983	Oil Fields Fire Station - FF	5.18	Reverse	[11.7]	376
400	Coalinga-04	1983	Oil Fields Fire Station - Pad	5.18	Reverse	[11.7]	376
401	Coalinga-04	1983	Palmer Ave	5.18	Reverse	[13.8]	376
402	Coalinga-04	1983	Skunk Hollow	5.18	Reverse	[11.9]	376
403	Coalinga-04	1983	Sulphur Baths (temp)	5.18	Reverse	[15.4]	617
404	Coalinga-04	1983	Transmitter Hill	5.18	Reverse	[10.0]	376
405	Coalinga-05	1983	Burnett Construction	5.77	Reverse	[11.5]	352
408	Coalinga-05	1983	Oil Fields Fire Station - FF	5.77	Reverse	[11.1]	376
410	Coalinga-05	1983	Palmer Ave	5.77	Reverse	[12.3]	376
414	Coalinga-05	1983	Sulphur Baths (temp)	5.77	Reverse	[11.4]	617
419	Coalinga-07	1983	Sulphur Baths (temp)	5.21	Reverse	[12.1]	617
423	Coalinga-08	1983	Coalinga-14th & Elm (Old CHP)	5.23	Strike-Slip	[13.3]	339
424	Coalinga-08	1983	Sulphur Baths (temp)	5.23	Strike-Slip	[18.3]	617
453	Morgan Hill	1984	Fremont - Mission San Jose	6.19	Strike-Slip	31.3	368
455	Morgan Hill	1984	Gilroy Array #1	6.19	Strike-Slip	14.9	1428
463	Morgan Hill	1984	Hollister Diff Array #1	6.19	Strike-Slip	26.4	216
464	Morgan Hill	1984	Hollister Diff Array #3	6.19	Strike-Slip	26.4	216
465	Morgan Hill	1984	Hollister Diff Array #4	6.19	Strike-Slip	26.4	216
466	Morgan Hill	1984	Hollister Diff Array #5	6.19	Strike-Slip	26.4	216
467	Morgan Hill	1984	Hollister Diff. Array	6.19	Strike-Slip	26.4	216
470	Morgan Hill	1984	San Juan Bautista- 24 Polk St	6.19	Strike-Slip	27.1	371
471	Morgan Hill	1984	San Justo Dam (L Abut)	6.19	Strike-Slip	31.9	623
472	Morgan Hill	1984	San Justo Dam (R Abut)	6.19	Strike-Slip	31.9	623
498	Hollister-04	1986	Hollister Diff Array #1	5.45	Strike-Slip	[14.1]	216
499	Hollister-04	1986	Hollister Diff Array #3	5.45	Strike-Slip	[14.1]	216
501	Hollister-04	1986	SAGO South - Surface	5.45	Strike-Slip	[12.2]	685
516	N. Palm Springs	1986	Cranston Forest Station	6.06	Reverse-Oblique	27.5	371
519	N. Palm Springs	1986	Hemet Fire Station	6.06	Reverse-Oblique	34.7	339
521	N. Palm Springs	1986	Hurkey Creek Park	6.06	Reverse-Oblique	29.8	339
522	N. Palm Springs	1986	Indio	6.06	Reverse-Oblique	35.6	208
526	N. Palm Springs	1986	Landers Fire Station	6.06	Reverse-Oblique	35.4	345
535	N. Palm Springs	1986	San Jacinto - Valley Cemetary	6.06	Reverse-Oblique	31	339
545	Chalfant Valley-01	1986	Bishop - Paradise Lodge	5.77	Strike-Slip	15.1	345

Table F.1 (cont.)

551	Chalfant Valley-02	1986	Convict Creek	6.19	Strike-Slip	31.2	339
556	Chalfant Valley-02	1986	McGee Creek - Surface	6.19	Strike-Slip	30.1	359
563	Chalfant Valley-04	1986	Zack Brothers Ranch	5.44	Strike-Slip	[10.6]	271
590	Whittier Narrows-01	1987	Altadena - Eaton Canyon	5.99	Reverse-Oblique	19.5	371
592	Whittier Narrows-01	1987	Arcadia - Campus Dr	5.99	Reverse-Oblique	17.4	368
594	Whittier Narrows-01	1987	Baldwin Park - N Holly	5.99	Reverse-Oblique	16.7	309
608	Whittier Narrows-01	1987	Carson - Water St	5.99	Reverse-Oblique	30	161
613	Whittier Narrows-01	1987	Covina - W Badillo	5.99	Reverse-Oblique	18.6	271
616	Whittier Narrows-01	1987	El Monte - Fairview Av	5.99	Reverse-Oblique	15.7	309
622	Whittier Narrows-01	1987	Hacienda Heights - Colima	5.99	Reverse-Oblique	17.4	309
632	Whittier Narrows-01	1987	LA - Cypress Ave	5.99	Reverse-Oblique	17	446
634	Whittier Narrows-01	1987	LA - Fletcher Dr	5.99	Reverse-Oblique	18.9	446
637	Whittier Narrows-01	1987	LA - N Figueroa St	5.99	Reverse-Oblique	16.5	405
640	Whittier Narrows-01	1987	LA - S Grand Ave	5.99	Reverse-Oblique	20.5	309
643	Whittier Narrows-01	1987	LA - Wonderland Ave	5.99	Reverse-Oblique	27.6	1223
649	Whittier Narrows-01	1987	La Habra - Briarcliff	5.99	Reverse-Oblique	20.3	361
650	Whittier Narrows-01	1987	La Puente - Rimgrove Av	5.99	Reverse-Oblique	17.8	309
707	Whittier Narrows-02	1987	Alhambra - Fremont School	5.27	Reverse-Oblique	[11.8]	550
708	Whittier Narrows-02	1987	Altadena - Eaton Canyon	5.27	Reverse-Oblique	[15.5]	371
709	Whittier Narrows-02	1987	Downey - Co Maint Bldg	5.27	Reverse-Oblique	[18.5]	272
714	Whittier Narrows-02	1987	LA - Obregon Park	5.27	Reverse-Oblique	[13.5]	349
715	Whittier Narrows-02	1987	Mt Wilson - CIT Seis Sta	5.27	Reverse-Oblique	[19.9]	822
716	Whittier Narrows-02	1987	San Marino - SW Academy	5.27	Reverse-Oblique	[12.0]	379
731	Loma Prieta	1989	APEEL 10 - Skyline	6.93	Reverse-Oblique	41.9	392
732	Loma Prieta	1989	APEEL 2 - Redwood City	6.93	Reverse-Oblique	43.2	133
735	Loma Prieta	1989	APEEL 7 - Pulgas	6.93	Reverse-Oblique	41.9	415
736	Loma Prieta	1989	APEEL 9 - Crystal Springs Res	6.93	Reverse-Oblique	41	450
751	Loma Prieta	1989	Calaveras Reservoir	6.93	Reverse-Oblique	35.5	514
760	Loma Prieta	1989	Foster City - Menhaden Court	6.93	Reverse-Oblique	45.6	126
761	Loma Prieta	1989	Fremont - Emerson Court	6.93	Reverse-Oblique	39.9	285
762	Loma Prieta	1989	Fremont - Mission San Jose	6.93	Reverse-Oblique	39.5	368
772	Loma Prieta	1989	Halls Valley	6.93	Reverse-Oblique	30.5	282
781	Loma Prieta	1989	Lower Crystal Springs Dam dwnst	6.93	Reverse-Oblique	48.4	713
782	Loma Prieta	1989	Monterey City Hall	6.93	Reverse-Oblique	44.4	685
791	Loma Prieta	1989	SAGO South - Surface	6.93	Reverse-Oblique	34.3	685
800	Loma Prieta	1989	Salinas - John & Work	6.93	Reverse-Oblique	32.8	271
807	Loma Prieta	1989	Sunol - Forest Fire Station	6.93	Reverse-Oblique	47.6	401
812	Loma Prieta	1989	Woodside	6.93	Reverse-Oblique	34.1	454
931	Big Bear-01	1992	San Bernardino - E & Hospitality	6.46	Strike-Slip	[34.6]	271
934	Big Bear-01	1992	Silent Valley - Poppet Flat	6.46	Strike-Slip	[35.2]	685
935	Big Bear-01	1992	Snow Creek	6.46	Strike-Slip	[38.2]	345
942	Northridge-01	1994	Alhambra - Fremont School	6.69	Reverse	36.8	550
945	Northridge-01	1994	Anaverde Valley - City R	6.69	Reverse	38	446
947	Northridge-01	1994	Arcadia - Arcadia Av	6.69	Reverse	39.7	309
948	Northridge-01	1994	Arcadia - Campus Dr	6.69	Reverse	41.4	368
951	Northridge-01	1994	Bell Gardens - Jaboneria	6.69	Reverse	44.1	309
958	Northridge-01	1994	Camarillo	6.69	Reverse	40.3	235
962	Northridge-01	1994	Carson - Water St	6.69	Reverse	49.8	161
970	Northridge-01	1994	El Monte - Fairview Av	6.69	Reverse	44.8	309
971	Northridge-01	1994	Elizabeth Lake	6.69	Reverse	36.5	235

Table F.1 (cont.)

981	Northridge-01	1994	Inglewood - Union Oil	6.69	Reverse	42.2	316
984	Northridge-01	1994	LA - 116th St School	6.69	Reverse	41.2	301
990	Northridge-01	1994	LA - City Terrace	6.69	Reverse	36.6	365
991	Northridge-01	1994	LA - Cypress Ave	6.69	Reverse	30.7	446
993	Northridge-01	1994	LA - Fletcher Dr	6.69	Reverse	27.3	446
994	Northridge-01	1994	LA - Griffith Park Observatory	6.69	Reverse	23.8	1016
997	Northridge-01	1994	LA - N Figueroa St	6.69	Reverse	31.2	405
1000	Northridge-01	1994	LA - Pico & Sentous	6.69	Reverse	31.3	270
1001	Northridge-01	1994	LA - S Grand Ave	6.69	Reverse	34	309
1005	Northridge-01	1994	LA - Temple & Hope	6.69	Reverse	31.5	376
1008	Northridge-01	1994	LA - W 15th St	6.69	Reverse	29.7	405
1011	Northridge-01	1994	LA - Wonderland Ave	6.69	Reverse	20.3	1223
1019	Northridge-01	1994	Lake Hughes #1	6.69	Reverse	35.8	425
1021	Northridge-01	1994	Lake Hughes #4 - Camp Mend	6.69	Reverse	31.7	822
1022	Northridge-01	1994	Lake Hughes #4B - Camp Mend	6.69	Reverse	31.7	554
1026	Northridge-01	1994	Lawndale - Osage Ave	6.69	Reverse	39.9	361
1027	Northridge-01	1994	Leona Valley #1	6.69	Reverse	37.2	685
1028	Northridge-01	1994	Leona Valley #2	6.69	Reverse	37.2	446
1029	Northridge-01	1994	Leona Valley #3	6.69	Reverse	37.3	685
1030	Northridge-01	1994	Leona Valley #4	6.69	Reverse	37.6	446
1031	Northridge-01	1994	Leona Valley #5 - Ritter	6.69	Reverse	37.8	446
1032	Northridge-01	1994	Leona Valley #6	6.69	Reverse	38	327
1034	Northridge-01	1994	Malibu - Point Dume Sch	6.69	Reverse	33.7	350
1035	Northridge-01	1994	Manhattan Beach - Manhattan	6.69	Reverse	39.3	405
1038	Northridge-01	1994	Montebello - Bluff Rd.	6.69	Reverse	45	405
1041	Northridge-01	1994	Mt Wilson - CIT Seis Sta	6.69	Reverse	35.9	822
1053	Northridge-01	1994	Palmdale - Hwy 14 & Palmdale	6.69	Reverse	41.7	552
1055	Northridge-01	1994	Pasadena - N Sierra Madre	6.69	Reverse	36.1	455
1058	Northridge-01	1994	Point Mugu - Laguna Peak	6.69	Reverse	41.9	376
1070	Northridge-01	1994	San Gabriel - E Grand Ave	6.69	Reverse	39.3	401
1072	Northridge-01	1994	San Marino - SW Academy	6.69	Reverse	35	379
1074	Northridge-01	1994	Sandberg - Bald Mtn	6.69	Reverse	41.6	822
1631	Upland	1990	Pomona - 4th & Locust FF	5.63	Strike-Slip	[7.3]	230
1632	Upland	1990	Rancho Cucamonga - FF	5.63	Strike-Slip	[11.0]	390
1645	Sierra Madre	1991	Mt Wilson - CIT Seis Sta	5.61	Reverse	10.4	822
1646	Sierra Madre	1991	Pasadena - USGS/NSMP Office	5.61	Reverse	17.1	371
1647	Sierra Madre	1991	San Marino - SW Academy	5.61	Reverse	18.7	379
1688	Northridge-05	1994	Moorpark - Fire Sta	5.13	Reverse-Oblique	[20.1]	405
1693	Northridge-06	1994	Arleta - Nordhoff Fire Sta	5.28	Reverse	[12.2]	298
1697	Northridge-06	1994	Burbank - N Buena Vista	5.28	Reverse	[17.7]	271
1704	Northridge-06	1994	Jensen Filter Plant Generator	5.28	Reverse	[14.7]	526
1707	Northridge-06	1994	LA - Century City CC North	5.28	Reverse	[19.8]	278
1709	Northridge-06	1994	LA - Griffith Park Observatory	5.28	Reverse	[21.8]	1016
1711	Northridge-06	1994	LA - N Faring Rd	5.28	Reverse	[17.2]	405
1715	Northridge-06	1994	LA - Wonderland Ave	5.28	Reverse	[17.2]	1223
1722	Northridge-06	1994	Northridge - 17645 Saticoy St	5.28	Reverse	[11.3]	281
1723	Northridge-06	1994	Pacoima KageI Canyon	5.28	Reverse	[17.3]	508
1725	Northridge-06	1994	Panorama City - Roscoe	5.28	Reverse	[11.8]	271
1733	Northridge-06	1994	Sun Valley - Roscoe Blvd	5.28	Reverse	[12.3]	309
1734	Northridge-06	1994	Sun Valley - Sunland	5.28	Reverse	[15.3]	271

Table F.1 (cont.)

1735	Northridge-06	1994	Sunland - Mt Gleason Ave	5.28	Reverse	[20.0]	446
1736	Northridge-06	1994	Sylmar - Converter Sta	5.28	Reverse	[14.7]	251
1737	Northridge-06	1994	Sylmar - Converter Sta East	5.28	Reverse	[14.8]	371
1738	Northridge-06	1994	Sylmar - Sayre St	5.28	Reverse	[15.6]	339
1739	Northridge-06	1994	Tarzana - Cedar Hill A	5.28	Reverse	[13.3]	257
1740	Little Skull Mtn-NV	1992	Station #1-Lathrop Wells	5.65	Normal	16.1	275
1758	San Juan Bautista	1998	Hollister Diff. Array	5.17	Strike-Slip	[16.2]	216
1846	Yountville	2000	Benicia Fire Station #1	5	Strike-Slip	[41.6]	155
1852	Yountville	2000	Larkspur Ferry Terminal (FF)	5	Strike-Slip	[48.2]	170
1861	Yountville	2000	Richmond Rod & Gun Club	5	Strike-Slip	[44.0]	155
1866	Yountville	2000	Sonoma Fire Station #1	5	Strike-Slip	[12.4]	155
2462	Chi-Chi- Taiwan-03	1999	CHY029	6.2	Reverse	31.8	545
2466	Chi-Chi- Taiwan-03	1999	CHY035	6.2	Reverse	34.5	555
2490	Chi-Chi- Taiwan-03	1999	CHY074	6.2	Reverse	28.7	553
2616	Chi-Chi- Taiwan-03	1999	TCU063	6.2	Reverse	34.2	476
2618	Chi-Chi- Taiwan-03	1999	TCU065	6.2	Reverse	26.1	306
2619	Chi-Chi- Taiwan-03	1999	TCU067	6.2	Reverse	28.5	434
2631	Chi-Chi- Taiwan-03	1999	TCU082	6.2	Reverse	35.6	473
2646	Chi-Chi- Taiwan-03	1999	TCU109	6.2	Reverse	34.8	424
2651	Chi-Chi- Taiwan-03	1999	TCU117	6.2	Reverse	46.3	199
2656	Chi-Chi- Taiwan-03	1999	TCU123	6.2	Reverse	31.8	242
2663	Chi-Chi- Taiwan-03	1999	TCU141	6.2	Reverse	33.6	209
2700	Chi-Chi- Taiwan-04	1999	CHY025	6.2	Strike-Slip	29.2	278
2704	Chi-Chi- Taiwan-04	1999	CHY029	6.2	Strike-Slip	25.8	545
2708	Chi-Chi- Taiwan-04	1999	CHY034	6.2	Strike-Slip	28.5	379
2709	Chi-Chi- Taiwan-04	1999	CHY035	6.2	Strike-Slip	25.1	555
2712	Chi-Chi- Taiwan-04	1999	CHY042	6.2	Strike-Slip	34.1	680
2741	Chi-Chi- Taiwan-04	1999	CHY082	6.2	Strike-Slip	48.9	194
2742	Chi-Chi- Taiwan-04	1999	CHY086	6.2	Strike-Slip	33.7	680
2746	Chi-Chi- Taiwan-04	1999	CHY092	6.2	Strike-Slip	33	254
2754	Chi-Chi- Taiwan-04	1999	CHY104	6.2	Strike-Slip	31.5	223
2821	Chi-Chi- Taiwan-04	1999	KAU054	6.2	Strike-Slip	30.2	577
2871	Chi-Chi- Taiwan-04	1999	TCU084	6.2	Strike-Slip	27.1	680
2873	Chi-Chi- Taiwan-04	1999	TCU089	6.2	Strike-Slip	27.5	680
2888	Chi-Chi- Taiwan-04	1999	TCU116	6.2	Strike-Slip	28.8	493
2897	Chi-Chi- Taiwan-04	1999	TCU138	6.2	Strike-Slip	33.6	653
2997	Chi-Chi- Taiwan-05	1999	HWA005	6.2	Reverse	33.6	489
3008	Chi-Chi- Taiwan-05	1999	HWA020	6.2	Reverse	34.9	502
3019	Chi-Chi- Taiwan-05	1999	HWA032	6.2	Reverse	32.3	515
3021	Chi-Chi- Taiwan-05	1999	HWA034	6.2	Reverse	33.5	379
3264	Chi-Chi- Taiwan-06	1999	CHY024	6.3	Reverse	31.1	428
3268	Chi-Chi- Taiwan-06	1999	CHY028	6.3	Reverse	33.6	543
3300	Chi-Chi- Taiwan-06	1999	CHY074	6.3	Reverse	29.3	553
3456	Chi-Chi- Taiwan-06	1999	TCU049	6.3	Reverse	32	487
3457	Chi-Chi- Taiwan-06	1999	TCU050	6.3	Reverse	36.6	471
3458	Chi-Chi- Taiwan-06	1999	TCU051	6.3	Reverse	33.9	468
3459	Chi-Chi- Taiwan-06	1999	TCU052	6.3	Reverse	30.1	579
3460	Chi-Chi- Taiwan-06	1999	TCU053	6.3	Reverse	34.6	455
3461	Chi-Chi- Taiwan-06	1999	TCU056	6.3	Reverse	36.1	440
3462	Chi-Chi- Taiwan-06	1999	TCU057	6.3	Reverse	38	479

Table F.1 (cont.)

3464	Chi-Chi- Taiwan-06	1999	TCU060	6.3	Reverse	38.6	496
3469	Chi-Chi- Taiwan-06	1999	TCU068	6.3	Reverse	35.7	487
3477	Chi-Chi- Taiwan-06	1999	TCU082	6.3	Reverse	31.2	473
3488	Chi-Chi- Taiwan-06	1999	TCU100	6.3	Reverse	38.3	479
3489	Chi-Chi- Taiwan-06	1999	TCU102	6.3	Reverse	35.5	714
3495	Chi-Chi- Taiwan-06	1999	TCU109	6.3	Reverse	37.9	424
3496	Chi-Chi- Taiwan-06	1999	TCU110	6.3	Reverse	36.5	213
3502	Chi-Chi- Taiwan-06	1999	TCU120	6.3	Reverse	32.5	459
3503	Chi-Chi- Taiwan-06	1999	TCU122	6.3	Reverse	31.3	476
3509	Chi-Chi- Taiwan-06	1999	TCU138	6.3	Reverse	33.6	653

Table F.2 Details of Moderate Suite of Earthquake Records

NGA Sequence #	Event Name	Year	Station	Magnitude	Fault Mechanism	Closest Distance (km)	Vs30 (m/s)
12	Kern County	1952	LA - Hollywood Stor FF	7.36	Reverse	117.8	316.5
28	Parkfield	1966	Cholame - Shandon Array #12	6.19	Strike-Slip	17.6	408.9
30	Parkfield	1966	Cholame - Shandon Array #5	6.19	Strike-Slip	9.6	289.6
31	Parkfield	1966	Cholame - Shandon Array #8	6.19	Strike-Slip	12.9	256.8
33	Parkfield	1966	Temblor pre-1969	6.19	Strike-Slip	16	527.9
71	San Fernando	1971	Lake Hughes #12	6.61	Reverse	19.3	602.1
95	Managua- Nicaragua-01	1972	Managua- ESSO	6.24	Strike-Slip	4.1	288.8
125	Friuli- Italy-01	1976	Tolmezzo	6.5	Reverse	15.8	424.8
146	Coyote Lake	1979	Gilroy Array #1	5.74	Strike-Slip	10.7	1428
147	Coyote Lake	1979	Gilroy Array #2	5.74	Strike-Slip	9	270.8
148	Coyote Lake	1979	Gilroy Array #3	5.74	Strike-Slip	7.4	349.9
149	Coyote Lake	1979	Gilroy Array #4	5.74	Strike-Slip	5.7	221.8
150	Coyote Lake	1979	Gilroy Array #6	5.74	Strike-Slip	3.1	663.3
155	Norcia- Italy	1979	Bevagna	5.9	Normal	[31.4]	1000
158	Imperial Valley-06	1979	Aeropuerto Mexicali	6.53	Strike-Slip	0.3	274.5
159	Imperial Valley-06	1979	Agrarias	6.53	Strike-Slip	0.7	274.5
161	Imperial Valley-06	1979	Brawley Airport	6.53	Strike-Slip	10.4	208.7
162	Imperial Valley-06	1979	Calexico Fire Station	6.53	Strike-Slip	10.4	231.2
164	Imperial Valley-06	1979	Cerro Prieto	6.53	Strike-Slip	15.2	659.6
165	Imperial Valley-06	1979	Chihuahua	6.53	Strike-Slip	7.3	274.5
167	Imperial Valley-06	1979	Compuertas	6.53	Strike-Slip	15.3	274.5
171	Imperial Valley-06	1979	EC Meloland Overpass FF	6.53	Strike-Slip	0.1	186.2
173	Imperial Valley-06	1979	El Centro Array #10	6.53	Strike-Slip	6.2	202.8
174	Imperial Valley-06	1979	El Centro Array #11	6.53	Strike-Slip	12.4	196.2
175	Imperial Valley-06	1979	El Centro Array #12	6.53	Strike-Slip	17.9	196.9
178	Imperial Valley-06	1979	El Centro Array #3	6.53	Strike-Slip	12.8	162.9
187	Imperial Valley-06	1979	Parachute Test Site	6.53	Strike-Slip	12.7	348.7
189	Imperial Valley-06	1979	SAHOP Casa Flores	6.53	Strike-Slip	9.6	338.6
192	Imperial Valley-06	1979	Westmorland Fire Sta	6.53	Strike-Slip	15.2	193.7
199	Imperial Valley-07	1979	El Centro Array #11	5.01	Strike-Slip	[15.3]	196.2
200	Imperial Valley-07	1979	El Centro Array #2	5.01	Strike-Slip	[18.8]	188.8
201	Imperial Valley-07	1979	El Centro Array #3	5.01	Strike-Slip	[16.3]	162.9
204	Imperial Valley-07	1979	El Centro Array #6	5.01	Strike-Slip	[10.4]	203.2
230	Mammoth Lakes-01	1980	Convict Creek	6.06	Normal-Oblique	6.6	338.5
231	Mammoth Lakes-01	1980	Long Valley Dam (Upr L Abut)	6.06	Normal-Oblique	15.5	345.4
232	Mammoth Lakes-01	1980	Mammoth Lakes H. S.	6.06	Normal-Oblique	4.7	370.8
235	Mammoth Lakes-02	1980	Mammoth Lakes H. S.	5.69	Strike-Slip	9.1	370.8
240	Mammoth Lakes-04	1980	Convict Creek	5.7	Strike-Slip	[5.3]	338.5
249	Mammoth Lakes-06	1980	Fish & Game (FIS)	5.94	Strike-Slip	[12.2]	338.5
269	Victoria- Mexico	1980	Victoria Hospital Sotano	6.33	Strike-Slip	7.3	274.5
284	Irpinia- Italy-01	1980	Auletta	6.9	Normal	9.6	1000
285	Irpinia- Italy-01	1980	Bagnoli Irpinio	6.9	Normal	8.2	1000
286	Irpinia- Italy-01	1980	Bisaccia	6.9	Normal	21.3	1000
289	Irpinia- Italy-01	1980	Calitri	6.9	Normal	17.6	600
292	Irpinia- Italy-01	1980	Sturno	6.9	Normal	10.8	1000
295	Irpinia- Italy-02	1980	Auletta	6.2	Normal	29.9	1000
296	Irpinia- Italy-02	1980	Bagnoli Irpinio	6.2	Normal	19.6	1000
297	Irpinia- Italy-02	1980	Bisaccia	6.2	Normal	14.7	1000
300	Irpinia- Italy-02	1980	Calitri	6.2	Normal	8.8	600

Table F.2 (cont.)

303	Irpinia- Italy-02	1980	Sturno	6.2	Normal	20.4	1000
316	Westmorland	1981	Parachute Test Site	5.9	Strike-Slip	16.7	348.7
317	Westmorland	1981	Salton Sea Wildlife Refuge	5.9	Strike-Slip	7.8	191.1
319	Westmorland	1981	Westmorland Fire Sta	5.9	Strike-Slip	6.5	193.7
326	Coalinga-01	1983	Parkfield - Cholame 2WA	6.36	Reverse	44.7	184.8
338	Coalinga-01	1983	Parkfield - Fault Zone 14	6.36	Reverse	29.5	338.5
373	Coalinga-02	1983	Anticline Ridge Pad	5.09	Reverse	[11.6]	376.1
398	Coalinga-04	1983	Oil City	5.18	Reverse	[9.5]	376.1
406	Coalinga-05	1983	Coalinga-14th & Elm (Old CHP)	5.77	Reverse	[10.8]	338.5
409	Coalinga-05	1983	Oil Fields Fire Station - Pad	5.77	Reverse	[11.1]	376.1
411	Coalinga-05	1983	Pleasant Valley P.P. - FF	5.77	Reverse	[16.1]	257.4
412	Coalinga-05	1983	Pleasant Valley P.P. - yard	5.77	Reverse	[16.1]	257.4
413	Coalinga-05	1983	Skunk Hollow	5.77	Reverse	[11.8]	376.1
448	Morgan Hill	1984	Anderson Dam (Downstream)	6.19	Strike-Slip	3.3	488.8
454	Morgan Hill	1984	Gilroy - Gavilan Coll.	6.19	Strike-Slip	14.8	729.6
455	Morgan Hill	1984	Gilroy Array #1	6.19	Strike-Slip	14.9	1428
456	Morgan Hill	1984	Gilroy Array #2	6.19	Strike-Slip	13.7	270.8
457	Morgan Hill	1984	Gilroy Array #3	6.19	Strike-Slip	13	349.9
458	Morgan Hill	1984	Gilroy Array #4	6.19	Strike-Slip	11.5	221.8
459	Morgan Hill	1984	Gilroy Array #6	6.19	Strike-Slip	9.9	663.3
460	Morgan Hill	1984	Gilroy Array #7	6.19	Strike-Slip	12.1	333.9
461	Morgan Hill	1984	Halls Valley	6.19	Strike-Slip	3.5	281.6
497	Nahanni- Canada	1985	Site 3	6.76	Reverse	5.3	659.6
502	Mt. Lewis	1986	Halls Valley	5.6	Strike-Slip	[13.5]	281.6
514	N. Palm Springs	1986	Cabazon	6.06	Reverse-Oblique	7.8	345.4
518	N. Palm Springs	1986	Fun Valley	6.06	Reverse-Oblique	14.2	345.4
527	N. Palm Springs	1986	Morongo Valley	6.06	Reverse-Oblique	12.1	345.4
537	N. Palm Springs	1986	Silent Valley - Poppet Flat	6.06	Reverse-Oblique	17	684.9
547	Chalfant Valley-01	1986	Zack Brothers Ranch	5.77	Strike-Slip	6.4	271.4
549	Chalfant Valley-02	1986	Bishop - LADWP South St	6.19	Strike-Slip	17.2	271.4
550	Chalfant Valley-02	1986	Bishop - Paradise Lodge	6.19	Strike-Slip	18.3	345.4
587	New Zealand-02	1987	Matahina Dam	6.6	Normal	16.1	424.8
589	Whittier Narrows-01	1987	Alhambra - Fremont School	5.99	Reverse-Oblique	14.7	550
595	Whittier Narrows-01	1987	Bell Gardens - Jaboneria	5.99	Reverse-Oblique	17.8	308.6
608	Whittier Narrows-01	1987	Carson - Water St	5.99	Reverse-Oblique	30	160.6
619	Whittier Narrows-01	1987	Garvey Res. - Control Bldg	5.99	Reverse-Oblique	14.5	468.2
639	Whittier Narrows-01	1987	LA - Obregon Park	5.99	Reverse-Oblique	15.2	349.4
643	Whittier Narrows-01	1987	LA - Wonderland Ave	5.99	Reverse-Oblique	27.6	1222.5
718	Superstition Hills-01	1987	Wildlife Liquef. Array	6.22	Strike-Slip	17.6	207.5
721	Superstition Hills-02	1987	El Centro Imp. Co. Cent	6.54	Strike-Slip	18.2	192.1
728	Superstition Hills-02	1987	Westmorland Fire Sta	6.54	Strike-Slip	13	193.7
732	Loma Prieta	1989	APEEL 2 - Redwood City	6.93	Reverse-Oblique	43.2	133.1
739	Loma Prieta	1989	Anderson Dam (Downstream)	6.93	Reverse-Oblique	20.3	488.8
740	Loma Prieta	1989	Anderson Dam (L Abut)	6.93	Reverse-Oblique	20.3	488.8
752	Loma Prieta	1989	Capitola	6.93	Reverse-Oblique	15.2	288.6
755	Loma Prieta	1989	Coyote Lake Dam (SW Abut)	6.93	Reverse-Oblique	20.3	597.1
757	Loma Prieta	1989	Dumbarton Bridge West End FF	6.93	Reverse-Oblique	35.5	274.5
759	Loma Prieta	1989	Foster City - APEEL 1	6.93	Reverse-Oblique	43.9	116.3
760	Loma Prieta	1989	Foster City - Menhaden Court	6.93	Reverse-Oblique	45.6	126.4
763	Loma Prieta	1989	Gilroy - Gavilan Coll.	6.93	Reverse-Oblique	10	729.6

Table F.2 (cont.)

764	Loma Prieta	1989	Gilroy - Historic Bldg.	6.93	Reverse-Oblique	11	338.5
765	Loma Prieta	1989	Gilroy Array #1	6.93	Reverse-Oblique	9.6	1428
766	Loma Prieta	1989	Gilroy Array #2	6.93	Reverse-Oblique	11.1	270.8
768	Loma Prieta	1989	Gilroy Array #4	6.93	Reverse-Oblique	14.3	221.8
769	Loma Prieta	1989	Gilroy Array #6	6.93	Reverse-Oblique	18.3	663.3
776	Loma Prieta	1989	Hollister - South & Pine	6.93	Reverse-Oblique	27.9	370.8
786	Loma Prieta	1989	Palo Alto - 1900 Embarc.	6.93	Reverse-Oblique	30.8	209.9
787	Loma Prieta	1989	Palo Alto - SLAC Lab	6.93	Reverse-Oblique	30.9	425.3
801	Loma Prieta	1989	San Jose - Santa Teresa Hills	6.93	Reverse-Oblique	14.7	671.8
802	Loma Prieta	1989	Saratoga - Aloha Ave	6.93	Reverse-Oblique	8.5	370.8
809	Loma Prieta	1989	UCSC	6.93	Reverse-Oblique	18.5	714
810	Loma Prieta	1989	UCSC Lick Observatory	6.93	Reverse-Oblique	18.4	714
821	Erzican- Turkey	1992	Erzincan	6.69	Strike-Slip	4.4	274.5
832	Landers	1992	Amboy	7.28	Strike-Slip	69.2	271.4
836	Landers	1992	Baker Fire Station	7.28	Strike-Slip	87.9	271.4
837	Landers	1992	Baldwin Park - N Holly	7.28	Strike-Slip	131.9	308.6
841	Landers	1992	Boron Fire Station	7.28	Strike-Slip	89.7	345.4
849	Landers	1992	Covina - W Badillo	7.28	Strike-Slip	128.1	271.4
852	Landers	1992	Duarte - Mel Canyon Rd.	7.28	Strike-Slip	126.3	446
854	Landers	1992	Featherly Park - Maint	7.28	Strike-Slip	121.8	308.6
858	Landers	1992	Glendora - N Oakbank	7.28	Strike-Slip	122.6	446
860	Landers	1992	Hemet Fire Station	7.28	Strike-Slip	68.7	338.5
885	Landers	1992	Pomona - 4th & Locust FF	7.28	Strike-Slip	117.5	229.8
886	Landers	1992	Puerta La Cruz	7.28	Strike-Slip	94.5	370.8
887	Landers	1992	Riverside Airport	7.28	Strike-Slip	96	370.8
888	Landers	1992	San Bernardino - E & Hospitality	7.28	Strike-Slip	79.8	271.4
949	Northridge-01	1994	Arleta - Nordhoff Fire Sta	6.69	Reverse	8.7	297.7
953	Northridge-01	1994	Beverly Hills - 14145 Mulhol	6.69	Reverse	17.1	355.8
954	Northridge-01	1994	Big Tujunga- Angeles Nat F	6.69	Reverse	19.7	446
957	Northridge-01	1994	Burbank - Howard Rd.	6.69	Reverse	16.9	821.7
959	Northridge-01	1994	Canoga Park - Topanga Can	6.69	Reverse	14.7	267.5
960	Northridge-01	1994	Canyon Country - W Lost Cany	6.69	Reverse	12.4	308.6
962	Northridge-01	1994	Carson - Water St	6.69	Reverse	49.8	160.6
989	Northridge-01	1994	LA - Chalon Rd	6.69	Reverse	20.4	740
994	Northridge-01	1994	LA - Griffith Park Observatory	6.69	Reverse	23.8	1015.9
999	Northridge-01	1994	LA - Obregon Park	6.69	Reverse	37.4	349.4
1007	Northridge-01	1994	LA - Univ. Hospital	6.69	Reverse	34.2	376.1
1011	Northridge-01	1994	LA - Wonderland Ave	6.69	Reverse	20.3	1222.5
1012	Northridge-01	1994	LA 00	6.69	Reverse	19.1	706.2
1016	Northridge-01	1994	La Crescenta - New York	6.69	Reverse	18.5	446
1042	Northridge-01	1994	N Hollywood - Coldwater Can	6.69	Reverse	12.5	446
1050	Northridge-01	1994	Pacoima Dam (downstr)	6.69	Reverse	7	2016.1
1052	Northridge-01	1994	Pacoima Kagel Canyon	6.69	Reverse	7.3	508.1
1078	Northridge-01	1994	Santa Susana Ground	6.69	Reverse	16.7	715.1
1082	Northridge-01	1994	Sun Valley - Roscoe Blvd	6.69	Reverse	10.1	308.6
1083	Northridge-01	1994	Sunland - Mt Gleason Ave	6.69	Reverse	13.3	446
1111	Kobe- Japan	1995	Nishi-Akashi	6.9	Strike-Slip	7.1	609
1116	Kobe- Japan	1995	Shin-Osaka	6.9	Strike-Slip	19.1	256
1141	Dinar- Turkey	1995	Dinar	6.4	Normal	3.4	219.8
1164	Kocaeli- Turkey	1999	Istanbul	7.51	Strike-Slip	52	424.8

Table F.2 (cont.)

1170	Kocaeli- Turkey	1999	Mecidiyekoy	7.51	Strike-Slip	53.4	424.8
1177	Kocaeli- Turkey	1999	Zeytinburnu	7.51	Strike-Slip	53.9	274.5
1181	Chi-Chi- Taiwan	1999	CHY004	7.62	Reverse-Oblique	47.3	271.3
1183	Chi-Chi- Taiwan	1999	CHY008	7.62	Reverse-Oblique	40.4	210.7
1187	Chi-Chi- Taiwan	1999	CHY015	7.62	Reverse-Oblique	38.1	228.7
1190	Chi-Chi- Taiwan	1999	CHY019	7.62	Reverse-Oblique	50.5	478.3
1196	Chi-Chi- Taiwan	1999	CHY027	7.62	Reverse-Oblique	42	210
1199	Chi-Chi- Taiwan	1999	CHY032	7.62	Reverse-Oblique	35.4	192.7
1200	Chi-Chi- Taiwan	1999	CHY033	7.62	Reverse-Oblique	43.8	197.6
1210	Chi-Chi- Taiwan	1999	CHY050	7.62	Reverse-Oblique	44.8	432.9
1211	Chi-Chi- Taiwan	1999	CHY052	7.62	Reverse-Oblique	39	574.7
1212	Chi-Chi- Taiwan	1999	CHY054	7.62	Reverse-Oblique	48.5	172.1
1228	Chi-Chi- Taiwan	1999	CHY076	7.62	Reverse-Oblique	42.2	169.8
1230	Chi-Chi- Taiwan	1999	CHY079	7.62	Reverse-Oblique	47.5	550.8
1232	Chi-Chi- Taiwan	1999	CHY081	7.62	Reverse-Oblique	41.7	575.1
1233	Chi-Chi- Taiwan	1999	CHY082	7.62	Reverse-Oblique	36.1	193.7
1239	Chi-Chi- Taiwan	1999	CHY093	7.62	Reverse-Oblique	49.8	190.5
1243	Chi-Chi- Taiwan	1999	CHY100	7.62	Reverse-Oblique	53.5	230.1
1247	Chi-Chi- Taiwan	1999	CHY107	7.62	Reverse-Oblique	50.6	175.7
1248	Chi-Chi- Taiwan	1999	CHY109	7.62	Reverse-Oblique	41	557.4
1258	Chi-Chi- Taiwan	1999	HWA005	7.62	Reverse-Oblique	47.6	489.2
1259	Chi-Chi- Taiwan	1999	HWA006	7.62	Reverse-Oblique	47.9	490.8
1262	Chi-Chi- Taiwan	1999	HWA011	7.62	Reverse-Oblique	53.2	241.7
1266	Chi-Chi- Taiwan	1999	HWA015	7.62	Reverse-Oblique	51.1	334.6
1267	Chi-Chi- Taiwan	1999	HWA016	7.62	Reverse-Oblique	52.2	344
1600	Duzce- Turkey	1999	Arcelik	7.14	Strike-Slip	131.4	523
1601	Duzce- Turkey	1999	Aslan R.	7.14	Strike-Slip	130.8	274.5
1621	Duzce- Turkey	1999	Yarimca	7.14	Strike-Slip	97.5	297
1634	Manjil- Iran	1990	Abhar	7.37	Strike-Slip	75.6	274.5
1640	Manjil- Iran	1990	Tonekabun	7.37	Strike-Slip	93.6	274.5
1641	Sierra Madre	1991	Altadena - Eaton Canyon	5.61	Reverse	13.2	370.8
1709	Northridge-06	1994	LA - Griffith Park Observatory	5.28	Reverse	[21.8]	1015.9
1715	Northridge-06	1994	LA - Wonderland Ave	5.28	Reverse	[17.2]	1222.5
1763	Hector Mine	1999	Anza - Pinyon Flat	7.13	Strike-Slip	90	724.9
1764	Hector Mine	1999	Anza - Tripp Flats Training	7.13	Strike-Slip	102.4	684.9
1767	Hector Mine	1999	Banning - Twin Pines Road	7.13	Strike-Slip	83.4	684.9
1771	Hector Mine	1999	Bombay Beach Fire Station	7.13	Strike-Slip	120.7	257
1773	Hector Mine	1999	Cabazon	7.13	Strike-Slip	76.9	345.4
1846	Yountville	2000	Benicia Fire Station #1	5	Strike-Slip	[41.6]	155.4
1852	Yountville	2000	Larkspur Ferry Terminal (FF)	5	Strike-Slip	[48.2]	169.7
1861	Yountville	2000	Richmond Rod & Gun Club	5	Strike-Slip	[44.0]	155.4
1866	Yountville	2000	Sonoma Fire Station #1	5	Strike-Slip	[12.4]	155.4
2458	Chi-Chi- Taiwan-03	1999	CHY025	6.2	Reverse	28.7	277.5
2509	Chi-Chi- Taiwan-03	1999	CHY104	6.2	Reverse	35	223.2
2622	Chi-Chi- Taiwan-03	1999	TCU071	6.2	Reverse	16.5	624.9
2625	Chi-Chi- Taiwan-03	1999	TCU074	6.2	Reverse	16.6	549.4
2626	Chi-Chi- Taiwan-03	1999	TCU075	6.2	Reverse	19.6	573
2627	Chi-Chi- Taiwan-03	1999	TCU076	6.2	Reverse	14.7	615
2628	Chi-Chi- Taiwan-03	1999	TCU078	6.2	Reverse	7.6	443
2629	Chi-Chi- Taiwan-03	1999	TCU079	6.2	Reverse	8.5	364

Table F.2 (cont.)

2632	Chi-Chi- Taiwan-03	1999	TCU084	6.2	Reverse	9.3	680
2635	Chi-Chi- Taiwan-03	1999	TCU089	6.2	Reverse	9.8	680
2649	Chi-Chi- Taiwan-03	1999	TCU115	6.2	Reverse	35.2	215.3
2651	Chi-Chi- Taiwan-03	1999	TCU117	6.2	Reverse	46.3	198.6
2655	Chi-Chi- Taiwan-03	1999	TCU122	6.2	Reverse	19.3	475.5
2699	Chi-Chi- Taiwan-04	1999	CHY024	6.2	Strike-Slip	19.7	427.7
2703	Chi-Chi- Taiwan-04	1999	CHY028	6.2	Strike-Slip	17.7	542.6
2705	Chi-Chi- Taiwan-04	1999	CHY030	6.2	Strike-Slip	30.5	204.7
2710	Chi-Chi- Taiwan-04	1999	CHY036	6.2	Strike-Slip	30.9	233.1
2734	Chi-Chi- Taiwan-04	1999	CHY074	6.2	Strike-Slip	6.2	553.4
2739	Chi-Chi- Taiwan-04	1999	CHY080	6.2	Strike-Slip	12.5	680
2741	Chi-Chi- Taiwan-04	1999	CHY082	6.2	Strike-Slip	48.9	193.7
3317	Chi-Chi- Taiwan-06	1999	CHY101	6.3	Reverse	36	258.9
3470	Chi-Chi- Taiwan-06	1999	TCU072	6.3	Reverse	13	468.1
3473	Chi-Chi- Taiwan-06	1999	TCU078	6.3	Reverse	11.5	443

Table F.3 Details of Severe Suite of Earthquake Records (NGA)

NGA Sequence #	Event Name	Year	Station	Magnitude	Fault Mechanism	Closest Distance (km)	Vs30 (m/s)
77	San Fernando	1971	Pacoima Dam (upper left abut)	6.61	Reverse	1.8	2016.1
126	Gazli- USSR	1976	Karakyr	6.8	Unkown	5.5	659.6
139	Tabas- Iran	1978	Dayhook	7.35	Reverse	13.9	659.6
143	Tabas- Iran	1978	Tabas	7.35	Reverse	2	766.8
146	Coyote Lake	1979	Gilroy Array #1	5.74	Strike-Slip	10.7	1428
155	Norcia- Italy	1979	Bevagna	5.9	Normal	[31.4]	1000
160	Imperial Valley-06	1979	Bonds Corner	6.53	Strike-Slip	2.7	223
170	Imperial Valley-06	1979	EC County Center FF	6.53	Strike-Slip	7.3	192.1
171	Imperial Valley-06	1979	EC Meloland Overpass FF	6.53	Strike-Slip	0.1	186.2
174	Imperial Valley-06	1979	El Centro Array #11	6.53	Strike-Slip	12.4	196.2
175	Imperial Valley-06	1979	El Centro Array #12	6.53	Strike-Slip	17.9	196.9
178	Imperial Valley-06	1979	El Centro Array #3	6.53	Strike-Slip	12.8	162.9
179	Imperial Valley-06	1979	El Centro Array #4	6.53	Strike-Slip	7	208.9
180	Imperial Valley-06	1979	El Centro Array #5	6.53	Strike-Slip	4	205.6
181	Imperial Valley-06	1979	El Centro Array #6	6.53	Strike-Slip	1.4	203.2
182	Imperial Valley-06	1979	El Centro Array #7	6.53	Strike-Slip	0.6	210.5
183	Imperial Valley-06	1979	El Centro Array #8	6.53	Strike-Slip	3.9	206.1
184	Imperial Valley-06	1979	El Centro Differential Array	6.53	Strike-Slip	5.1	202.3
185	Imperial Valley-06	1979	Holtville Post Office	6.53	Strike-Slip	7.7	202.9
192	Imperial Valley-06	1979	Westmorland Fire Sta	6.53	Strike-Slip	15.2	193.7
199	Imperial Valley-07	1979	El Centro Array #11	5.01	Strike-Slip	[15.3]	196.2
200	Imperial Valley-07	1979	El Centro Array #2	5.01	Strike-Slip	[18.8]	188.8
201	Imperial Valley-07	1979	El Centro Array #3	5.01	Strike-Slip	[16.3]	162.9
250	Mammoth Lakes-06	1980	Long Valley Dam (Upr L Abut)	5.94	Strike-Slip	[16.2]	345.4
265	Victoria- Mexico	1980	Cerro Prieto	6.33	Strike-Slip	14.4	659.6
266	Victoria- Mexico	1980	Chihuahua	6.33	Strike-Slip	19	274.5
284	Irpinia- Italy-01	1980	Auletta	6.9	Normal	9.6	1000
285	Irpinia- Italy-01	1980	Bagnoli Irpinio	6.9	Normal	8.2	1000
286	Irpinia- Italy-01	1980	Bisaccia	6.9	Normal	21.3	1000
292	Irpinia- Italy-01	1980	Sturno	6.9	Normal	10.8	1000
295	Irpinia- Italy-02	1980	Auletta	6.2	Normal	29.9	1000
296	Irpinia- Italy-02	1980	Bagnoli Irpinio	6.2	Normal	19.6	1000
297	Irpinia- Italy-02	1980	Bisaccia	6.2	Normal	14.7	1000
303	Irpinia- Italy-02	1980	Sturno	6.2	Normal	20.4	1000
317	Westmorland	1981	Salton Sea Wildlife Refuge	5.9	Strike-Slip	7.8	191.1
319	Westmorland	1981	Westmorland Fire Sta	5.9	Strike-Slip	6.5	193.7
326	Coalinga-01	1983	Parkfield - Cholame 2WA	6.36	Reverse	44.7	184.8
368	Coalinga-01	1983	Pleasant Valley P.P. - yard	6.36	Reverse	8.4	257.4
372	Coalinga-02	1983	Anticline Ridge Free-Field	5.09	Reverse	[11.6]	376.1
407	Coalinga-05	1983	Oil City	5.77	Reverse	[8.5]	376.1
415	Coalinga-05	1983	Transmitter Hill	5.77	Reverse	[9.5]	376.1
418	Coalinga-07	1983	Coalinga-14th & Elm (Old CHP)	5.21	Reverse	[10.9]	338.5
451	Morgan Hill	1984	Coyote Lake Dam (SW Abut)	6.19	Strike-Slip	0.5	597.1
455	Morgan Hill	1984	Gilroy Array #1	6.19	Strike-Slip	14.9	1428
495	Nahanni- Canada	1985	Site 1	6.76	Reverse	9.6	659.6
529	N. Palm Springs	1986	North Palm Springs	6.06	Reverse-Oblique	4	345.4
540	N. Palm Springs	1986	Whitewater Trout Farm	6.06	Reverse-Oblique	6	345.4
558	Chalfant Valley-02	1986	Zack Brothers Ranch	6.19	Strike-Slip	7.6	271.4
568	San Salvador	1986	Geotech Investig Center	5.8	Strike-Slip	6.3	545

Table F.3 (cont.)

569	San Salvador	1986	National Geografical Inst	5.8	Strike-Slip	7	350
585	Baja California	1987	Cerro Prieto	5.5	Strike-Slip	[4.5]	659.6
608	Whittier Narrows-01	1987	Carson - Water St	5.99	Reverse-Oblique	30	160.6
643	Whittier Narrows-01	1987	LA - Wonderland Ave	5.99	Reverse-Oblique	27.6	1222.5
721	Superstition Hills-02	1987	El Centro Imp. Co. Cent	6.54	Strike-Slip	18.2	192.1
728	Superstition Hills-02	1987	Westmorland Fire Sta	6.54	Strike-Slip	13	193.7
732	Loma Prieta	1989	APEEL 2 - Redwood City	6.93	Reverse-Oblique	43.2	133.1
741	Loma Prieta	1989	BRAN	6.93	Reverse-Oblique	10.7	376.1
753	Loma Prieta	1989	Corralitos	6.93	Reverse-Oblique	3.9	462.2
759	Loma Prieta	1989	Foster City - APEEL 1	6.93	Reverse-Oblique	43.9	116.3
760	Loma Prieta	1989	Foster City - Menhaden Court	6.93	Reverse-Oblique	45.6	126.4
765	Loma Prieta	1989	Gilroy Array #1	6.93	Reverse-Oblique	9.6	1428
767	Loma Prieta	1989	Gilroy Array #3	6.93	Reverse-Oblique	12.8	349.9
779	Loma Prieta	1989	LGPC	6.93	Reverse-Oblique	3.9	477.7
811	Loma Prieta	1989	WAHO	6.93	Reverse-Oblique	17.5	376.1
825	Cape Mendocino	1992	Cape Mendocino	7.01	Reverse	7	513.7
826	Cape Mendocino	1992	Eureka - Myrtle & West	7.01	Reverse	42	338.5
827	Cape Mendocino	1992	Fortuna - Fortuna Blvd	7.01	Reverse	19.9	457.1
828	Cape Mendocino	1992	Petrolia	7.01	Reverse	8.2	712.8
829	Cape Mendocino	1992	Rio Dell Overpass - FF	7.01	Reverse	14.3	311.8
830	Cape Mendocino	1992	Shelter Cove Airport	7.01	Reverse	28.8	513.7
838	Landers	1992	Barstow	7.28	Strike-Slip	34.9	370.8
850	Landers	1992	Desert Hot Springs	7.28	Strike-Slip	21.8	345.4
855	Landers	1992	Fort Irwin	7.28	Strike-Slip	63	345.4
862	Landers	1992	Indio - Coachella Canal	7.28	Strike-Slip	54.2	345.4
864	Landers	1992	Joshua Tree	7.28	Strike-Slip	11	379.3
879	Landers	1992	Lucerne	7.28	Strike-Slip	2.2	684.9
880	Landers	1992	Mission Creek Fault	7.28	Strike-Slip	27	345.4
881	Landers	1992	Morongo Valley	7.28	Strike-Slip	17.3	345.4
882	Landers	1992	North Palm Springs	7.28	Strike-Slip	26.8	345.4
884	Landers	1992	Palm Springs Airport	7.28	Strike-Slip	36.1	207.5
891	Landers	1992	Silent Valley - Poppet Flat	7.28	Strike-Slip	50.9	684.9
897	Landers	1992	Twentynine Palms	7.28	Strike-Slip	41.4	684.9
900	Landers	1992	Yermo Fire Station	7.28	Strike-Slip	23.6	353.6
901	Big Bear-01	1992	Big Bear Lake - Civic Center	6.46	Strike-Slip	[9.4]	338.5
952	Northridge-01	1994	Beverly Hills - 12520 Mulhol	6.69	Reverse	18.4	545.7
962	Northridge-01	1994	Carson - Water St	6.69	Reverse	49.8	160.6
983	Northridge-01	1994	Jensen Filter Plant Generator	6.69	Reverse	5.4	525.8
994	Northridge-01	1994	LA - Griffith Park Observatory	6.69	Reverse	23.8	1015.9
1004	Northridge-01	1994	LA - Sepulveda VA Hospital	6.69	Reverse	8.4	380.1
1011	Northridge-01	1994	LA - Wonderland Ave	6.69	Reverse	20.3	1222.5
1013	Northridge-01	1994	LA Dam	6.69	Reverse	5.9	629
1044	Northridge-01	1994	Newhall - Fire Sta	6.69	Reverse	5.9	269.1
1045	Northridge-01	1994	Newhall - W Pico Canyon Rd.	6.69	Reverse	5.5	285.9
1050	Northridge-01	1994	Pacoima Dam (downstr)	6.69	Reverse	7	2016.1
1051	Northridge-01	1994	Pacoima Dam (upper left)	6.69	Reverse	7	2016.1
1063	Northridge-01	1994	Rinaldi Receiving Sta	6.69	Reverse	6.5	282.2
1080	Northridge-01	1994	Simi Valley - Katherine Rd	6.69	Reverse	13.4	557.4
1106	Kobe- Japan	1995	KJMA	6.9	Strike-Slip	1	312
1119	Kobe- Japan	1995	Takarazuka	6.9	Strike-Slip	0.3	312

Table F.3 (cont.)

1120	Kobe- Japan	1995	Takatori	6.9	Strike-Slip	1.5	256
1148	Kocaeli- Turkey	1999	Arcelik	7.51	Strike-Slip	13.5	523
1162	Kocaeli- Turkey	1999	Goy nuk	7.51	Strike-Slip	31.7	424.8
1165	Kocaeli- Turkey	1999	Izmit	7.51	Strike-Slip	7.2	811
1166	Kocaeli- Turkey	1999	Iznik	7.51	Strike-Slip	30.7	274.5
1176	Kocaeli- Turkey	1999	Yarimca	7.51	Strike-Slip	4.8	297
1180	Chi-Chi- Taiwan	1999	CHY002	7.62	Reverse-Oblique	25	235.1
1182	Chi-Chi- Taiwan	1999	CHY006	7.62	Reverse-Oblique	9.8	438.2
1184	Chi-Chi- Taiwan	1999	CHY010	7.62	Reverse-Oblique	20	549.6
1186	Chi-Chi- Taiwan	1999	CHY014	7.62	Reverse-Oblique	34.2	560.3
1193	Chi-Chi- Taiwan	1999	CHY024	7.62	Reverse-Oblique	9.6	427.7
1194	Chi-Chi- Taiwan	1999	CHY025	7.62	Reverse-Oblique	19.1	277.5
1195	Chi-Chi- Taiwan	1999	CHY026	7.62	Reverse-Oblique	29.5	226
1197	Chi-Chi- Taiwan	1999	CHY028	7.62	Reverse-Oblique	3.1	542.6
1198	Chi-Chi- Taiwan	1999	CHY029	7.62	Reverse-Oblique	11	544.7
1199	Chi-Chi- Taiwan	1999	CHY032	7.62	Reverse-Oblique	35.4	192.7
1200	Chi-Chi- Taiwan	1999	CHY033	7.62	Reverse-Oblique	43.8	197.6
1201	Chi-Chi- Taiwan	1999	CHY034	7.62	Reverse-Oblique	14.8	378.8
1202	Chi-Chi- Taiwan	1999	CHY035	7.62	Reverse-Oblique	12.7	555.2
1203	Chi-Chi- Taiwan	1999	CHY036	7.62	Reverse-Oblique	16.1	233.1
1204	Chi-Chi- Taiwan	1999	CHY039	7.62	Reverse-Oblique	31.9	201.2
1205	Chi-Chi- Taiwan	1999	CHY041	7.62	Reverse-Oblique	19.8	492.3
1206	Chi-Chi- Taiwan	1999	CHY042	7.62	Reverse-Oblique	28.2	680
1208	Chi-Chi- Taiwan	1999	CHY046	7.62	Reverse-Oblique	24.1	442.1
1209	Chi-Chi- Taiwan	1999	CHY047	7.62	Reverse-Oblique	24.1	291.9
1212	Chi-Chi- Taiwan	1999	CHY054	7.62	Reverse-Oblique	48.5	172.1
1227	Chi-Chi- Taiwan	1999	CHY074	7.62	Reverse-Oblique	10.8	553.4
1228	Chi-Chi- Taiwan	1999	CHY076	7.62	Reverse-Oblique	42.2	169.8
1231	Chi-Chi- Taiwan	1999	CHY080	7.62	Reverse-Oblique	2.7	680
1233	Chi-Chi- Taiwan	1999	CHY082	7.62	Reverse-Oblique	36.1	193.7
1234	Chi-Chi- Taiwan	1999	CHY086	7.62	Reverse-Oblique	28.4	680
1235	Chi-Chi- Taiwan	1999	CHY087	7.62	Reverse-Oblique	28.9	505.2
1236	Chi-Chi- Taiwan	1999	CHY088	7.62	Reverse-Oblique	37.5	366.2
1238	Chi-Chi- Taiwan	1999	CHY092	7.62	Reverse-Oblique	22.7	253.7
1239	Chi-Chi- Taiwan	1999	CHY093	7.62	Reverse-Oblique	49.8	190.5
1240	Chi-Chi- Taiwan	1999	CHY094	7.62	Reverse-Oblique	37.1	221.9
1244	Chi-Chi- Taiwan	1999	CHY101	7.62	Reverse-Oblique	10	258.9
1245	Chi-Chi- Taiwan	1999	CHY102	7.62	Reverse-Oblique	37.7	679.9
1246	Chi-Chi- Taiwan	1999	CHY104	7.62	Reverse-Oblique	18	223.2
1380	Chi-Chi- Taiwan	1999	KAU054	7.62	Reverse-Oblique	30.9	577.4
1476	Chi-Chi- Taiwan	1999	TCU029	7.62	Reverse-Oblique	28.1	426.3
1477	Chi-Chi- Taiwan	1999	TCU031	7.62	Reverse-Oblique	30.2	489.2
1479	Chi-Chi- Taiwan	1999	TCU034	7.62	Reverse-Oblique	35.7	393.8
1480	Chi-Chi- Taiwan	1999	TCU036	7.62	Reverse-Oblique	19.8	495
1481	Chi-Chi- Taiwan	1999	TCU038	7.62	Reverse-Oblique	25.4	229.3
1482	Chi-Chi- Taiwan	1999	TCU039	7.62	Reverse-Oblique	19.9	540.7
1483	Chi-Chi- Taiwan	1999	TCU040	7.62	Reverse-Oblique	22.1	362
1484	Chi-Chi- Taiwan	1999	TCU042	7.62	Reverse-Oblique	26.3	424
1486	Chi-Chi- Taiwan	1999	TCU046	7.62	Reverse-Oblique	16.7	465.6
1488	Chi-Chi- Taiwan	1999	TCU048	7.62	Reverse-Oblique	13.6	551.2

Table F.3 (cont.)

1489	Chi-Chi- Taiwan	1999	TCU049	7.62	Reverse-Oblique	3.8	487.3
1490	Chi-Chi- Taiwan	1999	TCU050	7.62	Reverse-Oblique	9.5	470.7
1491	Chi-Chi- Taiwan	1999	TCU051	7.62	Reverse-Oblique	7.7	467.5
1492	Chi-Chi- Taiwan	1999	TCU052	7.62	Reverse-Oblique	0.7	579.1
1493	Chi-Chi- Taiwan	1999	TCU053	7.62	Reverse-Oblique	6	454.6
1494	Chi-Chi- Taiwan	1999	TCU054	7.62	Reverse-Oblique	5.3	460.7
1495	Chi-Chi- Taiwan	1999	TCU055	7.62	Reverse-Oblique	6.4	447.8
1496	Chi-Chi- Taiwan	1999	TCU056	7.62	Reverse-Oblique	10.5	440.2
1497	Chi-Chi- Taiwan	1999	TCU057	7.62	Reverse-Oblique	11.8	479.3
1498	Chi-Chi- Taiwan	1999	TCU059	7.62	Reverse-Oblique	17.1	230.3
1499	Chi-Chi- Taiwan	1999	TCU060	7.62	Reverse-Oblique	8.5	495.8
1500	Chi-Chi- Taiwan	1999	TCU061	7.62	Reverse-Oblique	17.2	320.3
1501	Chi-Chi- Taiwan	1999	TCU063	7.62	Reverse-Oblique	9.8	476.1
1502	Chi-Chi- Taiwan	1999	TCU064	7.62	Reverse-Oblique	16.6	357.5
1503	Chi-Chi- Taiwan	1999	TCU065	7.62	Reverse-Oblique	0.6	305.9
1504	Chi-Chi- Taiwan	1999	TCU067	7.62	Reverse-Oblique	0.6	433.6
1505	Chi-Chi- Taiwan	1999	TCU068	7.62	Reverse-Oblique	0.3	487.3
1506	Chi-Chi- Taiwan	1999	TCU070	7.62	Reverse-Oblique	19	401.3
1507	Chi-Chi- Taiwan	1999	TCU071	7.62	Reverse-Oblique	5.3	624.9
1508	Chi-Chi- Taiwan	1999	TCU072	7.62	Reverse-Oblique	7	468.1
1509	Chi-Chi- Taiwan	1999	TCU074	7.62	Reverse-Oblique	13.5	549.4
1510	Chi-Chi- Taiwan	1999	TCU075	7.62	Reverse-Oblique	0.9	573
1511	Chi-Chi- Taiwan	1999	TCU076	7.62	Reverse-Oblique	2.8	615
1512	Chi-Chi- Taiwan	1999	TCU078	7.62	Reverse-Oblique	8.2	443
1513	Chi-Chi- Taiwan	1999	TCU079	7.62	Reverse-Oblique	11	364
1515	Chi-Chi- Taiwan	1999	TCU082	7.62	Reverse-Oblique	5.2	472.8
1517	Chi-Chi- Taiwan	1999	TCU084	7.62	Reverse-Oblique	11.2	680
1519	Chi-Chi- Taiwan	1999	TCU087	7.62	Reverse-Oblique	7	561.8
1521	Chi-Chi- Taiwan	1999	TCU089	7.62	Reverse-Oblique	8.9	680
1527	Chi-Chi- Taiwan	1999	TCU100	7.62	Reverse-Oblique	11.4	479.3
1528	Chi-Chi- Taiwan	1999	TCU101	7.62	Reverse-Oblique	2.1	504.4
1529	Chi-Chi- Taiwan	1999	TCU102	7.62	Reverse-Oblique	1.5	714.3
1530	Chi-Chi- Taiwan	1999	TCU103	7.62	Reverse-Oblique	6.1	494.1
1531	Chi-Chi- Taiwan	1999	TCU104	7.62	Reverse-Oblique	12.9	543.8
1532	Chi-Chi- Taiwan	1999	TCU105	7.62	Reverse-Oblique	17.2	575.5
1533	Chi-Chi- Taiwan	1999	TCU106	7.62	Reverse-Oblique	15	418.8
1534	Chi-Chi- Taiwan	1999	TCU107	7.62	Reverse-Oblique	16	418.7
1535	Chi-Chi- Taiwan	1999	TCU109	7.62	Reverse-Oblique	13.1	424.2
1536	Chi-Chi- Taiwan	1999	TCU110	7.62	Reverse-Oblique	11.6	212.7
1537	Chi-Chi- Taiwan	1999	TCU111	7.62	Reverse-Oblique	22.1	237.5
1538	Chi-Chi- Taiwan	1999	TCU112	7.62	Reverse-Oblique	27.5	201
1539	Chi-Chi- Taiwan	1999	TCU113	7.62	Reverse-Oblique	31.1	230.3
1540	Chi-Chi- Taiwan	1999	TCU115	7.62	Reverse-Oblique	21.8	215.3
1541	Chi-Chi- Taiwan	1999	TCU116	7.62	Reverse-Oblique	12.4	493.1
1542	Chi-Chi- Taiwan	1999	TCU117	7.62	Reverse-Oblique	25.4	198.6
1543	Chi-Chi- Taiwan	1999	TCU118	7.62	Reverse-Oblique	26.8	201
1544	Chi-Chi- Taiwan	1999	TCU119	7.62	Reverse-Oblique	38	201
1545	Chi-Chi- Taiwan	1999	TCU120	7.62	Reverse-Oblique	7.4	459.3
1547	Chi-Chi- Taiwan	1999	TCU123	7.62	Reverse-Oblique	14.9	241.7
1546	Chi-Chi- Taiwan	1999	TCU122	7.62	Reverse-Oblique	9.3	475.5

Table F.3 (cont.)

1548	Chi-Chi- Taiwan	1999	TCU128	7.62	Reverse-Oblique	13.2	599.6
1550	Chi-Chi- Taiwan	1999	TCU136	7.62	Reverse-Oblique	8.3	538
1551	Chi-Chi- Taiwan	1999	TCU138	7.62	Reverse-Oblique	9.8	652.9
1552	Chi-Chi- Taiwan	1999	TCU140	7.62	Reverse-Oblique	33	201
1553	Chi-Chi- Taiwan	1999	TCU141	7.62	Reverse-Oblique	24.2	209.2
1602	Duzce- Turkey	1999	Bolu	7.14	Strike-Slip	12	326
1605	Duzce- Turkey	1999	Duzce	7.14	Strike-Slip	6.6	276
1611	Duzce- Turkey	1999	Lamont 1058	7.14	Strike-Slip	0.2	424.8
1612	Duzce- Turkey	1999	Lamont 1059	7.14	Strike-Slip	4.2	424.8
1613	Duzce- Turkey	1999	Lamont 1060	7.14	Strike-Slip	25.9	782
1614	Duzce- Turkey	1999	Lamont 1061	7.14	Strike-Slip	11.5	481
1615	Duzce- Turkey	1999	Lamont 1062	7.14	Strike-Slip	9.2	338
1616	Duzce- Turkey	1999	Lamont 362	7.14	Strike-Slip	23.4	517
1617	Duzce- Turkey	1999	Lamont 375	7.14	Strike-Slip	3.9	424.8
1618	Duzce- Turkey	1999	Lamont 531	7.14	Strike-Slip	8	659.6
1619	Duzce- Turkey	1999	Mudurnu	7.14	Strike-Slip	34.3	659.6
1620	Duzce- Turkey	1999	Sakarya	7.14	Strike-Slip	45.2	471
1627	Caldiran- Turkey	1976	Maku	7.21	Unkown	50.8	274.5
1636	Manjil- Iran	1990	Qazvin	7.37	Strike-Slip	50	274.5
1637	Manjil- Iran	1990	Rudsar	7.37	Strike-Slip	64.5	274.5
1709	Northridge-06	1994	LA - Griffith Park Observatory	5.28	Reverse	[21.8]	1015.9
1715	Northridge-06	1994	LA - Wonderland Ave	5.28	Reverse	[17.2]	1222.5
1728	Northridge-06	1994	Rinaldi Receiving Sta	5.28	Reverse	[13.0]	282.2
1762	Hector Mine	1999	Amboy	7.13	Strike-Slip	43	271.4
1766	Hector Mine	1999	Baker Fire Station	7.13	Strike-Slip	64.8	271.4
1768	Hector Mine	1999	Barstow	7.13	Strike-Slip	61.2	370.8
1770	Hector Mine	1999	Big Bear Lake - Fire Station	7.13	Strike-Slip	61.9	338.5
1776	Hector Mine	1999	Desert Hot Springs	7.13	Strike-Slip	56.4	345.4
1785	Hector Mine	1999	Fun Valley	7.13	Strike-Slip	54.7	345.4
1786	Hector Mine	1999	Heart Bar State Park	7.13	Strike-Slip	61.2	684.9
1787	Hector Mine	1999	Hector	7.13	Strike-Slip	11.7	684.9
1794	Hector Mine	1999	Joshua Tree	7.13	Strike-Slip	31.1	379.3
1795	Hector Mine	1999	Joshua Tree N.M. - Keys View	7.13	Strike-Slip	50.4	684.9
1813	Hector Mine	1999	Morongo Valley	7.13	Strike-Slip	53.2	345.4
1816	Hector Mine	1999	North Palm Springs Fire Sta #36	7.13	Strike-Slip	61.8	345.4
1836	Hector Mine	1999	Twentynine Palms	7.13	Strike-Slip	42.1	684.9
1838	Hector Mine	1999	Whitewater Trout Farm	7.13	Strike-Slip	62.9	345.4
1846	Yountville	2000	Benicia Fire Station #1	5	Strike-Slip	[41.6]	155.4
1852	Yountville	2000	Larkspur Ferry Terminal (FF)	5	Strike-Slip	[48.2]	169.7
1861	Yountville	2000	Richmond Rod & Gun Club	5	Strike-Slip	[44.0]	155.4
1866	Yountville	2000	Sonoma Fire Station #1	5	Strike-Slip	[12.4]	155.4
2095	Denali- Alaska	2002	Anchorage - DOI Off. of Aircraft	7.9	Strike-Slip	272.5	279.4
2096	Denali- Alaska	2002	Anchorage - Dowl Eng Warehouse	7.9	Strike-Slip	270.3	360
2097	Denali- Alaska	2002	Anchorage - K2-02	7.9	Strike-Slip	264.5	366
2098	Denali- Alaska	2002	Anchorage - K2-03	7.9	Strike-Slip	263.6	474
2099	Denali- Alaska	2002	Anchorage - K2-04	7.9	Strike-Slip	273.6	279.4
2100	Denali- Alaska	2002	Anchorage - K2-05	7.9	Strike-Slip	269.1	284
2101	Denali- Alaska	2002	Anchorage - K2-06	7.9	Strike-Slip	268.2	491
2102	Denali- Alaska	2002	Anchorage - NOAA Weather Fac.	7.9	Strike-Slip	275.1	274.5
2103	Denali- Alaska	2002	Anchorage - New Fire Station #1	7.9	Strike-Slip	266.6	274.5

Table F.3 (cont.)

2104	Denali- Alaska	2002	Anchorage - New Fire Station #7	7.9	Strike-Slip	275.9	274.5
2105	Denali- Alaska	2002	Anchorage - Police Headquarters	7.9	Strike-Slip	269	467.9
2106	Denali- Alaska	2002	Anchorage - State Fish & Game	7.9	Strike-Slip	272.6	360
2107	Denali- Alaska	2002	Carlo (temp)	7.9	Strike-Slip	50.9	963.9
2108	Denali- Alaska	2002	Eagle River - AK Geologic Mat	7.9	Strike-Slip	246.2	274.5
2109	Denali- Alaska	2002	Fairbanks - Ester Fire Station	7.9	Strike-Slip	139.8	274.5
2110	Denali- Alaska	2002	Fairbanks - Geophysic. Obs- CIGO	7.9	Strike-Slip	141.3	424.8
2111	Denali- Alaska	2002	R109 (temp)	7.9	Strike-Slip	43	963.9
2112	Denali- Alaska	2002	TAPS Pump Station #08	7.9	Strike-Slip	104.9	424.8
2113	Denali- Alaska	2002	TAPS Pump Station #09	7.9	Strike-Slip	54.8	382.5
2114	Denali- Alaska	2002	TAPS Pump Station #10	7.9	Strike-Slip	2.7	329.4
2115	Denali- Alaska	2002	TAPS Pump Station #11	7.9	Strike-Slip	126.4	376.1
2116	Denali- Alaska	2002	TAPS Pump Station #12	7.9	Strike-Slip	164.7	338.6
2118	Denali- Alaska	2002	Valdez - Valdez Dock Company	7.9	Strike-Slip	239.5	659.6
2457	Chi-Chi- Taiwan-03	1999	CHY024	6.2	Reverse	19.6	427.7
2651	Chi-Chi- Taiwan-03	1999	TCU117	6.2	Reverse	46.3	198.6
2658	Chi-Chi- Taiwan-03	1999	TCU129	6.2	Reverse	12.8	664.4
2741	Chi-Chi- Taiwan-04	1999	CHY082	6.2	Strike-Slip	48.9	193.7
3474	Chi-Chi- Taiwan-06	1999	TCU079	6.3	Reverse	10.1	364
3475	Chi-Chi- Taiwan-06	1999	TCU080	6.3	Reverse	10.2	509

Table F.4 Details of Severe Suite of Earthquake Records (K-NET)

Tohoku Sequence #	Event Name	Year	Station	Magnitude	Fault Mechanism
AKT011	Tohoku - 1	2011	MIYATA	9.0	Reverse
AKT016	Tohoku - 1	2011	OHMAGARI	9.0	Reverse
AOM007	Tohoku - 1	2011	MINAMIDOHRI	9.0	Reverse
AOM010	Tohoku - 1	2011	NOHEJI	9.0	Reverse
AOM011	Tohoku - 1	2011	MISAWA	9.0	Reverse
AOM012	Tohoku - 1	2011	HACHINOHE	9.0	Reverse
AOM013	Tohoku - 1	2011	NAMBU	9.0	Reverse
CHB003	Tohoku - 1	2011	SHIROI	9.0	Reverse
CHB004	Tohoku - 1	2011	SAWARA	9.0	Reverse
CHB005	Tohoku - 1	2011	CHOHSHI	9.0	Reverse
CHB006	Tohoku - 1	2011	NARITA	9.0	Reverse
CHB007	Tohoku - 1	2011	SAKURA	9.0	Reverse
CHB010	Tohoku - 1	2011	YOHKAICHI	9.0	Reverse
CHB011	Tohoku - 1	2011	HASUNUMA	9.0	Reverse
CHB012	Tohoku - 1	2011	TOHGANE	9.0	Reverse
CHB014	Tohoku - 1	2011	ANEZAKI	9.0	Reverse
CHB016	Tohoku - 1	2011	MISAKI	9.0	Reverse
CHB028	Tohoku - 1	2011	ICHIKAWA-KITA	9.0	Reverse
FKS001	Tohoku - 1	2011	SOHMA	9.0	Reverse
FKS002	Tohoku - 1	2011	YANAGAWA	9.0	Reverse
FKS003	Tohoku - 1	2011	FUKUSHIMA	9.0	Reverse
FKS004	Tohoku - 1	2011	IITATE	9.0	Reverse
FKS005	Tohoku - 1	2011	HARAMACHI	9.0	Reverse
FKS006	Tohoku - 1	2011	KATSURAO	9.0	Reverse
FKS008	Tohoku - 1	2011	FUNEHKI	9.0	Reverse
FKS009	Tohoku - 1	2011	ONO	9.0	Reverse
FKS010	Tohoku - 1	2011	HIRONO	9.0	Reverse
FKS011	Tohoku - 1	2011	IWAKI	9.0	Reverse
FKS012	Tohoku - 1	2011	NAKOSO	9.0	Reverse
FKS013	Tohoku - 1	2011	FURUDONO	9.0	Reverse
FKS014	Tohoku - 1	2011	YAMATSURI	9.0	Reverse
FKS015	Tohoku - 1	2011	TANAGURA	9.0	Reverse
FKS016	Tohoku - 1	2011	SHIRAKAWA	9.0	Reverse
FKS017	Tohoku - 1	2011	SUKAGAWA	9.0	Reverse
FKS018	Tohoku - 1	2011	KOHRIYAMA	9.0	Reverse
FKS019	Tohoku - 1	2011	NIHOMMATSU	9.0	Reverse
FKS020	Tohoku - 1	2011	INAWASHIRO	9.0	Reverse
FKS022	Tohoku - 1	2011	NISHIAIDU	9.0	Reverse
FKS023	Tohoku - 1	2011	AIDUWAKAMATSU	9.0	Reverse
FKS024	Tohoku - 1	2011	NAKANO	9.0	Reverse
FKS025	Tohoku - 1	2011	SHIMOGOH	9.0	Reverse
FKS027	Tohoku - 1	2011	TAKINOHARA	9.0	Reverse
FKS031	Tohoku - 1	2011	KAWAUCHI	9.0	Reverse
GNM002	Tohoku - 1	2011	MINAKAMI	9.0	Reverse
GNM009	Tohoku - 1	2011	KIRYUH	9.0	Reverse
GNM010	Tohoku - 1	2011	TATEBAYASHI	9.0	Reverse
IBR001	Tohoku - 1	2011	DAIGO	9.0	Reverse
IBR002	Tohoku - 1	2011	TAKAHAGI	9.0	Reverse
IBR003	Tohoku - 1	2011	HITACHI	9.0	Reverse

Table F.4 (cont.)

IBR004	Tohoku - 1	2011	OHMIYA	9.0	Reverse
IBR005	Tohoku - 1	2011	KASAMA	9.0	Reverse
IBR006	Tohoku - 1	2011	MITO	9.0	Reverse
IBR007	Tohoku - 1	2011	NAKAMINATO	9.0	Reverse
IBR008	Tohoku - 1	2011	SHIMODATE	9.0	Reverse
IBR009	Tohoku - 1	2011	KOGA	9.0	Reverse
IBR010	Tohoku - 1	2011	SHIMOTSUMA	9.0	Reverse
IBR011	Tohoku - 1	2011	TSUKUBA	9.0	Reverse
IBR012	Tohoku - 1	2011	ISHIOKA	9.0	Reverse
IBR013	Tohoku - 1	2011	HOKOTA	9.0	Reverse
IBR014	Tohoku - 1	2011	TSUCHIURA	9.0	Reverse
IBR015	Tohoku - 1	2011	IWAI	9.0	Reverse
IBR016	Tohoku - 1	2011	TORIDE	9.0	Reverse
IBR017	Tohoku - 1	2011	EDOSAKI	9.0	Reverse
IBR018	Tohoku - 1	2011	KASHIMA	9.0	Reverse
IWT001	Tohoku - 1	2011	TANEICHI	9.0	Reverse
IWT002	Tohoku - 1	2011	KUJI	9.0	Reverse
IWT003	Tohoku - 1	2011	FUDAI	9.0	Reverse
IWT005	Tohoku - 1	2011	MIYAKO	9.0	Reverse
IWT007	Tohoku - 1	2011	KAMAISHI	9.0	Reverse
IWT009	Tohoku - 1	2011	DAITOH	9.0	Reverse
IWT010	Tohoku - 1	2011	ICHINOSEKI	9.0	Reverse
IWT011	Tohoku - 1	2011	MIZUSAWA	9.0	Reverse
IWT012	Tohoku - 1	2011	KITAKAMI	9.0	Reverse
IWT013	Tohoku - 1	2011	TOHNO	9.0	Reverse
IWT014	Tohoku - 1	2011	ISHIDORIYA	9.0	Reverse
IWT016	Tohoku - 1	2011	KAWAI	9.0	Reverse
IWT017	Tohoku - 1	2011	KADOMA	9.0	Reverse
IWT018	Tohoku - 1	2011	MORIOKA	9.0	Reverse
IWT019	Tohoku - 1	2011	IWAIZUMI	9.0	Reverse
IWT020	Tohoku - 1	2011	YABUKAWA	9.0	Reverse
IWT021	Tohoku - 1	2011	NISHINE	9.0	Reverse
IWT022	Tohoku - 1	2011	ASHIRO	9.0	Reverse
IWT023	Tohoku - 1	2011	KUZUMAKI	9.0	Reverse
IWT024	Tohoku - 1	2011	NINOHE	9.0	Reverse
IWT025	Tohoku - 1	2011	OHSHIDA	9.0	Reverse
IWT026	Tohoku - 1	2011	AISARI	9.0	Reverse
KNG001	Tohoku - 1	2011	KAWASAKI	9.0	Reverse
KNG002	Tohoku - 1	2011	YOKOHAMA	9.0	Reverse
KNG006	Tohoku - 1	2011	FUTAMATAGAWA	9.0	Reverse
KNG008	Tohoku - 1	2011	SAGAMIHARA	9.0	Reverse
KNG009	Tohoku - 1	2011	ATSUGI	9.0	Reverse
KNG010	Tohoku - 1	2011	HIRATSUKA	9.0	Reverse
KNG013	Tohoku - 1	2011	ODAWARA	9.0	Reverse
KNG201	Tohoku - 1	2011	HIRATSUKA-ST1	9.0	Reverse
KNG202	Tohoku - 1	2011	HIRATSUKA-ST2	9.0	Reverse
KNG205	Tohoku - 1	2011	HIRATSUKA-ST5	9.0	Reverse
KNG206	Tohoku - 1	2011	HIRATSUKA-ST6	9.0	Reverse
MYG001	Tohoku - 1	2011	KESENNUMA	9.0	Reverse
MYG002	Tohoku - 1	2011	UTATSU	9.0	Reverse
MYG003	Tohoku - 1	2011	TOHWA	9.0	Reverse

Table F.4 (cont.)

MYG004	Tohoku - 1	2011	TSUKIDATE	9.0	Reverse
MYG005	Tohoku - 1	2011	NARUKO	9.0	Reverse
MYG006	Tohoku - 1	2011	FURUKAWA	9.0	Reverse
MYG007	Tohoku - 1	2011	TOYOSATO	9.0	Reverse
MYG009	Tohoku - 1	2011	TAIWA	9.0	Reverse
MYG010	Tohoku - 1	2011	ISHINOMAKI	9.0	Reverse
MYG012	Tohoku - 1	2011	SHIOGAMA	9.0	Reverse
MYG013	Tohoku - 1	2011	SENDAI	9.0	Reverse
MYG014	Tohoku - 1	2011	SAKUNAMI	9.0	Reverse
MYG015	Tohoku - 1	2011	IWANUMA	9.0	Reverse
MYG016	Tohoku - 1	2011	SHIROISHI	9.0	Reverse
MYG017	Tohoku - 1	2011	KAKUDA	9.0	Reverse
TCG001	Tohoku - 1	2011	KUROISO	9.0	Reverse
TCG005	Tohoku - 1	2011	YAITA	9.0	Reverse
TCG006	Tohoku - 1	2011	OGAWA	9.0	Reverse
TCG008	Tohoku - 1	2011	KANUMA	9.0	Reverse
TCG009	Tohoku - 1	2011	IMAICHI	9.0	Reverse
TCG011	Tohoku - 1	2011	KUZUU	9.0	Reverse
TCG012	Tohoku - 1	2011	OYAMA	9.0	Reverse
TCG013	Tohoku - 1	2011	MOOKA	9.0	Reverse
TCG014	Tohoku - 1	2011	MOTEGI	9.0	Reverse
TKY017	Tohoku - 1	2011	TATSUMI	9.0	Reverse
YMN009	Tohoku - 1	2011	ROKUGOH	9.0	Reverse
YMT005	Tohoku - 1	2011	HIJIORI	9.0	Reverse
YMT006	Tohoku - 1	2011	OBANAZAWA	9.0	Reverse
YMT007	Tohoku - 1	2011	HIGASHINE	9.0	Reverse
YMT009	Tohoku - 1	2011	SAGAE	9.0	Reverse
YMT010	Tohoku - 1	2011	YAMAGATA	9.0	Reverse
YMT011	Tohoku - 1	2011	KAMINOYAMA	9.0	Reverse
YMT015	Tohoku - 1	2011	YONEZAWA	9.0	Reverse
FKS023	Tohoku - 2	2011	AIDUWAKAMATSU	6.8	Reverse
MYG002	Tohoku - 2	2011	UTATSU	6.8	Reverse
FKS004	Tohoku - 3	2011	IITATE	5.8	Reverse
FKS005	Tohoku - 3	2011	HARAMACHI	5.8	Reverse
FKS008	Tohoku - 3	2011	FUNEHKI	5.8	Reverse
FKS009	Tohoku - 3	2011	ONO	5.8	Reverse
FKS010	Tohoku - 3	2011	HIRONO	5.8	Reverse
FKS012	Tohoku - 3	2011	NAKOSO	5.8	Reverse
FKS014	Tohoku - 3	2011	YAMATSURI	5.8	Reverse
FKS015	Tohoku - 3	2011	TANAGURA	5.8	Reverse
FKS016	Tohoku - 3	2011	SHIRAKAWA	5.8	Reverse
FKS018	Tohoku - 3	2011	KOHRİYAMA	5.8	Reverse
FKS019	Tohoku - 3	2011	NIHOMMATSU	5.8	Reverse
IBR001	Tohoku - 3	2011	DAIGO	5.8	Reverse
IBR002	Tohoku - 3	2011	TAKAHAGI	5.8	Reverse
IBR003	Tohoku - 3	2011	HITACHI	5.8	Reverse
IBR004	Tohoku - 3	2011	OHMIYA	5.8	Reverse
MYG015	Tohoku - 3	2011	IWANUMA	5.8	Reverse
TCG009	Tohoku - 3	2011	IMAICHI	5.8	Reverse
FKS001	Tohoku - 4	2011	SOHMA	6.4	Reverse
FKS002	Tohoku - 4	2011	YANAGAWA	6.4	Reverse

Table F.5 Component Peak Parameters for Slight Record Suite

Record ID	Length (s)	Trans PGA (g)	Long PGA (g)	Vert PGA (g)	Trans PGD (cm)	Long PGD (cm)	Vert PGD (cm)
1000	40.0	0.10	0.19	0.07	3.72	2.37	1.69
1001	30.0	0.29	0.26	0.09	2.42	1.87	0.67
1005	40.0	0.13	0.18	0.10	3.14	2.74	1.35
1008	40.0	0.10	0.16	0.05	5.74	3.30	1.38
1011	30.0	0.11	0.17	0.11	1.78	2.77	1.12
1019	32.0	0.09	0.08	0.10	3.70	2.40	3.39
1021	32.0	0.06	0.08	0.05	3.90	2.25	3.03
1022	32.0	0.04	0.06	0.04	2.16	1.94	3.44
1026	40.0	0.08	0.15	0.05	2.90	2.59	1.78
1027	32.0	0.09	0.07	0.05	1.62	1.77	2.15
1028	32.0	0.09	0.06	0.06	1.65	1.59	2.08
1029	32.0	0.08	0.11	0.05	2.18	1.73	2.33
1030	32.0	0.08	0.06	0.05	1.74	1.99	2.34
1031	32.0	0.15	0.09	0.10	2.34	2.67	2.55
1032	32.0	0.18	0.13	0.06	2.06	1.22	2.08
1034	40.0	0.13	0.08	0.09	2.09	1.77	1.00
1035	35.0	0.20	0.13	0.08	1.86	4.63	2.04
1038	21.8	0.18	0.13	0.08	1.51	2.22	0.48
1041	40.0	0.23	0.13	0.09	0.70	0.45	0.57
1053	60.0	0.06	0.07	0.04	1.84	2.01	1.38
1055	19.9	0.24	0.17	0.14	1.08	1.57	0.57
1058	32.0	0.13	0.22	0.07	1.36	1.87	0.49
1070	35.0	0.14	0.26	0.07	2.21	2.79	1.49
1072	40.0	0.12	0.15	0.08	1.10	0.72	0.39
1074	40.0	0.09	0.10	0.04	4.75	4.59	3.65
122	39.9	0.06	0.09	0.03	3.03	3.08	3.33
130	26.4	0.11	0.09	0.07	2.22	1.62	1.58
132	22.0	0.26	0.21	0.10	1.07	1.82	1.35
133	16.5	0.06	0.13	0.06	1.14	1.98	2.11
145	28.8	0.16	0.28	0.12	1.31	2.33	0.67
146	26.8	0.10	0.13	0.07	0.48	1.52	0.41
154	28.5	0.11	0.11	0.12	0.95	1.02	0.95
155	23.8	0.04	0.02	0.02	0.41	0.06	0.09
156	12.0	0.16	0.15	0.20	0.62	0.43	1.68
157	24.9	0.05	0.04	0.04	0.11	0.14	0.18
1631	40.0	0.19	0.21	0.10	1.24	1.25	0.57
1632	40.0	0.23	0.24	0.16	0.39	0.64	0.24
1645	40.0	0.28	0.20	0.24	1.80	1.07	0.75
1647	40.0	0.17	0.14	0.13	1.16	0.91	0.50
1688	20.0	0.02	0.02	0.01	0.12	0.10	0.04
1693	20.0	0.12	0.13	0.12	0.36	0.34	0.39
1697	7.7	0.14	0.20	0.14	0.32	0.64	0.13
1707	20.0	0.16	0.09	0.03	0.54	0.47	0.18
1711	7.5	0.11	0.12	0.05	0.49	0.31	0.07
1715	5.7	0.05	0.05	0.05	0.07	0.13	0.07
1722	5.7	0.17	0.17	0.11	0.90	0.80	0.20
1723	20.0	0.15	0.23	0.10	0.63	1.36	0.41
1725	7.2	0.09	0.15	0.17	0.47	0.43	0.30
1733	6.2	0.12	0.12	0.16	0.34	0.61	0.19

Table F.5 (cont.)

1734	7.7	0.32	0.25	0.14	0.84	0.60	0.18
1735	8.7	0.09	0.07	0.08	0.25	0.24	0.23
1736	6.5	0.22	0.29	0.08	1.63	1.61	0.41
1737	6.5	0.16	0.13	0.04	0.85	0.26	0.17
1738	6.0	0.26	0.25	0.06	1.67	1.15	0.15
1739	45.1	0.37	0.31	0.13	0.89	1.11	0.30
1740	111.7	0.13	0.21	0.08	0.49	0.97	0.45
186	40.0	0.11	0.07	0.03	6.90	5.21	2.03
188	18.7	0.04	0.06	0.03	1.33	1.91	0.98
191	40.0	0.12	0.17	0.06	1.83	1.02	0.71
193	19.9	0.08	0.10	0.05	0.34	1.42	0.02
195	19.4	0.12	0.07	0.03	0.87	0.51	0.05
198	10.4	0.07	0.04	0.02	0.25	0.43	0.06
199	10.9	0.12	0.17	0.06	0.74	1.02	0.08
200	10.9	0.15	0.07	0.03	0.95	0.22	0.06
201	11.0	0.18	0.11	0.03	0.97	0.30	0.07
202	19.6	0.26	0.16	0.10	0.64	0.65	0.13
203	19.2	0.24	0.24	0.08	0.75	1.06	0.07
205	17.3	0.13	0.19	0.06	0.52	1.00	0.06
206	10.7	0.12	0.14	0.07	0.36	0.87	0.08
207	19.4	0.17	0.13	0.10	0.82	0.41	0.08
208	19.6	0.13	0.21	0.04	0.56	2.14	0.08
214	21.0	0.15	0.08	0.04	6.11	1.69	0.45
215	40.0	0.06	0.04	0.02	1.00	1.24	0.40
219	20.5	0.04	0.04	0.03	0.14	0.33	0.13
221	20.0	0.26	0.23	0.10	0.55	1.18	0.17
222	24.0	0.20	0.25	0.08	1.02	1.30	0.39
223	21.7	0.30	0.10	0.04	2.82	0.62	0.50
225	10.3	0.11	0.13	0.05	0.11	0.49	0.08
226	10.2	0.13	0.08	0.07	0.17	0.06	0.06
227	10.3	0.06	0.07	0.04	0.35	0.16	0.09
233	30.0	0.16	0.18	0.13	1.95	2.27	1.05
234	30.0	0.19	0.07	0.04	0.65	0.59	0.29
236	40.0	0.22	0.21	0.19	4.87	2.29	1.59
237	40.0	0.11	0.07	0.08	1.21	1.33	0.42
238	40.0	0.10	0.08	0.07	1.06	1.69	0.45
239	40.0	0.48	0.19	0.12	1.77	3.28	0.52
23	39.7	0.10	0.11	0.05	0.19	0.43	0.18
241	40.0	0.09	0.05	0.06	0.59	0.35	0.12
242	40.0	0.08	0.07	0.06	1.65	0.51	0.31
243	40.0	0.24	0.20	0.15	1.56	0.82	0.36
2462	52.0	0.07	0.03	0.07	10.48	1.93	7.32
2466	94.0	0.09	0.04	0.20	6.05	1.95	4.98
248	26.0	0.27	0.32	0.19	1.74	3.19	1.62
2490	46.0	0.08	0.03	0.06	3.27	2.88	3.80
2616	101.0	0.04	0.03	0.05	1.78	4.16	4.90
2618	105.0	0.28	0.05	0.35	5.50	1.93	6.65
2619	94.0	0.21	0.07	0.17	1.51	4.02	4.69
2631	41.0	0.05	0.02	0.04	1.58	0.34	1.51
2646	125.0	0.07	0.03	0.11	2.18	0.88	5.94
2651	106.0	0.03	0.02	0.06	1.78	2.10	10.85

Table F.5 (cont.)

2656	105.0	0.06	0.03	0.08	8.22	6.60	8.97
2663	115.0	0.05	0.07	0.05	1.06	4.16	6.07
2700	79.0	0.07	0.06	0.07	9.42	3.95	7.55
2704	110.0	0.07	0.04	0.06	11.72	2.86	5.34
2708	73.0	0.05	0.10	0.08	1.06	2.06	2.63
2709	75.0	0.12	0.05	0.13	2.67	1.78	2.65
2712	49.1	0.08	0.04	0.09	1.78	0.81	1.90
2741	69.0	0.03	0.03	0.03	1.62	1.86	6.33
2742	68.0	0.11	0.05	0.11	3.04	1.29	2.33
2746	71.0	0.05	0.05	0.05	3.62	5.59	10.15
2754	101.0	0.04	0.05	0.05	4.83	6.14	11.84
2821	50.0	0.08	0.08	0.09	0.44	0.42	0.41
284	34.3	0.06	0.06	0.04	3.19	3.68	1.28
285	36.9	0.14	0.20	0.11	9.26	9.59	5.75
286	38.3	0.10	0.08	0.07	14.76	2.92	11.02
2871	51.0	0.06	0.02	0.04	2.24	0.70	1.75
2873	39.0	0.02	0.01	0.03	0.30	0.76	0.68
287	38.5	0.04	0.05	0.02	0.33	0.30	0.19
2888	68.0	0.11	0.04	0.09	3.22	0.62	2.28
2897	58.0	0.02	0.05	0.04	2.58	2.97	6.25
290	42.7	0.09	0.15	0.05	1.31	1.78	0.26
291	37.2	0.11	0.10	0.07	0.65	1.22	0.90
295	32.0	0.02	0.02	0.02	0.72	0.84	0.64
296	42.0	0.05	0.06	0.03	0.52	0.68	0.73
297	37.7	0.08	0.07	0.05	4.61	5.43	3.69
2997	88.0	0.07	0.08	0.09	0.42	0.72	1.03
3008	54.0	0.06	0.03	0.06	0.31	0.24	0.28
3019	62.0	0.15	0.06	0.10	0.57	0.26	0.34
3021	66.0	0.08	0.07	0.08	0.76	0.32	0.59
303	30.3	0.07	0.08	0.04	0.93	0.74	0.40
314	28.4	0.17	0.17	0.10	3.09	0.48	0.23
315	40.0	0.10	0.18	0.13	0.69	0.80	0.47
317	28.7	0.20	0.18	0.21	4.44	2.33	1.08
318	28.4	0.07	0.12	0.05	0.24	0.49	0.09
320	40.0	0.17	0.15	0.10	2.05	2.88	1.65
321	40.0	0.15	0.10	0.07	0.97	1.50	0.75
3264	66.0	0.14	0.07	0.13	3.01	5.27	10.80
3268	65.1	0.14	0.06	0.15	4.21	4.30	3.94
326	40.0	0.11	0.11	0.04	2.60	1.79	1.39
3300	65.1	0.16	0.06	0.13	1.69	1.22	3.58
335	40.0	0.07	0.13	0.04	7.06	3.14	2.57
336	40.0	0.10	0.09	0.04	2.34	1.83	1.80
337	40.0	0.11	0.11	0.07	3.24	5.67	2.10
339	40.0	0.17	0.12	0.08	4.94	2.94	2.07
340	40.0	0.20	0.12	0.06	3.48	1.83	1.91
341	40.0	0.12	0.13	0.04	6.06	4.40	0.93
342	40.0	0.14	0.16	0.05	4.74	4.95	2.31
343	40.0	0.07	0.12	0.05	3.35	4.43	2.29
344	40.0	0.05	0.06	0.03	3.84	3.19	1.74
3456	53.0	0.04	0.02	0.04	1.27	0.67	0.95
3457	54.0	0.04	0.02	0.04	0.75	0.50	0.85

Table F.5 (cont.)

3458	61.0	0.05	0.02	0.05	1.09	0.75	1.20
3459	71.0	0.05	0.03	0.07	1.94	0.87	1.41
345	40.0	0.12	0.12	0.06	7.32	3.36	2.18
3460	51.0	0.04	0.02	0.05	0.78	0.45	0.92
3461	49.0	0.05	0.03	0.05	1.02	0.80	1.07
3462	51.0	0.03	0.02	0.04	0.91	0.78	0.93
3464	49.0	0.03	0.02	0.03	0.70	0.43	0.72
3469	55.0	0.04	0.02	0.04	2.45	0.38	1.78
346	40.0	0.13	0.12	0.05	4.24	1.70	1.65
3477	50.0	0.04	0.02	0.05	1.67	1.11	1.69
347	32.0	0.06	0.05	0.03	2.92	2.45	1.62
3488	53.0	0.04	0.01	0.04	1.04	0.57	1.29
3489	57.0	0.05	0.03	0.05	2.62	1.07	1.19
348	40.0	0.12	0.06	0.04	4.52	2.58	1.16
3495	75.0	0.07	0.11	0.09	2.08	2.18	1.82
3496	75.0	0.08	0.10	0.06	3.35	0.66	4.59
349	28.0	0.07	0.08	0.03	1.73	1.40	0.91
3502	60.0	0.06	0.06	0.06	0.86	1.84	1.58
3503	61.0	0.13	0.13	0.13	2.24	3.92	6.30
3509	71.0	0.08	0.07	0.06	2.64	4.07	2.68
350	40.0	0.08	0.07	0.04	3.70	2.63	1.58
351	40.0	0.09	0.07	0.05	2.86	1.55	1.50
356	40.0	0.06	0.09	0.03	2.64	1.76	1.65
357	24.0	0.15	0.11	0.03	2.91	1.37	1.07
358	34.0	0.06	0.07	0.03	2.34	1.39	0.89
360	40.0	0.08	0.09	0.07	2.11	2.40	1.49
362	30.0	0.07	0.08	0.06	1.46	1.21	1.52
363	40.0	0.10	0.14	0.06	2.96	2.57	1.75
364	30.0	0.06	0.05	0.02	1.38	0.94	0.71
369	30.0	0.17	0.15	0.05	4.17	2.71	2.41
371	40.0	0.29	0.22	0.05	0.77	0.64	0.10
374	10.5	0.09	0.10	0.08	0.37	0.35	0.15
375	40.0	0.14	0.11	0.05	0.46	0.33	0.12
376	40.0	0.08	0.15	0.07	0.13	0.67	0.10
377	16.6	0.13	0.08	0.06	0.49	0.38	0.18
379	10.0	0.25	0.28	0.10	0.71	0.39	0.13
380	40.0	0.31	0.34	0.08	0.41	0.56	0.07
381	10.3	0.25	0.18	0.15	0.34	0.26	0.11
382	10.4	0.20	0.29	0.09	0.34	0.75	0.13
383	9.8	0.08	0.22	0.10	1.04	0.51	0.16
384	35.8	0.14	0.24	0.07	0.70	0.68	0.15
385	16.6	0.12	0.22	0.08	0.85	1.42	0.15
386	10.5	0.17	0.10	0.08	0.49	0.37	0.12
387	40.0	0.01	0.00	0.01	0.04	0.03	0.06
388	40.0	0.13	0.09	0.08	0.97	0.69	0.35
389	24.3	0.15	0.12	0.06	1.09	0.75	0.19
391	20.3	0.16	0.19	0.08	2.42	1.91	0.80
392	40.0	0.05	0.06	0.03	1.96	1.95	0.76
393	40.0	0.04	0.04	0.03	2.29	1.64	1.47
394	20.1	0.33	0.27	0.11	1.20	0.46	0.43
395	20.1	0.38	0.26	0.14	1.03	0.52	0.34

Table F.5 (cont.)

396	19.0	0.12	0.15	0.07	0.50	0.52	0.26
397	40.0	0.20	0.17	0.08	0.62	0.38	0.21
399	21.1	0.09	0.10	0.06	0.26	0.71	0.22
400	20.8	0.09	0.11	0.07	0.53	0.32	0.20
401	20.0	0.11	0.21	0.07	0.24	0.43	0.10
402	20.6	0.19	0.14	0.16	0.32	0.37	0.19
403	40.0	0.06	0.07	0.04	0.21	0.15	0.09
404	20.7	0.21	0.19	0.11	1.34	0.87	0.35
405	21.6	0.27	0.32	0.21	2.32	1.43	1.09
408	17.2	0.22	0.19	0.14	2.85	3.82	2.84
410	21.6	0.27	0.29	0.20	3.30	3.32	1.35
414	40.0	0.14	0.13	0.08	0.79	0.66	0.69
419	40.0	0.15	0.23	0.14	1.27	0.76	0.32
423	40.0	0.02	0.03	0.03	0.09	0.07	0.07
424	40.0	0.01	0.02	0.02	0.06	0.06	0.04
453	36.0	0.03	0.02	0.02	0.77	1.03	0.30
455	30.0	0.07	0.10	0.09	1.26	1.02	1.06
45	13.6	0.15	0.08	0.15	0.23	0.10	0.18
463	26.9	0.09	0.10	0.21	1.76	1.53	0.90
464	40.0	0.08	0.08	0.24	1.90	1.49	0.97
465	40.0	0.09	0.10	0.28	1.90	1.69	1.04
466	40.0	0.10	0.10	0.25	1.99	1.88	1.12
467	28.6	0.09	0.09	0.22	1.88	1.71	0.81
470	28.0	0.04	0.04	0.05	1.73	1.52	1.35
471	28.3	0.08	0.07	0.03	2.60	1.86	0.52
472	28.3	0.08	0.06	0.04	3.08	2.18	1.04
498	40.0	0.10	0.11	0.17	1.95	2.29	0.56
499	40.0	0.11	0.10	0.12	1.60	1.41	0.51
501	40.0	0.04	0.09	0.05	1.27	1.70	0.53
50	16.7	0.20	0.08	0.16	0.62	0.25	1.02
516	11.1	0.15	0.17	0.12	0.92	1.15	0.55
519	30.0	0.14	0.13	0.09	0.73	0.39	0.24
521	11.2	0.24	0.19	0.10	0.45	0.89	0.55
522	30.0	0.06	0.12	0.09	2.22	3.62	1.40
526	30.0	0.08	0.10	0.05	0.42	0.52	0.41
535	40.0	0.07	0.06	0.05	0.99	1.24	0.30
545	39.9	0.05	0.09	0.07	0.24	1.69	0.96
551	40.0	0.06	0.07	0.04	1.54	1.07	1.09
556	20.1	0.08	0.08	0.07	0.66	0.89	0.52
563	39.9	0.06	0.06	0.05	0.91	0.84	0.37
585	16.0	1.39	0.89	0.59	11.50	7.62	2.52
590	40.0	0.30	0.15	0.16	1.20	0.50	0.44
592	34.9	0.30	0.16	0.23	3.11	0.72	0.56
594	25.6	0.13	0.06	0.08	2.49	0.54	0.75
608	29.7	0.10	0.13	0.05	1.90	1.53	0.23
613	30.9	0.13	0.08	0.08	1.33	0.63	0.22
616	28.3	0.12	0.23	0.14	0.92	4.05	0.45
622	35.3	0.20	0.20	0.10	0.83	0.61	0.24
632	19.9	0.16	0.14	0.08	0.87	1.35	0.29
634	32.0	0.17	0.21	0.10	2.16	1.45	1.03
637	34.9	0.15	0.17	0.17	1.10	1.81	0.47

Table F.5 (cont.)

63	30.0	0.07	0.11	0.04	0.68	1.08	0.73
640	36.7	0.19	0.15	0.12	0.75	1.19	0.29
643	18.2	0.04	0.05	0.02	0.17	0.15	0.09
649	27.1	0.18	0.13	0.06	2.22	1.09	0.31
650	37.4	0.14	0.12	0.08	1.04	0.41	0.19
707	22.0	0.17	0.18	0.08	0.90	0.87	0.26
708	22.0	0.26	0.20	0.12	0.78	0.81	0.27
709	22.0	0.07	0.07	0.05	0.55	0.58	0.14
714	22.0	0.37	0.26	0.10	0.98	2.57	0.35
715	22.0	0.16	0.14	0.09	0.24	0.20	0.16
716	22.0	0.16	0.21	0.08	1.01	1.50	0.26
731	40.0	0.10	0.09	0.04	8.59	7.30	3.72
732	35.8	0.27	0.22	0.08	12.61	6.84	3.15
735	40.0	0.16	0.09	0.06	7.76	8.33	3.09
736	39.0	0.11	0.10	0.05	5.77	8.08	2.11
751	39.1	0.07	0.12	0.06	4.26	6.30	5.70
760	30.0	0.11	0.12	0.08	7.99	3.94	2.71
761	39.7	0.19	0.14	0.07	5.51	8.33	6.34
762	40.0	0.12	0.11	0.08	5.43	4.40	5.29
772	40.0	0.13	0.10	0.06	3.31	5.46	4.06
782	40.0	0.07	0.06	0.03	1.42	2.88	0.92
791	40.0	0.07	0.07	0.06	6.45	6.38	5.84
800	40.0	0.09	0.11	0.10	8.51	7.97	2.39
807	39.1	0.08	0.07	0.03	3.87	6.08	6.53
812	40.0	0.08	0.08	0.05	8.42	8.91	2.76
81	27.3	0.14	0.05	0.10	1.61	0.95	1.56
87	29.7	0.21	0.06	0.15	2.87	1.77	2.30
931	100.0	0.09	0.10	0.07	3.52	3.36	1.13
934	40.0	0.06	0.07	0.05	0.34	0.30	0.27
935	60.0	0.16	0.12	0.09	0.77	0.56	0.53
93	40.0	0.11	0.03	0.10	5.01	2.59	5.77
942	60.0	0.10	0.08	0.05	2.53	1.32	1.12
945	40.0	0.04	0.06	0.04	1.09	1.53	1.69
947	35.0	0.10	0.08	0.09	1.58	1.61	0.56
948	35.0	0.09	0.11	0.06	1.29	1.73	0.59
951	35.0	0.10	0.07	0.05	3.56	2.47	1.90
958	65.0	0.12	0.12	0.05	3.46	3.25	1.28
962	40.0	0.09	0.09	0.04	1.59	1.92	0.25
970	35.0	0.12	0.16	0.06	4.22	1.88	1.36
971	40.0	0.15	0.11	0.05	2.70	1.53	1.47
97	23.2	0.11	0.08	0.05	2.59	0.80	0.39
981	36.0	0.09	0.10	0.05	2.29	3.21	1.05
984	40.0	0.21	0.13	0.06	2.67	2.83	1.45
990	40.0	0.26	0.32	0.13	2.88	2.42	1.84
991	29.6	0.21	0.15	0.09	2.01	2.23	0.44
993	30.0	0.16	0.24	0.11	2.86	3.60	1.19
994	46.9	0.16	0.13	0.29	2.40	1.61	3.88
997	30.0	0.13	0.17	0.10	1.43	1.28	0.78

Table F.6 Component Peak Parameters for Moderate Record Suite

Record ID	Length (s)	Trans PGA (g)	Long PGA (g)	Vert PGA (g)	Trans PGD (cm)	Long PGD (cm)	Vert PGD (cm)
1007	40.0	0.493	0.21	0.12	2.39	2.37	1.37
1011	30.0	0.112	0.17	0.11	1.78	2.77	1.12
1012	60.0	0.261	0.39	0.18	4.81	4.55	2.48
1016	30.0	0.178	0.16	0.11	1.14	3.00	0.87
1042	21.9	0.298	0.27	0.29	6.33	11.53	4.14
1050	20.0	0.415	0.43	0.19	4.99	4.53	1.38
1052	40.0	0.301	0.43	0.17	11.21	7.95	4.13
1078	57.3	0.232	0.16	0.29	7.08	2.49	4.53
1082	30.3	0.303	0.44	0.31	7.86	10.05	5.01
1083	30.0	0.127	0.16	0.19	5.55	4.36	2.34
1111	41.0	0.509	0.50	0.37	9.52	11.26	5.63
1116	41.0	0.243	0.21	0.06	8.54	7.64	2.16
1141	28.0	0.352	0.28	0.14	9.41	5.58	3.06
1164	138.8	0.044	0.05	0.04	12.67	8.23	6.44
1170	44.0	0.054	0.07	0.03	4.75	10.11	4.68
1177	129.3	0.108	0.11	0.05	12.98	18.20	8.56
1181	150.0	0.041	0.10	0.10	5.34	17.51	15.41
1183	150.0	0.075	0.13	0.12	8.53	20.21	13.84
1187	150.0	0.032	0.15	0.16	5.47	9.83	13.17
1190	107.0	0.024	0.05	0.06	5.02	6.66	4.22
1196	90.0	0.053	0.05	0.06	14.42	6.43	19.00
1199	90.0	0.078	0.06	0.09	19.00	5.95	17.75
1200	90.0	0.062	0.04	0.07	16.63	7.24	16.74
1210	90.0	0.069	0.03	0.11	7.74	5.29	4.51
1211	116.0	0.039	0.09	0.15	5.45	6.91	9.40
1212	90.0	0.097	0.03	0.09	13.75	6.43	11.86
1228	90.0	0.073	0.03	0.07	16.97	7.24	20.38
1230	90.0	0.050	0.03	0.04	4.19	4.78	5.62
1232	90.0	0.045	0.03	0.05	7.66	4.86	7.18
1233	90.0	0.063	0.08	0.07	25.79	6.34	20.71
1239	150.0	0.036	0.05	0.07	5.84	13.74	12.79
1243	150.0	0.029	0.07	0.06	5.49	8.28	12.50
1247	150.0	0.043	0.10	0.09	7.87	13.42	15.39
1248	89.0	0.043	0.03	0.04	1.80	5.03	1.63
1258	80.0	0.051	0.15	0.14	7.15	8.22	9.18
1259	80.0	0.063	0.09	0.08	6.81	6.11	5.89
125	36.3	0.351	0.31	0.27	4.11	5.09	2.50
1262	90.0	0.102	0.04	0.09	13.77	10.86	26.84
1266	90.0	0.073	0.05	0.11	8.42	9.86	23.84
1267	90.0	0.080	0.05	0.10	5.65	10.39	12.88
12	70.0	0.042	0.06	0.02	4.76	1.86	2.54
146	26.8	0.103	0.13	0.07	0.48	1.52	0.41
147	26.9	0.211	0.34	0.17	2.29	5.81	1.18
148	26.8	0.272	0.23	0.16	3.42	4.86	1.26
149	27.2	0.248	0.27	0.39	2.59	4.78	2.47
150	27.1	0.434	0.32	0.15	7.67	3.84	3.92
155	23.8	0.040	0.02	0.02	0.41	0.06	0.09
158	11.2	0.327	0.26	0.14	10.25	3.59	2.46
159	28.4	0.221	0.83	0.37	11.70	5.01	10.02

Table F.6 (cont.)

1600	51.4	0.008	0.01	0.01	3.25	3.10	2.28
1601	57.8	0.017	0.01	0.01	3.66	4.46	2.91
161	37.8	0.160	0.22	0.15	22.36	13.50	3.48
1621	72.5	0.022	0.02	0.01	8.64	3.64	3.92
162	37.8	0.275	0.20	0.19	8.98	9.19	2.48
1634	29.5	0.132	0.21	0.08	8.35	27.25	2.69
1640	35.5	0.089	0.14	0.04	4.42	5.89	2.67
1641	40.0	0.448	0.18	0.15	3.00	0.87	0.53
164	63.7	0.157	0.21	0.17	7.98	3.27	4.24
165	40.0	0.254	0.22	0.27	12.90	1.28	9.14
167	36.0	0.147	0.07	0.19	2.49	0.97	2.89
1715	5.7	0.048	0.05	0.05	0.07	0.13	0.07
171	40.0	0.314	0.30	0.25	25.58	31.64	8.34
173	37.0	0.171	0.22	0.11	31.13	19.50	6.90
174	39.0	0.364	0.38	0.14	16.08	18.63	6.79
175	39.0	0.143	0.12	0.07	11.31	11.97	5.32
1767	67.8	0.020	0.02	0.02	5.27	5.15	1.58
178	39.5	0.266	0.22	0.13	18.90	23.27	4.72
187	39.3	0.111	0.20	0.16	12.32	9.96	4.76
189	15.7	0.287	0.51	0.38	2.64	5.47	1.17
192	40.0	0.074	0.11	0.08	16.54	10.00	2.60
199	10.9	0.124	0.17	0.06	0.74	1.02	0.08
200	10.9	0.150	0.07	0.03	0.95	0.22	0.06
201	11.0	0.179	0.11	0.03	0.97	0.30	0.07
204	19.7	0.189	0.37	0.08	1.15	2.83	0.11
230	30.0	0.416	0.44	0.39	4.66	5.41	5.94
231	30.0	0.430	0.27	0.12	7.52	3.06	1.72
232	30.0	0.321	0.24	0.25	1.57	1.64	2.54
235	30.0	0.390	0.44	0.26	2.71	2.27	1.57
240	40.0	0.380	0.43	0.35	1.16	2.30	0.52
2458	102.0	0.128	0.07	0.10	10.18	13.83	16.28
249	11.5	0.395	0.40	0.18	1.84	1.39	1.68
2509	117.0	0.043	0.11	0.08	9.00	13.86	14.33
2622	96.1	0.380	0.14	0.19	1.72	1.16	1.54
2625	63.0	0.047	0.02	0.04	0.62	2.06	0.60
2626	124.1	0.153	0.10	0.22	1.06	1.29	5.21
2627	96.0	0.156	0.25	0.52	3.57	5.12	9.61
2628	65.0	0.278	0.24	0.47	2.05	1.40	5.10
2629	73.0	0.262	0.17	0.34	0.82	0.90	2.26
2632	94.0	0.067	0.05	0.14	8.15	0.92	6.85
2635	96.0	0.085	0.04	0.09	0.80	0.52	2.70
2649	124.0	0.040	0.03	0.05	9.88	0.64	12.22
2651	106.0	0.032	0.02	0.06	1.78	2.10	10.85
2655	97.0	0.170	0.10	0.20	4.67	17.19	16.98
2699	51.1	0.072	0.05	0.07	2.30	4.39	8.29
269	18.3	0.045	0.03	0.02	2.65	1.68	0.65
2703	75.0	0.123	0.07	0.20	7.07	2.34	5.29
2705	114.0	0.078	0.03	0.08	14.73	2.95	6.98
2710	114.0	0.086	0.05	0.09	16.46	1.98	4.70
2734	112.0	0.347	0.30	0.32	9.53	4.92	10.84
2739	98.0	0.120	0.08	0.13	6.96	2.23	4.04

Table F.6 (cont.)

2741	69.0	0.029	0.03	0.03	1.62	1.86	6.33
284	34.3	0.058	0.06	0.04	3.19	3.68	1.28
285	36.9	0.139	0.20	0.11	9.26	9.59	5.75
286	38.3	0.100	0.08	0.07	14.76	2.92	11.02
289	35.2	0.132	0.18	0.15	4.71	4.91	2.16
28	44.1	0.063	0.05	0.06	3.54	2.11	2.56
292	39.3	0.251	0.36	0.26	11.37	32.02	10.27
295	32.0	0.019	0.02	0.02	0.72	0.84	0.64
296	42.0	0.049	0.06	0.03	0.52	0.68	0.73
297	37.7	0.076	0.07	0.05	4.61	5.43	3.69
300	49.5	0.177	0.16	0.15	6.73	6.61	12.56
303	30.3	0.071	0.08	0.04	0.93	0.74	0.40
30	43.9	0.367	0.14	0.44	3.84	2.67	5.11
316	40.0	0.242	0.16	0.16	26.88	12.95	1.78
317	28.7	0.199	0.18	0.21	4.44	2.33	1.08
319	40.0	0.368	0.50	0.84	10.59	10.91	0.46
31	26.1	0.273	0.12	0.25	3.22	1.48	3.56
326	40.0	0.109	0.11	0.04	2.60	1.79	1.39
3317	72.0	0.146	0.04	0.13	6.86	6.62	13.70
338	40.0	0.282	0.27	0.10	8.09	5.10	4.12
33	30.3	0.272	0.14	0.36	3.37	1.11	3.81
3470	57.0	0.088	0.04	0.08	0.74	0.78	1.80
3473	60.0	0.386	0.31	0.25	5.85	5.20	4.76
373	9.9	0.452	0.41	0.42	0.85	1.27	0.20
398	20.6	0.387	0.37	0.21	1.59	0.88	0.29
406	40.0	0.324	0.61	0.20	1.39	2.32	1.10
409	19.5	0.217	0.21	0.15	2.88	4.38	3.16
411	20.6	0.228	0.41	0.13	6.20	5.63	2.52
412	21.7	0.602	0.33	0.32	8.06	2.32	0.92
413	21.3	0.375	0.23	0.23	6.24	2.65	2.88
448	28.3	0.423	0.29	0.20	4.58	6.35	1.81
454	30.0	0.114	0.09	0.11	0.88	0.94	0.25
455	30.0	0.069	0.10	0.09	1.26	1.02	1.06
456	30.0	0.162	0.21	0.58	1.42	2.09	0.92
457	40.0	0.194	0.20	0.40	2.41	3.46	1.22
458	40.0	0.224	0.35	0.41	4.34	3.11	1.70
459	30.0	0.222	0.29	0.41	2.46	6.13	1.86
460	30.0	0.190	0.11	0.43	2.05	1.78	0.92
461	40.0	0.156	0.31	0.11	1.84	7.65	1.25
497	19.1	0.148	0.14	0.14	3.10	0.99	3.01
502	40.0	0.140	0.16	0.07	1.65	4.41	0.56
514	20.6	0.217	0.21	0.36	1.96	2.24	0.84
518	20.1	0.129	0.12	0.07	1.06	1.38	0.67
527	20.2	0.218	0.20	0.40	8.50	15.02	1.61
537	24.0	0.139	0.11	0.09	0.55	0.79	0.47
547	39.9	0.285	0.21	0.21	3.99	5.40	2.06
549	40.0	0.248	0.17	0.14	7.05	6.68	2.24
550	40.0	0.165	0.16	0.13	2.16	3.28	1.41
587	27.0	0.256	0.34	0.15	6.39	2.66	3.39
589	40.0	0.333	0.41	0.19	2.42	2.32	0.85
595	34.3	0.219	0.21	0.10	2.53	4.82	0.40

Table F.6 (cont.)

608	29.7	0.104	0.13	0.05	1.90	1.53	0.23
619	26.0	0.384	0.46	0.36	2.49	4.30	0.75
639	40.0	0.450	0.40	0.14	2.18	2.53	0.59
643	18.2	0.039	0.05	0.02	0.17	0.15	0.09
718	29.8	0.132	0.13	0.19	7.32	5.19	2.26
71	36.6	0.283	0.17	0.37	3.03	0.65	1.68
721	40.0	0.358	0.26	0.13	17.56	20.08	4.90
728	40.0	0.172	0.21	0.25	13.06	20.27	4.18
732	35.8	0.274	0.22	0.08	12.61	6.84	3.15
739	39.6	0.244	0.24	0.15	7.69	6.70	3.18
740	39.0	0.064	0.08	0.05	11.79	5.53	4.06
752	40.0	0.529	0.44	0.54	9.12	5.49	2.63
755	40.0	0.151	0.48	0.08	7.33	15.07	3.81
757	65.0	0.129	0.13	0.06	10.34	6.20	3.63
759	60.0	0.268	0.29	0.10	6.28	15.03	3.27
760	30.0	0.107	0.12	0.08	7.99	3.94	2.71
763	40.0	0.357	0.33	0.19	6.36	4.56	5.74
764	40.0	0.284	0.24	0.15	11.12	3.67	6.00
765	39.9	0.411	0.47	0.21	6.35	8.05	5.55
766	40.0	0.367	0.32	0.29	7.15	12.08	4.68
768	40.0	0.417	0.21	0.16	7.10	10.09	5.09
769	40.0	0.126	0.17	0.10	4.74	3.80	4.07
776	60.0	0.371	0.18	0.20	30.30	18.13	7.06
786	40.0	0.213	0.20	0.08	17.20	11.71	3.35
787	39.6	0.194	0.28	0.09	9.97	9.72	2.82
801	50.0	0.275	0.23	0.21	13.35	6.23	5.74
802	40.0	0.512	0.32	0.39	16.24	27.61	15.21
809	25.0	0.311	0.39	0.23	5.93	5.07	5.79
810	40.0	0.450	0.39	0.37	3.83	5.03	5.38
821	21.3	0.515	0.25	0.50	27.66	7.55	21.93
832	50.0	0.115	0.15	0.09	11.32	7.49	3.44
836	50.0	0.108	0.11	0.06	6.25	7.91	3.59
837	34.3	0.028	0.03	0.02	4.86	5.19	1.25
841	40.0	0.119	0.09	0.05	9.06	3.52	3.04
849	55.8	0.057	0.05	0.03	9.60	2.09	2.42
852	37.0	0.026	0.02	0.02	0.86	1.05	1.14
854	44.0	0.051	0.05	0.03	3.48	2.36	0.86
858	56.8	0.039	0.06	0.03	1.37	2.79	0.60
860	56.0	0.081	0.10	0.06	1.35	2.20	1.33
885	55.0	0.067	0.04	0.04	6.91	3.52	1.35
886	65.0	0.047	0.04	0.04	0.38	0.56	0.43
887	50.0	0.043	0.04	0.04	1.72	1.40	0.79
888	120.0	0.078	0.09	0.06	10.49	7.63	2.63
949	40.0	0.344	0.31	0.55	15.07	10.65	8.62
953	30.0	0.416	0.52	0.33	13.14	11.07	2.56
954	30.0	0.163	0.25	0.17	0.83	1.12	0.56
957	30.0	0.120	0.16	0.08	2.25	1.81	1.49
959	25.0	0.356	0.42	0.49	9.11	20.26	5.49
95	26.0	0.337	0.38	0.42	8.23	3.10	6.01
960	20.0	0.410	0.48	0.32	11.69	12.53	5.17
962	40.0	0.089	0.09	0.04	1.59	1.92	0.25
989	31.1	0.225	0.19	0.17	3.39	5.77	1.09
994	46.9	0.164	0.13	0.29	2.40	1.61	3.88
999	40.0	0.355	0.56	0.11	1.48	2.67	1.32

Table F.7 Component Peak Parameters for Severe NGA Record Suite

Record ID	Length (s)	Trans PGA (g)	Long PGA (g)	Vert PGA (g)	Trans PGD (cm)	Long PGD (cm)	Vert PGD (cm)
1004	47.8	0.93	0.45	0.75	17.37	10.88	13.39
1011	30.0	0.11	0.17	0.11	1.78	2.77	1.12
1013	26.6	0.51	0.35	0.42	21.24	15.09	8.69
1044	40.0	0.58	0.59	0.55	17.74	38.13	14.95
1045	25.0	0.45	0.33	0.29	56.62	16.10	13.48
1050	20.0	0.42	0.43	0.19	4.99	4.53	1.38
1051	40.0	1.58	1.29	1.23	5.72	23.07	12.21
1063	19.9	0.83	0.49	0.83	29.61	26.94	10.05
1080	25.0	0.88	0.64	0.40	5.28	5.09	2.18
1106	48.0	0.82	0.60	0.34	17.68	19.95	10.29
1119	41.0	0.69	0.69	0.43	26.66	16.76	12.38
1120	41.0	0.61	0.62	0.27	35.77	32.73	4.47
1148	30.0	0.15	0.09	0.22	35.57	5.53	13.65
1162	25.5	0.13	0.12	0.11	3.05	3.95	7.60
1165	30.0	0.22	0.15	0.15	17.13	9.81	6.67
1166	30.0	0.14	0.10	0.08	17.45	7.73	4.26
1176	35.0	0.27	0.35	0.24	57.02	50.98	29.56
1180	150.0	0.09	0.12	0.15	15.50	45.42	59.82
1182	150.0	0.20	0.36	0.35	11.63	25.59	15.18
1184	132.0	0.13	0.23	0.17	5.16	7.26	11.07
1186	149.0	0.10	0.23	0.26	5.16	6.21	6.57
1193	90.0	0.18	0.15	0.28	31.05	34.80	43.62
1194	90.0	0.15	0.16	0.16	24.47	29.88	36.78
1195	90.0	0.07	0.07	0.08	26.97	15.35	35.24
1197	90.0	0.82	0.34	0.65	23.29	13.56	14.68
1198	90.0	0.24	0.16	0.28	29.11	9.82	14.73
1199	90.0	0.08	0.06	0.09	19.00	5.95	17.75
1200	90.0	0.06	0.04	0.07	16.63	7.24	16.74
1201	197.0	0.09	0.25	0.31	8.37	11.46	16.54
1202	90.0	0.25	0.10	0.25	16.87	5.99	12.03
1203	90.0	0.21	0.10	0.29	34.17	10.18	21.19
1204	90.0	0.10	0.04	0.11	14.66	7.27	17.46
1205	90.0	0.64	0.12	0.30	11.25	6.38	8.62
1206	90.0	0.07	0.06	0.10	7.97	4.72	6.50
1208	90.0	0.18	0.08	0.14	11.90	6.21	10.29
1209	150.0	0.09	0.17	0.19	8.56	10.28	13.65
1212	90.0	0.10	0.03	0.09	13.75	6.43	11.86
1227	90.0	0.16	0.09	0.23	11.75	9.40	19.04
1228	90.0	0.07	0.03	0.07	16.97	7.24	20.38
1231	90.0	0.90	0.72	0.97	33.98	27.82	18.60
1233	90.0	0.06	0.08	0.07	25.79	6.34	20.71
1234	90.0	0.20	0.05	0.11	7.89	4.79	6.66
1235	90.0	0.13	0.06	0.14	8.11	5.77	7.19
1236	90.0	0.22	0.04	0.14	14.21	4.93	8.06
1238	150.0	0.12	0.11	0.08	26.67	37.27	30.54
1239	150.0	0.04	0.05	0.07	5.84	13.74	12.79
1240	150.0	0.05	0.07	0.05	9.27	19.53	19.77
1244	90.0	0.44	0.16	0.35	68.76	19.73	45.29
1245	90.0	0.05	0.03	0.04	4.15	5.06	5.36

Table F.7 (cont.)

1246	150.0	0.12	0.16	0.19	20.49	36.15	47.24
126	16.3	0.61	0.72	1.26	25.37	23.71	30.12
1380	90.0	0.08	0.03	0.08	3.56	4.66	6.00
139	23.8	0.41	0.18	0.33	9.09	4.67	11.59
143	32.8	0.85	0.69	0.84	95.01	16.39	38.64
146	26.8	0.10	0.13	0.07	0.48	1.52	0.41
1476	90.0	0.20	0.06	0.17	40.19	26.82	44.57
1477	90.0	0.12	0.07	0.11	31.11	29.00	47.96
1479	90.0	0.11	0.07	0.25	21.66	14.93	46.08
1480	90.0	0.13	0.06	0.14	42.18	22.51	63.61
1481	90.0	0.17	0.07	0.14	43.61	28.80	64.18
1482	90.0	0.14	0.14	0.21	44.54	45.99	76.79
1483	90.0	0.12	0.08	0.15	50.21	16.99	57.39
1484	90.0	0.20	0.09	0.25	23.86	24.09	46.92
1486	85.0	0.12	0.10	0.13	23.19	37.75	37.32
1488	90.0	0.18	0.10	0.12	53.56	21.65	52.19
1489	90.0	0.25	0.17	0.29	51.30	21.83	65.29
1490	90.0	0.13	0.10	0.15	52.05	27.59	54.69
1491	90.0	0.23	0.11	0.19	56.52	24.56	70.27
1492	90.0	0.42	0.24	0.35	246.19	163.54	184.45
1493	90.0	0.14	0.12	0.22	48.06	23.45	59.53
1494	90.0	0.19	0.13	0.15	52.23	24.66	59.43
1495	56.0	0.20	0.17	0.24	47.17	39.59	9.95
1496	90.0	0.13	0.11	0.13	54.56	27.08	50.78
1497	90.0	0.09	0.08	0.12	56.23	29.01	56.71
1498	90.0	0.17	0.06	0.17	53.53	12.06	63.66
1499	90.0	0.11	0.09	0.20	45.57	24.82	51.90
1500	90.0	0.14	0.09	0.14	36.21	24.17	37.05
1501	90.0	0.13	0.13	0.17	59.25	40.03	59.20
1502	90.0	0.12	0.08	0.11	59.04	24.51	51.84
1503	90.0	0.60	0.27	0.81	60.75	53.71	92.58
1504	90.0	0.33	0.23	0.50	45.96	28.49	93.11
1505	90.0	0.46	0.49	0.57	430.08	266.60	324.16
1506	90.0	0.17	0.09	0.26	56.68	30.94	48.10
1507	90.0	0.65	0.45	0.57	49.07	31.32	13.76
1508	90.0	0.40	0.28	0.49	41.29	27.28	38.64
1509	90.0	0.35	0.29	0.60	15.70	7.75	20.45
1510	90.0	0.26	0.23	0.33	33.24	25.63	86.47
1511	90.0	0.42	0.28	0.30	35.38	17.39	31.48
1512	90.0	0.29	0.18	0.44	9.17	14.19	31.25
1513	90.0	0.39	0.39	0.74	13.78	12.59	11.11
1515	90.0	0.19	0.13	0.22	53.80	25.50	71.49
1517	90.0	0.42	0.34	1.16	21.27	11.94	31.44
1519	90.0	0.12	0.11	0.13	25.55	51.33	62.63
1521	79.0	0.25	0.19	0.33	32.30	23.91	18.53
1527	90.0	0.12	0.09	0.12	53.51	33.74	51.96
1528	49.0	0.25	0.17	0.20	35.12	39.20	75.37
1529	90.0	0.17	0.19	0.30	44.88	48.75	89.20
1530	90.0	0.16	0.15	0.13	15.98	42.37	87.56
1531	90.0	0.09	0.08	0.11	52.71	20.60	51.98
1532	90.0	0.13	0.06	0.11	45.60	18.41	48.60

Table F.7 (cont.)

1533	90.0	0.13	0.12	0.16	35.83	20.65	43.33
1534	90.0	0.16	0.09	0.12	32.80	21.70	39.82
1535	90.0	0.16	0.14	0.16	34.75	20.28	46.50
1536	90.0	0.18	0.12	0.18	35.30	26.90	40.98
1537	90.0	0.10	0.08	0.14	31.30	22.39	55.23
1538	90.0	0.07	0.06	0.08	37.44	22.07	30.06
1539	90.0	0.07	0.08	0.07	27.13	17.03	22.22
1540	90.0	0.12	0.08	0.10	33.03	21.95	37.82
1541	90.0	0.15	0.12	0.18	30.07	31.66	49.23
1542	90.0	0.12	0.09	0.12	45.55	19.91	49.01
1543	90.0	0.09	0.12	0.11	36.49	21.28	23.88
1544	90.0	0.06	0.06	0.07	19.75	13.68	22.53
1545	90.0	0.19	0.16	0.23	33.31	22.35	54.10
1546	90.0	0.26	0.24	0.22	36.09	33.78	43.03
1547	90.0	0.14	0.09	0.16	27.31	26.85	33.48
1548	90.0	0.17	0.10	0.14	41.88	34.78	90.63
1550	90.0	0.12	0.17	0.18	30.20	66.50	44.83
1551	150.0	0.11	0.19	0.22	19.74	36.43	26.10
1552	150.0	0.07	0.07	0.06	17.10	21.44	17.53
1553	150.0	0.10	0.11	0.08	21.83	35.00	23.11
155	23.8	0.04	0.02	0.02	0.41	0.06	0.09
1602	55.9	0.73	0.82	0.20	23.07	13.55	14.29
1605	25.9	0.35	0.54	0.36	42.09	51.60	19.40
160	37.6	0.59	0.77	0.42	16.76	15.00	4.06
1616	43.2	0.04	0.02	0.03	8.09	4.34	10.12
1617	41.5	0.97	0.19	0.51	5.48	6.20	7.51
1618	41.5	0.16	0.07	0.12	7.85	7.53	9.52
1619	28.8	0.12	0.06	0.06	7.63	15.38	7.33
1620	60.0	0.02	0.02	0.01	5.80	7.34	4.00
1627	28.2	0.06	0.10	0.05	0.72	1.17	1.28
1636	60.4	0.18	0.13	0.09	3.91	3.38	3.94
1637	52.2	0.10	0.09	0.09	2.21	6.43	1.36
170	40.0	0.21	0.23	0.25	15.95	39.40	9.65
1715	5.7	0.05	0.05	0.05	0.07	0.13	0.07
171	40.0	0.31	0.30	0.25	25.58	31.64	8.34
1728	6.0	0.65	0.43	0.60	2.48	1.54	0.74
174	39.0	0.36	0.38	0.14	16.08	18.63	6.79
175	39.0	0.14	0.12	0.07	11.31	11.97	5.32
1762	60.0	0.18	0.15	0.13	13.62	17.28	4.39
1766	60.0	0.09	0.13	0.07	4.00	4.11	2.43
1768	60.0	0.06	0.08	0.04	2.41	4.57	1.28
1770	50.0	0.16	0.17	0.04	8.35	11.10	1.38
1776	50.0	0.07	0.08	0.07	3.94	3.58	2.29
1786	60.0	0.08	0.08	0.06	9.87	8.57	2.54
1787	45.3	0.34	0.15	0.27	13.96	6.92	22.53
178	39.5	0.27	0.22	0.13	18.90	23.27	4.72
1794	50.0	0.15	0.19	0.12	7.25	5.38	4.17
1795	71.7	0.08	0.09	0.04	7.60	2.56	2.90
179	39.0	0.49	0.36	0.25	20.08	59.04	10.71
180	39.3	0.52	0.38	0.54	35.39	63.06	19.80
181	39.0	0.41	0.44	1.66	27.56	65.81	25.81

Table F.7 (cont.)

182	36.8	0.34	0.46	0.54	24.64	44.71	9.32
1836	60.0	0.07	0.07	0.04	7.18	2.71	2.45
183	37.6	0.60	0.45	0.44	32.33	35.56	11.92
184	39.0	0.35	0.48	0.71	45.81	14.03	11.60
185	37.7	0.25	0.22	0.23	31.62	31.89	5.73
192	40.0	0.07	0.11	0.08	16.54	10.00	2.60
199	10.9	0.12	0.17	0.06	0.74	1.02	0.08
200	10.9	0.15	0.07	0.03	0.95	0.22	0.06
201	11.0	0.18	0.11	0.03	0.97	0.30	0.07
2095	172.0	0.01	0.02	0.01	7.13	4.15	1.57
2096	300.0	0.01	0.01	0.01	4.88	2.97	1.52
2097	300.0	0.01	0.01	0.01	4.66	2.53	1.54
2098	280.0	0.01	0.01	0.01	4.27	2.64	1.65
2099	300.0	0.01	0.01	0.01	4.81	4.54	1.68
2100	300.0	0.02	0.01	0.01	4.91	3.35	1.31
2101	293.0	0.01	0.01	0.01	3.56	3.78	1.21
2102	163.0	0.01	0.02	0.01	4.87	4.73	1.47
2103	169.0	0.02	0.02	0.01	5.14	3.36	1.53
2104	188.0	0.02	0.02	0.01	4.96	3.89	1.45
2105	300.0	0.01	0.01	0.01	4.46	2.89	1.75
2106	300.0	0.01	0.01	0.01	4.77	3.35	1.58
2108	50.0	0.01	0.01	0.00	3.91	2.08	1.72
2109	300.0	0.05	0.04	0.02	3.29	4.66	4.60
2110	234.0	0.09	0.07	0.05	3.98	3.48	4.12
2112	75.5	0.05	0.04	0.02	3.62	3.42	2.90
2113	164.5	0.06	0.07	0.06	8.99	11.01	4.41
2115	164.8	0.07	0.09	0.03	9.42	13.42	9.12
2116	104.6	0.04	0.03	0.02	4.21	5.12	3.72
2118	86.0	0.01	0.01	0.01	5.65	5.58	2.66
2457	99.0	0.09	0.07	0.19	11.20	15.54	19.59
250	26.0	0.92	0.41	0.31	3.17	6.42	1.08
2651	106.0	0.03	0.02	0.06	1.78	2.10	10.85
2658	104.0	0.40	0.19	0.95	1.80	4.85	7.80
265	24.5	0.62	0.59	0.30	13.07	9.47	4.88
266	26.9	0.09	0.10	0.15	9.96	2.50	9.17
2741	69.0	0.03	0.03	0.03	1.62	1.86	6.33
284	34.3	0.06	0.06	0.04	3.19	3.68	1.28
285	36.9	0.14	0.20	0.11	9.26	9.59	5.75
286	38.3	0.10	0.08	0.07	14.76	2.92	11.02
292	39.3	0.25	0.36	0.26	11.37	32.02	10.27
295	32.0	0.02	0.02	0.02	0.72	0.84	0.64
296	42.0	0.05	0.06	0.03	0.52	0.68	0.73
297	37.7	0.08	0.07	0.05	4.61	5.43	3.69
303	30.3	0.07	0.08	0.04	0.93	0.74	0.40
317	28.7	0.20	0.18	0.21	4.44	2.33	1.08
319	40.0	0.37	0.50	0.84	10.59	10.91	0.46
326	40.0	0.11	0.11	0.04	2.60	1.79	1.39
3474	70.0	0.62	0.58	0.77	3.25	1.79	7.53
3475	93.0	0.54	0.48	0.47	5.21	2.24	5.57
368	40.0	0.59	0.55	0.35	8.80	3.96	2.35
372	9.8	0.58	0.67	0.25	0.96	1.18	0.11

Table F.7 (cont.)

407	21.2	0.87	0.45	0.57	6.14	2.23	1.20
415	21.8	0.84	1.08	0.39	6.82	5.42	3.59
418	40.0	0.43	0.73	0.33	1.21	5.23	0.61
451	30.0	0.71	1.30	0.39	12.01	9.56	2.66
455	30.0	0.07	0.10	0.09	1.26	1.02	1.06
495	20.6	0.98	1.10	2.09	9.64	14.52	12.28
529	20.0	0.59	0.69	0.43	11.46	3.88	1.16
540	20.0	0.49	0.61	0.47	6.39	4.58	1.02
558	40.0	0.45	0.40	0.32	7.00	8.59	2.82
568	9.0	0.87	0.48	0.39	12.35	14.19	2.11
569	20.3	0.41	0.61	0.48	15.64	10.19	2.36
585	16.0	1.39	0.89	0.59	11.50	7.62	2.52
608	29.7	0.10	0.13	0.05	1.90	1.53	0.23
643	18.2	0.04	0.05	0.02	0.17	0.15	0.09
721	40.0	0.36	0.26	0.13	17.56	20.08	4.90
728	40.0	0.17	0.21	0.25	13.06	20.27	4.18
732	35.8	0.27	0.22	0.08	12.61	6.84	3.15
741	25.0	0.48	0.53	0.50	11.68	11.86	9.14
753	39.9	0.64	0.48	0.46	10.82	11.29	7.11
759	60.0	0.27	0.29	0.10	6.28	15.03	3.27
760	30.0	0.11	0.12	0.08	7.99	3.94	2.71
765	39.9	0.41	0.47	0.21	6.35	8.05	5.55
767	39.9	0.56	0.37	0.34	8.25	19.33	6.97
779	25.0	0.97	0.59	0.89	65.79	24.46	65.14
77	41.6	1.16	0.70	1.23	11.79	18.20	35.41
811	25.0	0.40	0.67	0.27	6.63	8.35	3.97
825	30.0	1.50	1.04	0.75	39.71	12.20	110.28
826	44.0	0.15	0.18	0.04	5.85	11.39	2.61
827	44.0	0.12	0.11	0.05	27.50	12.74	3.70
828	36.0	0.59	0.66	0.16	21.92	28.97	28.44
829	36.0	0.39	0.55	0.20	21.63	19.52	7.03
830	36.0	0.23	0.19	0.05	0.40	0.52	0.21
838	40.0	0.13	0.14	0.07	20.61	18.72	4.18
850	50.0	0.17	0.15	0.17	12.96	7.44	3.20
855	40.0	0.11	0.12	0.06	3.60	21.76	3.90
862	60.0	0.10	0.11	0.04	5.07	9.62	3.99
864	44.0	0.27	0.28	0.18	9.53	14.31	8.87
879	48.1	0.73	0.79	0.82	262.64	69.76	22.23
880	70.0	0.13	0.13	0.08	2.32	24.33	1.69
881	70.0	0.19	0.14	0.16	9.47	6.30	3.29
882	70.0	0.14	0.13	0.11	4.98	5.57	2.38
884	60.0	0.08	0.09	0.11	6.95	5.25	3.09
891	55.0	0.05	0.04	0.04	1.96	4.07	1.97
897	50.0	0.08	0.06	0.04	2.26	4.12	1.73
900	44.0	0.24	0.15	0.14	43.83	24.62	4.97
901	60.0	0.48	0.54	0.19	4.05	4.05	2.96
952	24.0	0.62	0.44	0.31	8.56	4.83	1.30
962	40.0	0.09	0.09	0.04	1.59	1.92	0.25
983	28.6	1.02	0.82	0.57	24.69	14.64	42.40
994	46.9	0.16	0.13	0.29	2.40	1.61	3.88

Table F.8 Component Peak Parameters for Severe Tohoku Record Suite

Tohoku Sequence #	N-S PGA (gal)	E-W PGA (gal)	U-D PGA (gal)	N-S PGA (g)	E-W PGA (g)	U-D PGA (g)
AKT011	111	104	63	0.11	0.11	0.06
AKT016	109	108	36	0.11	0.11	0.04
AOM007	256	191	62	0.26	0.19	0.06
AOM010	126	93	43	0.13	0.09	0.04
AOM011	137	127	67	0.14	0.13	0.07
AOM012	185	194	75	0.19	0.20	0.08
AOM013	98	67	28	0.10	0.07	0.03
CHB003	473	463	269	0.48	0.47	0.27
CHB004	277	301	179	0.28	0.31	0.18
CHB005	174	176	54	0.18	0.18	0.06
CHB006	242	230	173	0.25	0.23	0.18
CHB007	1036	491	200	1.06	0.50	0.20
CHB010	188	188	88	0.19	0.19	0.09
CHB011	142	151	73	0.14	0.15	0.07
CHB012	212	215	119	0.22	0.22	0.12
CHB014	100	130	65	0.10	0.13	0.07
CHB016	71	98	30	0.07	0.10	0.03
CHB028	218	244	279	0.22	0.25	0.28
FKS001	619	552	331	0.63	0.56	0.34
FKS002	478	557	196	0.49	0.57	0.20
FKS003	328	299	150	0.33	0.30	0.15
FKS004	568	504	254	0.58	0.51	0.26
FKS005	735	445	264	0.75	0.45	0.27
FKS006	478	525	203	0.49	0.54	0.21
FKS008	1012	736	327	1.03	0.75	0.33
FKS009	492	793	301	0.50	0.81	0.31
FKS010	1116	882	436	1.14	0.90	0.44
FKS011	374	312	300	0.38	0.32	0.31
FKS012	356	250	231	0.36	0.25	0.24
FKS013	296	353	222	0.30	0.36	0.23
FKS014	196	227	165	0.20	0.23	0.17
FKS015	275	211	114	0.28	0.22	0.12
FKS016	1295	949	441	1.32	0.97	0.45
FKS017	672	493	298	0.69	0.50	0.30
FKS018	745	1069	457	0.76	1.09	0.47
FKS019	392	404	171	0.40	0.41	0.17
FKS020	241	276	96	0.25	0.28	0.10
FKS022	138	118	56	0.14	0.12	0.06
FKS023	451	421	128	0.46	0.43	0.13
FKS024	330	328	221	0.34	0.33	0.23
FKS025	97	147	137	0.10	0.15	0.14
FKS027	150	177	66	0.15	0.18	0.07
FKS031	451	408	271	0.46	0.42	0.28
GNM002	138	87	34	0.14	0.09	0.03
GNM009	281	354	157	0.29	0.36	0.16
GNM010	178	170	113	0.18	0.17	0.12
IBR001	304	400	265	0.31	0.41	0.27
IBR002	525	588	496	0.54	0.60	0.51
IBR003	1598	1186	1166	1.63	1.21	1.19

Table F.8 (cont.)

IBR004	1283	1007	775	1.31	1.03	0.79
IBR005	967	596	465	0.99	0.61	0.47
IBR006	779	786	427	0.79	0.80	0.44
IBR007	546	512	412	0.56	0.52	0.42
IBR008	259	290	161	0.26	0.30	0.16
IBR009	200	158	108	0.20	0.16	0.11
IBR010	309	408	206	0.31	0.42	0.21
IBR011	329	343	154	0.34	0.35	0.16
IBR012	287	302	230	0.29	0.31	0.23
IBR013	1355	1070	811	1.38	1.09	0.83
IBR014	382	496	247	0.39	0.51	0.25
IBR015	321	291	155	0.33	0.30	0.16
IBR016	470	517	251	0.48	0.53	0.26
IBR017	417	412	363	0.43	0.42	0.37
IBR018	494	651	268	0.50	0.66	0.27
IWT001	213	242	65	0.22	0.25	0.07
IWT002	126	123	40	0.13	0.13	0.04
IWT003	115	148	72	0.12	0.15	0.07
IWT005	199	164	236	0.20	0.17	0.24
IWT007	631	697	440	0.64	0.71	0.45
IWT009	570	512	299	0.58	0.52	0.30
IWT010	998	852	353	1.02	0.87	0.36
IWT011	199	342	167	0.20	0.35	0.17
IWT012	591	455	198	0.60	0.46	0.20
IWT013	352	438	205	0.36	0.45	0.21
IWT014	239	189	109	0.24	0.19	0.11
IWT016	229	236	90	0.23	0.24	0.09
IWT017	273	329	122	0.28	0.34	0.12
IWT018	163	249	112	0.17	0.25	0.11
IWT019	316	260	201	0.32	0.27	0.20
IWT020	249	246	116	0.25	0.25	0.12
IWT021	328	261	114	0.33	0.27	0.12
IWT022	111	96	50	0.11	0.10	0.05
IWT023	109	142	34	0.11	0.14	0.03
IWT024	161	134	77	0.16	0.14	0.08
IWT025	164	137	42	0.17	0.14	0.04
IWT026	310	396	214	0.32	0.40	0.22
KNG001	149	148	87	0.15	0.15	0.09
KNG002	138	165	59	0.14	0.17	0.06
KNG006	86	100	35	0.09	0.10	0.04
KNG008	96	116	49	0.10	0.12	0.05
KNG009	152	115	48	0.15	0.12	0.05
KNG010	92	80	55	0.09	0.08	0.06
KNG013	97	164	66	0.10	0.17	0.07
KNG201	107	124	15	0.11	0.13	0.02
KNG202	95	150	48	0.10	0.15	0.05
KNG205	158	150	21	0.16	0.15	0.02
KNG206	209	368	62	0.21	0.38	0.06
MYG001	412	426	258	0.42	0.43	0.26
MYG002	643	658	362	0.66	0.67	0.37
MYG003	570	781	303	0.58	0.80	0.31

Table F.8 (cont.)

MYG004	2700	1268	1880	2.75	1.29	1.92
MYG005	254	206	158	0.26	0.21	0.16
MYG006	444	571	239	0.45	0.58	0.24
MYG007	568	651	243	0.58	0.66	0.25
MYG009	450	548	216	0.46	0.56	0.22
MYG010	458	377	332	0.47	0.38	0.34
MYG012	758	1969	501	0.77	2.01	0.51
MYG013	1517	982	290	1.55	1.00	0.30
MYG014	496	418	214	0.51	0.43	0.22
MYG015	411	353	254	0.42	0.36	0.26
MYG016	406	359	203	0.41	0.37	0.21
MYG017	317	349	160	0.32	0.36	0.16
TCG001	362	412	155	0.37	0.42	0.16
TCG005	253	290	86	0.26	0.30	0.09
TCG006	378	376	181	0.39	0.38	0.18
TCG008	311	293	187	0.32	0.30	0.19
TCG009	1017	1186	493	1.04	1.21	0.50
TCG011	159	145	72	0.16	0.15	0.07
TCG012	298	420	254	0.30	0.43	0.26
TCG013	414	422	300	0.42	0.43	0.31
TCG014	711	1205	494	0.72	1.23	0.50
TKY017	219	158	82	0.22	0.16	0.08
YMN009	115	114	37	0.12	0.12	0.04
YMT005	113	95	83	0.12	0.10	0.08
YMT006	239	172	57	0.24	0.18	0.06
YMT007	184	200	90	0.19	0.20	0.09
YMT009	108	71	52	0.11	0.07	0.05
YMT010	103	96	61	0.10	0.10	0.06
YMT011	134	123	54	0.14	0.13	0.06
YMT015	193	199	79	0.20	0.20	0.08
FKS023	131	106	22	0.13	0.11	0.02
MYG002	83	79	28	0.08	0.08	0.03
FKS004	159	147	49	0.16	0.15	0.05
FKS005	208	258	85	0.21	0.26	0.09
FKS008	98	127	44	0.10	0.13	0.04
FKS009	67	162	25	0.07	0.17	0.03
FKS010	209	115	33	0.21	0.12	0.03
FKS012	68	101	68	0.07	0.10	0.07
FKS014	83	138	52	0.08	0.14	0.05
FKS015	95	109	32	0.10	0.11	0.03
FKS016	101	115	38	0.10	0.12	0.04
FKS018	39	103	30	0.04	0.10	0.03
FKS019	82	130	35	0.08	0.13	0.04
IBR001	92	136	87	0.09	0.14	0.09
IBR002	75	126	61	0.08	0.13	0.06
IBR003	277	249	126	0.28	0.25	0.13
IBR004	99	80	55	0.10	0.08	0.06
MYG015	67	107	43	0.07	0.11	0.04
TCG009	147	162	35	0.15	0.17	0.04
FKS001	94	53	44	0.10	0.05	0.04
FKS002	78	105	17	0.08	0.11	0.02

APPENDIX G. STRUCTURAL ANALYSIS RESULTS

The following plots present the results of the automated procedure to identify performance points indicative of achieving the slight, moderate, and extensive limit states in the experimental results from the hybrid simulation. These points are based off of measured strain values, reductions in stiffness, loss of load capacity, and physical observation of cracking and spalling. Following assessment of these results, further modifications are made based off of pier responses for the calibrated models subjected to varying earthquake records. The final limit states used to develop fragility relationship parameters take into account data from each of these approaches.

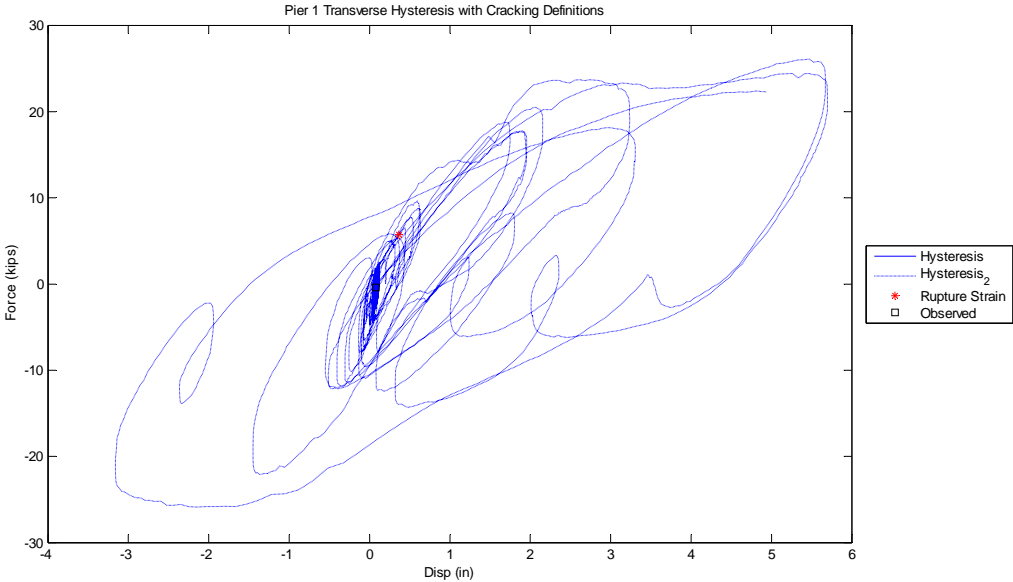


Figure G.1 Pier 1 Transverse Displacement Cracking Definition

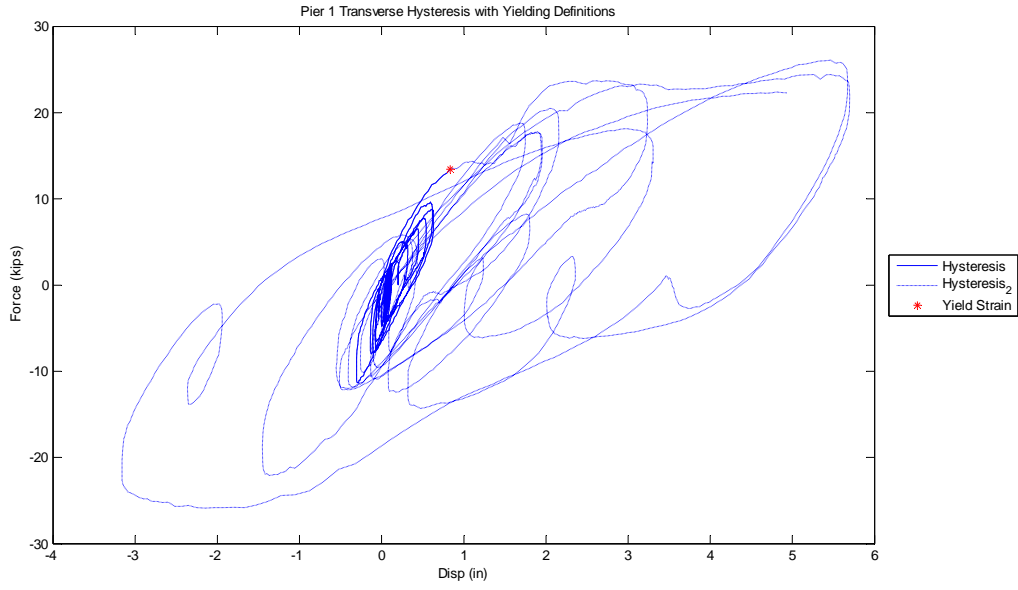


Figure G.2 Pier 1 Transverse Displacement Yield Definition

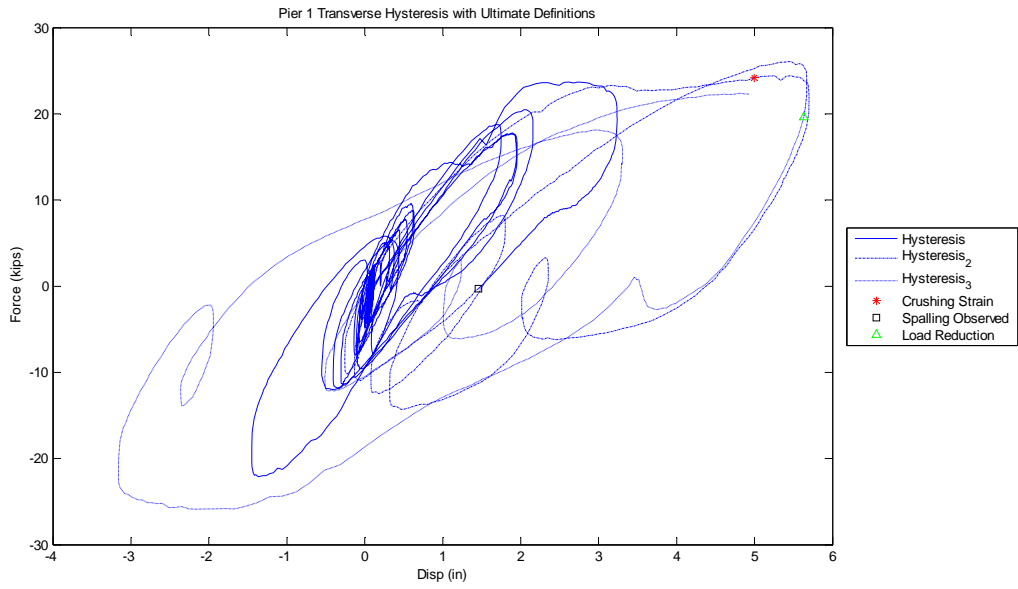


Figure G.3 Pier 1 Transverse Displacement Ultimate Definition

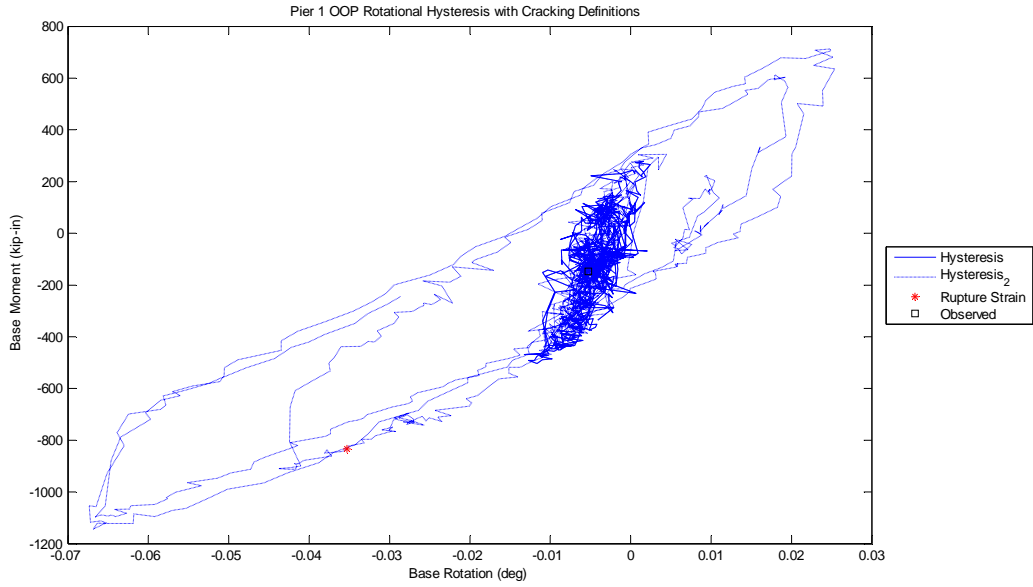


Figure G.4 Pier 1 OOP Rotation Cracking Definition

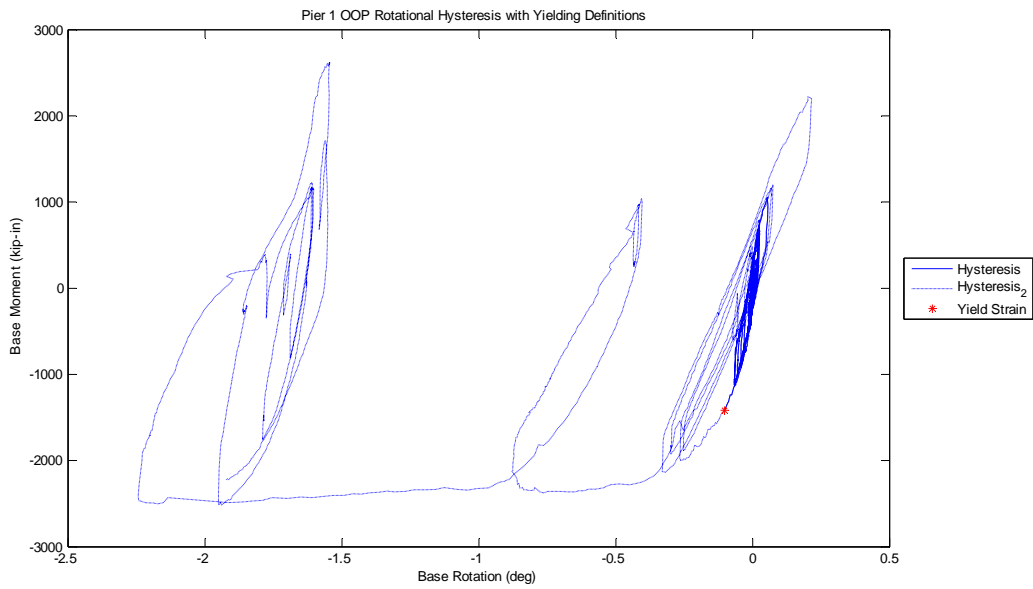


Figure G.5 Pier 1 OOP Rotation Yield Definition

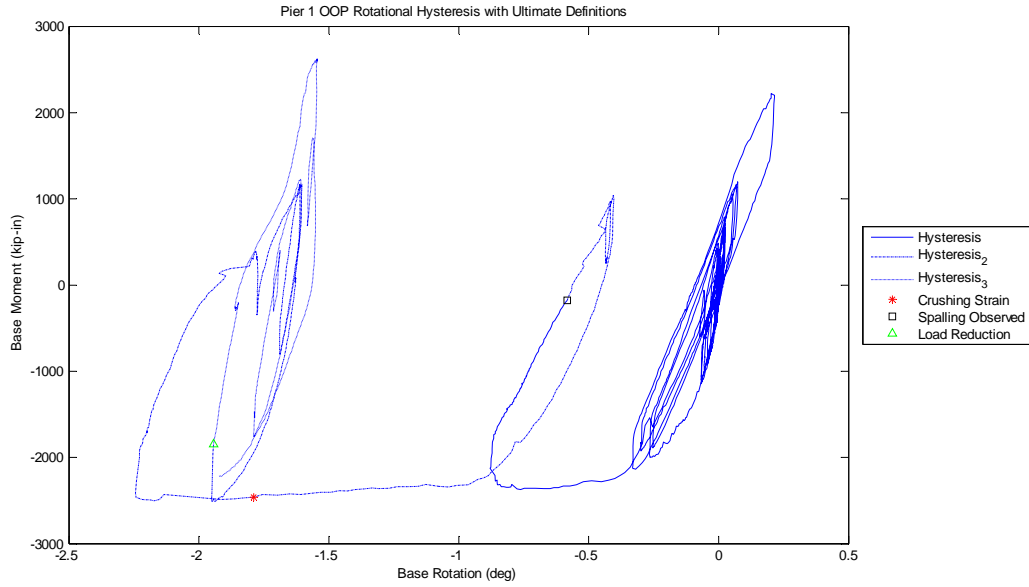


Figure G.6 Pier 1 OOP Rotation Ultimate Definition

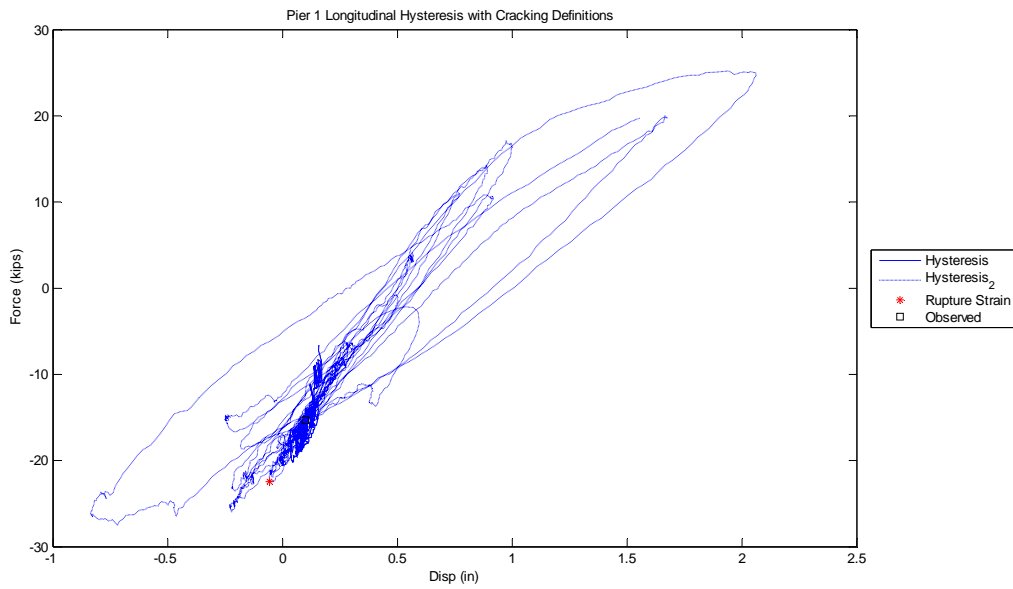


Figure G.7 Pier 1 Longitudinal Displacement Cracking Definition

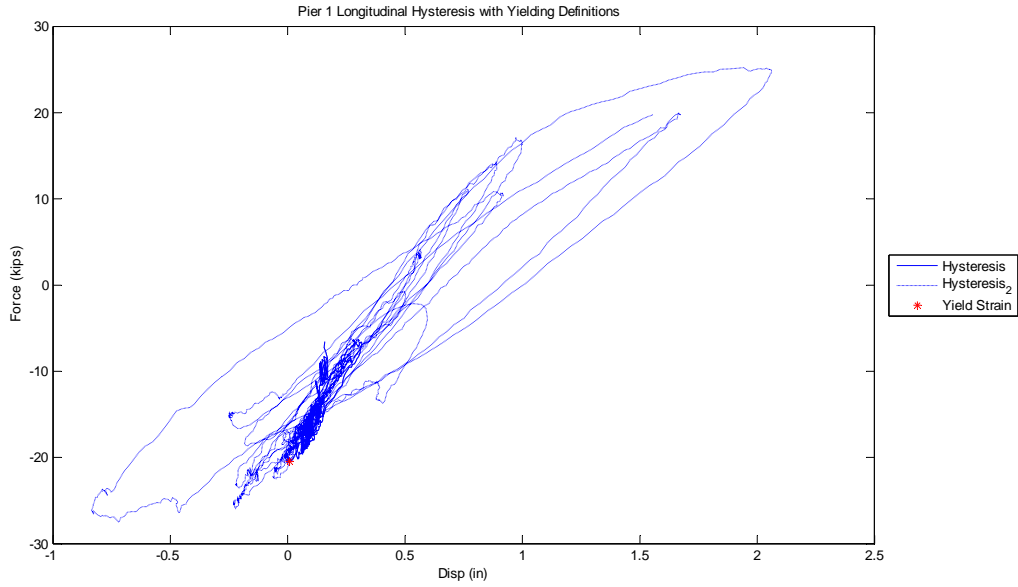


Figure G.8 Pier 1 Longitudinal Displacement Yield Definition

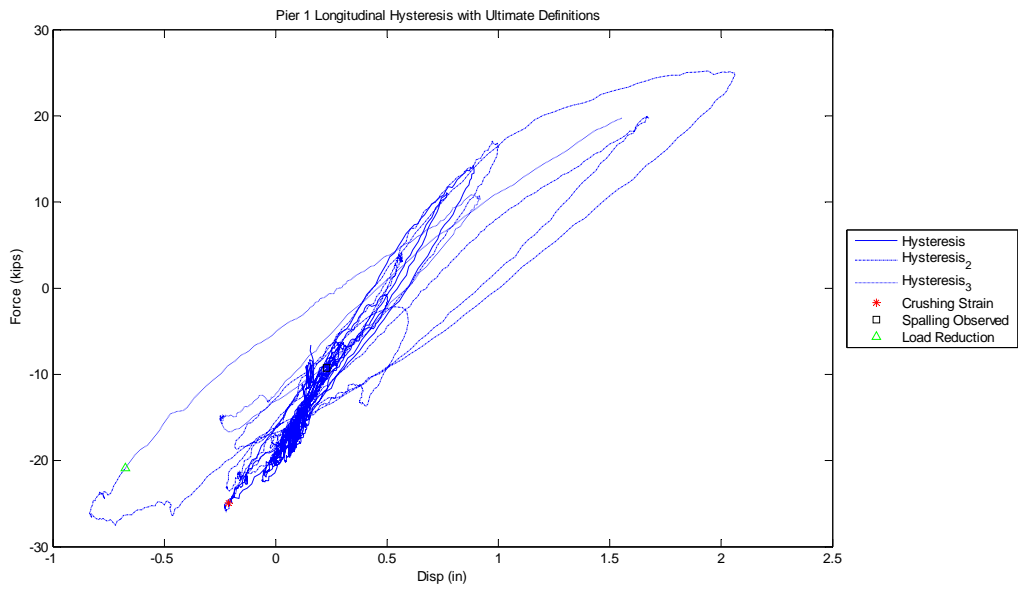


Figure G.9 Pier 1 Longitudinal Displacement Ultimate Definition

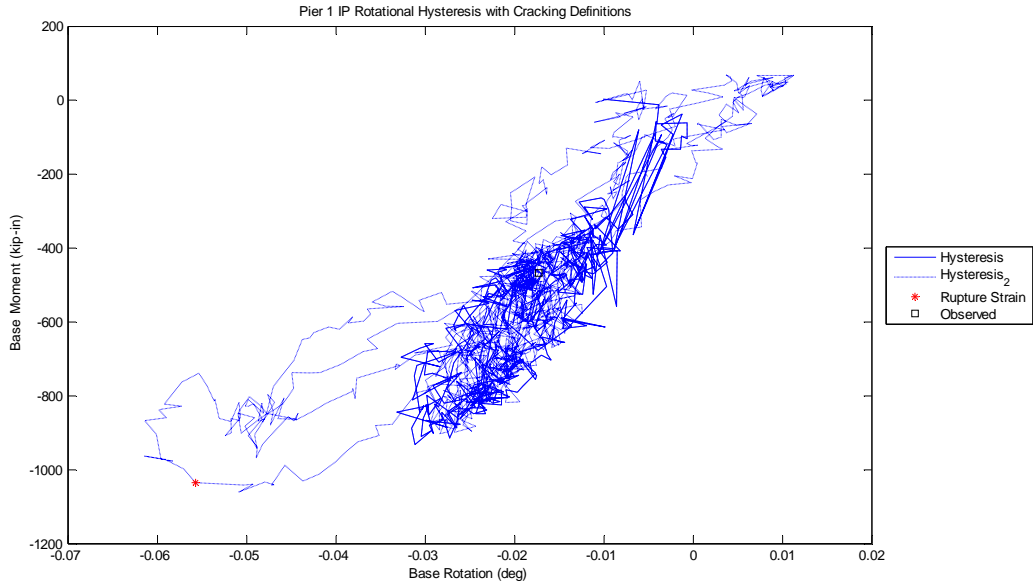


Figure G.10 Pier 1 IP Rotation Cracking Definition

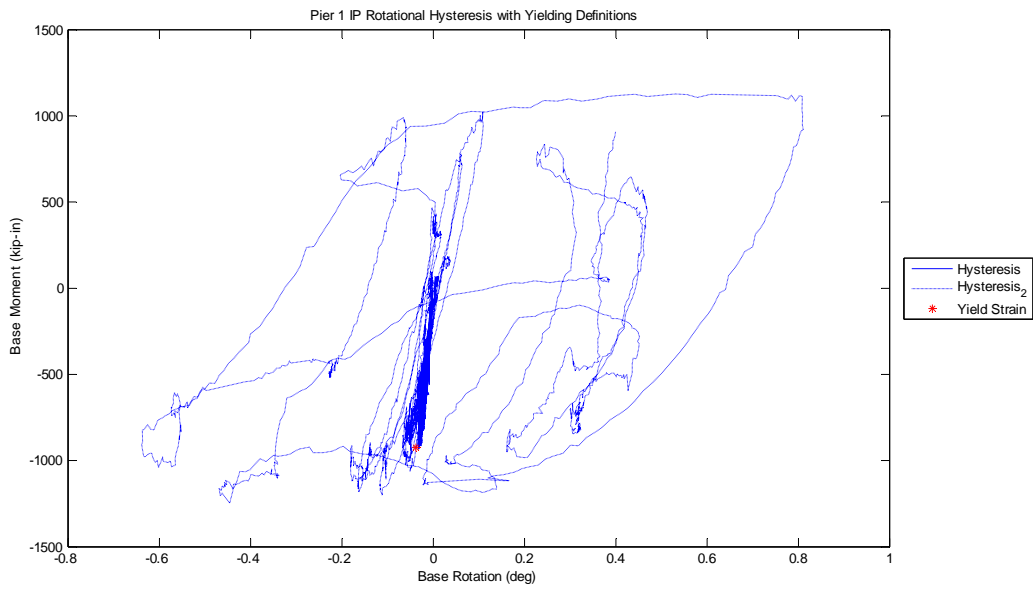


Figure G.11 Pier 1 IP Rotation Yield Definition

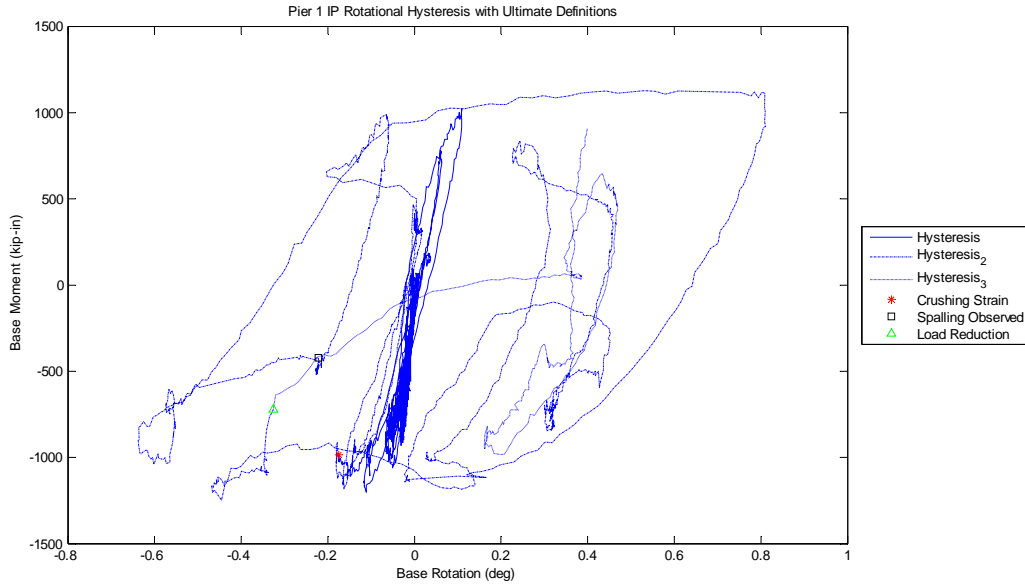


Figure G.12 Pier 1 IP Rotation Ultimate Definition

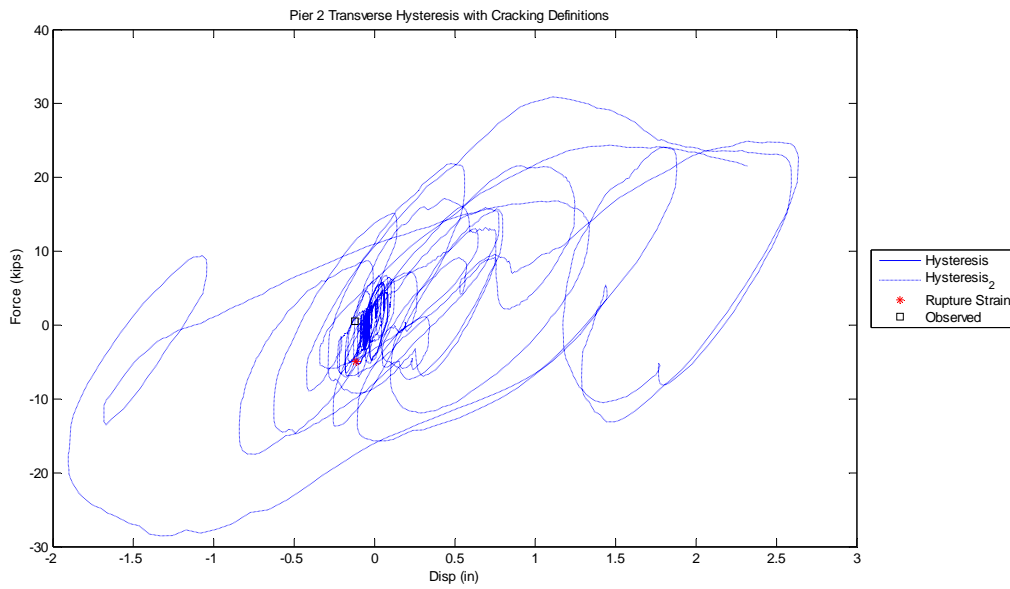


Figure G.13 Pier 2 Transverse Displacement Cracking Definition

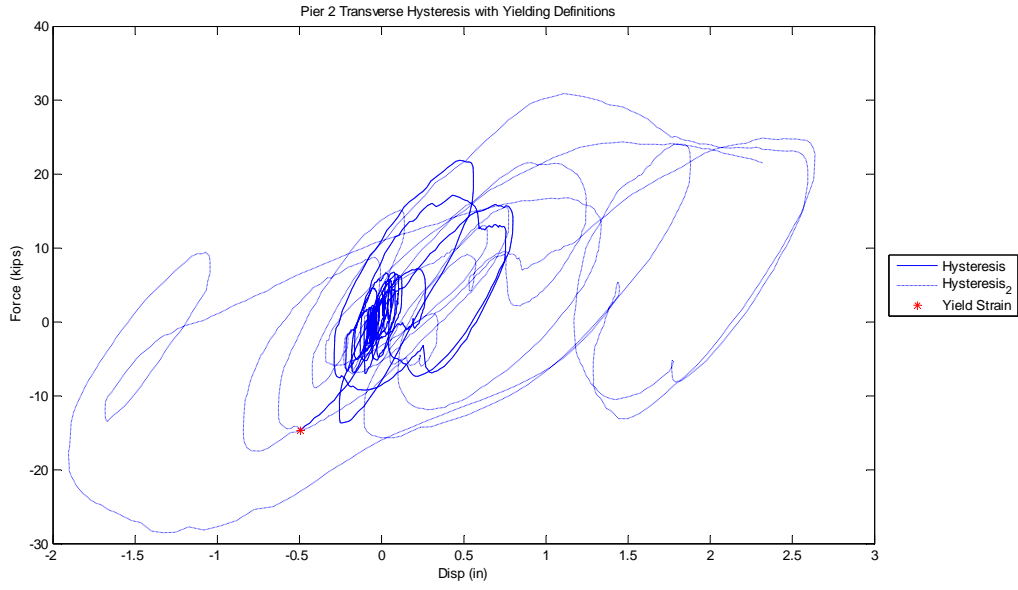


Figure G.14 Pier 2 Transverse Displacement Yield Definition

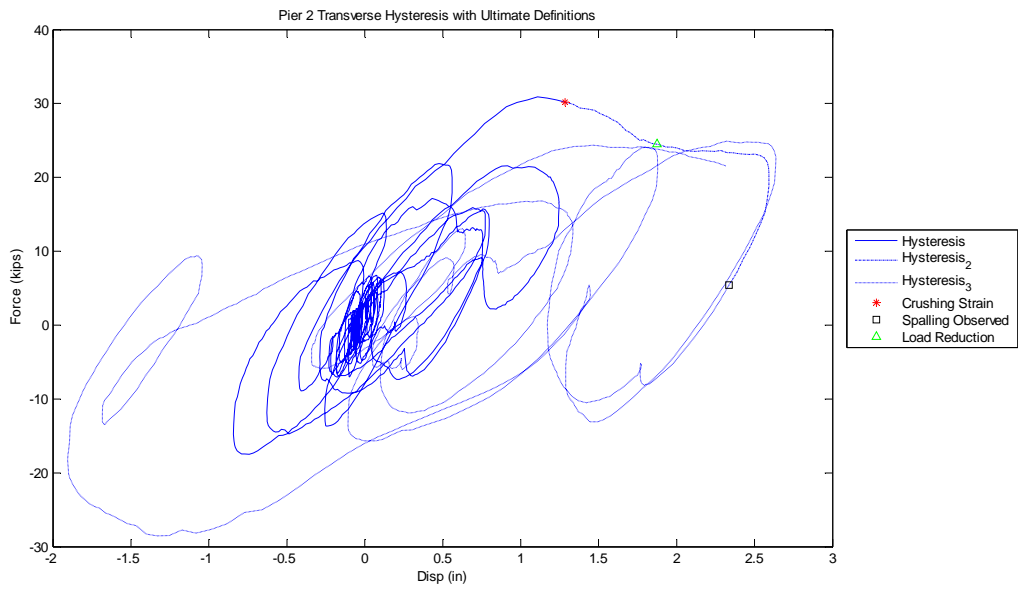


Figure G.15 Pier 2 Transverse Displacement Ultimate Definition

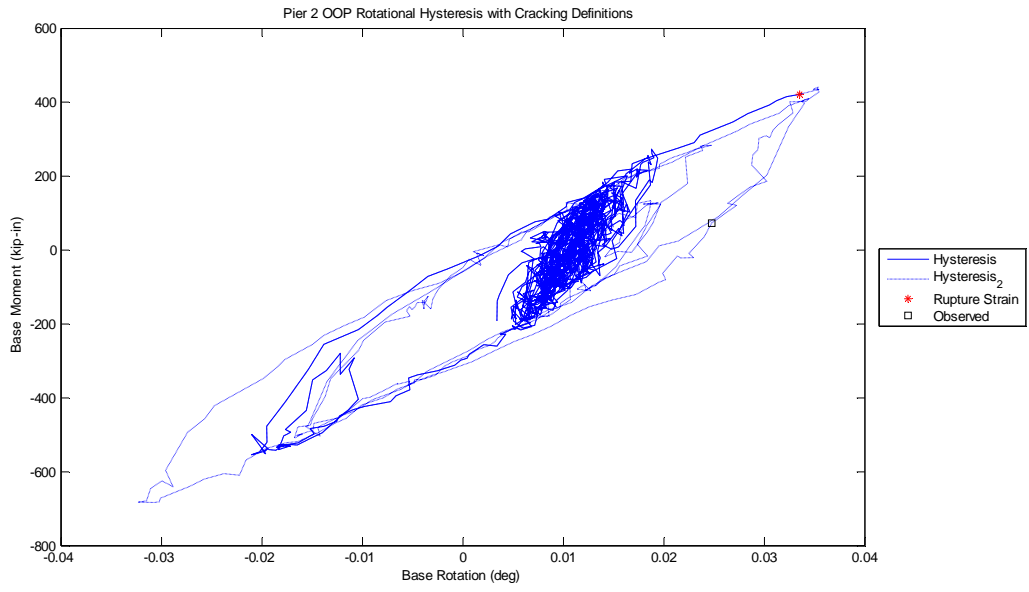


Figure G.16 Pier 2 OOP Rotation Cracking Definition

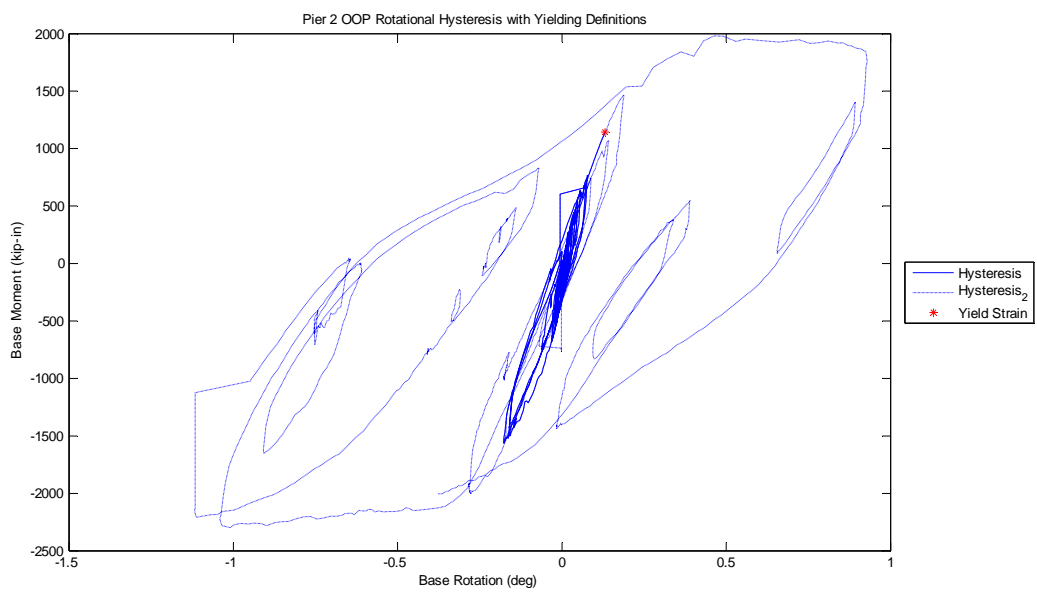


Figure G.17 Pier 2 OOP Rotation Yield Definition

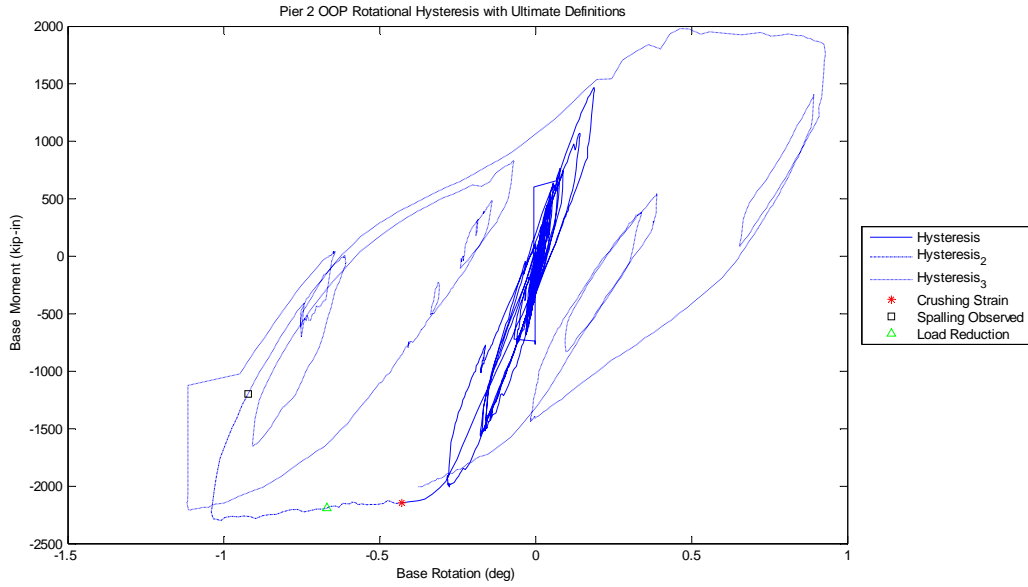


Figure G.18 Pier 2 OOP Rotation Ultimate Definition

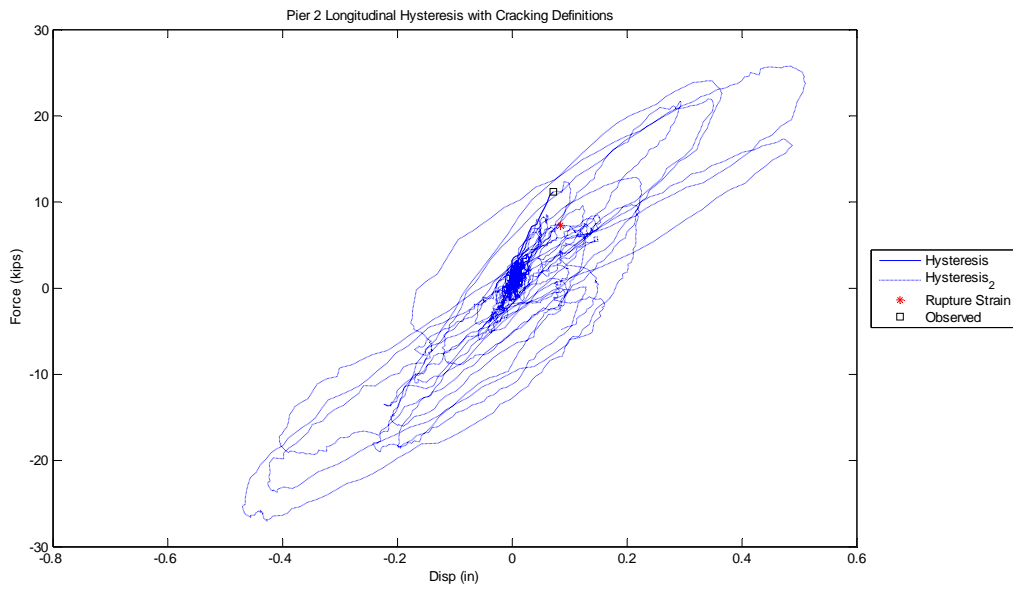


Figure G.19 Pier 2 Longitudinal Displacement Cracking Definition

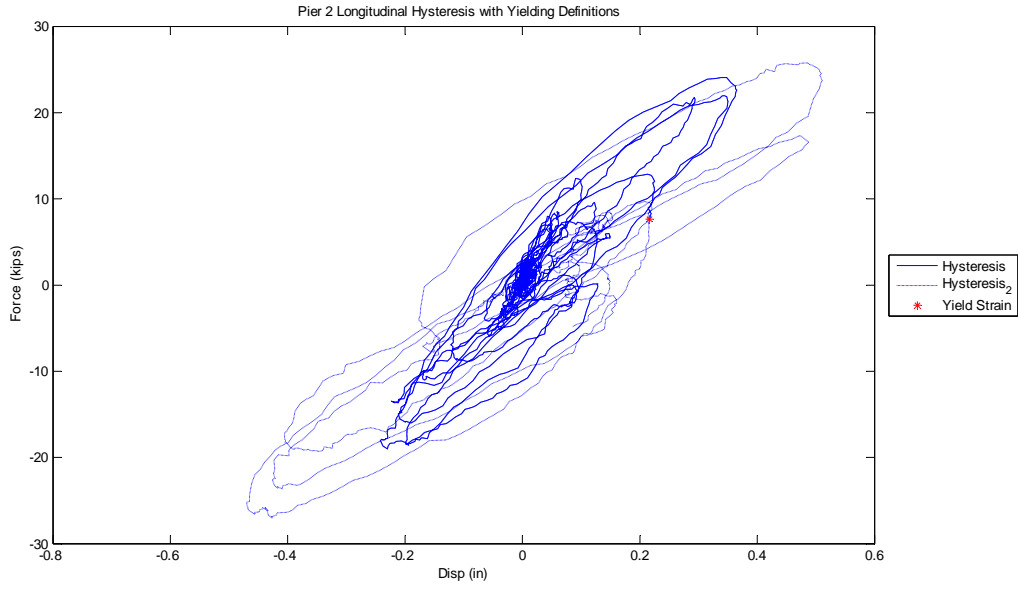


Figure G.20 Pier 2 Longitudinal Displacement Yield Definition

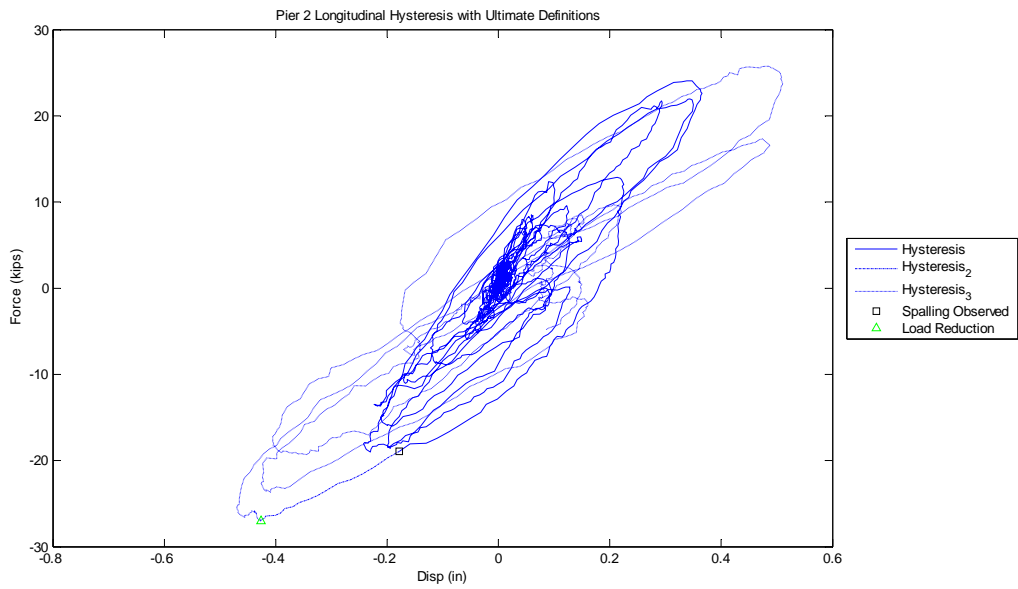


Figure G.21 Pier 2 Longitudinal Displacement Ultimate Definition

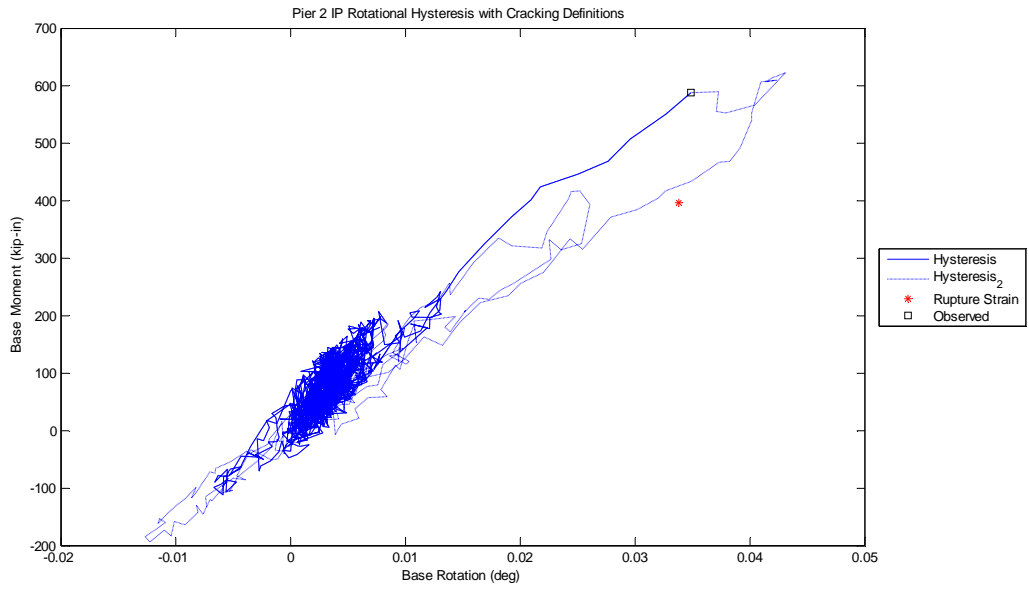


Figure G.22 Pier 2 IP Rotation Cracking Definition

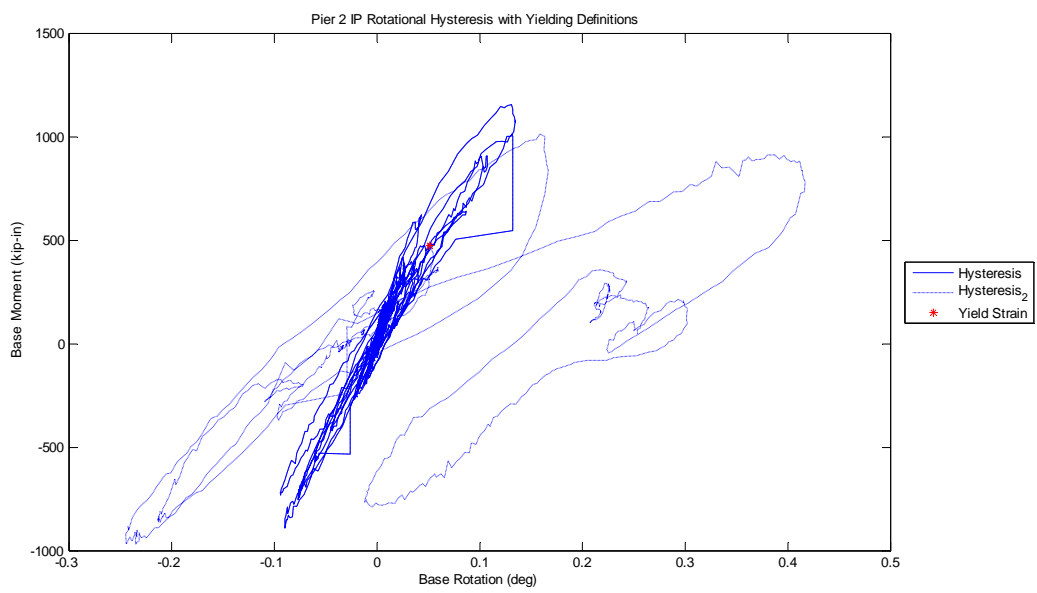


Figure G.23 Pier 2 IP Rotation Yield Definition

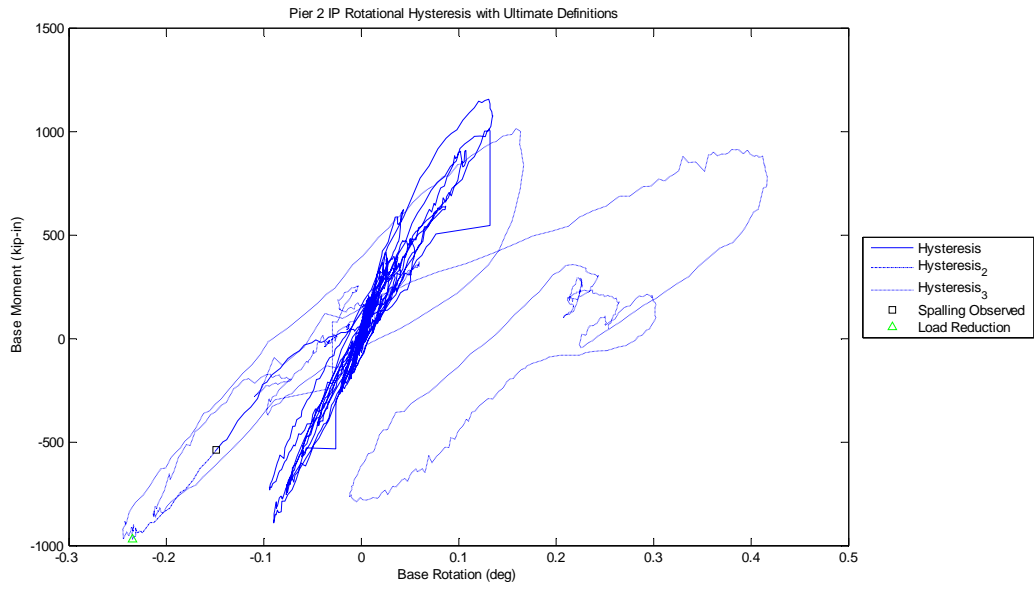


Figure G.24 Pier 2 IP Rotation Ultimate Definition

APPENDIX H. STATISTICAL ANALYSIS RESULTS

This chapter presents the full suite of fragility curves developed in this study. Fragility curves for each case of parameters are plotted, followed by variations on each parameter to illustrate its effective influence on the resulting vulnerability relationships.

The notation used in the legends of each of these plots is provided below.

Table H.1 Key for plot legend notation

Calibration	Geometry	Limit State	Applied Loading	Notation
Calibrated	Curved	Slight	TD	'CCSA'
Calibrated	Curved	Slight	BD	'CCSH'
Calibrated	Curved	Slight	UD-L	'CCSL'
Calibrated	Curved	Slight	UD-T	'CCST'
Calibrated	Curved	Moderate	TD	'CCMA'
Calibrated	Curved	Moderate	BD	'CCMH'
Calibrated	Curved	Moderate	UD-L	'CCML'
Calibrated	Curved	Moderate	UD-T	'CCMT'
Calibrated	Curved	Severe	TD	'CCVA'
Calibrated	Curved	Severe	BD	'CCVH'
Calibrated	Curved	Severe	UD-L	'CCVL'
Calibrated	Curved	Severe	UD-T	'CCVT'
Calibrated	Straight	Slight	TD	'CSSA'
Calibrated	Straight	Slight	BD	'CSSH'
Calibrated	Straight	Slight	UD-L	'CSSL'
Calibrated	Straight	Slight	UD-T	'CSST'
Calibrated	Straight	Moderate	TD	'CSMA'
Calibrated	Straight	Moderate	BD	'CSMH'
Calibrated	Straight	Moderate	UD-L	'CSML'
Calibrated	Straight	Moderate	UD-T	'CSMT'
Calibrated	Straight	Severe	TD	'CSVA'
Calibrated	Straight	Severe	BD	'CSVH'
Calibrated	Straight	Severe	UD-L	'CSVL'
Calibrated	Straight	Severe	UD-T	'CSVV'

Table H.1 (cont.)

Calibration	Geometry	Limit State	Applied Loading	Notation
Uncalibrated	Curved	Slight	TD	'UCSA'
Uncalibrated	Curved	Slight	BD	'UCSH'
Uncalibrated	Curved	Slight	UD-L	'UCSL'
Uncalibrated	Curved	Slight	UD-T	'UCST'
Uncalibrated	Curved	Moderate	TD	'UCMA'
Uncalibrated	Curved	Moderate	BD	'UCMH'
Uncalibrated	Curved	Moderate	UD-L	'UCML'
Uncalibrated	Curved	Moderate	UD-T	'UCMT'
Uncalibrated	Curved	Severe	TD	'UCVA'
Uncalibrated	Curved	Severe	BD	'UCVH'
Uncalibrated	Curved	Severe	UD-L	'UCVL'
Uncalibrated	Curved	Severe	UD-T	'UCVT'
Uncalibrated	Straight	Slight	TD	'USSA'
Uncalibrated	Straight	Slight	BD	'USSH'
Uncalibrated	Straight	Slight	UD-L	'USSL'
Uncalibrated	Straight	Slight	UD-T	'USST'
Uncalibrated	Straight	Moderate	TD	'USMA'
Uncalibrated	Straight	Moderate	BD	'USMH'
Uncalibrated	Straight	Moderate	UD-L	'USML'
Uncalibrated	Straight	Moderate	UD-T	'USMT'
Uncalibrated	Straight	Severe	TD	'USVA'
Uncalibrated	Straight	Severe	BD	'USVH'
Uncalibrated	Straight	Severe	UD-L	'USVL'
Uncalibrated	Straight	Severe	UD-T	'USVT'

H.1 Limit States for Each Case

The tables provided below present the median and coefficient of variation fragility parameters for each of the curves generated in this study.

The following plots display the three fragility relationships developed for each limit state within a given case. There are sixteen cases, comprising of each combination of curved and straight, calibrated and un-calibrated models subjected to one of four directions or combinations of applied seismic loading.

Table H.2 Fragility parameters for Calibrated Curved bridges

	Slight		Moderate		Severe	
	Median	CoV	Median	CoV	Median	CoV
Tri-directional including vertical	0.040	1.151	0.226	0.734	0.825	0.498
Bi-directional horizontal	0.037	1.199	0.230	0.743	0.825	0.498
Uni-directional longitudinal	0.065	0.722	0.221	0.600	0.715	0.355
Uni-directional transverse	0.092	1.064	0.425	0.332	1.040	0.254

Table H.3 Fragility parameters for Calibrated Straight bridges

	Slight		Moderate		Severe	
	Median	CoV	Median	CoV	Median	CoV
Tri-directional including vertical	0.055	1.000	0.284	0.632	0.814	0.499
Bi-directional horizontal	0.054	1.020	0.284	0.632	0.814	0.499
Uni-directional longitudinal	0.070	0.574	0.252	0.520	0.797	0.252
Uni-directional transverse	0.187	0.714	0.491	0.189	1.029	0.273

Table H.4 Fragility parameters for Uncalibrated Curved bridges

	Slight		Moderate		Severe	
	Median	CoV	Median	CoV	Median	CoV
Tri-directional including vertical	0.000	0.500	0.155	1.258	0.345	0.574
Bi-directional horizontal	0.015	1.205	0.132	0.947	0.345	0.574
Uni-directional longitudinal	0.046	0.705	0.151	0.704	0.400	0.388
Uni-directional transverse	0.023	1.385	0.302	0.553	0.438	0.406

Table H.5 Fragility parameters for Uncalibrated Straight bridges

	Slight		Moderate		Severe	
	Median	CoV	Median	CoV	Median	CoV
Tri-directional including vertical	0.029	1.019	0.169	0.783	0.359	0.460
Bi-directional horizontal	0.027	1.118	0.172	0.800	0.358	0.465
Uni-directional longitudinal	0.050	0.641	0.177	0.751	0.425	0.385
Uni-directional transverse	0.065	1.091	0.360	0.523	0.464	0.429

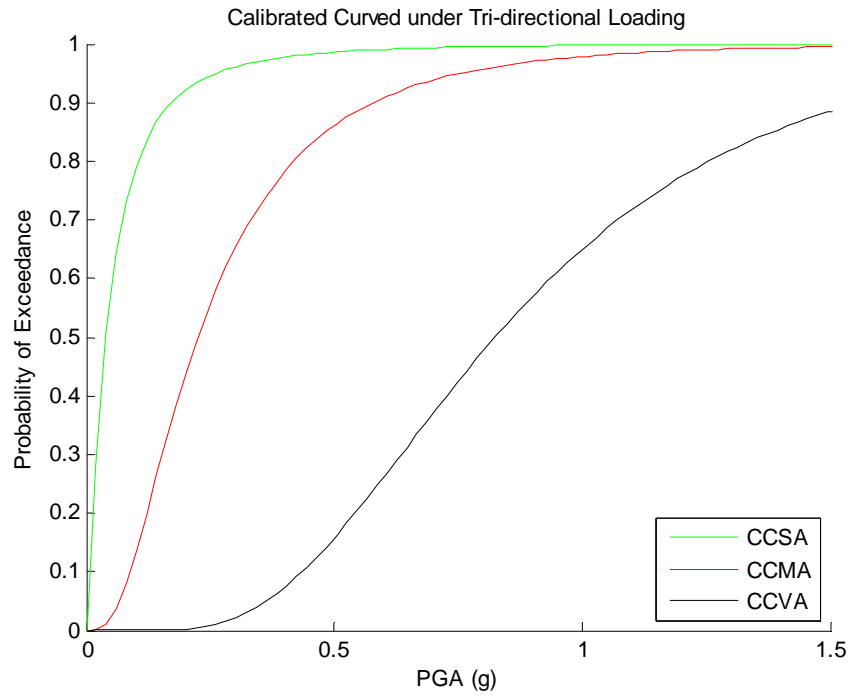


Figure H.1 Calibrated Curved bridge subjected to Tri-Directional loading

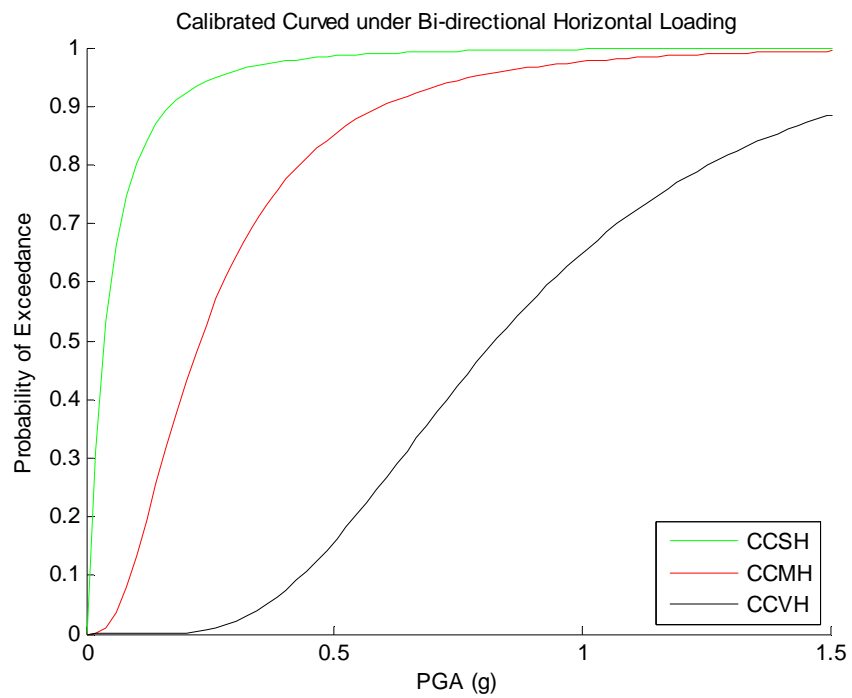


Figure H.2 Calibrated Curved bridge subjected to Bi-Directional horizontal loading

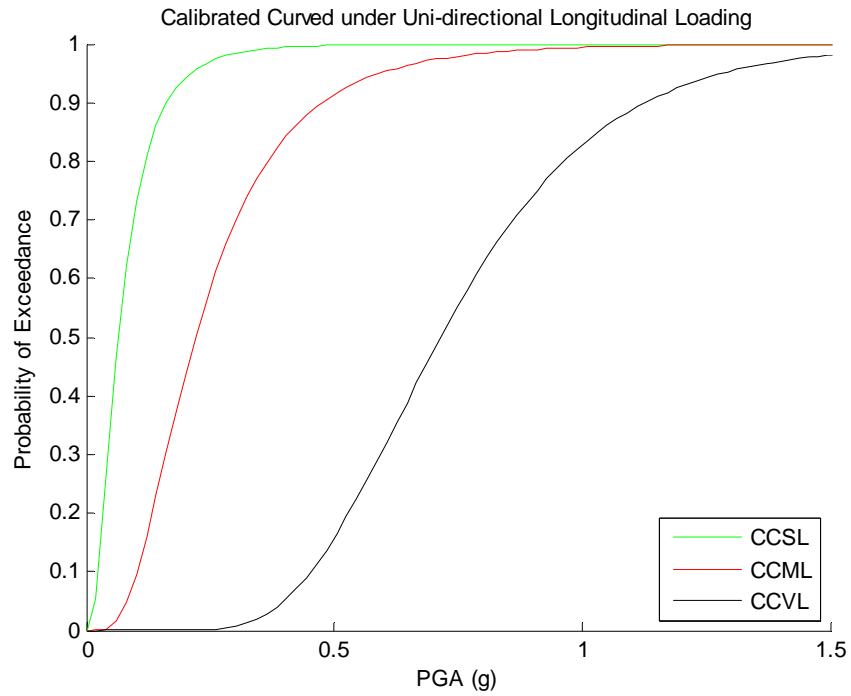


Figure H.3 Calibrated Curved bridge subjected to Uni-Directional Longitudinal loading

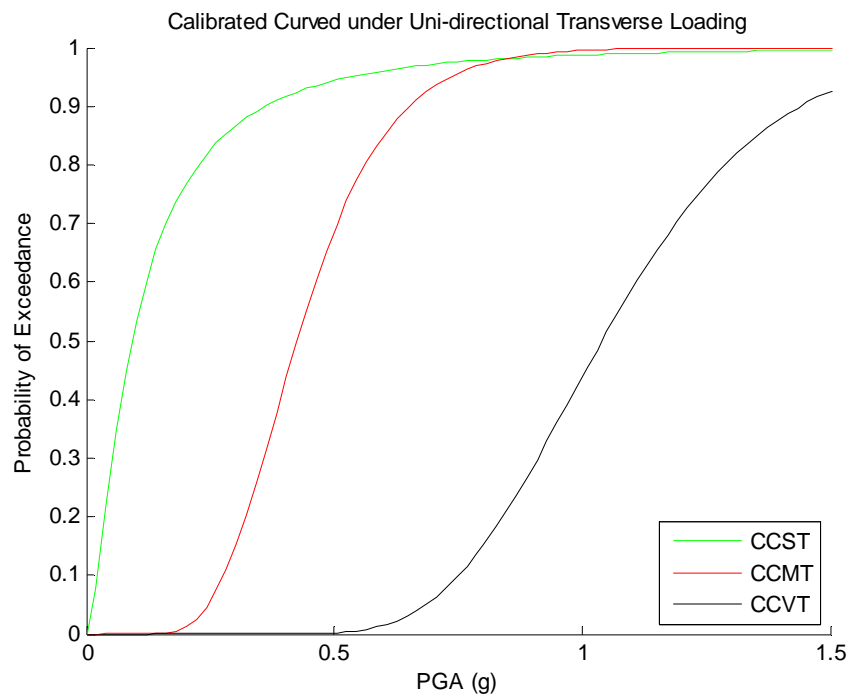


Figure H.4 Calibrated Curved bridge subjected to Uni-Directional Transverse loading

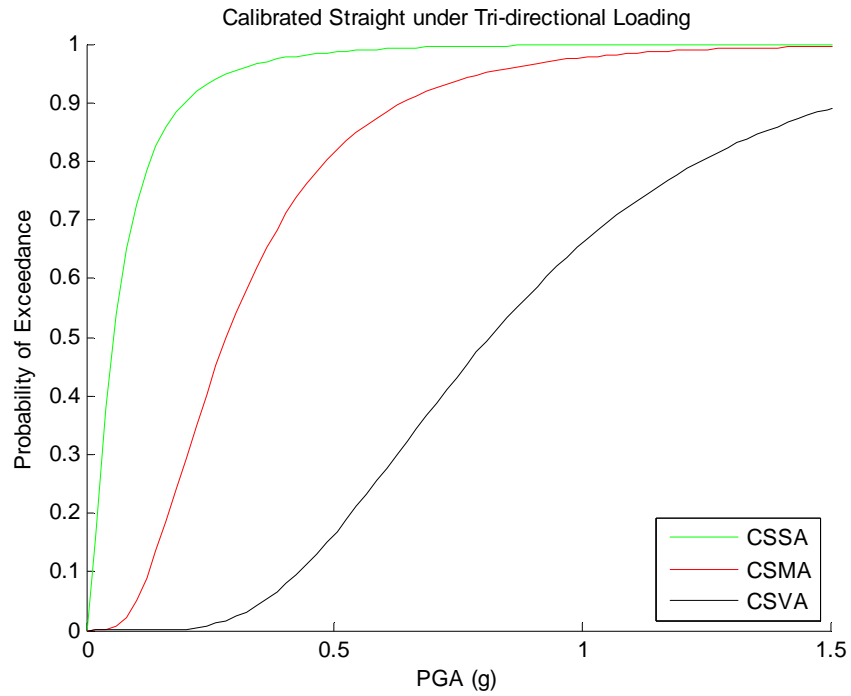


Figure H.5 Calibrated Straight bridge subjected to Tri-Directional loading

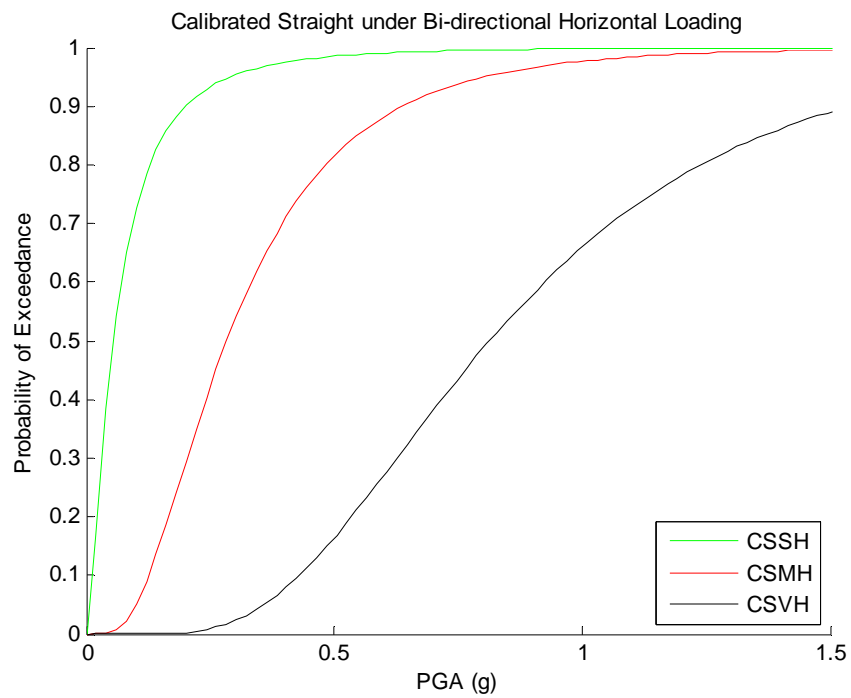


Figure H.6 Calibrated Straight bridge subjected to Bi-Directional horizontal loading

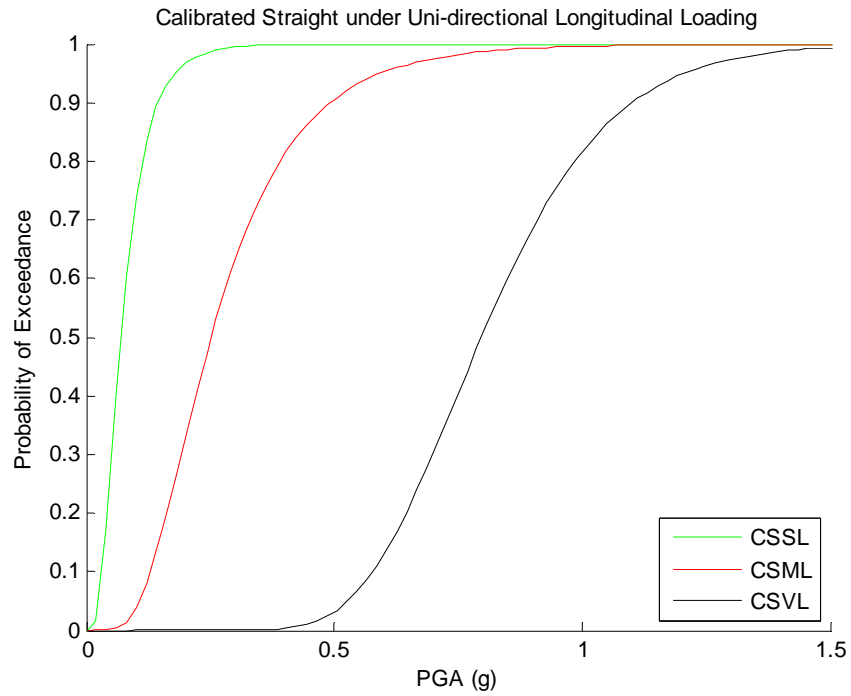


Figure H.7 Calibrated Straight bridge subjected to Uni-Directional Longitudinal loading

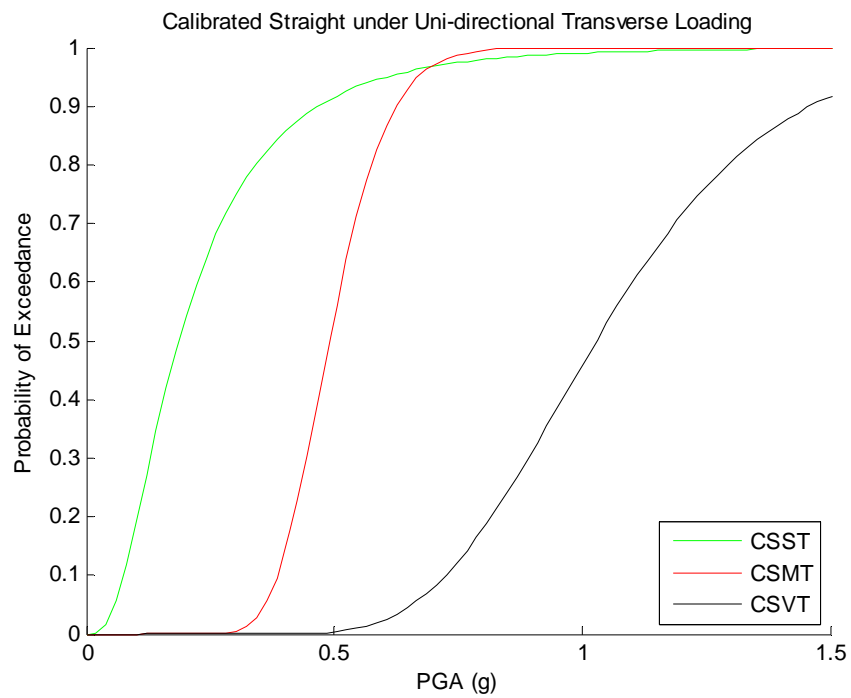


Figure H.8 Calibrated Straight bridge subjected to Uni-Directional Transverse loading

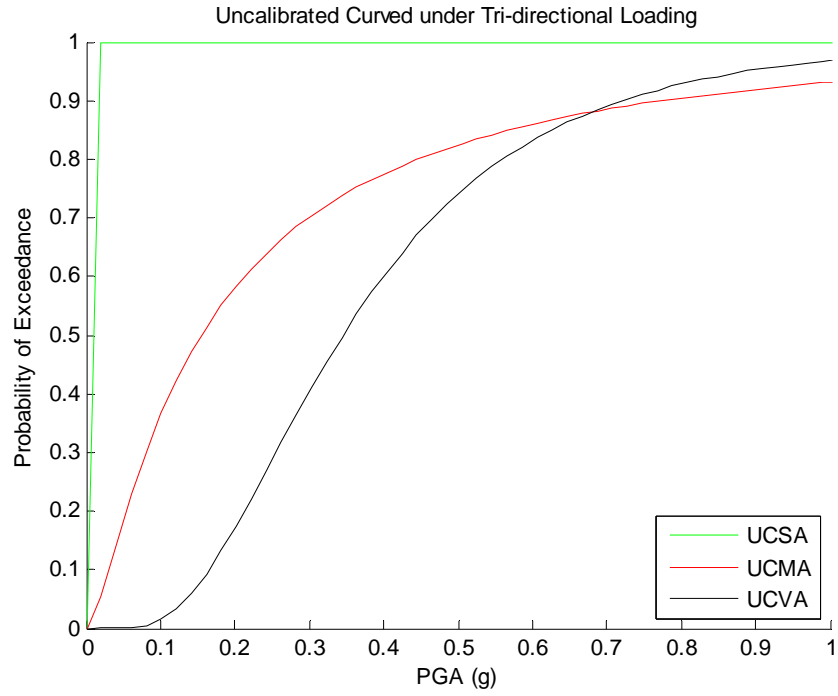


Figure H.9 Uncalibrated Curved bridge subjected to Tri-Directional loading

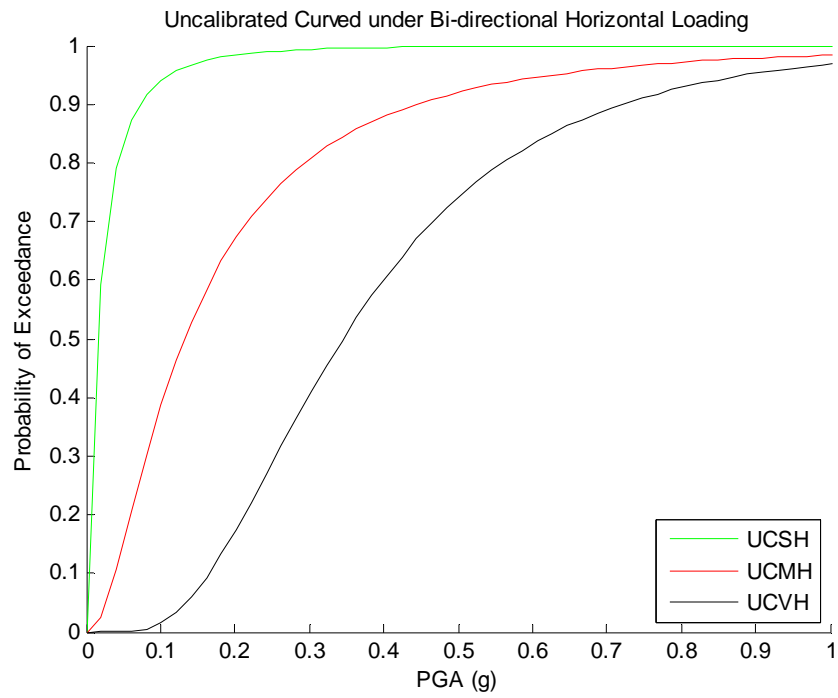


Figure H.10 Uncalibrated Curved bridge subjected to Bi-Directional horizontal loading

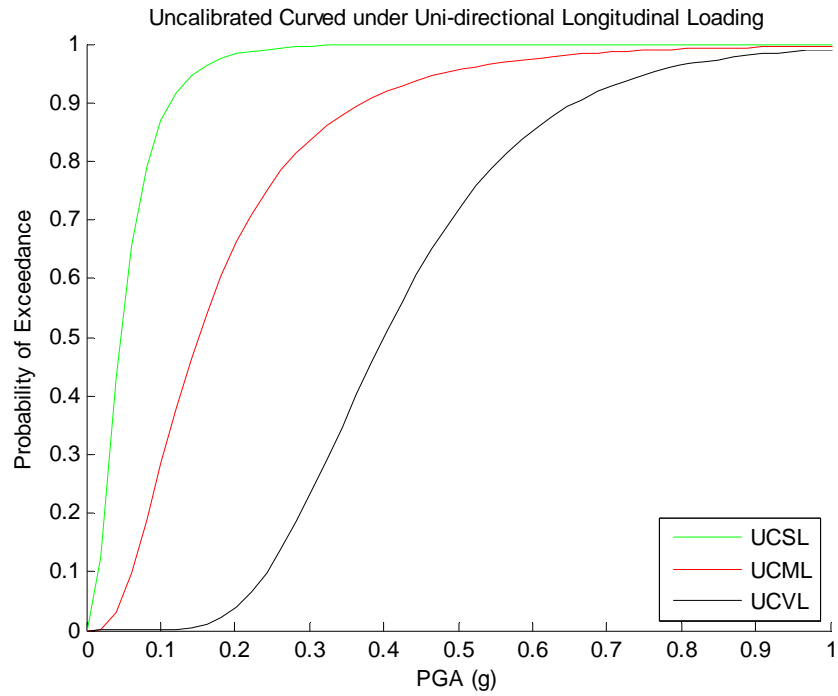


Figure H.11 Uncalibrated Curved bridge subjected to Uni-Directional Longitudinal loading

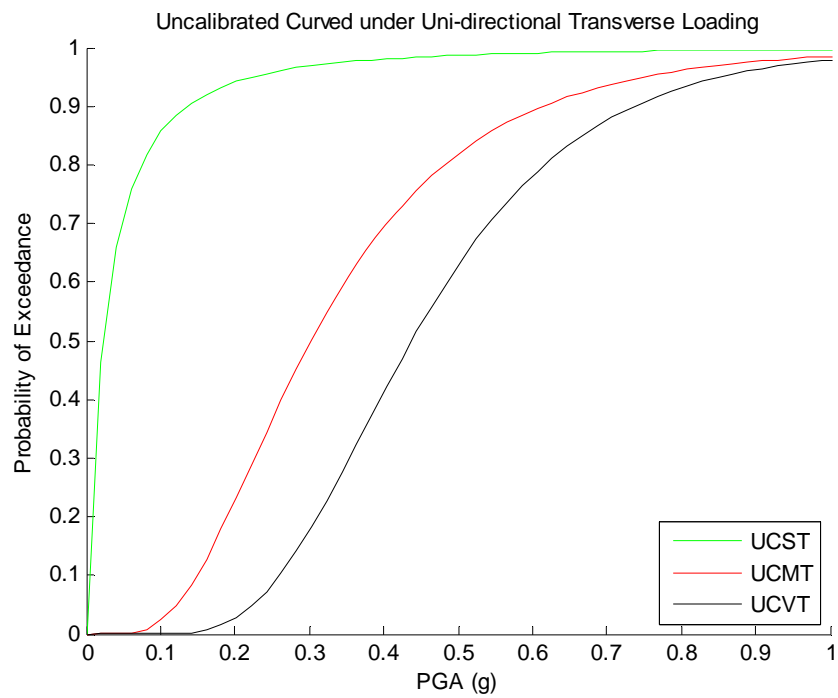


Figure H.12 Uncalibrated Curved bridge subjected to Uni-Directional Transverse loading

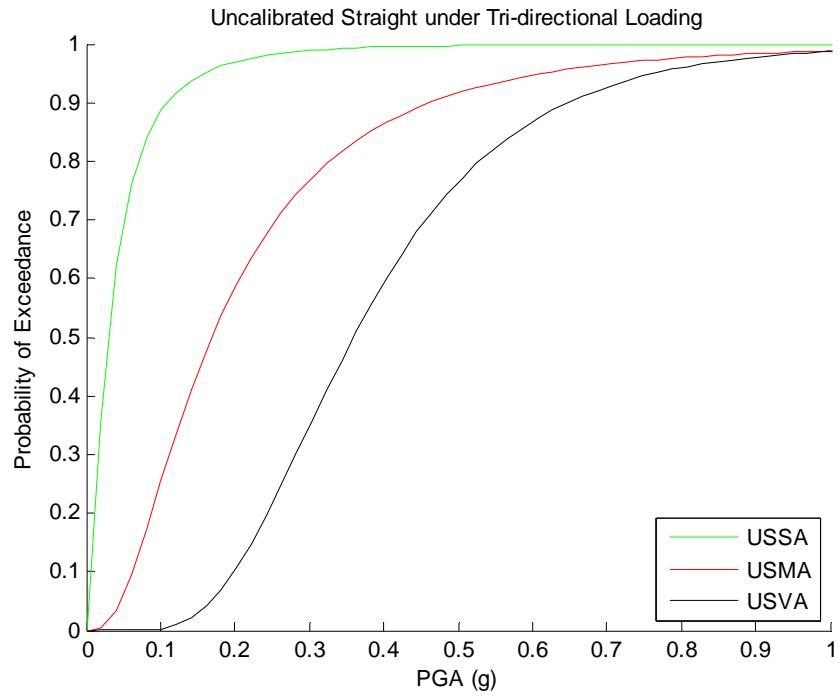


Figure H.13 Uncalibrated Straight bridge subjected to Tri-Directional loading

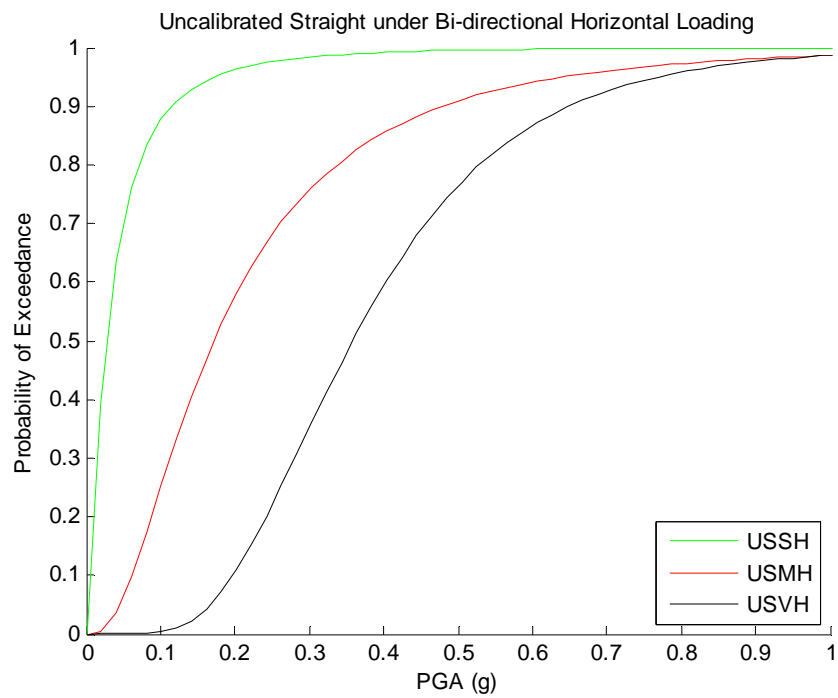


Figure H.14 Uncalibrated Straight bridge subjected to Bi-Directional horizontal loading

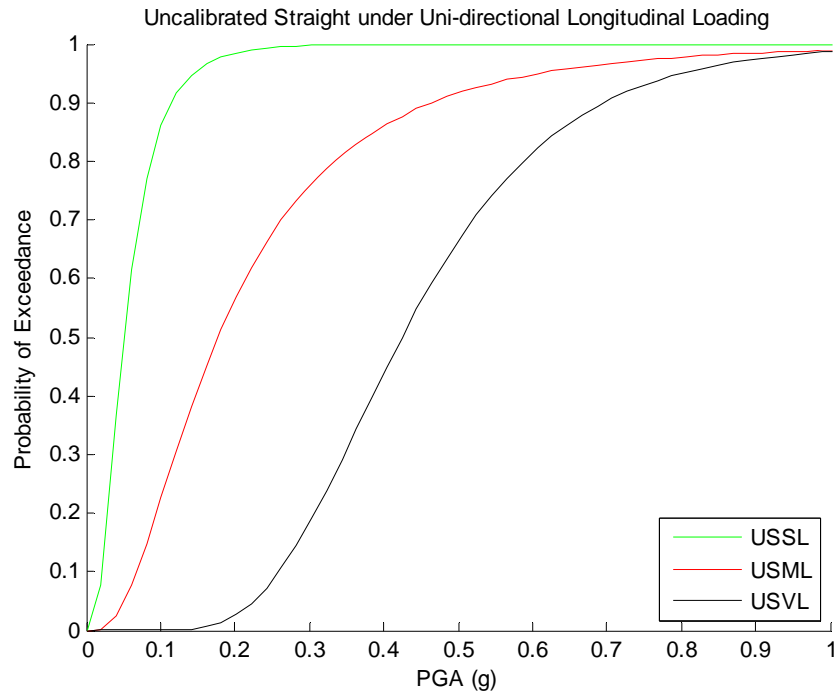


Figure H.15 Uncalibrated Straight bridge subjected to Uni-Directional Longitudinal loading

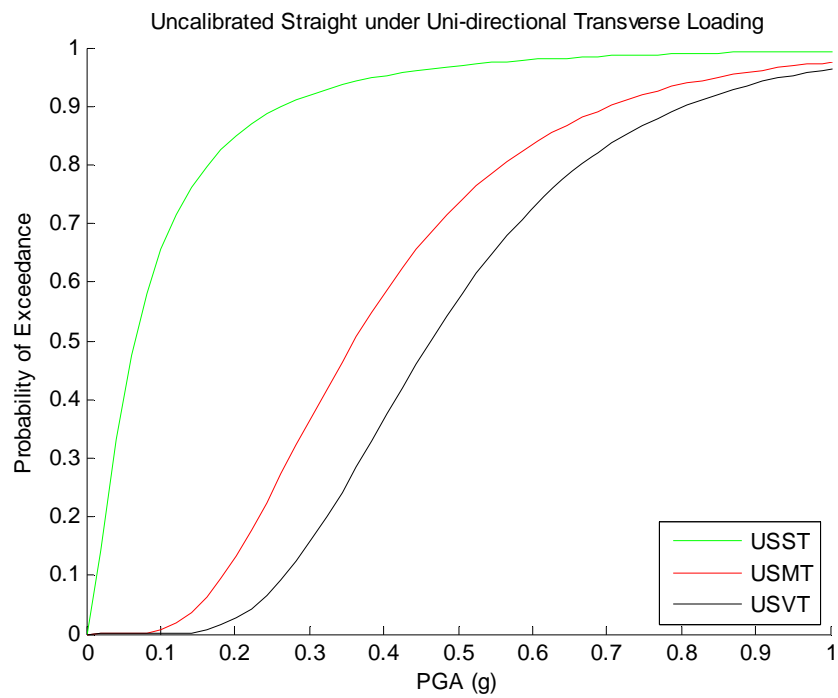


Figure H.16 Uncalibrated Straight bridge subjected to Uni-Directional Transverse loading

H.2 Influence of Geometry

The following eight plots display the influence of changing only the geometry parameter, from straight to curved, with identical loading and calibration parameters within each plot. All three limit states are presented in each case.

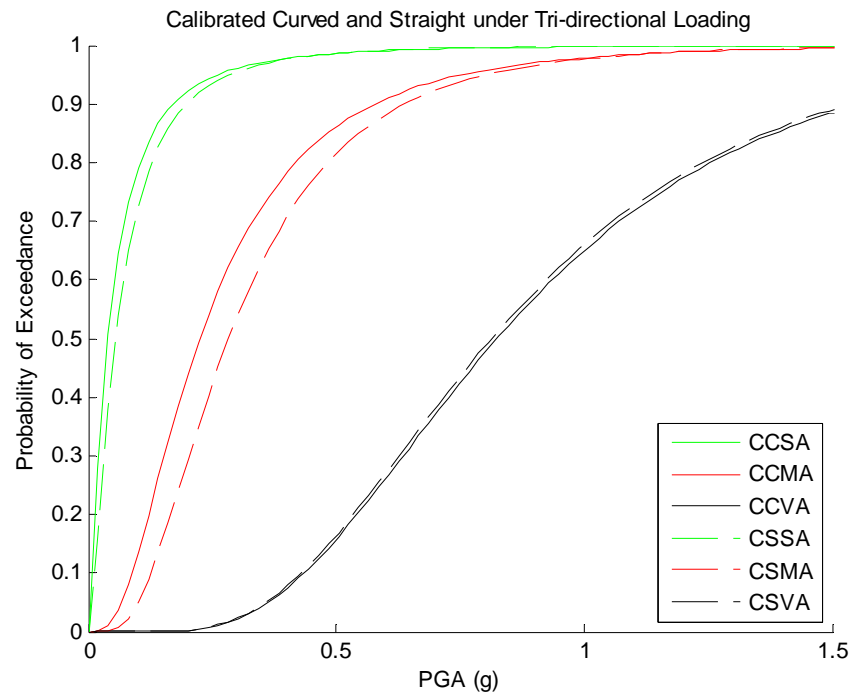


Figure H.17 Calibrated Curved and Straight bridges subjected to Tri-Directional loading

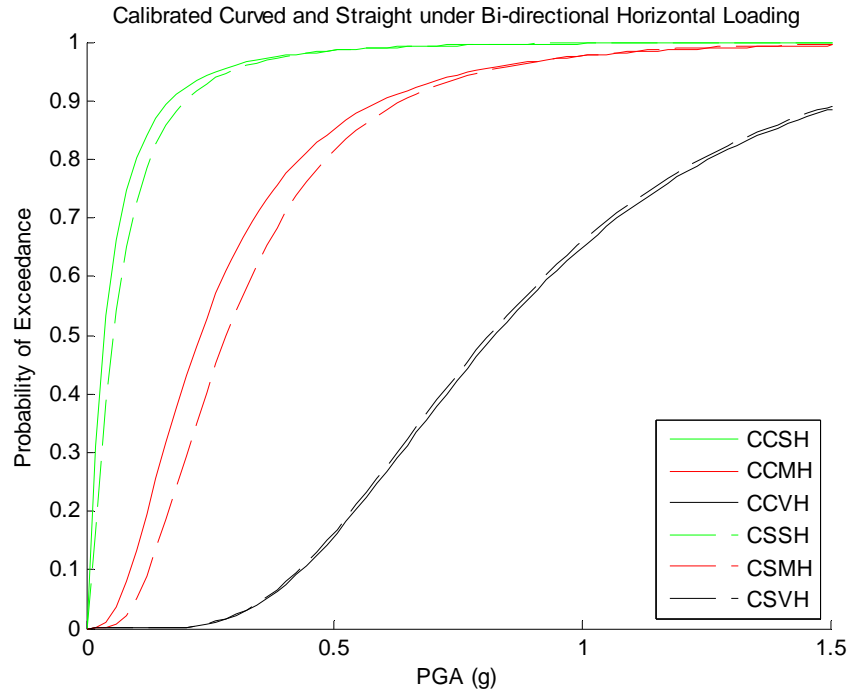


Figure H.18 Calibrated Curved and Straight bridges subjected to Bi-Directional loading

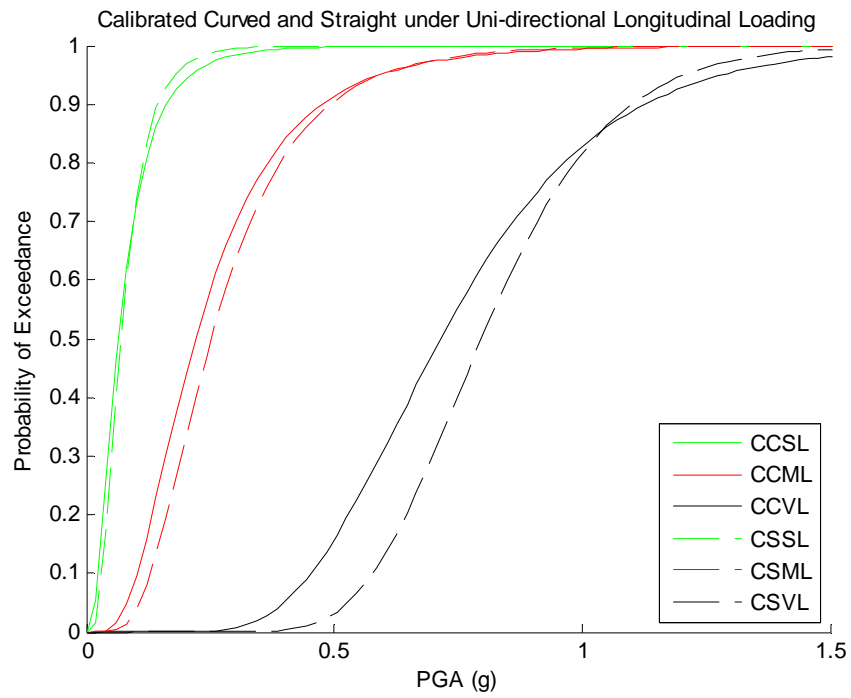


Figure H.19 Calibrated Curved and Straight bridges subjected to Uni-Directional Longitudinal loading

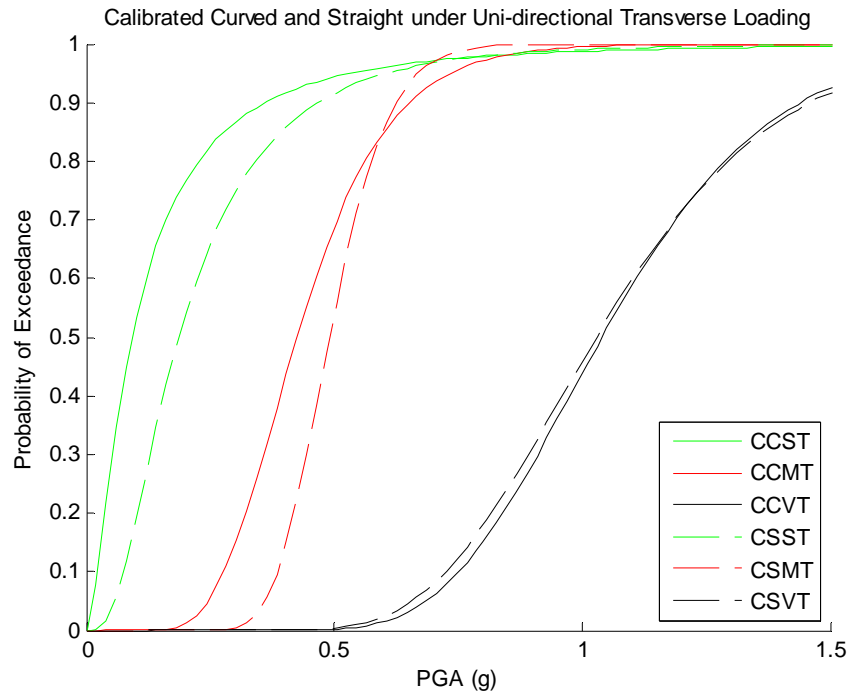


Figure H.20 Calibrated Curved and Straight bridges subjected to Uni-Directional Transverse loading

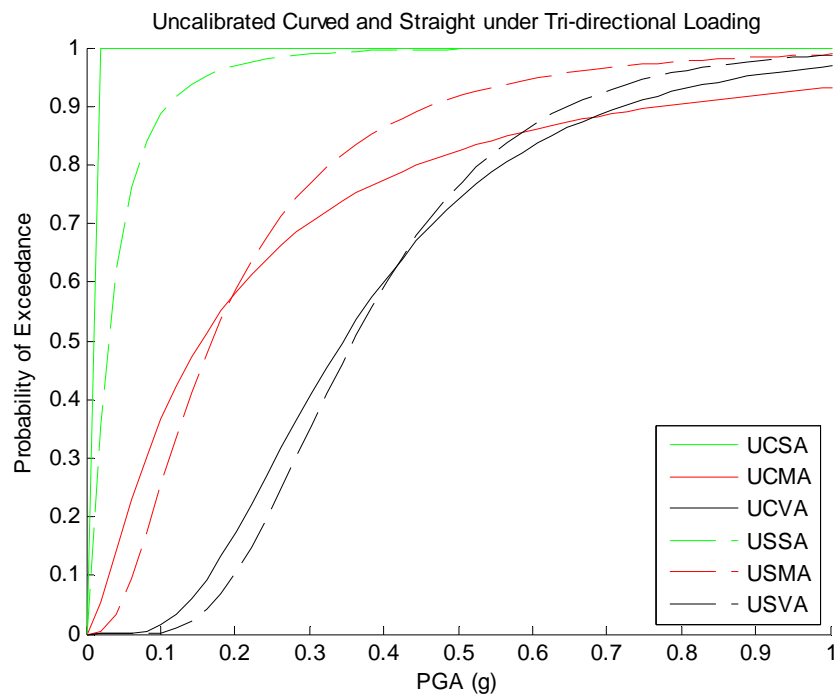


Figure H.21 Uncalibrated Curved and Straight bridges subjected to Tri-Directional loading

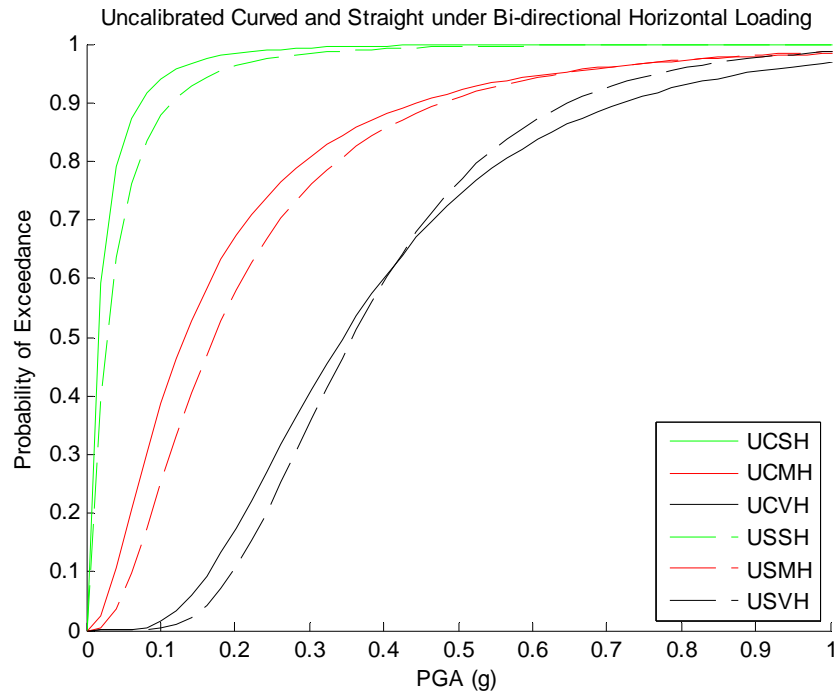


Figure H.22 Uncalibrated Curved and Straight bridges subjected to Bi-Directional loading

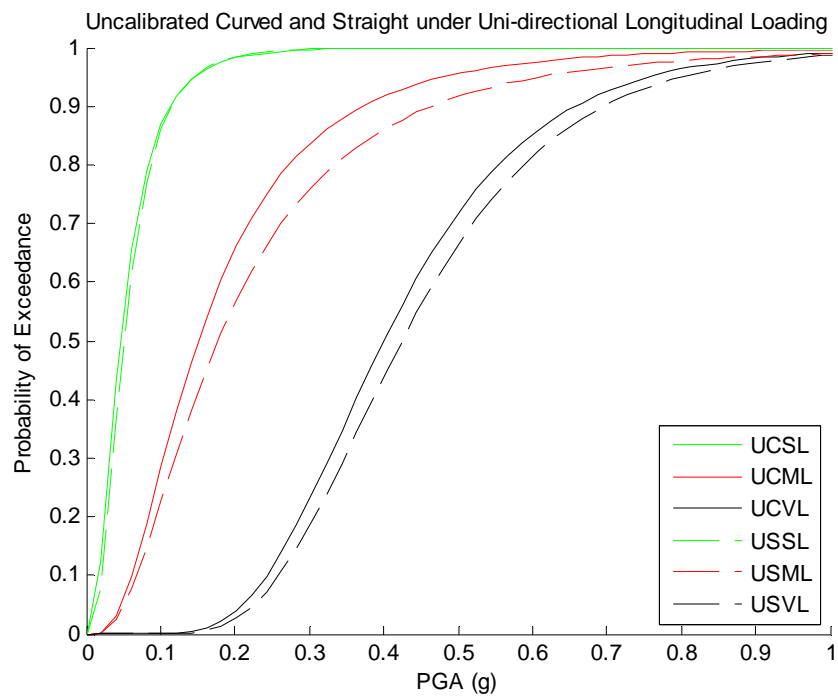


Figure H.23 Uncalibrated Curved and Straight bridges subjected to Uni-Directional Longitudinal loading

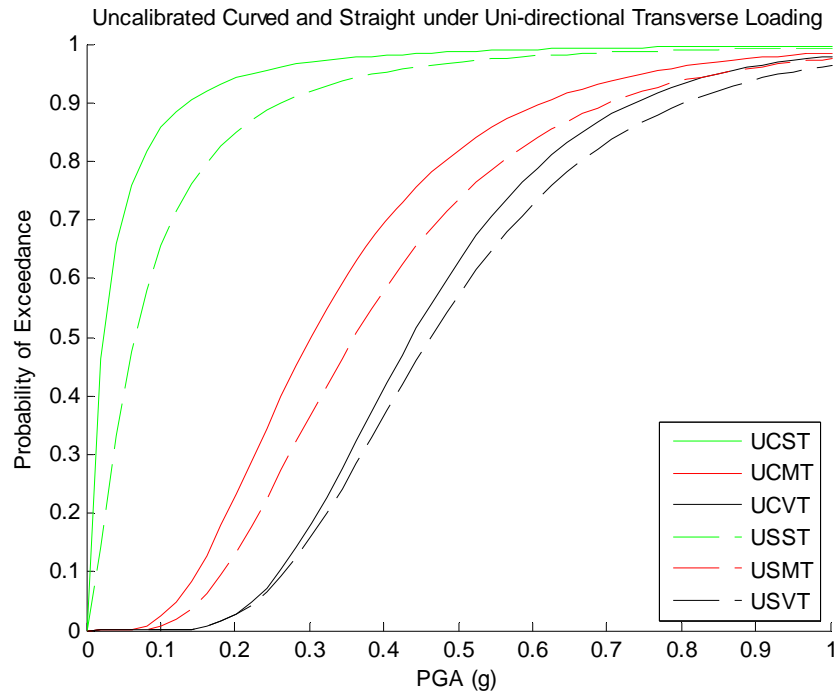


Figure H.24 Uncalibrated Curved and Straight bridges subjected to Uni-Directional Transverse loading

H.3 Influence of Load Application

The following twelve plots display the influence of changing the orientation and combination of applied seismic loading. Uni-directional transverse, uni-directional longitudinal, bi-directional horizontal, and tri-directional loading including vertical accelerations are examined in each plot. Each figure represents the same bridge geometry and calibration parameter, and is displayed for only one of the three limit states.

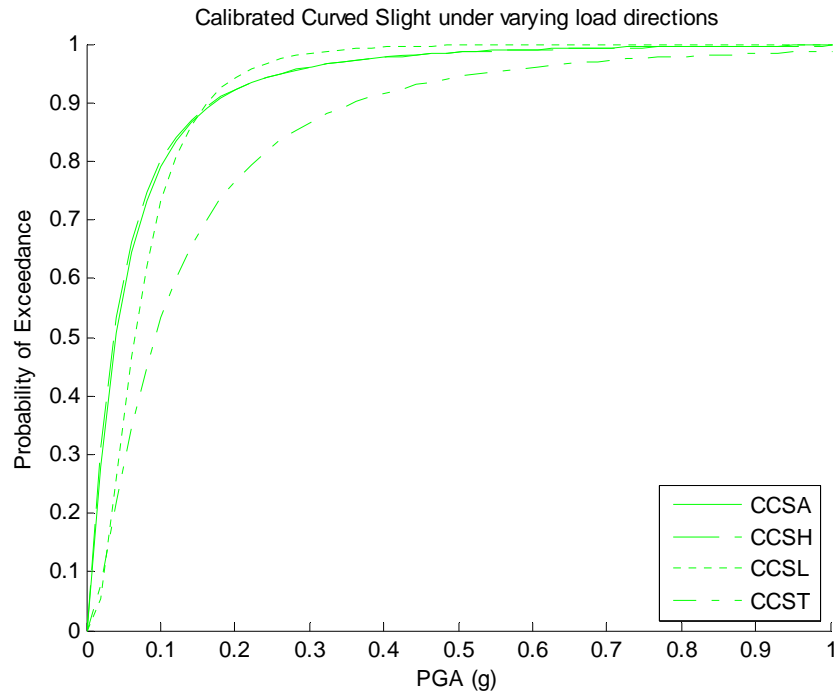


Figure H.25 Calibrated Curved Bridge - Slight limit for varied loading

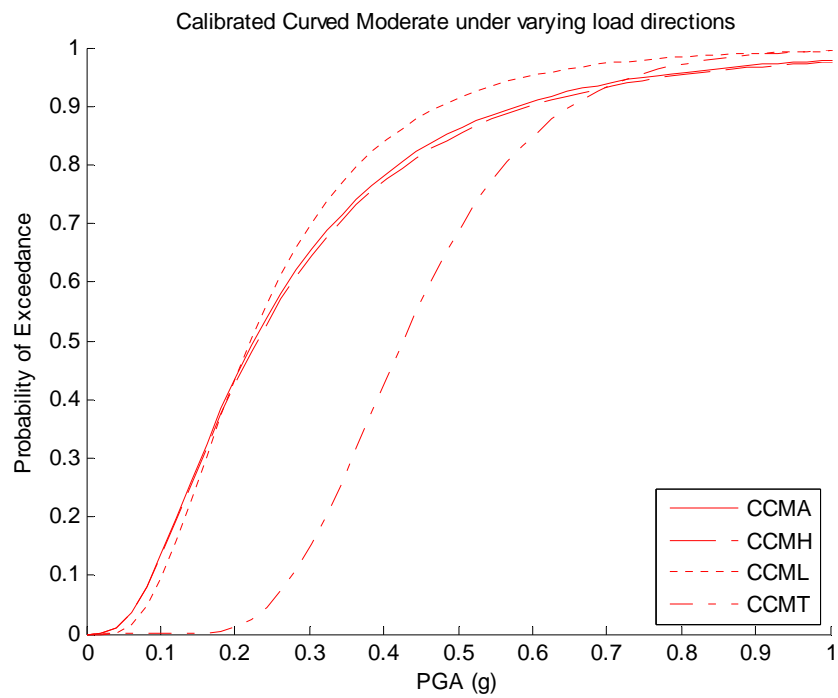


Figure H.26 Calibrated Curved Bridge - Moderate limit for varied loading

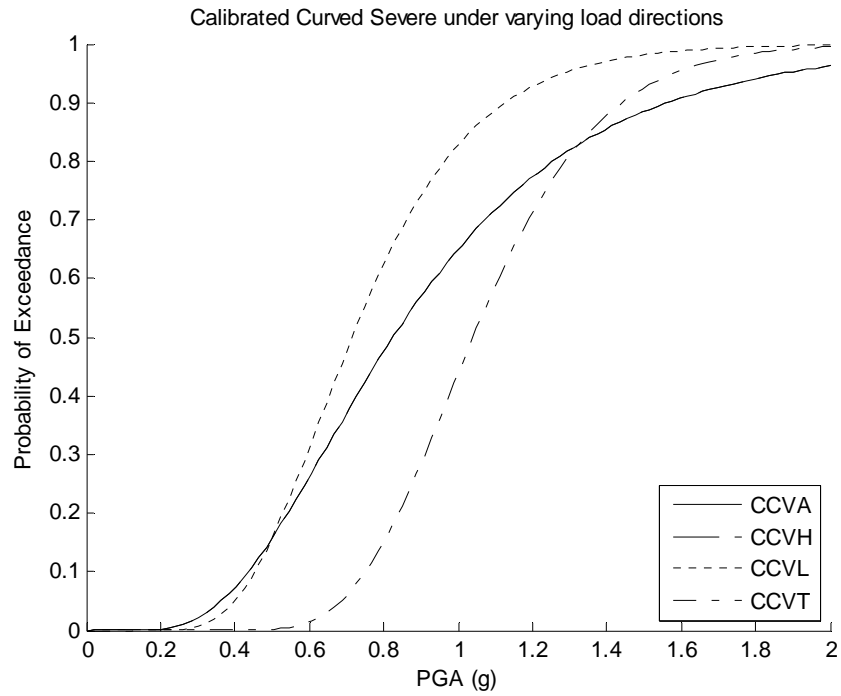


Figure H.27 Calibrated Curved Bridge - Severe limit for varied loading

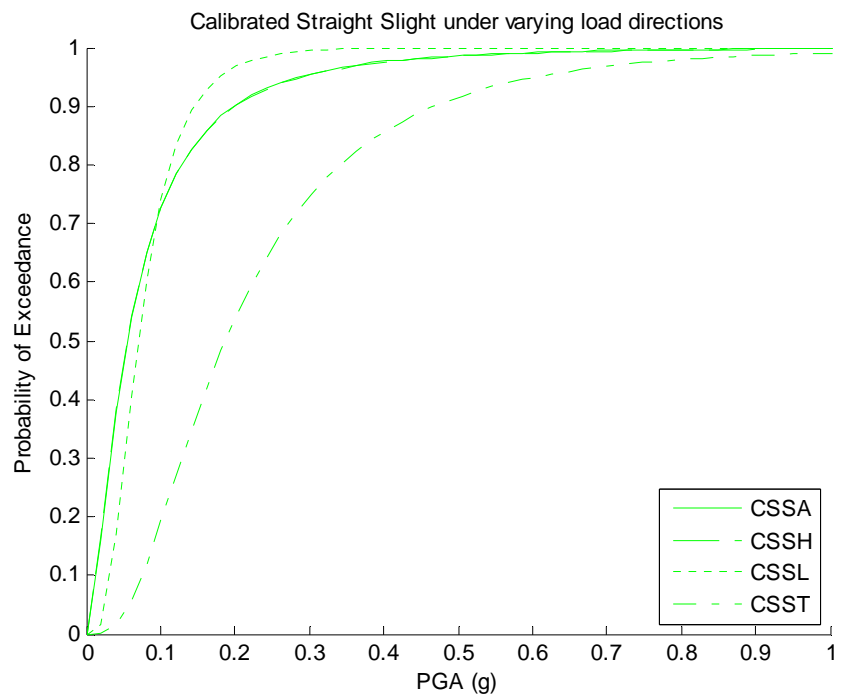


Figure H.28 Calibrated Straight Bridge - Slight limit for varied loading

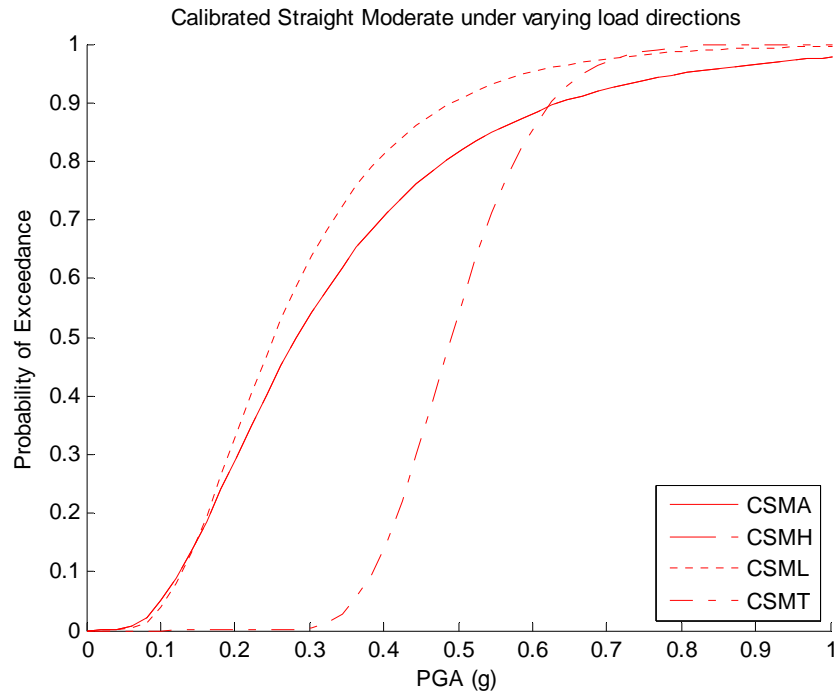


Figure H.29 Calibrated Straight Bridge - Moderate limit for varied loading

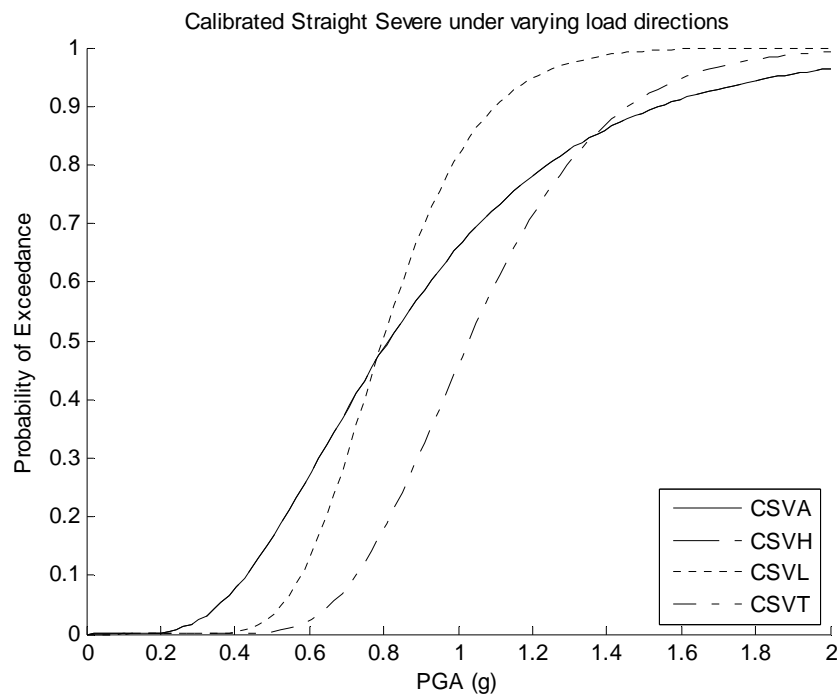


Figure H.30 Calibrated Straight Bridge - Severe limit for varied loading

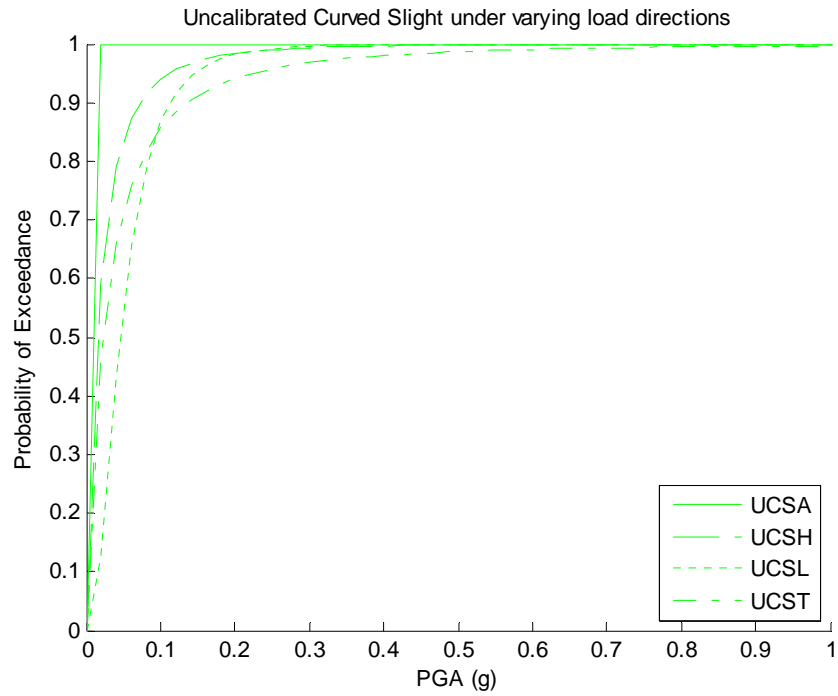


Figure H.31 Uncalibrated Curved Bridge - Slight limit for varied loading

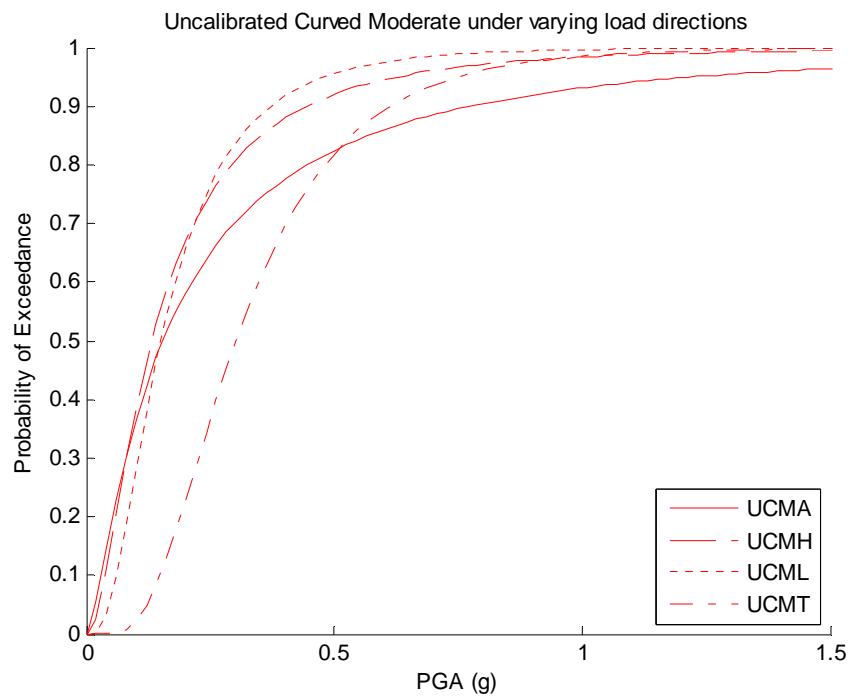


Figure H.32 Uncalibrated Curved Bridge - Moderate limit for varied loading

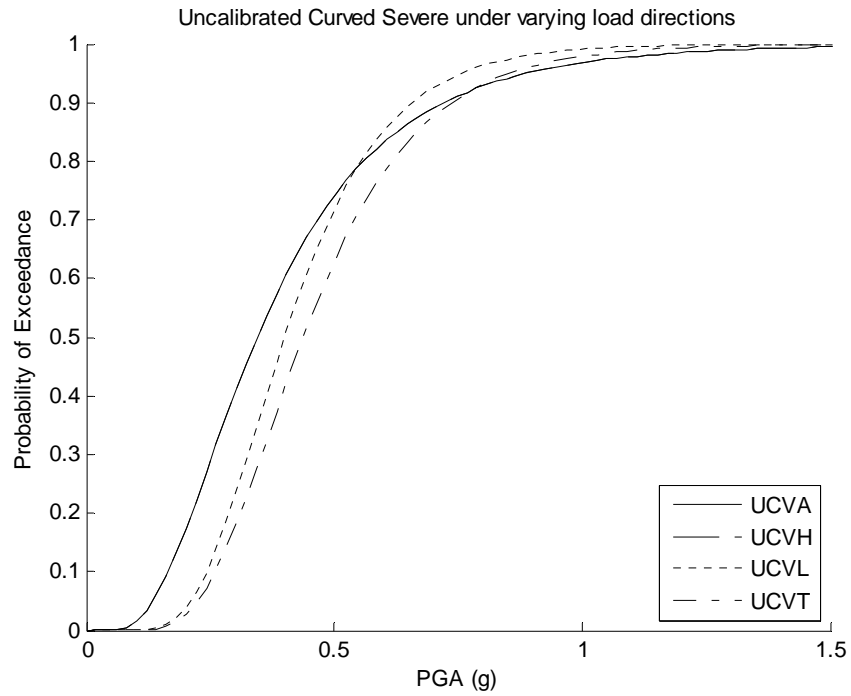


Figure H.33 Uncalibrated Curved Bridge - Severe limit for varied loading

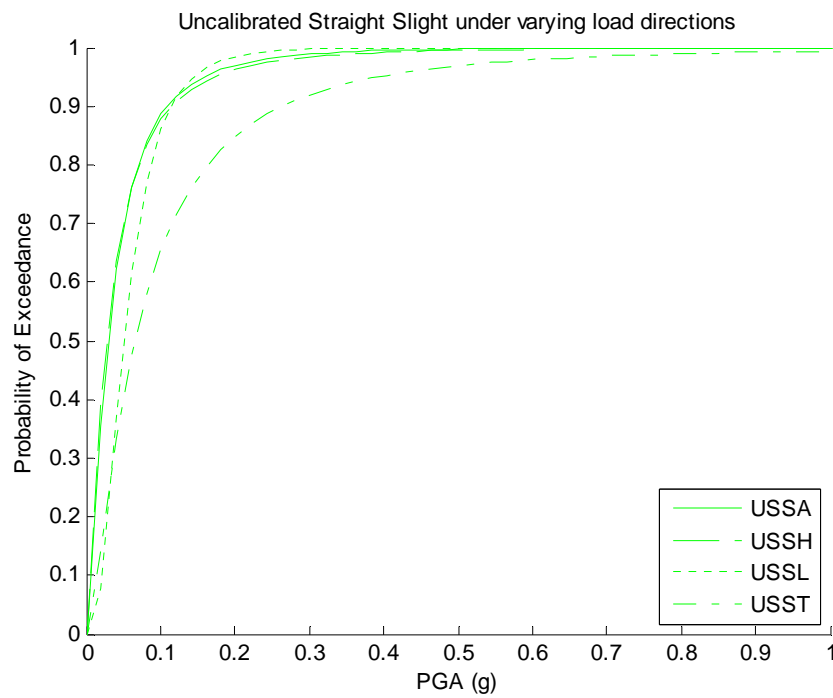


Figure H.34 Uncalibrated Straight Bridge - Slight limit for varied loading

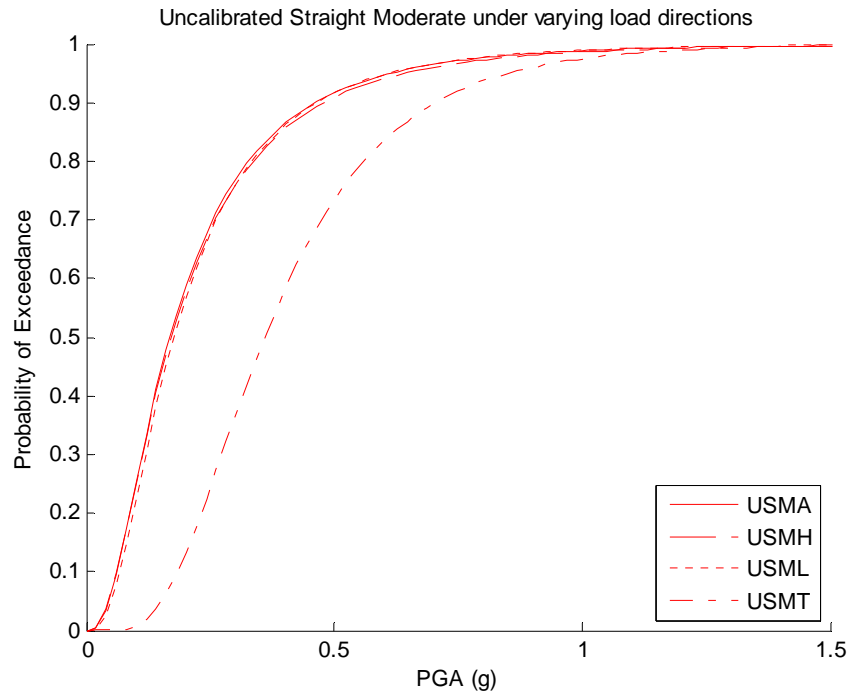


Figure H.35 Uncalibrated Straight Bridge - Moderate limit for varied loading

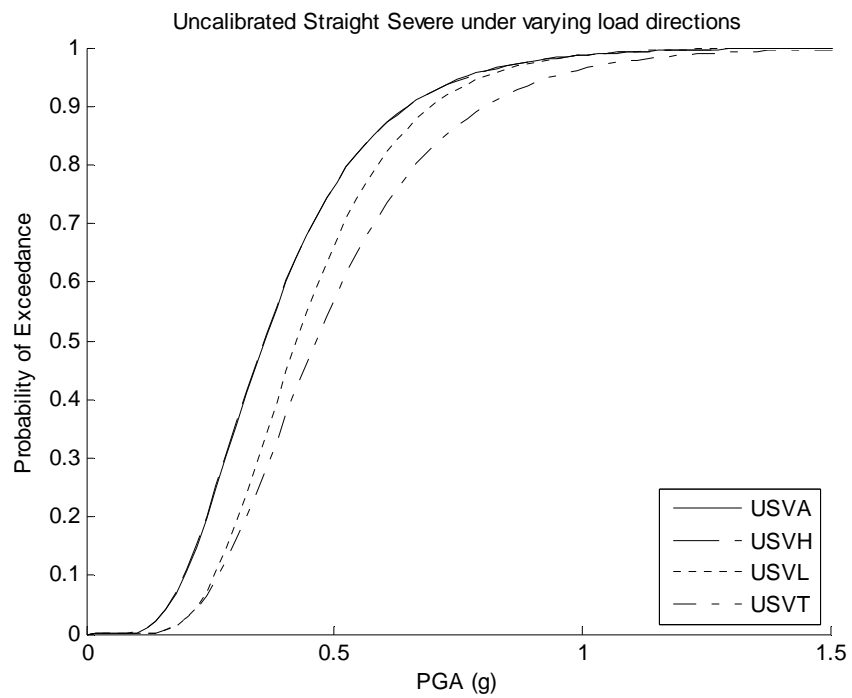


Figure H.36 Uncalibrated Straight Bridge - Severe limit for varied loading

H.4 Influence of Model Calibration

The following eight plots display the influence of varying the model calibration parameter between un-calibrated and calibrated. Each figure represents the same geometry and loading parameters. All three limit states are presented for each case.

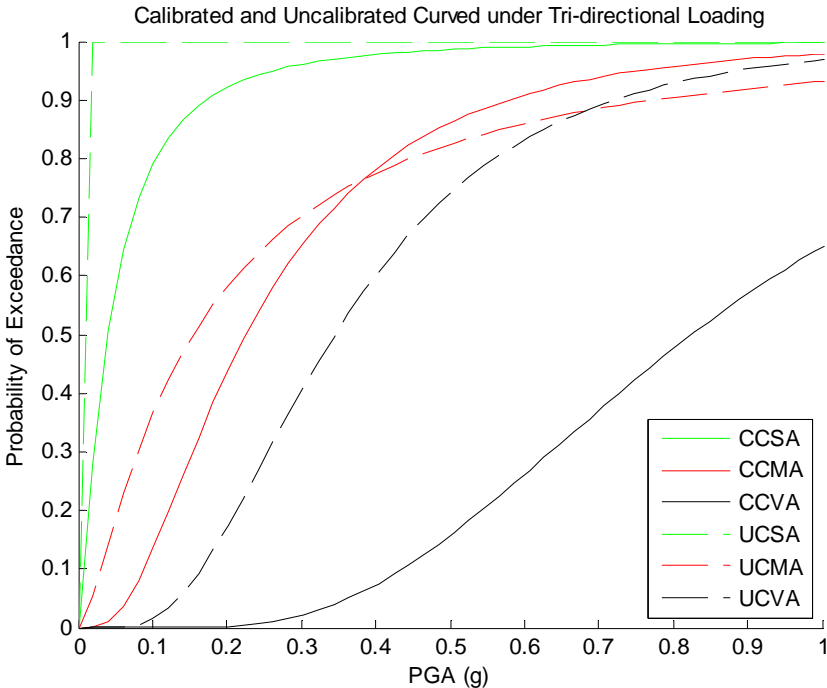


Figure H.37 Calibrated and Uncalibrated Curved bridge subjected to Tri-Directional loading

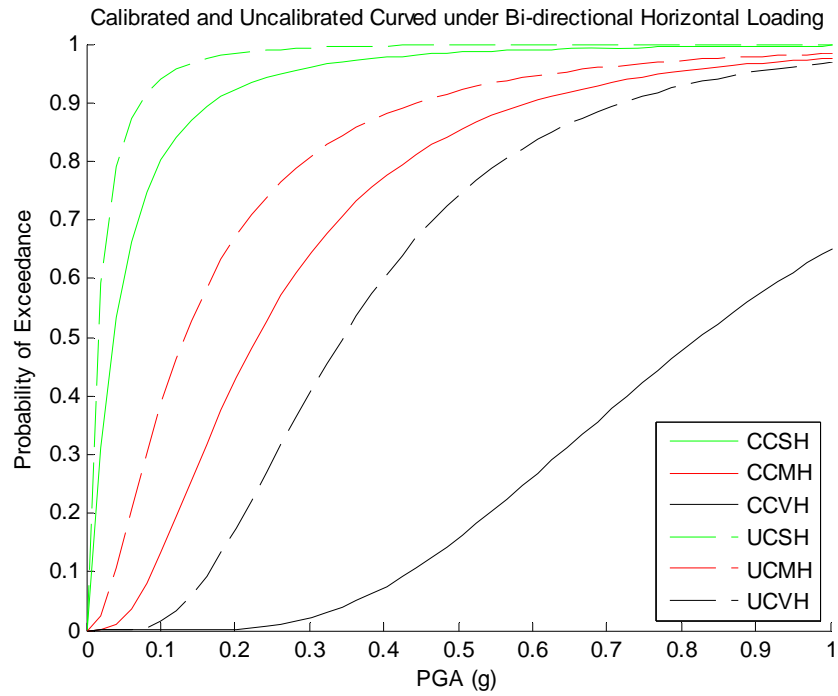


Figure H.38 Calibrated and Uncalibrated Curved bridge subjected to Bi-Directional loading

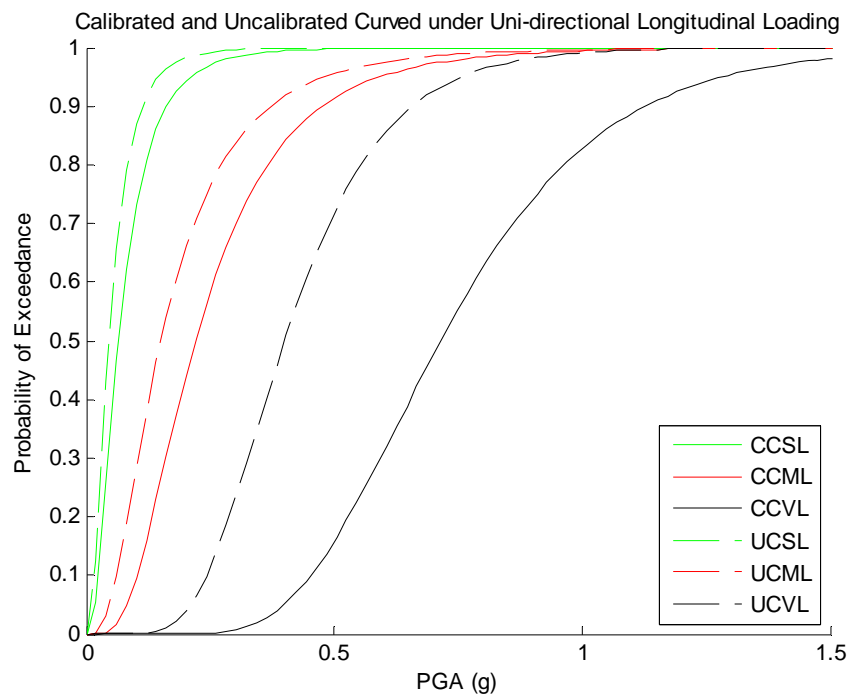


Figure H.39 Calibrated and Uncalibrated Curved bridge subjected to Uni-Directional Longitudinal loading

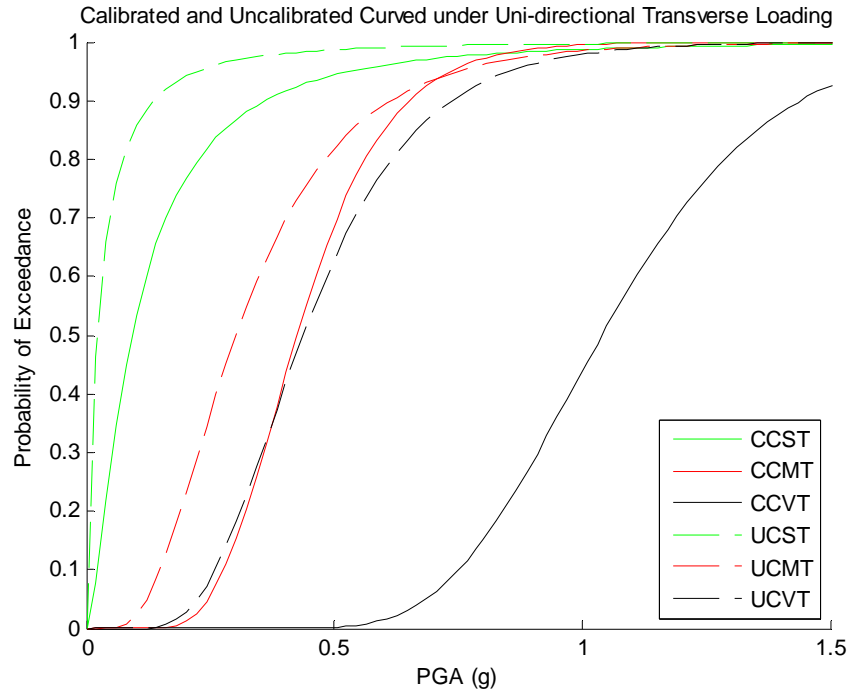


Figure H.40 Calibrated and Uncalibrated Curved bridge subjected to Uni-Directional Transverse loading

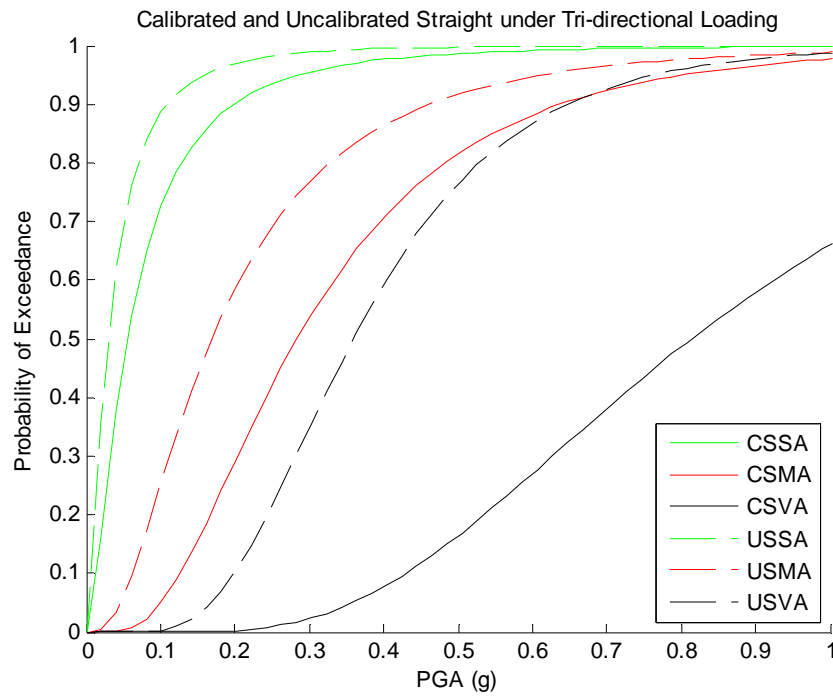


Figure H.41 Calibrated and Uncalibrated Straight bridge subjected to Tri-Directional loading

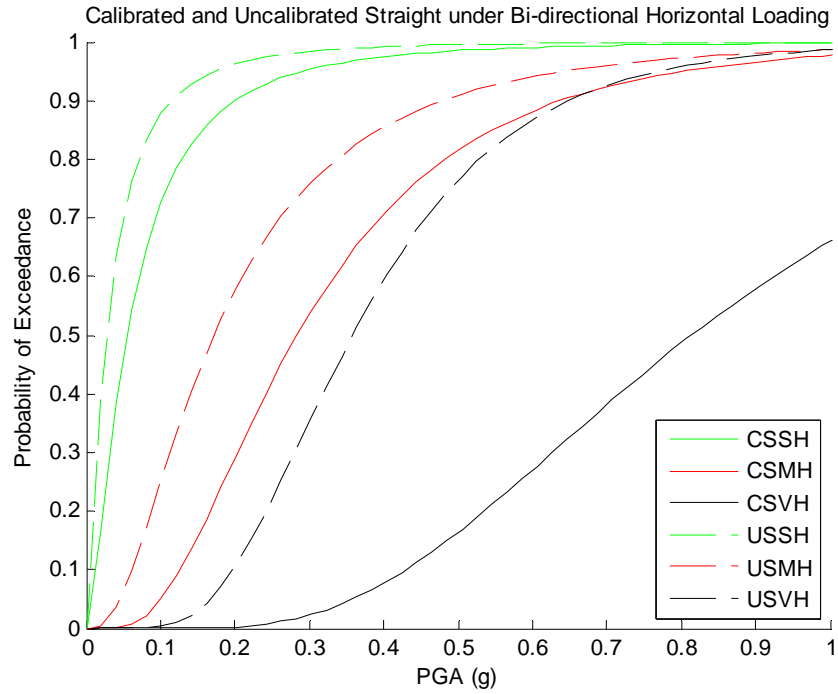


Figure H.42 Calibrated and Uncalibrated Straight bridge subjected to Bi-Directional loading

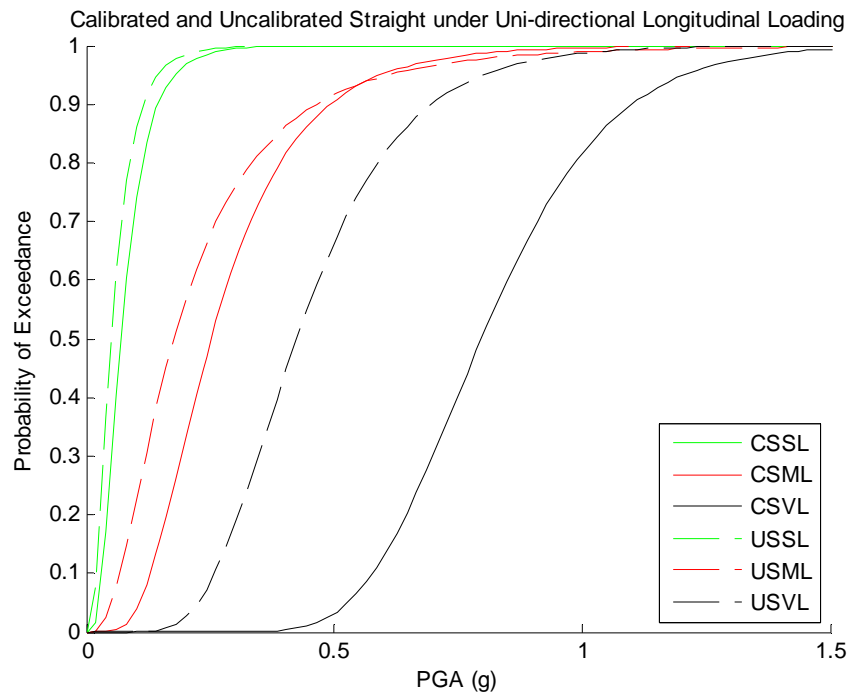


Figure H.43 Calibrated and Uncalibrated Straight bridge subjected to Uni-Directional Longitudinal loading

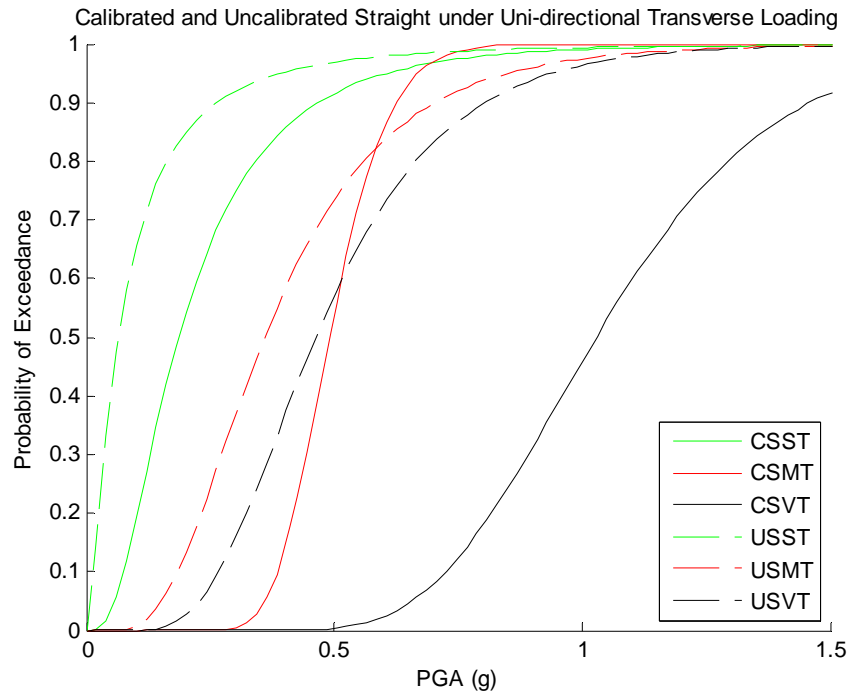


Figure H.44 Calibrated and Uncalibrated Straight bridge subjected to Uni-Directional Transverse loading

H.5 Modification Factors

Presented below are plots of the distribution of absolute and relative changes in fragility curve parameters due to change in geometry, model calibration, and load combination. Average influence for each method of defining the change in the parameter is provided as well.

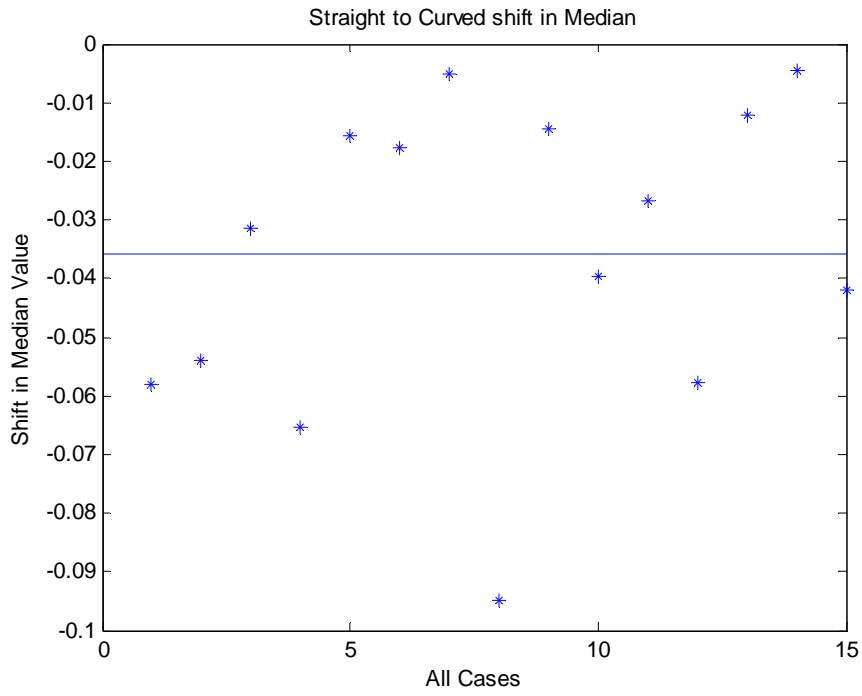


Figure H.45 Shift in median value resulting from bridge curvature

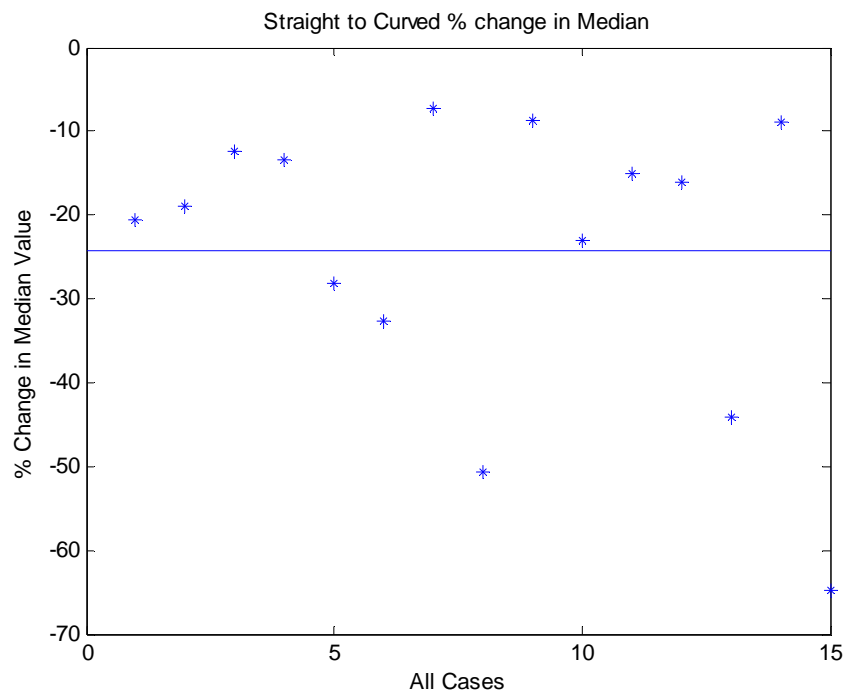


Figure H.46 Percent change in median value resulting from bridge curvature

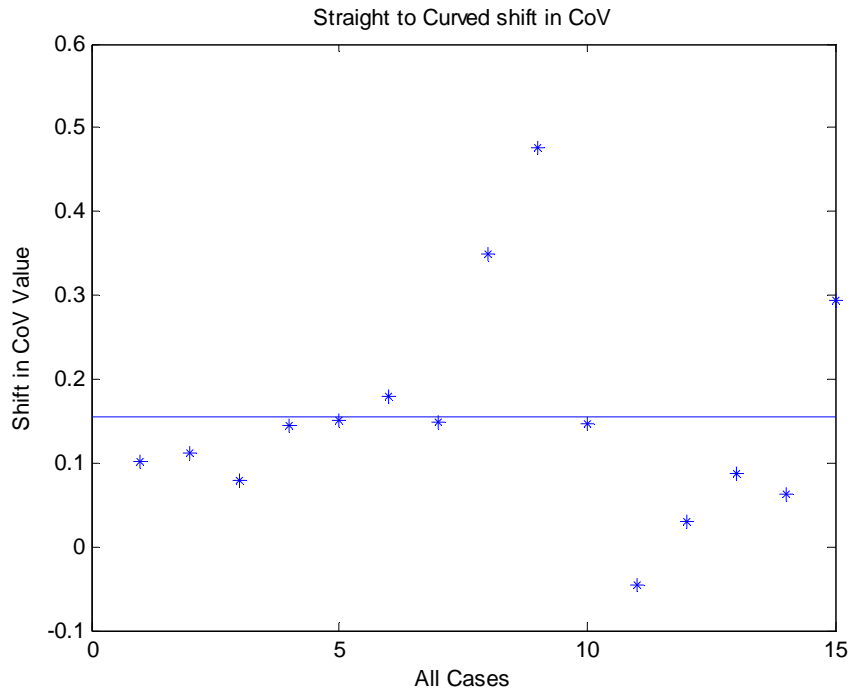


Figure H.47 Shift in coefficient of variation resulting from bridge curvature

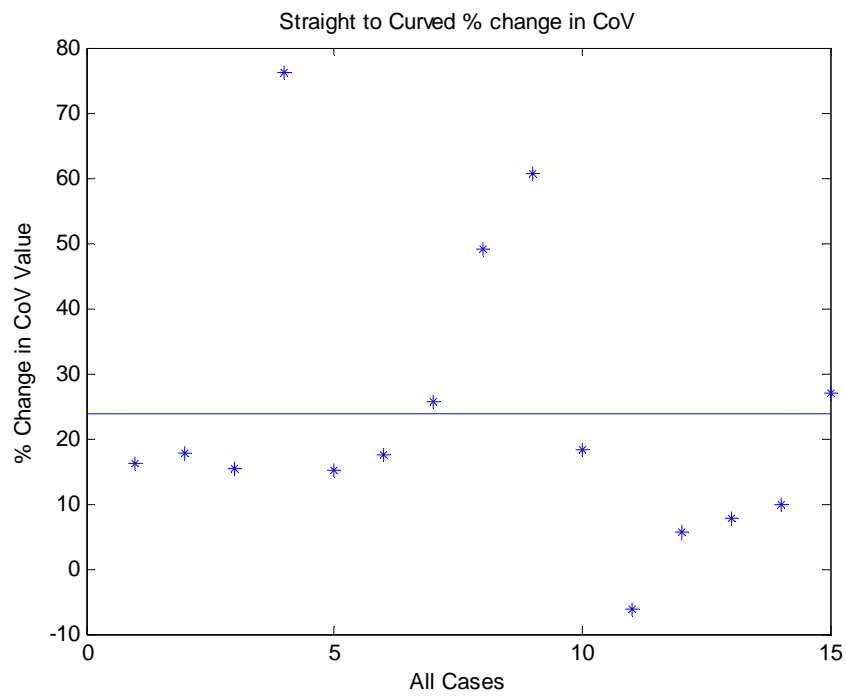


Figure H.48 Percent change in coefficient of variation resulting from bridge curvature

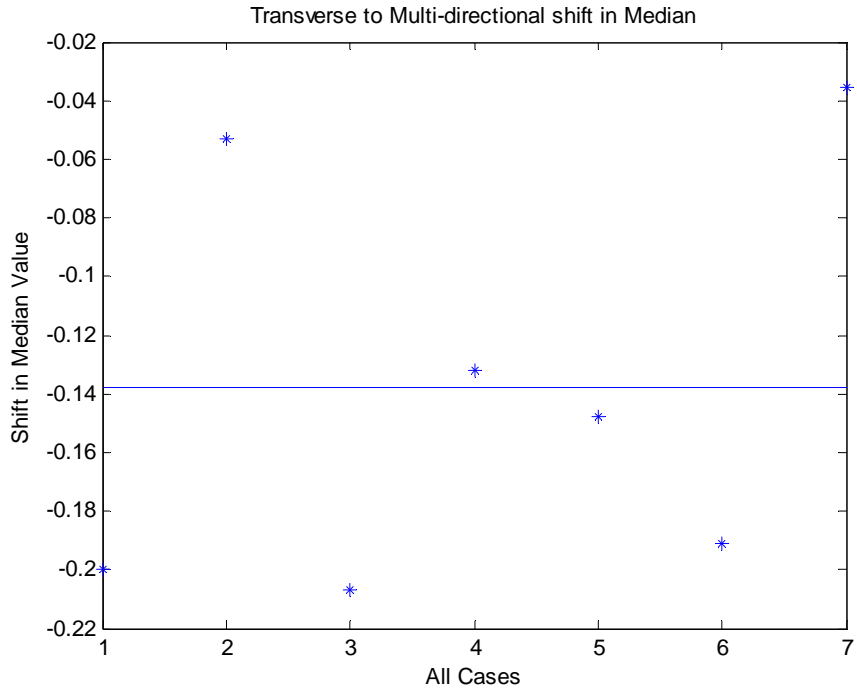


Figure H.49 Shift in median value resulting from multi-directional loading

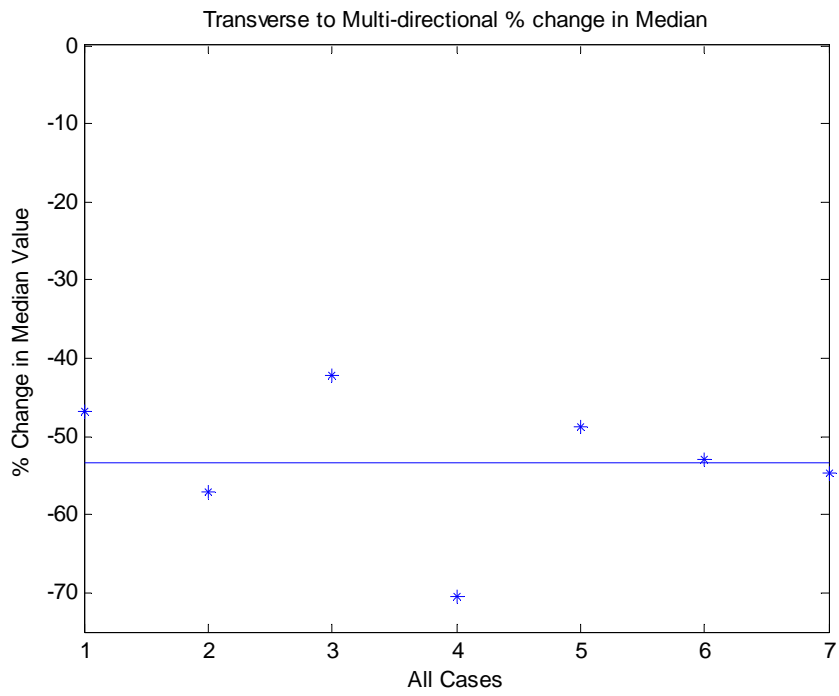


Figure H.50 Percent change in median value resulting from multi-directional loading

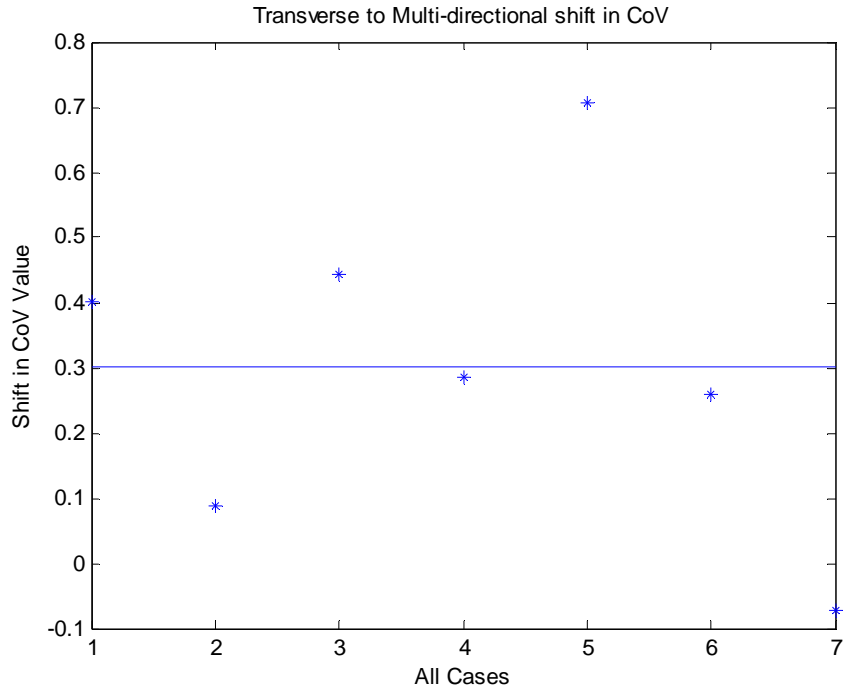


Figure H.51 Shift in coefficient of variation resulting from multi-directional loading

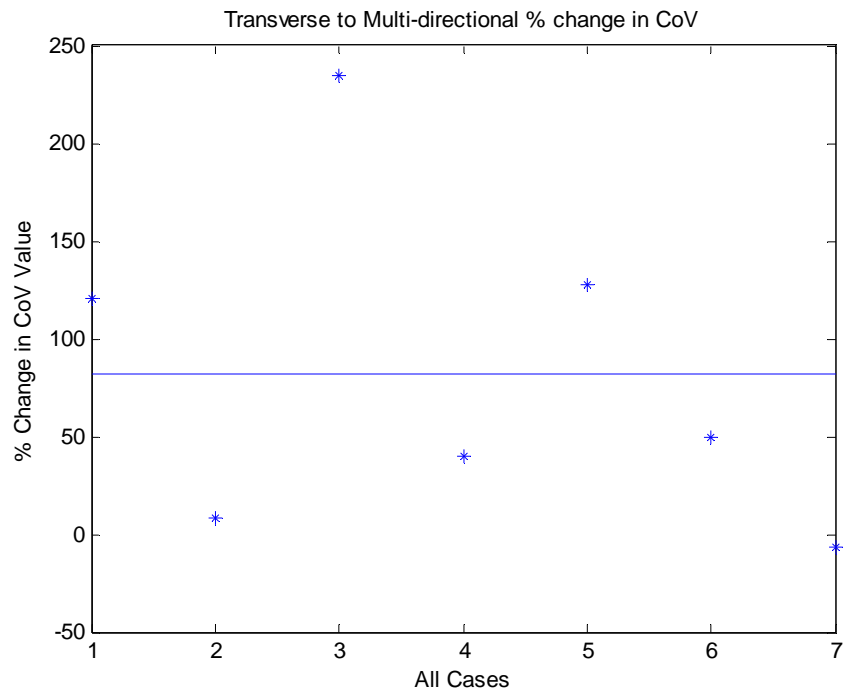


Figure H.52 Percent change in coefficient of variation resulting from multi-directional loading

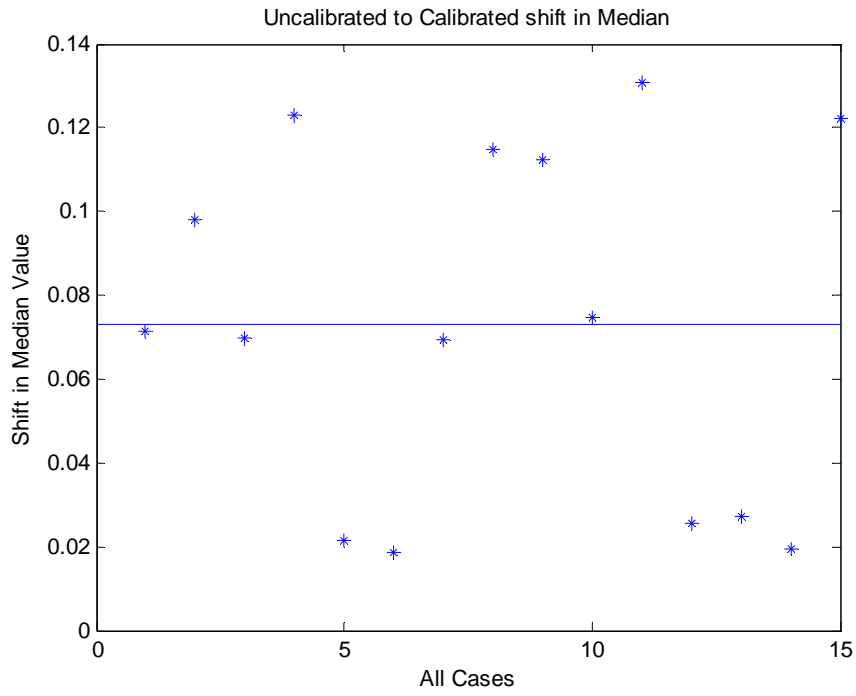


Figure H.53 Shift in median value resulting from model calibration

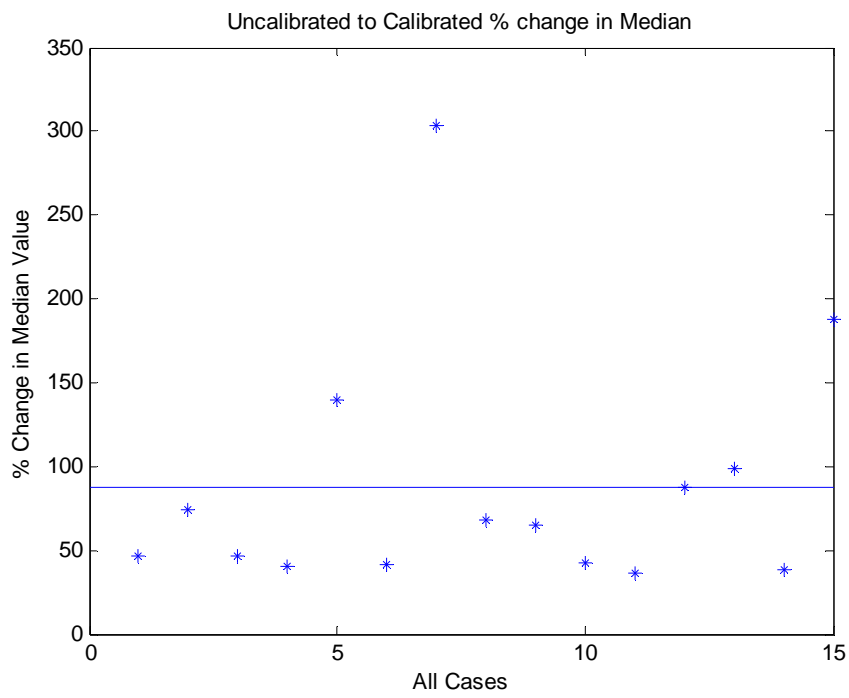


Figure H.54 Percent change in median value resulting from model calibration

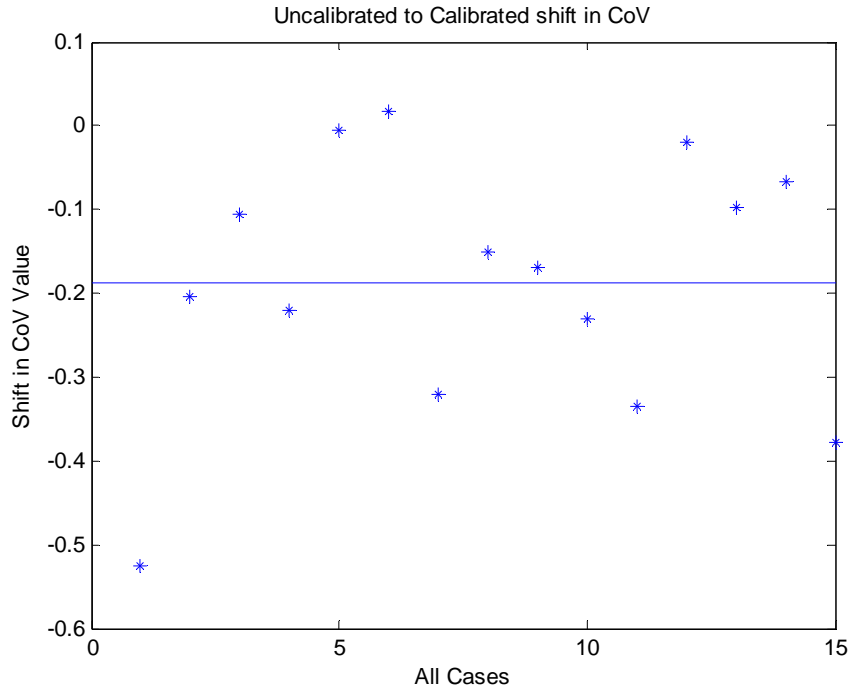


Figure H.55 Shift in coefficient of variation resulting from model calibration

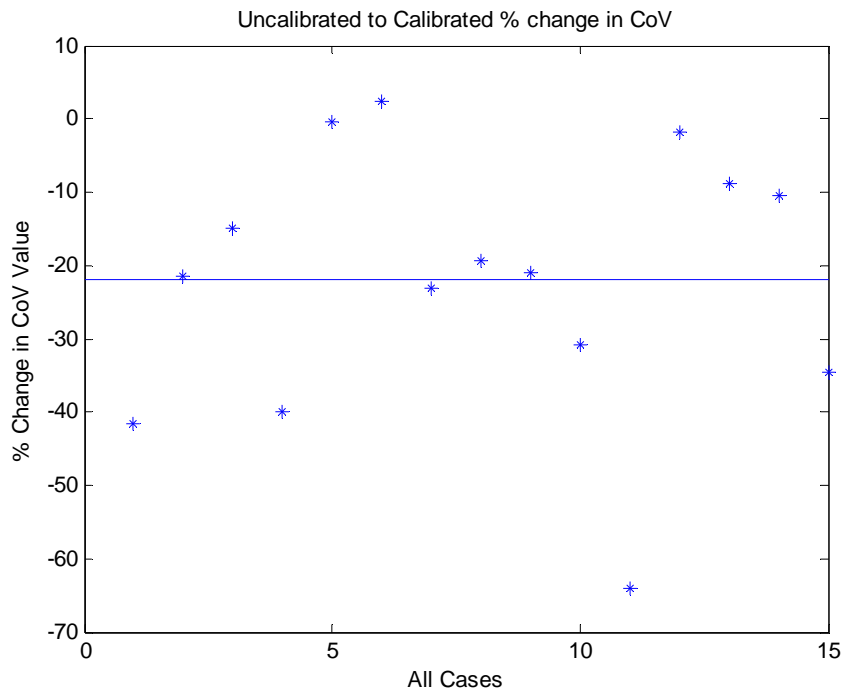


Figure H.56 Percent change in coefficient of variation resulting from model calibration

APPENDIX I. DIGITAL APPENDICES

Appendix A – Material Properties

- Concrete cylinder crushing tests: cylinder3_tmf.10.24.2011 (folder)
- Rebar tensile tests: rebar4_tmf.01.26.2010 (folder)

Appendix C – DAQ Test Data

- DAQ data: DAQdata.mat
- Portable LBCB data: data_portable.mat
- Large-scale dual LBCB data: data_twobox.mat
- Strain gage data: strain_data.mat

Appendix C – Key Events

- 167 .emf images of format step####_pier#.emf

Appendix C – Krypton Test Data

- Derived 6DOF plots: folder with 25 .emf images of format P#_6DOF_#
- Pier 1 6DOF data: Kto6DOF_pier1.mat
- Pier 2 6DOF data: Kto6DOF_pier2.mat
- Pier 1 raw data: Pier_krypton_data1.mat
- Pier 2 raw data: Pier_krypton_data2.mat

Appendix C – Test Photos

- 12 folders of 10 .jpeg images of format pic_#####.jpeg
- For beginning and end of static and dynamic loading, and every 500 steps in between

Appendix F – Seismic Records

- 3 intensity level folders with 3 .txt files for each record of format rec_###_*.txt

Appendix G – Structural Response

- 48 folders with key_output.txt files containing the analytical results described in Table 4.7

BIBLIOGRAPHY

- Abrams, D. P. (1987). Influence of Axial Force Variations on Flexural Behavior of Reinforced Concrete Columns. *ACI Structural Journal*, 246-254.
- Acun, B., & Sucuoglu, H. (2010). Performance of Reinforced Concrete Columns Designed for Flexure under Severe Displacement Cycles. *ACI Structural Journal*, 364-371.
- ASCE/SEI-41. (2007). *Seismic Rehabilitation of Existing Buildings*. Reston, VA: American Society of Civil Engineers.
- ATC. (1985). *Earthquake Damage Evaluation Data for California, Report No. ATC-13*. Applied Technology Council, Redwood City, CA.
- ATC. (1991). *Seismic Vulnerability and Impact of Disruption of Lifelines in the Conterminous United States, Report No. ATC-25*. Applied Technology Council, Redwood City, CA.
- Baker, J. W., & Cornell, C. A. (2006, February). Correlation of response spectral values for multicomponent ground motions. *Bulletin of the Seismological Society of America*, 96(1), 215-227.
- Banerjee, S., & Shinozuka, M. (2007). Nonlinear Static Procedure for Seismic Vulnerability Assessment of Bridges. *Computer-Aided Civil and Infrastructure Engineering*, 22, 293-305.
- Basoz, N., & Kiremidjian, A. S. (1999). Development of empirical fragility curves for bridges. *Proceedings of the 1999 5th U.S. Conference on Lifeline Earthquake Engineering: Optimizing Post-Earthquake Lifeline System Reliability*. 16, pp. 693-702. Seattle, WA: Technical Council on Lifeline Earthquake Engineering Monograph.
- Belarbi, A., Prakash, S. S., & Silva, P. (2008). Flexure-shear-torsion interaction of RC bridge columns. *Proceedings of the Concrete Bridge Conference, Paper No. 6*. St. Louis, USA.
- Belarbi, A., Prakash, S., & You, Y. M. (2009). Effect of Spiral Reinforcement on Flexural-Shear-Torsional Seismic Behavior of Reinforced Concrete Circular Bridge Columns. *Structural Engineering and Mechanics*, 33(2), 137-158.
- Caltrans. (2006). *Seismic Design Criteria Guidelines Version 1.4*.

- Choe, D. E., Gardoni, P., & Rosowsky, D. (2007). Closed-Form Fragility Estimates, Parameter Sensitivity, and Bayesian Updating for RC Columns. *Journal of Engineering Mechanics*, 833-843.
- Choe, D., Gardoni, P., & Rosowsky, D. (2010). Fragility increment functions for deteriorating reinforced concrete bridge columns. *ASCE Journal of Engineering Mechanics*, 136(8), 969-978.
- Choi, E., DesRoches, R., & Nielson, B. (2004). Seismic Fragility of Typical Bridges in Moderate Seismic Zones. *Engineering Structures*, 26, 187-199.
- Desroches, R., & Fenves, G. L. (1997). Evaluation of Recorded Earthquake Response of a Curved Highway Bridge. *Earthquake Spectra*, 13(3), 363-386.
- Dutta, A. (1999). On energy based seismic analysis and design of highway bridges. *Ph.D. Thesis*. State University of New York at Buffalo.
- Elwood, K. J., & Eberhard, M. O. (2009). Effective Stiffness of Reinforced Concrete Columns. *ACI Structural Journal*, 476-484.
- FEMA. (2003). *HAZUS-MH MRI: Technical Manual*. Federal Emergency Management Agency, Washington, D.C.
- Furlong, R. W., Hsu, C. T., & Mirza, S. A. (2004). Analysis and Design of Concrete Columns for Biaxial Bending - Overview. *ACI Structural Journal*, 413-423.
- Gardoni, P., Der Kiureghian, A., & Mosalam, K. M. (2002). Probabilistic Capacity Models and Fragility Estimates for Reinforced Concrete Columns based on Experimental Observations. *Journal of Engineering Mechanics*, 1024-1038.
- Gardoni, P., Mosalam, K. M., & Der Kiureghian, A. (2003). Probabilistic seismic demand models and fragility estimates for RC bridges. *Journal of Earthquake Engineering*, 7(Special Issue 1), 79-106.
- Greene Jr., G., & Belarbi, A. (2009a). Model for Reinforced Concrete Members under Torsion, Bending, and Shear. I: Theory. *Journal of Engineering Mechanics*, 961-969.

- Greene Jr., G., & Belarbi, A. (2009b). Model for Reinforced Concrete Members under Torsion, Bending, and Shear. II: Model Application and Validation. *Journal of Engineering Mechanics*, 970-977.
- Hindi, R. A., & Browning, B. J. (2011). Torsionally Loaded Circular Concrete Members Confined with Spirals. *ACI Structural Journal*, 139-147.
- Holub, C. (2005). *Similitude Considerations for Small Scale Distributed Hybrid Testing of Reinforced Concrete Bridges*. M.S. Thesis, University of Illinois at Urbana-Champaign, Urbana, IL.
- Hwang, H., Jernigan, J. B., & Lin, Y. W. (2000). Evaluation of seismic damage to Memphis bridges and highway systems. *Journal of Bridge Engineering*, 5(4), 322-330.
- Hwang, H., Liu, J. B., & Chiu, Y. H. (2001). *Seismic Fragility Analysis of Highway Bridges*. The University of Memphis. Mid-America Earthquake Center.
- Jeng, C. H. (2010). Simple Rational Formulas for Cracking Torque and Twist of Reinforced Concrete Members. *ACI Structural Journal*, 189-198.
- Kang, T. H.-K., Kim, W., Massone, L. M., & Galleguillos, T. A. (2012). Shear-Flexure Coupling Behavior of Steel Fiber-Reinforced Concrete Beams. *ACI Structural Journal*, 435-444.
- Kappos, A. J., Manolis, G. D., & Moschona, I. F. (2002). Seismic assessment and design of R/C bridges with irregular configuration, including SSI effects. *Engineering Structures*, 24, 1337-1348.
- Karim, K. R., & Yamazaki, F. (2003). A Simplified Method of Constructing Fragility Curves for Highway Bridges. *Earthquake Engineering and Structural Dynamics*, 32, 1603-1626.
- Kawashima, K., & Tirasit, P. (2008). Effect of Nonlinear Seismic Torsion on the Performance of Skewed Bridge Piers. *Journal of Earthquake Engineering*, 12(6), 980-998.
- Kim, S. H., & Shinozuka, M. (2004). Development of fragility curves of bridges retrofitted by column jacketing. *Probabilistic Engineering Mechanics*, 19(1-2), 105-112.
- Kim, S. J., Holub, C. J., & Elnashai, A. S. (2011). Analytical Assessment of the Effect of Vertical Earthquake Motion on RC Bridge Piers. *Journal of Structural Engineering*, 137(2), 252-260.

- Kim, S. J., Holub, C. J., & Elnashai, A. S. (2011). Experimental Investigation of the Behavior of RC Bridge Piers Subjected to Horizontal and Vertical Earthquake Motion. *Engineering Structures*, 33, 2221-2235.
- Kunnath, S. K., El-Bahy, A., Taylor, A. W., & Stone, W. C. (1997). *Cumulative Seismic Damage of Reinforced Concrete Bridge Piers*. National Institute of Standards and Technology, Gaithersburg, MD.
- Kwon, O. S., & Elnashai, A. S. (2006). The effect of material and ground motion uncertainty on the seismic vulnerability curves of RC structure. *Engineering Structures*, 28, 289-303.
- Kwon, O. S., Nakata, N., Elnashai, A. S., & Spencer, B. F. (2005). A Framework for Multi-Site Distributed Simulation and Application to Complex Structural Systems. *Journal of Earthquake Engineering*, 9(5), 741-753.
- Lee, D. H., & Elnashai, A. S. (2001). Seismic Analysis of RC Bridge Columns with Flexure-Shear Interaction. *Journal of Structural Engineering*, 546-553.
- Lee, D. H., & Elnashai, A. S. (2002). Inelastic Seismic Analysis of RC Bridge Piers Including Flexure-Shear-Axial Interaction. *Structural Engineering and Mechanics*, 13(3), 241-260.
- Lee, D. H., Choi, E., & Zi, G. (2005). Evaluation of Earthquake Deformation and Performance for RC Bridge Piers. *Engineering Structures*, 27, 1451-1464.
- Li, J., Spencer, B. F., & Elnashai, A. S. (2013). Bayesian Updating of Fragility Functions Using Hybrid Simulation. *Journal of Structural Engineering*, 139, 1160-1171.
- Li, Q., Belarbi, A., & Prakash, S. S. (2010). Seismic Performance of Square RC Bridge Columns under Combined Loading including Torsion with Low Shear. *Earth and Space 2010: Engineering, Science, Construction, and Operations in Challenging Environments* (pp. 3011-3018). Honolulu, HI: ASCE.
- Mackie, K., & Stojadinovic, B. (2004). Fragility curves for reinforced concrete highway overpass bridges. *13th World Conference on Earthquake Engineering*. Vancouver, B.C.
- Mander, J. B. (1998). *Fragility Curve Development for Assessing the Seismic Vulnerability of Highway Bridges*. University at Buffalo, State University of New York. MCEER.

- Mander, J. B., & Basoz, N. (1999). Seismic fragility curve theory for highway bridges. *Proceedings of the 1999 5th U.S. Conference on Lifeline Earthquake Engineering: Optimizing Post-Earthquake Lifeline System Reliability*, 16, pp. 31-40. Seattle, WA: Technical Council on Lifeline Earthquake Engineering Monograph.
- Maruyama, K., Ramirez, H., & Jirsa, J. O. (1984). Short RC columns under bilateral load histories. *ASCE Journal of Structural Engineering*, 110(1), 120-137.
- McMullen, A. E., & Warwaruk, J. M. (1970). Concrete beams in bending, torsion and shear. *Journal Struct. Div.*, 96(5), 885-903.
- Mostafaei, H., & Kabeyasawa, T. (2007). Axial-Shear-Flexure Interaction Approach for Reinforced Concrete Columns. *ACI Structural Journal*, 218-226.
- Mostafaei, H., Vecchio, F. J., & Kabeyasawa, T. (2009). Deformation Capacity of Reinforced Concrete Columns. *ACI Structural Journal*, 187-195.
- Moustafa, K. F., Sanders, D., Saiidi, M. S., & El-Azazy, S. (2011). Seismic Performance of Reinforced Concrete Bridge Bents. *ACI Structural Journal*, 23-33.
- NIED. (2013). K-NET. Tsukuba, Ibaraki, Japan.
- Nielson, B. G., & DesRoches, R. (2007). Analytical Seismic Fragility Curves for Typical Bridges in the Central and Southeastern United States. *Earthquake Spectra*, 23(3), 615-633.
- Otsuka, H., Takeshita, E., Yabuki, W., Wang, Y., Yoshimura, T., & Tsunomoto, M. (2004). Study on the seismic performance of reinforced concrete columns subjected to torsional moment, bending moment and axial force. *Proceedings of the 13th World Conference on Earthquake Engineering, Paper No. 393*. Vancouver, Canada.
- Ozcebe, G., & Saatcioglu, M. (1989). Hysteretic shear model for reinforced concrete members. *Journal of Structural Engineering*(115), 132-148.
- Park, R., Priestley, M. J., & Gill, W. D. (1982). Ductility of square-confined concrete columns. *ASCE J. Struct. Div.*, 108(4), 929-950.
- PEER. (2010). PEER Ground Motion Database. Berkeley, CA: PEER Center.

- Prakash, S. S., & Belarbi, A. (2010). Towards Damage-Based Design Approach for RC Bridge Columns Under Combined Loadings Using Damage Index Models. *Journal of Earthquake Engineering*, 14(3), 363-389.
- Prakash, S. S., Li, Q., & Belarbi, A. (2012). Behavior of Circular and Square Reinforced Concrete Bridge Columns under Combined Loading Including Torsion. *ACI Structural Journal*, 317-327.
- Prakesh, S., Belarbi, A., & You, Y. M. (2010). Seismic Performance of Circular RC Columns Subjected to Axial Force, Bending, and Torsion with Low and Moderate Shear. *Engineering Structures*, 32, 46-59.
- Priestley, M. J., & Benzoni, G. (1996). Seismic performance of circular columns with low longitudinal reinforced ratios. *ACI Structural Journal*, 93(4), 474-485.
- Priestley, M. J., & Park, R. (1987). Strength and Ductility of Concrete Bridge Columns under Seismic Loading. *ACI Structural Journal*, 84(1).
- Rahal, K. N., & Collins, M. P. (1995). Analysis of Sections Subjected to Combined Shear and Torsion - A Theoretical Model. *ACI Structural Journal*, 459-469.
- Ramanathan, K., DesRoches, R., & Padgett, J. E. (2012). A comparison of pre- and post-seismic design considerations in moderate seismic zones through the fragility assessment of multispan bridge classes. *Engineering Structures*, 45, 559-573.
- Saadeghvaziri, M. A., & Foutch, D. A. (1991). Dynamic Behaviour of R/C Highway Bridges Under the Combined Effect of Vertical and Horizontal Earthquake Motions. *Earthquake Engineering and Structural Dynamics*, 20, 535-549.
- Saatcioglu, M., & Ozcebe, G. (1989). Response of reinforced concrete columns to simulated seismic loading. *ACI Structural Journal*, 86(1), 120-137.
- Shinozuka, M., Feng, M. Q., Kim, H. K., & Kim, S. H. (2000). Nonlinear static procedure for fragility curve development. *Journal of Engineering Mechanics*, 126(12), 1287-1296.
- Shome, N., Cornell, C. A., Bazzurro, P., & Carballo, J. E. (1998). Earthquakes, Records, and Nonlinear Responses. *Earthquake Spectra*, 14(3), 469-500.

- Silva, P. F., Megally, S., & Seible, F. (2003). Seismic Performance of Sacrificial Interior Shear Keys. *ACI Structural Journal*, 100(2), 177-187.
- Subramaniam, K. V., Popovics, J. S., & Shah, S. P. (1998). Testing Concrete in Torsion: Instability Analysis and Experiments. *Journal of Engineering Mechanics*, 1258-1268.
- Sucuoglu, H., & Acun, B. (2012). Energy-Based Hysteresis Model for Flexural Response of Reinforced Concrete Columns. *ACI Structural Journal*, 541-550.
- Takeda, T., Sozen, M. A., & Nielsen, N. N. (1970). Reinforced concrete response to simulated earthquakes. *ASCE Journal of Structural Division*, 96(12), 2557-2573.
- Tavares, D. H., Padgett, J. E., & Paultre, P. (2012). Fragility curves of typical as-built highway bridges in eastern Canada. *Engineering Structures*, 40, 107-118.
- Tirasit, P., & Kawashima, K. (2007). Seismic Performance of Square Reinforced Concrete Columns under Combined Cyclic Flexural and Torsional Loadings. *Journal of Earthquake Engineering*, 11, 425-452.
- Tsuchiya, S., Maekawa, K., & Kawashima, K. (2007). Three-Dimensional Cyclic Behavior Simulation of RC Columns under Combined Flexural Moment and Torsion Coupled with Axial and Shear Forces. *Journal of Advanced Concrete Technology*, 5(3), 409-421.
- Wen, Y. K., & Ellingwood, B. R. (2005). The Role of Fragility Assessment in Consequence-Based Engineering. *Earthquake Spectra*, 21(3), 861-877.
- Wen, Y. K., & Wu, C. L. (2001). Uniform Hazard Ground Motions for Mid-America Cities. *Earthquake Spectra*, 17(2), 359-384.
- Xie, L., Bentz, E. C., & Collins, M. P. (2011). Influence of Axial Stress on Shear Response of Reinforced Concrete Elements. *ACI Structural Journal*, 745-754.
- Xu, S. Y., & Zhang, J. (2011). Hysteretic Shear-Flexure Interaction Model of Reinforced Concrete Columns for Seismic Response Assessment of Bridges. *Earthquake Engineering and Structural Dynamics*, 40, 315-337.
- Xu, S. Y., & Zhang, J. (2012). Axial-Shear-Flexure Interaction Hysteretic Model for RC Columns Under Combined Actions. *Engineering Structures*, 34, 548-563.

- Yamazaki, F., Hamada, T., Motoyama, H., & Yamauchi, H. (1999). Earthquake damage assessment of expressway bridges in Japan. *Proceedings of the 1999 5th U.S. Conference on Lifeline Earthquake Engineering: Optimizing Post-Earthquake Lifeline System Reliability*. 16, pp. 361-370. Seattle, WA: Technical Council on Lifeline Earthquake Engineering Monograph.
- Zhang, J., & Xu, S. Y. (2009). Seismic response simulations of bridges considering shear-flexural interaction of columns. *Structural Engineering and Mechanics*, 31(5), 545-566.
- Zhang, J., Xu, S. Y., & Tang, Y. (2011). Inelastic Displacement Demand of Bridge Columns Considering Shear-Flexure Interaction. *Earthquake Engineering and Structural Dynamics*, 40, 731-748.
- Zhiguo, S., Bingjun, S., Dongsheng, W., & Xun, G. (2008). Experimental Research and Finite Element Analysis of Bridge Piers Failed in Flexure-Shear Modes. *Earthquake Engineering and Engineering Vibration*, 7(4), 403-414.